Sediment Dynamics in a Bedrock Channel

Bishnu Prasad Sharma

Abstract

Headwater systems often comprise alluvial rivers interrupted by reaches with partly or entirely rock beds, indicate a local change in bedload conveyance relative to sediment supply. Detailed knowledge of sediment dynamics in bedrock-alluvial systems is crucial for a better understanding of bedrock incision and sediment delivery downstream, but field evidence is lacking. This thesis reports a field investigation in this topic. Coarse bedload transport was studied in alluvial, semi-alluvial and bare rock segments of Trout Beck in North England by monitoring two sets of 270 magnet-tagged pebbles over a period of nineteen months. At-a-station hydraulic geometry, flow resistance and shear stress were estimated using stage recorders, water surface profiles and salt-wave measurements in five short sub-reaches. Thresholds of motion were investigated using tracer-pebble data and bedload impact counts. Tracers seeded in the upstream alluvial channel moved more slowly. Tracers seeded in a bare rock gorge dispersed quickly at first but accumulated in a coarse-sediment zone at the start of the next partial cover. Bedload transport was size selective over alluvial or semi-alluvial segments but not over bare rock. Flow resistance, as quantified by Manning's n or Darcy-Weisbach f, varies considerably with both discharge and bed character. The estimated bedload conveyance is highest in reaches with entirely or mainly rock bed, and lowest in alluvial and boulder-rich segments. The boulder-rich segment has high shear stress, but presumably its threshold stress is also high due to form drag from boulders, as evidenced by very high values of n and f. No standard resistance law describes flow in Trout Beck accurately from measured bed D_{84}. This study demonstrates how bedrock reaches control sediment processes and how they are different from alluvial reaches.

Sediment Dynamics in a Bedrock Channel

Bishnu Prasad Sharma

Department of Geography

Durham University

Thesis submitted for the degree of Doctor of Philosophy

September 2016

Table of Contents

List of Tables

List of Figures

List of Abbreviations

AHG	At-a-station Hydraulic Geometry
AL	Upper Alluvial
Bath.	Bathurst
BLL	Bottom Left Logger
BRL	Bottom Right Logger
CEH	Centre for Ecology & Hydrology
DEM	Digital Elevation Model
dGPS	Differential GPS
d/S	Downstream
EA	Environment Agency
EC	Electrical Conductivity
ECM	Electromagnetic Current Meter
ECN	Environmental Change Network
FDC	Flow Duration Curve
F1	Sub-reach 1 (Field 1)
F2	Sub-reach 2
F3	Sub-reach 3
F4	Sub-reach 4
F5	Sub-reach 5
GEV1	Generalised Extreme Value Type1
GSD	Grain Size Distribution
HM	Harmonic mean
LAL	Lower Alluvial
LSA	Lower Semi-alluvial
Max.	Maximum
Min.	Minimum
min	Minute
ML	Middle Logger
M-S	Manning-Strickler

NERC	Natural Environment Research Council
NNR	National Nature Reserve
NS	Not Significant
PIT	Passive Integrated Transponder
PT	Pressure Transducer
RL	Roughness Layer
RQ	Research Question
RR	Rickenmann and Recking (2011)
RFID	Radio Frequency Identification
SA	Upper Semi-alluvial
TBG	Trout Beck Gauge Board
TLL	Top Left Logger
TLS	Terrestrial Laser Scanning (Scanner)
TRL	Top Right Logger
u/s	Upstream
VPE	Variable Power Equation
WSL	Water Surface Level

List of Symbols

A	Cross-Sectional Area
Ai	Wetted area for a cross-section
$<A>$	Average wetted area for a sub-reach
A_{IP}	Plan area occupied by immobile grains
A_m	Plan area occupied by mobile grains
A_t	Plan area occupied by total bed
a	Coefficient of width in Hydraulic Geometry relation ($w= aQ^b$)
b	Exponent of width in Hydraulic Geometry relation ($w = aQ^b$)
b	Intermediate (b-axis diameter) diameter of a particle
^{0}C	Degree Celsius
c	Coefficient of depth in Hydraulic Geometry relation ($d = cQ^f$)
C	Chezy's coefficient
C	Corey Sphericity
CD (= C_d)	Coefficient of Drag
CF	Concentration Factor
C_I	Drag coefficient for immobile grains
C_m	Drag coefficient for mobile grains
D	Grain diameter
D_x	Refers to the grain size in cumulative frequency distribution for which x% of the distribution is smaller in size (e.g. D_{84} = 84% grains are finer than this size)
d	flow depth
F_I	Water shear force on immobile grains
F_m	Water shear force on mobile grains
F_t	Total downward water shear force
Fr	Froude Number
f	Darcy-Weisbach friction factor
f	Exponent of depth (d) in Hydraulic Geometry relation ($d = cQ^f$)
g	Acceleration due to gravity

H	Water stage
I	Number of impact counts in 5 min interval
k	Coefficient of velocity (V) in Hydraulic Geometry relation ($V= kQ^m$)
k_s	Effective Roughness height
κ	von Karman constant
L	Sub-reach length
M	Mass
m	Exponent of width (V) in Hydraulic Geometry relation ($V= kQ^m$)
N	No of cross-sections in a sub-reach/ no. of samples
n	Manning's roughness coefficient
p	Protrusion
P	Wetted perimeter
P_i	Wetted perimeter for a cross-section
$<P>$	Average wetted perimeter for a sub-reach
P_1	Upper probe for salt-wave measurements in a sub-reach
P_2	Upper probe for salt-wave measurements in a sub-reach
Q	River Discharge
Q_{avg}	Average of Q_1 and Q_2
Q_b	Bedload transport rate
Q_c	Critical or threshold discharge
Q_{EA}	Discharge at EA gauging station
Q_m	Long-term mean discharge
Q_{MED}	Median annual discharge (2 years' flood)
Q_{site}	Discharge at Trout Beck study site
Q_p (= Q_{peak})	Peak discharge
Q_t	Bedload conveyance or potential transport rate
Q_{TBG}	Discharge estimated from TBG rating curve
Q_1	Discharge at upper probe
Q_2	Discharge at lower probe
q	Unit discharge

q_b	Bedload transport rate per unit width
q_c	Unit critical discharge
q_t	Potential transport rate per unit width
q^*	Non-dimensional discharge
q^{**}	Non-dimensional discharge
R	Hydraulic Radius
R_i	Hydraulic radius for a cross-section
$<R>$	Average hydraulic radius for a sub-reach
R/D_{84}	Relative submergence
S	Energy slope
S_b	Channel bed (talweg) slope
S_w	Water surface slope
SE	Standard Error of the mean
u^*	Shear velocity
V	Mean velocity
V_{avg}	Average of V_c and V_{HM})
V_c	Velocity from Centroid method
V_{cont}	Velocity from continuity equation ($V = Q/<A>$)
V_{HM}	Velocity from Harmonic Mean (HM) method
V_{salt}	Velocity from salt dilution
V^*	Non-dimensional velocity
V^{**}	Non-dimensional velocity
w	wetted channel width
WL_1	Water surface level at probe 1 (upstream probe)
WL_2	Water surface level at probe 2 (downstream probe)
X_b	Flow-facing cross-sectional area of a boulder
z_0	Roughness height
Z_m	Average height of mobile sediment from the base of the immobile grains
τ	Mean boundary shear stress
τ_b	Stress on boulders (= τ_I)

τ_c	Critical or threshold stress
τ_I	Stress on large immobile grains (= τ_b)
τ_m	Stress on mobile bed
τ_R	Reynolds Stress
τ_t (= τ)	Total boundary shear stress
τ^*_c	Non-dimensionless critical shear stress (critical value of τ^*)
τ^*	Non-dimensional Shields number
ρ	Density of water
ρ_s	Density of sediment
σ	Standard deviation
λ	Spacing of the immobile grains
φ	Phi (grain size)
ω	Unit stream power
ω_c	Critical stream power
ω_{*c}	Non-dimensional critical stream power

Dissemination

Papers:

1) Ferguson, R. I., B. P. Sharma, R. A. Hodge, R. J. Hardy and J. Warburton (in review), Bedload tracer mobility in a mixed bedrock/alluvial channel, Journal of Geophysical Research: Earth Surface.

2) Ferguson, R. I., B. P. Sharma, R. A. Hodge, R. J. Hardy and J. Warburton (in review), Flow resistance and hydraulic geometry in contrasting reaches of a bedrock channel, Water Resources Research.

Statement of Copyright

Acknowledgements

First and foremost, I would like to express my sincere gratitude to my four supervisors Dr Richard Hardy, Dr Jeff Warburton, Dr Rebecca Hodge and Emeritus Professor Rob Ferguson. They have all given me the opportunity to undertake this research and invaluable supervision, support, encouragement and field assistance during the course of this study. Dr Hardy, whom I contacted first about this PhD has been a constant source of inspiration and without his support this PhD would not have been possible. I thank him also for his support on administrative matters during the course of this research. Dr Warburton has been a source of constant support, always motivated me for critical thinking. He deserves particular thanks for all his work in setting up and maintaining loggers and other instrumentation and without his support my heavily field-based research would not have been possible. Dr Hodge has always been supportive and provided ideas and insights to this research. Prof. Ferguson has been a constant source of encouragement, support and motivation, and provided insightful ideas and stimulating contributions to this research. I would like to thank him also for checking my calculations and the endless English corrections. It was a great privilege to study in this world-class university under all these great academics.

My research was supported by a Durham University doctoral studentship, with some additional funding support from the Department of Geography at Durham and a small grant for additional fieldwork from the British Society for Geomorphology (BSG).

I am thankful to the Centre for Ecology and Hydrology (CEH) who kindly allowed access to the field site at Moor House and the Environment Agency discharge data. All of my colleagues who assisted me with my cold and wet fieldwork at Trout Beck, I hope, with delight they all have fond memories and I would like to thank all of them. Special thanks go to Rosie Fewings, Chris Longley, Ramjee Bhandari, Marisa Saltamontes and Jitendra Thakur. I would like to thank my fellow postgraduates, academic colleagues, all the technical staff in the Department of Geography at Durham. In particular, Mervyn Brown who has been extremely helpful to assist me with the field equipment and Mark Kincey for help with GIS and use of field equipment. I would like to acknowledge my wife Sushila for help with fieldwork, pebble drilling and painting, and my daughters Riju and Riya for supporting me to put the labels in the pebbles.

I would like to thank my whole combined family and in particular my mother, parents-in-law, sisters, cousin brother, brothers-in-law, sisters-in-law, nieces, nephews, wife and

three beautiful daughters for their love, understanding, devotion, sacrifices. In particular, my wife without her unending support none of this would have been possible. For the final year of completing my PhD, I would like to acknowledge and raise thanks to two new members of my family Jamil Mahmood and Du Lujie. Finally, I would like to thank all my friends and relatives who have offered support and advice when needed.

Thank you to you all.

Dedication

I would like to dedicate my PhD to my beloved family,

My mother

Who raised and educated me and made me who I am

My late father

Who always wanted me to be an engineer but did not stay here long to see his dream coming true, I think about him always

My lovely wife

For supporting me all the way, without her, none of my success would be possible

My sisters

For all their prayers, love and support

And last but not least, my lovely daughters Riju, Riya and Riva

The most beautiful gifts the world has given to us, for their love and smiles.

1 Introduction

Most rivers flow along alluvial channels in which the bed and banks are composed of sediments transported and deposited by the river. The morphology and functioning of alluvial rivers has been studied for hundreds of years by engineers and geomorphologists – the engineers more interested in maintaining navigation, providing irrigation and preventing major instability, whereas the geomorphologists were concerned with the river patterns to know more about the river history and behaviour. We now have a fairly good understanding of channel form and fluvial processes in alluvial rivers; it is summarised later in this chapter (Section 1.1). These self-formed channels can adapt quite quickly in various ways to any change in external controls (hydrology, coarse sediment supply, base level).

In some rivers alluvial cover is absent or so thin that bedrock is exposed in some or all of the bed/banks. Many upland rivers have such situations where the alluvial reaches are interspersed with partly or fully bedrock reaches. Many researchers consider that these bedrock reaches/channels (which will be defined later in this chapter) are more widespread than have been reported (Montgomery *et al.*, 1996; Tinkler & Wohl, 1998b). The bedrock channels which occur in mountain areas are usually steep, shallow and contain coarse sediment cover. Therefore some similarities to steep coarse-bed (gravel-bed) alluvial rivers are expected. But there are also differences: morphological change in bedrock reaches is much slower, apart from changes in sediment cover; flow resistance of bare rock is likely to be different from that of sediment; and likewise threshold discharge and shear stress for sediment transport are probably different.

However, despite the ubiquitous presence of bedrock channels, there is far less research on bedrock rivers than on alluvial rivers, very little until recently, and much of it consists of modelling or simplified experiments rather than field process studies. A detailed literature review follows later in this chapter (Section 1.3).

A quantitative understanding of the processes of flow, erosion and sediment transport in bedrock channels is important for two main reasons. First, incision of bedrock rivers controls long-term landscape evolution in mountain/upland environments because bedrock channels set the local base elevation for hillslopes and are the first components of the landscape to respond to regional changes in base level (Howard, 1994; Howard, 1998; Whipple & Tucker, 2002). Bedrock incision affects the stability and erosion rates

of adjoining hillslopes (Burbank *et al.*, 1996) and hence the amount of sediment supply to the channels (Wohl, 1999; Korup *et al.*, 2004; Whipple, 2004) for which much attention has been given to the tools and cover balance (Gilbert, 1877; Sklar & Dietrich, 1998, 2004). Incision depends on the balance between tool and cover effects but previous research on this is based either on infrequent observations (Turowski *et al.*, 2008a) or on untested assumptions about how sediment supply varies with discharge (e.g. Lague, 2010). The models which have been developed to study landscape evolution need to make assumptions about the incision processes (Hancock *et al.*, 1998; Anders *et al.*, 2009) which need checking through field and laboratory studies. Secondly, if there are differences in hydraulic and sediment transport behaviour in bedrock rivers compared to alluvial rivers they could be relevant to engineering, flood routing and ecological assessment. As sediment cover can change more quickly than bed morphology, for river management purposes such as to plan and manage infrastructure projects, reduce flood risk, prevent bank erosion and preserve habitats (Carling, 1995; Tinkler & Wohl, 1998a; Lane *et al.*, 2007; Raven *et al.*, 2009) it is more important to understand hydraulic and sediment transport processes than bedrock incision.

This thesis reports a field process study, designed to identify any differences in bulk hydraulics and bedload mobility between short reaches of contrasting character (alluvial, bedrock, mixed) in a bedrock channel and to see how observed behaviour compares with assumptions made by modellers. This chapter is divided into five sections. Section 1.1 reviews process-based understanding of alluvial channels; section 1.2 discusses the differences between bedrock and alluvial channels; section 1.3 discusses previous research on bedrock channel processes and identifies some knowledge gaps; section 1.4 formulates the general aim and specific research questions of this research and the objectives that had to be achieved to answer the questions; and finally section 1.5 outlines the structure of the thesis.

1.1 Process-based understanding of alluvial channels

This section summarises the feedback links between channel configuration and fluvial processes in alluvial channels. Channel configuration here includes the size, shape and gradient of the channel and also the size distribution and structure of its bed sediment. The processes involved include the flow of water along the channel and the entrainment, transport, and deposition of bed material. A distinction is generally made between sand-bed and gravel-bed rivers, since channels with approximately equal proportions of sand

and gravel are rare (Howard, 1980) and there are some important differences between rivers whose beds are mainly or entirely sand and those whose beds are mainly gravel or coarser sediment. One difference is that sand-bed rivers have little scope for coarsening and fining of the bed but bedforms become relevant. Another is that much of the bed-material transport in sand-bed rivers occurs in suspension, whereas in gravel-bed rivers it is predominantly or entirely bedload transport, meaning movement along the riverbed by rolling, sliding or saltation. What sediment there is in a bedrock river is generally coarse, so in the rest of this discussion of alluvial channel processes the emphasis is on gravel-bed rivers.

Figure 1.1 shows a form-process diagram to illustrate the interrelations between channel configuration, flow hydraulics and bedload transport in a gravel-bed alluvial river. This diagram is from Ashworth and Ferguson (1986) with slight modifications. The channel flow (characterised by flow width w, depth d, velocity V, shear stress τ, and stream power τV) depends on channel slope, width and bed roughness together with the imposed water discharge Q. The bedload transport rate Q_b and the grain-size distribution (GSD) of the transported sediment depend on the flow and the bed material GSD. More specifically, the transport rate is widely accepted as being negligibly small in flows below some threshold value of shear stress or stream power. The threshold is higher for coarser bed material, and in near-threshold conditions only finer grains are moved. Above the threshold, the transport rate increases with shear stress or stream power and the GSD of the transported material becomes progressively closer to that of the bed.

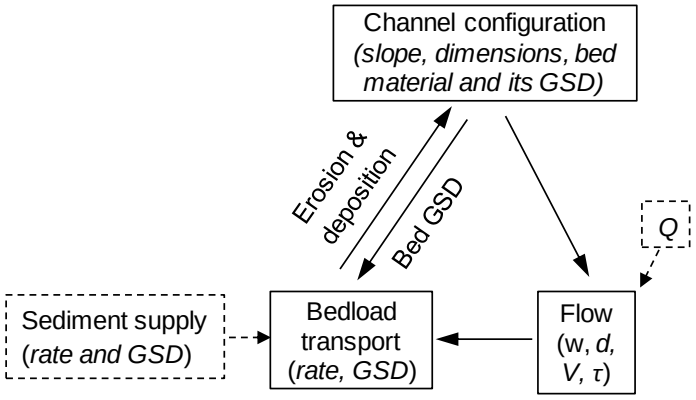

Figure 1.1. Form-process diagram showing the interrelationships among channel configuration, flow and bedload transport in gravel-bed alluvial channels. Flow implies bulk hydraulics such as channel width (w), depth (d), velocity (V) and shear stress (τ). The sediment supply (rate and grain size distribution GSD) and discharge (Q), shown by dashed arrows, are external controls.

The bed GSD is a main control which regulates the system via size-selective entrainment and deposition. Any imbalance between transport rate (Q_b) and bed-

material sediment supply (Q_s) causes changes in one or more of channel width, depth, and slope through aggradation and degradation of the bed and banks and/or coarsening and fining of the bed. These changes lead to a new channel geometry and the cycle continues. This has been a well-established paradigm for gravel-bed rivers for many decades (e.g. Ashworth & Ferguson, 1986), and most of the recent literature is about trying to quantify the details of the various links in the system using a mechanistic approach.

The current understanding about sediment dynamics in gravel-bed rivers is discussed in the following sections under various headings: grain size distribution, at-a-station hydraulic geometry, flow resistance, non-dimensional hydraulic geometry, bed shear stress, threshold of motion and bedload measurements.

1.1.1 Grain size distribution

Both the rate of bedload transport in a gravel-bed river and the size distribution of the transported material depend on the grain sizes available in the bed, so quantification of the bed GSD is required in order to predict the bedload flux and composition (Parker, 1990; Ferguson, 1994). A representative average grain size (normally the median, D_{50}) is invariably used as the basis for estimating the threshold of motion, and a representative coarse grain size such as D_{84} (84% grains are finer than this size) or D_{90} is generally used to estimate the roughness of an alluvial bed on the assumption that large grains account for most of the resistance. Bed grain sizes vary greatly along river systems according to slope and sediment supply. Many alluvial channels show downstream fining, with the average size of surface grains gradually decreasing from the headwaters to downstream sections because of abrasion and sorting (Ferguson *et al.*, 1996), however exceptions to the exponential trend in the downstream fining have been reported.

The bed GSD can be measured by bulk sampling (e.g. Mosley & Tindale, 1985) or clast measurements and counts (e.g. Wolman, 1954; Leopold, 1970) and in each approach the spatial variability along the channel bed needs to be addressed. Bias is likely in small samples, therefore poorly sorted river gravels require large samples to achieve good precision (Ferguson & Paola, 1997). Recently, air-or ground-based imagery (e.g. Carbonneau *et al.*, 2005; Heritage & Milan, 2009; Hodge *et al.*, 2009a) which can be digitally processed to obtain spatially extensive data are also in use. Wolman (1954)

method uses the sample size of 100 grains which remains the mostly used sample size (Wohl, 2013), but probably insufficient to characterise coarser pebbles.

1.1.2 At-a-station hydraulic geometry (AHG)

The at-a station hydraulic geometry of a river, conceived by Leopold and Maddock (1953) based on low-gradient alluvial channels, relates changes over time in the mean width (w), depth (d), and velocity (V) at a particular place in a channel to changes in discharge (Q) by power-law relations:

$$w = aQ^b \quad \text{Eq. 1.1}$$

$$d = cQ^f \quad \text{Eq. 1.2}$$

$$V = kQ^m \quad \text{Eq. 1.3}$$

where a, c, k, b, f and m are numerical constants. The coefficients a, c, and k indicate an estimation of the variable when $Q = 1\ m^3\ s^{-1}$ (for e.g. $w = a$ when $Q = 1\ m^3\ s^{-1}$), whereas the exponents b, f, and m indicate the rate of increase of the parameter with discharge irrespective to channel size. At any station at a certain time these three variables are interrelated by the continuity equation ($Q = wdV$), which means that any change in Q will be accommodated by suitable changes in w or d or V (Ferguson, 1986). These equations have been used to characterise and compare channels formed under different settings by comparing the likeness of the exponents, and are a useful tool to describe the complex processes that link the channel form and dynamic variables (Rhodes, 1977). These relationships are useful to estimate mean depth based on Q. At-a-station hydraulic geometry (AHG) can be used to estimate the hydraulic conditions at different periods on the same station, for example to know a dam's effect in downstream reaches, and for other various purposes such as flood routing (Snell & Sivapalan, 1995) and sediment transport (Richards, 1982).

Since the AHG relations give the information about the rate of change in velocity and flow depth in the stream these will be a useful tool to quantify flow resistance in steep mountainous rivers (David *et al.*, 2010). However, there is a great scatter in the exponent and coefficient values at local scales even within alluvial reaches (Table 4 in Comiti *et al.*, 2007). Ferguson (1986) suggests that the scatter is expected and it is not necessary that the power-law trends are followed given the wide variety of channel cross-sections which affect the rate of change of width with depth and friction characteristics. He pointed out the connection between at-a-station hydraulic geometry

and flow resistance, and this is now widely accepted (Gleason & Smith, 2014; Gleason, 2015). Most researchers have used a single power-law for the entire range of discharges from low to bankfull discharges, but Richards (1973) noted that this is not always appropriate. Navratil and Albert (2010) after studying 15 alluvial reaches in France found that a single power function (log-log linear) is not applicable for most of the reaches. They proposed two power functions; one for low to moderate discharge (30% of median flood) which is useful for habitat studies and another for moderate to bankfull discharge which is relevant for flood routing and sediment transport. They suggested that the non-linearity could result from different reasons such as a change in flow resistance with the depth or the presence of lateral gravel bars.

There are many studies on at-a-station hydraulic geometry in low-land alluvial streams (e.g. Leopold & Maddock, 1953; Richards, 1973; Rhodes, 1977), shallow/steep alluvial rivers (e.g. Beven *et al.*, 1979; Lee & Ferguson, 2002; Comiti *et al.*, 2007; Parker *et al.*, 2007; Reid & Hickin, 2008; David *et al.*, 2010; Navratil & Albert, 2010) and alluvial streams with large bed elements (e.g. Judd & Peterson, 1969; Beven *et al.*, 1979).

1.1.3 Flow resistance

Flow resistance is a collective term for the various frictional forces retarding the flow of a river. Hydraulic calculations have to make some assumptions about flow resistance since this is what determines flow depth at a given discharge and therefore affects shear stress and sediment transport. Flow resistance and bed roughness can be quantified at a range of scales. The emphasis in this thesis is on bulk flow at the reach or sub-reach scale, where reach scale conventionally means along-channel distances of at least 10 times the channel width (Ferguson, 2007b) and sub-reach scale means a few channel widths.

Flow resistance is a fundamental control on flow hydraulics in rivers and it controls four bulk flow properties – flow velocity (V), flow depth (d), energy slope (S), and boundary shear stress (τ) (Powell, 2014). If the velocities in different cross-sections along a reach are similar for a given discharge then the energy slope S (also called friction slope) is parallel to the bed slope and water surface slope (*i.e.* flow is uniform), but if the velocities are different then the flow is non-uniform, and the water surface slope needs to be corrected by the change along the reach in the local velocity head $V^2/2g$ to obtain the energy slope (Chow, 1959). The quantification of flow resistance is important for every hydraulic calculation including flood estimation, river habitat prediction,

engineering design, geomorphological and sediment routing models, and other scientific and river management applications (Ferguson, 2007a).

Flow resistance is traditionally regarded as having two components: 'grain resistance' or 'skin drag' that arises because of the contact of the flow with the skin of the boundary (grain surface, exposed channel bed and walls) and 'form drag' which arises due to the pressure difference between upstream and downstream side of the grains or undulations or large roughness elements (Ferguson, 2013; Powell, 2014). The part of the total flow resistance that is due to wakes, spill and other frictional losses other than the skin resistance are considered to be form resistance (Ferguson, 2013). In rivers different parts of the boundary (grains and other roughness elements) are aligned differently with respect to the flow therefore the flow will receive both skin and form drags and their relative importance varies with the relative submergence (R/D, where R is hydraulic radius and D the representative size of the bed material) (Powell, 2014). As the water depth increases the individual grains affect a smaller portion of the total flow, so the effect of grain resistance decreases as the depth increases (Wohl, 2013); this is why flow resistance decreases with discharge (Ferguson, 2010) if the boundary does not have boulders or large roughness elements. In boulder areas, the effect of form (pressure) drag will be high until the boulders become fully submerged; once they are fully submerged the pressure drag will decrease (Bathurst, 1993).

However, the hydraulics of steep/shallow channels containing coarser grains are different to the low-gradient reaches; because of the smaller catchment area and steeper gradient the relative submergence is small, and the GSD includes grain sizes ranging from finer more mobile patches to large immobile boulders which usually form riffle, steps and cascades (e.g. Yager *et al.*, 2007). The coarse grains and immobile boulders in steep channels obstruct the flow (Bathurst, 1978; Wiberg & Smith, 1991; Byrd *et al.*, 2000), increase turbulence (Papanicolaou *et al.*, 2001) and change the flow resistance (Bathurst, 1985; Marcus *et al.*, 1992). Because of these complexities in coarse-grained steep channels the conventional resistance equations cannot accurately predict the flow velocities (Bathurst, 1985; Marcus *et al.*, 1992; Bathurst, 2002; Katul *et al.*, 2002), and also the velocity profile may not be logarithmic which means the law-of-the-wall to calculate bed shear stress and the resistance laws based on log law (such as Keulegan equations) may not be applicable.

Flow resistance can be predicted reasonably well in low-gradient alluvial rivers but there is a lack of well-examined and reliable equations for upland rivers (Ferguson, 2007a; Wohl, 2013). Flow resistance is typically defined with a roughness or friction parameter, namely Chezy's coefficient C ($m^{1/2}$ s^{-1}), Manning's n ($m^{-1/3}$ s) and Darcy-Weisbach friction factor f (Chow, 1959; Ferguson, 2007a; Ferguson, 2012). These are defined as

$$C = V(RS)^{-1/2} \quad \text{Eq. 1.4}$$

$$n = \frac{1}{V} R^{2/3} S^{1/2} \quad \text{Eq. 1.5}$$

$$f = \frac{1}{V^2} 8gRS \quad \text{Eq. 1.6}$$

where g is acceleration due to gravity (9.81 m s^{-2}), and S is energy slope. The mean depth d and hydraulic radius R are often seen as interchangeable in relatively wide channels (width > 40 times depth). Manning and other researchers demonstrated that Chezy's C was likely to vary with the depth and therefore not suitable for velocity prediction. This then led to the development of Manning's equation where n is traditionally considered as a constant for a reach (Ferguson, 2010). In engineering n appears to be more common for open channel and f for pipe flows; however in geomorphology n and f appear to have been used interchangeably. The value of n is selected based on experience or the published values for different kind of channels (Chow, 1959) or based on bed-grain size using the Manning-Strickler approach. Strickler (1923) related Manning's n to the 1/6th power of median surface grain size (D_{50}) as

$$n \approx 0.047\, D_{50}^{1/6} \approx 0.039 D_{84}^{1/6} \quad \text{Eq. 1.7}$$

(Ferguson, 2010). The combination of Equations 1.5 and 1.7 is called Manning-Strickler and can be expressed as a 1/6-power relation between relative velocity and relative submergence:

$$V/u^* = a_1 (R/D)^{1/6} \quad \text{Eq. 1.8}$$

where V/u^* is relative velocity [$=(8/f)^{1/2}$, shear or friction velocity $u^* = (\tau/\rho)^{1/2}$ and water density ρ = 1000 kg m^{-3}], constant a_1 is generally taken 6.7 with D_{50}, 7.3 to 8.2 with D_{84} or D_{90} (Ferguson, 2007a). This equation can be seen as a power-law approximation of the logarithmic equation discussed below (Eq.1.9), for deep flow, but not in shallow

flows (*i.e*. for low R/D). In shallow flows, such as step-pool streams or larger rivers with boulders, the power-law exponent is more like 1 (Ferguson, 2007a).

Based on the Prandtl-Karman logarithmic law of the wall for turbulent boundary layers and the experimental work of Nikuradse (1933) on flow resistance in circular pipes, Keulegan (1938) proposed a flow resistance formula for an open channel relating the friction factor f to the Nikuradse roughness height k_s:

$$(8/f)^{0.5} = V/u^* = 2.5 \ln (12.2\ R/k_s) = 6.25 + 5.75 \log (R/k_s) \qquad \text{Eq. 1.9}$$

The value of k_s can be expressed in the form of a bed grain-size or some researchers have estimated it from geometric measures of bed roughness including rock bed (Ferguson, 2013). This Keulegan equation (also known as Colebrook-White equation) is commonly used for gravel-bed rivers and even for sand beds without dunes (Ferguson, 2013). For a well-sorted bed, k_s can be approximated as D_{50} or D_{65} but for poorly sorted river beds or channels with large roughness elements such as boulders k_s can be expressed as a multiple of some coarse percentile of the GSD such as D_{84} or D_{90}. Data from gravel bed rivers have shown that this multiplying factor can vary from 2 to 4 (Bray, 1979; Hey, 1979; Bathurst, 1985; Ferguson, 2007a). Bathurst (1985) fitted a modified log law to measured flow resistance in steep streams:

$$(8/f)^{1/2} = 4 + 5.62 \log (R/D_{84}) \qquad \text{Eq. 1.10}$$

Because of the complexity of the flow resistance processes in steep mountain rivers, many authors (Bray, 1979; Griffiths, 1981; Bathurst, 2002; Lee & Ferguson, 2002) have proposed empirical power laws in terms of the submergence ratio. Bathurst (2002) suggested that the bed grain roughness (D_{84}), bed material distribution (GSD) and the channel slope are the key factors that control flow resistance. He believed the power law can more accurately describe the flow resistance relation with relative submergence than the use of log laws and proposed the equations:

For $S < 0.008$ (S is energy slope)

$$(8/f)^{1/2} = V/u^* = 3.84(R/D)^{0.547} \qquad \text{Eq. 1.11}$$

For $S > 0.008$

$$(8/f)^{1/2} = V/u^* = 3.10(R/D)^{0.93} \quad \text{Eq. 1.12}$$

Ferguson (2007a) developed an alternative equation which he termed the Variable Power Equation (VPE) by assuming that f is the sum of two components, one for skin friction and having a 1/6-power dependence on submergence (like Manning-Strickler) and the other for form drag and having a linear (power 1) dependence on submergence. This gives

$$(8/f)^{1/2} = V/u^* = a_1 a_2 (R/D_{84}) / [a_1^2 + a_2^2 (R/D_{84})^{5/3}]^{1/2} \quad \text{Eq. 1.13}$$

where a_1 and a_2 are coefficients. The best fit to a large data set (N = 376) spanning a wide range of channel character (S = 0.0007 – 0.21; D_{84} = 0.05 – 0.8; R/D_{84} = 0.1 – 26 with one value 87) was found with $a_1 \sim 6.5$ and $a_2 \sim 2.5$. Eq. 1.13 is asymptotic to Eq. 1.8 in deep flows but steeper in shallow flows, though less so than Eq.1.9.

There are some limitations of estimating f or n using grain sizes D_{84} or D_{50} as the flow resistance is not only the result of the grains but also of the form drag on elements such as immobile boulders, woody debris, vegetation, morphology of walls, rock characteristics and bedforms etc. The local-scale surface topography of a coarse bed has an important role in flow hydraulics for a number of reasons such as the variability in surface friction angles, grains protrusion, hydraulic roughness and the near-bed flow field (Kirchner *et al.*, 1990). Direct measurement and quantification of bed topography have been attempted by many researchers (e.g. Furbish, 1987; Hodge *et al.*, 2009b; Richards & Clifford, 2011) but this has never been straightforward. The variability in friction angle and grain protrusion within the bed surface affects the variation in flow resistance, velocity profiles and hence the shear stress distribution, this means that the size distribution of the grains is not the sole descriptor of the flow resistance.

1.1.4 Non-dimensional hydraulic geometry

Discharge measurements in small, steep and rough channels are relatively accurate compared to the water depth measurements which are carried out for velocity calculation, because the flow resistance which determines the depth is controlled by bed topography and channel geometry which are often irregular and vary between the reaches. Therefore several authors (Rickenmann, 1991; Aberle & Smart, 2003; Comiti *et al.*, 2007; Ferguson, 2007a; Rickenmann & Recking, 2011) proposed an idea of dimensionless hydraulic geometry equations to relate the flow velocity with the flow discharge so that different reaches should all follow the same trend. Following the work

of previous researchers (e.g. Rickenmann, 1991; Aberle & Smart, 2003), Ferguson (2007a) proposed a non-dimensional hydraulic geometry relation as

$$V^* = a^{1-m} S^{\frac{(1-m)}{2}} q^{*m} \quad \text{Eq. 1.14}$$

where V^* is non-dimensional velocity [= $V/\sqrt{(gD_{84})}$, where g is acceleration due to gravity = 9.8 m s^{-1}], and q^* is the non-dimensional discharge [= $q/\sqrt{(gD_{84}{}^3)}$, where $q = Q/w$] and m is a constant. Using this equation the velocity can be predicted for a known slope, grain size and unit discharge from which the depth (= Q/wV) and the shear stress (= ρgRS, Eq. 1.20) can then be calculated. Ferguson (2007a) argued that the V^*–q^* relation ought to shift up/down according to slope (S) and he proposed two power laws one for deep flows ($q^* > 2$) and the other for shallow flows ($q^* < 2$) with different values of a and m in Eq.(1.14). They are:

$$V^* = a_1{}^{0.6} q^{*0.4} S^{0.3} \quad \text{[deep flows]} \quad \text{Eq. 1.15}$$

$$V^* = a_2{}^{0.4} q^{*0.6} S^{0.2} \quad \text{[shallow flows]} \quad \text{Eq. 1.16}$$

Comiti et al (2007) combined field data from 10 step-pool and cascade reaches with the data from the literature to find that the non-dimensional unit discharge (q^*) was the key variable to describe the observed variations in velocity and flow resistance, followed by channel gradient and the ratio of step height to step length. Comiti *et al.* (2007) plotted V^* against q^* and found that the points collapsed onto a single trend giving an equation.

$$V^* = 0.92 q^{*0.66} \quad \text{Eq. 1.17}$$

This is a generalised form of Ferguson's equation (1.14) without the slope term and Comiti *et al.* (2007) found no clear effect of slope.

Rickenmann and Recking (2011) tested several flow resistance equations using a large set of data (2 890 measurements) for shallow flows and found that Ferguson's VPE was the best of the equations using R/D_{84}, therefore based on VPE they proposed new non-dimensional variables V^{**} and q^{**} and a relation between them as:

For $1 \leq q^{**} < 100$

$$V^{**} = 1.60 q^{**0.545} \quad \text{Eq. 1.18}$$

For $q^{**} < 1$

$$V^{**} = 1.55q^{**0.706}$$ Eq. 1.19

where $V^{**}=V/\sqrt{(gSD_{84})}$, and $q^{**}=q/\sqrt{(gSD_{84}^3)}$. The $V^{**} - q^{**}$ relation is an improvement on Ferguson's $V^{*} - q^{*}$ equation (Eq. 1.15 and 1.16) as they save recalculating the formula with a different slope for each reach.

1.1.5 Bed shear stress

Bed shear stress τ (N m^{-2}) is the tangential force per unit area that moving water exerts on its boundary. It is of fundamental importance to sediment transport processes (Bauer *et al.*, 1992; Wilcock, 1996) and is a critical control on sediment entrainment (Lane, 1995). Boundary shear stress τ is often quantified in terms of shear or friction velocity (u_*). Bed shear stress in rivers cannot be measured directly but can be estimated from observations of flow geometry or velocity profiles or turbulence; this is particularly difficult in complex flow fields when the flow is highly three-dimensional. Commonly employed methods to estimate bed shear stress are the depth-slope product method for the reach and sub-reach scale; the law-of-the-wall method for the local or within sub-reach scale; and Reynolds stress and turbulence kinetic energy methods for the point scale. The depth-slope product (also called the Du Boys method) defines the reach-average mean shear stress τ (N m^{-2}) as a function of energy slope (S) and hydraulic radius R (m):

$$\tau = \rho g R S$$ Eq. 1.20

This is a simple force balance equation for uniform flow obtained by equating the downstream component of water weight over unit bed area to the frictional retardation and is commonly employed in studies of flow resistance (Hey, 1988; Griffiths, 1989) as well as flow competence and bed load transport relationships (Andrews, 1983; Carling, 1983). This equation gives the total boundary shear stress that includes both skin and form drag components (Robert, 1997). However, not all of this energy will be available for sediment transport and so the shear stress is sometimes partitioned into form drag and skin friction components (Robert, 1990; Lawless & Robert, 2001; Yager *et al.*, 2007) with only the latter regarded as available to drive bedload transport. This approach is also standard for predictions of bedload transport in rivers with dune beds (e.g. Meyer-Peter & Müller, 1948). Alternatively the critical shear stress (discussed below) can be increased to allow for the effect of the form drag (Ferguson, 2012), this will be further discussed in the next section (Section 1.1.6).

The law-of- the-wall method of calculating shear stress is based on the assumption that the velocity profile in the lower portion of an open channel flow has a logarithmic structure in the form

$$\frac{u}{u_*} = \frac{1}{k} ln \left(\frac{z}{z_0}\right) \qquad \text{Eq. 1.21}$$

where u is the time-averaged streamline velocity at elevation z above the bed, k the von Karman's constant (generally set to 0.40), and z_0 the roughness height *i.e*. the height above bed where velocity goes to zero. Measurements of local velocity at different heights allow u_*, and thus τ, to be estimated by fitting a regression equation. In general, z_0 is supposed to be proportional to the saltation height of the moving particle, or controlled by an average grain size that represents bed material or mobile grains. In shallow and steep gravel bed rivers the law-of-the-wall equation may not be fully applicable as the velocity profiles over mobile beds and larger size particles may not be logarithmic (Wohl, 2000), however in large gravel bed rivers the profile is found approximately logarithmic through the depth (Wiberg & Smith, 1991).

The Reynolds shear stress τ_R (N m^{-2}) acting on the plane can be expressed as

$$\tau_R = \rho \overline{u'w'} \qquad \text{Eq. 1.22}$$

where u' (= $u - u_m$) and w' (= $w - w_m$) are the velocity fluctuations (m s^{-1}) away from mean values in streamline and upward direction respectively, u and w are the measured velocities (m s^{-1}) and u_m and w_m are the mean values (m s^{-1}) in respective directions. The kinematic Reynolds shear stresses (e.g. Lane, 1995) are a measure of momentum exchange at a given point in the flow and can also be considered as a direct method of shear stress measurement. However, as it measures the shear stress at a point in the flow, not even on the bed, therefore may not be much useful for estimating mean bed shear stresses.

Measurement of the shear stress in bedrock and upland reaches is complex primarily because of the spatially and temporally varied channel-bed roughness and resulting turbulence and velocities (Dietrich & Whiting, 1989; Wohl, 2013). Reach-averaged bed shear stress (τ) is frequently determined from the depth-slope product mainly because the stresses in such channels are highly varied cross-wise and along the channel (Dietrich & Whiting, 1989) and also this method is easy to use in the field.

1.1.6 Threshold of motion and effective stress

Incipient motion of a sediment grain occurs when the drag and lift forces applied by the flow start to overcome the inertial forces. This point is called the threshold of particle entrainment and the associated shear stress is called the critical or threshold shear stress (τ_c). The bed materials in most gravel-bed rivers are immobile in normal flow conditions but they start to move during floods when the flow exceeds the threshold condition (Ferguson, 1994). If the threshold of motion for different sizes within the bed is dependent on grain size then entrainment is described as size selective.

The traditional way of predicting threshold of motion is using Shields' criterion:

$$\tau_c^* = \tau_c/(\rho_s\text{-}\rho)gD = \text{constant} \qquad \text{Eq. 1.23}$$

where τ_c^* is dimensionless critical shear stress or Shields stress (Shields, 1936), τ_c the critical shear stress (N m^{-2}), ρ_s the grain density (~2650 kg m^{-3}), D the mean grain diameter (m) which is often replaced by the median diameter D_{50} of the bed material. From a laboratory experiment with uniform spheres of varied grain size and density on a plane bed in a rough turbulent flow Shields (1936) found a constant τ_c^* of about 0.05 – 0.06 for particles coarser than 0.1 mm (Ferguson, 1994). His bedload was the same diameter as his bed material. However in gravel-bed rivers there is a wide range of grain sizes. It is to be noted that the D_{50} used here is of the bed material, not the bedload, so D_{50} is a major control over transport rate which alters τ_c.

The shear stress required to move individual grains that are coarser or finer than D_{50} depends on hiding, protrusion and pivot angles. Using eight decades of data Buffington and Montgomery (1997) studied the grain entrainment in gravel-bed rivers, and their analysis showed that τ_c^* of the median grain size as determined from bedload transport rates ranges from 0.052 – 0.086, but based on visual observation of grain motion the values are slightly lower 0.030 – 0.073. Mueller *et al.* (2005) estimated a high-value of τ_c^* up to 0.12 for steep gravel bed rivers, whereas Mao *et al.* (2008) found τ_c^* values up to 0.20 for two upland torrents. Conventionally, channel beds are considered to become mobile at a certain value of τ_c^* but various studies have shown that the value of τ_c^* is higher for steep shallow flows such as those found in headwater channels (Lamb *et al.*, 2008b; Ferguson, 2012). Many studies have shown that slope strongly influences the threshold of motion (Neill, 1968; Buffington & Montgomery, 1997; Mueller *et al.*, 2005; Lamb *et al.*, 2008b). Ferguson (2012) described how the slope dependency is because of the increase in bulk flow resistance. Lamb *et al.* (2008b) advise that the grain

entrainment is a function of relative flow roughness (*D/h*, where *D* is grain diameter and *h* water depth), which both vary with slope.

Several authors have tried to predict incipient motion by using critical discharge (Q_c) instead of critical threshold stress (τ_c). This was first done by Schoklitsch (1962) who developed an equation for unit critical discharge q_c in $m^2\ s^{-1}$ (= Q_c/w) for onset of motion using field data as

$$q_c = 0.26(\frac{\rho_s}{\rho} - 1)^{5/3} \frac{{D_{40}}^{3/2}}{S^{7/6}} \qquad \text{Eq. 1.24}$$

where ρ_s is the density of sediment (2650 kg m^{-3}). Schoklitsch's formula is based on Manning-Strickler and τ_c^* as a constant. Bagnold (1980) subsequently proposed an equation for critical stream power (ω_c), which can be converted to unit critical discharge q_c or critical discharge Q_c (= w x q_c) when the slope S is known:

$$q_c = \frac{\omega_c}{\rho g S} \qquad \text{Eq. 1.25}$$

Later works include Bathurst *et al.* (1987a), Petit *et al.* (2005), Ferguson (2005), Parker *et al.* (2011) and Ferguson (2012). The critical stream power (ω_c) can be expressed as

$$\omega_c = \omega_{*c}\rho[g\left(\frac{\rho_s}{\rho} - 1\right)D_{50}]^{3/2} \qquad \text{Eq. 1.26}$$

(Parker *et al.*, 2011; Ferguson, 2012). In terms of critical discharge (q_c), this can be expressed as

$$q_c = \frac{\omega_c}{\rho g S} = \omega_{*c}\, g^{0.5}(\frac{\rho_s}{\rho} - \rho)^{1.5} {D_{50}}^{1.5} S^{-1} \qquad \text{Eq. 1.27}$$

Parker *et al.* (2011) suggested that ω_{*c} is typically close to 0.1 based on an analysis of published and flume data, and Ferguson (2012) provided some theoretical backing for it using the VPE resistance law. Commonly used slope-based empirical formulas for dimensionless critical shear stress are by Mueller *et al.* (2005) as

$$\tau^*_c = 2.18\ S + 0.021 \qquad \text{Eq. 1.28}$$

and Lamb *et al.* (2008b) as

$$\tau^*_c = 0.15\ S^{0.25} \qquad \text{Eq. 1.29}$$

Those authors (e.g. Mueller *et al.*, 2005; Lamb *et al.*, 2008b; Ferguson, 2012) who have identified an increase in threshold stress in steep channels have all used the threshold

stress in relation to total stress as they figure that the reason for the higher threshold is due to higher form drag from immobile clasts.

Effective shear stress is the part of total shear stress that is available for bedload transport after subtracting losses due to form drag. This concept was originally applied to sand-bed rivers where the form drag is due to dunes, but is also used by other researchers (e.g. Yager *et al.*, 2007; Yager *et al.*, 2012) for situations where some of the bed material is so coarse that it is not available for transport but still extracts momentum from the flow. From a flume experiment Yager *et al.* (2007) developed sets of equations to partition the total shear stress into the stress that is available for mobile grains and immobile large boulders. The field data required for this approach include the diameter of the immobile grains, their spacing, and protrusion along with the channel slope, width, discharge, and diameter of mobile grains. These equations were later tested in the field (Yager *et al.*, 2012). They will be discussed again in section 4.6.1.

Many bedload transport equations are based on the excess-stress law of Meyer-Peter and Muller (MPM) form

$$q_b = k\,(\tau - \tau_c)^n \qquad \text{Eq. 1.30}$$

(e.g. Meyer-Peter & Müller, 1948), where q_b is the bedload transport rate per unit width (kg m^{-1} s^{-1}) and k and n are empirically determined values, with n typically being greater than one (Montgomery & Buffington, 1998). The transport rate (Q_b) through a channel section can be calculated by multiplying q_b by channel width (w). Once the shear stress exceeds the threshold value for entrainment, the bedload entrainment and transport rate increase in a rapid but nonlinear way with excess shear stress (τ-τ_c). Therefore an accurate estimation of the threshold shear stress (τ_c) is crucial as it affects the duration of competent flow and bedload flux calculation (Wilcock, 1996; Wohl, 2000; Ferguson, 2012). The estimation of dimensionless critical shear stress (τ_c^*) and the representative grain size (D_{50}) for the mobile grains are also difficult for the complex bed structure of bedrock rivers. Research has shown that most of the existing bedload formulas which were developed based on data from low-gradient alluvial rivers, overpredict sediment flux in steep rivers by several orders of magnitude (e.g. Bathurst *et al.*, 1987a; Rickenmann, 1997; D'Agostino & Lenzi, 1999).

1.1.7 Bedload measurements

Bedload movement is inherently stochastic at the local scale and collecting a representative sample is a difficult task (Ryan & Troendle, 1999; Wohl, 2013) for reasons that include difficult access due to rugged topography, the episodic nature of high-flow events and sediment discharge and in some cases extreme climatic conditions. Three aspects of the bedload transport that are difficult to measure and predict are: (i) grain entrainment under extremely spatially and temporally variable circumstances, (ii) the effect of sediment supply limitations on grain entrainment and transport, and (iii) the stability of the bed material surface layer and of bedforms (Wohl, 2013). The most commonly used techniques for bedload measurements are Helley-Smith bedload samplers (Helley & Smith, 1971; Warburton, 1992) or other portable trap samplers (e.g. Bunte *et al.*, 2003; Bunte *et al.*, 2004; Bunte *et al.*, 2007), fixed sediment traps or retention basins (e.g. Reid *et al.*, 1980; Lenzi *et al.*, 1990; Habersack *et al.*, 2001; Rickenmann & McArdell, 2007), pebble tracing (e.g. Ergenzinger & Conrady, 1982; Hassan *et al.*, 1984; Ferguson & Wathen, 1998; Hassan & Ergenzinger, 2003), and impact or pressure sensors (Rickenmann, 1994; Bogen & Møen, 2001; Carling *et al.*, 2002a; Raven *et al.*, 2010; Rickenmann *et al.*, 2014). The bedload samplers are at risk of being washed away or destroyed; the handheld or cable suspended samplers are logistically challenging to deploy at high discharges; and the safety of the field workers in flood conditions is always at high risk. The other two methods pebble tracing and bedload impact sensors are discussed below.

Pebble tracing

Tracer-pebble methods have been widely used in gravel-bed rivers for over three decades for incipient motion studies, in particular to study the effect of discharge on particle entrainment and transport distances (e.g. Ergenzinger & Conrady, 1982; Hassan *et al.*, 1992; Bunte, 2010), particle shape (e.g. Ergenzinger & Schmidt, 1990; Schmidt & Ergenzinger, 1992; Schmidt & Gintz, 1995; Demir, 2000; Warburton & Demir, 2000), size (Hassan *et al.*, 1984; e.g. Church & Hassan, 1992; Ferguson & Wathen, 1998) and particle packing (e.g. Laronne & Carson, 1976). Using this method the bedload mobility, transport rates and size selectivity can be determined (Ergenzinger & Conrady, 1982; Hassan *et al.*, 1984; Haschenburger & Church, 1998; Ferguson *et al.*, 2002; Hodge *et al.*, 2011). Pebble tracing may have some uncertainties including the recovery rate, but it supplies plenty of good information on sediment transport which may not be available from other methods (Ferguson *et al.*, 2002). Recovery rates will

vary immensely depending on the size of the river, extent of transport and time between surveys. Mainly there are two kinds of tracers- passive and active (Schmidt & Ergenzinger, 1992). The passive tracers use iron or magnetic cores with or without paint and after floods they are located using a metal detector. The passive tracers provide information about the cumulative travel length and the spatial locations of the tracers, and this technique has been used for last four decades (e.g. Ergenzinger & Conrady, 1982; Hassan *et al.*, 1984; Ferguson *et al.*, 2002). The active tracers use the radio-frequency identification (RFID) tags but they will be only activated when they are within the range of antenna. The RFID system has been used by many researchers (Ergenzinger & Schmidt, 1990; Lamarre *et al.*, 2005; Lamarre & Roy, 2008a, 2008b; Schneider *et al.*, 2010) for faster searching and higher recovery rate but there are also potential issues with active tracers too, for example antennas can miss grains if they are next to each other.

Bedload impact plates

A bedload impact plate is a metal plate fixed on the stream bed which receives bedload impacts and the attached sensor (logger) records these impacts of the clasts moving over the plate. The sound produced by particle impacts was initially used by Mulhofer (1933) to detect bedload transport. Later Richards and Milne (1979) used a piezo-electric transducer to convert sound energy to electric signals. Bänziger and Burch (1991) and (Rickenmann *et al.*, 1997) detailed a system for a hydrophone that detects the impacts generated by particles passing over a metal plate. The impact sensors are of a non-invasive or minimally invasive nature and have a very minimal effect on the flow field near the sensors (Rickenmann & McArdell, 2007). The hydrophones, piezoelectric bedload impact sensors (PBIS), geophone sensors, and the sediment impact sensor as introduced by Carling *et al.* (2002a) and Richardson *et al.* (2003) have been used by many researches to estimate the volume of bedload transport (e.g. Rickenmann & McArdell, 2007; Mizuyama *et al.*, 2010; Rickenmann & Fritschi, 2010; Rickenmann *et al.*, 2014). Bedload data are needed to calibrate impact sensors; such data are generally obtained from the retention basin (Rickenmann & McArdell, 2008; Rickenmann *et al.*, 2012) and/or the bedload samplers (Rickenmann *et al.*, 2014; Wyss *et al.*, 2014). There are some uncertainties in understanding the sensor data but research attempting to establish a relation between the sensor signals and the grain size distribution of bedload (e.g. Wyss *et al.*, 2014; Barrière *et al.*, 2015) and to develop a rating curve of bedload transport rates (Rickenmann *et al.*, 2014) is underway, but strong relationships between

the impact counts and total bedload mass has already been established by various authors (e.g. Rickenmann & McArdell, 2007; Rickenmann & McArdell, 2008; Turowski & Rickenmann, 2011; Beylich & Laute, 2014; Rickenmann *et al.*, 2014).

1.2 Differences between bedrock and alluvial channels

A channel with some exposed rock on its boundary (bed/banks) can be considered as a bedrock channel. Bedrock channels can either be purely bedrock (almost no sediment on its bed) or partly alluvial and partly bare rock surfaces on its boundary (semi-alluvial). Several definitions of bedrock channel exist, but generally they can be defined as a channel that cannot widen, deepen or shift its channel substantially without eroding rock (Whipple, 2004; Turowski *et al.*, 2008b). Fully alluvial and pure bedrock reaches can be considered as end members of a continuum; the intermediate points on the continuum are semi-alluvial channels which comprise both alluvium and exposed rock (Ashley *et al.*, 1988). A schematic of the bedrock-alluvial continuum is shown in Figure 1.2 which illustrates four channel types: type *a* is a bedrock channel confined wholly in bedrock with negligible sediment deposit, type *b* is confined with rock walls but the channel bed is sediment; type *c* is a channel with exposed rock on the bed but remains within an alluvial plain, and finally type *d* is a fully alluvial channel. This thesis uses the term 'bedrock river' to describe all three types of bedrock channels (*a* to *c*). However, in reach classifications the term 'bare rock' or 'bedrock' will be used to describe type *a* and 'semi-alluvial' to describe types *b* or *c* channels. Figure 1.3 illustrates the sections of an alternating sequence of bare rock, semi-alluvial and alluvial reaches of Trout Beck, an upland channel in the North Pennines, UK.

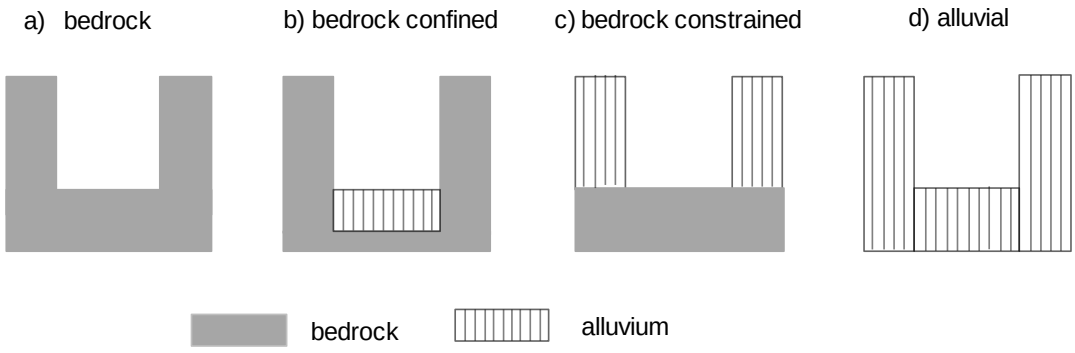

Figure 1.2. The end members in the continuum of channel types from bedrock to alluvial character. A slightly modified version of Meshkova *et al.* (2012), but originally from Turowski *et al.* (2008b).

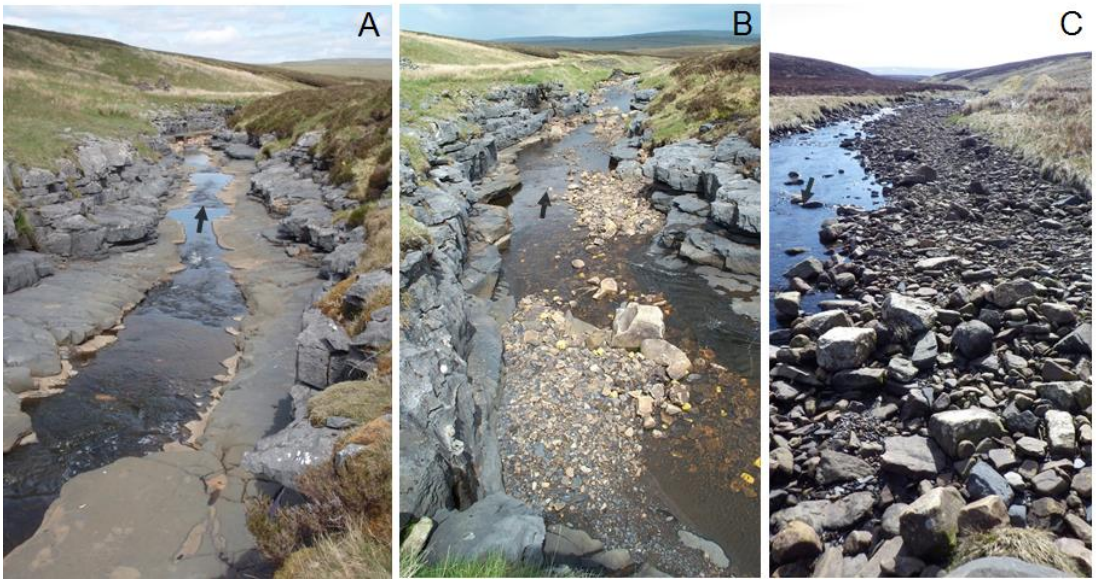

Figure 1.3. An upland river showing the alternating sequence of A) bare rock, B) semi-alluvial, and C) fully alluvial reaches (Trout Beck, North Pennines, UK). Arrows show flow direction.

Bedrock rivers are traditionally associated with incision during tectonic uplift, but can also occur in tectonically inactive areas where there are contrasts in lithology along the river. In general, bedrock rivers have stronger and more stable channel boundaries than alluvial rivers (Tinkler & Wohl, 1998b; Montgomery & Gran, 2001; Whipple, 2004; Goode & Wohl, 2010a), so that the flow is more rigidly confined by the channel geometry. In the long run the hydraulic forces may be able to adjust the geometry (Keller & Melhorn, 1978; Ashley *et al.*, 1988; Montgomery & Gran, 2001; Wohl & Merritt, 2001) but this most likely occurs over a longer period than in alluvial channels. Bedrock channels generally exhibit steeper gradients than alluvial rivers of similar size (Howard & Kerby, 1983; Tinkler & Wohl, 1998b; Gregory & Goudie, 2011) even though they may include some segments with low gradients (Miller, 1991b, 1991a). They are often described as having high velocities and very turbulent flows (Tinkler & Wohl, 1998b; Richardson & Carling, 2006) and are known to be competent to transport boulder-sized particles for long distances (Goode & Wohl, 2010b).

Where bedrock is exposed in over the full width of the bed of a river, there is no local sediment to entrain so the rate of coarse sediment transport cannot exceed the rate at which grains of transportable size are supplied from upstream or alongside. All bedload arriving from upstream is flushed over the exposed bedrock without accumulating as a sediment cover. This situation implies that the river is powerful enough that it could transport more bedload if only more sediment was available, either through an increase in the supply rate or through the existence of a partial sediment cover. Most previous

researchers have assumed that there is in principle some upper limit to the potential transport rate at a given water discharge, and that the limit is the transport rate that would occur if the bedrock was completely covered by sediment (e.g. Gilbert, 1877; Howard, 1980; Ashley *et al.*, 1988; Howard, 1994; Hancock *et al.*, 1998; Sklar & Dietrich, 1998; Whipple & Tucker, 2002; Turowski *et al.*, 2007; and many subsequent authors). Authors making this assumption have generally referred to the maximum potential transport rate as the 'transport capacity' of the bedrock channel, though that term will not be used in this thesis. In an extension of the same conceptual approach the continuum of zero to 100% sediment cover is regarded by many researchers as relating to differences in bedload supply rate, with little or no cover if the supply rate is very low relative to the power of the river but increasing progressively with higher supply rates until the cover becomes complete (e.g. Sklar & Dietrich, 1998; Turowski *et al.*, 2007; Lague, 2010; Johnson, 2014). The shape of the curve relating sediment cover to supply rate is relevant to river incision because of the trade-off (first recognised by Gilbert (1877)) between the 'tools effect' and the 'cover effect': a higher sediment supply rate provides more abrasive tools, but by increasing the sediment cover it protects more of the bed from abrasion (Gilbert, 1877; Sklar & Dietrich, 1998; Turowski *et al.*, 2007). If the maximum bedload transport rate is associated with a complete or almost complete cover, its value must depend on the same variables that are found empirically to influence the bedload transport rate in alluvial channels (section 1.1): the shear stress (or stream power) exerted by the flow and a threshold stress (or power) that depends on the character of the bed and in particular the average grain size.

Figure 1.4 shows the form-process diagrams prepared for bedrock channels (bare rock and semi-alluvial) alongside the alluvial-channel diagram of Figure 1.1 to bring out the differences. The fundamental difference between a bare rock channel (Figure 1.4b) and an alluvial channel (Figure 1.4a) lies in the channel configuration. The lack of alluvium on the channel bed means the flow resistance in the bare rock channel arises from exposed rock surfaces whereas it is from alluvial deposits (bed material/banks) in the alluvial channel. Therefore D_{84} (or any other grain size) cannot be used to predict the skin-friction part of the flow resistance of exposed bedrock, nor D_{50} to predict the threshold of transport; instead, both must depend in some way on the topographic roughness of the rock surface.

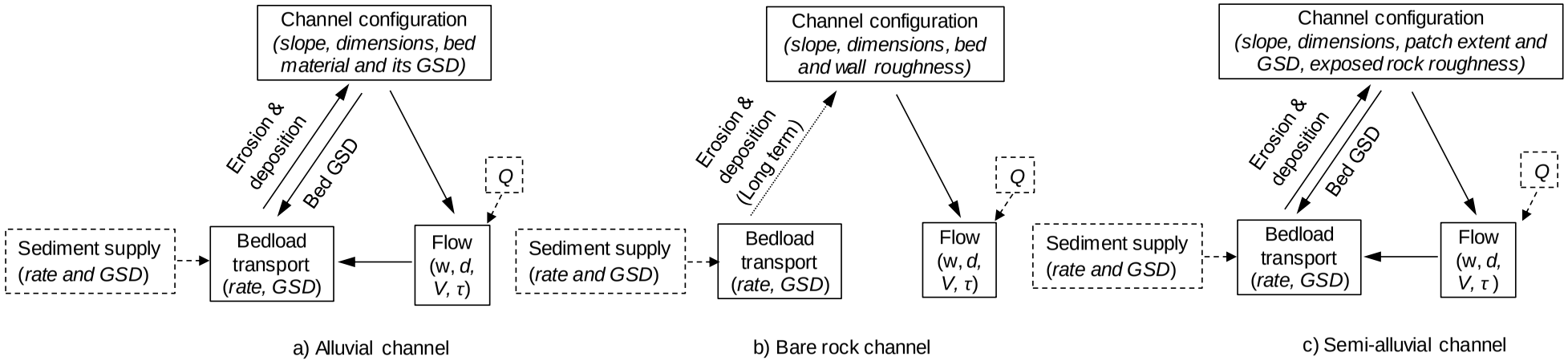

Figure 1.4. Form-process diagram for alluvial, semi-alluvial and bare rock channels. The sediment supply and discharge (Q) are external controls as shown by dashed arrows.

Another difference is that the critical shear stress and size selectivity of transport over rock may differ from normal alluvial conditions because of differences in flow resistance giving a different relationship between depth and velocity at a given discharge. Figure 1.4b shows no arrow from 'flow' to 'bedload transport' as the transport rate is controlled by supply: the flow would be capable of transporting more sediment if it was available. However, in the case of a bare-rock reach in an otherwise alluvial or semi-alluvial river, the sediment transported from upstream through the bare rock reach may be deposited and stored in the semi-alluvial and alluvial sections downstream and this may have important influences on form-process interactions there. The other important difference is that the channel morphology in bedrock reaches is relatively stable because the boundaries are resistant to erosion (Howard *et al.*, 1994; Howard, 1998; Tinkler & Wohl, 1998b): the fact that the flow could move more sediment than is supplied does not cause noticeable changes to the channel dimensions in the short term, in the way that alluvial channels can continually aggrade or degrade to a small degree. Erosion does occur in bare rock channels by abrasion of exposed surfaces and plucking of joint blocks, and this gives a local sediment supply, but rates of bedrock erosion are very low compared to rates of aggradation, degradation and bank retreat during floods in alluvial channels. Also, the products of abrasion are often fine-grained and removed as washload, rather than bedload.

Figure 1.4c shows the diagram for a semi-alluvial channel, which combines features of both the alluvial and bare rock channels. There is some sediment availability in patchy cover, so the cover GSD can adjust as in an alluvial channel, but also the extent of cover can adjust, approaching 100% (an alluvial channel) as the sediment supply increases but decreasing towards zero as the supply rate drops (e.g. Sklar & Dietrich, 1998; Turowski *et al.*, 2007). The resulting flow resistance is a composite of alluvium and exposed bedrock surface, in proportions that may vary temporally and spatially. The bedload transport rate depends on patch GSD and bed roughness via threshold shear stress. The varying sediment cover in semi-alluvial channels is a key mode of feedback as it affects the channel morphodynamics by linking feedbacks between supply, shear stress, erosion, and evolving channel form (Finnegan *et al.*, 2007; Johnson & Whipple, 2007; Turowski *et al.*, 2008a; Nelson & Seminara, 2011). This is a major difference from a bare rock or fully alluvial channel.

Bedrock channel morphology is influenced by physical (exposed rock and intermittent cover) as well as hydraulic and bedload transport characteristics (Ashley *et al.*, 1988).

Since the alluvial and bedrock systems have different channel forming processes (Turowski *et al.*, 2008b), fluvial geomorphology such as hydraulic geometry relations and standard resistance laws (Ferguson, 2007a; Rickenmann & Recking, 2011; Powell, 2014) based on alluvial channels may not work for bedrock channels (Tinkler & Wohl, 1998b).

1.3 Previous research on bedrock channel processes

Differences in the behaviour of bedrock and alluvial rivers were recognised more than a century ago by Gilbert (1877), but until the 1990s there was very little subsequent research on bedrock rivers. Since then there has been a rapid increase in number of publications, mostly stimulated by the importance of bedrock river incision in tectonic geomorphology. Four approaches can be identified to investigate bedrock rivers: (1) analytical/numerical modelling of incision processes/rates (making assumptions about processes), (2) dating studies of particular gorges to see whether long-term incision rates can help discriminate between models (e.g. Van Der Beek & Bishop, 2003; Valla *et al.*, 2010), (3) experiments in flumes or artificial channels, and (4) field observations/measurements in natural bedrock rivers. The thesis is about short-term processes rather than exogenic forcing, so strand (2) of the literature is not relevant and will not be reviewed. The following sections discuss the other three approaches, reviewing assumptions in incision models and empirical findings from work on flume/artificial and natural bedrock channels.

1.3.1 Hydraulic assumptions in analytical/numerical modelling of incision processes

Depending on the amount of material carried by bedrock rivers this can either promote incision (tools effect) or inhibit incision (cover effect), therefore these bedrock reaches control the rate of channel incision (Whipple, 2004; Yanites *et al.*, 2011; Inoue *et al.*, 2014; Johnson, 2014) which constrains landscape evolution in uplifted and/or tectonically active mountain ranges (e.g. Himalayas, New Zealand, Taiwan). Most of the work in bedrock rivers has chosen the first approach (modelling) even though sufficient general theory for incision and sediment transport by bedrock rivers is lacking (Carling, 2006), for example by making assumptions about how sediment supply varies with discharge and about how sediment transport varies with shear stress and hence discharge. Nearly all landscape evolution models from Howard (1994) onwards have assumed the incision rate is a function of bed shear stress (Eq. 1.20) where they estimate the shear stress (τ) from the unit discharge (q), slope (S) and assumed roughness

parameters ($\tau = \rho g d S$; $d = q/V$; V from flow resistance law). Mechanistic models have also been developed for specific incision processes such abrasion and plucking (Lamb *et al.*, 2008a; Chatanantavet & Parker, 2009), for the evolution of bedrock channel geometry (e.g. Turowski *et al.*, 2008b), and for the interrelation among alluvial cover, bed roughness, sediment transport and incision (Inoue *et al.*, 2014; Johnson, 2014).

Some researchers have used a constant value of Manning's n (e.g. Howard, 1994; Turowski *et al.*, 2007; Turowski *et al.*, 2008a), others have used a fixed value of Darcy-Weisbach f, equivalently Chezy's coefficient C (e.g. Whipple & Tucker, 1999; Chatanantavet & Parker, 2009; Zhang *et al.*, 2015), whilst Lague *et al.* (2005) used both approaches. Sediment cover is often assumed to be a simple function of sediment supply (Sklar & Dietrich, 2004), but the roughness of the exposed surface is also important (Davis *et al.*, 2005; Chatanantavet & Parker, 2008) and has been included in recent models (e.g. Inoue *et al.*, 2014; Johnson, 2014; Zhang *et al.*, 2015). Chatanantavet and Parker (2008) used the Manning-Strickler formula ($n \propto k_s^{1/6}$ or $V/u^* \propto (R/k_s)^{1/6}$) in their model to back calculate the roughness height k_s from measurements in artificial bedrock channels. Most cover models use different relationships between cover percentage and other reach variables such as slope, flow, sediment supply and grain size, however, Johnson (2014) considered that without incorporating surface roughness these models cannot predict the cover behaviours accurately and he developed a 1-dimensional model using the bed roughness as a main control for shear stress and threshold stress and hence for potential transport rate; the shear stress was calculated as a function of flow resistance ($\tau = \rho f V^2/8$) using the Manning-Strickler formula. He calculated separate roughness values for alluvial patches (based on grain size) and exposed bedrock surface (the standard deviation of bedrock elevation), and total flow resistance by taking a weighted average of spatial fractions of exposed bedrock and alluvial cover. Lamb *et al.* (2008a) and Nelson and Seminara (2012) have used logarithmic resistance law (Eq. 1.9), which imply that n or f decreases as the depth (or discharge) increases, in their models. Inoue *et al.* (2014) also used the logarithmic resistance law in their model to calculate the hydraulic roughness height of an experimental bedrock channel (channel excavated into bedrock) in the field.

Lague (2010) developed a model that links the sediment supply with the discharge and can model the sediment transport at a daily time scale. However field data such as how cover varies through a sequence of floods are lacking to provide insight into this process. With the lack of detailed and widespread field datasets of channel incision,

hillslope and channel processes, it is difficult to understand longitudinal profile development over long-term scales.

A lot of the literature is about what controls the extent of sediment cover and how it feeds back to processes. The extent and texture of alluvial cover in bedrock channels have been shown to vary with channel slope (Montgomery *et al.*, 1996) and channel roughness (Davis *et al.*, 2005; Inoue *et al.*, 2014; Johnson, 2014), which implies that channel slope and the roughness have strong links with the alluvial cover. Sediment cover controls the channel morphodynamics by moderating the interactions among sediment supply, shear stress and erosion (Johnson, 2014), and the extent of sediment cover is a function of threshold for grain entrainment (Inoue *et al.*, 2014). Cover varies over time, but there is disagreement about whether floods increase sediment cover or flush it away. The conceptual model developed by Turowski *et al.* (2013) describes two different types of behaviour of streams under flood conditions. Flood-cleaning streams evacuate sediment during extreme discharge events, while material is deposited during small and intermediate events. On the contrary, flood-depositing streams erode during small and intermediate events while deposition occurs in extreme events.

1.3.2 Experiments in flumes or artificial/experimental bedrock channels

Chatanantavet and Parker (2008) used tilting-bed flume experiments to investigate the factors controlling sediment cover in bedrock channels. They found that the major factors that control whether the bedrock surface is fully or partially exposed are sediment supply, channel slope, bed roughness, intensity/thickness of existing patches, and presence of boulders. As mentioned above in section 1.3.1, the hydraulic roughness height of the bedrock surface (k_{sb}) was back calculated using the Manning-Strickler relation when there was no sediment in the bed of the flume. They also calculated the standard deviation of the distribution of difference between the average flume slope and the surface topography as has been used to quantify bedrock roughness by Johnson and Whipple (2007) and Finnegan *et al.* (2007). On three out of four different bedrock topographies, they found the standard deviation values were very different from the hydraulic roughness height.

Inoue *et al.* (2014) measured the threshold of entrainment, alluvial cover and bedrock incision for range of discharges, sediment supply, grain sizes and bed roughness in an experimental bedrock channel excavated alongside a bedrock river (Ishikari) in Japan. The result showed that the dimensionless critical shear stress (τ_c^*) increases with

increasing relative roughness (k_s/D, where D is the grain size) and there is an interaction between bed roughness (k_s) and the alluvial cover in which k_s decreases as the cover increases. As mentioned earlier in section 1.3.1, in their model they considered both topographic roughness as well as hydraulic roughness. According to their definition, the topographic roughness was the measure of the standard deviation (Finnegan *et al.*, 2007; Johnson & Whipple, 2007, 2010) of the macro-roughness of the bedrock surface while the hydraulic roughness was back-calculated using Keulegan equation.

Siddiqui and Robert (2010) carried out both field and flume experiments to examine the erosive resistance of loose, discontinuous joint blocks which remained as a bed material in a bedrock channel incised into shale. This is discussed in the next section (see 'Threshold of motion and size selectivity').

Chatanantavet *et al.* (2013) studied the saltation dynamics (dimensionless critical shear stress; grain saltation length/height/velocity; and effect of shape) in a smooth bedrock channel by carrying out a flume experiment to determine whether the saltation is dependent on bed roughness or sediment size. They characterised the saltation dynamics using Froude number *Fr* as well as dimensionless critical shear stress τ_c^* (also called critical Shields stress). They found that the *Fr*-based scaling gave a better fit to the saltation data and is advantageous as it does not involve estimating τ_c^* which can vary up to two orders of magnitude (0.001-0.1, see Hodge *et al.* (2011)) and is also a difficult task to measure in bedrock channels with varied bed roughness and slopes. However, they also considered that the calculation of Froude number ($F = V/(gd)^{1/2}$) requires estimation of flow velocity (V) based on flow resistance which is equally challenging for bedrock channels. The results showed that the saltation velocity is independent of particle size and density and is a linear function of flow velocity. They suggested that either the roughness coefficient or τ_c^* must be properly estimated in saltation-abrasion model to get accurate results.

1.3.3 Field observations/measurements in bedrock channels

The literature on field experiments to measure/observe the processes in bedrock channels is discussed below under various headings.

Flow resistance

A solute dispersion study (series of dye dilution experiments) carried out by Richardson and Carling (2006) in a small bedrock channel with very little sediment cover (Birk

Beck, UK) showed that the study reach behaved differently with respect to the dispersive properties with increasing discharge. They found slightly lower values of *n* and *f* at low discharge when the velocity (*V*) was calculated from the advective time delay (between fluorimeters at upper and lower of the reach) compared to that from continuity equation (*V* = discharge *Q*/average cross-sectional area *A*). The results also show that *n* initially declines rapidly with increasing discharge but remains constant at high flows (*n* ~ 0.037). The *n* value at higher discharges in Birk Beck was found to be lower than those of alluvial channels of similar slope and depth as predicted by the empirical equation of Jarrett (1984) for high-gradient streams.

Other studies measured water surface profile to estimate mean depth, mean velocity, and flow resistance in bedrock reaches where discharge could be estimated separately. Heritage *et al.* (2004) measured the water surface profiles using crest stage devices for known discharges in five short reaches of a large and partly anastomosed bedrock-dominated river (Sabie, South Africa). They found that the reach-averaged values of *n* and *f* decrease with increasing discharge from low to moderate flow, and then remained almost constant at higher flows, as also found in many shallow/steep gravel-bed rivers (e.g. Kellerhals *et al.*, 1972; Hicks & Mason, 1991; Lee & Ferguson, 2002; Reid & Hickin, 2008). They also found that the flow resistance was very high at low flows, higher than any reported value in the literature. They explained that the higher flow resistance probably reflects the hydraulic jumps and internal distortions of the flow caused by shallow flow and large roughness elements such as irregular bedrock outcrops and boulders. Based on field estimation of Manning's *n* using a range of approximate techniques (visual and semi-empirical equations) and the stage indicator of recent moderate flood, Kidson *et al.* (2006) calibrated a hydraulic model for reconstruction of palaeoflood discharge for a bedrock channel Mae Chaem in northern Thailand. They also checked the uncertainty in estimation of *n* values from these approximate techniques within a hydraulic model for a large flood of known discharge (*Q*). They found that the *n* values estimated from both approximate techniques and existing model (predicting stage-roughness variations) underestimate the actual roughness; also they found a complex *Q*-*n* relation for this river.

Hydraulic geometry

Since the side walls of bedrock channels are usually more resistant to erosion than the banks of alluvial rivers, it might be thought that bedrock rivers have, on average, lower

channel widths than alluvial rivers with the same discharge or the same drainage area, and consequently greater average flow depths. Wohl and David (2008) investigated this by comparing field data on the channel geometry of 47 bedrock sites with nearby alluvial reaches of the same rivers. They analysed the data in several ways, some of which showed a slight tendency for bedrock reaches to be narrower, but mostly there was no significant difference. The results also show that the width to depth (w/d) ratio varies greatly between bedrock channels.

There are very few field studies that report on at-a-station hydraulic geometry (AHG) for bedrock channels. Beven *et al.* (1979) reported the exponents in the AHG relation between velocity and discharge (V-Q) for two bedrock reaches in the headwaters of the River Severn. Turowski *et al.* (2008b) studied the AHG relation between width and discharge (w-Q) in alluvial and bedrock reaches in Taiwan (total 81 river stations, for each station with >1000 discharge data and 100 width measurements) and found no systematic difference between the width exponents for alluvial and bedrock reaches. They found that the hydraulic geometry of bedrock channels in Taiwan was adapted to the sediment load, which normally does not happen to other mountainous rivers (Turowski *et al.*, 2008b).

Threshold of motion and size selectivity

As mentioned earlier in section 1.3.2, Siddiqui and Robert (2010) carried out both field and flume studies to determine the threshold of entrainment of loose blocks of various sizes which remained as bed material in a semi-alluvial channel (Etobicoke Creek, Canada). They measured the transport distances of various clasts in the field during different flood events which demonstrated that the transport distances were directly related to the shear stresses, and larger clasts were found to have moved shorter distances and smaller ones moved longer distances (size-selective). The flume experiment showed that the resistance to entrainment provided by the clasts depended on their orientation. The platy nature of the rocks, their orientation and their imbrication significantly affected the threshold of erosion. Based on their current meter measurements they found that n and f varied according to the stage.

Isolated or clustered big boulders are generally observed in bedrock channels. Some of these might have been detached from the bed or side walls whilst others might have been transported by floods (Carling *et al.*, 2002b). Carling and Tinkler (1998) carried out a theoretical review and an experiment in a steep flume-like natural channel to

investigate the entrainment of cuboid boulders in bedrock channels. The study showed that incipient motion of large boulders on bedrock surfaces is linked to the Froude number being near 1 *i.e.* when the flow is near critical, which occurs when the flow depth is similar to the height of the boulder. As bedrock rivers may not adjust the boundaries to the flow regime, the bed slope and geometry may be adjusted to maximize the unit discharge through a minimisation of the mean specific energy ($d + V^2/2g$) (Grant, 1997; Chanson, 1999) and this condition occurs when the flow is critical. Therefore the largest boulders may be subject to sub-critical, critical or super-critical flows depending on the discharge amount. The bed surface of the semi-alluvial reaches could be physically-smooth and boulders may be flat rather than rounded, therefore the mechanism of entrainment of such boulders could be by sliding as well as pivoting which occurs with critical or supercritical flow. Hydraulic jumps can also help generate the vibrations and pressures to move these obstacle particles (Carling *et al.*, 2002b).

Goode and Wohl (2010b) from a tracer-pebble experiment in a bedrock river (Ocoee, USA) with a complex topography (with bedrock ribs) found that the bedrock topography has a strong control on bedload transport. The result showed that the transport was significantly dependent on grain size where the bedrock ribs were longitudinal to flow, as in alluvial rivers (e.g. Church & Hassan, 1992; Ferguson & Wathen, 1998), but it was independent to size where the ribs were oblique to flow.

Hodge *et al.* (2011), based on theoretical analysis and tracer pebble data, showed how the degree of alluvial cover affects grain entrainment, transport and deposition in a bedrock channel. Their theoretical analysis showed that grain entrainment is size-independent in bedrock rivers. They compared the tracer data from three rivers of comparable slope, size and GSD but contrasting alluvial cover (Allt Dubhaig: fully alluvial 100% cover, South Fork Eel: bedrock 80% cover, Calder: bedrock 20% cover). The field data showed that the transport distances in bedrock-dominated Calder River was fully size-independent whereas in the other two rivers the transport was size dependent. They estimated τ_c^* = 0.038 for River Calder, a slightly lower value than generally reported for alluvial rivers, though is still within the range of alluvial river 0.030 – 0.086 according to Buffington and Montgomery (1997). Their theoretical analysis showed that the τ_c^* on bedrock channels could be an order of magnitude lower than on alluvial channels for the same size grains, they considered the possible reasons for this are poorly-packed scattered patches, shallow sediment depths and absence of

surface coarsening. The result also showed that the virtual velocities (travel distance divided by the duration of competent flow) (Einstein, 1937; Hassan *et al.*, 1992; Ferguson & Wathen, 1998; Haschenburger & Church, 1998) are higher in the bedrock River Calder than in the alluvial River Allt Dubhaig.

Sediment supply and cover

Variation in sediment supply affects the sediment flux and hence sediment cover and bedrock erosion. Turowski *et al.* (2008a) observed that the sedimentation along the channel talweg of the Liwu River in Taiwan during high floods encouraged bank erosion and the tools-and-cover effects dictated the partitioning of lateral and bed erosion.

1.3.4 Knowledge gaps

From the above studies it appears that the knowledge of flow and sediment transport processes in bedrock channels has been further advanced in the last two decades but the understanding is still poor compared to well-studied alluvial channels, primarily due to a lack of detailed observational data. Furthermore, most of these process understandings are based on theoretical analysis, flume studies and very limited field studies which do not cover a wide variety of bedrock channels and all aspects of sediment transport processes. The key gaps in knowledge and differences of opinion on how to model the processes are summarised below, based on which the aim, research questions and the objectives of this research were identified (which will be discussed in next section).

1) The studies show that authors have used different resistance laws (e.g. Manning's *n*, Darcy-Weisbach *f*, Manning-Strickler, log law) in the incision models but because of very limited field data the suitability of these relations for bedrock channels is not known.
2) How the flow resistance behaviour of bedrock rivers compares with that of steep and coarse alluvial channels is not known, but the presence of some coarse sediment in most bedrock channels suggests that it is worth investigating. The log law, variable power equation (VPE) and non-dimensional hydraulic geometry equations are considered to be the best resistance laws for coarse alluvial rivers but how these perform in bedrock reaches is not known.
3) Most incision models use constant *n* or *f*, but the limited field measurements in bedrock channels show that there is a stage-related variance in *n* and *f*, also there is a

large variation in flow resistance between sites. To guide the modellers, it is essential to have more field data from bedrock reaches of different bed character.

4) Field investigations by various researchers show the importance of partial sediment cover in moderating incision (e.g. Cowie *et al.*, 2008; Johnson *et al.*, 2009; Turowski & Rickenmann, 2009; Yanites *et al.*, 2011) and several efforts have been made to develop a fully process-based mathematical model to reproduce the erosion processes (e.g. Whipple & Tucker, 2002; Sklar & Dietrich, 2004; Turowski, 2012; Inoue *et al.*, 2014; Johnson, 2014; Zhang *et al.*, 2015), but field data covering the wide range of bedrock channels are still lacking; which prevents the validation and testing of the assumptions in the models
5) Bedrock reaches are often quite short and interspersed between alluvial reaches. Moreover, the sediment cover and grain sizes can vary between different short segments of a single bedrock reach. There has been only one field study of bedload mobility in bedrock reaches of contrasting bed character (Goode & Wohl, 2010b), and it considered only differences in the character of exposed bedrock, not differences in the extent of sediment cover. Also it is not fully known how the mobility in bedrock reaches (bare rock and semi-alluvial) compare with adjacent fully alluvial reaches; the comparison in Hodge *et al.* (2011) was between three different rivers.
6) The very limited field data on size selectivity of bedload transport in bedrock channels shows selective transport in some situations but not others (Goode & Wohl, 2010b; Hodge *et al.*, 2011), and neither study investigated the possibility of selective transport according to grain shape as well as size. This suggests the desirability of examining size/shape selectivity in different varieties of bedrock channels.
7) Some incision models predict the incision rate directly from the bed shear stress, which is calculated from the local discharge, slope and assumed flow resistance parameter. More detailed models predict the potential bedload transport rate from excess shear stress, but how the shear stress and threshold stresses (also threshold discharges) vary in bedrock reaches and how they compare with alluvial reaches are not fully understood. It is good to have a field investigation to assess the controlling factors for threshold stress and bedload conveyance.

1.4 Aim and objectives

There has been more modelling of bedrock processes than empirical research, and much of the empirical work has been with artificial 'bedrock', so there is a need for detailed field investigations of processes in natural bedrock channels. The general aim of this thesis is to contribute to filling this gap. Field process measurements are time-consuming so the thesis is restricted to one site, but in order to learn as much as possible from one field site, a site was chosen that allowed for comparative measurements in contrasting parts of the river (fully alluvial, extensive partial cover, limited partial cover, and bare rock). The emphasis will be on bulk flow and sediment transport, since they are key parts of the process system and not well understood, but can be studied within the duration of a PhD since there are certain to be at least some transport events. There is unlikely to be measurable incision within 2-3 years, so that is not considered; and previous work at the chosen field site (Smith, 2004; Cray, 2010) suggests sediment cover changes significantly only in extreme floods, so trying to study that within the PhD timescale would be risky.

It is clear from the review of previous research (Section 1.3) that sediment transport processes in bedrock systems are still poorly understood and that field measurements of bulk hydraulics and sediment transport are lacking. The main uncertainties in bulk hydraulics are: how at-a-point hydraulic geometry and flow resistance in bedrock channels compare with fully alluvial channels; how flow resistance varies with discharge on different kinds of bed; and whether the standard resistance laws based on alluvial rivers are applicable to bedrock rivers. The uncertainties about sediment transport include: how bed character affects critical shear stresses and sediment mobility; and how selective, if at all, is sediment transport in bedrock systems. A general aim and series of research questions and objectives have been devised to investigate these processes by studying the morphology, flow and sediment transport in a bedrock channel.

1.4.1 Aim and research questions

The aim of this research is to find out more about flow and bedload transport in natural bedrock channels. In particular, the PhD aims to undertake an intensive field programme of direct measurement of coarse sediment dynamics through a sequence of reaches of contrasting character in a bedrock channel. In order to achieve this aim, four research questions (RQs) have been devised:

RQ 1. How do bulk flow properties vary according to bed character and with discharge?

Bedrock channels contain exposed rock and alluvial cover which ranges from a few isolated patches to an almost complete cover. Roughness resulting from alluvial patches, rock bed, rock walls, and immobile boulders makes the prediction of reach-scale flow resistance complex. Various sub-questions will be answered to address this question including: how at-a-station hydraulic geometry varies along the study channel; how flow resistance and shear stress vary along the channel and with the flow; how the large roughness elements reduce the total shear stress for sediment transport; and how the bulk flow properties in bedrock segments compare with an adjacent alluvial segment.

RQ 2. How does sediment mobility vary according to bed character?

Exposed rock in the channel bed implies that sediment mobility is higher compared to the areas with alluvial cover, and an alternation of alluvial and bedrock reaches therefore implies spatial differences in sediment mobility. A series of observations and measurements of coarse sediment movement will be undertaken to discover how sediment mobility varies with bed character and series of sub-questions will be answered including: how the mobility of sediment varies in fully alluvial, bare rock and semi-alluvial reaches; how the mobility varies in different floods; what areas have the higher concentration of sediment; where the grains are most and least mobile; and what factors control the mobility.

RQ 3. How selective is bedload transport?

Previous tracer pebble experiments in alluvial rivers have shown that the transport distances vary with pebble size and shape. There are very limited similar studies in bedrock channels; some have shown that transport is size selective, some that it is not, and none has considered shape selectivity. In this section a series of sub-questions will be answered such as: whether the bedload transport in bedrock reaches is selective according to size or shape; how the size selectivity varies between fully bedrock and partial-cover reaches; and how the degree of selectivity in bedrock reaches compares with alluvial reaches.

RQ 4. How do the flow and shear stress at initiation and cessation of bedload transport compare and vary according to bed character?

Transport rate is expected to depend on threshold stress as well as shear stress, and therefore to vary according to bed character. In this section an analysis will be undertaken to answer a series of sub-questions including: how the threshold discharge and threshold shear stress vary in fully bare rock, semi-alluvial and alluvial segments, how the threshold values at initiation and cessation of bedload motion compare; and how the field estimated threshold values compare with the estimates from empirical formulas.

1.4.2 Objectives

In order to address the general aim and research questions, three objectives have been drawn up which are set out below.

(1) To observe and measure how bulk flow properties (mean depth, mean hydraulic radius, mean velocity, mean flow resistance, mean shear stress) vary over time and how they differ in fully alluvial, fully bedrock and semi-alluvial sub-reaches;
(2) To observe and measure sediment transport on fully alluvial, fully bedrock and semi-alluvial sub-reaches and investigate the degree of size selectivity and any differences in the flow and shear stress at initiation and cessation of motion;
(3) To investigate the extent to which the bedload mobility can be explained by the bulk hydraulics and variation in channel bed structure in the sub-reaches.

1.5 Structure of the thesis

This thesis is an attempt to investigate the coarse sediment dynamics in different reaches of a bedrock channel and compares that with an adjacent alluvial reach. This thesis reports the results of field work carried out at a suitable upland channel in the UK comprising reaches from across the alluvial-bedrock continuum. In doing so it also enables a greater understanding of how different reaches of varying bed character affect the overall bedload conveyance of a channel. In particular, this research will look into bulk hydraulics, bedload transport, the linkage between the flow and transport results and comparisons between the field results and what process assumptions are made in long-term incision models. This thesis deals with these components through the use of field experimentation and observation to improve the knowledge of sediment transport through a bedrock channel.

Chapters 2 discusses the study site and the results of the topographic survey, grain size distribution and sediment cover mapping. Chapter 3 discusses the methodologies for studying hydraulics and sediment transport. Chapter 4 presents the results of the flow measurements, calculations and analysis. This includes measurements of discharge, velocity and stage; and calculation of hydraulic geometry, flow resistance and shear stresses over spatial and temporal scales. These bulk hydraulics results allow the bedload conveyance to be assessed in a greater detail. Chapter 5 reports the results from a tracer pebble experiment and investigates the bedload mobility, size selectivity and thresholds of motion in the contrasting bed segments for a range of flow conditions. Chapter 6 presents and analyses the data from bedload impact sensors. The transport distance of the tracers and the impact counts from the sediment impact sensors will allow the threshold conditions to be examined thoroughly. All through the thesis the interplay between flow, sediment supply and morphology are examined at different temporal and spatial scales. Finally, chapter 7 offers answers to the research questions (Section 1.4.1), discusses the key findings of the thesis, implications of the results and future avenues, and provides the conclusions of the thesis.

2 Field site

This thesis is concerned with the sediment transport processes through the contrasting reaches of a mixed alluvial-bedrock channel which required a combination of experimentation and monitoring to carry out an in-depth field measurement of channel topography, bed sediment including effects of big boulders, flow hydraulics and bedload transport (Section 1.4.2). Therefore an upland bedrock channel consisting of alternating reaches of alluvial, bedrock and partial alluvial sections was the key consideration in identifying a suitable field site. The study channel should experience frequent floods and needed to be active in terms of bedload transport so that the threshold conditions for bedload entrainment could be studied under range of flow conditions. Since the research involves the collection of flow and sediment transport data using in-situ instrumentation, frequent surveys and detailed measurements good site and land access and permission for the instrumentation were also crucial to the success of the research. Furthermore a hydrological and meteorological monitoring station in the vicinity which could provide the historical flow data would be an added advantage.

Based on above criteria a study site in Moor House on Trout Beck (NY 758 335), a tributary of River Tees in the North Pennines, UK was considered suitable for the purposes of this research. Trout Beck is a small perennial bedrock stream with alternating reaches of alluvial, bedrock and mixed alluvial-bedrock sections. This site has an added benefit of being a centre for large amount of earlier research in hydrology, geology and sediment transport (Garnett *et al.*, 1997; Evans *et al.*, 1999; Demir, 2000; Holden, 2000; Holden & Burt, 2003; Smith, 2004; Crowe & Warburton, 2007; Cray, 2010; Tancock, 2014). Previous studies on this study reach (e.g. Demir, 2000; Cray, 2010) demonstrated that Trout Beck was active in terms of sediment transport and frequent high-flow events, which ensured that the data could be collected. The river discharge on Trout Beck has been monitored as part of the UK's Environmental Change Network (Sykes & Lane, 1996) at a compound crump weir maintained by the Environment Agency (EA), which is located approximately 800 m downstream of the study site. Access to the study site is from Garrigill, a small village near the town of Alston, which is 10 kilometres distant from the study site.

Standard surveying and grain size distribution (GSD) techniques are used for the site description in this chapter and are only outlined briefly; the field results of topographic surveying, GSD and sediment cover survey are also included in this chapter. The methods used to quantify processes (discharge, hydraulics and sediment transport) are described in the next chapter. This chapter is divided into five sections. Sections 2.1 describes the Trout Beck catchment and geology, section 2.2 reports the climate and hydrology of the study catchment; section 2.3 discusses the channel morphology of the study reach, methodology for topographic survey, and summarises the reach characteristics; section 2.4 explains the survey methods for determining sediment cover, GSD and boulders measurement, and reports the field results; and finally section 2.5 discusses the sub-reaches for detailed study and presents the channel cross-sections for each sub-reach.

2.1 Catchment and geology

2.1.1 Trout Beck catchment

Figure 2.1 shows the location of the study site and the catchment. The altitude of Trout Beck (NY 75 33) catchment ranges from 527 m, at the confluence with River Tees, to 848 m at Great Dun Fell, the highest peak of the catchment. The Trout Beck channel, from its origin near Great Dun Fell to the River Tees, is approximately 6 km long and with the elevation difference of 320 m the overall gradient of Trout Beck is 5.4 %. The other peaks in the watershed include Hard Hill (678 m), Knock Fell (794 m) and Dufton Fell (768 m). Trout Beck has its entire catchment within the Moor House – Upper Teesdale National Nature Reserve (NNR). Moor House and Upper Teesdale were two separate NNRs until 1999. Meteorological recording began at Moor House in 1932, and the Moor House Reserve, owned by English Nature, has been a centre for diverse scientific research particularly in the field of natural flora, biology and hydrology. A large part of the River Tees catchment also lies within the Reserve. The total drainage area of Trout Beck at the EA gauging station (535 m) at Moor House is 11.46 km^2. Smith (2004) classified the channel sections in River Tees and Trout Beck by dividing the channels into five classes from bedrock to fully alluvial sections and found that 82 % of Trout Beck was alluvial, 13 % semi-alluvial (3 % with <50% sediment cover, 8 % from 51 – 90 % cover, and 2 % mobile sediment) and 5 % are bare rock sections. The River Tees had similar classification with slightly higher bedrock proportion (81%, alluvial, 9 % semi-alluvial and 10% bedrock.

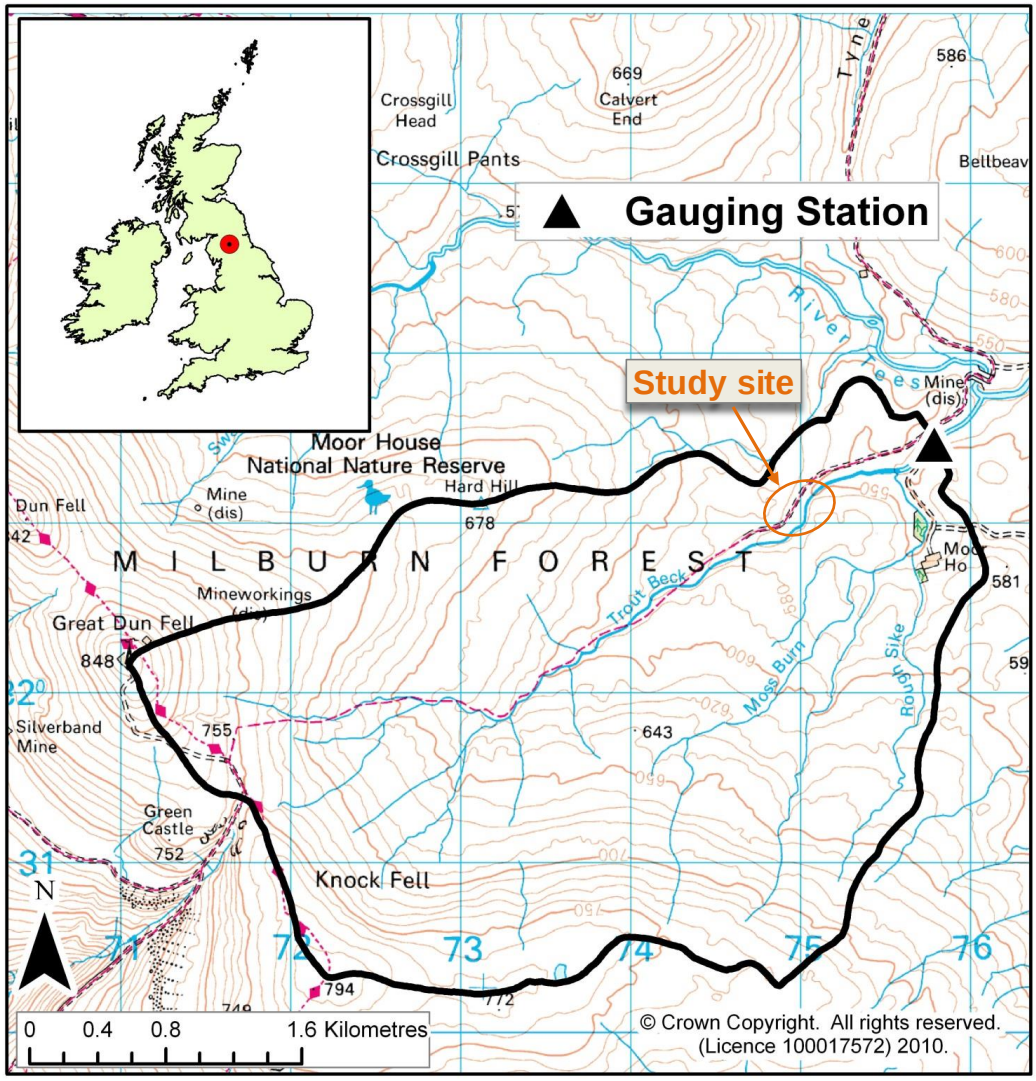

Figure 2.1. Location map of Trout Beck study site (NY 758 335) in Moor House in the Northern England showing Trout Beck catchment (black line), and the Environment Agency gauging station (black triangle). Map source: http://data.ecn.ac.uk/sites/ecnsites.asp?site=R22.

2.1.2 Regional geology

Johnson (1963) carried out a detailed survey of the study region in 1954, and published a descriptive memoir on the geology of the area in 1963. A map showing a geological setting of North England with boundaries of Moor House NNR and a generalised section showing the geological sequence of the Moor House Reserve, taken from the monograph of Johnson (1963), are shown in Figures 2.2 and 2.3. The North Pennines, a remote area of upland moorland, is at the northern end of the Pennines chain. Most of the area lies above 450 m and the highest peak is Cross Fell (893 m). The North Pennine block is made up of two fault-bounded crustal blocks: the 'Alston Block' to the north in the counties of Durham, Cumbria and Northumberland and the 'Askrigg Block' to the south in North Yorkshire (Figure 2.2). These blocks represent areas of crustal

uplift and are adjacent to areas of crustal subsidence; the Northumberland Basin to the north, the Stainmore Trough between the two blocks, and the Craven Basin to the south.

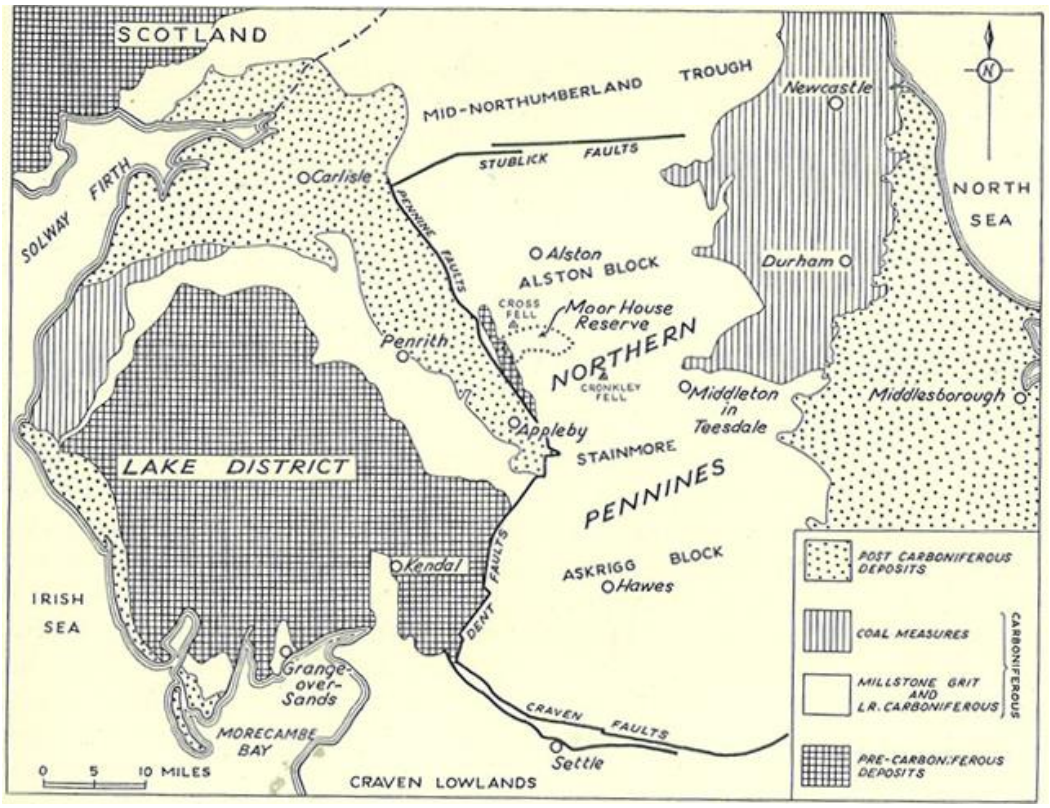

Figure 2.2. Map of Northern England and Borders showing the position of the Moor House NNR (dotted line) in which the geological boundaries are based on the maps of the Geological Survey (From Johnson, 1963).

Figure 2.3 shows that the western escarpment is sloping steeply in a sequence of benches and falling to the plains over which the River Eden flows. To the east of the Reserve, the moorland is sloping gently. The glacial till overlies on the gently sloping eastern plateau where drainage is poor and develops surface of blanket bog with peat (Johnson, 1963). Channels incise into the peat and bedrock, and carry tributaries into the Tees, which pass through the valley bottom. The underlying rocks are Carboniferous in age, with alternating layers of limestone, sandstone, and shale; with intrusion of the Great Whin Sill of quartz dolerite (Johnson, 1963). The Ordovician shales and slates outcrop at the foot of western escarpment are part of the Palaeozoic succession of Cross Fell Inlier. The summit ridge of the escarpment is formed by the tops of Great Dun Fell, Little Dun Fell and Knock fell which are continuous with Cross Fell.

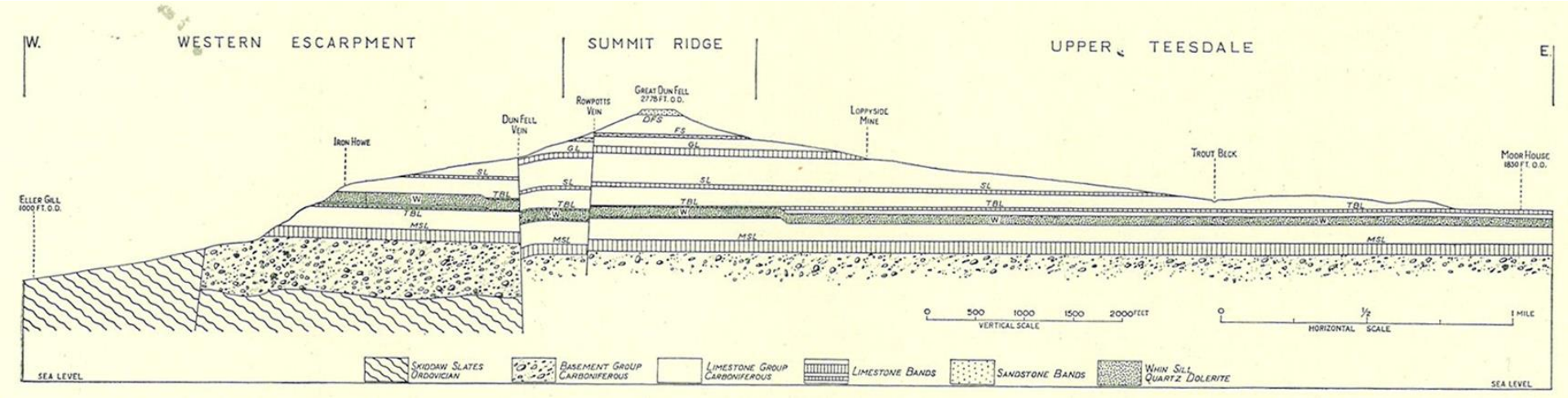

Figure 2.3. Generalised section of the Moor House Nature Reserve showing the disposition of the geological formations and location of Trout Beck (From Johnson, 1963).

The summit ridge divides the watershed; it drains to the Tees in the east and to the Eden in the west. To the east of the summit ridge, a long spur 'Knock Ridge' runs into the Tees valley, and is the southern boundary of the reserve. The Tees is the northern boundary of the reserve. Another ridge runs to the east from Great Dun Fell and divides the drainage of the Tees from Trout Beck. Within the reserve area the outcropping of almost all the strata of the Carboniferous sequence of the North Pennines are visible, and Great Dun Fell is the only place where the continuous layers of the upper part of the Carboniferous rocks in the region are exposed. Several mineral layers of lead, zinc, fluorite and barytes are exposed on the reserve. Glacial deposits of boulder clay and moraine gravels including moraines are present in the region about the reserve, including the moraines produced by the last glaciation of the Pennines that only ended some 10,000 years ago (Johnson, 1963). Historically this area was considered of high economic value because of sheep grazing, mineral deposits and large limestone quarries. A geological map of Moor House NNR is shown in Figure 2.4 and the geological sequence of the reserve comprises overlying superficial and underlying solid formations in Table 2.1.

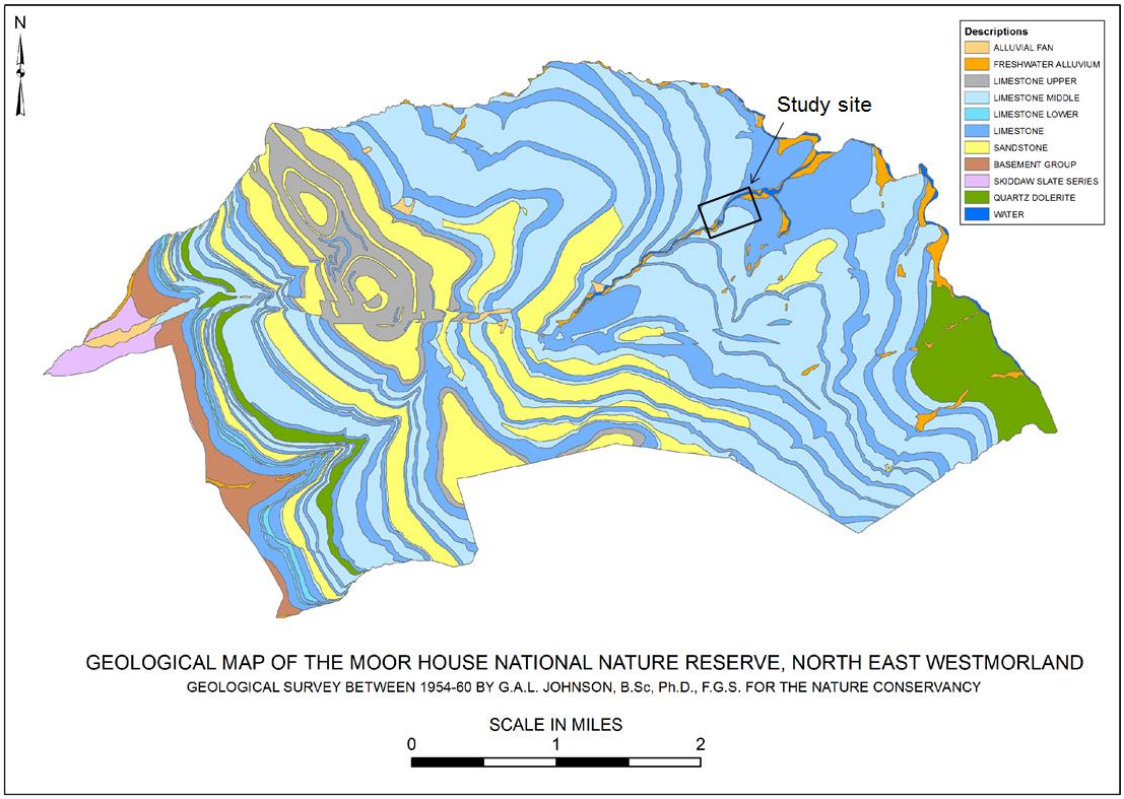

Figure 2.4. Geological map of the Moor House NNR (adapted from Johnson, 1963). Map prepared by C.M. Wood, Centre for Ecology & Hydrology (CEH), version 1, 6/12/2013.

Table 2.1. Geological sequence of Moor House NNR (From Johnson, 1963).

Superficial formations	Solid formations
Recent and post glacial Blanket-peat, basin-peat, alluvium, and alluvial fans *Glacial and Periglacial* Solifluxion deposits (sandy and strong clays), and boulder clay	*Upper Carboniferous* Upper Limestone Group: sandstone, grits and shales with coal seams and limestone bands *Lower Carboniferous* Middle Limestone Group: a rhythmic sequence of limestones, shales, sandstones and coal seams Lower Limestone Group: massive limestone overlain by thin bands of shale, sandstone and limestone *Basement Series* Upper division: sandstone and shales with thin limestones. Lower division: massive conglomerates with inter-bedded sandstones *Ordovician (great unconformity)* Skiddaw Slate Series: slates, flags, tuffs and lavas

Table 2.1 shows that Trout Beck study site geology belongs to the Lower Limestone Group of Lower Carboniferous sequence that includes massive limestone overlain by thin bands of shale, sandstone and limestone. These rocks provide a base for glacial boulder clay at the site. The surface geology comprises periglacial deposits of reworked till and overbank deposits that are covered by blanket peat of 1 to 3 m thickness (Warburton & Evans, 2011). This clay impedes drainage contributing to the development of blanket peat which covers, 90% of the reserve in thicknesses up to 3 m deep (Holden & Burt, 2003). Warburton and Evans (2011) found that peat blocks are widespread and they contribute notably to the channel roughness and control the channel sedimentation. Demir (2000) found that about 95% of the sample bed materials on Trout Beck are sandstone and remaining 5% are shales and limestones.

2.2 Climate and hydrology

Professor Gordon Manley started the climatological recording at Moor House in 1932 and a full climatological office started in 1952 (Manley, 1936; Rawes, 1981). The climate in Trout Beck catchment is cold and wet and has been variously described as sub-alpine and Atlantic (Eddy *et al.*, 1968), sub-arctic oceanic (Evans *et al.*, 1999). The rainfall quickly converts into runoff and the site hydrograph is typically flashy (Evans *et al.*, 1999). The North Pennines moorland comprises some of the coldest places in the

England and there occur occasional unusually violent thunderstorms and the well-known “helm wind” (Manley, 1936). Strong winds are experienced on the exposed moors all year round. The water logged soil with peats is common in this wet climate environment.

The Environment Change Network (ECN) monitors the terrestrial and freshwater measurements in Moor House – Teesdale NNR. The meteorological station (Grid ref. NY 757328) is at Moor House (556 m) (Holden & Adamson, 2002) and the discharge monitoring station (Grid ref. NY 758 335) is at Compound Crump weir on Trout Beck (535 m). The measurements at Moor House include hourly automatic weather (meteorological) data which are validated every week by manual measurements, stage and discharge measurements every 15 minutes, hourly record of stream temperature etc.

2.2.1 Temperature

The temperature at Moor House is low and the winters are harsh as most winters record the temperatures below -15 ^{0}C (Holden, 2000). The long-term average temperatures at Moor House station as reported by Holden and Adamson (2002) are: 5.2 ^{0}C for 1931 – 1952, 5.3 ^{0}C for 1953 – 1979, 4.9 ^{0}C for 1980 – 1990, and 5.8 ^{0}C for 1991 – 2000 which shows that the temperature for the period 1991-2000 was significantly warmer but Garnett *et al.* (1997) claims that the Moor House record up to 1995 gives no evidence for significant change in the temperature. The 21 years of recent data (1991 – 2011) of maximum, minimum and mean temperatures at Moor House are plotted in Figure 2.5 and also shown in Table 2.2.

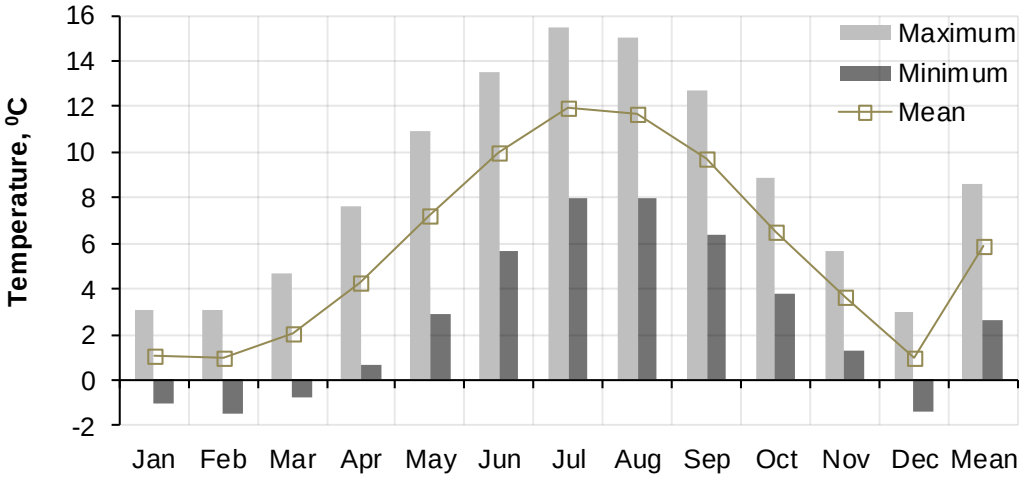

Figure 2.5. Maximum, minimum and mean monthly temperatures at Moor House for 1991 – 2011. (Data downloaded on 20.12.2015 from ECN site: http://data.ecn.ac.uk/tsv/results_datatables.asp?mcode=MA).

Table 2.2. Maximum, minimum and mean monthly temperatures at Moor House for 1991-2011. (Data downloaded on 20.12.2015 from ECN site: http://data.ecn.ac.uk/tsv/results_datatables.asp?mcode=MA).

Months	Monthly temperature, ^{0}C (1991-2011)		
	Maximum	Minimum	Mean
Jan	3.0	-1.1	1.1
Feb	3.1	-1.5	1.0
Mar	4.7	-0.7	2.1
Apr	7.6	0.6	4.3
May	10.9	2.9	7.2
Jun	13.5	5.7	10.0
Jul	15.5	8.0	12.0
Aug	15.0	8.0	11.7
Sep	12.7	6.4	9.7
Oct	8.9	3.8	6.5
Nov	5.6	1.3	3.6
Dec	3.0	-1.4	1.0
Mean	*8.6*	*2.7*	*5.8*

The mean seasonal temperatures are: 11.2 ^{0}C for summer (Jun – Aug), 6.6 ^{0}C for autumn (Sep – Nov), 1^{0}C for winter (Dec – Feb), and 4.5 ^{0}C for spring (Mar – May); and the mean annual temperature is 5.8 ^{0}C (Table 2.2). In the winter months the day time mean maximum temperature rises to 3.1 ^{0}C and the night time mean minimum drops down to -1 to -1.5 ^{0}C. The mean minimum temperatures are below 0 ^{0}C in December to March and the highest mean maximum temperature occurs in July – August.

2.2.2 Precipitation

The rainfall at Moor House is high. According to Holden (2000), the mean annual precipitation based on historical data for 1953 – 2000 is 1 953 mm, with 240 average rainfall days in a year, and the total rainfall varies year to year from 1 345 mm in 1971 to 2 930 mm in 1979. The mean annual rainfall for 1991 – 2012 is 2 065 mm; the rainfall ranges from 1 374 mm in 2010 to 2 763 mm in 2000 as shown in Figure 2.6a and Table 2.3. Similarly, the mean monthly rainfall at for 1911 – 2011 is 170 mm; the rainfall ranges from 100 mm in June to 233 mm in November.

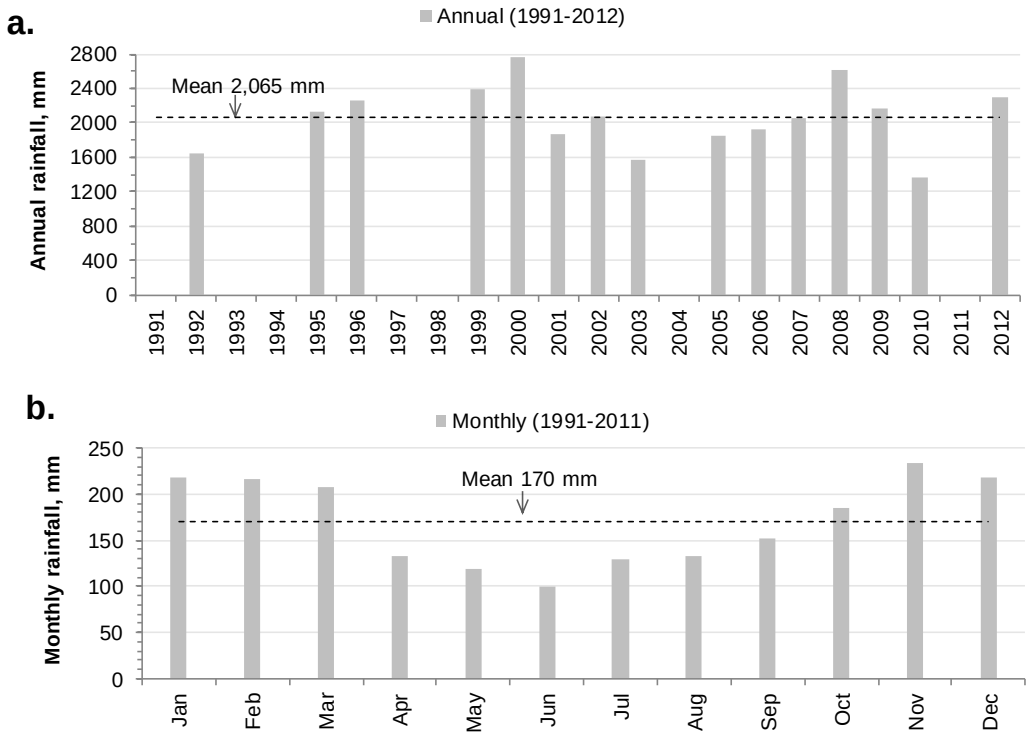

Figure 2.6. Rainfall at Moor House: a) mean annual; b) mean monthly.

Table 2.3. Mean annual and monthly rainfall at Moor House. (Data downloaded on 20.12.2015 from : http://data.ecn.ac.uk/tsv/results_datatables_annual.asp?mcode=MA).

Annual rainfall, mm (1991-2012)			
1991	-	2002	2078
1992	1640	2003	1561
1993	-	2004	-
1994	-	2005	1844
1995	2126	2006	1922
1996	2261	2007	2063
1997	-	2008	2617
1998	-	2009	2173
1999	2388	2010	1374
2000	2763	2011	-
2001	1867	2012	2294
Mean			*2065*

Monthly rainfall, mm (1991-2011)	
Jan	219
Feb	216
Mar	207
Apr	132
May	119
Jun	100
Jul	129
Aug	132
Sep	151
Oct	184
Nov	233
Dec	219
Mean	*170*

A significant amount of winter precipitation in the higher areas of the Pennines falls as snow. The mean annual snow cover increases from 55 days at 500 m elevation to 100 days on the summits (Archer & Stewart, 1995). These figures are in agreement with the data from Moor House, the measured albedo for three consecutive years indicates that number of days of snow cover were 52, 59 and 45 in years 1995, 1996 and 1997

respectively; and the longest continuous period of snow at site in these three years period was 24 days from December to January in 1997 (Evans *et al.*, 1999).

2.2.3 Discharge at Trout Beck Environment Agency gauging station

The longitudinal concave profile of Trout Beck is shown in Figure 2.7. For the first 2.5 km from upstream the channel is narrow and steep (8%), after this the channel slope is gentle (Demir, 2000). The drainage density (3.57 km km^{-2}) in the catchment is high (Demir, 2000). Several small tributaries feed into the main stem of Trout Beck, among them Rough Sike (with Moss Burn), which joins 300 m upstream of the EA gauging station, contributes about one third of the drainage area.

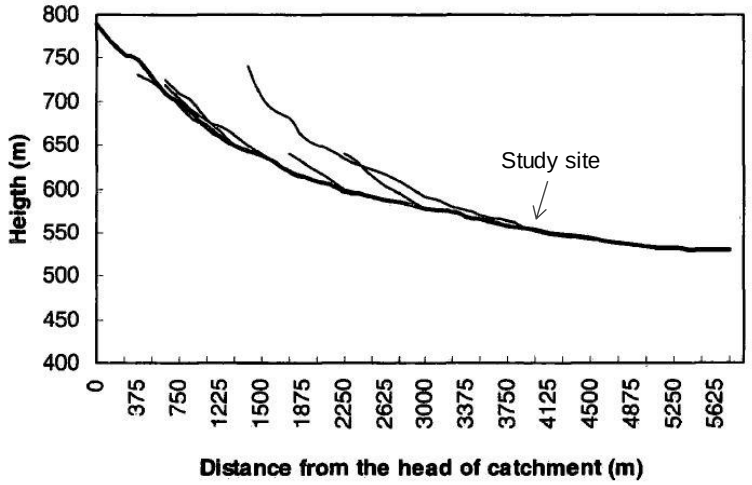

Figure 2.7. Longitudinal profile of Trout Beck and its major tributaries, based on 1: 25,000 Ordnance Survey Map. The thicker line is the main channel profile.(From Demir, 2000)

Trout Beck gauging station has a long record of discharge (*Q*) data. The daily discharge series (measured one time in a day) for 1957 – 1979 and quarter-hourly (measured every 15 minutes) series for 1991 – 2015 were made available for this study. The data gap in the discharge series between 1979 and 1991 represents the hiatus in monitoring between the end of the Nature Conservancy Council involvement at the site and start of the Environmental Change Network. Based on daily-mean data series for 1957 – 1979, the minimum and maximum annual peak discharges are 5 and 28 $m^3 s^{-1}$. But it is to be noted that the discharge values based on the daily-mean data will be lower compared to the 15 min data for the same period as the extreme discharges are lost in the averaging. Figure 2.8 plots quarter-hourly runoff data from the Trout Beck catchment during the study period and the flashiness of the stream response is obvious. The maximum, mean and minimum discharges at EA gauging station during the study period are 14.2, 0.61 and 0.01 $m^3 s^{-1}$ respectively.

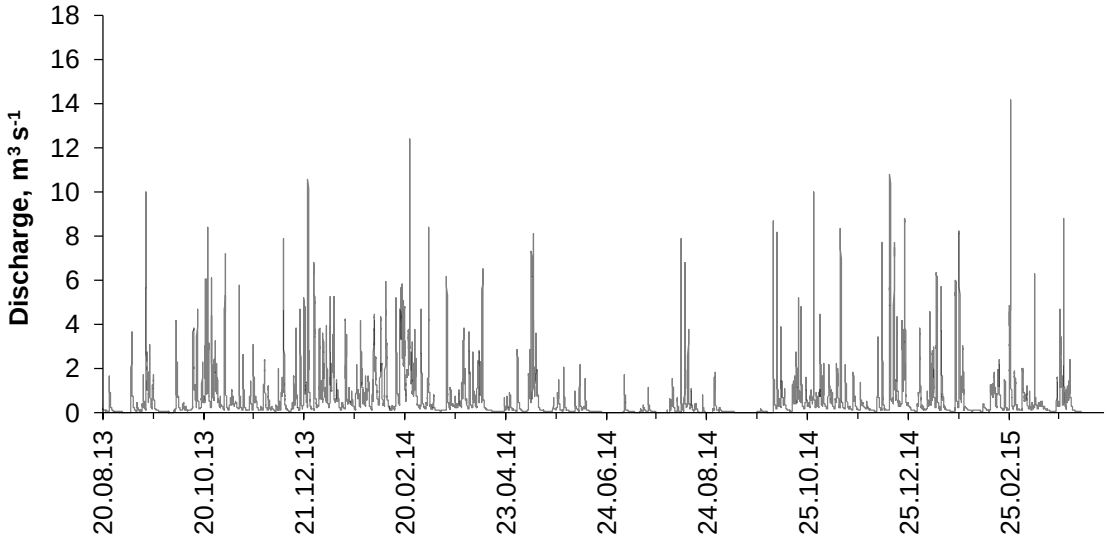

Figure 2.8. 15 min runoff at Trout Beck EA gauging station during study period.

Figure 2.9 plots a flow duration curve (FDC) from 15 min data series for 1991 – 2014, which shows the mean discharge (Q_m) is 0.62 $m^3 s^{-1}$. It also shows 75 % of the time the discharge is below Q_m, and 50 % of the time the discharge is below 0.20 $m^3 s^{-1}$ which indicates that there was a negligible amount of groundwater flow from the peat (Evans *et al.*, 1999).

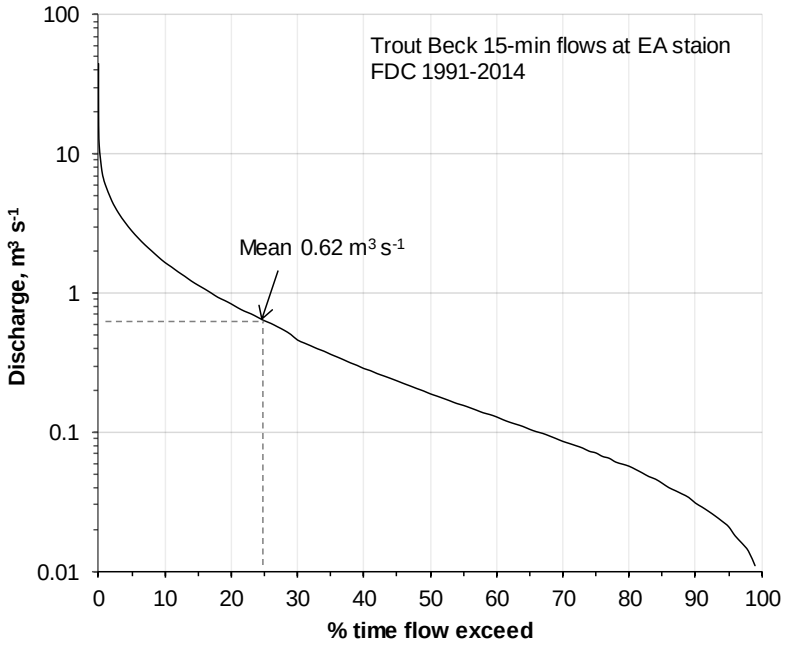

Figure 2.9. Flow duration curve (1991 – 2014) at EA station based on 15 min data. The mean flow 0.62 $m^3 s^{-1}$ exceeds 25% of the time as shown by the dashed line.

Evans *et al.* (1999) studied the runoff generation in Trout Beck catchment which shows a strong correlation of flow and rainfall, a high mean runoff ratio (% of catchment rainfall that becomes streamflow) of 40 % was observed, which was along the lines of

some previous works on blanket peats (Conway & Millar, 1960; Crisp, 1966). The high runoff ratio is because of the efficient transfer of water to the channel by quick overland flow or near surface storm flow (Burt *et al.*, 1997; Warburton *et al.*, 2004). Holden and Burt (2003) studied the catchment efficiency in relation to the runoff production in the different sized catchments on the peaty ground of Moor House and found that the lag times from mean rainfall peak to discharge peak were 2.7, 2.1 and 3.2 hours for the catchment area 11.4, 0.83 and 0.44 km^2 respectively. The mean lag time of 2.7 hours was very close to 2.8 hours as observed by Evans *et al.* (1999) for the same catchment. In Trout Beck, overland flow is dominant, hence the runoff is flashy, typically the overland flow contributes 80% of the runoff and the remaining contribution from upper 10 cm of the peat layer (Holden & Burt, 2003).

2.2.4 Scaled down discharge at study site

The drainage area at the upstream end of the bedrock gorge in the study site is 7.1 km^2, which is 62 % of the Trout Beck catchment defined at EA gauging station. This means the area above the fieldwork site is 38 % smaller. On the grounds of hydrological similarity it is reasonable to expect discharges at the gorge to be 38 % lower on average. Though this study collected the primary data from the site, the EA data have been used to check the measured data and fill any missing data gaps. The EA discharge data have been scaled down by a catchment area ratio (Hirsch, 1979) of 0.62 to obtain the discharge series for the study site (e.g. Hirsch, 1979). The flow duration curve (FDC) developed for the study site for 1991 – 2014 is presented in Figure 2.10.

The mean monthly discharges and annual maximum floods for EA station and the study site are plotted in Figure 2.11. These plots show that the maximum mean monthly flow at study site is 0.56 $m^3 s^{-1}$ in December and minimum is 0.2 $m^3 s^{-1}$ in November. Similarly the maximum and minimum annual peaks at site are 27.7 $m^3 s^{-1}$ (2002) and 6.3 $m^3 s^{-1}$ (2001) respectively.

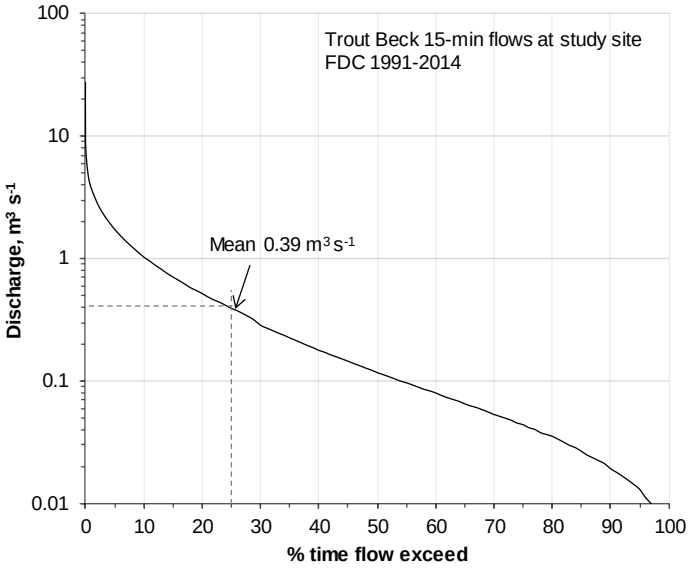

Figure 2.10. Flow duration curve for the 1991-2014 at study site based on scaled down quarter-hourly data. The mean flow 0.39 $m^3 s^{-1}$ exceeds 25% time of the year.

In Trout Beck high runoff is generated by heavy frontal rainfall or rapid snowmelt or both or sometimes by the thunderstorms. The largest floods in Moor House are related to rain-on-snow events, the recession limb of snowmelt flood hydrograph is less steep than the rain-driven flood hydrograph (Evans *et al.*, 1999). The time series of scaled down discharges for the study site for 1957 – 1979 (daily mean) and 1991 – 2015 (quarter-hourly) are shown in Figure 2.12.

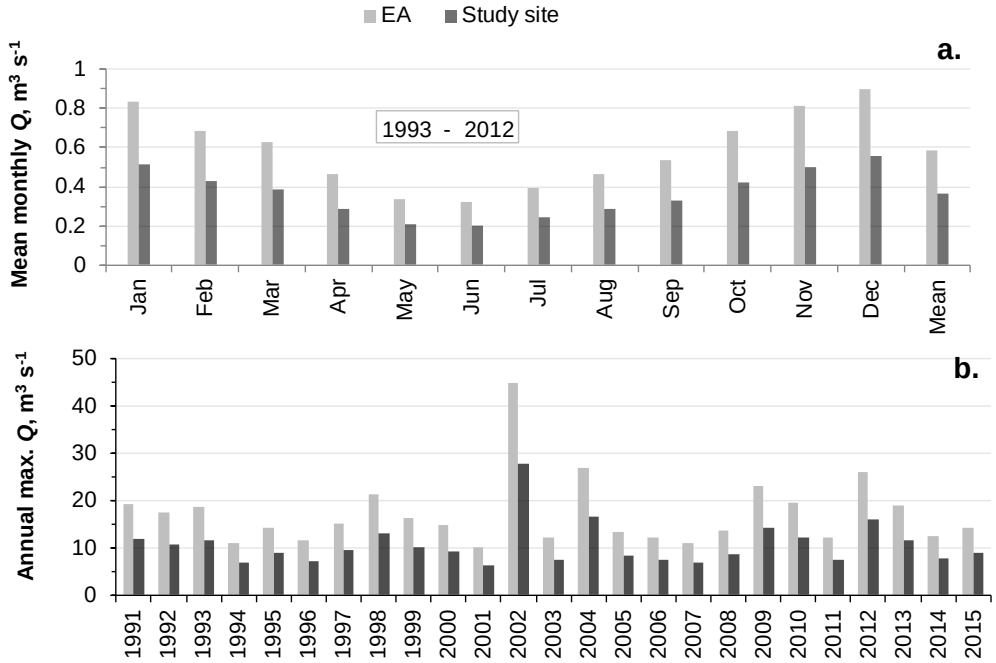

Figure 2.11. Trout Beck EA and scaled-down discharge for study site: a) mean monthly *Q for* 1993 – 2012; b) annual maximum *Q* for 1991 – 2015.

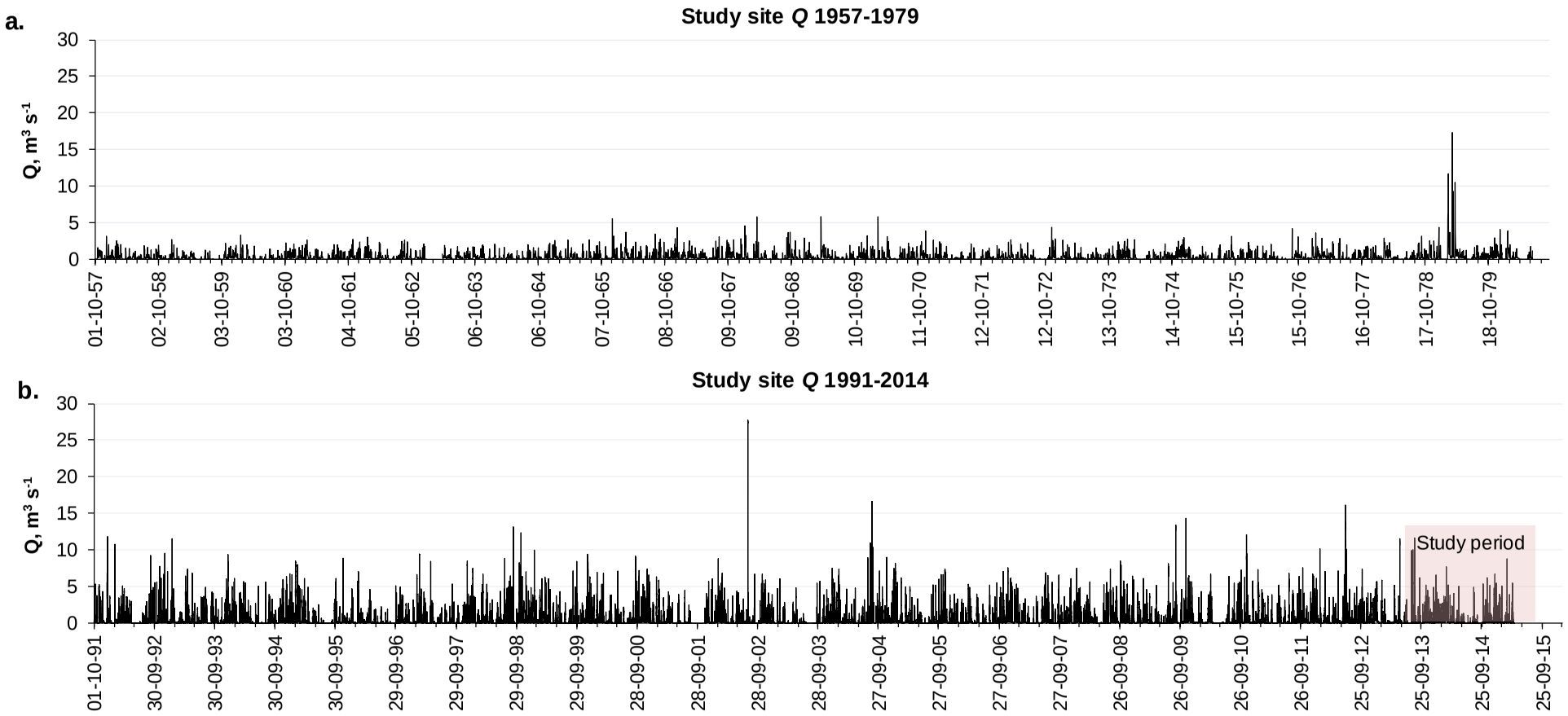

Figure 2.12. Trout Beck study site discharge data scaled down from EA data: a) daily flow series for 1957-1979, the maximum annual peak Q = 17.4 $m^3 s^{-1}$ on 25.03.1979; b) 15 min flow series for 1991 – 2015, the maximum annual peak Q = 27.7 $m^3 s^{-1}$ on 30.07.2002. The study period is marked.

Flood frequency and probabilities

The 25 years' annual maximum series (1991 – 2015) (Table 2.4) are used for the flood frequency and probability analysis; the pre-1980 daily data are not used as they are not comparable with the 15 min data (Figure 2.12). Figure 2.13 shows the Gumbel plot for the study site.

Table 2.4. Annual maximum discharges for 1991 – 2015 at EA station (Q_{EA}) and study site (Q_{site}). The maximum and minimum annual peak discharges are highlighted.

Year	Q_{EA} $m^3 s^{-1}$	Q_{site} $m^3 s^{-1}$
1991	19.1	11.8
1992	17.4	10.8
1993	18.6	11.6
1994	10.9	6.8
1995	14.3	8.8
1996	11.4	7.1
1997	15.2	9.4
1998	21.2	13.2
1999	16.2	10.0
2000	14.8	9.2
2001	10.3	6.4
2002	44.7	27.7
2003	12.1	7.5
2004	26.80	16.6
2005	13.25	8.2
2006	12.21	7.6
2007	11.10	6.9
2008	13.70	8.5
2009	23.1	14.3
2010	19.5	12.1
2011	12.2	7.6
2012	26.0	16.1
2013	18.8	11.7
2014	12.4	7.7
2015	14.2	8.8

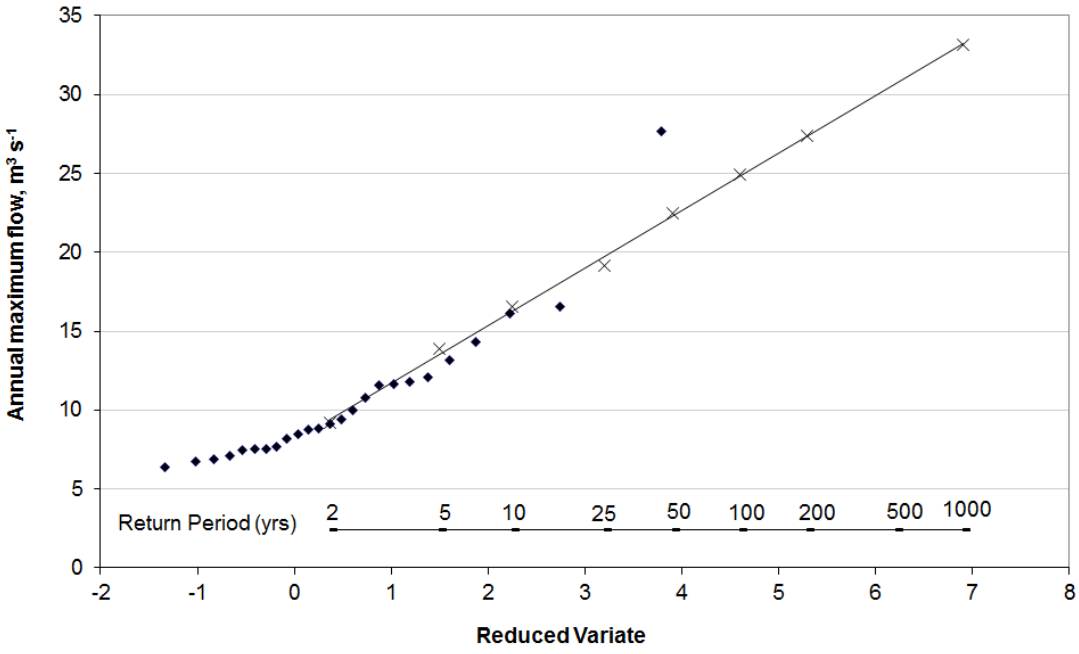

Figure 2.13. Flood frequency at study site (Gumbel plot).

The annual maxima values in Figure 2.13 are plotted using Gringorten formula and fitted with Generalised Extreme Value Type1 (GEV1), also called as Gumbel

distribution (Shaw, 1994) and is a commonly used method for flood frequency analysis in the UK (Castellarin *et al.*, 2012). Flood frequency analysis includes the estimation of peak discharge which is likely to be equalled or exceeded once in a specified period, called as return period or recurrence interval (Shaw, 1994). The estimated *Q* for various return periods are summarised in Table 2.5 which shows that the 2-year return period (median annual Q_{MED}) flood is 9.1 $m^3 s^{-1}$ for the study site and 14.7 $m^3 s^1$ for the EA station. The mean annual flood MAF (return period of 2.33 years) is 10.6 $m^3 s^{-1}$ for the study site and 17.2 $m^3 s^1$ for the EA station. The Gumbel plot suggests that the highest peak *Q* of 2002 (Table 2.4) is equivalent to the return period of 220 years.

Table 2.5. Return periods at study site (Gumbel method using annual peak discharges).

Return Period	Flow, $m^3 s^{-1}$
1	3.1
2	9.1
5	13.9
10	16.6
20	19.1
50	22.5
100	24.9
200	27.4
1000	33.1

Summary

The mean annual temperature in Moor House is low (5.8 ^{0}C), the winters are harsh, and it's a high rainfall area with mean annual precipitation 2,065 mm. The 25 years of quarter-hourly discharge data (1991 – 2015) are available for the nearby EA gauging station and on grounds of hydrological similarity the discharge series for the study site are obtained by applying the catchment area ratio of 0.62. The minimum and maximum annual peak discharges during 25 years of period are 10.2 $m^3 s^{-1}$ (2001) and 44.7 $m^3 s^{-1}$ (2002); the equivalent discharges scaled down to study site are 6.3 and 27.7 $m^3 s^{-1}$ respectively. The long term mean discharge for the EA station and study site are 0.62 and 0.39 $m^3 s^{-1}$ respectively. According to the GEV1 flood frequency analysis the median annual flood (2 year return flood) is 9.1 $m^3 s^{-1}$ and the highest flood of 2002 is equivalent to 220 years of return period.

2.3 Morphology of study reach

The morphology of the study reach was surveyed using the terrestrial laser scanning (TLS), and the channel cross-sections and longitudinal profile were carried out using differential GPS (dGPS). A brief methodology of TLS, dGPS survey and reach characteristics will be discussed in this section. Figure 2.14 shows a field measurement framework showing the field activities with the duration and frequency of measurements in order to address the research questions identified in chapter 1.

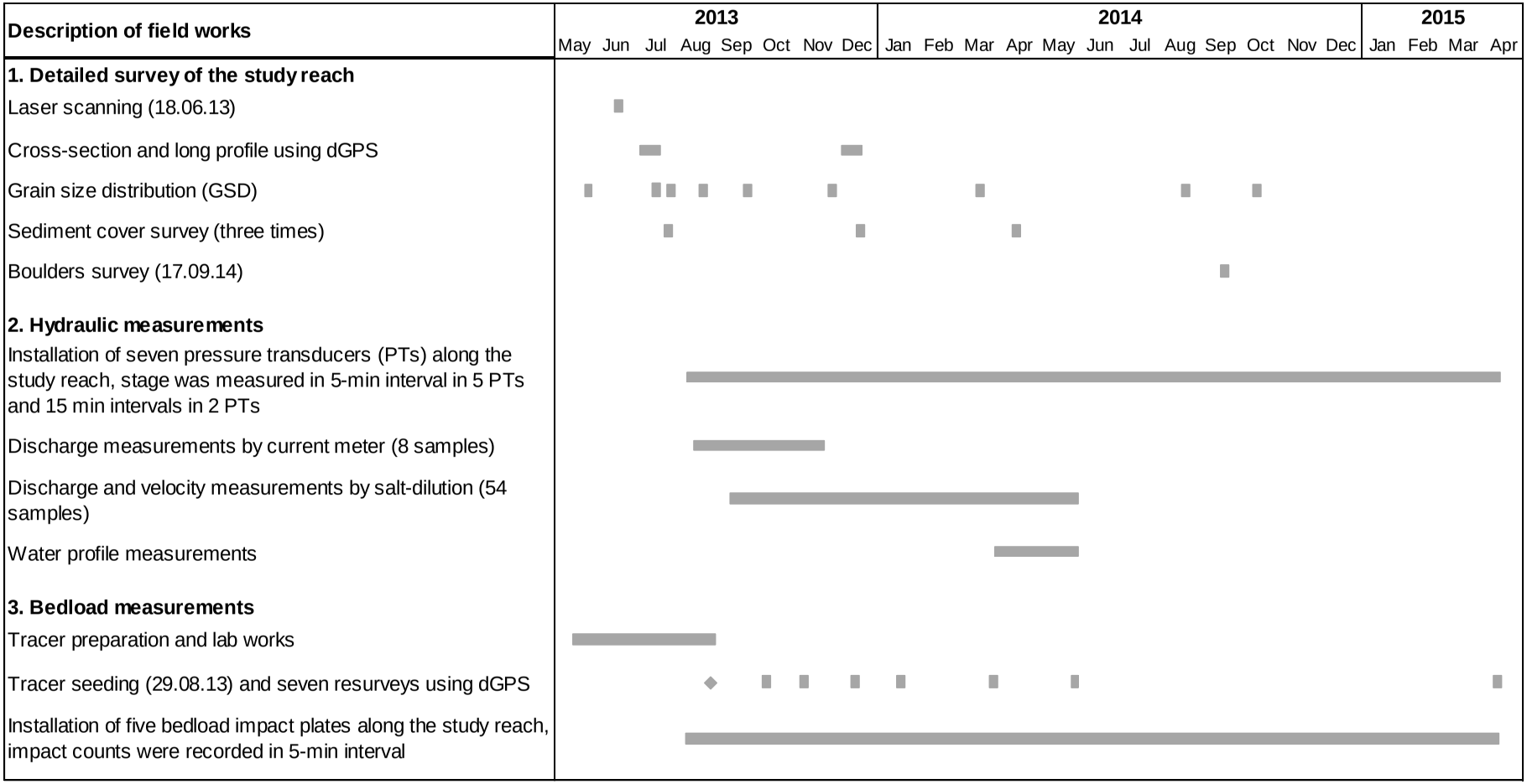

Figure 2.14. Field measurement framework showing the field activities, frequency and duration of measurements undertaken at Trout Beck study site over the period of two years. The methods related to the channel survey as shown in item 1 will be discussed in this chapter, whilst the methods for items 2 and 3 will be discussed in chapter 3.

2.3.1 Channel survey

Detailed topographic survey of the study reach using the terrestrial laser scanner RIEGL VZ – 1000 (Riegl, 2015) was carried out in June 2013. As TLS does not scan through water, the scanning was undertaken on a dry and low flow day to maximise the exposed bed area. A total of 10 scan positions and 10 target positions (reflectors/tie points) were chosen to cover the entire study reach; and at least four targets were used for each scan position to scan the data from all sides. The study reach with scan and target positions are indicated in Figure 2.15.

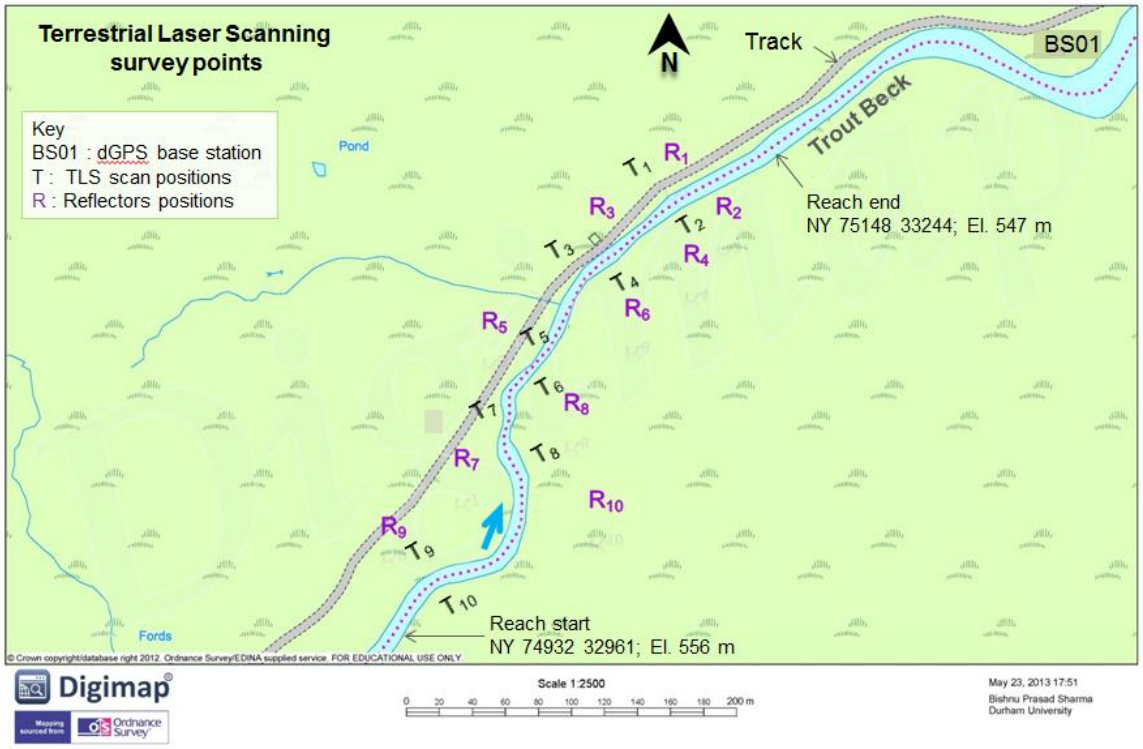

Figure 2.15. The survey points for TLS where BS01 is the dGPS base station, T_1 to T_{10} are scanner's positions, and R_1 to R_{10} are reflectors positions. The blue arrow indicates the flow direction. Start and end of the study reach with coordinates are shown.

The effect of channel geometry and different surface reflectivity was reduced by scanning each target, and subsequently the channel from multiple locations. The TLS records the topographic data at a high resolution with a precision and accuracy of 5 and 8 mm respectively for both vertical and horizontal measurements (Riegl, 2015). Accuracy is the closeness of a measured value to the true value whilst precision is the degree to which the repeated measurements give the same result. The post processing of the TLS data was carried out in RiSCAN PRO. Around 90 million points of the merged scan data from all 10 scan positions were reduced to 30 million by Octree filter process. The point cloud of the reduced number of points was further processed in RiSCANPRO, and also in ENVI, to prepare a 2.5 dimensional digital elevation model

(DEM). The DEM is shown in Figure 2.16 along with the longitudinal profile of the channel talweg. The DEM has been used to plot the data from tracer surveys, patch mapping, and to measure the distance and areas of a channel segments. The cover surveys (will be discussed in section 2.4.1) and visual observations indicated that during the two years' study period there were no significant floods to make any significant changes in the channel morphology; therefore the TLS survey was not repeated.

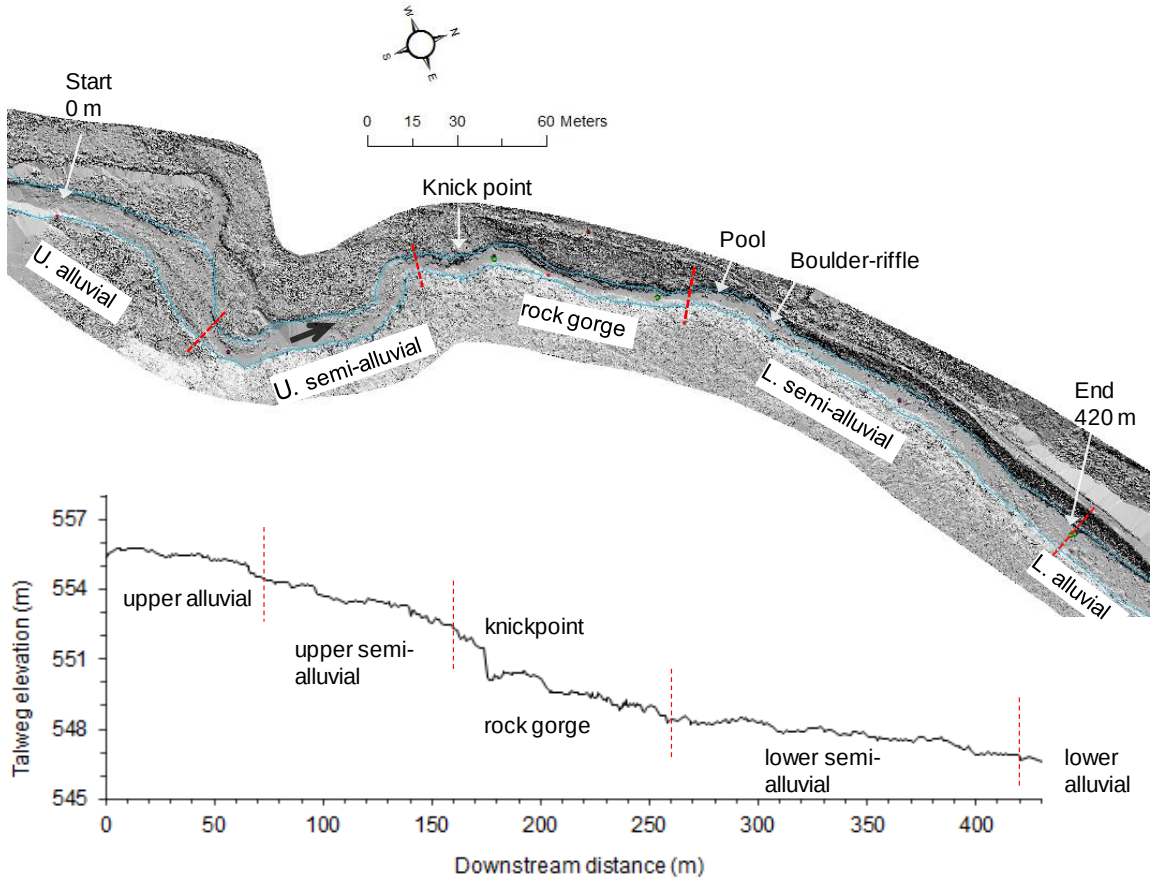

Figure 2.16. The digital elevation model (DEM) prepared from TLS showing sequence of contrasting reaches (marked by red lines) from upper alluvial, through upper semi-alluvial, to bare rock, lower semi-alluvial, and back to fully alluvial. The start (x = 0 m, where x is downstream distance) and end of study reach (x = 420 m); a knickpoint in the gorge; pool followed by a boulder-riffle in lower semi-alluvial are shown. The channel talweg long profile measured by dGPS is shown. The lower alluvial reach (fifth reach), though shown here, is outside the study reach (> 420 m).

A dGPS using Leica 1200 system (Leica, 2008) was used to set up the base station or survey benchmark and to record the coordinates of the TLS scan and target positions (Figure 2.15). The longitudinal profile of the study reach (Figure 2.16) and channel cross-sections which will be discussed in section 0 were surveyed using the dGPS. The accuracy of the dGPS was 10 mm + 1 ppm for horizontal and 20 mm +1 ppm for vertical measurements respectively (Leica, 2008).

2.3.2 Morphological reach characteristics

Based on the characteristics of the channel bed the study channel has been broadly classified into four distinct morphological reaches: upper alluvial, upper semi-alluvial, bare rock gorge and lower semi-alluvial reach. The 420 m long study reach (main focus area) with 2% average gradient does not include the lower alluvial reach as no detailed hydraulic measurements were carried out there. However, the grain size measurements and tracer searching activities were carried out also in that reach. These four morphological reaches are shown in Figure 2.17 and the reach characteristics based on the field surveys are presented in Table 2.6. There are five hydraulic sub-reaches: one in upper alluvial reach, one in bare rock gorge and three in lower semi-alluvial reach, which will be discussed in section 2.5. The channel section fully covered with alluvium is classified as alluvial reach, the section partly covered with sediments and partly with exposed rock is classified as semi-alluvial, and the section with exposed rock with no or very little sediment except in some hydraulically sheltered regions is classified as bare rock reach (rock gorge). There are no significant tributary inputs and so discharge can be assumed constant throughout.

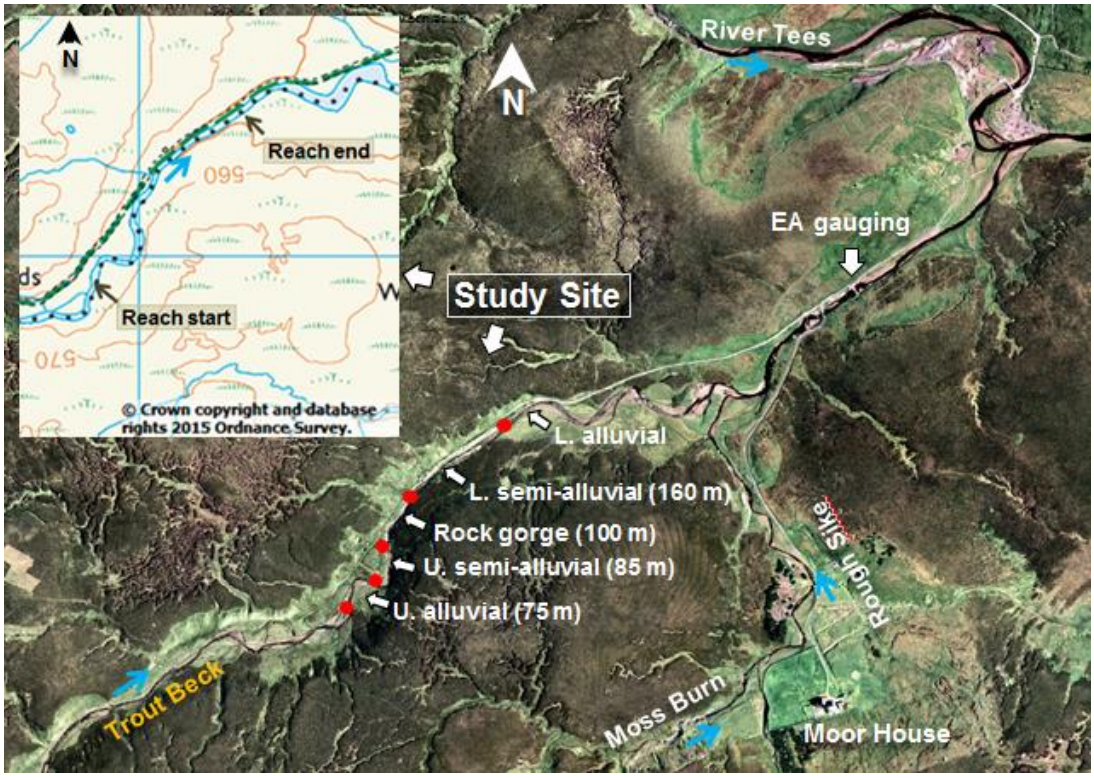

Figure 2.17. The 420 m long study channel showing upper alluvial, upper semi-alluvial, bare rock gorge and lower semi-alluvial reach. The red dots mark the boundary between the reaches. The EA gauging station ~800 m downstream of the study site is shown. A major tributary Rough Sike joins Trout Beck ~300 m upstream of EA station. Trout Beck joins River Tees ~370 m downstream of EA station. The inset map shows the contours and start and end of study reach with grid reference. The base map aerial photo was received from NERC.

Table 2.6. Morphological reach characteristics.

Study reach (Length)	Distance m	Average width m	Bed Slope (S_b)	Alluvial cover	Bed characteristics
1. Upper alluvial (75 m)	0 – 75	10.3	1.41 %	100 %	Fully alluvial, shallow banks
2. Upper semi-alluvial (85 m)	75 – 160	8.7	2.40 %	45 %	Fractured shale rock wall on the right bank and gravel bars on the left bank
3. Bare rock gorge (100 m)	160 – 260	5.9	4.15 %*	1 %	Shallow limestone gorge, narrow width, bare rock, rock walls
4. Lower semi-alluvial (160 m)					
a) Upper part (100 m)	260 – 360	5.7	0.70 %**	55 %	Comprises pool, boulders, and gravels. Rock walls on both sides >2/3rd length.
b) Lower part (60 m)	360 – 420	8.5	1.13 %	30 %	Exposed rock on ~2/3rd of the channel bed with dead zones/ cavities. Few boulders, gravels on ~1/3rd bed. Alluvial banks.
Total (420 m)	0 – 420		2.04 %		

* S_b between PT_3 and the bottom of rock gorge (192 – 260 m) is ~3.31%.

** S_b in the pool (260 – 285 m) is 0.04 % and in boulder-riffle (285 – 305 m) is 1.1 %.

The 75 m long upper alluvial reach is on average 10.3 m wide, 1.41% steep (Table 2.6) and comprises a big lateral gravel bar on the right bank (Figure 2.18). The upper semi-alluvial reach (85 m) immediately downstream of the alluvial reach is 2.40% steep and 8.7 m wide which contains some patches of sediment on the channel bed, two big exposed bars on the left bank (Figure 2.18) and a fractured shale and limestone wall on the right bank (Figure 2.21a).

Figure 2.18. Photograph showing the start of study reach, upper alluvial and upper semi-alluvial reaches. The line 1 (red) indicates the end of the upper alluvial and start of the upper semi-alluvial reach. Line 2 indicates the end of upper semi-alluvial and start of bare rock gorge. The black arrow indicates the flow direction. (Scale: Line 1 ~10 m).

Then the rock gorge (bare rock reach) starts which is about 100 m long, and on average 5.9 m wide and 4.15% steep (Figure 2.19). The channel drops about 1.5 m in knickpoint, near the head of the gorge, makes a small pool, then widens little bit but after a small rapid it becomes narrower again. It is a shallow (< 3 m) limestone gorge with almost no bed sediments except few in a plunge pool below the knickpoint and other small areas such as potholes, groves and troughs. The limestone rock walls in the gorge are nearly vertical and hydraulically rough as they have protrusions and re-entrants, but the channel bed is very smooth.

Figure 2.19. Photograph showing: a) upper part of the rock gorge showing the knickpoint and plunge pool. Line 2 indicates the end of upper semi-alluvial reach and start of the rock gorge; b) rock gorge and the upper part of lower semi-alluvial reach. Line 3 indicates the end of rock gorge and start of the lower semi-alluvial reach. (Scale: Line 3 ~5 m).

The channel enters the lower semi-alluvial reach at the bottom of the rock gorge but the rock walls still continue. Considering the proportion of sediment cover (or exposed rock) the lower semi-alluvial reach can be further divided into upper and lower part (Table 2.6). The 100 m long upper part with average width 5.7 m and gradient 0.70% (Figure 2.20a) includes pool, boulders and gravel section with almost similar proportion of sediments and exposed rock whereas the 60 m long lower part with average width 8.5 m and gradient 1.13% (Figure 2.20b) is largely covered with the exposed rock with lots of pot holes, groves and troughs and low sediment cover.

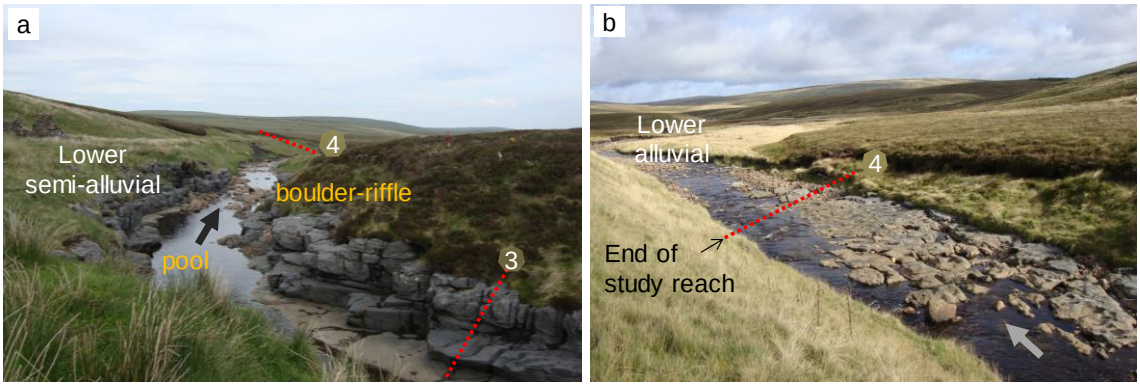

Figure 2.20. Photograph showing: a) upper part of lower semi-alluvial reach comprising pool, boulder-riffle and gravels zone; b) lower part of the lower semi-alluvial reach comprising significant exposed rock with pot holes and cavities. Line 4 indicates the end of semi-alluvial reach and start of the lower alluvial reach.

The first 20 m of lower semi-alluvial reach can be considered as a shallow 'pool' which is also a location for sediment storage and the next 25 m is a boulder-riffle zone with numerous boulders (*b*-axis > 256 mm) of up to 1.2 m diameter and is hydraulically rougher than the rock gorge (Figure 2.20a). The rock wall continues up to the end of the boulder-riffle on the left bank, and then an alluvial wall starts. On the right bank the rock wall continues further downstream, and channel expands to 8 – 10 m. The fully alluvial reach starts again after the lower semi-alluvial reach. Figure 2.21 shows some bank erosion along the study reach.

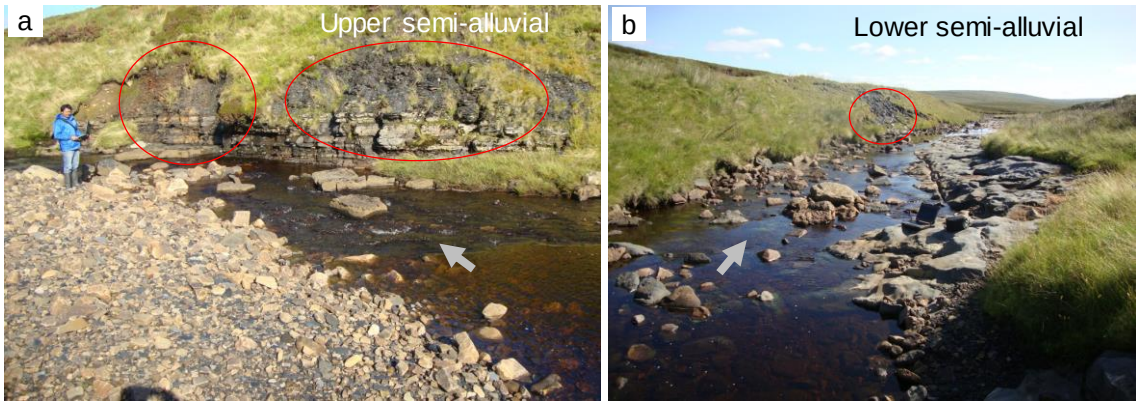

Figure 2.21. Photograph showing: a) fractured shale and limestone with an eroded area, a potential source of local sediment supply; b) the erosion on the left bank of the lower semi-alluvial reach.

The main source of sediment supply to the gorge and lower semi-alluvial reaches is the upstream alluvial reach. The upper semi-alluvial right bank is a fractured rock and some erosion is evident (Figure 2.21a). As the rock gorge is surrounded by rock walls there is no possibility of supply of material within the channel. In lower semi-alluvial reach there are occasional bank slips and erosion is on the left bank (Figure 2.21b). The

sediment cover is ~1% in the bare rock gorge while it varies from 30 – 55% in semi-alluvial reach; these percentages are based on the cover survey which will be discussed in next section 2.4.1.

2.4 Downstream variation in sediment cover and grain size distribution (GSD)

2.4.1 Sediment cover

From field observations it was evident that there was spatial variation in sediment storage in the study reach, therefore sediment cover surveys were carried out to investigate the variation of sediment cover along the study reach over time. The first cover survey was carried out in July 2013 which was repeated in December 2013 and April 2014. The cover surveys mapped the extent of the sediment patches in the bare rock and semi-alluvial reaches using dGPS. The depth of the sediment cover was measured using a metal rod as well as estimated by visual inspection; there was little sediment in the gorge but in the semi-alluvial reaches the cover depth was shallow, typically about a grain size. The dGPS points from the cover survey are plotted in DEM and percentage sediment cover for every 10 m downstream distance is calculated. The plan area of the sediment patches and the channel bed was measured from DEM. Figure 2.22 shows the cover maps of 31st July 2013, 17th December 2013 and 10th April 2014 illustrating the sedimentation pattern in bare rock and semi-alluvial reaches. These three maps are largely similar in terms of the extent and the pattern of sedimentation and percentage cover.

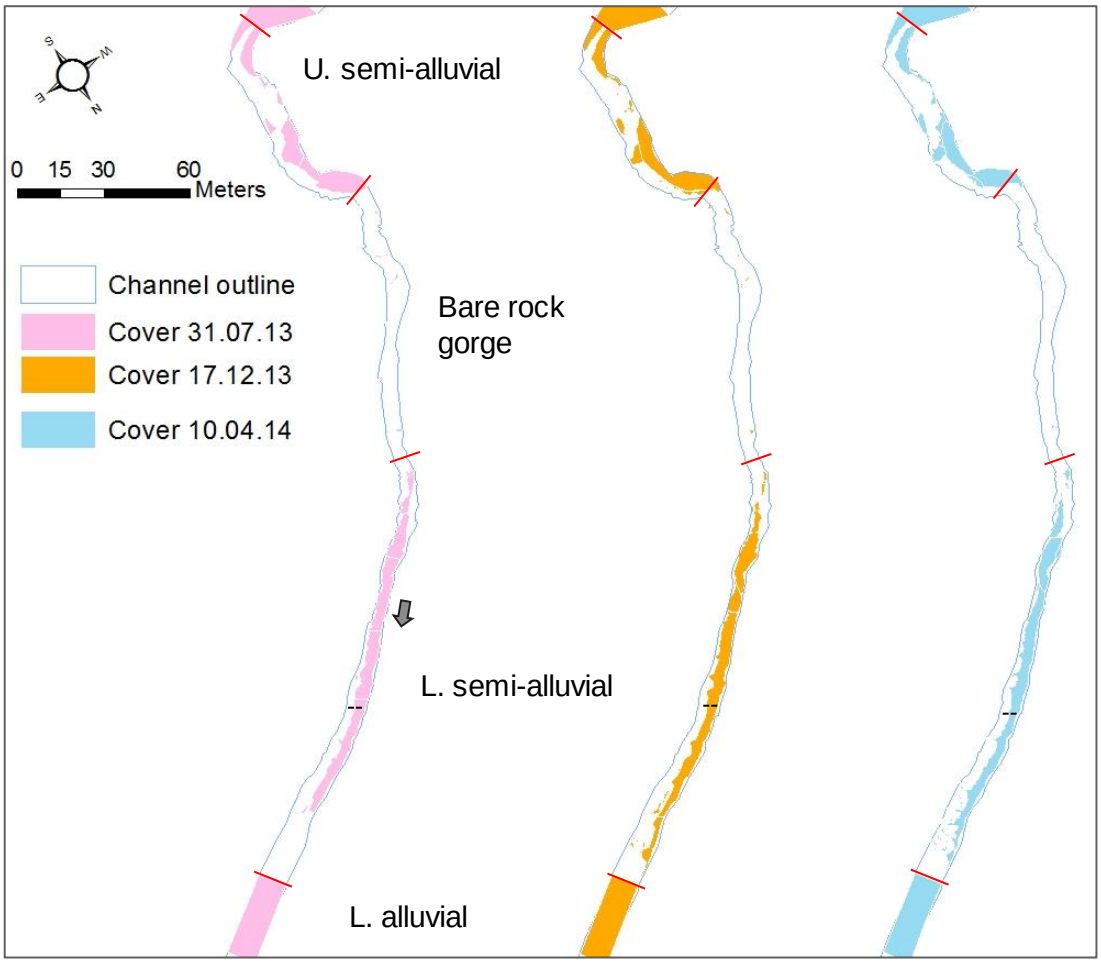

Figure 2.22. Cover maps as of 31.07.13 (pink), 17.12.13 (orange) and 10.04.14 (blue). Red lines show the reach boundaries, and a dotted black line separates the upper and lower parts of the lower semi-alluvial reach. The arrow indicates the flow direction.

Figure 2.23 shows a detailed map of the sedimentation on 10th April 2014 along the study reaches and the % cover is also plotted in Figure 2.24. The upper semi-alluvial reach has 45% cover which comprises gravels, pebbles and boulders and the exposed bars on the left bank. The bare rock gorge was almost free of sediment (1% cover) except few small patches in deep areas, grooves and troughs. The overall percentage of sediment cover in lower semi-alluvial reach is 45% of which the upper part (pool, boulder-riffle and gravel bed; total length 100 m) has 55% while the lower part (mostly gravels and rough exposed rock) has 30% cover. The upper and lower alluvial reach are fully covered (100%).

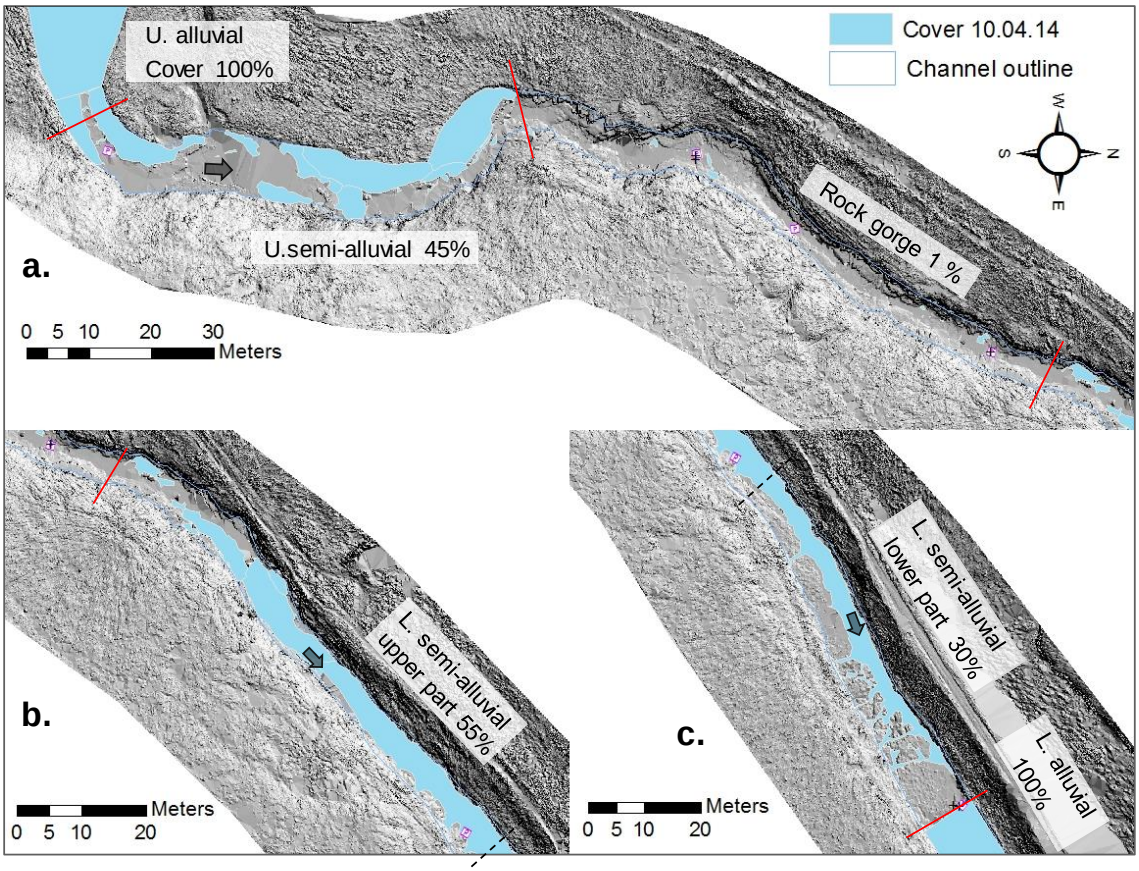

Figure 2.23. A DEM showing sediment cover (blue area) as of 10th April 2014. The red line shows the reach boundaries and arrow shows the flow direction: a) the cover in upper alluvial, upper semi-alluvial and rock gorge are 100%, 45% and 1.0% respectively; b) the upper part of the lower semi-alluvial reach (marked by black dashed line) has 55% cover; and c) the lower part of the semi-alluvial reach has 30% cover.

Figure 2.24 shows the percentage cover decreases rapidly as it starts the upper-semi alluvial reach, then rises again because of the exposed bars, but drops again to almost zero when it enters the rock gorge. The cover rises again as it starts the lower semi-alluvial reach and reaches the peak (86 %) at the boulder-riffle and drops to almost zero near the end of the lower semi-alluvial reach. The results from previous two surveys are very similar to this, therefore are not included here.

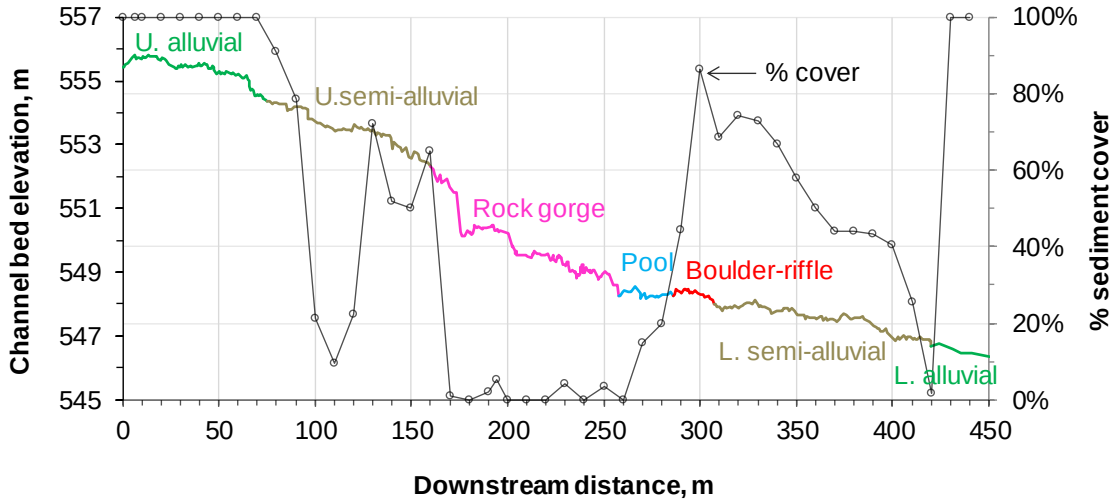

Figure 2.24. Plot showing % cover as of 10th April 2014 (black line with markers) and long-profile of the talweg: alluvial (green), semi-alluvial (grey), bare rock (pink), pool (blue), and boulder-riffle (red).

Figure 2.25 compares the latest cover map with the historical maps of 2002-03 (Smith, 2004) and 2009 (Cray, 2010). Figure 2.26 shows the long-term discharge series showing the dates of current and the historical cover maps. Looking at the 2002-03 maps the sediment patches mainly from the boulder-riffle area were gradually developed over the period of six months from Nov 2002 to May 2003. A major flood of 27.7 $m^3 s^{-1}$ at study site (~220 years return period, section 2.2.4) in July 2002 stripped sediment cover from the gorge, but partial cover re-formed within one year. Since then there has been no major flood. Figure 2.25 shows that the latest map of April 2014 is not greatly dissimilar to the map of 2009 which suggests that there has been no major evacuation of sediment from the study reaches after the extreme event of 2002. This indicates that Trout Beck is flood cleaning stream that evacuates sediment during extreme flood events, while material is deposited during small and intermediate events (Turowski *et al.*, 2013).

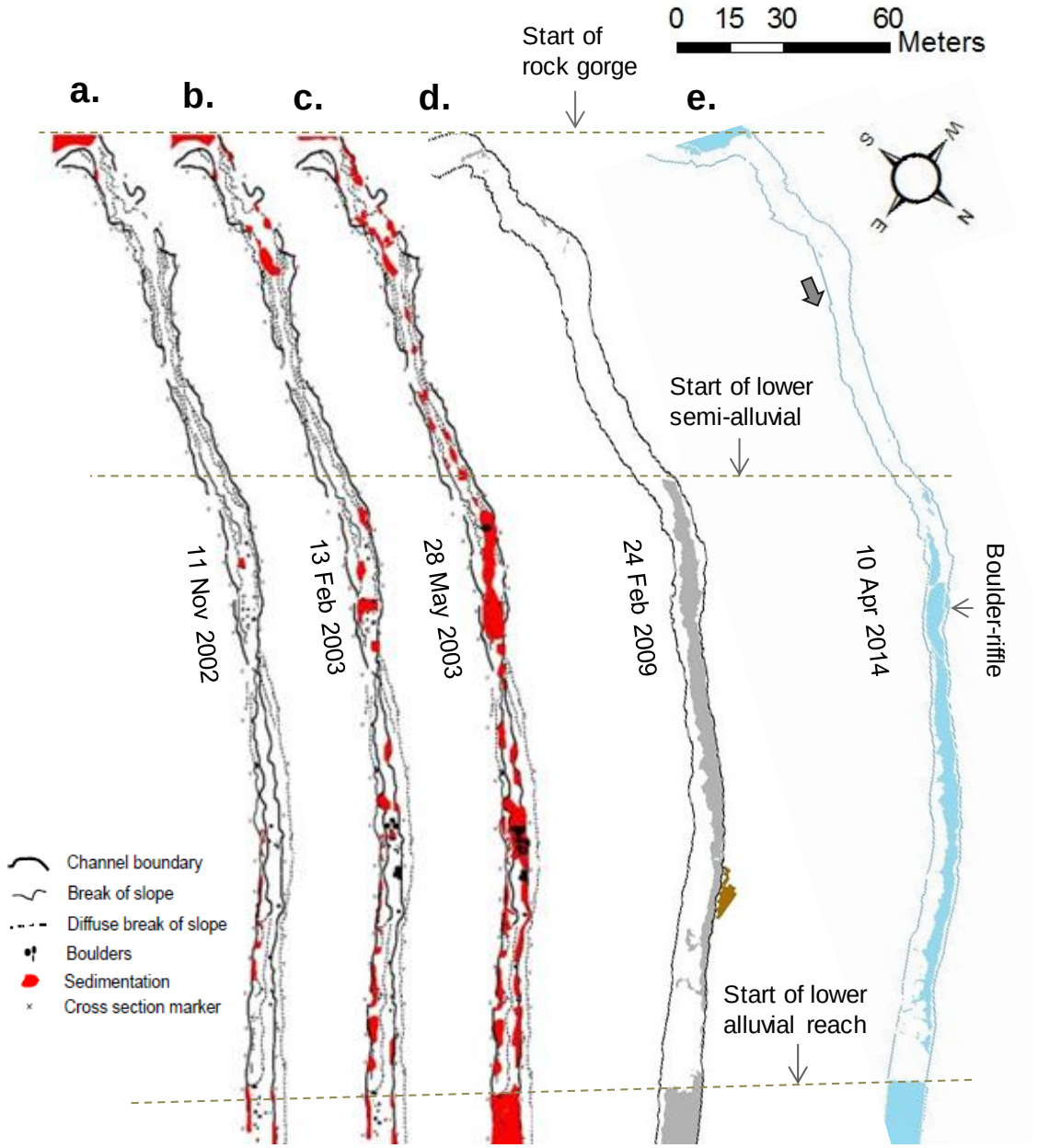

Figure 2.25. Historical and current maps showing variation in sediment cover: a) maps of Nov 2002, Feb 2003 and May 2003 (From Smith, 2004) showing evolution of the patches over time after a big event of July 2002; b) Feb 2009 map (From Cray, 2010) indicating there were no major changes since 2003; c) latest map of Dec 2013 (this study) suggesting no major changes since 2003.The sedimentation in historical maps and current map are in different colours (red, grey and blue).

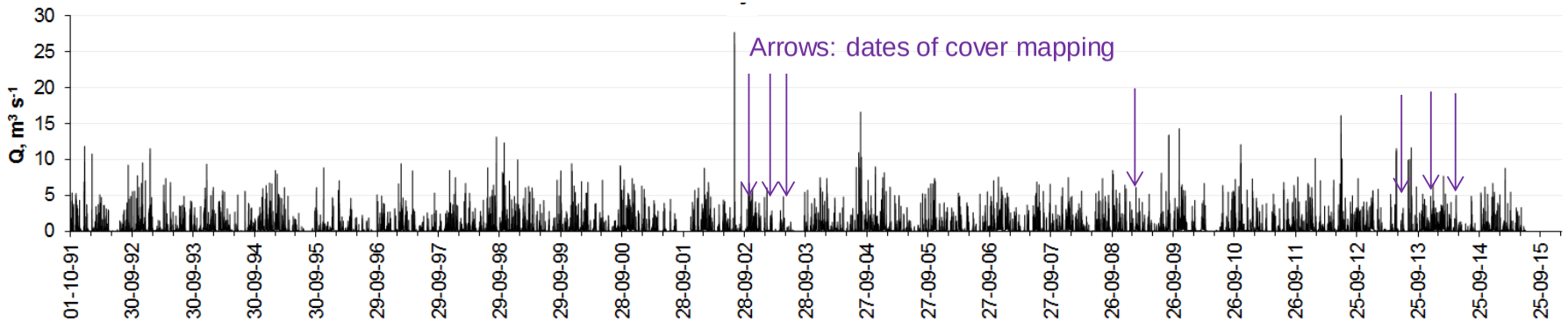

Figure 2.26. Discharge series at study site for 1991 – 2015 showing the current and historical cover mapping dates: first 3 arrows indicate Nov 2002, Feb 2003 and May 2003 surveys carried out by Smith (2004), the middle arrow indicates the Feb 2009 survey undertaken by Cray (2010) and the last three rows show the surveys carried out for this study in Jul 2013, Dec 2013 and Apr 2014..

2.4.2 Grain size distribution (GSD)

The general sizes of the sediment in the channel are explained by the grain size distribution. The GSD measurement of the exposed bars and the bed sediment was undertaken using Wolman pebble count method which requires 100 grains to be sampled at random at each site to accurately quantify pebble distributions (Wolman, 1954). The 20 m length of a measuring tape was spread over the area where the grains were to be measured, and one grain lying on every 20 cm interval was hand-picked and measured at half-phi intervals using a gravelometer. The tape was spread either laterally and/or longitudinally or in a zigzag pattern to make the sample most representative for the site. The grain sampling was repeated in few of the sites to assess how the GSD varied in the reach over time. However, the resampling at dates 18.11.13 and 24.10.14 in upper alluvial reach; at dates 31.07.13, 18.11.13 and 24.03.14 in upper semi-alluvial reach; at dates 31.07.13, 19.08.13 and 22.09.13 in lower semi-alluvial reach; and at dates 30.05.13, 16.07.13 and 24.03.14 in lower alluvial reach showed little variation over time. The measurements were carried out both in river bed and exposed bars. The bars are formed from the transported sediment, therefore they are also considered as a proxy for the channel bed sediment. Figure 2.27 shows the location of 14 sites from where 19 samples of the surface grains were collected in eight different dates; the photographs taken during the GSD measurements are shown in Figure 2.28.

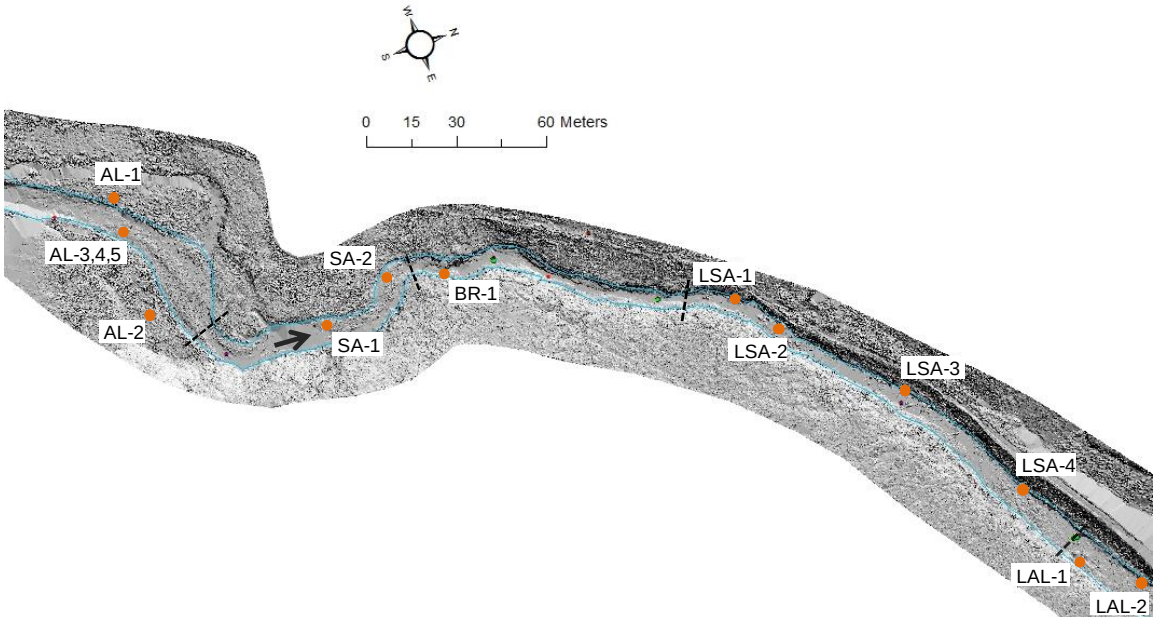

Figure 2.27. The study reach showing the locations of the grain size measurements (orange circle).The AL-1 to AL-5 are the measurements from upper alluvial reach; SA-1 and SA-2 from upper semi-alluvial; BR-1 from rock gorge; LSA-1 to LSA-4 from lower semi-alluvial; and LAL-1 and LA-2 from lower alluvial reach.

Figure 2.28. Photographs taken during GSD measurements and show the sample locations: a, b) upper alluvial; c, d) upper semi-alluvial; e) rock gorge; f to i) lower semi-alluvial; and j) lower alluvial reach with a gravelometer used to measure GSD. Black arrow shows flow direction.

These measurements cover all reaches in the study site. Out of total 19 measurements, six were taken from the submerged bed which include three from upper alluvial (AL-3, AL-4, AL-5) and three from lower semi-alluvial reach (LSA-2, LSA-3, LSA-4). Other 13 samples were measured from the exposed bars which will also be under water at moderate to high flows. The graphical plots of cumulative percentage finer against the

grain sizes for different reaches along with the values of D_{16}, D_{50} and D_{84} are shown in Figure 2.29 which are also summarised in Table 2.7. The only one sample collected from the rock gorge was BR-1 which was measured in a small bar of fine particles (Figure 2.28e). There were some other patches of few grains on the gorge but they were not enough (<< 100 clasts) to calculate the GSD. A sample from the plunge pool below the knickpoint shows that 16 out of 20 grains were in the range 45 to 90 mm size. Therefore the BR-1 sample is not considered a representative sample for the gorge, hence is not shown in Figure 2.29 and further analysis including the overall average (Figure 2.29e).

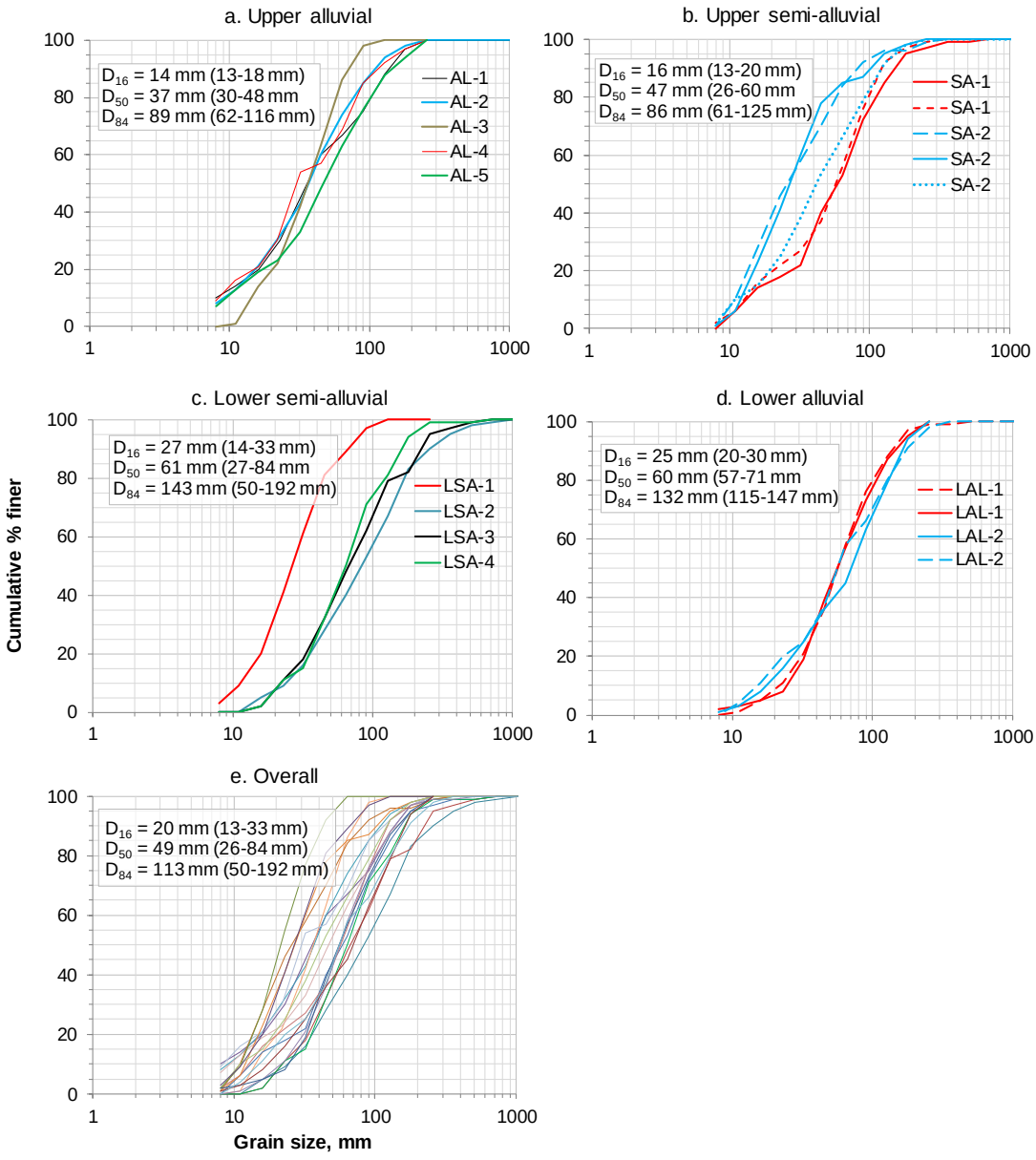

Figure 2.29. Grain size distribution along the study reaches: a to d) GSD plots for different reaches along with the average value (the range in brackets) for D_{16}, D_{50} and D_{84}. The LSA-1 is finer than other samples in lower semi-alluvial reach (c); e) plots from all the reaches showing the overall average values.

Table 2.7. Summary of GSD for different reaches along the study reach. Sorting coefficient σ (φ units) according to Folk and Ward (1957) is shown.

Reach	D_{16}, mm		D_{50}, mm		D_{84}, mm		Sorting coefficient σ
	Range	average	Range	average	Range	average	
Upper Alluvial	13-18	14	30-48	38	62-116	94	1.3
Upper Semi-alluvial	13-20	16	26-60	43	61-125	93	1.2
Lower semi-alluvial	14-33	27	27-84	61	50-192	143	1.2
Lower alluvial	20-30	25	57-71	60	115-147	132	1.2
Overall	13-33	20	26-84	49	50-192	113	1.2

The measured data show a wide range of grain sizes in the study site. The ranges of values for the entire study site are D_{16} = 13 to 33 mm, D_{50} = 26 to 84 mm, and D_{84} = 50 to 192 mm, and the overall average values are D_{16} = 20 mm, D_{50} = 49 mm, and D_{84} = 113 mm (Table 2.7). Across the reaches the D_{16} has a narrow range but the D_{50} and D_{84} have wide ranges. The D_{50} for alluvial, upper semi-alluvial, lower semi-alluvial and lower alluvial reaches are respectively 37, 47, 61 and 60 mm; and D_{84} are 89, 86, 143 and 132 mm respectively. The cumulative grain size distributions for upper alluvial and upper semi-alluvial are very similar and so are the lower semi-alluvial and lower alluvial reaches. The sample LSA-1 (Figure 2.29c) is finer than the other three samples in the lower semi-alluvial reach, and this sample was from a small bar at the start of the lower semi-alluvial therefore can also be considered as of bare rock reach. If this is excluded, the average D_{50} and D_{84} for lower semi-alluvial reach becomes 72 and 174 mm respectively, a bit coarser than the downstream alluvial reach. Table 2.7 includes sorting coefficient σ (in φ units) based on Folk and Ward (1957) which is calculated as

$$\sigma = (\varphi 84 - \varphi 16)/4 + (\varphi 95 - \varphi 5)/6.6 \qquad \text{Eq. 2.1}$$

where φ84, φ16 φ95 and φ5 represent the φ values (= -Log$_2$$D$) at 84, 16, 95 and 5 percentiles. The σ values for study site all lie between 1 and 2 which represents poorly sorted grains in Trout Beck study site (Folk & Ward, 1957).

The above GSD plots and data suggest that the spatial variability of the grain size in study site is medium to high. The grains in the lower semi-alluvial reach are relatively coarser and the grains from boulder-riffle are the coarsest (refer LSA-2 in Figure 2.29c) of all the samples. The grains at the lower semi-alluvial reach and lower alluvial reach are of moderate size, finer than the grains from boulder areas but coarser than from the

upper alluvial reach. The data show no trend of downstream fining or coarsening of the grains over the entirety of the study reach.

2.4.3 Boulder survey

Boulder survey was carried out to test the stress partitioning formulas proposed by Yager *et al.* (2007) (Section 4.6). The boulder survey was carried out on a low flow day to measure the required parameters for these formulas such as number of boulders, diameter of each boulder, protrusion, plan, and flow facing area of the boulder. The protrusion height and the *b*-axis of the boulder were estimated at site. Four to six dGPS points were taken for each boulder which allowed the plan area to be calculated from the DEM. The survey data were plotted in the DEM from where the spacing of the boulders and the plan area of each boulder were calculated. The flow velocity and depth were measured at site; the methods for bulk hydraulics measurement will be discussed in chapter 3.

All the grains with longest visible axis greater than 256 mm were mapped on 17th September 2014 which shows that there were 270 grains in the lower semi-alluvial reach out of which 103 were in boulder-riffle area. However, by the standard definition of the boulder (*i.e.* grains with *b*-axis >256 mm) there were 120 boulders in lower semi-alluvial reach and 54 in boulder-riffle area. The stress partitioning calculations for boulder-riffle zone (Chapter 4) will use all the surveyed grains (103) as they were considered immobile at moderate to high flows. During survey, the surveyed grains were logged with distinct identification as B1 to B270 as seen in Figure 2.30. The surveyed grains are also plotted in DEM in Figure 2.31.

Figure 2.30. Photograph dated 17.09.14, during the boulder survey of lower semi-alluvial reach. The photo was taken looking downstream from the start of the reach.

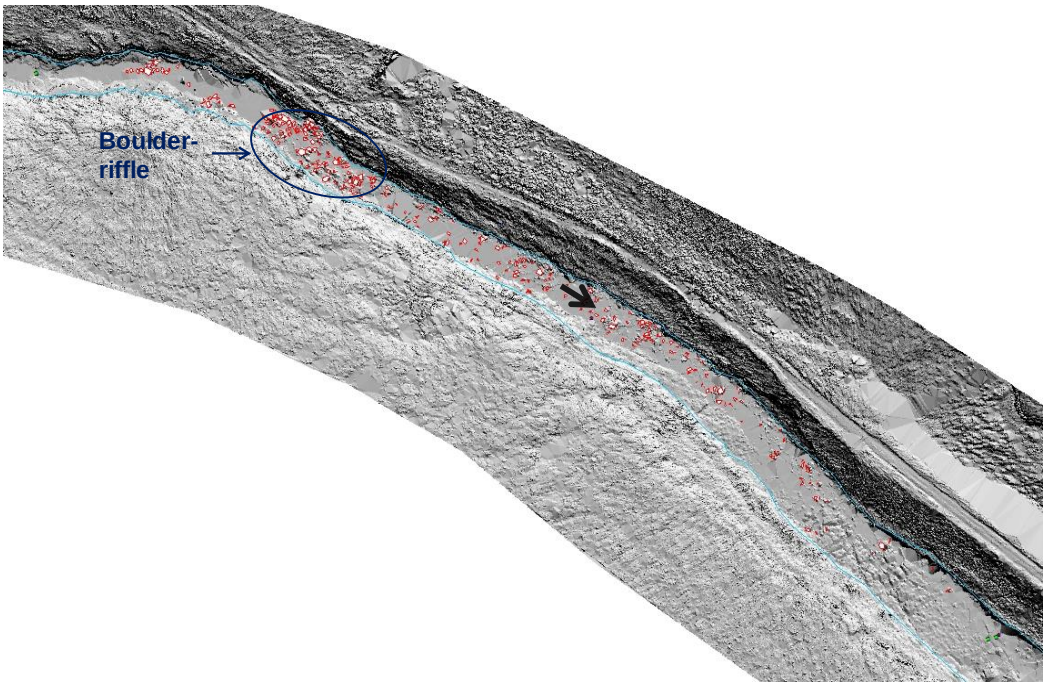

Figure 2.31. The dGPS-surveyed boulders (all boulders which have at least one axis >256 mm) plotted in DEM. The boulder-riffle zone for which the stress partitioning will be applied is encircled. The flow direction is shown by thick black arrow.

2.5 Sub-reaches for detailed study of hydraulics

To understand the effect of bed morphology on velocity, flow resistance and shear stress the bulk hydraulics were measured in short sub-reaches using repeated salt-wave travel time measurements (salt-dilution method will be discussed in chapter 3). The overall criteria for choosing the sub-reaches was to find the best available sites with contrasting bed types; fairly homogeneous along the 25 to 30 m length; convenient places to position the logger, fix the probes and inject the salt; and to avoid the area of large steps, pool, dead zones, back eddies etc as they would affect the results in multiple ways. For instance if a knickpoint was included in a sub-reach then the hydraulic calculations for that sub-reach would be complex due to the break of slope. The cable length of the double-probes conductivity meter was 15 m for each probe which dictated the length of these short sub-reaches (or test sites) which varied between 25 to 30 m. Five identified sub-reaches are shown in Figure 2.32 which include one in fully alluvial reach (F1), one in bare rock (F2), and three in lower semi-alluvial reach (F3: boulders in rock bed, F4: gravels in rock bed, and F5: very low cover in rock bed) (Table 2.6).

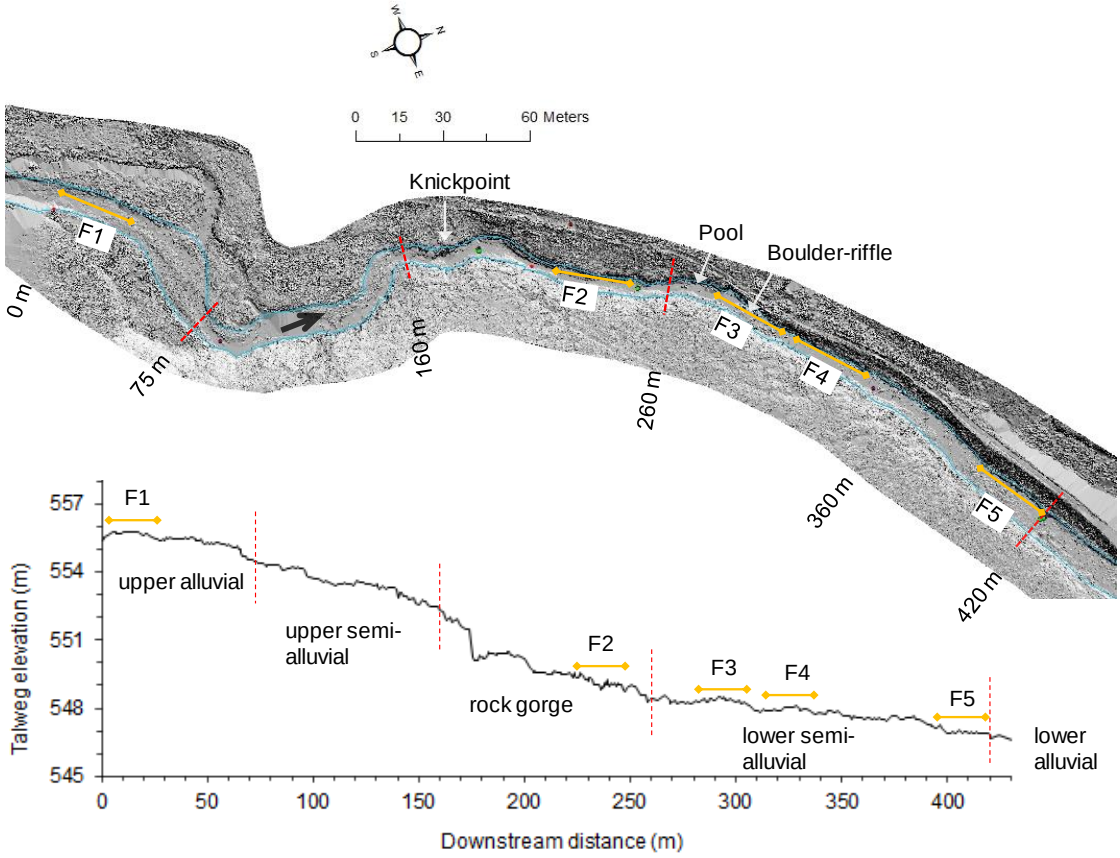

Figure 2.32. A DEM and channel bed long-profile showing five sub-reaches/sites for salt-wave measurements: sub-reach F1 in upper alluvial; F2 in rock gorge; F3, F4, and F5 in lower semi-alluvial reach. Morphological reach boundaries are marked by red lines and sub-reach lengths are indicated by orange lines. The black arrow in DEM indicates the flow direction.

The photographs showing the locations of these sub-reaches are shown in Figures 2.33 to 2.37. The upper alluvial and bedrock reach are of relatively short sections (< 100 m) and have similar substrates within the reach, therefore only one sub-reach per reach is chosen in these reaches (F1: Figure 2.33, F2: Figure 2.34). The lower semi-alluvial reach, however, has more varied bed morphology which comprises segments of varied grain sizes, sediment cover and rock exposures and therefore three sub-reaches F3, F4 and F5 (Figures 2.35 to 2.37) were identified for this sub-reach. No sub-reach was needed in upper semi-alluvial reach as there are three sub-reaches from lower semi-alluvial reach which cover varieties of bed character in semi-alluvial reach.

Figure 2.33. Photograph, taken at a very low flow day (~0.050 $m^3 s^{-1}$) showing sub-reach F1 in the upper alluvial reach. The double-headed arrow indicates the length of the sub-reach whilst the one way thick arrow shows the flow direction.

Figure 2.34. Photograph showing the sub-reach F2 in the bare rock gorge. The nearly-vertical walls in the gorge with numerous re-entrants and spurs.

The boulder-riffle sub-reach F3 (Figure 2.35) is surrounded by limestone walls on both sides and the bed is fully covered with gravels, cobbles and boulders (Section 2.4.3). The short stretch immediately downstream of the boulder-riffle sub-reach was chosen as another sub-reach F4 (Figure 2.36) which is relatively straight and uniform for a

distance, the channel bed was fully covered with gravels and some boulders. The lowermost sub-reach F5 (Figure 2.37) was chosen at the downstream end of the lower semi-alluvial reach which comprises significant rock exposure with potholes, grooves and few gravels along the talweg on the left side of the channel.

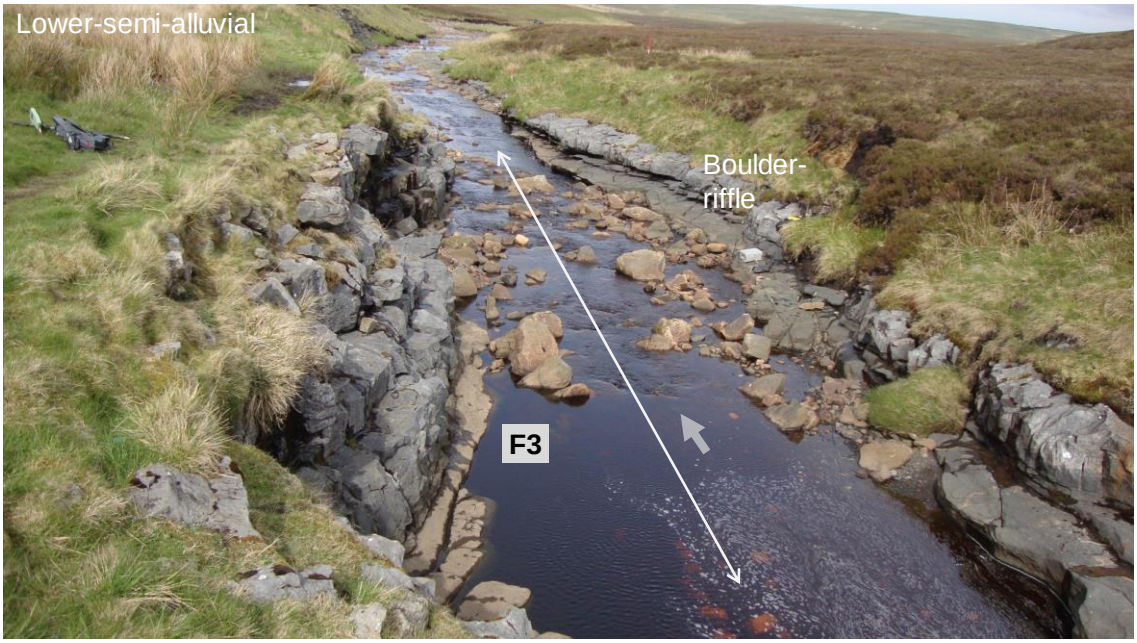

Figure 2.35. Photograph showing the boulder-riffle sub-reach F3 in the lower semi-alluvial reach. Sub-reach F4 (next Figure) is immediately downstream of F3.

Figure 2.36. Photograph showing the sub-reach F4 in the semi-alluvial reach.

Figure 2.37. Photograph showing the sub-reach F5 at the end of the lower semi-alluvial reach.

The sub-reach characteristics including the tape-measured sub-reach length, the dGPS-measured bed slopes (based on the levels at two ends of the sub-reach), the average grain sizes (D_{16}, D_{50} and D_{84}) are summarised in Table 2.8. Several salt-waves were measured across a range of flow conditions, the results of salt-wave measurements are discussed in chapter 4.

Table 2.8. Characteristics of five hydraulic sub-reaches.

Sub-reach	Length (m)	Distance from start of study reach (PT_1), m	Bed slope, S_b	D_{16} (mm)	D_{50} (mm)	D_{84} (mm)	Alluvial cover
F1	25.10	0	0.015	14	36	116	100%
F2	26.00	222.7	0.019	-	-	-	1%
F3	24.40	281.1	0.013	32	84	190	70%
F4	27.55	311.5	0.003	30	68	190	70%
F5	26.15	393.3	0.014	32	64	140	20%

In addition to these five short sub-reaches some hydraulic calculations such as shear stresses have been calculated for slightly longer sub-reaches (*i.e.* between two pressure transducers located either side of the short sub-reach), which will be discussed in section 4.5. The lengths between the two PTs are: $PT_1 – PT_2$ (84.7 m), $PT_2 – PT_3$ (107.4 m), $PT_3 – PT_5$ (58.7 m), $PT_5 – PT_6$ (91.9 m) and $PT_6 – PT_7$ (77.3 m). These lengths are also shown in Figure 2.40.

2.5.1 Survey of channel cross-sections at sub-reaches

To compute the mean velocity (V) in a sub-reach using continuity equation ($V = Q/A$) the mean cross-sectional area (A) of that sub-reach is needed which requires the measurement of channel cross-sections within each sub-reach. At each sub-reach seven to ten cross-sections were surveyed using the Leica 1200 dGPS. Sub-reaches F1, F2 and F5 each have eight cross-sections, F3 has seven and F4 has 10 cross-sections. The cross-sections within the sub-reach were measured at 2 to 3 metres spacing and also where the abrupt change in the channel width or slope was noticed. Figure 2.38 shows the cross-sections for F1 – F3, whilst Figure 2.39 shows for F4 and F5. The channel cross-sections at each pressure transducer PT_1 to PT_7 (will be discussed in Chapter 3, Section 3.2.4) will be used in hydraulic calculations which are shown in Figure 2.40. The water levels at Q = 2.0 and 6.0 $m^3 s^{-1}$ are marked in all these cross-sections to indicate the extent of submergence in moderate and high flows. The visual observation (photographs of 06.10.2014 at Q = 5.0 to 5.5 $m^3 s^{-1}$) suggest the bankfull flows in the upper and lower alluvial reaches are around 6-7 $m^3 s^{-1}$.

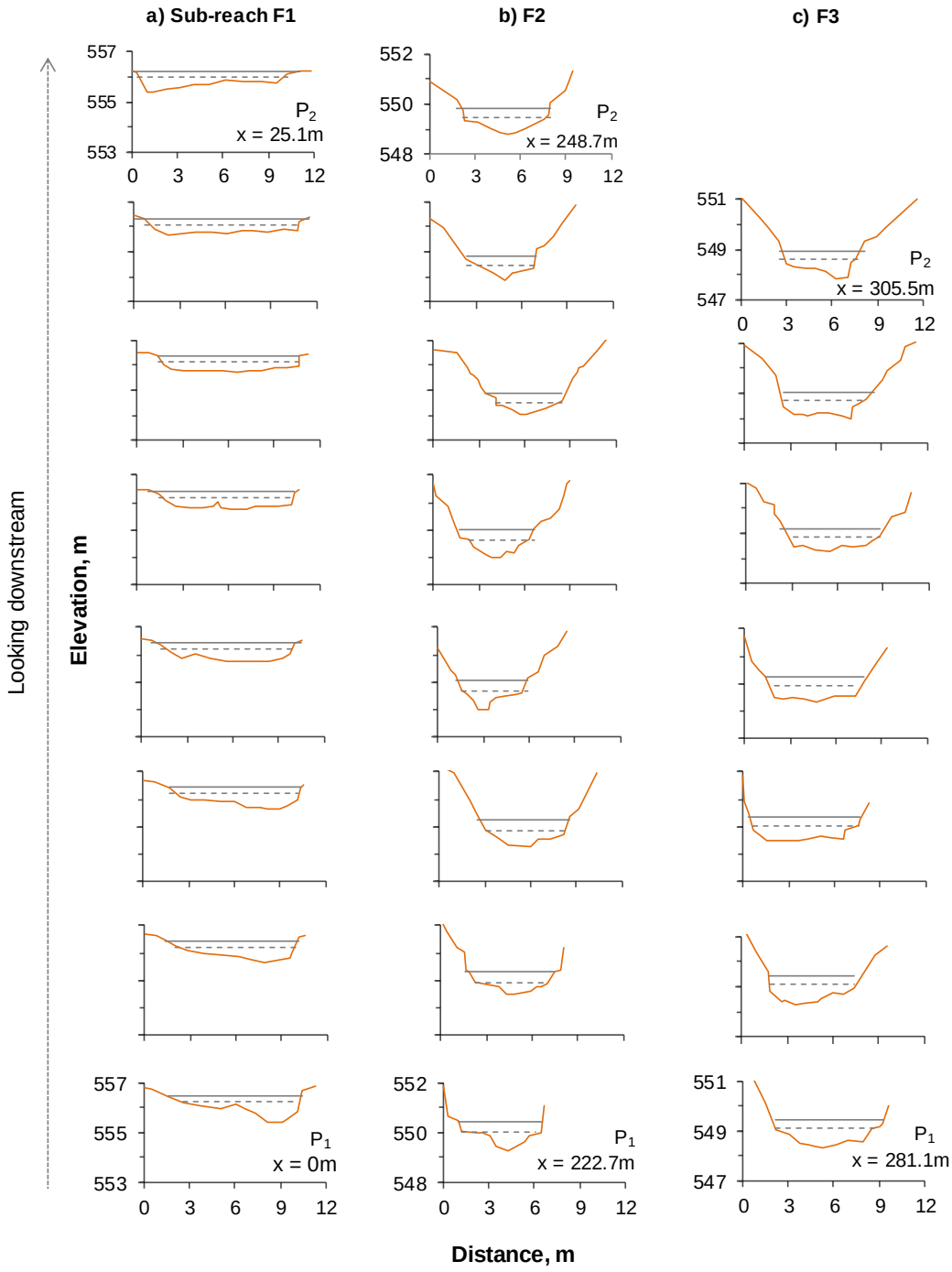

Figure 2.38. Channel cross-sections at sub-reaches F1 to F3 (a to c) looking downstream. Water levels at 2 $m^3 s^{-1}$ (dashed) and 6 $m^3 s^{-1}$ (solid) and downstream distance 'x' from the first pressure transducer PT_1 (start of the study reach) are shown. The cross-sections labelled as P_1 (upper probe for salt-dilution) and P_2 (lower probe) are respectively the uppermost and lowermost cross-sections within the sub-reach, others are intermediate cross-sections.

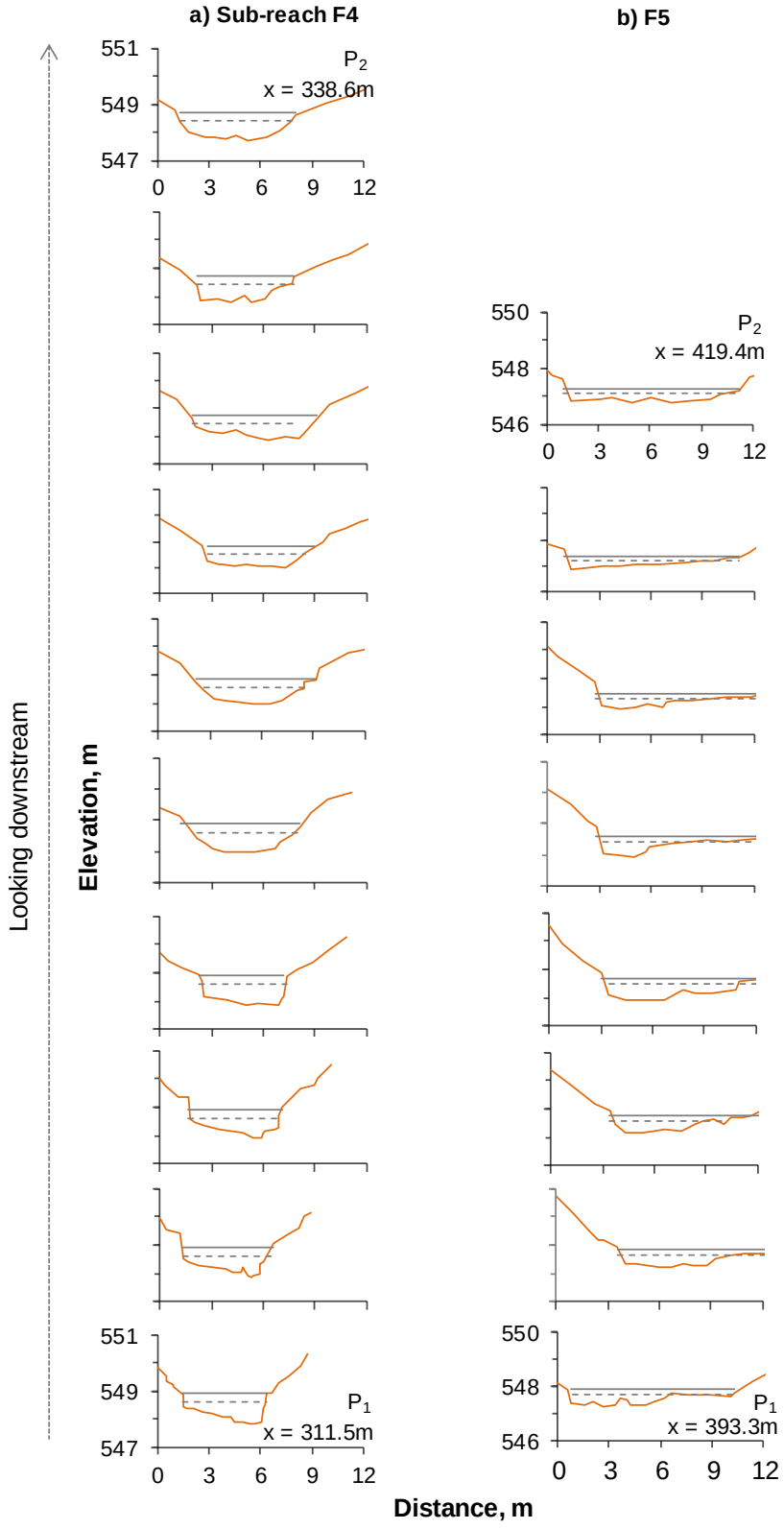

Figure 2.39. Channel cross-sections at sub-reaches F4 and F5 (a, b) looking downstream. Water levels at 2 $m^3 s^{-1}$ (dashed) and 6 $m^3 s^{-1}$ (solid) and downstream distance 'x' from PT_1 is shown. Probe locations P_1 and P_2 for salt dilution are shown.

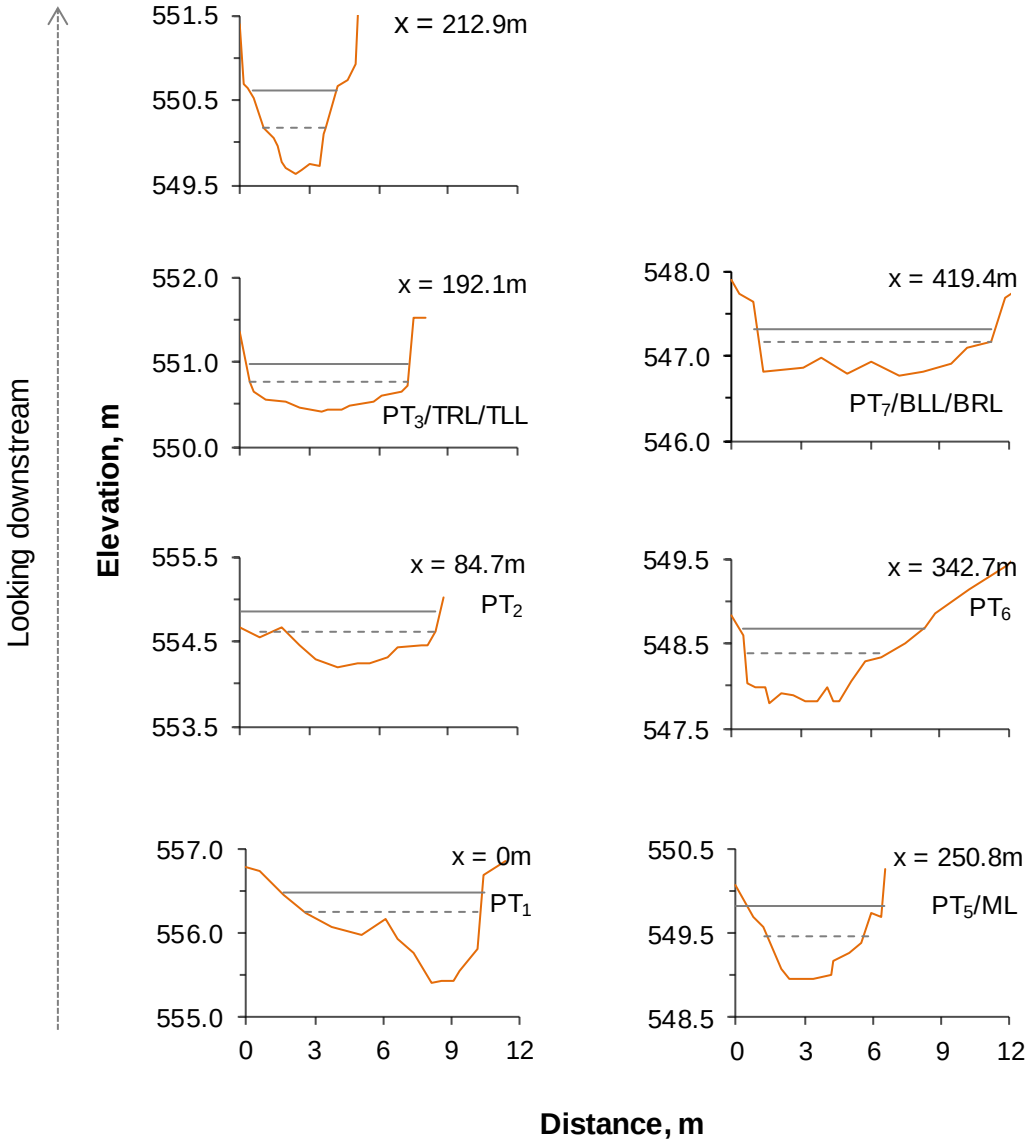

Figure 2.40. Channel cross-sections (orange) looking downstream at pressure transducers PT_1 to PT_7. The bedload impact plates TLL/TRL are also next to PT_3, ML next to PT_5 and BLL/BRL next to PT_7; these plates will be discussed in Section 3.3). Water levels at moderate discharge 2 $m^3 s^{-1}$ (dashed line) and high discharge 6 $m^3 s^{-1}$ (solid) are shown. Downstream distance 'x' from PT_1 (x =0 m at PT_1 and 419.4 m at PT_7) are shown.

This chapter has outlined the study site and explained how the reach was divided into four morphological reaches and five hydraulic sub-reaches, and what the morphological characteristics are of each of the reaches and sub-reaches. The methods for hydraulic measurements, pebble tracing and bedload impact sensors will be discussed in next chapter.

3 Methods for studying hydraulics and sediment transport

This chapter explains the field measurement methods for studying bulk hydraulics and bedload transport through the sequence of contrasting reaches in Trout Beck. In particular this chapter will detail the following:

- the field methods and calculation process to measure the spatial and temporal patterns of variation in stream velocity and other bulk flow properties including mean depth, hydraulic radius, flow resistance and shear stress using a series of pressure transducers, water profile measurements using dGPS, and repeated current meter and salt dilution methods in short sub-reaches. This also includes the stress partitioning to split the total stress in a boulder-riffle sub-reach F3;
- the field experiment to measure movement of coarse sediment through a sequence of contrasting reaches using magnetically-tagged tracer pebbles; and
- the field methods to establish the critical discharge for bedload movement in different reaches using bedload impact plates.

The bulk hydraulics measurements, tracer-pebble and impact plate experiments were started in August 2013 and continued until April 2015. However, the preparation and laboratory works including tracer collection, drilling and painting were started in May 2013 (refer field measurement framework in Figure 2.14). This chapter is divided into three sections: section 3.1 details the methodologies for flow monitoring and hydraulic calculations; section 3.2 describes the methods for magnetic tracer pebbles; and finally section 3.3 discusses the methods for bedload impact plates.

3.1 Flow monitoring for hydraulic calculations

The methods for measuring river discharge, velocity and stage and calculation of bulk flow properties averaged over the width of the stream are discussed in this section. These measurements were required to investigate the extent to which the bed load mobility can be explained by the bulk hydraulics and substrate in the contrasting reaches of a mixed alluvial-bedrock system.

The river discharge (Q) was monitored in situ by the velocity-area method using current meter and sudden-injection salt dilution. The main aim of the discharge measurement was to establish a stage-discharge rating curve, establish critical discharge for bedload transport and to observe the spatial and temporal patterns of variation in stream velocity

to study the shear stress and flow resistance. The *Q* is also estimated by scaling the EA discharge by using the catchment area ratio (Hirsch, 1979). The velocity-area and dilution gauging are well-recognised and widely used methods for estimating river discharges (Church & Kellerhals, 1970; Day, 1976; Gees, 1990; Herschy, 1993, 1998). Each method has its own advantages and limitations. The velocity-area method using current meter is more appropriate for rivers with uniform and steady flows whereas the salt-wave method is more suitable in turbulent headwater streams which often have irregular cross-sections and intermittent flow regime (Day, 1977a; Elder *et al.*, 1990). Salt-wave measurements are relatively quick and safe compared to the current meter measurements, especially for measuring the rising or falling limbs of a flood in a flashy stream such as Trout Beck. Moreover, the current meter method may not be practical in most parts of the channel, whereas salt dilution can be done anywhere along it. Because of the above advantages the salt dilution method was used as a main method in this study for discharge measurements. An additional advantage of this method was that the sub-reach velocity could also be measured. However, the current meter was also used to verify the discharge estimates from salt dilution. Since there are no tributaries entering within the study reach, a constant *Q* is assumed throughout the study reach. The sub-reach velocity was measured by salt-wave travel time measurements as well as by using the continuity equation for which the water surface profiles were measured using the dGPS and the quasi-continuous water stages were recorded using pressure transducers (PTs). The measured discharge, flow velocity, stage and channel cross-sections are used to estimate the bulk hydraulics for sub-reaches. The rating curves are developed by using the measured discharge and stages which are used to estimate the bulk properties for high flow conditions. The procedures for measuring stage and discharge and calculating the bulk flow properties are illustrated in a flow chart in Figure 3.1.

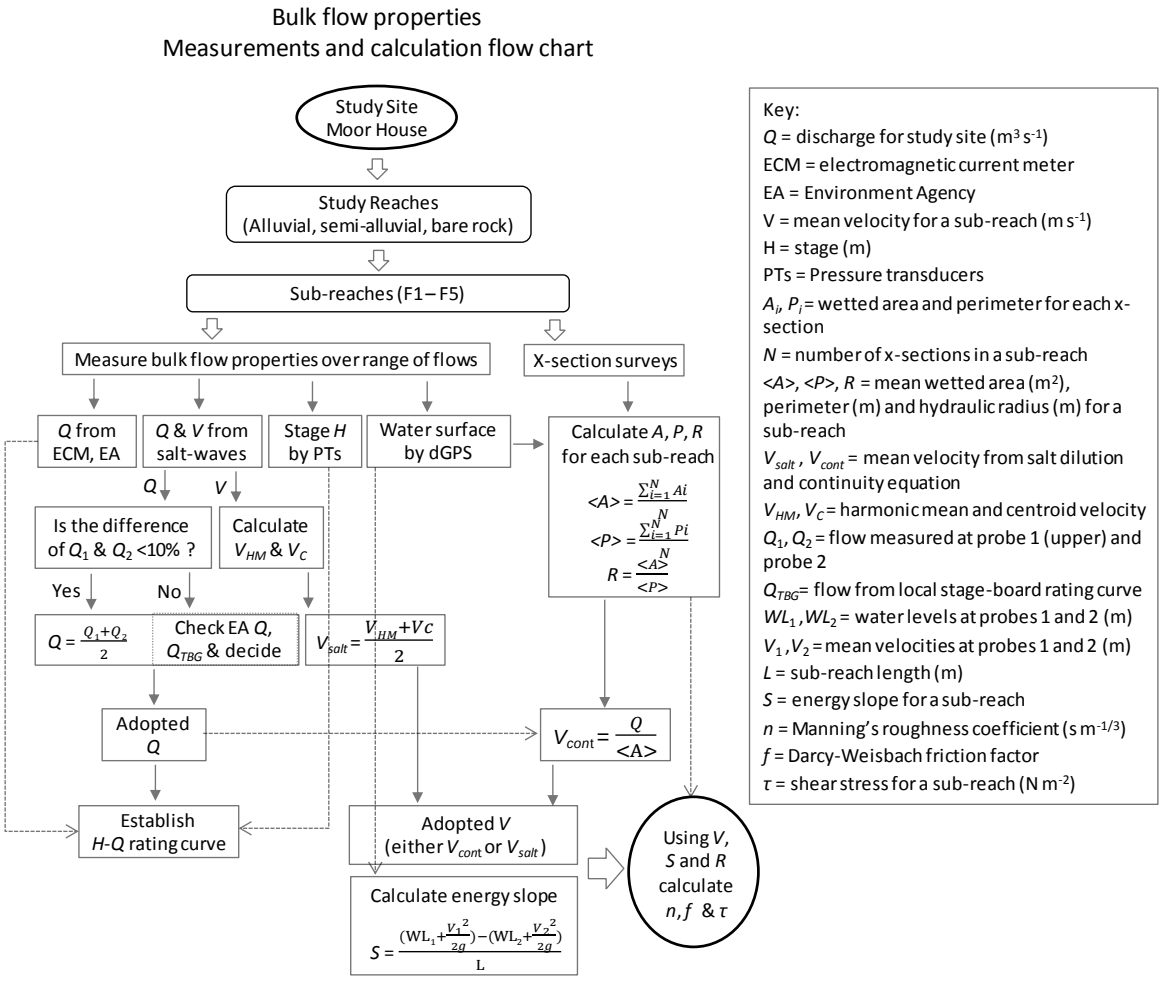

Figure 3.1. Flow chart for bulk flow properties measurement and calculations.

The discharge measurement methods (current meter, salt dilution and catchment area ratio), stage and velocity measurement methods and the procedures for calculating bulk flow properties are discussed below.

3.1.1 Discharge measurement using current meter

A Valeport single axis version 3.10 (flat) electromagnetic current meter (ECM) was used to measure the stream velocity in a cross-section. The ECM provided both the streamwise and lateral velocities averaged over an averaging period and standard deviation of the velocities. The discharge estimate used only the streamwise velocity. The standard deviation, calculated from real time samples during the averaging period, gives an indication of the quality of the measurements; a high standard deviation indicates either a high variability in the flow, or the probe has not been held steady during the measurement. This is a high precision instrument, with an accuracy of ± 0.5 % of reading plus 5 mm s^{-1} over a wide range of flows (± 5 m s^{-1}), the required minimum depth for this equipment is only 5 cm (Valeport, 2011). The electrodes on the

flat sensor are located on the top surface of the sensor above which the flow is measured. The sampling volume for the flat sensor (~3 cm^3) is a small cylinder whose diameter is the distance between the electrodes (~20 mm), and whose height extends ~10 mm above the surface of the sensor. The smaller sampling volume means the flat sensor is more suitable for shallow flows and/or confined spaces. However, in the turbulent flows as the sensing volume is small, more fluctuations in the real time readings are expected in the flat sensor than in the cylindrical sensor but a long averaging-period (> 30 seconds) can minimise this effect. The larger sampling volume of the cylindrical sensor reduces the turbulence noise, but it needs a greater depth of water for velocity measurements. The sensor is aligned into the flow to measure the velocity profile but perpendicular to a tape stretched across river to measure the velocity for discharge calculation. The flow is calibrated as positive when the sensor is facing upstream of the wading rod.

All the ECM measurements were carried out in a single cross-section, called as ECM gauging section, in sub-reach F4 immediately downstream of the boulder-riffle area in the lower semi-alluvial reach, which is relatively a straight and uniform stretch to provide uniform flow through the measuring section (Figure 3.2). For the current meter measurements the 6-m wide measuring section was divided into 20 vertical subsections at regular interval of 0.3 m to ensure none of the subsection spaced at intervals greater than 1/20th of the width (Shaw, 1994).

Figure 3.2. Velocity measurement using 801 single axis electromagnetic current meter at ECM gauging section in sub-reach F4. The picture was dated 17.09.2013 at Q = 1.2 $m^3 s^{-1}$. The arrow shows the flow direction.

Assuming the velocity profile was logarithmic, the velocities were measured at 0.2 and 0.8 of the total depth and then averaged to obtain an average velocity for the vertical (Shaw, 1994). The discharge in each subsection was calculated by multiplying the subsection area by the mean velocity using mean section method (Herschy, 1998). The total discharge through the cross-section was the sum of the discharges at each subsection.

3.1.2 Discharge measurement by salt dilution

Theory

The basic theory of dilution gauging is the conservation of mass of a conservative tracer. A known mass of tracer is added to the channel, either continuously at a steady rate or all at once (gulp- or slug-injection method), and its concentration is measured at a downstream point where the salt is fully mixed with the flow. The higher the discharge, the more the tracer is diluted. This study used the slug injection method (Elder *et al.*, 1990) where common salt (sodium chloride, NaCl) was used as a tracer (Day, 1977a; Hongve, 1987; Elder *et al.*, 1990; Gees, 1990; Kite, 1994; Hudson & Fraser, 2005). Sodium chloride is easily available, cheap and does not cause any health hazard (Day, 1976). Sodium chloride when in aqueous solution dissociates into ions (Na^+ and Cl^-) which conduct electricity. The more of these ions contained in the water, the higher the electrical conductivity which means the water has high ability to conduct an electric current. Therefore the electrical conductivity (EC) is directly proportional to the concentration of ions in the solution.

The slug injection involves a sudden injection of a known quantity of salt into the stream whose conductivity is constantly monitored at a certain distance downstream where the salt is vertically and laterally fully mixed with the stream flow (Elder *et al.*, 1990; Butterworth *et al.*, 2000; Hudson & Fraser, 2005). From conservation of mass, the discharge Q in ($m^3\ s^{-1}$) is calculated as

$$Q = \frac{M}{\int_0^t (c_t - c_0)dt} \qquad \text{Eq. 3.1}$$

where M is the mass of injected salt (kg), t is the time of passage of the salt wave (s), c_t is the concentration of the salt wave at time t (kg m^{-3}) and c_0 is the background concentration (kg m^{-3}) at the sampling point before the start of the salt wave.

In the field it is easier to measure conductivities than concentrations; therefore the discharge equation is rearranged as

$$Q = \frac{M}{\sum(EC_t - EC_0)CF.\Delta t.1000} \qquad \text{Eq. 3.2}$$

where EC_t is electrical conductivity at time t (µS cm^{-1}), EC_0 is background conductivity at the start of the salt waves (µS cm^{-1}), Δt is time interval between conductivity readings (s), *CF* is the concentration factor [mg $L^{-1}(\mu S)^{-1}cm$] which can be determined either in the field or laboratory.

Equipment

Salt waves were measured using two CS547A conductivity and temperature probes (Campbell Scientific, 2016) placed up to 30 m apart and connected to a single CR10X Campbell datalogger (Campbell Scientific, 2003) recording every two seconds. Other equipment required in the field include a field laptop, plastic buckets (~10 litres capacity), a stirring rod or wooden stake, a stop watch and adequate supply of table salt in pre-weighed packets (500 and 1000 g). The downloaded data comprises both the corrected (compensated for actual temperature) and uncorrected (measured at standard temperature 25^0C) *EC*s for each probe. The real time data displayed on the computer during the measurement are helpful to identify any errors on the measured data so that the errors can be fixed instantly at the field site. The logger recorded temperature-corrected conductivity; the maximum variation in temperature during a single measurement was found to be less than 0.5 ^{0}C.

Calibration for concentration factor (CF)

The conductivity (*EC*) when multiplied by the concentration factor (*CF*) gives the concentration of the solution. The concentration factor [mg $L^{-1}(\mu S)^{-1}cm$] is the slope of linear regression of the plot of concentration (mg L^{-1}) versus electrical conductivity (µS cm^{-1}). The calibration process required the CR10X logger with probes, a laptop, two 1000-mL graduated cylinders, two 10-mL glass pipettes, two stirring rods, adequate amount of deionised water and a standard solution. A standard solution of 2000 mg L^{-1} NaCl was used to make the concentrations of sample solutions closer to the expected range of peak concentrations at Trout Beck.

In laboratory, a range of conductivity and concentration values were measured for each probe by varying the concentration of a saline solution. The concentrations were plotted

against *EC*s and a linear regression fitted the slope of which is *CF*. The conversion factor, however, is not constant for all streams and is related to the background conductivity of the stream (Hongve, 1987). The calibration determined the *CF* values of 0.466 and 0.469 mg L^{-1} $(\mu S)^{-1}$cm for probes 1 and 2 respectively for *EC* range 20 – 100 µS cm^{-1}. Hongve (1987) found the *CF* value 0.47 mg L^{-1} $(\mu S)^{-1}$ cm for *EC* range 0 – 64 µS cm^{-1} and 0.51 mg L^{-1} $(\mu S)^{-1}$ cm for EC range 617 – 1990 µS cm^{-1}. The data show the background *EC* at Trout Beck varies from 20 to 100 µS cm^{-1} and are low at high flows and high at low flows. The reason for high background conductivity at low flow is that rain water arriving in a catchment has a low solute concentration, but once it is on or in the ground it acquires more solutes derived from rock weathering and soil cation exchange processes. The surrounding geology of the study site also contains peat and abandoned mine sites through which the ground water flows.

Field test sites

As detailed in section 2.5, the study reach was divided into five sub-reaches of contrasting bed morphology to carry out the salt dilution measurements. The five sub-reaches are: F1 in upper alluvial; F2 in bare rock gorge; F3, F4 and F5 in lower semi-alluvial reach. The positions for salt injection and two probes were all identified and marked in the field. The position of the upper probe P_1 was at the upstream end of the sub-reach whilst the lower probe P_2 was at the downstream end. The injection and probe positions for each sub-reach were kept fixed for all measurements to allow for easy comparison of the results at different discharges. The sub-reaches are marked in Figure 2.32 and sub-reach characteristics (length, slope, GSD, and sediment cover) are given in Table 2.8 in chapter 2.

Mixing length and salt quantity

Mixing length L_m is a distance between the injection point and a downstream point where the salt is fully mixed with the flow (Day, 1976; Day, 1977b). The L_m depends on the channel size, slope, flow width and the presence of turbulence in the test site (Day, 1977b). The vertical mixing is the result of turbulence in the flow whereas the lateral mixing is attributed to the velocity gradient in the cross-section. Beyond the L_m the concentrations are adequately uniform crosswise and depthwise and one dimensional spatial axis can be assumed to represent the spatial variation (Day, 1975; Waldon, 2004). If the distance from injection point to upper probe is shorter than the required L_m, the result will be erratic as the complete mixing of the salt in the entire flow may not

have achieved which may give a sharp peak. Also before attaining the mixing length the stream velocity will be slightly different from the salt-wave velocity. The lower probe also should not be too far downstream from the fully-mixed point as it will have a long tail and no distinct peak. Day (1977b) recommends a quick estimate for mixing length as 25 times the mean flow width based on the data of slug dilution gauging in mountain stream, whilst some other researchers (e.g. Hudson & Fraser, 2002; Lee & Ferguson, 2002) have suggested 20 times the channel width. These are just the guidelines and appear to be conservative since the channel width is estimated visually at site; some trials should be carried out on site to establish the optimal mixing length. Hudson and Fraser (2005) found the optimum mixing length to width ratio as low as 10. Based on the trials on site, the optimum location of injection points and the mixing lengths for low to medium flow for different sub-reaches were identified which are shown in Table 3.1.

Table 3.1. Mixing length for the sub-reaches. The mixing length shown here is also the distance between the injection point and the upstream probe P_1.

Sub-reach	Channel width (w) for measured range of Q up to 2 $m^3 s^{-1}$ (m)	Mixing length, L_m (m)	Mixing length to width ratio (L_m/w)
F1	8.5	130	15
F2	4.0	60	15
F3	6.0	90	15
F4	5.8	115	20
F5	7.0	110	16

While doing the trial tests to determine the optimum mixing lengths, some checks were applied such as whether the integral (or area) under the wave at P_1 and P_2 are similar, whether the discharge estimate at P_1 and P_2 are similar, and whether the wave curve for each probe is uniform with a single peak with smooth rising and falling limbs. However, the choice of injection point in the gorge was limited by difficulty of access when carrying a bucket of salt solution. The mixing lengths shown in Table 3.1 were determined after fulfilling the above criteria.

The amount of salt injected should also be optimum as too little salt creates potential errors and too much salt is difficult to handle. However, more salt means a strong solution that will maximise the peak and minimise the area under the tail. Initially 0.5 kg salt was tested for a 1 $m^3 s^{-1}$ flow and that gave a mean wave EC of 4 µS cm^{-1} above the background level which made the calculation of area under the wave rather imprecise, especially if there was any variability in the background reading. Therefore,

the salt was increased to 1.5 kg per $m^3 s^{-1}$ flow to obtain a satisfactory result. The actual amount of salt used for range of flows was 0.5 kg for < 0.2 $m^3 s^{-1}$ flow, 1 kg for 0.2 – 0.5 $m^3 s^{-1}$, 1.5 kg for 0.5 – 1 $m^3 s^{-1}$, and 2 kg for 1 – 2 $m^3 s^{-1}$. These salt quantities gave a satisfactory result; the mean *EC* of the salt waves were 10 µS cm^{-1} greater than the background values.

It can be difficult to define the end of the salt wave which is generally due to a change in the background conductivity during the measurement, or in some cases the difficulty was also because of the insufficient sampling time. Day (1976) reported that the back ground conductivity was different when the flow changes but generally remained constant during a single measurement. The background *EC* remained largely unchanged in this study during a single measurement but in few occasions it did not return to its original value and fluctuated by 1 or 2 µS cm^{-1} (1 to 4% of the initial value).

Measurement and calculation of Q

The salt-wave measurements were carried out at the sub-reaches for low to medium discharges and the data for probes P_1 and P_2 were downloaded from the datalogger from which the respective discharges Q_1 and Q_2 ($m^3 s^{-1}$) were calculated using the Eq. 3.2.

Problems and source of errors

The salt-wave results are sensitive to specific methodological details, extreme care was taken while collecting and analysing the data. The potential sources of errors may arise if:

- There is not enough salt. It is expected that the mean EC of the wave should be at least >10 µS cm^{-1} above background EC;
- the used salt is not fully dissolved in the bucket or salt is lost in the channel between the injection point and the probe locations;
- the probe is too close to the injection point i.e. before attaining full mixing;
- the probes are placed in a dead or recirculation zone. For example, the flow through boulder-riffle sub-reach (F3) is very complicated with lots of small dead zones;
- the probes are not fully submerged or they move after placement;
- the stream turbidity changes during measurement (Rantz, 1982); and
- the background conductivity changes during measurement or do not return to its original value.

3.1.3 Discharge estimation by catchment ratio

In addition to the study site *Q* obtained from ECM and salt-waves measurement, this study also uses the EA discharge, scaled by catchment ratio 0.62 as explained in section 2.2.4. The scaled-down EA data were used for several purposes such as to establish flow duration curves, calculate flood frequencies, verify the measured discharges, fill the missing gaps, extend the rating curves for high-discharges above the measured range and estimate the bulk hydraulics for high discharges.

3.1.4 Pressure transducers (PTs) for stage measurement and rating curves

Stage measurements were required to develop stage-discharge rating curve, calculate water slopes and establish critical discharge and shear stress for particle movement in different reaches and sub-reaches. Since the river discharge at study reach is much less than at the EA gauging station (catchment area ratio 0.62), a stage-discharge (*H: Q*) rating curve was needed to know the actual discharge series at the site. The pressure transducers (PTs) recorded the quasi-continuous water stages in study reach during the study period from which the rating curves are developed. The rating curves are established for each PT to perform the bulk hydraulics calculations for high flow conditions. These curves also allow comparison of the measured discharge with the computed discharges providing a quality check for the PT data.

Seven pressure transducers PT_1 to PT_7 at different locations along the study channel were installed as shown in Figure 3.3. The PT_1 and PT_4 were the pressure transducers linked to a Campbell CR10X datalogger (Campbell Scientific, 2003) whereas PT_2, PT_3, PT_5, PT_6 and PT_7 were the Mini-Divers (Schlumberger, 2014). All the PTs except PT_4 and PT_6 were installed in August 2013, the PT_6 was installed in September 2013 and PT_4 in May 2014. The Mini-Diver measures the absolute pressure which is equal to the weight of the water column above the measuring instrument plus the prevailing air pressure. Therefore the air pressure also needs to be measured which will then be deducted from the Mini-Divers' absolute pressure readings. A separate Mini-Diver (called TB baro) to measure the air pressure was installed next to PT4 logger in an enclosure (see green cage in Figure 3.5b). The air pressure measurements recorded by TB baro were then subtracted from the absolute pressure measurements recorded by various PTs and the corrected stage data were obtained.

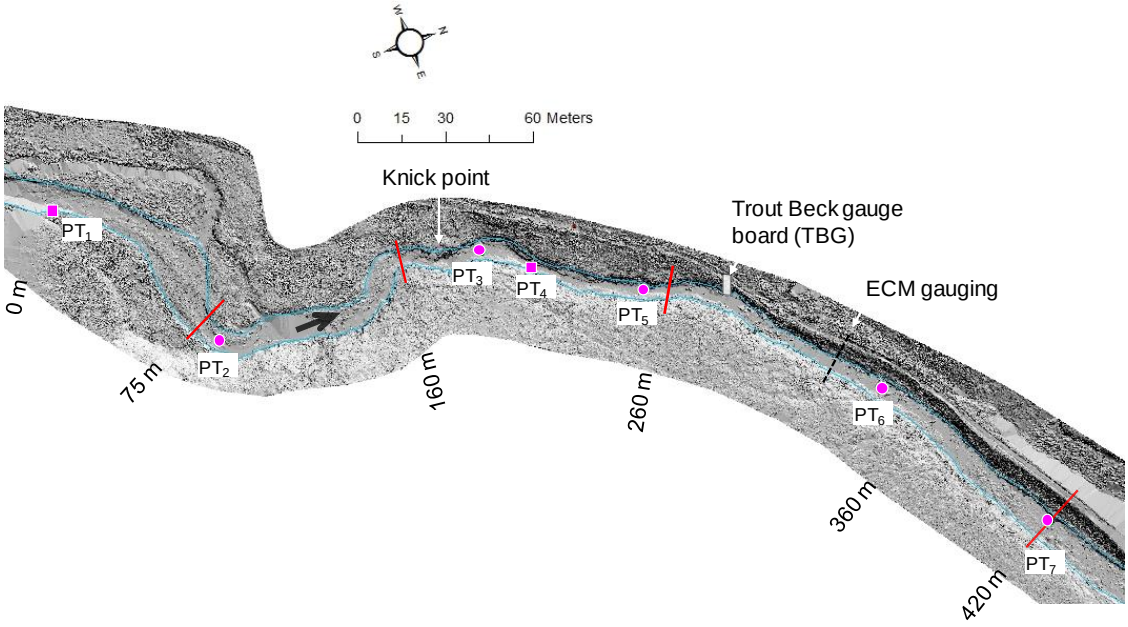

Figure 3.3. Location of stage recorders PT_1 to PT_7 in DEM (pink circle for Mini-Diver and square for Campbell logger). PT_1 in upper alluvial, PT_2 in upper semi-alluvial, PT_3/PT_4/PT_5 in bare rock gorge, PT_6 in lower semi-alluvial reach, and PT_7 at the end of the semi-alluvial study reach. The local stage board (TBG) and the ECM gauging section are shown and the reach boundaries are marked. The black arrow indicates the flow direction.

The PT_1 was installed in upper alluvial reach at x = 0 m (x is downstream distance from the PT_1, Figure 3.3) in an asymmetric wide cross-section (bankfull width ~9.0 m) with fully alluvial bed and walls (Figure 3.4a). The cross-sections at each PT locations are shown in Figure 2.40 in chapter 2. The PT_2 (x = 85 m) was installed in the upper semi-alluvial reach in a wide cross-section (~9.0 m) on bedrock bed with alluvial wall on the left bank and rock wall on the right bank (Figure 3.4b).

Figure 3.4. Photograph showing the pressure transducers: a) PT_1 in the upper alluvial reach which comprises a Campbell CR10X logger and the cable inside a stilling well; b) PT_2 (white circle) is a Mini-Diver (inset) in upper semi-alluvial reach. Thick arrows show the flow direction.

The PT_3 (x = 192 m) was installed on bare rock near the head of the rock gorge immediately after the knickpoint/plunge pool in a wide symmetrical cross-section (~7.0 m) with limestone rock walls on either side (Figure 3.5). The PT_4 (x = 213 m) was installed in a narrow (~4.0 m) and symmetrical section in the bedrock gorge with high rock walls (~3.0 m) on either side. The PT_5 (x = 251 m) was also installed in a narrow (~6.0 m) and symmetrical cross-section near the bottom of the rock gorge surrounded by rock walls on either side (Figure 3.5b). The PT_4 was installed in a short distance (21 m) from PT_3 because the PT_4 to PT_5 is comparatively a straight and uniform-width stretch with no major drops on the channel bed. Therefore PT_4 – PT5 section can be considered to be the best of the available sites for the detailed experiment.

Figure 3.5. a) Photograph of the gorge looking upstream showing PT_3 (Mini-Diver) and PT_4 (Campbell logger, the cable connecting to the CR10X logger). A small rapid immediately downstream of PT_3 is seen; b) Photograph looking downstream showing PT3, PT4 (the logger is inside the green cage), and PT5 (Mini-Diver). The TB baro to measure air pressure is kept in the green cage.

The PT_6 (x = 343 m) was installed in a wide (~8.0 m) asymmetrical cross-section in the semi-alluvial bed with alluvial banks (Figure 3.6a). The PT_7 (x = 420 m) was installed in a wide (~10.0 m) asymmetrical cross-section at the bottom end of the lower semi-alluvial reach with alluvial banks on either side of it (Figure 3.6b).

Figure 3.6. Photograph showing: a) PT_6 in lower semi-alluvial reach; and b) PT_7 at the lower end of the lower semi-alluvial reach. The arrow shows the flow direction.

All the Mini-Divers recorded the data every 5 minutes, but the Campbell loggers in every 15 minutes because of their smaller data storage. The sites for stage recorders PT_3, PT_5 and PT_7 were located next to the bedload impact sensors, which will be discussed in section 3.3. As both the impact sensor and stage recorders record the data at the same time interval and they are located next to each other, it allowed the flow and impact counts data to be correlated to understand the critical discharge for grain entrainment. Other PTs were placed in the best available sites. Using these stage data (H) and the measured discharges (Q) over as wide a range of flow events, the stage-discharge (H-Q) relationship were established. For higher flows (> 2 m^3 s^{-1}) for which

the discharge measurement at field was not possible, the discharge was obtained by applying catchment ratio to the EA discharge data.

Trout Beck stage board (TBG)

A staff gauge board (TBG: Trout Beck gauge board) was also established at the study site which allows a quick visual estimation of the river discharge (Figure 3.7). The stage readings were taken at regular intervals on the days of discharge measurements and a stage-discharge rating curve was developed.

Figure 3.7. Photo dated 01.04.2014 (Q~ 2.0 $m^3 s^{-1}$) showing the local staff gauge board (TBG) in the left bank at the bottom of the gorge near the start of the boulder-riffle sub-reach (F3). The black arrow shows the flow direction.

3.1.5 Stream velocity and other bulk flow properties

Mean velocity is required for flow resistance calculation such as Manning's *n* and Darcy –Weisbach's *f*. The mean velocity and other bulk flow parameters such as mean depth *d*, mean width *w*, mean wetted perimeter *P*, and mean hydraulic radius *R* (= *A*/*P*) vary according to the discharge *Q* as well as channel bed characteristics. Mean velocities in the sub-reaches were estimated by two alternative approaches: from salt wave travel time, and by using water level measurements and the continuity equation. For high-*Q* conditions for where the discharge measurements were not possible, the continuity equation was used using the channel cross-sections, the measured discharges and stages and the rating curves. The methodology for velocity measurement using salt-waves and continuity equation are explained below.

Velocity measurement from salt-waves

Once the required amount of salt was injected in the channel the probes placed at either end of the sub-reach measured the conductivity of the salt-waves at 2 second intervals until it returned to the background conductivity. Using these salt-waves recorded at two probes, the mean velocity through the sub-reach was estimated as the sub-reach length divided by the travel time of salt-wave (Beven *et al.*, 1979; Lee & Ferguson, 2002). Reach-average velocity can be determined as the reach length divided by the time difference between the centroids of the upper and lower waves (e.g. Lee & Ferguson, 2002) and is referred to as the centroid method. Waldon (2004) describes that for steady flow condition the mean velocity over a certain distance is same as the spatial harmonic mean velocity. Therefore the mean velocity from the point of injection to a measurement point is equal to the downstream distance divided by the harmonic mean time-of-travel of the salt wave. This is called the harmonic mean (HM) method and is in preference to the centroid method, as discussed below. Waldon (2004) describes the equations for centroid and harmonic mean travel times as below.

The centroid of a tracer wave is the mean tracer time-of-travel from the injection site to the downstream measurement site,

$$tc = \int_{t=0}^{\infty} tp_x\,(t)dt \qquad \text{Eq. 3.3}$$

The harmonic mean time-of-travel for tracer passing a fixed site,

$$t_{\mathrm{HM}} = \frac{1}{\int_{t=0}^{\infty} \frac{1}{t} p_x(t)dt} \qquad \text{Eq. 3.4}$$

Mean tracer velocity (V) through the reach from tracer injection to the measurement site,

Centroid method: $$V(x_1) = \frac{x_1}{t_c} \qquad \text{Eq. 3.5}$$

HM method: $$V(x_1) = \frac{x_1}{t_{\mathrm{HM}}} \qquad \text{Eq. 3.6}$$

where $p_x(t)$ is probability density function of travel time through study reach, t is time after tracer injection, t_c is temporal centroid (mean travel time through the study reach), t_{HM} is the harmonic mean time travel time through a study reach, x_1 is the distance of measurement site 1 from injection point, and $V(x_1)$ is mean water velocity through the study reach (0, x_1).

Both the centroid and harmonic mean (HM) methods were used to estimate the travel time between the two points in the reach such as point of salt injection to upstream probe P_1, between two probes, and between point of injection to downstream probe P_2. Most of the times these methods gave consistent results but in some occasions they were not in agreement and therefore the methods needed to be assessed.. The traditional, and intuitively best, method is to use wave centroids. Lee and Ferguson (2002) used the centroid method and assumed the error was within 5%. In this study an analysis was carried out for several salt waves in different sub-reaches and at different discharges and that suggested the centroid travel time was only slightly sensitive to the choice of when to define the end of the wave (e.g. first return to background conductivity or 1 or 2 minutes later). In some occasions the conductivity readings had some small fluctuations, the background conductivity never came back or the returned background conductivity was not stable for long and increased again. A protocol was therefore prepared to cover this, and to allow for possible hour-to-hour trend in background conductivity. Waldon (2004) suggests that harmonic means (HMs) should be used, but that is specifically for travel time from injection point to a single location at which tracer concentration is measured. In our application, the only valid way to use HMs would be to estimate sub-reach travel time as the difference between the HM travel time from injection to probe 1 and from injection to probe 2. The analysis suggested that this difference was more sensitive to definition of end of wave than was the case when using centroids. The analysis in the results section (Chapter 4, Section 4.2.1) showed that the velocities estimated from centroids and HM methods were close and therefore the average of the two to obtain the mean stream velocity was used.

Water surface measurement at sub-reaches

To calculate the velocity using the continuity equation, the water surface measurements at the locations of channel cross-sections were needed (Section 2.5.1). Most of the times during the salt-waves measurement, the water surface profile of the sub-reach was also measured using the Leica 1200 dGPS. Measurement of water surface exactly at the marked cross-section points was time consuming and therefore a water surface profile taking random points at the spacing of 1~2 m at each sub-reach were measured. The water profile points were plotted in DEM, and the exact water level at each cross-section was computed by interpolation of the upstream and downstream points. These water levels were used in the velocity computation using continuity equation for the measured discharges and the extended high-flows.

Velocity from continuity equation and calculation of bulk flow properties

This method estimates the mean velocity *V* and bulk flow parameters using the measured *Q* (low/moderate ~2 $m^3 s^{-1}$) and measured water levels (Figure 3.1). Based on these measured water levels at cross-sections the bulk flow parameters top width *w*, wetted area *A*, wetted perimeter *P*, depth *d*, and hydraulic radius *R* were calculated at each cross-section. The mean depth was calculated as the wetted area divided by wetted width (i.e $d = A/w$), and the hydraulic radius was calculated by as the wetted area divided by wetted perimeter (i.e $R = A/P$). The w, *P*, *A*, *d* and *R* values for all the cross-sections in the sub-reach were then averaged to obtain overall average values for that particular sub-reach. Mean velocities were calculated by dividing *Q* by either sub-reach average *A* ($<A>$) or the product of average *P* and average *R*; refer chapter 4 for results. The mean velocity obtained from the continuity equation ($V= Q/<A>$), not from the salt-waves, was used for later analysis, refer section 4.2.2 in chapter 4.

Calculation of energy slopes

The energy slope (*S*) is required to calculate the flow resistance and shear stress. The water surface slope (S_W) for a sub-reach was calculated as the difference in water elevations at upstream and downstream end (*i.e.* location of probe 1 and probe 2) divided by the sub-reach length. The energy slope (*S*) was then calculated by applying the corrections for the velocity head (Section 4.3.4).

Bulk flow properties for high discharges

Bedload transport generally occurs at high flows therefore the high discharge data will be required to study the bedload transport process. Direct measurements of some variables were only possible up to a moderate discharge of ~2 $m^3 s^{-1}$ because of a combination of flashiness, distance from Durham and safety considerations. Indirect methods were therefore necessary to estimate flow characteristics at the high discharges during which bedload moves in the reach. The peak discharge during the study period (8.8 $m^3 s^{-1}$) was slightly less than the median annual flood (9.1 $m^3 s^{-1}$). The water levels were estimated for range of discharges, up to 12 $m^3 s^{-1}$. Two approaches were considered to estimate the water level for a chosen discharge. The first method was to interpolate water levels at the measured cross-sections in a sub-reach by assuming straight-line water surface profiles between the nearest upstream and downstream PTs, utilising their stage data. This approach worked well for F2 (rock gorge) where the stage

recorders were not far from the ends of the sub-reach but not elsewhere. Therefore a second approach was adopted in which the principle of the calculation was to start from the highest measured free surface profile in each sub-reach, and raise it for progressively higher discharges in accordance with the *Q*-*H* rating curves for the nearest PT upstream and the nearest PT downstream. The water level at each cross-section within the short sub-reach was calculated with the contributions of the upstream and downstream PTs weighed inversely by their distance from each individual cross-section. The formula used to calculate the water level and the steps followed are shown in Figure 3.8. Once the water levels were estimated for a range of discharges, the bulk properties including the velocities were calculated using the same method used for field-measured discharges, as discussed earlier in this section.

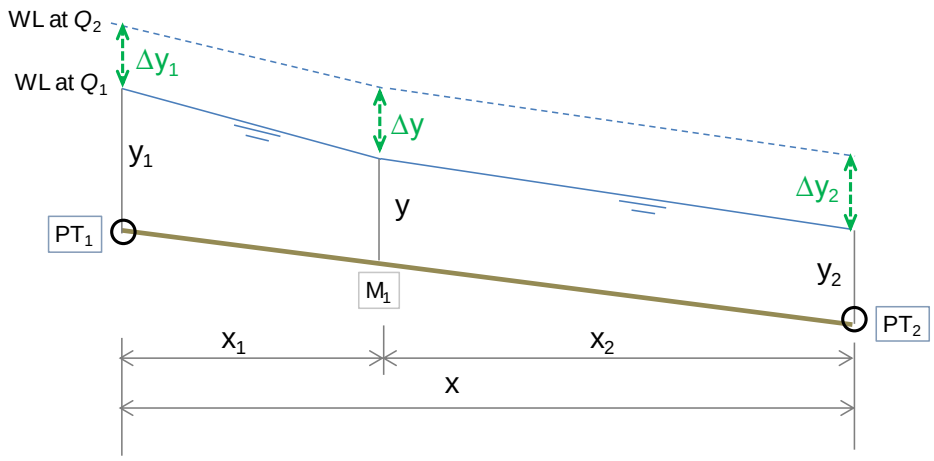

Steps to calculate water levels (WL) for high-*Q* at intermediate x-sections M_1, M_2…of a sub-reach located between two pressure transducers PT_1 and PT_2:

1) Start from the highest measured discharge (say Q_1). Note the WL at PT_1, M_1 and PT_2 (depths are y_1, y and y_2)
2) Calculate WL at M_1(=Δy) for progressively higher values of *Q* (say Q_2 =1.5, 2, 3 .....12 $m^3 s^{-1}$) using the formula:

$$\Delta y = \Delta y_1 \frac{X_2}{X} + \Delta y_2 \frac{X_1}{X}$$

where Δy_1 (and Δy_2) will be calculated using the stage-discharge equation $H = H_0 + cQ_2^d$ for PT_1 (and PT_2) for chosen discharge say Q_2=1.5 $m^3 s^{-1}$. Calculate *c* and *d* from respective rating-curve equations.

3) Repeat the calculation for 2, 3……12 $m^3 s^{-1}$ and calculate Δy for M_1
4) Repeat these calculations for other x-sections M_2, M_3….. in that sub-reach
5) Once the WLs are obtained for series of high discharges for the sub-reach, repeat process (1) to (4) for other sub-reaches.

Figure 3.8. Procedure developed to calculate water levels at sub-reaches for high *Q*.

Hydraulic geometry, flow resistance and shear stress

Hydraulic geometry relations (*w*-*Q*, *d*-*Q*, *V*-*Q*) are calculated as described in section 1.1.2. The flow resistance values using Manning's and Darcy-Weisbach's equations,

other resistance laws (e.g. logarithmic and variable power equations) and non-dimensional hydraulic geometry relations are calculated as described in sections 1.1.3 and 1.1.4. The total shear stress is calculated by the depth slope product as explained in section 1.1.5. The threshold of motion is calculated using the tracer data (Sections 5.2.3 and 5.2.4) and impact sensor data (Section 6.2) and compared with the empirical relations (Eq 1.24 and 1.27) as described in section 1.1.6.

3.1.6 Effective shear stress

As explained in section 1.1.6, the effective stress is a part of total stress (τ) that is available for bedload transport after subtracting losses due to form drag. The stress partitioning is useful to inform how much shear stress is available to move the mobile bedload as it splits the total available shear stress (τ_t) into two parts: the stress borne by mobile grains (τ_m), and stress borne by more-or-less immobile parts of the channel including rough walls and exposed rock as well as boulders (τ_i). Here the resistance from the channel walls and the bare rock bed are assumed to be negligible. The equation can be written as,

$$F_t = F_I + F_m \qquad \text{Eq. 3.7}$$

where F_t is the downstream component of total water force, F_m and F_I (or F_b) are the force applied on mobile grains and immobile boulders respectively. This can be written as,

$$\tau_t A_t = \tau_I A_{IP} + \tau_m A_m \qquad \text{Eq. 3.8}$$

where A_t is the total bed area, A_{IP} the plan area occupied by immobile boulders and A_m the bed area of mobile grains.

Yager *et al*. (2007 & 2012) discuss how the stress on the mobile sediment can be determined as long as the discharge and the boulder properties including size and average spacing are available. In these approaches, the drag coefficients can be calibrated to the required field site using the measured mean flow velocity and depth (or the discharge). Alternatively, the equations can also be tested how accurate they are predicting the mean flow by comparing the measured and predicted flow velocities (and/or depths). The Yager *et al*. (2007) assumes a regular array of identical boulders, whereas Yager *et al*. (2012) assumes boulders are in regularly-spaced transverse steps. In this study the stress-partitioning equations of Yager *et al.* (2007) were tested to the boulder-riffle sub-reach (F3) in Trout Beck. However, one particular concern with

Yager's model is that it neglects the stress to be borne by walls and also does not allow for exposed rock. The results (refer section 4.6.1) showed that the stress partitioning equations of Yager *et al.* (2007) did not perform well for Trout Beck, therefore an alternative method was also developed for this study which will be discussed in chapter 4 (Section 4.6.2).

3.2 Bedload transport using magnetic tracer pebbles

As discussed in section 1.1.7, the tracer-pebble technique is extremely useful to visualise the bedload transport and deposition (Bunte & Ergenzinger, 1989) and also to assess the threshold of motion. There have been several tracer experiments in gravel-bed rivers (e.g. Ashworth & Ferguson, 1989; Hassan *et al.*, 1992; Ferguson & Wathen, 1998; Lamarre *et al.*, 2005; Bunte, 2010; Schneider *et al.*, 2010), and a few in bedrock rivers (e.g. Demir, 2000; Cray, 2010; Hodge *et al.*, 2011), but none in a sequence of contrasting reaches (alluvial – semi-alluvial – bare rock – semi alluvial –alluvial) of the same stream. Trout Beck is a small channel, grains are easy to find in bedrock sections and do not get deeply buried, and frequent surveys all meant that a high recovery could be ensured. The previous tracer studies in Trout Beck (e.g. Demir, 2000; Smith, 2004; Cray, 2010) show that the recovery results are satisfactory and adequate to carry out further analysis. For example, Cray (2010) used magnetic tracer pebbles method on this reach and obtained a good recovery rate (78% after 3 months and 60% after ~6 months, the maximum flow during the period was 8.1 $m^3 s^{-1}$, just under the median annual flood of 9.1 $m^3 s^{-1}$). Therefore this study used tracer-pebble technique with painted and magnet embedded natural pebbles as 'tracers' to investigate the differences in bedload dynamics in a mixed alluvial-bedrock reach. The experimental design of tracers, tracer preparation, tracer seeding, methodology for repeat surveys and data analysis are discussed below.

3.2.1 Experimental design of tracers

Considering the alternating reaches of varied bed morphology, two sets of 270 magnetic tracer pebbles were seeded. The upper site tracers (set A) starts at upper alluvial bed and travels through upper semi-alluvial to bedrock and to semi-alluvial and finally enters into the lower alluvial reach whilst the lower site tracers (set B) starts at bare rock gorge and travels through the semi-alluvial reach which also includes the boulder-riffle section and finally reach the lower alluvial reach. These two sets of data provided useful information of coarse sediment transport though the reaches of contrasting bed characters within a single study site. In particular, the tracer data provide the

information whether there is any size or other selectivity within each set, as well as any difference in the overall mobility of each set. Since one of the aims of the research was to study about the size selectivity, the tracer sets would need a wide range of sizes. Many tracer studies have matched the GSD of the tracers to the GSD of the bed. The problem with this is that there will be very few of the much-coarser-than-average (e.g. D_{95}) and much-finer-than-average (e.g. D_5) particles which tell us the most about any difference in mobility according to size. In this study, the size selectivity and mobility were studied by comparing mean distances travelled by tracers in each half-phi size class following previous studies (e.g.Church & Hassan, 1992; Ferguson & Wathen, 1998; Ferguson *et al.*, 2002). The 95 % confidence interval for each mean is $t\sigma/N^{0.5}$, where t is the 5% exceedance value of the t-distribution with N-2 degrees of freedom, and is very close to 2.0 for $N > 20$, N is number of tracers in class and σ the standard deviation of distance travelled; so similar N in each class were used in order to obtain similar precision.

Each set of tracer pebbles comprises 30 – 50 pebbles in each of seven ½ φ size classes from φ = -5 to -8 (23 – 256 mm) spanning the surface D_{50} (Table 3.2). The size classes were measured at half-phi intervals using a gravelometer (Wolman plate) with standard metric size measurements (sizes: 8, 11, 16, 23, 32, 45, 64, 90, 128, 181 and 256 mm). The smallest hole in the gravelometer through which the grain passed was recorded as the tracer size. The average value of D_{50} for the study reach is 49 mm (range 26 – 84 mm) (Table 2.7).

Table 3.2. Number of tracer pebbles in each 1/2 φ size class deployed at alluvial site (set A) and bare rock site (set B). The equivalent metric sizes in millimetre are also shown.

Phi (φ) mm	< -8 < 256	< -7.5 < 180	< -7 < 128	< -6.5 < 90	< -6.0 < 64	< -5.5 < 45	< -5.0 < 32**	Total
Set A	30*	30	40	40	40	40	50	270
Set B	30*	30	40	40	40	40	50	270

*denotes non-magnetic tracers.

** < 32mm size class includes the pebbles from 23 – 32 mm.

The tracer size distribution does not include the finer pebbles <23 mm; the proportion of these finer pebbles on the river bed is from 5 – 15% (Figure 2.29) which means the tracer pebbles covers 85 – 95% of the site GSD. It was practically difficult to insert magnets in <16 mm pebbles as the pebbles break while drilling. Also the assumption was that finer pebbles were likely to be mobile in every flood and would not provide much information. Moreover, they were likely to be easily buried and would not give a

good recovery rate. Previous research indicates loss rates are higher for smaller pebbles (Ferguson & Hoey, 2002) and this risk therefore was minimised by increasing the number of pebbles in the smaller size classes (i.e. 50 tracers for < 32 mm size class, whereas for other size classes it was 40 except for the two largest size classes). Similarly the loss rates are lower for bigger size pebbles for which the smaller samples (i.e. 30 samples for 128 – 256 mm size) were used. Pebbles in the coarsest size class (180 – 256 mm) were painted and labelled in the field without putting magnets inside as they were unlikely to be buried and also too heavy to transport to the laboratory. The other size-class tracers were prepared in the laboratory.

Both sets of tracers were plotted in the Sneed and Folk (1958) classification system to see the distribution of the shapes. Figure 3.9 shows the percentage of tracers falling into ten shape-classes. Both set A and B have highest percentage of bladed shape 27 and 23 % respectively and both have 14% platy shapes. Both sets of tracers have similar shape distributions and do not have many tracers with very platy or very elongated shapes. The majority of the pebbles were within the central six classes in the diagram.

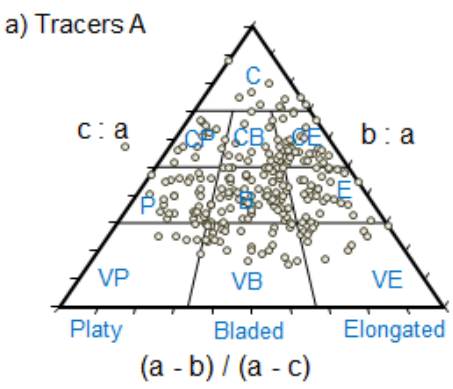

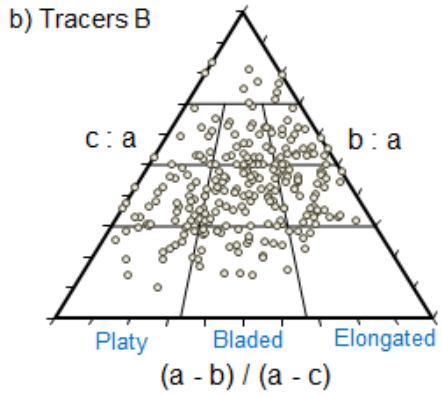

Sneed & Folk classes (A)		
Shape class	Count	Percent
Compact (C)	11	4
Compact-Platy (CP)	14	5
Compact-Bladed (CB)	17	6
Compact-Elongate (CE	32	12
Platy (P)	37	14
Bladed (B)	72	27
Elongate (E)	31	11
Very-Platy (VP)	10	4
Very-Bladed (VB)	31	11
Very-Elongate (VE)	15	6

Sneed & Folk classes (B)		
Shape class	Count	Percent
Compact	10	4
Compact-Platy	12	4
Compact-Bladed	28	10
Compact-Elongate	25	9
Platy	39	14
Bladed	61	23
Elongate	40	15
Very-Platy	19	7
Very-Bladed	32	12
Very-Elongate	4	1

Figure 3.9. Sneed and Folk classes for both A and B sets of tracers. The ten classes: compact (C) to very elongated (VE) are labelled in the first diagram.

To study the relationship between shape and travelled distance, the Zingg (1935) classification system was used in which the tracers were divided into 4 shapes: disc, sphere, blade, and rod as shown in Figure 3.10.

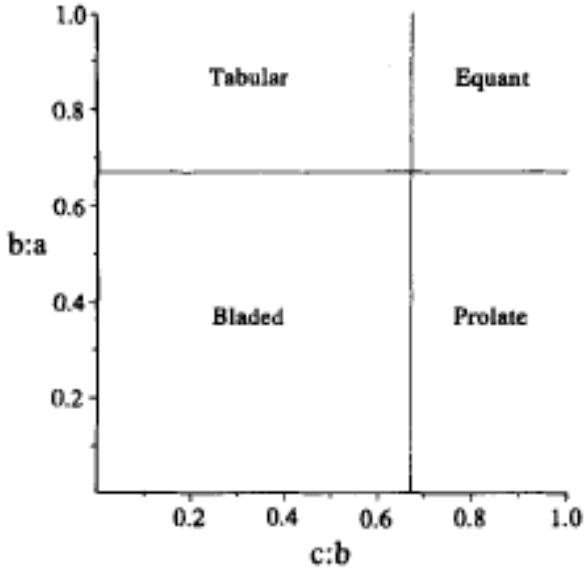

Figure 3.10. The Zingg (1935) diagram.

3.2.2 Tracer preparation

Pebbles of the required sizes were randomly collected from the river bed in the study site and all the pebbles, except the largest size class, were brought to the laboratory for drilling, insertion of magnets, painting and numbering. Each tracer was drilled and embedded with an Alcomax rod magnet. Three sizes of magnet were used (3 x 10 mm, 5.5 x 17 mm, and 6 x 20 mm), the smallest size 3 mm diameter magnet was used for the tracers below 64 mm size to avoid the possibility of breaking. Epoxy resin (Evo Stik Epoxy Express) was used to secure the magnet and plug the hole. To identify each tracer in the field, the tracers were labelled with identification (ID) numbers from 101 - 760 (*i.e.* ID 101 – 200 for < 32 mm tracers, 201 – 280 for < 45 mm tracers and so on). The ID labels were also secured by the epoxy resin. The tracers were painted with bright yellow masonry paint to make them visible in the channel. To make them stand out from A tracers, the B tracers were half-painted with red masonry paint on top of the yellow paint. The magnets in the pebbles allowed them to be located them when they were buried and when the paint was worn off. The tracers were photographed, weighed and *a*, *b* and *c* axes were measured to facilitate identification when their labels became illegible. The size (*b*-axis) and mass of the set-A and B tracers are plotted in Figure 3.11 which shows that the mass and size are very well correlated ($R^2 = 0.94$) and the best-fit exponents are close to what one would expect ($M \propto D^3$ for identical shape and density).

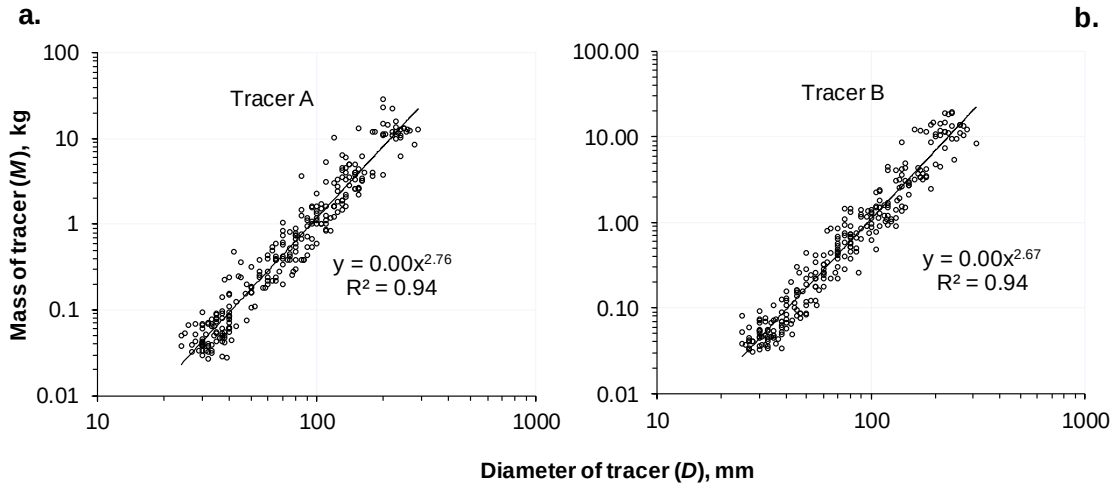

Figure 3.11. Mass *M* versus diameter *D* (*b*-axis) of the tracer pebbles. The best-fit equations for A and B tracers are $M \propto D^{2.76}$ and $M \propto D^{2.67}$.

The size distribution of the tracers for both sets was identical because each half-phi size class contained the same number of grains. The D_{16}, D_{50} and D_{84} for the tracers were 32, 67 and 157 mm respectively, the smaller size class was < 32 mm. Figure 3.12 shows the GSD of the tracer particles compared to four representative GSD samples from the study site (AL4: upper alluvial, SA-1: upper semi-alluvial, LSA-2: boulder-riffle, and LSA-4: near the bottom end of the lower semi-alluvial reach). This plot shows that the tracer sizes span most of the range of sizes in the bed.

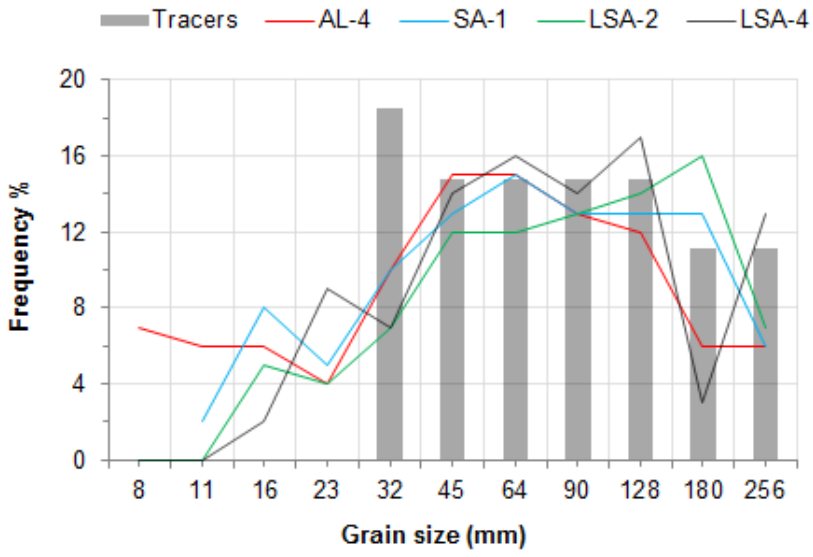

Figure 3.12. Grain size distribution for tracers compared with representative bed material samples from upper alluvial (red: AL-4), upper semi-alluvial bar (blue: SA-1), boulder-riffle (green: LSA-2), and bottom end in lower semi-alluvial reach (black: LSA-4).

3.2.3 Tracer seeding

Both sets of tracers were seeded on 29th August 2013, set A in the upper alluvial reach and set B in the bare rock gorge as shown in Figure 3.13.

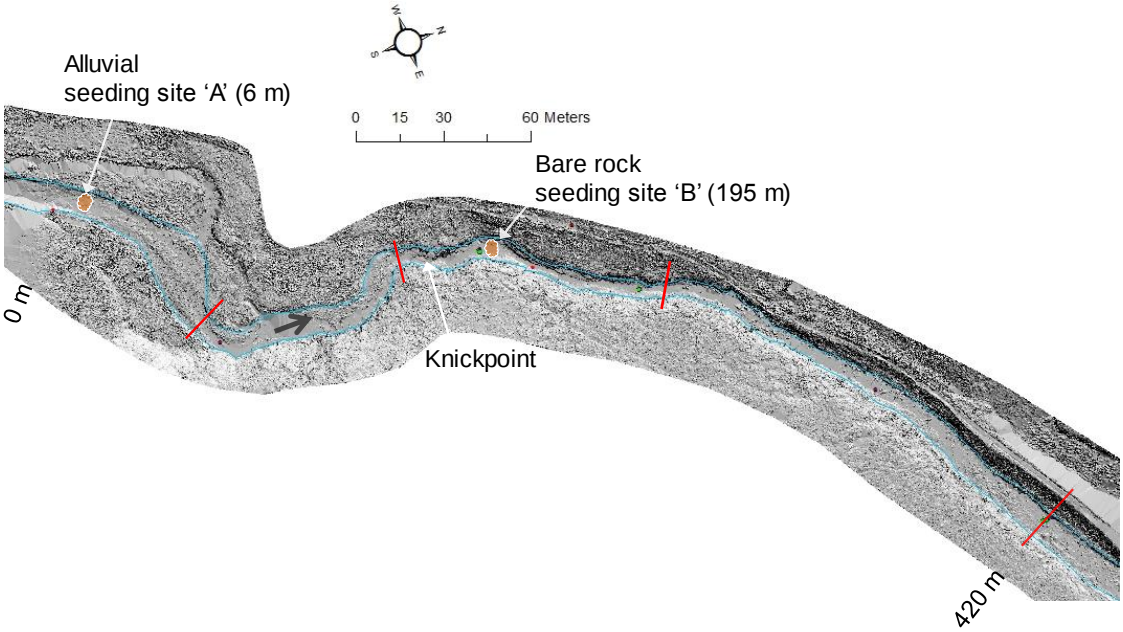

Figure 3.13. A DEM showing the tracer seeding sites A (alluvial bed, x = 6 m) and B (bare rock gorge, x = 195 m). The reaches are marked by red lines and black arrow indicates the flow direction.

The A tracers on the fully alluvial bed were laid out in the centre of the channel in a rectangular grid creating an artificial patch (Figure 3.14a). Similarly, the B tracers were emplaced on the rock bed just after the plunge pool at the base of the knickpoint but before a small rapid after which the channel width becomes narrow (Figure 3.14b, c).

Figure 3.14. Photographs taken at the time of tracers seeding on 29th Aug 2013: a) tracers at alluvial seeding site B; b) photograph of the rock gorge looking upstream showing seeding site B, plunge pool and knickpoint; and c) photograph of the gorge looking downstream showing the tracers at site B. The black arrow indicates the flow direction.

The A tracers have to travel 70 m in a fully alluvial reach and 85 m in the upper semi-alluvial reach before they enter the bare rock gorge. Similarly, the B tracers have to travel 65 m in the gorge, 45 m in the pool and boulder-riffle, and 115 m in the lower

semi-alluvial reach before they enter the downstream alluvial reach. The equal numbers of tracers deployed at the same time in alluvial and bare rock reaches allowed differences in bedload transport in a sequence of contrasting reaches to be identified.

3.2.4 Tracer surveys

Once the tracers were emplaced the routine surveys of the tracers were carried out, particularly after large flow events. Seven surveys were carried out for each set of tracers over the period of 19 months. The first six surveys were carried out in the nine months' period at an interval of one to two months either after a big event or a noticeable movement of the tracers was observed. No significant movement of the tracers occurred for a long period after the 6^{th} survey but as soon as a significant movement of the tracers was observed the final survey (7^{th}) was carried out on 10^{th} April 2014. In most occasions the stream flow was low and most tracers were found by sight. The few tracers that were buried or hidden (< 5% A tracers and < 10% B tracers) were located by using magnetic locators (magnetometers) (such as RD316), which can detect tracers at least 0.6 m below the surface (Ferguson & Wathen, 1998), and recovered by digging. The maximum recovery depth was < 0.30 m which was easily uncovered. The maximum burial depth was 0.15 m, Demir (2000) found the maximum burial depth in Trout Beck was 0.22 m. Once the tracers were found, the identity and position of each tracer was logged and mapped using dGPS. After logging the positions the tracers were left on surface where they were found even if they were found buried. The position of the tracers was also noted, for example whether it was isolated or in cluster, and whether it was on surface or buried. The tracers were searched in a systematic way in marked strips and the surveys generally covered the entire study reach and some 125 m further down in the lower alluvial reach, beyond which no tracers were visible. In last few surveys it was found that the identification labels of some recovered tracers (~ 10%) were not clearly readable and had to be identified from half phi size class, *a*/*b*/*c* axes and their positions in previous surveys. The information about the survey dates, recovery, dispersal and other results are detailed in chapter 5.

3.2.5 Tracer data analysis

The main aim of the tracer experiment was to investigate the bedload mobility, size selectivity, and the critical discharge. With the tracers data the transport distances against shape and size were analysed, critical discharge values were established and compared with the estimates from empirical relations and impact sensors data (Chapter 7).

This study analysed the movement of tracers from both sites over a period of 19 months. A record of flow events was obtained by flow and stage measurement, rating curves and data from EA gauging station (Section 3.1). Travel distances were calculated using the straight-line distance between the dGPS Easting and Northing coordinates of the seeding site and recovery site. The effect of Z-coordinates in the distance calculation found to be negligible (< 7 cm). For any A tracers that travelled past the knickpoint, because of the bend in the channel, the straight-line distance would be lesser than the actual channel distance, in such cases the distances were calculated as the sum of several short stretches. The virtual velocities (Section 5.3) were also calculated to quantify the bedload mobility.

Size selectivity was analysed in two ways: by regressing the travel distances of individual tracers on their *b*-axis diameter or mass as described by Ferguson *et al.* (2002), and by calculating and plotting the mean distance of transport from seeding to the tracers' positions for each half-phi size class. In addition to these two approaches, the virtual velocity approach was also used to investigate the size-selectivity, see below. This allowed differences in mobility both within the reaches (through size selectivity) and between the reaches to be identified. Dispersal of tracers was studied by plotting the cumulative percentage of tracers recovered at different distances downstream from each seeding sites. The relations between dispersion and alluvial cover, channel width and channel slope were studied (Section 5.2.1).

3.3 Bedload transport measurements using bedload impact plates

The bedload impact plates are alternative ways to gather some information on the bedload transport which is already discussed in section 1.1.7. These plates are attached with sensors and installed and downloaded at low flows. The sensors data are useful to investigate the threshold conditions for entrainment and cessation and also gives some information about the sediment supply conditions in the contrasting reaches of the study site.

3.3.1 Equipment

The impact sensors register vibrations generated by strikes of moving particles on a steel plate mounted in the river bed and record the number of impacts generating a signal above a threshold voltage in a set interval. The sensor device consisting of the *TGPR*-1200 data logger and an accelerometer was kept inside a watertight steel tube (60 mm diameter, 42 mm length) that was welded to a stainless steel impact plate

(150 x 130 x 6 mm in size). The open end of the tube was sealed with a laboratory bung and the plate was installed flush with the channel bed and fixed with the rock fixings. The tube was accommodated inside a recess made into the bare rock in the channel bed. It recorded the number of pings during each logging interval, which was set to 5 minutes to match the logging interval of pressure transducers (PTs). This required downloading every 55 days, and the battery needed replacing after about a year. The logger required Tinytag Explorer software (Gemini, 2014) and a USB cable. Downs *et al.* (2016) based on their flume test reported that this type of impact sensor (they called 'Benson-type') can detect the grain size of 12 mm and their field data indicated that the minimum detectable size could be in the range 9-12 mm.

3.3.2 Field sites

Five impact plates were installed in three locations of the channel (2-1-2): two in the top section in the bedrock gorge immediately upstream of the tracer seeding site (B), one in the middle section near the bottom of the rock gorge, and two in the bottom section at the end of lower semi-alluvial reach (Figure 3.15).

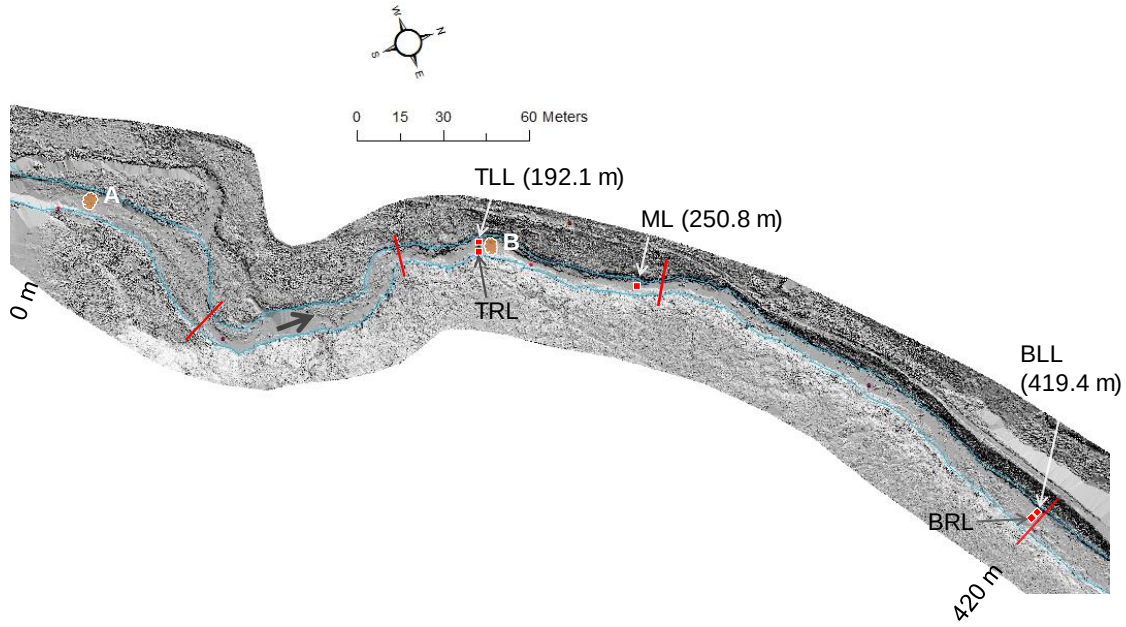

Figure 3.15. A DEM showing the bedload impact sensors (red squares). The TLL (top left logger) and TRL (top right logger) in the rock gorge (x=192.1 m) immediately upstream of the tracer seeding site B (195.0 m), the middle logger ML (250.8 m) near the end of the gorge; the BLL (bottom left logger) and BRL (bottom right logger) at the end of the lower semi-alluvial reach (419.4 m). The reach boundaries are marked by red lines, the tracer seeding sites A and B are shown. The thick black arrow shows the flow direction.

The site for upper plates TLL and TRL was chosen at the top of the bedrock gorge which allows the sensors to record the sediment entering into the bedrock gorge through the upper alluvial and semi-alluvial reach. The best available location at the top of the

gorge was immediately downstream of the knickpoint/plunge pool (Figure 3.16). This is a wide cross-section where two plates were installed adjacent to each other in order to study the lateral variation of the bedload movement. The plates were next to PT_3 (Figure 3.5) and few metres upstream of tracer seeding site B.

Figure 3.16. a) Photograph showing the knickpoint, plunge pool and upper site impact plates TLL and TRL. The sensor (inside the metal tube attached to the plate), the rubber bung that seals the sensor and the drilled hole where the plate was fixed are shown. b) Downstream view of the gorge showing the impact plates. The black arrow shows the flow direction.

The middle site for ML (Figure 3.17) was chosen near the end of the rock gorge so that it could record the bedload that entered the lower semi-alluvial reach and also it would

provide a check on the data recorded at upper site sensors in the gorge. The lower site for BLL and BRL (Figure 3.18) was chosen at the end of the study site which tells about the sediment transport through the lower semi-alluvial to the lower alluvial reach.

Figure 3.17. Photograph showing the ML in the gorge. The inset photograph shows the close view of the ML location.

Figure 3.18. Photograph showing the BLL and BRL at the bottom end of the lower semi-alluvial reach. The left side plate BLL was on the channel talweg.

Cray (2010) had also used these sites, but one sensor in one location, therefore one enclosure at each location was already there to put the sensor in the channel bed. The channel distance between the top and the middle section is ~60 m and between middle and the bottom section is ~170 m. Three loggers TLL, ML and BRL, one at each location, were installed on 7th August 2013. The TRL was added next to the TLL on 6th September 2013; and the BLL was added next to the BRL on 1st December 2013. The plates were installed and downloaded in low flow days. The data were collected for 20 months until the last downloading of 10th April 2015.

This chapter has outlined the methodologies and detailed how the field instrumentation and monitoring were carried out to investigate the bulk hydraulics (mean depth, velocity, wetted width, flow resistance, shear stress) and coarse sediment transport. The river discharges were measured using the electromagnetic current meter and salt-wave measurements. The flow velocities were estimated by salt-wave travel times and continuity equation by using the measured water surface profiles and channel cross-sections in hydraulic sub-reaches. The stage-discharge rating curves were developed using the measured quasi-continuous stages and the discharges. The coarse sediment transport was investigated by using two sets of 270 tracer pebbles, one starting in the upper alluvial reach and the other in the downstream bare rock gorge, monitored for nineteen months. The bedload impact plates were installed to record the impacts counts which provided the information about the start and end of the bedload transport which were used to investigate the critical discharge and shear stress in different reaches. The results are discussed in chapter 4 (bulk hydraulics), 5 (tracer pebbles) and 6 (impact sensors).

4 Bulk flow characteristics of sub-reaches

This chapter presents the results of measurements and calculations of bulk flow characteristics, averaged over the width of the stream, for the study reach and sub-reaches, in order to answer research question 1 (Section 1.4.1). In particular, the chapter describes and discusses how the mean depth, mean hydraulic radius, mean velocity, flow resistance and average shear stress vary with discharge and how they differ between the bare rock, semi-alluvial and alluvial reaches. The spatial and temporal variation of flow hydraulics along the channel has been studied as this is particularly important for bedload transport. The reach-averaged bed shear stress, the main driving force for bedload transport, is determined from the mean flow depth, which is dictated by the channel shape and bed roughness, and the channel slope. However, only the effective shear stress *i.e.* the portion of the average shear stress which is acting on the mobile grains is responsible for sediment transport. The remaining portion of the shear stress will be borne by the immobile parts of the channel including the elements of form resistance. This analysis allows comparisons with what others have found in other steep bedrock or alluvial channels and is also useful for understanding the tracer results. The objectives of this chapter are to:

- examine hydraulic geometry to understand tracer behaviour and for comparison with findings of at-a-station hydraulic geometry in other kinds of river. This includes how mean width, depth and velocity in each of the contrasting sub-reaches (Section 2.5) change with discharge
- investigate whether the flow resistance for contrasting sub-reaches varies with discharge and if so in what way
- analyse the differences in shear stress between sub-reaches, especially at high flow conditions to help understand tracer behaviour
- identify differences between sub-reaches in total shear stress and effective shear stress.

In order to achieve these objectives measurements of cross-section geometry, water stages, water surface profiles, velocity and discharge (Section 3.1) were carried out. The direct measurements of some variable such as discharge, water surface, and velocity were only possible up to moderate discharge; therefore indirect methods were also necessary for high-discharge flow characteristics (Section 3.1.5).

This chapter is divided into seven sections. Section 4.1 presents the results of stage and discharge measurements; section 4.2 discusses the results of velocity measurement from salt waves and the continuity equation; sections 4.3 to 4.6 investigate at-a-station hydraulic geometry, flow resistance, total shear stress, and effective shear stress respectively; and finally section 4.7 summarises the chapter.

4.1 Stage and discharge

Quasi-continuous water stages were recorded using seven pressure transducers (labelled PT_1 to PT_7) at different locations along the study channel (Section 3.1.4). PT_1 was installed in the upper alluvial reach, PT_2 in the upper semi-alluvial reach, PT_3 to PT_5 in the bare rock gorge, and PT_6 and PT_7 in the lower semi-alluvial reach. The two Campbell loggers PT_1 and PT_4 recorded the water levels at 15 min intervals while the other five Mini-Divers recorded at 5 min intervals; all loggers were synchronised. Figure 4.1 shows the stage hydrograph for each PT for the study period. A staff gauge board TBG (Figure 3.7) was also installed in the study reach where stages were recorded manually during field visits. The results of the discharge (Q) measurements using current meter, dilution gauging and catchment area ratio methods (Section 3.1) and the stage-discharge rating curves are discussed in this section.

4.1.1 Discharge measurement using current meter

The electromagnetic current meter (ECM) provided both the streamwise and lateral velocities averaged over a period of 30 seconds (Section 3.1.1). The discharge was calculated by the mean section method, with the velocity averaged at 0.2 and 0.8 times the depth (Shaw, 1994; Herschy, 1998). Table 4.1 summarises the Q ranging from 0.05 to 1.2 $m^3 s^{-1}$ measured on eight occasions at ECM gauging section (Figure 3.2).

Table 4.1. Discharge (Q) measurement by velocity-area method.

Date	Q ($m^3 s^{-1}$)
19.08.13	0.157
17.09.13	1.181
22.09.13	0.101
26.09.13	0.046
10.10.13	0.109
16.10.13	0.223
12.11.13	0.190
18.11.13	0.891

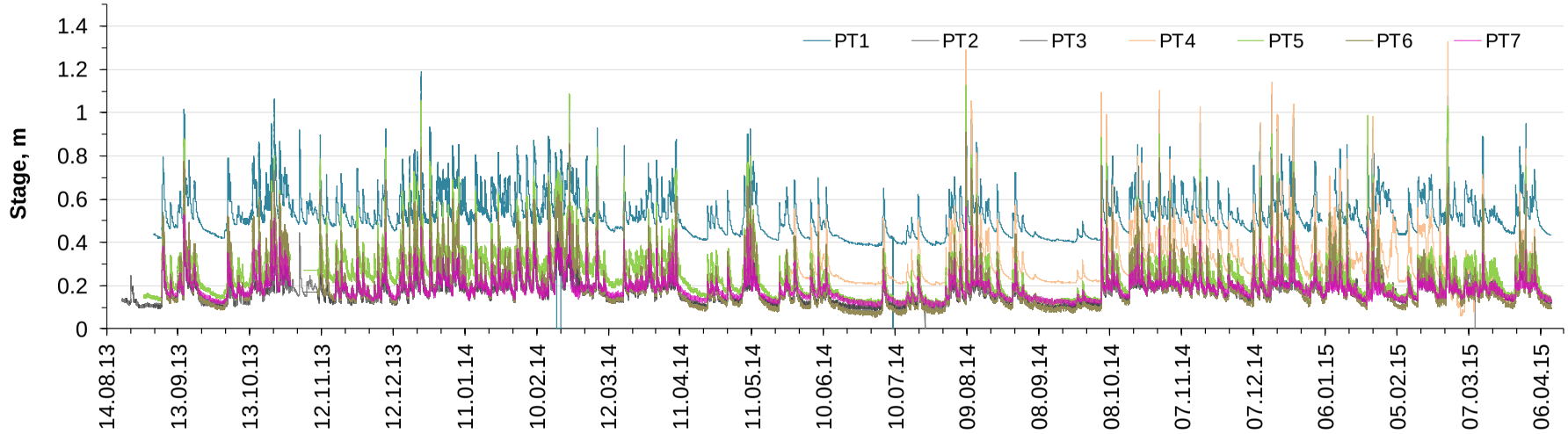

Figure 4.1. The water levels recorded by pressure transducers PT_1 to PT_7 at the study site.

4.1.2 Discharge measurement by salt dilution

A known mass of salt (tracer) dissolved in water was suddenly injected to the stream whose conductivity was constantly monitored at two downstream locations. The distance of upper probe from the point of injection (mixing length) and the salt quantity used in the dilution gauging are discussed in section 3.1.2. The measurements were made in five sub-reaches (24 to 28 m long) with contrasting beds: F1 (upper alluvial), F2 (bare rock), F3 (boulder-riffle), F4 (lower semi-alluvial, 70% cover), and F5 (semi-alluvial, 20% cover) (Section 2.5). A few measurements were carried out before finalising the sub-reach locations; these are used for rating curve development only, not for detailed hydraulic calculations for sub-reaches. Using the measured conductivity (EC) at upper probe P_1 and lower probe P_2 the respective discharges Q_1 and Q_2 were calculated using Eq. 3.2. A total of 52 salt-wave measurements were carried out over 14 dates. The results are shown in Table 4.2 which shows the measured discharges Q_1 and Q_2, the average of the two and the adopted discharge for further analysis which ranges from 0.05 to 2.1 $m^3 s^{-1}$. The chosen discharge (Q) for further analysis is generally the average of Q_1 and Q_2 (*i.e.* Q_{avg}), with a few exceptions as some of the values were found to be unexpectedly high or low, which are then rejected. Figure 4.2 shows the values that are replaced either by the Q estimate from TBG rating curve (will be discussed in 4.1.4) or one of the salt wave discharges (Q_1 or Q_2) after comparing with the EA scaled-down discharge. The data show that the Q estimates by salt dilution agreed well with each other (the 2 probes) and with the discharge measured using the velocity-area method (Section 4.1.1) on the same day.

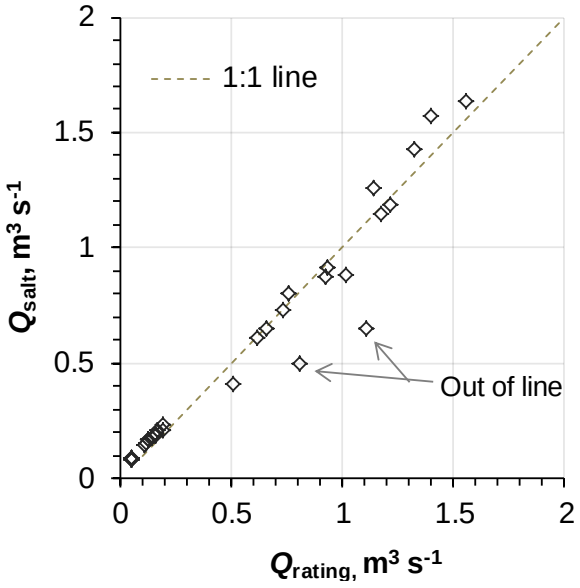

Figure 4.2. Average Q from salt-dilution (Q_{salt}) versus Q from TBG rating curve (Q_{rating}). The data away from 1:1 line were considered unrealistic and rejected.

Table 4.2. Discharge ($m^3 s^{-1}$) measured by salt-dilution: Q_1, Q_2, Q_{avg} are the discharges at probe P_1, probe P_2 and the average of the two. The unrealistic values were either replaced by rating-curve-derived Q (highlighted), or one of the two discharges was chosen (underlined). The adopted Q is the chosen discharge for further analysis. Measurements up to 30.12.2013 were carried out in slightly different locations but still within F2, F3 and F4 areas.

Sub-reach	Date (run)	Q_1	Q_2	Q_{avg}	Adopted Q
F1	31.03.14	0.13	0.18	0.16	0.13
	26.05.14	0.18	0.18	0.18	0.18
	10.04.14	0.18	0.18	0.18	0.18
	08.04.14	0.35	0.46	0.41	0.51
	11.05.14	0.82	0.95	0.89	0.89
	01.04.14	0.64	0.66	0.65	1.11
F2	27.05.14	0.08	0.08	0.08	0.08
	31.03.14	0.14	0.14	0.14	0.14
	26.05.14	0.17	0.17	0.17	0.17
	10.04.14	0.19	0.20	0.20	0.20
	08.04.14	0.59	0.63	0.61	0.61
	11.05.14	1.11	1.18	1.15	1.15
	01.04.14	1.16	1.21	1.19	1.19
Slightly downstream of F2	06.09.13r_1	0.06	0.05	0.05	0.05
	06.09.13r_2	0.08	0.07	0.07	0.07
	06.09.13r_4	0.55	0.47	0.51	0.51
	06.09.13r_6	1.29	1.00	1.15	1.00
Slightly upstream of F3	30.12.13r_2	0.99	1.19	1.09	1.09
	30.12.13r_3	1.11	1.12	1.11	1.11
	30.12.13r_4	1.21	1.12	1.16	1.16
F4	27.05.14	0.09	0.09	0.09	0.09
	31.03.14	0.14	0.13	0.14	0.14
	26.05.14	0.17	0.16	0.17	0.17
	10.04.14	0.21	0.20	0.21	0.21
	08.04.14	0.63	0.66	0.65	0.65
	11.05.14r_3	0.85	0.90	0.88	0.88
	11.05.14r_2	0.92	0.91	0.91	0.91
	11.05.14r1	1.49	1.37	1.43	1.43
	01.04.14	1.60	1.55	1.58	1.58
F3	26.09.13*	-	-	0.04	0.04
	27.05.14	0.09	0.08	0.08	0.08
	22.09.13	0.10	0.11	0.10	0.10
	31.03.14	0.14	0.14	0.14	0.14
	17.12.13r_2	0.15	0.15	0.15	0.15
	26.05.14	0.16	0.15	0.16	0.16
	17.12.13r_1	0.17	0.17	0.17	0.17
	10.04.14	0.22	0.20	0.21	0.21
	08.04.14	0.74	0.72	0.73	0.73
	18.11.13r_3	0.79	0.71	0.75	0.75
	18.11.13r_2	0.86	0.73	0.80	0.80
	18.11.13r_1	0.97	0.82	0.89	0.89
	30.12.13r_1	1.08	1.17	1.12	1.12
	11.05.14	1.22	1.30	1.26	1.26
	01.04.14	1.65	1.62	1.64	1.64
	17.09.13r_1	1.97	1.80	1.88	1.88
	17.09.13r_2	2.02	2.10	2.06	2.06
	17.09.13r_3	2.63	2.09	2.36	2.09
F5	27.05.14	0.09	0.09	0.09	0.09
	31.03.14	0.15	0.14	0.15	0.15
	10.04.14	0.22	0.24	0.23	0.23
	08.04.14	0.64	0.36	0.50	0.81
	11.05.14	0.79	0.80	0.80	0.80

*Measured by a single probe conductivity meter

4.1.3 Discharge estimation by catchment area ratio

The *Q* from the Environment Agency (EA) gauging station, scaled by the catchment area ratio, has also been used in the analysis to extend the rating curves and perform high *Q* calculations. As explained in section 3.1.5, direct measurement of high discharges, though attempted a few times, was not successful because of the flashiness of the channel. The EA discharges are plotted against the measured discharges at the study site in Figure 4.3 which shows a very strong linear correlation ($R^2 = 0.98$). The gradient of a linear fit is 0.63 which is very close to the catchment area ratio of 0.62 at the study site.

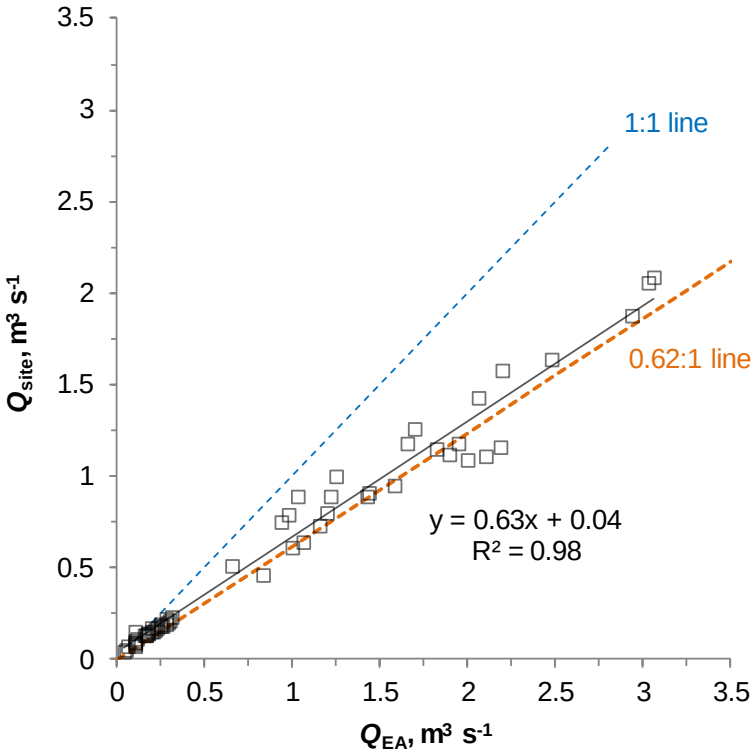

Figure 4.3. The linear relationship between discharge at study site and EA station. The regression equation is $Q_{site} = 0.63Q_{EA} + 0.04$ ($R^2 = 0.98$), the 95% confidence intervals are ±0.03 for the slope and ±0.04 for the intercept, and is significant at $p < 0.001$. The 1:1 line (blue) and 0.62:1 line (orange) are shown for comparison.

The discharges are also estimated for each PT using the stage-discharge rating curves which will be discussed below in section 4.1.4. The stage-derived discharges at each PT follow the same pattern as the EA discharges. This shows that the catchment area ratio works well for flood flows generated by frontal rainfall, though not necessarily for events generated by convective storms in summer (which occur only rarely). Figure 4.4 shows the study site hydrographs superimposed on each other: one is the scaled down *Q* whilst the other is derived from the PT_6 rating curve. Both the discharges agree well except in the thunderstorm event of 08.08.2014 (see Figure 4.6 f).

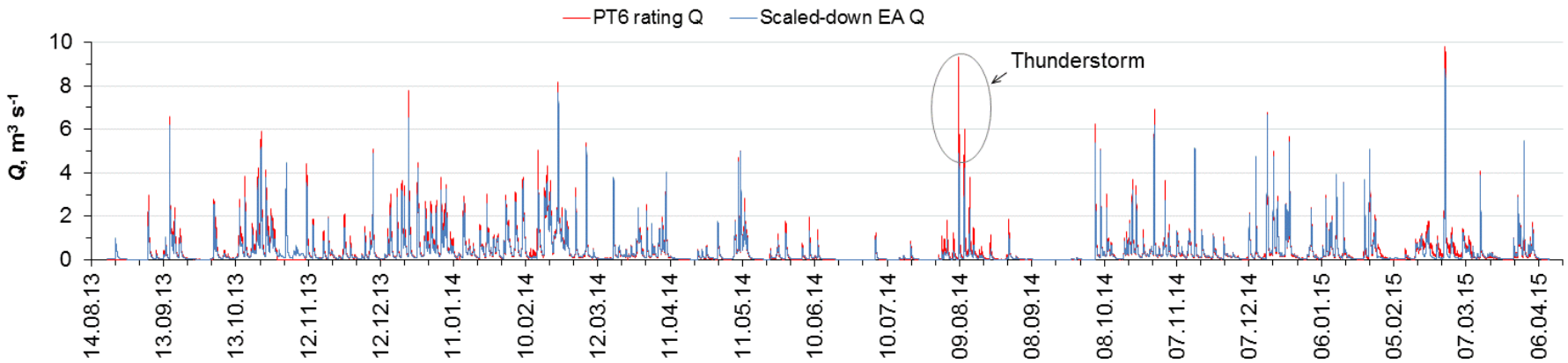

Figure 4.4. The study site *Q* obtained from PT_6 rating curve (red) and EA *Q* scaled by catchment area ratio (blue). The scaling ratio works well except for the event caused by thunderstorm (08.08.14).

4.1.4 Stage-discharge rating curve

A stage-discharge rating curve was developed for the local gauge board (TBG) as well as for each PT. At TBG the stage readings were taken at regular intervals during each day of salt-wave measurements. Figure 4.5 shows the TBG rating curve and a best-fit equation.

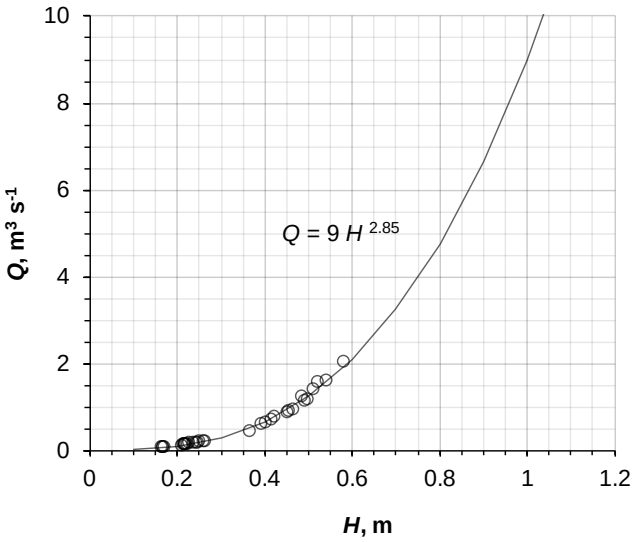

Figure 4.5. Stage-discharge rating curve for TBG based on the discharge measured by salt-dilution and stage manually recorded at TBG when at the field. The rating curve equation is $Q = 9H^{2.85}$, where Q is the measured discharge ($m^3 s^{-1}$) and H is the water stage (m). The correlation is significant at $p < 0.001$.

Stage data and discharges were used to establish a rating curve for each PT. Since the measured data only extended up to 2 $m^3 s^{-1}$ the scaled EA data were used to extend the rating curves by the following process: (i) create a flow almanac recording the dates and times when several discharges occurred on the rising and falling limbs each of six large frontal-rainfall flood events during the study period, (ii) scale the EA discharge by using the catchment area ratio of 0.62, (iii) tally each scaled discharge to the stage at each stage recorder 15 minutes earlier to allow for travel time, (iv) add these high-flow stage discharge pairs to the measured low-flow pairs, and fit a curve of the form $Q = a\,(H - H_0)^b$ for each pressure transducer. The stage-discharge rating curves and the equations fitted to the seven PTs are shown in Figure 4.6 which shows all the rating curves fitted well with the field-measured low-Q and scaled high-Q data. The fitted rating curves have a root mean square residual error of 0.3 to 0.5 $m^3 s^{-1}$, some of which is probably due to small departures from the 0.62 scaling; part of this could also be due to the location and the accuracy of the stage recorder. For example PT_5 was in a small supercritical zone immediately after a small drop (Figure 4.7) and the data there were more scattered.

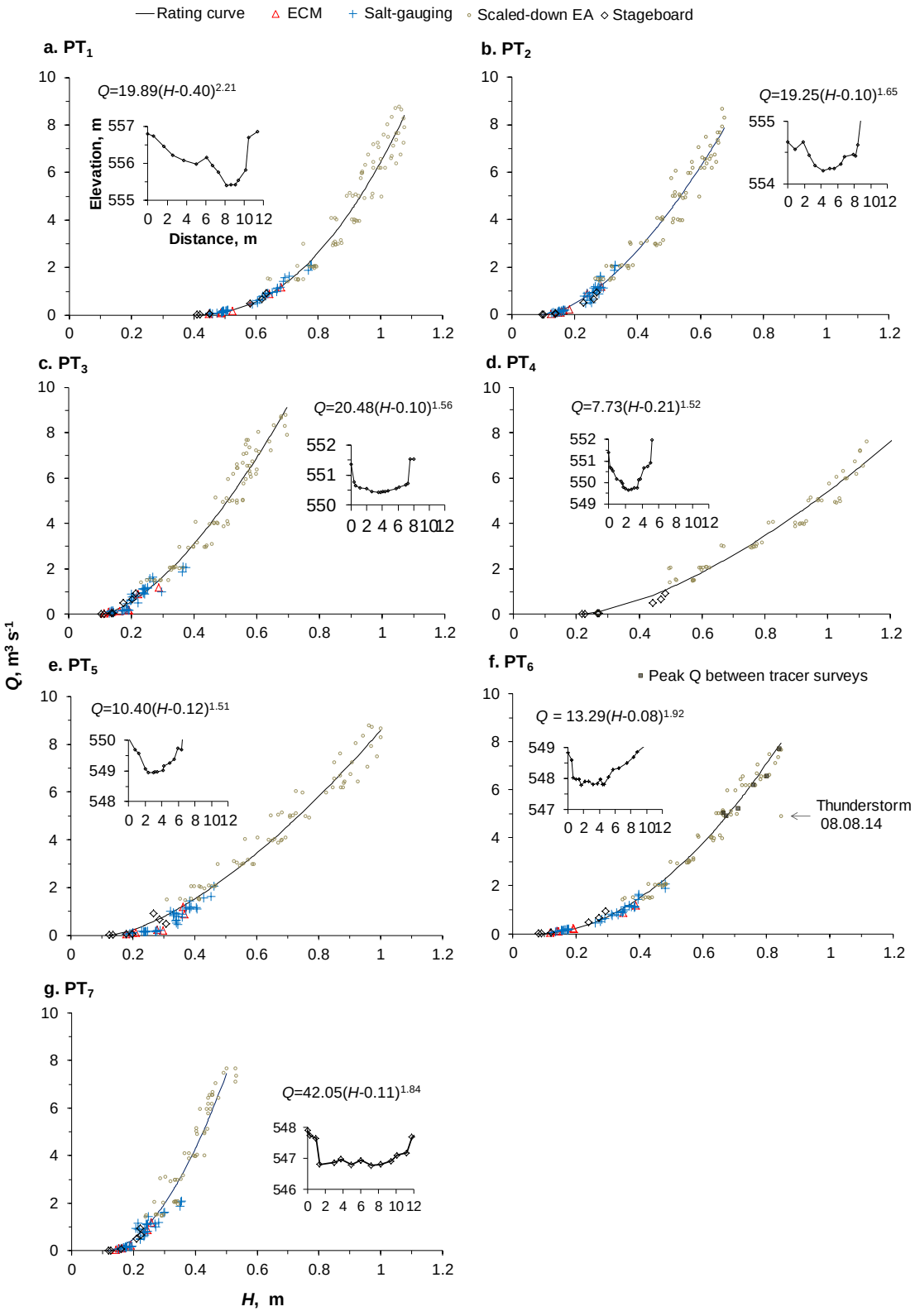

Figure 4.6. The stage-discharge rating curves and equations $Q = a\,(H - H_0)^{b}$ for PT_1 to PT_7 (a – g), cross-sections at each PT are also shown. The coloured markers indicate the type of Q: red (ECM), blue (salt-wave), black (TBG) and grey (scaled EA). The PT_6 curve (f) also shows the peak-Q during the successive tracer periods and the thunderstorm-induced event of 08.08.2014. All correlations are significant at $p < 0.01$.

Figure 4.7. The location of PT_5 immediately downstream of a small pool and a drop. Flow direction is shown by a white arrow.

Since there were two types of stage recorders, their precision might have some effect. PT_4 had not yet been installed when most of the salt-wave measurements were carried out so its rating curve is mainly based on EA scaled data and a few points from TBG. The scaled peak discharges between the successive tracer surveys (Table 5.1) are shown in Figure 4.6 (f). They agree closely with the rating curve, which implies that the rating curve works well at least up to 10 – 12 $m^3 s^{-1}$ discharge. Inverting these rating curves allows the stage at each PT to be predicted from the EA discharge with a root-mean-square error of 0.02 to 0.05 m (Figure 4.8). These inverted rating curves are of the form of $H = H_0+cQ^d$, where $c = (1/a)^d$, $d = 1/b$, and a and b are the coefficient and exponent of the equation $Q = a\,(H-H_0)^b$ shown in Figure 4.6.

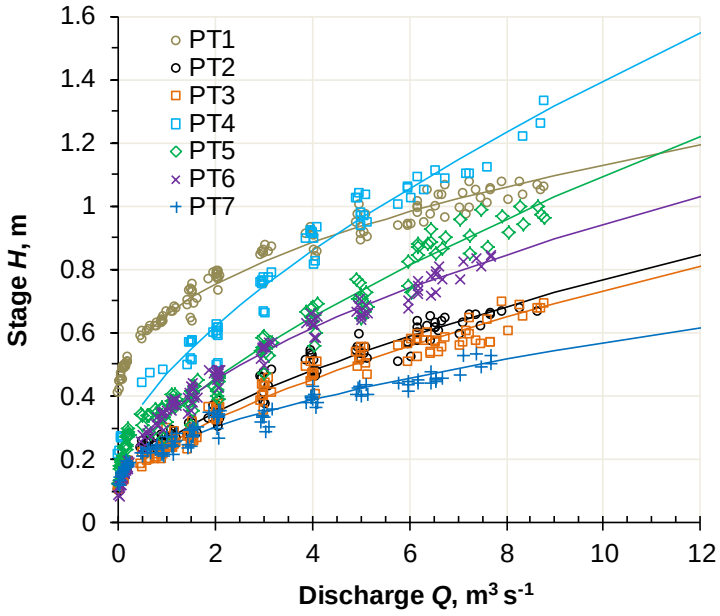

Figure 4.8. Inverted stage-discharge rating curves of the form $H = H_0+cQ^d$ for all PTs.

Summary

The discharge and stage measurements undertaken in this study provided reasonably good data sets with which to undertake the intended analysis; a few measurements were erroneous but were rejected after careful examination. The developed rating curve for each PT location was very useful to estimate bulk hydraulics properties at high discharges, as discussed later (Section 4.2.3). Salt dilution was the main method for *Q* measurement, though current metering was also used to supplement the dataset and check the salt-wave measurements. In steep/rough terrain in flashy rivers where the water levels rise or drop quickly, dilution gauging has some merits over current metering- it does not require a uniform section as for the ECM measurement and is quicker.

4.2 Velocity measurements and calculation of bulk properties

The bedload transport study requires an understanding of how the reach-average velocity and other bulk hydraulic properties vary with discharge and bed substrate. This is also important for comparison with what bedrock modellers assume about how depth and shear stress vary with discharge. Mean velocity in this study is required to calculate flow resistance coefficients including Manning's *n* and Darcy –Weisbach *f*. The mean velocity (*V)* was estimated from paired salt waves, as well as from the measured water levels and channel cross-sections using the continuity equation; the latter method also enabled calculations for flood flows. This section presents the observed bulk hydraulic characteristics and discusses how they varied with discharge along the study reaches of varying bed character.

4.2.1 Velocity from salt waves

The velocities were estimated from salt-wave travel time between two probes at either end of a sub-reach using centroid and harmonic mean methods (Section 3.1.5) for all 52 salt-wave measurements (Table 4.2). Some typical salt-wave plots of conductivity versus travel time from sub-reaches F1 to F4 are discussed below. The plots also show the velocities calculated using centroid (V_c) and harmonic mean (V_{hm}) methods and the difference between the two.

Sub-reach F1 (Upper alluvial)

Figure 4.9 shows the salt-wave plots recorded at probes P_1 and P_2 in the alluvial sub-reach F1 at different dates and discharges. The injection point was 130 m upstream of

P_1 (Table 3.1). The pairs of curves for each of the measurements show the expected pattern: the P_2 wave lags the P_1 wave and is more attenuated, with a lower peak. The data shown in Figure 4.9 demonstrate that the velocities increased with discharge. V_c and V_{hm} were in close agreement except in a few cases. The plot also shows the different background conductivity at different Q or dates, for *e.g.* 0.019 µS cm^{-1} for Q = 0.90 m^3 s^{-1} (11.05.14) and 0.057 µS cm^{-1} for 0.13 m^3 s^{-1} (31.03.14). The differences in the initial conductivities were as expected: higher background conductivity at lower Q, when most or entirely all of the base flow that has been in the ground and had the opportunity to dissolve weathering-product solutes adding to the solutes already present in rainwater.

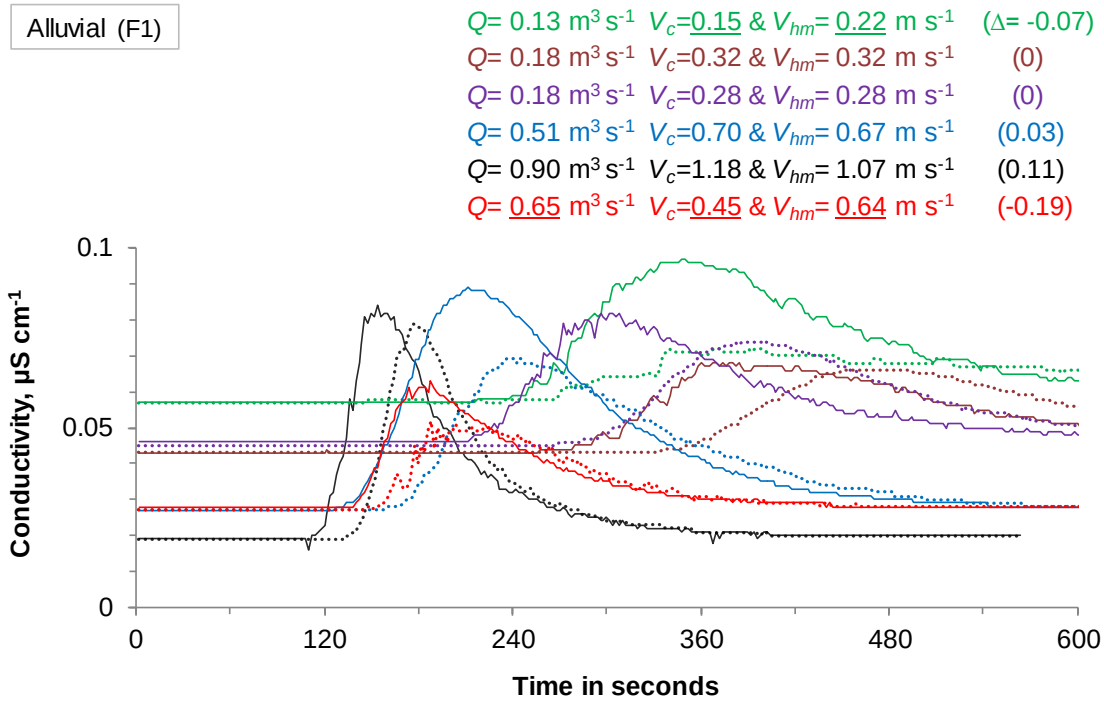

Figure 4.9. Plots of conductivity versus travel time at F1 (the time 0 sec is when the salt was injected) at different discharges (measured at different dates) shown by different colours. The solid lines are the waves at upper probe P_1 and dotted lines are at lower probe P_2, which were spaced 25.1 m apart. Q, V_c, V_{hm} and the difference ($\Delta = V_c - V_{hm}$) are shown in coloured text, same colour as in the curves. Unrealistic values of Q and V are underlined.

Sub-reach F2 (Bare rock gorge)

Salt-wave plots for the bare rock sub-reach F2 are shown in Figure 4.10, where the salt was injected at ~ 60 m upstream of P_1 (Table 3.1). V_c and V_{hm} in the rock gorge agree very closely. The blue curves for 08.04.14 (Q = 0.61 m^3 s^{-1}) have higher peaks than the black curves (1.15 m^3 s^{-1}; 11.05.14) and red curves (1.19 m^3 s^{-1}; 01.04.14) because more salt was used. The blue P_1 curve has a much higher peak than the blue P_2 curve,

possibly suggesting that full mixing at P_1 was not achieved on that occasion; perhaps because of this the Q_1 and Q_2 (0.59 and 0.63 $m^3 s^{-1}$) were slightly different (Table 4.2).

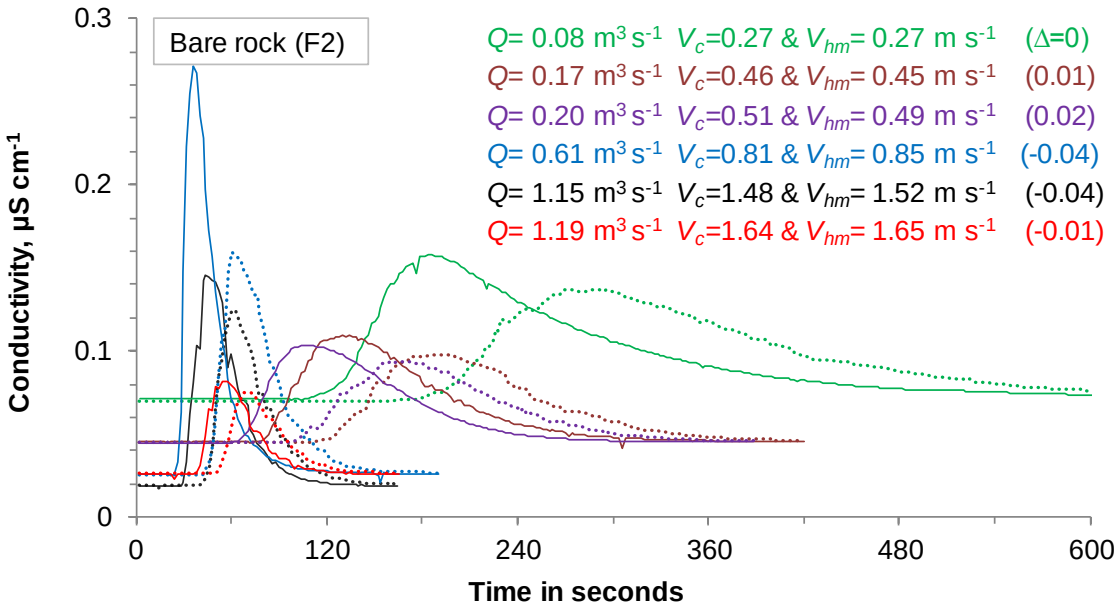

Figure 4.10. Plots for conductivity versus travel time for sub-reach F2. The solid and dotted lines respectively represent the observed waves at P_1 and P_2 spaced 26 m apart. The difference in velocity (in brackets) indicates the velocities in this sub-reach were in very good agreement.

Sub-reach F3 (Boulder-riffle)

Salt-wave plots for the boulder-riffle sub-reach F3 are shown in Figure 4.11. Contrary to the bare rock sub-reach, the V_c and V_{hm} estimates for this sub-reach are not consistent; sometimes the values were unrealistic and the difference was quite high. Three consecutive measurements carried out at F3 during a falling limb of a moderate flood of 11.05.14 are shown in Figure 4.12. The discharge dropped from 1.5 to 0.9 $m^3 s^{-1}$ from the first run (11:21:00 – 11:25:00) to the second (15:16 – 15:23) and third runs (15:39 – 15:45) within 4 hours 30 minutes. The jagged curves at the upper probe possibly indicate the intermittent presence of the probe in the main flow, with the probe moving back and forth between the main flow in the centre and the low-speed flow near the bank of the channel (Figure 4.13). This intermittency led to inaccuracies in the estimated velocities, clearly seen in the inconsistent and very high values of V_c and V_{hm} in the first run.

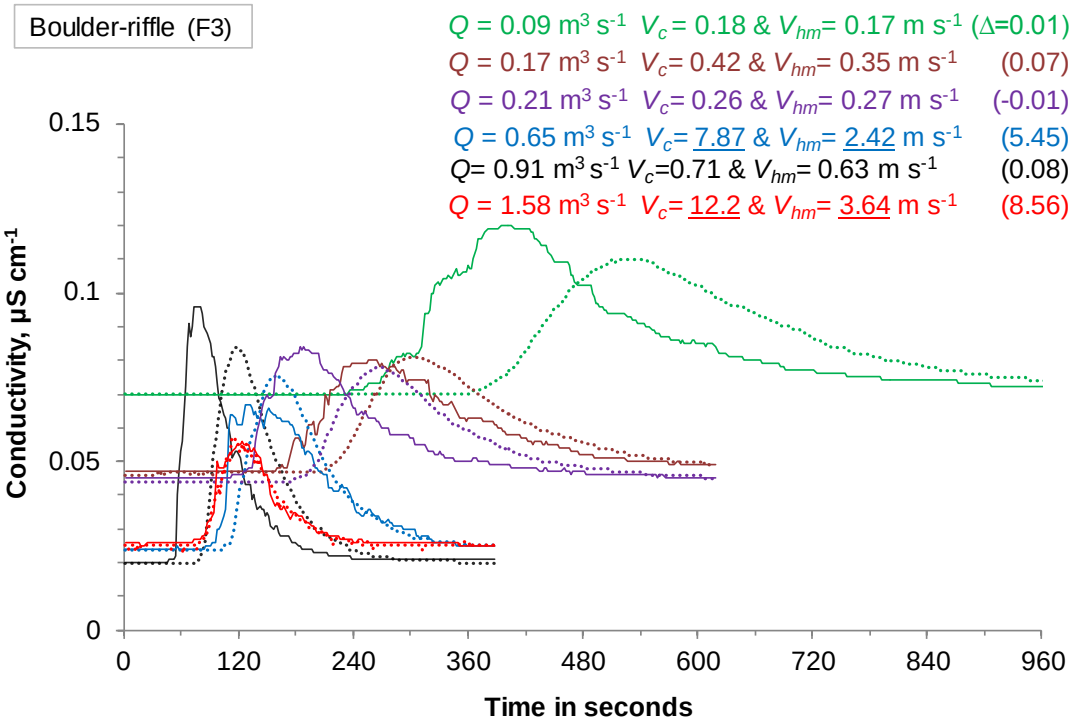

Figure 4.11. Plots of conductivity versus travel time for sub-reach F3. The solid and dotted lines respectively represent the observed waves at P_1 and P_2 spaced 24.4 m apart. The differences between V_c and V_{hm} (in brackets) are very high for some of the measurements.

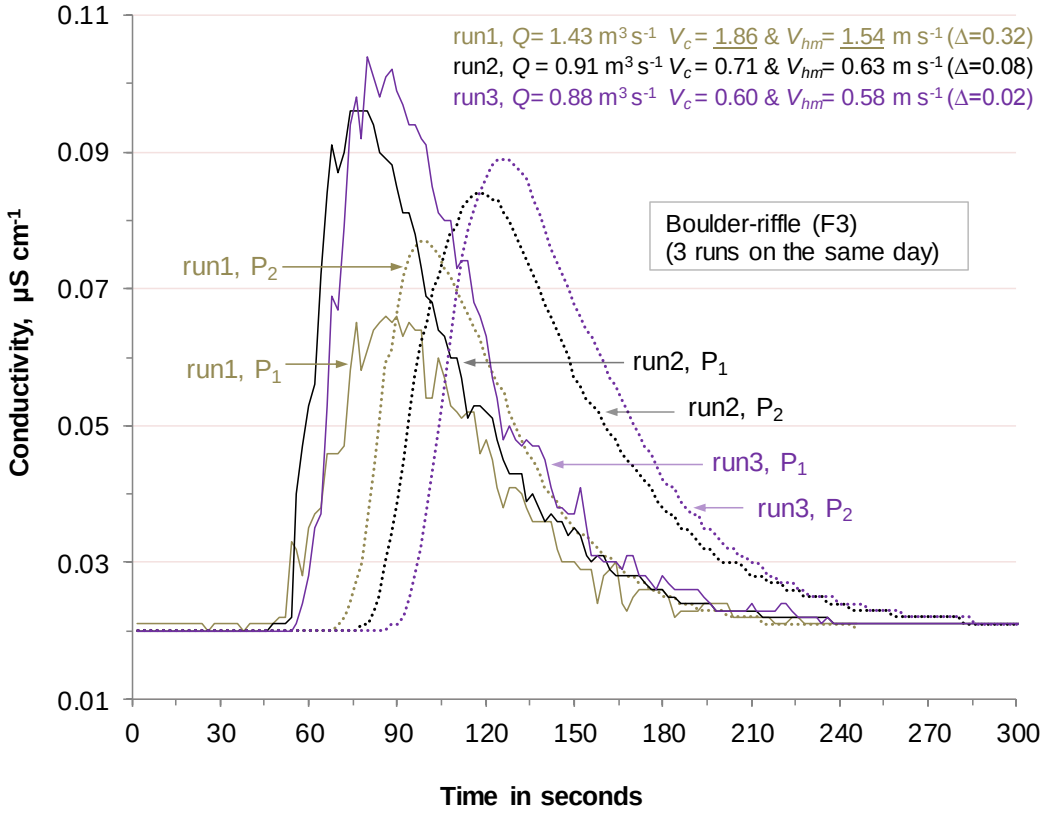

Figure 4.12. Conductivity plots from the boulder-riffle sub-reach F3 for three successive salt-wave measurements on 11.05.14 (Q ranged from 0.9 – 1.5 $m^3 s^{-1}$).

Figure 4.13. Photograph (Q = 0.8 $m^3 s^{-1}$) showing the location of the upper probe P_1 near TBG at the start of F3. The white foam near the bank indicates a very low velocity and the probe was moving back and forth between the main current and the edge, as indicated by the double-ended arrow. The black arrow shows flow direction.

Sub-reach F4 (Lower semi-alluvial, 70% cover)

The conductivity plots from sub-reach F4 are shown in Figure 4.14. As in F2, the centroid and harmonic mean velocities agree very closely. This was perhaps because this sub-reach is a relatively straight and uniform-width section with gentle slope (~0.8%).

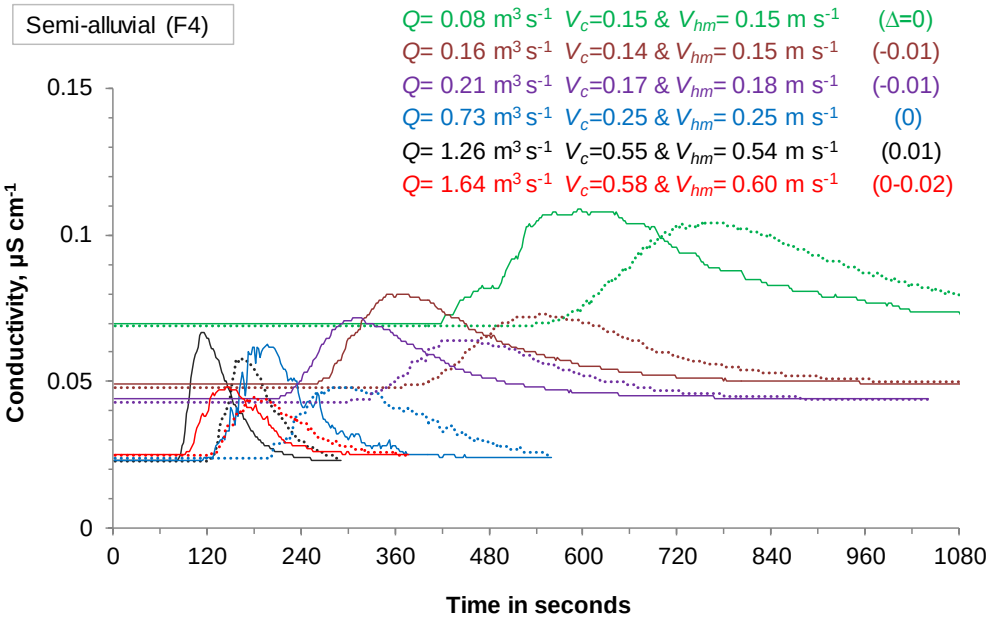

Figure 4.14. The salt-wave plots for sub-reach F4. The solid and dotted lines respectively represent the observed waves at different discharges at P_1 and P_2 spaced 27.6 m apart.

Most of the above examples, except a few from sub-reaches F3 and F5 show that the two velocities V_c and V_{hm} are in good agreement. However, $V_c \sim V_{hm}$ does not necessarily mean these values are correct, therefore these values will be further investigated by comparing with the velocity from the continuity equation in the following sections. The possible reasons for some erroneous measurements are: (i) either one or both probes were wobbling or at times they were not fully submerged, and (ii) the big boulders in F3 and the exposed rock with puddles and dead zones in F5 (Figure 2.37) might have affected the flow path causing flow separation and possibly the probes were not kept in the main flow path. In one occasion at F3 there was virtually no lag between the two waves, and in another occasion both waves looked very odd and very different from each other. The flow through this 'boulder riffle on bare rock' site appeared to be complicated with lots of little dead zones and the travel times of the flow along different flow paths might have varied especially at low flow. For example two points located at the same cross-section but in different flow paths might have drastically different travel times from the point of injection.

The range of measured Q and the average of V_c and V_{hm} velocities (V_{avg}) for all 52 salt-wave measurements are summarised in Table 4.3, and detailed data are presented in Table 4.4. A few measurements, especially at F1, F3 and F5, appeared to be in error as either one or both velocities (V_c and V_{hm}) appeared to be very high and different from each other. Therefore, as a check, the implied mean wetted perimeter [$= Q/(V_{avg}{}^{*}\langle R \rangle)$] is calculated. The highlighted P_i values in Table 4.4 are either too high or too low which indicates some error in the measured discharge and/or velocity. The centroid velocities are plotted against mean harmonic velocities for all five sub- reaches in Figure 4.15.

Table 4.3. Summary result of velocity measurement at sub-reaches using salt-waves. The V_{avg} is the average of V_c and V_{hm}. The unrealistic values are highlighted.

Sub-reach	No.of salt-wave measurements	Range of measured discharge Q ($m^3 s^{-1}$)	Range of measured velocity V_{avg} ($m s^{-1}$)
F1	6	0.18 – 1.11	0.18 – 1.13
F2	7	0.08 – 1.19	0.27 – 1.65
Slightly downstream of F2	4	0.05 – 1.00	0.15 – 1.67
Slightly upstream of F3	3	1.09 – 1.16	0.47 – 0.81
F3	9	0.09 – 1.58	0.18 – 7.92
F4	18	0.04 – 2.09	0.10 – 0.86
F5	5	0.09 – 0.81	0.07 – 5.00

Table 4.4. Discharge (Q) and mean velocities (V_c : centroid, V_{hm} : harmonic mean, V_{avg} : average) from salt-waves are shown for sub-reaches F1 to F5. Implied mean perimeter P_i (Q divided by V_{avg} and hydraulic radius R) is shown. Unrealistic values are highlighted. Empty cell for P_i indicates that the water level was not measured.

Sub-reach	Q, $m^3 s^{-1}$	V_c $m s^{-1}$	V_{hm} $m s^{-1}$	V_{avg} $m s^{-1}$	Pi, m
F1	0.13	0.15	0.22	0.18	3.1
	0.18	0.32	0.32	0.32	3.5
	0.18	0.28	0.28	0.28	4.0
	0.51	0.70	0.67	0.69	4.0
	0.89	1.18	1.07	1.13	3.5
	1.11	0.45	0.64	0.55	8.7
F2	0.08	0.27	0.27	0.27	2.2
	0.14	0.37	0.37	0.37	2.0
	0.17	0.46	0.45	0.45	2.4
	0.20	0.51	0.49	0.50	2.3
	0.61	0.81	0.85	0.83	3.4
	1.15	1.48	1.52	1.50	3.2
	1.19	1.64	1.65	1.65	2.9
Slightly d/s of F2	0.05	0.15	0.15	0.15	-
	0.07	0.09	0.09	0.09	-
	0.51	0.67	0.72	0.70	-
	1.00	1.00	2.35	1.67	-
Slightly u/s of F3	1.09	0.48	0.46	0.47	-
	1.11	0.68	0.70	0.69	-
	1.16	0.81	0.82	0.81	-
F3	0.09	0.18	0.17	0.18	3.5
	0.14	0.33	0.30	0.32	1.6
	0.17	0.42	0.35	0.39	2.2
	0.21	0.26	0.27	0.27	3.6
	0.65	7.87	2.42	5.15	0.4
	0.88	0.6	0.58	0.59	4.4
	0.91	0.71	0.63	0.67	3.9
	1.43	1.86	1.54	1.70	2.3
	1.58	12.2	3.64	7.92	0.5

Sub-reach	Q $m^3 s^{-1}$	V_c $m s^{-1}$	V_{hm} $m s^{-1}$	V_{avg} $m s^{-1}$	Pi
F4	0.04	0.14	0.15	0.14	5.8
	0.08	0.15	0.15	0.15	3.3
	0.10	0.15	0.07	0.11	
	0.14	0.14	0.14	0.14	4.5
	0.15	0.14	0.12	0.13	-
	0.16	0.14	0.15	0.14	5.8
	0.17	0.10	0.10	0.10	-
	0.21	0.17	0.18	0.18	5.4
	0.73	0.25	0.25	0.25	9.8
	0.75	0.46	0.46	0.46	-
	0.80	0.45	0.44	0.45	-
	0.89	0.57	0.57	0.57	-
	1.12	0.38	0.37	0.37	-
	1.26	0.55	0.54	0.55	6.5
	1.64	0.58	0.6	0.59	7.3
	1.88	0.81	0.77	0.79	-
	2.06	0.88	0.85	0.86	-
	2.09	0.86	0.84	0.85	-
F5	0.09	0.16	0.17	0.17	5.0
	0.15	0.29	0.07	0.18	3.9
	0.23	0.59	0.50	0.55	2.8
	0.81	0.05	0.08	0.07	58.9
	0.80	6.15	3.85	5.00	0.7

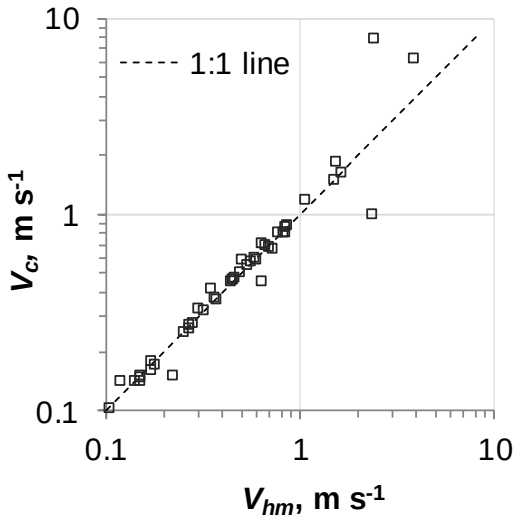

Figure 4.15. Velocities calculated from salt-wave travel time between probes at all five sub-reaches using centroid (V_c) and harmonic mean (V_{hm}) methods.

Figure 4.15 shows a generally good agreement between the two velocities but a few measurements are seen to be out of line. Therefore the sub-reach velocity is calculated as an average of the centroid and harmonic mean velocities (V_{avg}). These average velocities are plotted against discharge in Figure 4.16, which shows that most of the measured velocities in F1, F2, and F4 follow a power-law trend, though a few of them from F3 and F5 are away from other points and do not follow the main trend. These doubtful values are highlighted in Table 4.4.

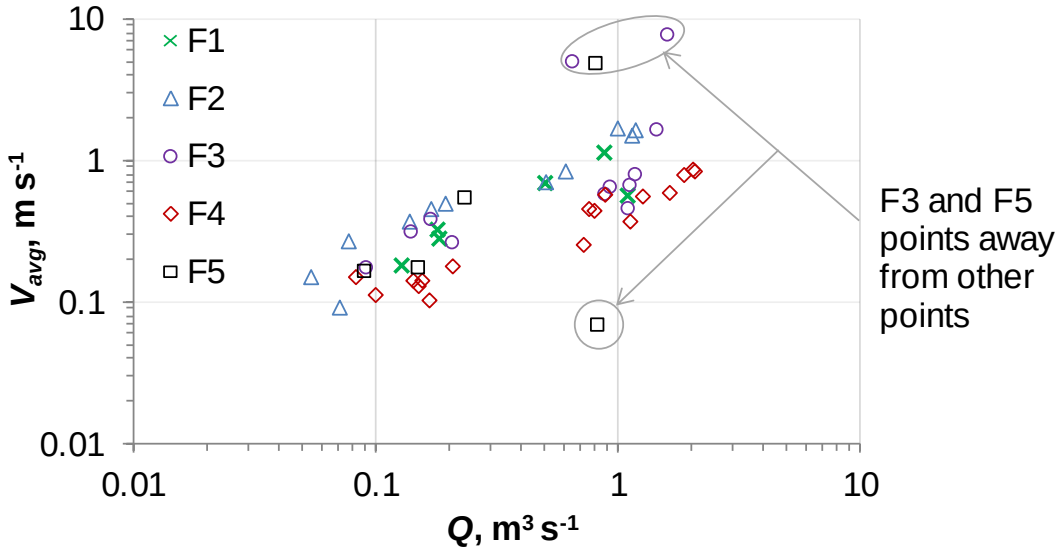

Figure 4.16. Log-log plot of V_{avg} (average of V_c and V_{hm}) against Q. The measured values that lie away from the majority of points are circled. The measurements at F1 (green), F2 (blue) and F4 (red) appear to follow power-line trends whereas the measurements at F3 (purple) and F5 (black) are more scattered.

4.2.2 Velocity from continuity equation and bulk properties for measured discharges

As described in section 3.1.5, the dGPS measurement of water levels and sub-reach cross-sections allow calculation of the top width *w*, wetted area *A*, perimeter *P*, mean depth *d* (= *A*/*w*), and hydraulic radius *R* (= *A*/*P*) for each cross-section within a sub-reach. These parameters from individual cross-sections are then averaged to obtain mean values <*w*>, <*A*>, <*P*>, <*d*> for the sub-reach. The sub-reach average *R* and *V* are calculated by <*A*>/<*P*> and *Q*/<*A*> respectively. The mean *V* is also calculated by *Q*/<*P*><*R*> and compared with *Q*/<*A*> in Figure 4.17. The plot shows that there is a very little difference between the two approaches as all the points lie on the 1:1 line. For further analysis this study uses *V* = *Q*/<*A*>.

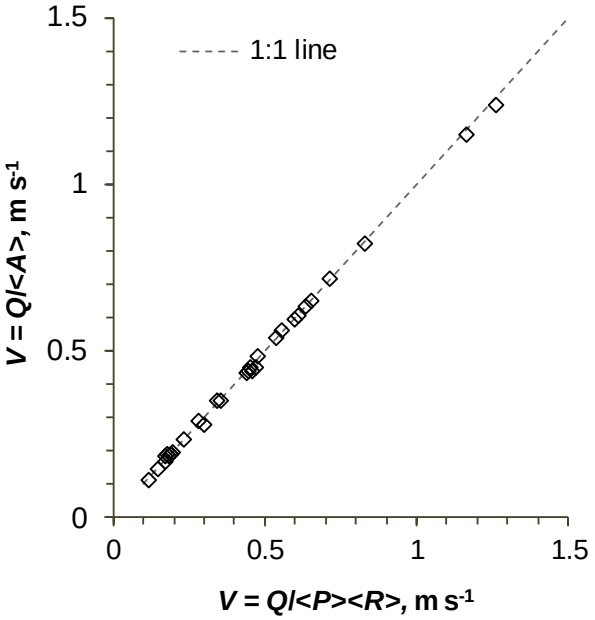

Figure 4.17. Relationship between velocity calculated using V = Q/<A> against velocity using *V* = *Q*/<*P*><*R*>; where <*A*>, <*P*> and <*R*> are the sub-reach-averaged area, perimeter and hydraulic radius. The 1:1 line shows that the two velocities are in close agreement.

The velocities obtained by the salt dilution and continuity equation methods are compared to choose the most reliable data for further analysis. The centroid and harmonic mean velocities after omitting suspicious values are plotted against the velocities obtained by the continuity equation method in Figure 4.18. These plots show that the correlation is good for velocities up to 1 m s^{-1}. Most of the data from sub-reach F5 and a few points from F3 are already rejected; therefore few data are left for this plot, especially at higher velocities (> 1 m s^{-1}). Sub-reach F4 appears to have a better correlation than the other sites. Though the correlation between these velocities is reasonably strong, these plots do not indicate which velocities should be preferred for

further analysis. To check this, all three velocities (V_c, V_{hm} and $V = Q/<A>$) were plotted against the measured Q in Figure 4.19 and the power-law trends are evaluated. These plots clearly show that the V-Q power line relation is best defined when using velocities from the continuity equation, so this method is adopted for further analysis. The velocities and other hydraulic properties for field-measured low/moderate discharges are summarised in Table 4.5.

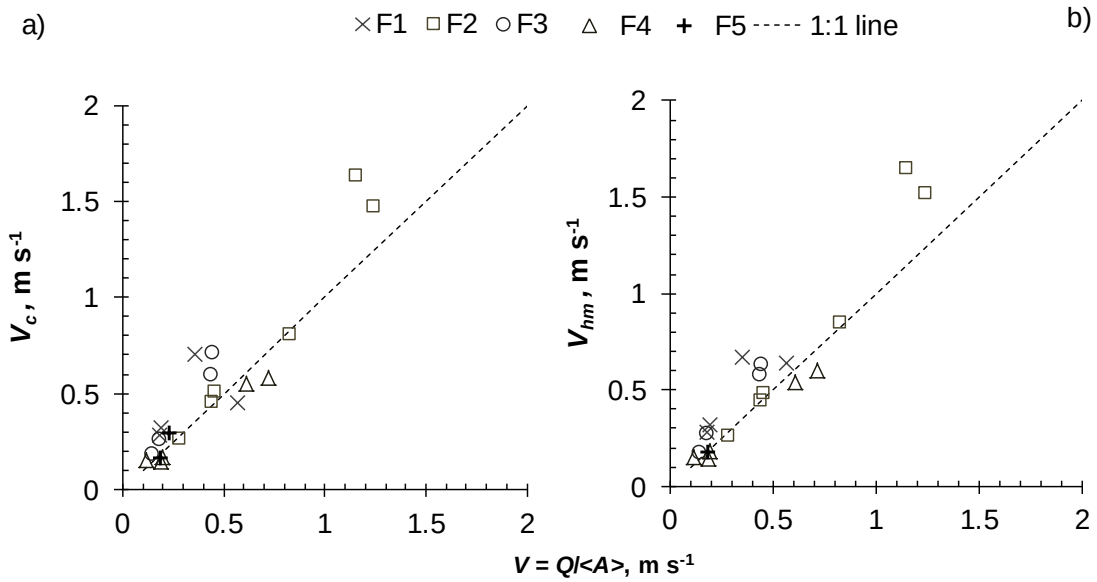

Figure 4.18. Salt wave velocities (V_c and V_{hm}) versus velocities from continuity equation $V = Q/<A>$, after removing the exceptionally high or low values. The 1:1 line is also shown.

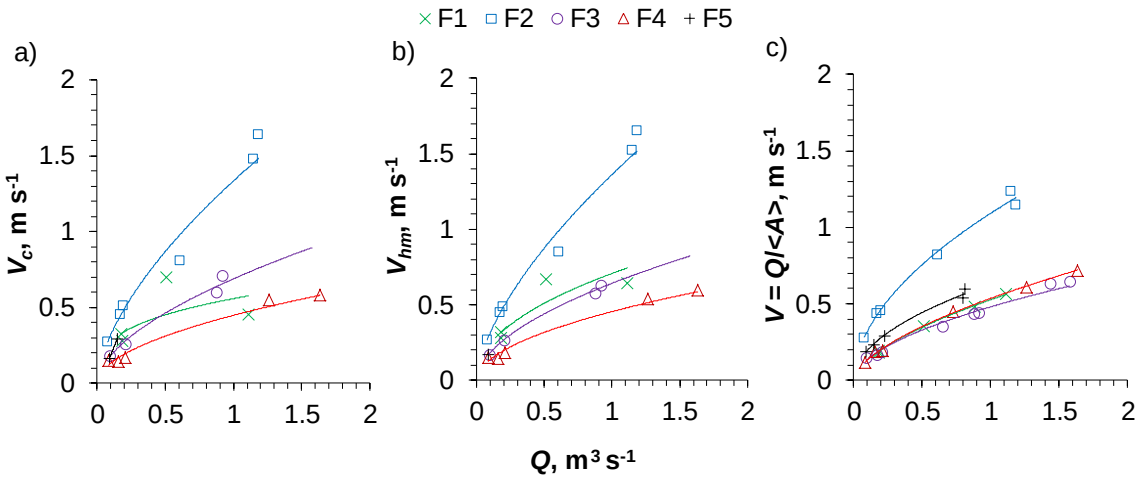

Figure 4.19. Plots of V_c, V_{hm} and V (= $Q/<A>$) versus Q. The data for each sub-reach and respective power trend lines are shown in different colours (F1: green cross, F2: blue square, F3: purple circle, F4: red triangle; and F5: black plus).

Table 4.5. Bulk hydraulics characteristics of F1 to F5 for measured discharges: mean width *w,* wetted perimeter *P*, wetted area *A*, depth *d* (= <*A*>/<*w*>), hydraulic radius *R* (= <*A*>/<*P*>), energy slope *S*, velocity *V* (= *Q*/<*A*>) *at* different dates and discharges. Width to depth ratio (*w*/*d*) is also shown.

Sub-Reach	Date (run)	*Q* ($m^3 s^{-1}$)	<*w*> (m)	<*P*> (m)	<*A*> (m^2)	<*d*> (m)	<*R*> (m)	*V* ($m\ s^{-1}$)	*w/d*
F1	26.05.14	0.18	6.13	6.25	0.93	0.15	0.15	0.19	40
	10.04.14	0.18	6.45	6.58	1.01	0.16	0.15	0.18	41
	08.04.14	0.51	7.73	7.91	1.44	0.19	0.18	0.35	42
	11.05.14	0.89	8.16	8.38	1.84	0.23	0.22	0.48	36
	01.04.14	1.11	8.26	8.50	1.97	0.24	0.23	0.57	35
F2	27.05.14	0.08	1.84	1.96	0.28	0.15	0.14	0.28	12
	26.05.14	0.17	2.18	2.31	0.39	0.18	0.17	0.44	12
	10.04.14	0.20	2.27	2.42	0.43	0.19	0.18	0.45	12
	08.04.14	0.61	3.17	3.37	0.74	0.23	0.22	0.82	14
	11.05.14	1.15	3.60	3.82	0.93	0.26	0.24	1.24	14
	01.04.14	1.19	3.86	4.10	1.03	0.27	0.25	1.15	14
F3	27.05.14	0.09	3.99	4.15	0.61	0.15	0.15	0.15	26
	26.05.14	0.17	4.71	4.93	0.98	0.21	0.20	0.17	23
	10.04.14	0.21	4.88	5.12	1.11	0.23	0.22	0.18	21
	08.04.14	0.65	5.39	5.75	1.84	0.34	0.32	0.35	16
	$11.05.14r_3$	0.88	5.52	5.90	2.01	0.36	0.34	0.44	15
	$11.05.14r_2$	0.91	5.55	5.95	2.06	0.37	0.35	0.44	15
	$11.05.14r_1$	1.43	5.67	6.10	2.26	0.40	0.37	0.63	14
	01.04.14	1.58	5.78	6.22	2.43	0.42	0.39	0.65	14
F4	27.05.14	0.08	4.06	4.26	0.72	0.18	0.17	0.12	23
	26.05.14	0.16	4.20	4.42	0.82	0.20	0.19	0.19	21
	10.04.14	0.21	4.62	4.88	1.08	0.23	0.22	0.19	20
	08.04.14	0.73	5.10	5.45	1.61	0.32	0.30	0.45	16
	11.05.14	1.26	5.38	5.80	2.07	0.38	0.36	0.61	14
	01.04.14	1.64	5.51	5.97	2.28	0.41	0.38	0.72	13
F5	27.05.14	0.09	4.37	4.48	0.47	0.11	0.11	0.19	40
	31.03.14	0.15	4.74	4.88	0.63	0.14	0.13	0.23	35
	10.04.14	0.23	5.27	5.44	0.78	0.16	0.15	0.28	34
	08.04.14	0.81	6.17	6.42	1.36	0.22	0.21	0.60	28
	11.05.14	0.80	6.46	6.72	1.49	0.23	0.22	0.54	28

Table 4.5 shows that the width to depth ratio (*w*/*d*) decreases as the discharges increases for all reaches except F2, which will be further discussed in section 4.3. The next section will discuss the bulk flow properties for high discharges.

4.2.3 Bulk flow properties for high discharges

Once the water levels at intermediate cross-sections within the sub-reach are estimated for high discharges following the method outlined in Figure 3.8 (Section 3.1.5) the mean velocity and other bulk hydraulic properties are calculated by the continuity equation in the same way as it is calculated for the measured discharge in section 4.2.2. The calculated bulk flow properties for the higher discharges (1.5 – 12 $m^3 s^{-1}$) for each PT are shown in Table 4.6.

Table 4.6. High-Q bulk hydraulic properties calculated from EA scaled *Q*, sub-reach cross-sections and stage data. Refer Table 4.5 caption for the description of the parameters.

Sub-Reach	*Q* ($m^3 s^{-1}$)	<*w*> (m)	<*P*> (m)	<*A*> (m^2)	<*d*> (m)	<*R*> (m)	*V* (m s^{-1})	*w/d*
F1	1.5	8.5	8.8	2.4	0.29	0.28	0.62	30
	2.0	8.6	8.9	2.8	0.32	0.31	0.72	27
	2.5	8.7	9.1	3.1	0.36	0.34	0.80	24
	3.0	8.8	9.2	3.4	0.39	0.37	0.88	23
	3.5	8.9	9.3	3.7	0.41	0.40	0.95	22
	4.0	9.0	9.4	3.9	0.44	0.42	1.02	21
	4.5	9.1	9.6	4.2	0.46	0.44	1.08	20
	5.0	9.2	9.7	4.4	0.48	0.46	1.13	19
	5.5	9.3	9.8	4.6	0.50	0.47	1.19	19
	6.0	9.5	10.0	4.9	0.51	0.49	1.24	19
	7.0	9.8	10.4	5.2	0.53	0.51	1.34	18
	8.0	10.1	10.6	5.7	0.56	0.53	1.41	18
	9.0	10.4	10.9	6.0	0.58	0.55	1.49	18
	12.0	10.7	11.3	7.1	0.66	0.63	1.69	16
F2	1.5	4.0	4.3	1.13	0.28	0.26	1.33	15
	2.0	4.4	4.7	1.39	0.31	0.30	1.44	15
	2.5	4.7	5.0	1.66	0.35	0.33	1.51	14
	3.0	4.8	5.2	1.91	0.40	0.37	1.57	13
	3.5	4.9	5.4	2.16	0.44	0.40	1.62	12
	4.0	5.0	5.5	2.40	0.48	0.44	1.67	11
	4.5	5.1	5.6	2.64	0.52	0.47	1.70	11
	5.0	5.1	5.7	2.87	0.56	0.50	1.74	10
	5.5	5.2	5.9	3.09	0.59	0.53	1.78	10
	6.0	5.3	6.0	3.31	0.63	0.55	1.81	10
	7.0	5.5	6.3	3.75	0.68	0.60	1.87	9
	8.0	5.7	6.5	4.18	0.74	0.64	1.91	9
	9.0	5.8	6.8	4.60	0.79	0.68	1.96	9
	12.0	6.3	7.5	5.86	0.92	0.78	2.05	8

Sub-Reach	Q ($m^3 s^{-1}$)	<w> (m)	<*P*> (m)	<*A*> (m^2)	<*d*> (m)	<*R*> (m)	V ($m\ s^{-1}$)	*w/d*
F3	1.5	5.7	6.2	2.3	0.41	0.38	0.64	14
	2.0	5.9	6.4	2.7	0.45	0.41	0.75	13
	2.5	6.1	6.6	3.0	0.49	0.45	0.84	12
	3.0	6.1	6.7	3.2	0.53	0.48	0.93	12
	3.5	6.2	6.8	3.5	0.57	0.51	1.00	11
	4.0	6.3	6.9	3.8	0.60	0.54	1.06	10
	4.5	6.3	7.0	4.0	0.63	0.57	1.13	10
	5.0	6.4	7.1	4.2	0.66	0.60	1.18	10
	5.5	6.4	7.2	4.5	0.70	0.62	1.23	9
	6.0	6.5	7.3	4.7	0.72	0.64	1.28	9
	7.0	6.6	7.5	5.1	0.78	0.68	1.37	9
	8.0	6.7	7.7	5.5	0.83	0.72	1.45	8
	9.0	6.8	7.8	5.9	0.87	0.76	1.52	8
	12.0	7.1	8.3	7.1	1.00	0.86	1.70	7
F4	1.5	5.5	5.9	2.2	0.41	0.38	0.67	13
	2.0	5.6	6.1	2.5	0.45	0.41	0.79	12
	2.5	5.7	6.3	2.8	0.49	0.45	0.89	12
	3.0	5.8	6.4	3.1	0.53	0.48	0.98	11
	3.5	5.8	6.5	3.3	0.56	0.51	1.07	10
	4.0	5.9	6.6	3.5	0.59	0.53	1.14	10
	4.5	6.0	6.7	3.7	0.62	0.55	1.21	10
	5.0	6.1	6.8	3.9	0.64	0.57	1.28	9
	5.5	6.2	7.0	4.1	0.67	0.59	1.34	9
	6.0	6.3	7.1	4.3	0.69	0.61	1.39	9
	7.0	6.4	7.3	4.7	0.73	0.64	1.50	9
	8.0	6.6	7.5	5.0	0.76	0.67	1.59	9
	9.0	6.8	7.8	5.4	0.79	0.69	1.67	9
	12.0	7.4	8.4	6.4	0.87	0.76	1.87	8
F5	1.5	6.7	6.9	1.6	0.24	0.23	0.93	27
	2.0	7.2	7.5	1.8	0.25	0.24	1.09	29
	2.5	7.9	8.3	2.1	0.26	0.25	1.22	31
	3.0	8.5	8.9	2.3	0.27	0.26	1.33	32
	3.5	8.8	9.1	2.5	0.28	0.27	1.42	31
	4.0	8.9	9.3	2.7	0.30	0.29	1.50	30
	4.5	9.2	9.6	2.9	0.31	0.30	1.57	29
	5.0	9.3	9.7	3.1	0.33	0.31	1.64	28
	5.5	9.4	9.8	3.2	0.35	0.33	1.70	27
	6.0	9.4	9.9	3.4	0.36	0.34	1.76	26
	7.0	9.5	10.0	3.7	0.39	0.37	1.87	24
	8.0	9.7	10.2	4.1	0.42	0.40	1.98	23
	9.0	9.8	10.3	4.4	0.45	0.42	2.07	22
	12.0	10.1	10.7	5.2	0.52	0.49	2.31	20

Tables 4.5and 4.6 show that both velocity and depth increase with increasing discharge, as in the low Q measured data. The w/d ratio decreases with increasing discharge, which is discussed in detail in the hydraulic geometry section (Section 4.3).

4.2.4 Energy slope

The bed slope (S_b), water surface slope (S_w) and energy slope (S) in a sub-reach will be parallel if the velocities in the sub-reach cross-sections are similar for a given Q, however this is not the case for Trout Beck sub-reaches. Therefore the energy slope is required to be used in the hydraulic calculations. The energy slope of a sub-reach is calculated as the difference between water level plus velocity head ($V^2/2g$) at upstream end and the water level plus velocity head at downstream end divided by the sub-reach length. The formula for the energy slope is,

$$S = \frac{(WL_1 + \frac{V_1^2}{2g}) - (WL_2 + \frac{V_2^2}{2g})}{L} \qquad \text{Eq. 4.1}$$

where WL_1 represent the water level (m) and V_1 the average velocity (m s^{-1}) at upstream end of the sub-reach; WL_2, V_2 at the downstream end; and L is the sub-reach length. The variation of water slope and energy slope with discharge is illustrated in Figure 4.20.

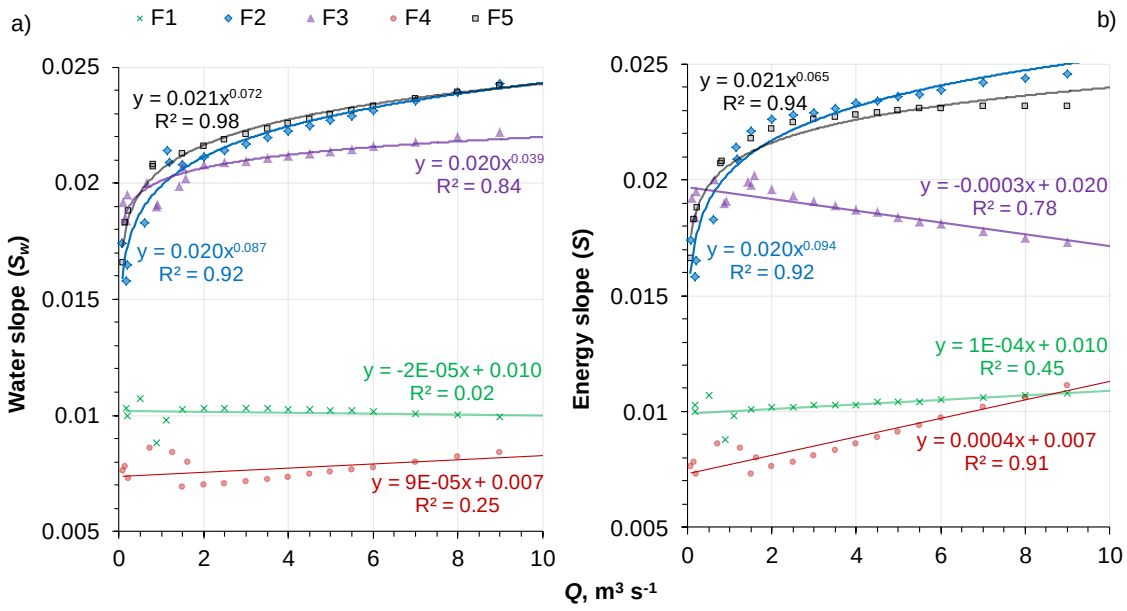

Figure 4.20. Relationship between: a) water slope S_w versus discharge Q; and b) energy slope S versus discharge Q. The best-fit line (power-law or straight line whichever has higher R^2) and equations are shown for each sub-reach: F2 (blue), F5 (black), F3 (purple), F1 (green), and F4 (red). The change in S_w with Q is not significant at the p =0.05 level in F1 and F4. All other trends are significant.

The above plots show that the S is almost equal to S_w for F2, and only slightly different for F1 and F5, but significantly different for F3 and F4 especially at high flow. If the

flow is accelerating (contracting flow, velocity increasing down-reach, wetted cross-section area A decreasing) the energy slope is less than the water slope, and vice versa for decelerating (expanding) flow. At F3, $S < S_w$ at high flow which must be because of a contraction of the channel; for example, at $Q = 5$ m^3 s^{-1} the wetted width reduces downstream from 6 to 5 m. Similarly, F4 has $S > S_w$ where the wetted width expands from 5.5 to 7 m at 5 m^3 s^{-1}. The other sites also have some expansion but not as abrupt as in F4. Figure 4.21 shows how the flow contracts along F3 then expands into F4.

Figure 4.21. Picture showing contraction along F3 and expansion along F4. The black arrow shows the flow direction.

Summary of velocity and bulk properties

The mean velocity in each sub-reach was measured by two methods: salt-wave method using double-probe conductivity meter and continuity equation method using water surface surveys. The salt-wave velocities calculated using centroid and harmonic-mean travel times are generally in close agreement, and are averaged to obtain the sub-reach velocity. Some suspicious measurements have been removed. For velocity by continuity equation and bulk properties calculation, the dGPS measured water levels, wetted perimeter, depth, width and area for several cross-sections are calculated and averaged to obtain mean values (<>) for a sub-reach. For example R is calculated as $\langle A \rangle / \langle P \rangle$ and $V = Q/\langle A \rangle$. The velocities calculated using this continuity equation method appear slightly more reliable and are used for further analysis.

Bedload transport occurs mainly or only at higher discharges but the water levels were only measured up to 1.6 $m^3 s^{-1}$. Therefore an indirect method to estimate the high *Q* hydraulic variables is adopted. The approach used is to take the highest measured water surface profile in each sub-reach and raise it for progressively higher discharges in accordance with the *Q-H* rating curves for the nearest stage recorders upstream and downstream. The velocity at the first and last cross-sections in a sub-reach are different at the same *Q*, hence the energy slope is different from the water slope. It is found that the energy slope (*S*) is less than the water surface slope (S_w) in sub-reach F3 at higher discharges, mainly because of a contraction. On the other hand, *S* is higher than S_w at high discharges in sub-reach F4 because of expansion. For other reaches the difference is minimal.

Flow resistance in rough and steep gradient channels can be highly sensitive to measurement errors, for example due to high frequency fluctuation of water levels at high flow conditions or multiple flow paths and dead zones around large bed elements at low flows. The high fluctuations at water levels can be seen in the stage data recorded by the pressure transducers as seen in Figure 4.22 and the *H-Q* rating curves in Figure 4.8.

Figure 4.22. Example of stage fluctuation at high flow in the gorge (*Q*~ 4 $m^3 s^{-1}$ on 06.10.14).

Moreover, holding the dGPS rover on top of water level to get the stable readings especially at high flow was another challenge; although a reading at a single cross-section could be out by at least 1 cm, with 7 to 10 cross-sections per sub-reach the error in mean hydraulic properties (area, width, perimeter, hydraulic radius) for sub-reach would be less significant. Also in a flashy river such as Trout Beck the water levels at

high flows can fluctuate even during a single measurement, but it is unlikely that this would be significant compared to the dGPS error as it takes only few minutes to survey the water surface profile in a sub-reach. Adequate precautions were taken to avoid the errors in the field measurements as velocity and flow resistance calculation for steep channels is sensitive to errors in the measurement of discharge, velocity, water surface elevations and channel geometry and also in the choice of representative cross-sections (Lee & Ferguson, 2002; Comiti *et al.*, 2007). The *R* and *d* can also be very variable in the steep channels but for this study mean *R*, rather than mean *d* is used because the cross-sections are fairly narrow and the walls are rough.

4.3 At-a-station hydraulic geometry

At-a-station hydraulic geometry (AHG) describes how reach-averaged velocity *V*, top width *w* and depth *d* vary with changes in *Q* at a particular location in a channel (Section 1.1.2). Table 4.7 presents the summary of the range of hydraulic geometry parameters for the measured and calculated data; for detailed data refer to Table 4.5 and Table 4.6.

Table 4.7. Range of measured and calculated hydraulic-geometry parameters (discharge *Q*, mean width *w*, mean depth *d*, and mean velocity *V*) for sub-reaches F1 – F5.

Sub-reach	Range of							
	Field-measured low-*Q* data				Rating curve derived high-*Q* data			
	Q ($m^3 s^{-1}$)	*w* (m)	*d* (m)	*V* ($m s^{-1}$)	*Q* ($m^3 s^{-1}$)	*w* (m)	*d* (m)	*V* ($m s^{-1}$)
F1	0.18–1.11	6.1–8.3	0.15–0.24	0.18–0.57	1.5–12	8.5–10.7	0.29–0.66	0.62–1.69
F2	0.08–1.19	1.8–3.9	0.15–0.27	0.28–1.24	1.5–12	4.0–6.3	0.28–0.92	1.33–2.05
F3	0.09–1.58	4.0–5.8	0.15–0.42	0.15–0.65	1.5–12	5.7–7.1	0.41–1.0	0.64–1.70
F4	0.08–1.64	4.1–5.5	0.18–0.41	0.12–0.72	1.5–12	5.5–7.4	0.41–0.87	0.67–1.87
F5	0.09–0.81	4.4–6.5	0.11–0.23	0.19–0.60	1.5–12	6.7–10.1	0.24–0.52	0.93–2.31

The relationships of *V*, *d* and w to *Q* ($V = kQ^m$, $w = aQ^b$, and $d = cQ^f$) (Leopold & Maddock, 1953) for each sub-reach are plotted on log scales in Figure 4.23. The *R*-*Q* plot is very like *d*-*Q* and *P*-*Q* is very like *w*-*Q*, therefore these plots and equations are not shown here. The alluvial or semi-alluvial sub-reaches all show that *V*, *d*, and *w* increase with increasing *Q*, but with offsets between the sub-reaches, for example F2 plots highest *V* but lowest *w* and F1 plots lowest *V* but highest *w*. At each field site, there is a general trend that the velocity, width and depth increase with discharge, but a single power-law over the full range of *Q* is not a good fit, therefore two power laws (for low and high *Q*) joining at a hinge are fitted.

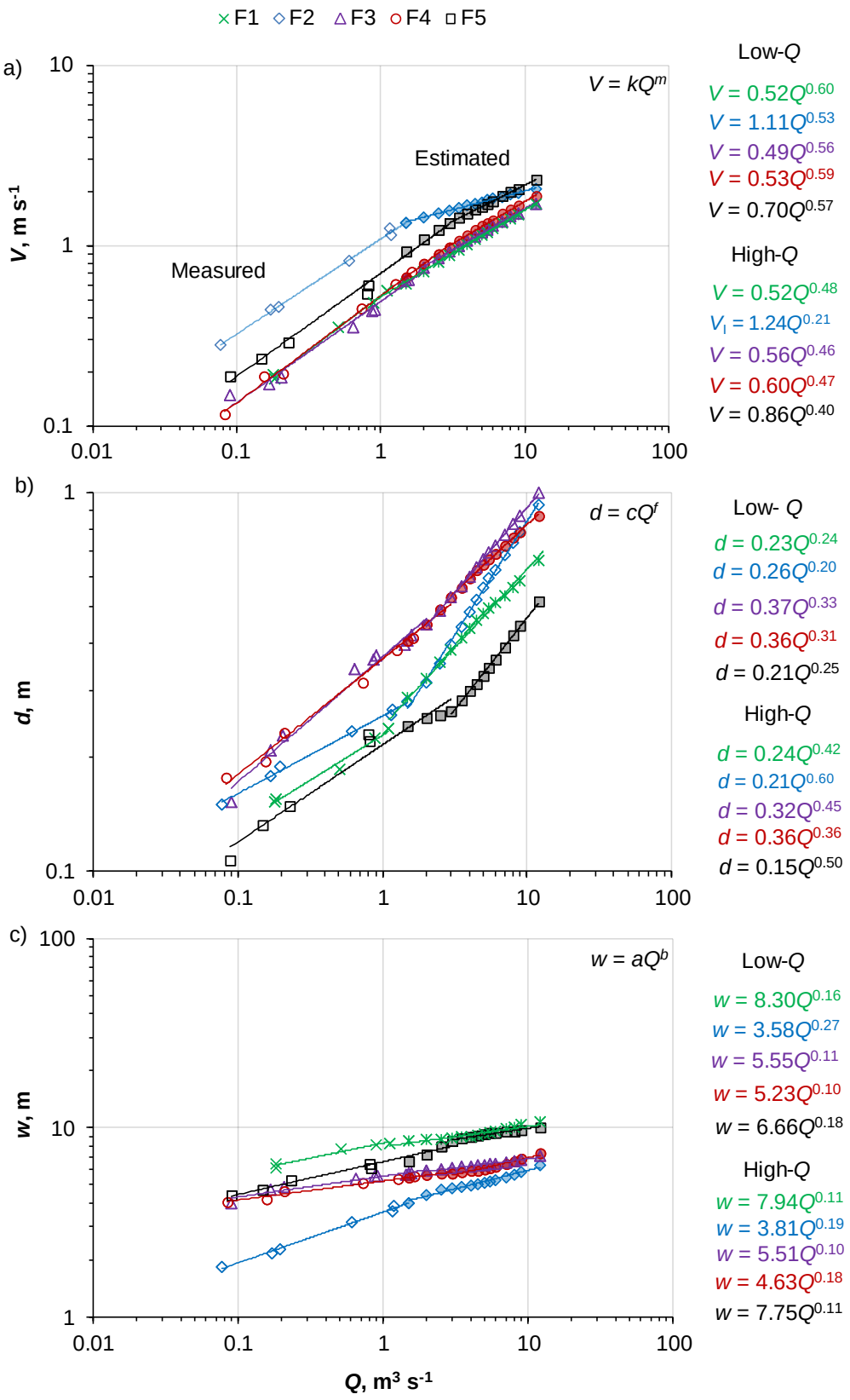

Figure 4.23. An at-a-station hydraulic geometry relations for sub-reaches: F1 (alluvial: green), F2 (bare rock: blue), F3 (boulder-riffle: purple), F4 (semi-alluvial 70% cover: red), F5 (semi-alluvial 20% cover: black). The open markers (in these and other figures below) indicate measured low-Q and filled markers indicate estimated high-Q. Two power equations ($V = kQ^m$, $d = cQ^f$, $w = aQ^b$) for each sub-reach are displayed in coloured text. All fitted power-law exponents are significantly different from zero at $p < 0.001$.

Navratil and Albert (2010) also found that a single power law was not appropriate at most of their 15 sites and they derived the relations for reach hydraulic geometry with two equations. Figure 4.23 shows that the kinks are prominent for sub-reaches F2 and F5 but minor for F1, F3 and F4 though they are also distinct in *n*-*Q*, *f*-*Q* and τ-*Q* plots which are shown in later sections (Figures 4.26 and 4.32). In the interests of maintaining the identity *wdv* = *Q*, separate low *Q* and high *Q* equations were fitted for all five sites. The reason for occurrence of these kinks is perhaps the presence of a smooth bed but rough near-vertical walls. For example in the bare rock sub-reach F2 the smoother bed may provide a small flow resistance at low flow but once the flow starts to rise above the bed the rough walls due to protrusions and re-entrants (Figure 2.34) may have caused the higher flow resistance. Also with the walls being nearly vertical the depth might increase faster than the velocity. Sub-reach F5 also has a rough wall in the left bank (Figure 3.18) which may have caused the distinct kink; however this left bank is not bedrock. The low *Q* equation is fitted from $Q = 0.08\ m^3s^{-1}$ to the hinge point and the high *Q* equation from the hinge point to 12 $m^3\ s^{-1}$. The hinges are at slightly different *Q* values for different sub-reaches: 1.1 $m^3\ s^{-1}$ for F1, 1.5 $m^3\ s^{-1}$ for F2, 2 $m^3\ s^{-1}$ for F3, and 3 $m^3\ s^{-1}$ for both F4 and F5. These are also the hinge points for *n*-*Q*, *f*-*Q*, τ-*Q* and other plots which are discussed later.

Table 4.8 summarises the coefficients and exponents of the AHG equations shown in Figure 4.23 which shows that *V* in each sub-reach generally increases faster with *Q* than does *w* or *d*, as also reported in other research on steep shallow streams (e.g. Lee & Ferguson, 2002). However, at high flow in, F2 and F5, *d* increases more rapidly with *Q* than does either *V* or *w*. This shows *V* in rock-exposed areas at higher flows increases slower but depth increases faster with discharge than elsewhere. The average value of the velocity exponent *m* (in $V = kQ^m$) for the Trout Beck site was 0.49. The average *m* values for low and high *Q* were 0.57 and 0.40 respectively (Table 4.8, Figure 4.23). The *m* value for F2 at high flow is much lower than elsewhere. The Trout Beck overall range of *m* (0.21 – 0.60) is very similar to the range 0.24 – 0.63 (most reaches had between 0.48 to 0.60) found by Comiti *et al.* (2007) from ten steep reaches in Rio Cordon, Italy. Similarly, Beven *et al.* (1979) found the range 0.50 – 0.87 in eight small steep reaches that included two bedrock reaches (*m* values for 2 bedrock reaches = 0.50 and 0.78), boulder and cobble sections and series of waterfalls and plunge pools. Lee and Ferguson (2002) found the range 0.51 – 0.84 from five small streams in England which included one semi-alluvial and five gravel-bed step-pool reaches. Both these ranges extend

slightly higher than the highest values from Trout Beck. The average exponent found by Judd and Peterson (1969) for their sites with large bed elements in USA is 0.48, similar to Trout Beck (0.49). The range for lowland rivers as stated by Knighton (1998) is 0.22 – 0.55, but the average value found by Leopold and Maddock (1953) from large rivers is rather low (0.34).

Table 4.8. At-a-station hydraulic geometry coefficients and exponents in $V = kQ^m$, $d = cQ^f$ $w = aQ^b$ for Trout Beck sub-reaches. Sub-reach average for low and high flows and the Trout Beck overall average (and range in brackets) for the entire flow range are shown.

Sub-reach	Low *Q*			High *Q*		
	Coefficients					
	k	*c*	*a*	*k*	*c*	*a*
F1	0.52	0.23	8.30	0.52	0.24	7.94
F2	1.11	0.26	3.58	1.24	0.21	3.81
F3	0.49	0.37	5.55	0.56	0.32	5.51
F4	0.53	0.36	5.23	0.60	0.36	4.63
F5	0.70	0.21	6.66	0.86	0.15	7.75
Sub-reach average	*0.67*	*0.29*	*5.86*	*0.76*	*0.26*	*5.93*
Overall average (range): k = 0.71 (0.49 –1.24), c = 0.27 (0.15 – 0.37), a = 5.93 (3.58 – 8.30)						
	Low *Q*			High *Q*		
	Exponents					
	m	*f*	*b*	*m*	*f*	*b*
F1	0.60	0.24	0.16	0.48	0.42	0.11
F2	0.53	0.20	0.27	0.21	0.60	0.19
F3	0.56	0.33	0.11	0.46	0.45	0.10
F4	0.59	0.31	0.10	0.47	0.36	0.18
F5	0.57	0.25	0.18	0.40	0.50	0.11
Sub-reach average	*0.57*	*0.27*	*0.16*	*0.40*	*0.47*	*0.14*
Overall average (range): m = 0.49 (0.21 – 0.60), f = 0.37 (0.20 – 0.60), b = 0.15 (0.10 – 0.27)						

The velocity coefficient *k* has an overall average of 0.71 (range 0.49 – 1.24), and average *k* values for low and high *Q* are 0.67 and 0.76 respectively (Table 4.8). The average value of *k* is a bit higher mainly because of the higher values of *k* for F2 and F5 which also suggests that exposed bedrock surface is smoother than sediment. In the low flow range, the *k* for F2 (1.11) is more than twice the value of F1, F3, and F4 (0.49 – 0.53) and the *m* value for all four sites is about the same (0.53 – 0.60). This indicates that for a given *Q* the average velocity in the rock gorge was about two times more than elsewhere. This is clearly seen in Figure 4.23 (a) where F2 plots highest and F3 (along with F1 and F4) plots lowest. This is consistent with F2 being a bare rock site with smoother bed and high energy slope (*S*) whereas F3 is the boulder riffle site with the coarsest bed and slightly lesser energy slope than F2 (Figure 4.20). Sub-reaches F1 and

F4 have rather lesser energy slope but also slightly less coarse beds than F3 therefore they plot lower, very similar to F3. The *k* values at higher discharges also show a similar pattern but the velocity at F2 is not double as *m* is rather lower (0.21) than elsewhere (0.40 to 0.48). The *k* value for F5 (0.70) is close to the average value (0.67) therefore it plots midway in the chart.

The depth exponent *f* (in $d = cQ^f$) and width exponent *b* (in $w = aQ^b$) in Table 4.8 show only a small variation among the sub-reaches. The *d* increases with *Q* faster than does *w* (*i.e.* $f > b$), similar to what Leopold and Maddock (1953) found for alluvial sites, as also indicated by *w*/*d* ratio (Tables 4.5 and 4.6) which decreases as the discharge increases (Rhodes, 1977). The only exception to this is F2 at low flow for which $f < b$, this was possibly because some sections in F2 have a compound shape with a small inner channel no more than 1 m wide; once the water level overtops this, width increases rapidly to 3 – 4 m, and at this condition the *w*/*d* ratio increases with increasing discharge (see F2 in Table 4.5). The overall average *f* value for Trout Beck is 0.37 but the low-*Q* average is 0.27 and the high-*Q* average is 0.47. The *f* values for F2 and F5 at higher discharges are high (0.60 and 0.50), showing that depth is increasing more rapidly than velocity. The values of the depth coefficient *c* are similar for all sub-reaches, with an overall average 0.27 (range 0.15 – 0.37). The *b* exponents across the sites and flow range are similar except for a slightly higher value for F2 (0.27, low flow); the overall average is 0.15. The slightly higher value of *b* for F2 ties in with the much lower flow widths at low *Q*. The average value of the width coefficient *a* is high for wide sub-reaches (F1 and F5) and low for the narrow sub-reach (F2) but the average value for all sub-reaches at low flow (5.86) is very similar to the average value at high flow (5.93).

Lee and Ferguson (2002) found similar low-*Q* values of *f* (range 0.19 – 0.36) and *b* (0.11 –0.21) in their six step-pool reaches. Judd and Peterson (1969) found average values $f = 0.42$ and $b = 0.11$ which are very similar to the values for fully or partial alluvial sub-reaches at Trout Beck at high *Q*. Leopold and Maddock (1953) from low gradient alluvial channels also found the similar value of $f = 0.40$ but slightly higher $b = 0.26$. Typical *f* values for lowland alluvial rivers are rather higher (0.30 – 0.57) and *b* values have a wide range (0 – 0.48) according to (Knighton, 1998). David *et al.* (2010) studied at-a-station hydraulic geometry of nine step pools, five cascade and one plane-bed in Colorado and found the average values of *m*, *f* and *b* were 0.49, 0.39 and 0.16 which are similar to the average values for Trout Beck. They also found that the

bed slope and the plan wetted-area are the main drivers that influence how velocity, depth and width vary with discharge.

The ratio *of* the rate of change of velocity to the rate of change of depth (m/f) varies from 0.35 (F2 at high Q) to 2.65 (F2 at low Q). Similarly, the ratio of the rate of change of depth to the rate of change of width (f/b) varies from 0.74 (F2 at low Q) to 4.55 (F3 at high Q). Wilcock (1971) argued that a channel experiences an increase in competence in sediment transport if $m/f \geq 1$, which is the case in all Trout Beck sub-reaches except F2 at higher discharges. All Trout Beck sub-reaches had $m > b + f$ at low flow, and according to Rhodes (1977) this condition occurs when the velocity increases faster than the cross-sectional area and for this condition the grain resistance is likely to be dominant, otherwise (if $m < b + f$) the form resistance will prevail (David *et al.*, 2010). Rhodes' (1977) *b–f–m* diagram relates the exponents with Froude number (*Fr*). The *Fr* – *Q* plot for Trout Beck is shown in Figure 4.24 (refer Tables 4.11 and 4.12 for data). According to the diagram, when $m > f/2$ the *Fr* increases with increasing *Q* and when $m < f/2$ the *Fr* decreases with increasing *Q*. Both these conditions are valid for Trout Beck (Figure 4.24). For all sub-reaches, bulk flow is sub-critical ($Fr < 1$) over the full range of flow except at F5 for $Q \geq 10$ m^3 s^{-1}. At low/moderate flow the nearest to critical flow ($Fr = 0.82$) occurs at 2 m^3 s^{-1} in F2. It has been suggested that large sections of the flow in bedrock channels are critical ($Fr = 1$) or supercritical ($Fr > 1$) at high *Q* (Tinkler & Wohl, 1998b) but this plot does not show this. However, even though the bulk *Fr* does not reach or exceed 1, there are localised hydraulic jumps, as can be seen in Figure 4.22.

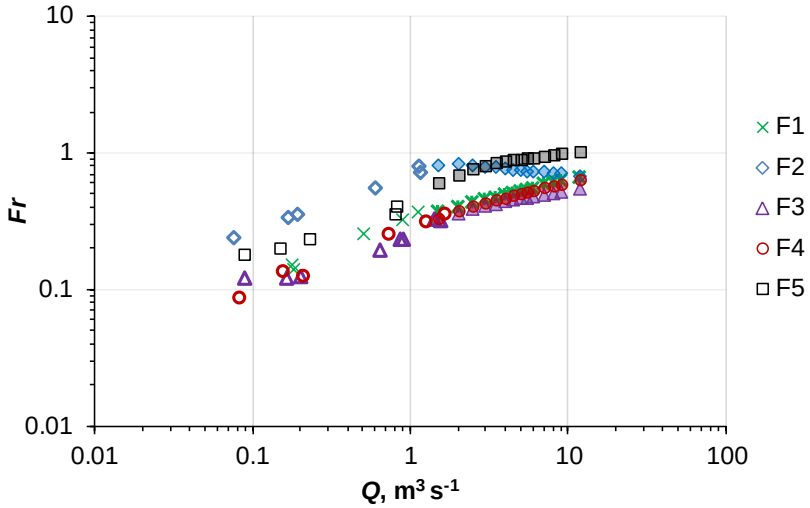

Figure 4.24. Froude number (*Fr*) for sub-reaches. The open markers indicate the low *Q* field-measured data whilst the filled markers indicate the high *Q* estimated data. All correlations are significant at $p < 0.001$.

Summary

At-a-station hydraulic geometry relations of *V*, *d* and *w* to *Q* in the study site do not follow a single power law; therefore two power laws (low-*Q* *a*nd high-*Q*) are fitted. The velocity generally increases faster with *Q* than *w* or *d* *(m > f > b)* for all sites over the range of flows, but at higher discharges the sub-reaches F2 and F5 have *f* > *m* > *b*. At-a-station hydraulic geometry can be useful to know how the flow resistance varies in high-gradient mountainous rivers. Figure 4.25 compares the Trout Beck exponent values (*m*, *f*, *b*) with other rivers.

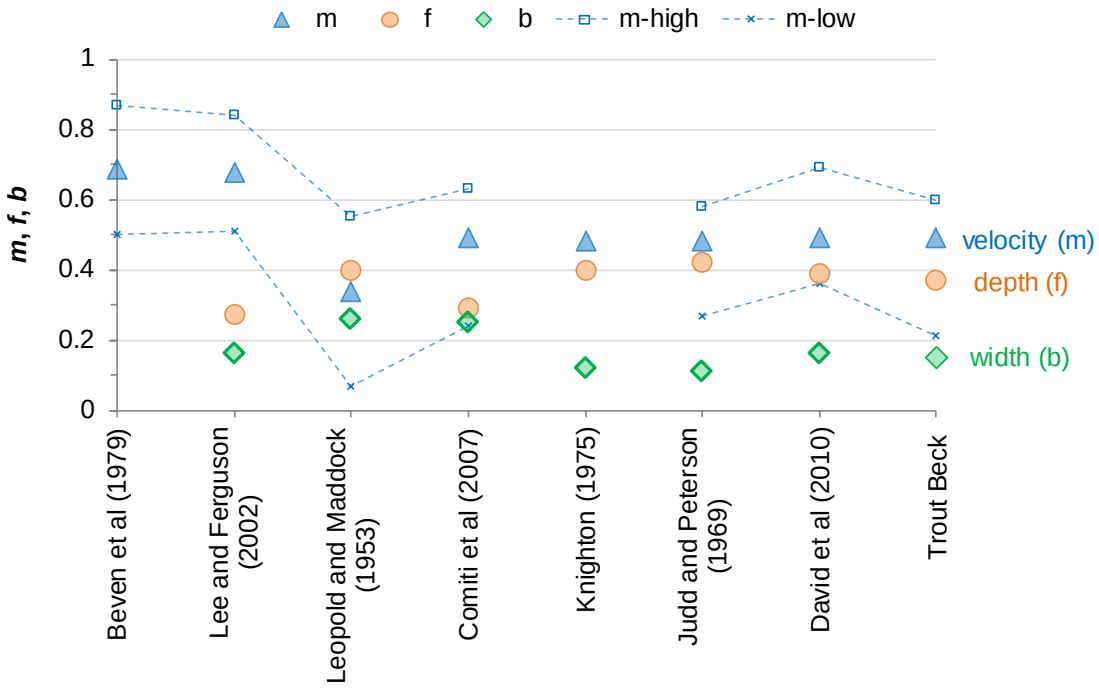

Figure 4.25. Comparison of average values of exponents for velocity (*m*: blue), depth (*f*: orange) and width (*b*: green) of Trout Beck with previous projects. The low and high range for *m*-values are also shown by dotted lines. The average value for Lee and Ferguson (2002) and Beven *et al.* (1979) are not available; for this comparison the average value is calculated as an average of lowest and highest values in the range.

Figure 4.25 shows the average velocity exponent (*m*) from Trout Beck (0.49) is within the range of values obtained from steep mountainous streams including from UK (e.g. Knighton, 1975; Lee & Ferguson, 2002) but is considerably higher than the values from large alluvial rivers (0.34) (Leopold & Maddock, 1953). The average width exponent *b* (0.15) is also within the range reported for boulders and step-pool reaches but lower than the Rio Cordon (Comiti *et al.*, 2007) value 0.25 which is similar to Leopold and Maddock (1953) value (0.26). The average depth exponent *f* (0.37) is also within the range reported for other gravel bed rivers but slightly higher than 0.29 for the Rio Cordon (Comiti *et al.*, 2007). The high value of *m* and *f* in Trout Beck indicates that

there is rapid reduction in flow resistance with the discharge. This is because as the flow depth increases the skin and form-resistance components expose only to the smaller proportion of the flow. Going from low to high flow, the average value of *m* decreases from 0.57 to 0.40 whilst *f* increases from 0.27 to 0.47 and *b* decreases from 0.16 to 0.14, which implies that increased discharge is accommodated more by increasing flow depth than by increasing velocity. Trout Beck sites have $m > f + b$ at shallow flows and according to David *et al.* (2010) this indicates that skin friction is the dominant source of flow resistance and not the form/spill resistance (David *et al.*, 2010). The velocity varies inversely with flow resistance which decreases most rapidly with the depth when the grain resistance is the main source of the flow resistance (Knighton, 1975). All the sub-reaches in Trout Beck have $m < f + b$ at deep flows therefore according to David *et al.* (2010) the form/spill resistance may be the principal source of hydraulic resistance as the discharge increases.

4.4 Flow resistance

4.4.1 Flow resistance coefficients

As discussed in chapter 1 (Section 1.1.3), accurate estimates of flow resistance coefficients such as Manning's *n* (Eq. 1.5) or Darcy-Weisbach *f* (Eq. 1.6) are required to estimate the reach-average velocity when the channel depth and slope are known. However, this is not straightforward in steep channels as the flow resistance is the result of interactions of the channel morphology with dynamic variables, and depends on several parameters such as roughness elements (grain size, homogeneity of the bed and bed roughness, boulders, woody debris, vegetation), channel planform, energy dissipating structures in the channel, and flow depth. The flow resistance coefficient *n* has been traditionally considered to be constant for a reach, with a value selected based on experience or tables based on the qualitative description of the channel (e.g. Chow, 1959). Similarly, the friction factor *f* is often estimated using the Keulegan equation (Eq. 1.9) (Ferguson, 2013). However, in this study *n* and *f* are back calculated using the field data on *V*, *R* and *S* (Tables 4.5 and 4.6). Table 4.9 shows a grand average *n* value of 0.08 (0.041 – 0.273 range) and *f* value of 1.11 (0.16 – 10.1 range) for Trout Beck. The highest value in the range relates to low flow, whilst the smallest to the high flow.

Table 4.9. Manning's *n* and Darcy-Weisbach *f* values for range of discharges (~1 to 12 $m^3 s^{-1}$) for sub-reaches F1 to F5, and overall. The range, mean, standard deviation (σ), and standard error of the mean (SE =$\sigma/\sqrt{N}$, where *N* is the number of samples) are shown.

Sub-reach	Channel description	Manning's *n*				Darcy-Weisbach *f*			
		range	mean	σ	*SE*	range	mean	σ	*SE*
F1	Fully alluvial	0.046 - 0.156	0.069	0.032	0.007	0.19 - 3.6	0.73	0.98	0.22
F2	Bare rock	0.046 - 0.128	0.061	0.020	0.004	0.25 - 2.5	0.50	0.53	0.12
F3	Boulder-riffle	0.068 - 0.273	0.124	0.066	0.014	0.39 - 10.1	2.37	3.2	0.68
F4	Semi-alluvial (70% cover)	0.049 - 0.230	0.076	0.048	0.011	0.21 - 7.5	1.01	1.78	0.40
F5	Semi-alluvial (20% cover)	0.041 - 0.151	0.065	0.038	0.009	0.16 - 3.8	0.80	1.13	0.26
Overall (F1 to F5 combined)		0.041 - 0.273	0.080	0.050	0.005	0.16 - 10.1	1.11	1.93	0.19

Table 4.9 shows the lowest values of *n* and *f* are observed in the bare rock gorge (average $n = 0.061$, $f = 0.50$) because of fastest velocity despite the highest energy slope and rapidly rising depth (Figures 4.23 and 4.20). Likewise, the highest values of *n* and *f* are observed in the boulder riffle sub-reach (average $n = 0.124$, $f = 2.37$) as it has the lowest *V*, highest *d* and moderately high *S*. Sub-reaches F1 and F5 have very similar values of *n* or *f*. The *n* values for Trout Beck are higher than the values stated by Chow (1959), who suggests 0.05 (range 0.03 – 0.07) for mountain streams with cobbles and boulders. Collated *n* and *f* values from the literature are shown in Table 4.10 for comparison. The highest values of *n* and *f* observed in Trout Beck are respectively 0.273 and 10.1 (F3) but these values are not as high as in some other channels. For example, Beven *et al.* (1979) observed a maximum value of $f = 1\,328$ in a site with waterfalls and plunge pool in a headwater of the River Severn at the very low discharge of 0.015 $m^3 s^{-1}$ (Table 4.10).

Table 4.10. Flow resistance coefficients *n* and *f* for a variety of channel conditions, taken from Heritage *et al.* (2004).

Reference	Channel description	Manning's '*n*'	Friction factor *f*
Chow (1959)	Vegetation infested	0·1	–
	Dense brush and willows	0·16 (max)	–
	Cobble bottom	0·05 (max)	–
Barnes (1967)	Bedrock base with boulders. High slope, low depth	0·075	–
Bathurst (1978)	Mountain stream, low flow	–	3·12 (max)
Bathurst *et al.* (1981)	Flume study, large-scale roughness	–	4·79 (max)
Richards (1982)	Clean natural channel	0·03	0·072
	Weedy natural channel	0·07	0·4
	Mountain stream with boulders	0·05	0·196
Thorne and Zevenbergen (1985)	Mountain stream, large boulders	0·11 (max)	1·55 (max)
Bathurst (1985)	Mountain river, high slope	–	0·65
			5·46 (max)
Hicks and Mason (1991)	Boulder bed, low flow	0·27	–
	Large boulder and bedrock, high flow	0·2	–
Whittaker and Jaeggi (1982)	Step–pool mountain streams	–	44·9 (max)
Beven *et al.* (1979)	Waterfalls and plunge pools; low flow	–	1328 (max)
	Straight, pools and cobbled riffles	–	48
Bridge and Gabel (1992)	Low sinuosity, braided	–	0·07
			0·13 (max)
Bakry *et al.* (1992)	Vegetation-infested canals	0·05	–
		0·074 (max)	
Hall and Freeman (1994)	Flume study, dense vegetation	0·27	–
		0·7 (max)	

Lee and Ferguson (2002) found very high and generally inconsistent values of flow resistance in step-pool streams, for example $n > 0.10$ in all sites even at high discharge, $n \sim 1$ at low flow, with maximum value of 8.0 in a very steep channel with large boulders. The maximum value of *f* found by Heritage *et al.* (2004) in a bedrock distributary of the Sabie River in South Africa is 3 733. Hicks and Mason (1991) report *n* values of 0.27 at low flow and 0.2 at high flow (Table 4.10) in a channel with large boulders, and these low flow values are similar to the boulder-riffle sub-reach (F3) at Trout Beck. The *f* values in excess of 40 have been reported from step-pool mountain streams and channel with cobble riffles (e.g. Beven *et al.*, 1979; Whittaker & Jaeggi, 1982) (Table 4.10) From a flow resistance study of five small catchments in British Columbia Reid and Hickin (2008) found that *n* varied from 0.047 to 7.95 and *f* from 0.29 to 12 700.

The *n* and *f* and other relevant hydraulic properties for the field-measured low *Q* data are presented in Table 4.11. Similarly, the high *Q* estimated data based on site rating curves, sub-reach cross-sections and measured water levels for low *Q* data are summarised in Table 4.12. These tables also include the inverse of resistance

$(8f)^{1/2}$ (= V/u^*), relative submergence R/D_{84} and shear stress (τ) which will be discussed in later sections.

Table 4.11. Bulk hydraulic characteristics of sub-reaches: measured discharge Q, mean velocity V, energy slope S, shear velocity u^* (= $(gRS)^{1/2}$ where R is hydraulic radius), Manning's n (=$R^{2/3}S^{1/2}/V$), Darcy-Weisbach f (= $8gRS/V^2$), Froude number Fr (= $V/(gd)^{1/2}$ where d is mean depth), inverse of resistance $(8f)^{1/2}$ [=V/u^*=$(0.319R^{1/6})/n$], relative submergence R/D_{84}, and shear stress τ (= ρgRS).

Sub-reach	Q ($m^3 s^{-1}$)	V ($m\ s^{-1}$)	S ($m\ m^{-1}$)	u^* ($m\ s^{-1}$)	n ($s\ m^{-3}$)	f	F_r	$(8/f)^{1/2}$	R/D_{84} ($m\ m^{-1}$)	τ ($N\ m^{-2}$)
F1	0.18	0.19	0.010	0.12	0.148	3.24	0.15	1.57	1.29	15
	0.18	0.18	0.010	0.12	0.156	3.60	0.14	1.49	1.32	15
	0.51	0.35	0.011	0.14	0.094	1.22	0.26	2.56	1.57	19
	0.89	0.48	0.009	0.14	0.071	0.65	0.32	3.51	1.89	19
	1.11	0.57	0.010	0.15	0.066	0.56	0.37	3.79	1.99	22
F2	0.08	0.28	0.017	0.16	0.128	2.48	0.23	1.80	-	24
	0.17	0.44	0.016	0.16	0.087	1.08	0.33	2.72	-	26
	0.19	0.45	0.017	0.17	0.089	1.12	0.35	2.68	-	29
	0.61	0.82	0.018	0.20	0.060	0.47	0.54	4.13	-	40
	1.15	1.24	0.021	0.23	0.046	0.27	0.78	5.48	-	51
	1.19	1.15	0.021	0.23	0.050	0.31	0.71	5.05	-	52
F3	0.09	0.15	0.019	0.17	0.260	10.1	0.12	0.89	0.77	28
	0.17	0.17	0.018	0.19	0.271	9.86	0.12	0.90	1.05	36
	0.21	0.18	0.020	0.20	0.273	9.76	0.12	0.91	1.14	42
	0.65	0.35	0.020	0.25	0.188	4.08	0.19	1.40	1.68	63
	0.88	0.44	0.019	0.25	0.154	2.67	0.23	1.73	1.79	63
	0.91	0.44	0.019	0.25	0.154	2.65	0.23	1.74	1.83	65
	1.43	0.63	0.020	0.27	0.115	1.44	0.32	2.36	1.95	72
	1.58	0.65	0.020	0.28	0.117	1.47	0.32	2.34	2.05	77
Sub-reach	Q ($m^3 s^{-1}$)	V ($m\ s^{-1}$)	S ($m\ m^{-1}$)	u^* ($m\ s^{-1}$)	n ($s\ m^{-3}$)	f	F_r	$(8/f)^{1/2}$	R/D_{84} ($m\ m^{-1}$)	τ ($N\ m^{-2}$)
F4	0.08	0.12	0.008	0.11	0.230	7.49	0.09	1.03	0.89	13
	0.16	0.19	0.008	0.12	0.153	3.20	0.14	1.58	0.98	14
	0.21	0.19	0.007	0.13	0.161	3.37	0.13	1.54	1.16	16
	0.73	0.45	0.009	0.16	0.091	0.98	0.26	2.86	1.55	25
	1.26	0.61	0.008	0.17	0.076	0.63	0.31	3.55	1.88	29
	1.64	0.72	0.008	0.17	0.066	0.46	0.36	4.15	2.01	30
F5	0.09	0.19	0.017	0.13	0.151	3.81	0.18	1.45	0.75	17
	0.15	0.23	0.018	0.15	0.147	3.37	0.20	1.54	0.92	23
	0.23	0.29	0.019	0.16	0.129	2.49	0.24	1.79	1.03	27
	0.81	0.60	0.021	0.21	0.086	0.97	0.41	2.87	1.51	43
	0.80	0.54	0.021	0.21	0.098	1.24	0.36	2.54	1.58	45

Table 4.12. Summary of bulk hydraulics for high *Q* data. Refer caption of Table 4.11 for description of characteristics.

Sub-reach	Q ($m^3 s^{-1}$)	V ($m\ s^{-1}$)	S ($m\ m^{-1}$)	u^* ($m\ s^{-1}$)	n ($s\ m^{-3}$)	f	F_r	$(8/f)^{1/2}$	R/D_{84} ($m\ m^{-1}$)	τ ($N\ m^{-2}$)
F1	1.5	0.62	0.010	0.17	0.069	0.58	0.37	3.72	2.39	28
	2.0	0.72	0.010	0.18	0.065	0.49	0.40	4.05	2.69	31
	2.5	0.80	0.010	0.19	0.062	0.42	0.43	4.34	2.96	34
	3.0	0.88	0.010	0.19	0.059	0.38	0.45	4.57	3.19	37
	3.5	0.95	0.010	0.20	0.057	0.35	0.47	4.76	3.41	40
	4.0	1.02	0.010	0.21	0.056	0.33	0.49	4.96	3.59	42
	4.5	1.08	0.010	0.21	0.055	0.31	0.51	5.10	3.77	45
	5.0	1.13	0.010	0.22	0.053	0.29	0.52	5.26	3.92	46
	5.5	1.19	0.010	0.22	0.052	0.27	0.54	5.42	4.06	48
	6.0	1.24	0.011	0.22	0.051	0.26	0.55	5.53	4.18	50
	7.0	1.34	0.011	0.23	0.049	0.23	0.58	5.84	4.36	53
	8.0	1.41	0.011	0.24	0.048	0.22	0.60	5.97	4.60	56
	9.0	1.49	0.011	0.24	0.047	0.21	0.62	6.15	4.78	59
	12.0	1.69	0.011	0.26	0.046	0.19	0.66	6.45	5.44	69
F2	1.5	1.33	0.022	0.24	0.046	0.26	0.81	5.54	-	57
	2.0	1.44	0.023	0.26	0.046	0.25	0.82	5.63	-	65
	2.5	1.51	0.023	0.27	0.048	0.26	0.81	5.54	-	74
	3.0	1.57	0.023	0.29	0.049	0.27	0.80	5.47	-	82
	3.5	1.62	0.023	0.30	0.051	0.28	0.78	5.36	-	91
	4.0	1.67	0.023	0.32	0.053	0.29	0.77	5.27	-	100
	4.5	1.70	0.023	0.33	0.054	0.30	0.76	5.19	-	108
	5.0	1.74	0.024	0.34	0.056	0.31	0.75	5.12	-	116
	5.5	1.78	0.024	0.35	0.057	0.31	0.74	5.08	-	123
	6.0	1.81	0.024	0.36	0.058	0.32	0.73	5.03	-	130
	7.0	1.87	0.024	0.38	0.059	0.33	0.72	4.95	-	142
	8.0	1.91	0.024	0.39	0.061	0.34	0.71	4.89	-	153
	9.0	1.96	0.025	0.40	0.062	0.34	0.70	4.83	-	164
	12.0	2.05	0.025	0.44	0.066	0.37	0.68	4.65	-	194
Sub-reach	Q ($m^3 s^{-1}$)	V ($m\ s^{-1}$)	S ($m\ m^{-1}$)	u^* ($m\ s^{-1}$)	n ($s\ m^{-3}$)	f	Fr	$(8/f)^{1/2}$	R/D_{84} ($m\ m^{-1}$)	τ ($N\ m^{-2}$)
F3	1.5	0.64	0.020	0.27	0.115	1.44	0.32	2.36	2.00	74
	2.0	0.75	0.020	0.28	0.104	1.13	0.36	2.66	2.18	80
	2.5	0.84	0.019	0.29	0.097	0.96	0.39	2.89	2.37	85
	3.0	0.93	0.019	0.30	0.092	0.84	0.41	3.08	2.54	90
	3.5	1.00	0.019	0.31	0.089	0.77	0.42	3.23	2.71	95
	4.0	1.06	0.019	0.32	0.085	0.70	0.44	3.37	2.86	100
	4.5	1.13	0.019	0.32	0.083	0.66	0.45	3.49	3.00	104
	5.0	1.18	0.018	0.33	0.081	0.62	0.46	3.60	3.13	107
	5.5	1.23	0.018	0.33	0.080	0.58	0.47	3.70	3.26	111
	6.0	1.28	0.018	0.34	0.078	0.56	0.48	3.79	3.38	114
	7.0	1.37	0.018	0.35	0.076	0.51	0.50	3.95	3.60	120
	8.0	1.45	0.018	0.35	0.074	0.47	0.51	4.11	3.80	124
	9.0	1.52	0.017	0.36	0.072	0.45	0.52	4.23	4.00	129
	12.0	1.70	0.017	0.37	0.068	0.39	0.54	4.54	4.51	140

F4	1.5	0.67	0.007	0.16	0.067	0.48	0.33	4.07	1.98	27
	2.0	0.79	0.008	0.18	0.061	0.39	0.37	4.50	2.18	31
	2.5	0.89	0.008	0.19	0.058	0.34	0.41	4.83	2.35	34
	3.0	0.98	0.008	0.19	0.056	0.31	0.43	5.05	2.52	38
	3.5	1.07	0.008	0.20	0.054	0.29	0.45	5.26	2.66	41
	4.0	1.14	0.009	0.21	0.053	0.27	0.47	5.40	2.80	45
	4.5	1.21	0.009	0.22	0.052	0.26	0.49	5.52	2.91	48
	5.0	1.28	0.009	0.23	0.051	0.25	0.51	5.66	3.01	51
	5.5	1.34	0.009	0.23	0.051	0.24	0.52	5.73	3.11	54
	6.0	1.39	0.010	0.24	0.051	0.24	0.53	5.78	3.21	58
	7.0	1.50	0.010	0.25	0.050	0.23	0.56	5.91	3.37	64
	8.0	1.59	0.011	0.26	0.050	0.22	0.58	6.02	3.52	70
	9.0	1.67	0.011	0.27	0.049	0.22	0.60	6.08	3.65	76
	12.0	1.87	0.012	0.30	0.050	0.21	0.64	6.15	4.01	93
F5	1.5	0.93	0.022	0.22	0.060	0.46	0.60	4.17	1.66	50
	2.0	1.09	0.022	0.23	0.053	0.36	0.69	4.74	1.74	53
	2.5	1.22	0.023	0.23	0.049	0.30	0.76	5.21	1.77	55
	3.0	1.33	0.023	0.24	0.046	0.26	0.82	5.58	1.82	57
	3.5	1.42	0.023	0.25	0.044	0.24	0.84	5.77	1.93	60
	4.0	1.50	0.023	0.25	0.044	0.23	0.87	5.92	2.05	64
	4.5	1.57	0.023	0.26	0.043	0.22	0.90	6.07	2.13	67
	5.0	1.64	0.023	0.27	0.043	0.21	0.91	6.16	2.24	71
	5.5	1.70	0.023	0.27	0.043	0.21	0.92	6.23	2.35	75
	6.0	1.76	0.023	0.28	0.042	0.20	0.93	6.29	2.46	78
	7.0	1.87	0.023	0.29	0.042	0.19	0.95	6.42	2.67	85
	8.0	1.98	0.023	0.30	0.042	0.19	0.97	6.57	2.84	90
	9.0	2.07	0.023	0.31	0.041	0.18	0.99	6.67	3.02	96
	12.0	2.31	0.023	0.33	0.041	0.16	1.03	6.96	3.47	110

4.4.2 Variation of flow resistance coefficients with discharge

It is often assumed that the resistance of a particular channel can be represented by some particular value of *n*, but several authors (e.g. Chow, 1959; Sargent, 1979; Ferguson, 2010, 2013) have shown that *n* tends to decrease as *Q* increases within a reach. Trout Beck *n* and *f* data (Tables 4.11 and 4.12) are plotted against *Q* in Figure 4.26. These diagrams show that all sub-reaches except bare rock (F2) follow the similar trend of *n* and *f* declining steadily from low flow to moderate and then decreasing very slowly with subsequent increases in *Q*. This is mainly because the influence of grain roughness is drowned out giving a negative value for the exponent *y* ($n = tQ^y$). The trend for the bare rock sub-reach (F2) is different; *n* and *f* decrease rapidly from low to moderate flows, achieve a minimum value then start to rise again as the discharge increases. This must be a consequence of flow rising up the very rough walls in this sub-reach. The walls in other reaches are less rough, giving less contrast with the bed.

The other reaches are all wider than F2, so their walls make up a smaller proportion of the wetted perimeter. Two power equations are shown in the form $n = tQ^y$ and $f = hQ^p$ (Knighton, 1998; Reid & Hickin, 2008).

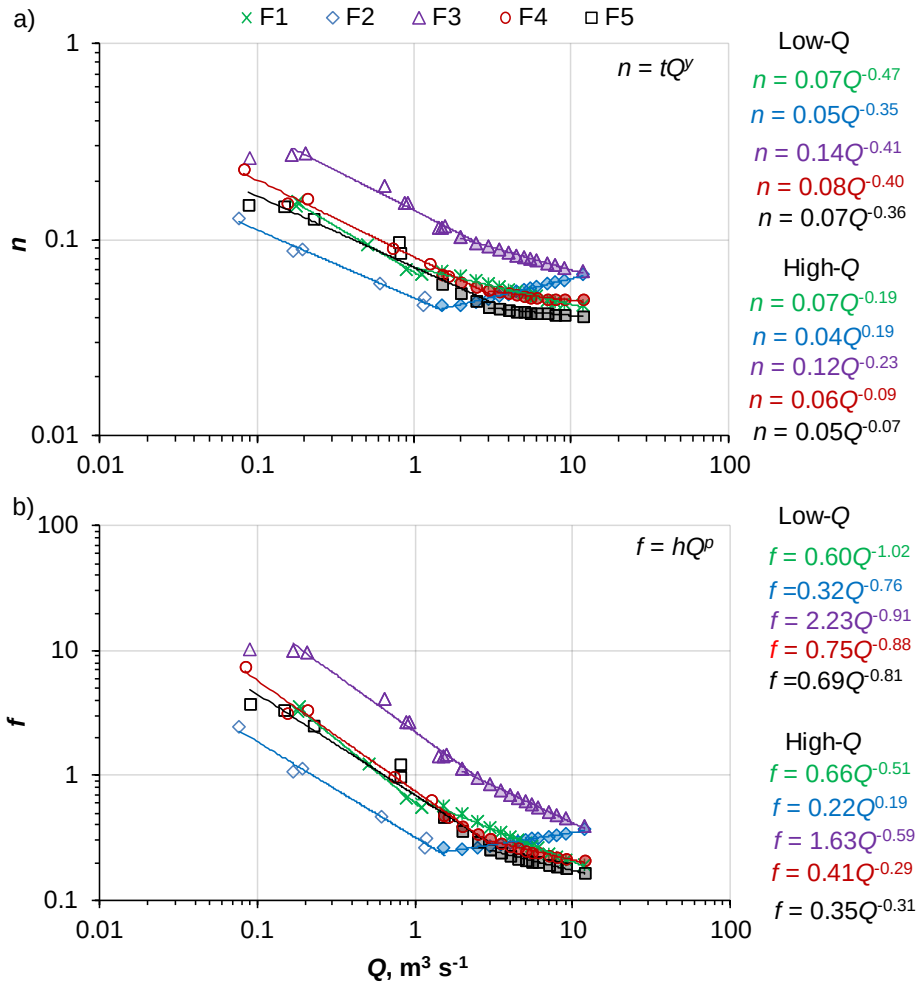

Figure 4.26. Variation in *n* and *f* with *Q* in Trout Beck sub-reaches: F1 (alluvial: green), F2 (bare rock: blue), F3 (boulder-riffle: purple), F4 (semi-alluvial 70% cover: red), F5 (semi-alluvial 20% cover: black). The open and filled markers represent the measured and estimated data. Two power equations in the form $n = tQ^y$ and $f = hQ^p$ are displayed in coloured text. All fitted power-law exponents are significantly different from zero at $p < 0.001$.

The general pattern of the *n*-*Q* and *f*-*Q* curves is very similar, with both *n* and *f* decreasing as *Q* increases. For example for F3 the highest (or close to the highest) values of *n* and *f* are 0.273 and 10.1 at the lowest discharge of 0.09 $m^3 s^{-1}$ (Table 4.11) and the lowest values of *n* and *f* are 0.068 and 0.39 at the highest discharge of 12 $m^3 s^{-1}$ (Table 4.12). Table 4.13 summarises the coefficients and exponents of *n*-*Q* and *f*-*Q* equations displayed in Figure 4.26.

Table 4.13. Coefficients and exponents in $n = tQ^y$, and $f = hQ^p$ for sub-reaches. All sub-reaches have negative exponents except bare rock (F2) at high Q (highlighted). The average values for sub-reach with and without F2, and overall average without F2 (and range) are shown.

Sub-reach	Low Q		High Q	
	Coefficients			
	t	*h*	*t*	*h*
F1	0.07	0.60	0.07	0.66
F2	0.05	0.32	0.04	0.22
F3	0.14	2.23	0.12	1.63
F4	0.08	0.75	0.06	0.41
F5	0.07	0.69	0.05	0.35
Sub-reach average	*0.08*	*0.92*	*0.07*	*0.65*
Sub-reach average excl. F2	*0.09*	*1.07*	*0.08*	*0.76*
*Overall average excluding F2 : t = 0.08 (*range: *0.07 to 0.14), h = 0.92 (*range: *0.32 to 2.23),*				
	Low Q		High Q	
	Exponents			
	y	*p*	*y*	*p*
F1	-0.47	-1.02	-0.19	-0.51
F2	-0.35	-0.76	0.19	0.19
F3	-0.41	-0.91	-0.23	-0.59
F4	-0.40	-0.88	-0.09	-0.29
F5	-0.36	-0.81	-0.07	-0.31
Sub-reach average	*-0.40*	*-0.88*	*-0.08*	*-0.30*
Sub-reach average excl. F2	*-0.41*	*-0.91*	*-0.15*	*-0.43*
*Overall average excluding F2 : y = -0.28 (*range: *-0.07 to -0.47), p = -0.67 (*range: *-0.29 to -1.02)*				

Table 4.13 shows that the average value of the *n*-*Q* exponent (*y*) for alluvial and semi-alluvial sub-reaches is -0.28 (range: -0.07 to -0.47). The average *y* values for low and high *Q* are -0.41 (-0.36 to -0.47) and -0.15 (-0.07 to -0.23) respectively. The bare rock sub-reach F2 has similar negative *y* (-0.35) at low flow but has positive *y* at high flow (0.19) because *n* starts to rise again with increasing *Q*. The possible reason why *n* decreases to the lowest value and then increases could be because of the rock walls that are hydraulically rougher than the bed because of the various protrusions and re-entrants as mentioned earlier in section 4.3. That would give minimum flow resistance when the water has risen to occupy the full bed width but is only just starting to rise up the walls. That is also the level at which the slope of the *d*-*Q* curve changes (Figure 4.23b). For sub-reaches F4 and F5, *n* is almost constant once the channel discharge exceeds a moderately high value (3 $m^3 s^{-1}$) as reflected by their very small *y* values (-0.09 and -0.07) (Figure 4.26a).

Sub-reach F3 plots highest in the *n*-*Q* chart, hence it has the highest coefficient *t* (0.12 – 0.14), while F2 plots lowest (*t* = 0.04 – 0.05). The low or high value of *y* shows the rate of change in *n*, whereas the low or high value of *t* indicates where they plot in the graph. Much higher resistance in F3 is possibly due to the higher form drag from the boulders, and the reason why *n* is not flattened off (*y* = -0.23) even at median annual flood (9.1 $m^3 s^{-1}$) is possibly because some of the large boulders are not fully submerged. Sub-reaches F1, F4 and F5 plot about midway between F2 and F3 as also indicated by the respective *t* values (0.05 – 0.08). Reid and Hickin (2008) found the average value of *y* varies from -0.27 to -0.56 and the coefficient *t* from 0.07 to 0.29, both these *y* and *t* values are higher than even the low flow values in Trout Beck.

The average value of the *f*-*Q* exponent (*p*) for alluvial and semi-alluvial sub-reaches is -0.67 (range: -0.29 to -1.02). The *p* value for low *Q* is -0.91 (-0.81 to -1.02) and for high *Q* is -0.43 (-0.29 to -0.59). In most of the Rio Cordon reaches in Italy, Comiti *et al.* (2007) found *p* between -0.35 and -0.60. These are rather lower values than for Trout Beck at low to moderate *Q*, but are very similar to the high *Q* values from Trout Beck. Reid and Hickin (2008) found the average *p* varies from -0.63 to -1.19 and the coefficient *h* from 0.46 to 4.68, which are higher values than in Trout Beck. Typical values of *y* for lowland stream are, in the range -0.01 to -0.24 whereas the values of *p* for the same rivers are in the range -0.14 to -0.61 according to Knighton (1998), slightly lower than in Trout Beck. This also shows that the *y* exponents are generally smaller than *p* exponents. Though the *n*-*Q* and *f*-*Q* plots appear very similar their coefficients and exponents are different (Table 4.13). For example, the average *n*-*Q* coefficient for Trout Beck (*t* = 0.08) is very different from the *f*-*Q* coefficient (*h* = 0.92), and similarly the exponent *y* (-0.28) is different from exponent *p* (-0.67). The *n*-*Q* plots for F4 and F5 are nearly flattened off at high discharge (*y* = -0.09 and -0.07) whereas the *f* is still declining with a moderately high rate (*p* = - 0.29 and -0.31). This shows that *n* and *f* decrease with increasing discharge but the rate of decrease is higher for *f* than *n*.

4.4.3 Variation in *n* with discharge and depth and comparison with channels of different character

The *n* values from Trout Beck sub-reaches and other channels of different character (large, small, sand/gravel-bed, pool-riffle, cobble/boulder cascade, bedrock reaches) are plotted against discharge in Figure 4.27, for comparison. The data of the global rivers are taken from published literature.

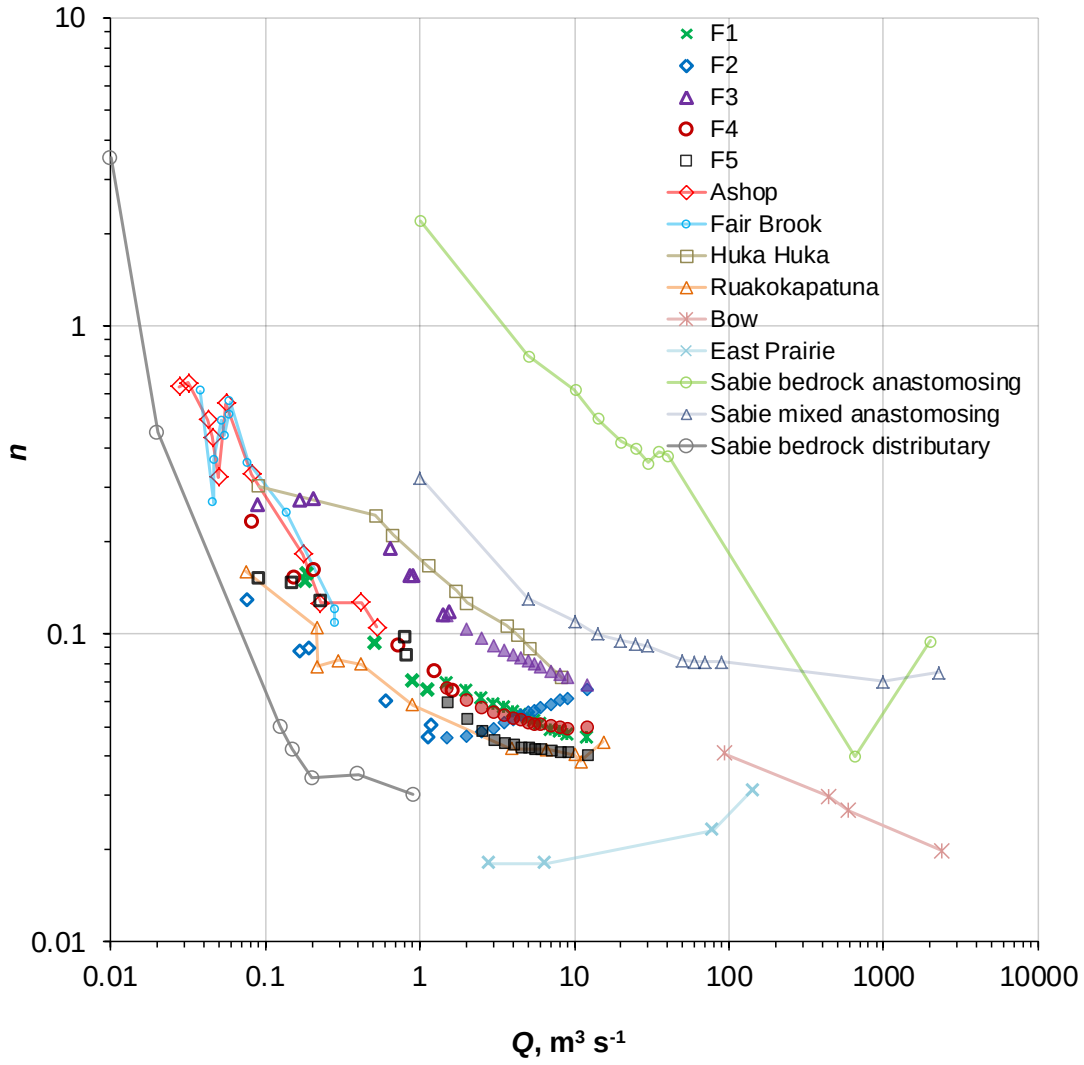

Figure 4.27. Variation in *n* with discharge in Trout Beck and other channels of different character: Ashop/Fair Brook – small rivers from England, Huka Huka/Ruakokapatuna – small rivers from New Zealand, Bow/East Prairie – large alluvial rivers from Canada; Sabie River (bedrock anastomosing/ mixed bedrock-alluvial anastomosing, and bedrock distributary channel) – large bedrock dominated river in South Africa. Trout Beck sub-reaches (F1 – F5) are shown by markers only (open markers: measured, filled markers: estimated) while other rivers by line with markers.

Ashop is a small cobble/boulder cascade reach in England (slope = 2.6%, width = 5.1 m, D_{84} = 296 mm, Q = 0.03 – 0.53 $m^3 s^{-1}$), the data are taken from Ferguson (2010). Fair Brook is another steep channel from England (S = 6.6%, w = 3.1 m, D_{84}= 480 mm, Q = 0.04 – 0.28 $m^3 s^{-1}$) with some exposed rock in its bed (near-horizontal sandstone/shale), so not so different from Trout Beck (data source: Lee & Ferguson, 2002). Figure 4.27 shows that both Ashop and Fair Brook data overlap each other, and are in good agreement with Trout Beck, though all their Q values are < 0.60 $m^3 s^{-1}$. Huka Huka and Ruakokapatuna are two small rivers from New Zealand (data source: Hicks & Mason, 1991). Huka Huka is a boulder bed river (S = 4%, D_{84} = 260 mm, Q =0.1 – 8.3 $m^3 s^{-1}$) whose data plot slightly higher but the trend is very similarly to the

boulder-riffle site (F3) of Trout Beck. Ruakokapatuna is a gravel-bed pool-riffle river (Q = 0.1 – 15.3 m^3 s^{-1}) and plots very similar to the F2 site (bedrock) of Trout Beck. River Bow and East Prairie are alluvial rivers from Canada (data source: Kellerhals *et al.*, 1972). Bow is a large gravel-bed river and is not comparable to Trout Beck, but it shows that *n* behaves similarly, declining with increasing discharge. East Prairie is a sand bed river at which *n* increases as the *Q* decreases and this appears to be because of the developed bedforms.

Sabie is a large bedrock-dominated river in South Africa (Data from Fig. 8/10 of Heritage *et al.*, 2004) and the data from three channels on the Sabie River are included in the plot.

a. 'Sabie bedrock anastomosing' is a cohesive mixed anastomosing reach with negligible sediment cover and includes a bedrock distributary (individual active channel flowing over bedrock), rapids (steep bedrock sections) and pools. The very high roughness is due to steep gradient and large roughness elements such as irregular bedrock outcrops and large boulders. This is a big anastomosing river and not directly relevant to Trout Beck but it shows that the flow resistance varies in bedrock and it could be much higher than is generally thought. Heritage *et al.* (2004) speculate that the high flow resistance generated from the exposed irregular bedrock (cohesive mixed anastomosed and mixed pool-rapid) perhaps reflects energy dissipation by internal distortion and hydraulic jumps, but this macro-scale roughness and energy dissipation effect seems to be drowned out as the discharge increases. From low to moderately high flow, *n* rapidly declines with discharge, and after reaching a minimum value it starts to increase again in the same way bare rock sub-reach F2 in Trout Beck does.
b. 'Sabie mixed anastomosing' is an uncohesive mixed anastomosing reach and includes a mixed distributary (individual active channel flowing over alluvial and bedrock bed), rapids and pools. The data from these channels plot lower than the pure bedrock anastomosing reach (because of the lower gradient) but the slope of the curve is parallel to Trout Beck and *n* flattens off and stabilises at high flow similar to semi-alluvial sub-reaches F4 and F5 in Trout Beck (Figure 4.27).
c. 'Sabie bedrock distributary' refers to the active distributary channel in the main anastomosing channel flowing over the bedrock, and the plotted data are

the field-measured low flow data (< 0.05 to 1 $m^3 s^{-1}$) from these bedrock morphological units. The *n* declines rapidly than in F2 because the Sabie channels are steeper and smoother than the bare rock gorge in Trout Beck.

All these bedrock-dominated channels of Sabie River show that the flow resistance rapidly declines from low flow and then it either stabilises or rises again as the discharge rises. According to Heritage *et al.* (2004), once *n* and *f* values become stabilised they will be similar to the values reported in mountains streams and slightly higher than those in typical braided rivers at high flows. These examples show that channel types with a high degree of bedrock influence have high values of flow resistance and in such circumstances the channel form resistance is more important than grain roughness.

As stated earlier, Manning's *n* which is frequently used in engineering design and landscape modelling works is often taken from textbooks (e.g. Chow, 1959) and these values are mainly based on large alluvial rivers. Figure 4.27 shows how *n* varies with discharge in large sand or gravel-bed rivers but it is interesting to see how *n* varies with mean depth (*d*) in Trout Beck and other rivers. Figure 4.28 plots the *d* in Trout Beck sub-reaches against *n*. For comparison, it also includes *d*-*n* plots for large alluvial rivers (Mississippi (USA), Tennessee (USA) and Irrawaddy (Burma)), taken from Chow (1959). All these examples demonstrate that the plots do not follow any particular trend but show that *n* is high at low depth, *n* steadily decreases as the depth increases up to a certain depth and then *n* either starts to rise a bit with the depth (as in Trout Beck sub-reach F2, Mississippi and Irrawaddy) or stabilises at almost a constant value or decreases very slowly (e.g. F1, F3, F4, F5 and Tennessee). Figure 4.28 (a) shows that F5 after achieving a depth of ~0.3 m the *n* value stabilises and has almost a constant value (~0.04) for any higher depth. However, in other alluvial and semi-alluvial sub-reaches the *n* value is still declining with rising depth, however F1 and F4 get stabilised at *d* ~0.60 m but F3 still continues to decline with rising depth. A possible reason why *n* for F3 is not stabilised at that depth (~1 m) is because the form drag increases with the depth (e. g. Andrews, 2000) or possibly some of the boulders are still not fully submerged.

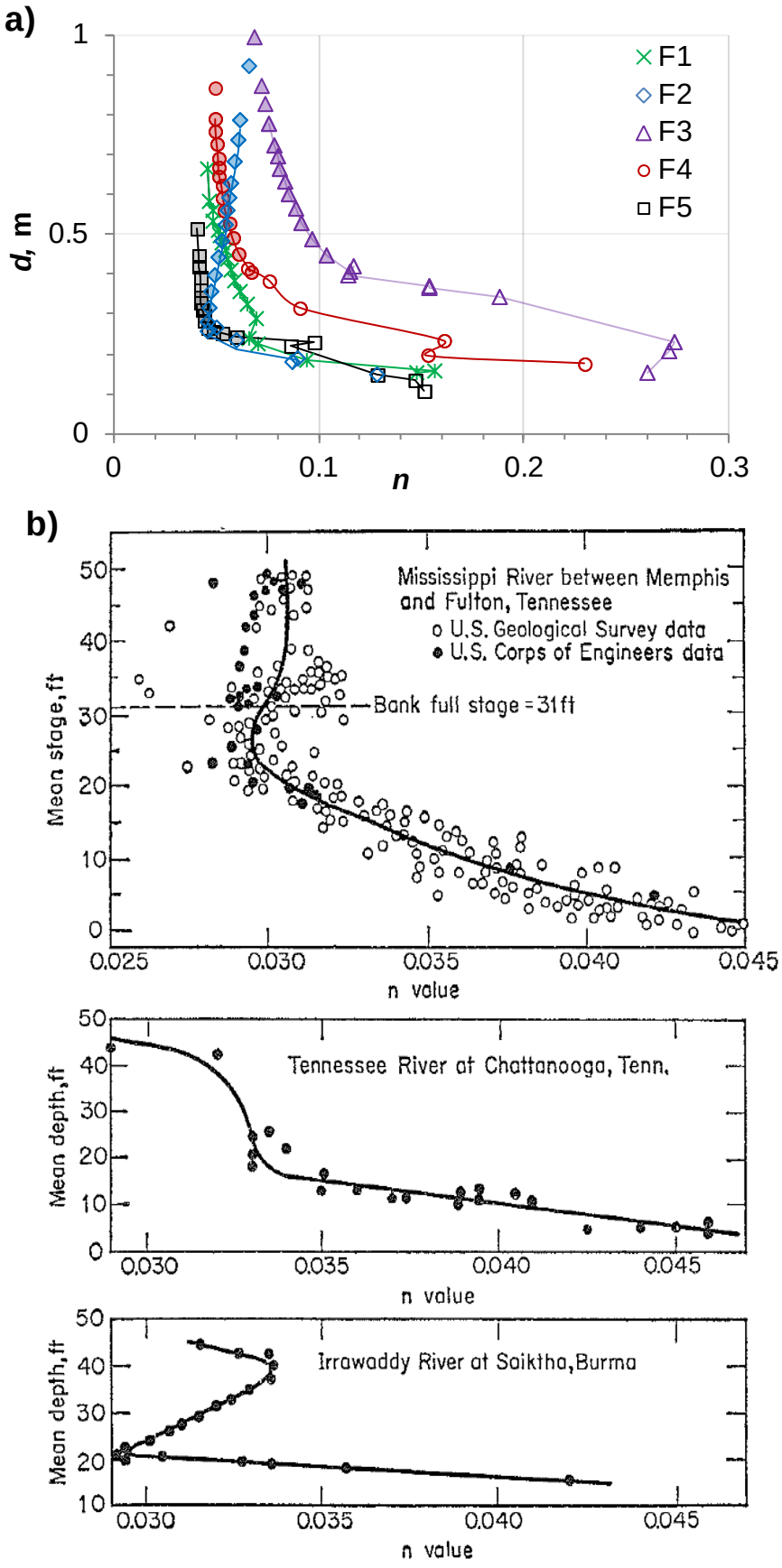

Figure 4.28. Variations of Manning's *n* with mean depth (*d*): a) Trout Beck sub-reaches F1 – F5; b) large alluvial rivers Mississippi, Tennessee, and Irrawaddy (Chow, 1959).

4.4.4 Relationship of flow resistance to relative submergence

Most flow resistance equations proposed for alluvial channels can be expressed by some relation to predict the relative velocity V/u^* [= $(8/f)^{½}$], as described in chapter 1 (Section 1.1.3). The inverse of flow resistance $(8/f)^{½}$ is plotted against R/D_{84} in Figure 4.29 to investigate how flow resistance varies with relative submergence (R/k_s, where k_s is roughness height and can be expressed in terms of D_{84}) in Trout Beck sub-reaches. In Trout Beck for a given range of Q from 0.08 to 12 $m^3 s^{-1}$, the submergence ratio R/D_{84} varies from 0.75 to 5.4 (for F1 = 1.3 to 5.4, F3 = 0.8 to 4.5, F4 = 0.9 to 4.0, and F5 = 0.75 to 3.5). Figure 4.29 also compares the Trout Beck data with the predictions by the commonly used power and log law equations as discussed in section 1.1.3. The upper and lower envelopes of Rickenmann and Recking's (2011) comprehensive data compilation are also shown for comparison. The D_{84} is undefined for the bare rock sub-reach F2 as there is no sediment on the main part of the bed; therefore F2 is not included in these plots.

Figure 4.29 (a) shows that the exponent b when the power law $(8/f)^{1/2} = a\,(R/D_{84})^b$ is fitted to Trout beck sub-reaches varies from 1.5 to 2.5 at low flow and 0.32 to 0.73 at high flow. The expected limits on b are 1/6 according to Manning – Strickler (M-S) (Eq. 1.8) and 1 according to the roughness-layer (RL) relation which forms the shallow-flow asymptote of the VPE (Ferguson, 2007a) (Eq. 1.13). The roughness layer approach assumes that in shallow flows ($R/k_s < \sim 4$), there is no boundary layer as such and the roughness elements affect all levels in the flow. Therefore, M-S can be considered as one end member to represent deep flows whilst RL is the other end member to represent shallow flows (Ferguson, 2007a). The b values for Trout Beck shows that Manning–Strickler overestimates velocity at all discharges in all sub-reaches. However, the high Q data are within the RL limit ($b < 1$).

Figure 4.29 (b) compares several flow resistance equations in terms of $(8/f)^{1/2}$ versus R/D_{84}. Some flow resistance equations are not straight lines in a log-log plot of $(8/f)^{1/2}$ versus R/D_{84}. The Keulegan-type log law (Eq. 1.9) for flow resistance which is based on logarithmic velocity profile in boundary layers will be a linear trend in a plot of $(8/f)^{1/2}$ versus $\log(R/D_{84})$, therefore the semilog plot is also shown in Figure 4.29 (c) to see whether any of the sub-reaches show a near-linear trend consistent with the Keulegan equation. The Manning – Strickler equation plots far higher than any Trout Beck data. Bathurst's (2002) power-law equation for slope $S > 0.008$ (Eq. 1.12) is close to the F5 data but still the curve is not parallel to the Trout Beck high flow data. The Bathurst

(2002) equation for $S < 0.008$ (Eq. 1.11) is close to the F5 data but this sub-reach is steeper than 0.8 % slope; the only sub-reach that has ≤ 0.8 % slope is F4.

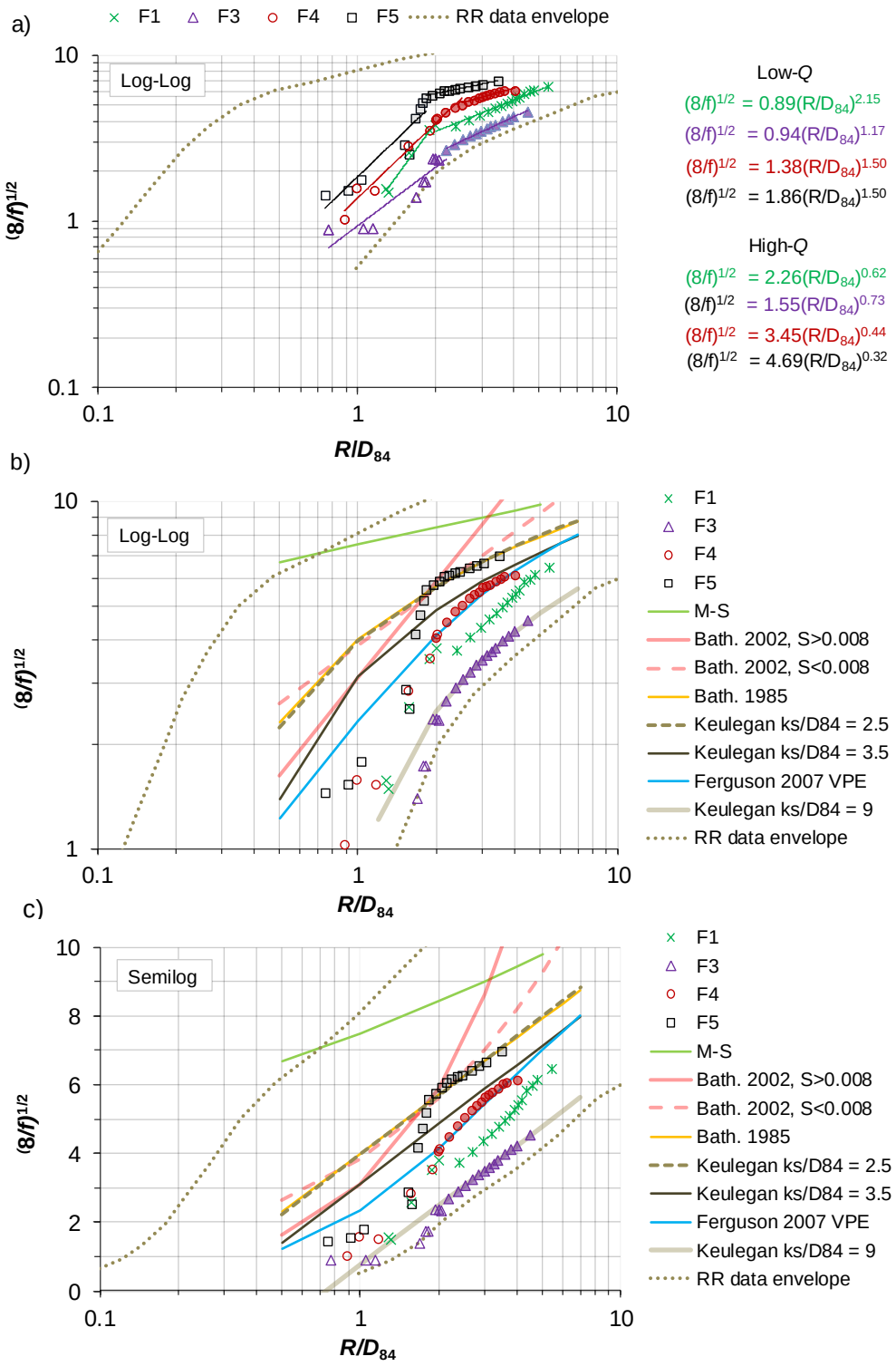

Figure 4.29. a) Log-log plot of $(8/f)^{½}$ ($=V/u^*$) against relative submergence R/D_{84} for Trout Beck sub-reaches. The RR data envelope from Figure 1 of Rickenmann and Recking (2011) is shown for comparison. All fitted power-law exponents are significantly different from zero at $p < 0.001$; b) Log-log plot of Trout Beck data with prediction curves by (from top to bottom) the Manning-Strickler (M-S) equation with constant 7.5, Bathurst (2002) equations for S > 0.8% and < 0.8%, Bathurst (1985) equation, the Keulegan equation with $k_s = 2.5$ and 3.5 times D_{84}, Ferguson (2007) VPE, and the Keulegan equation with $k_s = 9\ D_{84}$; c) Semilog plot of Figure (b).

The Bathurst (1985) equation (Eq. 1.10) overlaps with the Keulegan equation with k_s/D_{84} = 2.5 and these curves are close to the F5 data at higher submergence. Keulegan with k_s/D_{84} = 3.5, following Hey (1979), plots between the high flow data of F4 and F5, but very close to F4. Ferguson's (2007) VPE plots well overall and very close to the high flow data for F4. The Keulegan equation is tried with different values of $k_s/D_{84;}$ the value 9 fits very well with F3 data. Any error in Trout Beck D_{84} estimates would shift the data curves sideways in Figure 4.29 but there would have to be a massive error to bring F3 into line, and a big error to bring F1 into line. Figure 4.29 also shows that the Trout Beck data are within the envelopes of the data used by Rickenmann and Recking (2011), but F3 is right at the lower (high resistance) edge at low Q.

4.4.5 Non-dimensional hydraulic geometry

The non-dimensional velocity V^* [= $V/\sqrt{(gD_{84})}$] has been plotted against non-dimensional discharge unit q^* [= $q/\sqrt{(gD_{84}^3)}$] (Section 1.1.4). Figure 4.30 plots the V^*against q^* for Trout Beck sub-reaches, except F2. The regression lines for sub-reach F1, F3 and F4 are almost identical but F5 is out-of-line. The Comiti *et al.* (2007) equation $V^*= 0.92q^{*0.66}$ plots higher than the Trout Beck data because it was fitted to data from a much steeper channel: the channel slope for their reaches varies from 0.08 to 0.21 compared to ~0.02 for Trout Beck.

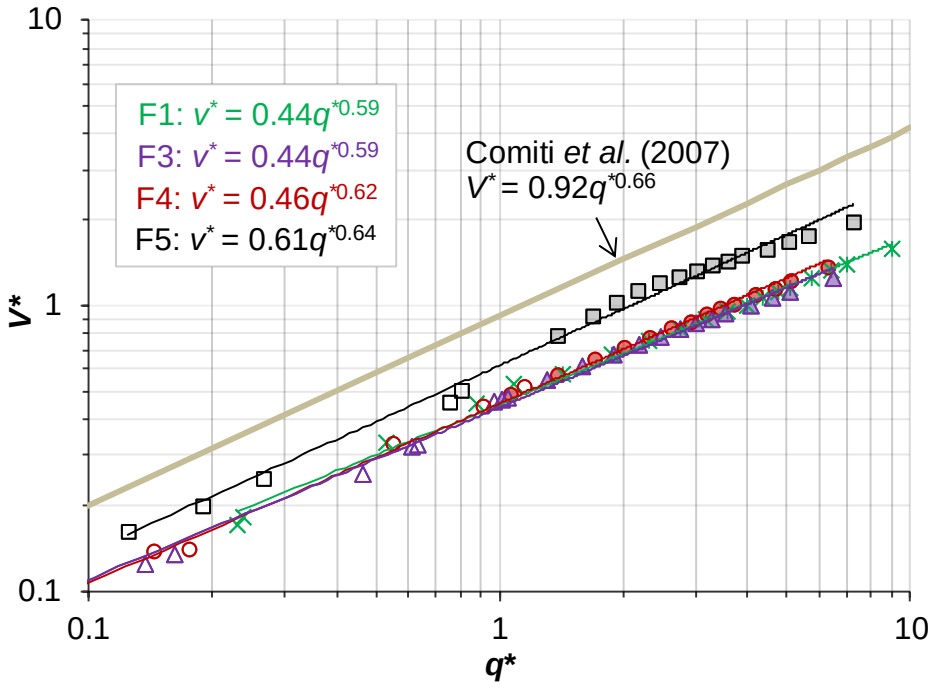

Figure 4.30. Relationship between dimensionless velocity (V^*) and unit discharge (q^*) for Trout Beck alluvial and semi-alluvial sub-reaches. The fitted equations for the data for each sub-reach are shown. The line predicted by Comiti *et al.* (2007) equation is shown for comparison.

The reason why F5 is out of line is perhaps because the used D_{84} = 140 mm (Table 2.8) is not properly representative of the effective roughness of the channel bed because of very low cover in sub-reach F5. In particular, the right hand side of F5 is exposed rock and could have a different effective roughness than the left hand side where the grain sizes were measured. This means that the D_{84} based on the GSD of few exposed patches in the left side of the channel may not be representative of the full channel width. The equation by Comiti *et al.* (2007) (Eq. 1.17) does not contain a channel slope term. Ferguson (2007a) argued that the $V^* - q^*$ relation ought to shift up/down according to slope (S). This is the reason why it is not expected all five sub-reaches to collapse onto a single trend in Figure 4.30, because they have different slopes and the exponent of slope in the formula of V^* (Eq. 1.15 and 1.16) causes an offset in the expected trend.

Figure 4.31 shows the $V^{**} - q^{**}$ plots for Trout Beck where $V^{**} = V/\sqrt{(gSD_{84})}$ and $q^{**} = q/\sqrt{(gSD_{84}^3)}$ (Section 1.1.4) and the Rickenmann and Recking (2011) trend lines (Eq. 1.18 and 1.19) along with the upper and lower boundaries of their data. Figure 4.31a shows the Trout Beck data plot slightly lower than as predicted by the Rickenmann and Recking (2011) equations, however the data envelope of Rickenmann and Recking (2011) (termed as RR) demonstrates that the Trout Beck data are within the envelope of their original data from which these $V^{**} - q^{**}$ equations were developed. The upper and lower envelopes of the RR's data set show that the Trout Beck results are within the envelopes, F3 is right at the lower edge, as is F2 at high Q. All the Trout Beck data apart from F5 plot below the RR trend, suggesting that Trout Beck generally has more resistance than D_{84} would suggest.

The $V^{**} - q^{**}$ plot automatically corrects for differences in slope, therefore Figure 4.31b shows the value of effective k_s for each sub-reach which brings the $V^{**} - q^{**}$ data into line with the RR curve. It is to be noted that all sub-reaches except F1 (alluvial) have two roughness scales: rock and sediment in F3, F4 and F5, and rock bed and rock walls in F2. The measured D_{84} gives an idea of k_s for alluvial bed, but the overall k_s will be some kind of average of k_s in sediment and k_s in rock. Figure 4.31b illustrates that the effective k_s of 0.20 m for F1 implies that the roughness is higher than D_{84} (0.12 m) (Table 2.8). Similarly the effective k_s for F2 = 0.11 m, F3 = 0.55 m > D_{84} (0.19 m), F4 = 0.26 m > D_{84} (0.19 m), and F5 = 0.12 m < D_{84} (0.14 m). This shows that effective roughness is higher than D_{84} in all sub-reaches except F5, and particularly high in the boulder-riffle sub-reach F3.

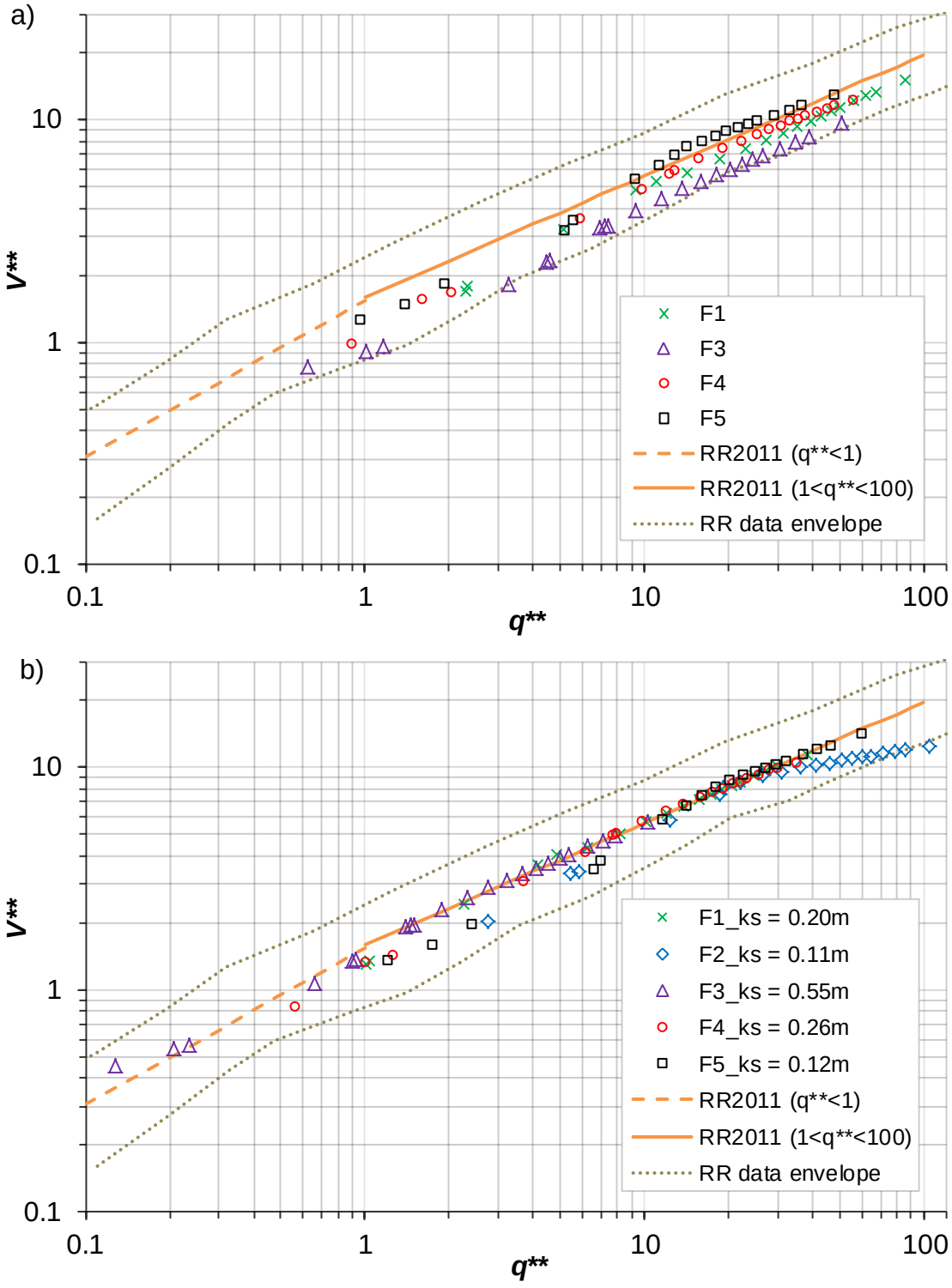

Figure 4.31. a) V^{**} versus q^{**} for Trout Beck sub-reaches as calculated using D_{84} (F1: green, F3: purple, F4: red and F5: black). The Rickenmann and Recking 2011 (RR2011) trend lines for q^{**} <1 (orange dashed) and q^{**} >1 (orange solid) are also shown, as are the upper and lower boundaries of the RR2011 data compilation (Fig 5a of Rickenmann & Recking, 2011) using dotted grey lines. The sub-reaches that plot below the RR trend have higher effective roughness than D_{84}; b) Effective k_s values that would be needed to bring the sub-reaches into RR line are shown, for *e.g.* k_s = 0.55 m would be needed to collapse the F3 data into the RR trend line.

The F2 data at the top right of Figure 4.31b are seen to start falling below the general trend when the water rises up the rough walls, as discussed in the hydraulic geometry

section (Section 4.3), which means at high Q the effective roughness is higher than 0.11 m.

Summary of flow resistance results

Flow resistance coefficients n and f are calculated for two sets of data: measured low Q and estimated high Q data. The field measured and estimated data range from 0.08 - 1.6 $m^3 s^{-1}$ and 1.5 - 12 $m^3 s^{-1}$ respectively. The data were measured for five sub-reaches F1 to F5 of distinct bed character. The average values and the range for Trout Beck site are n = 0.08 (range 0.041- 0.273) and f = 1.11 (0.16 – 10.1). The highest value in the range corresponds to low flow while the lowest value to high flow. The observed n and f values vary slightly between the sites but are within the expected range and are comparable with the values from similar sized steep-gradient coarse-bed rivers. The minimum value of n is observed in the bare rock sub-reach (average 0.061) while the maximum value is in the boulder-riffle sub-reach (0.124 average). These average values of n are higher than the values suggested by Chow (1959) for mountainous streams with cobbles and boulders (0.05). Lee and Ferguson (2002) found a very high value of n up to 8 in a steep channel with step-pool morphology and Heritage *et al.* (2004) found a f value of up to 3,733 but both these values appear to have observed at very low flow of <0.020 $m^3 s^{-1}$. In Trout Beck the n and f vary with the depth of the flow but not as much as some other researchers found, e.g. Reid and Hickin (2008) found small boulder-bed streams where the value of f varies over 6 orders of magnitude. In Trout Beck reaches from low to high flow range n varies from 3 to 5 times and f from 10 to 36 times.

The alluvial and semi-alluvial sites all show similar trends of n and f decreasing as Q increasing, but the bare rock has a different trend: n and f decrease to a minimum and then increase. Flow resistance in each sub-reach is reasonably described by a power function ($n = tQ^y$ and $f = hQ^p$) though a single power law does not give a good fit over the full range of discharge, therefore separate equations are fitted for low Q and high Q. The coefficients and exponents in n-Q and f-Q plots vary for each site and between the two flow ranges, but mostly are similar for alluvial and semi-alluvial sites. Though the n and f have very similar trends with discharge the coefficients y and p of their power functions are notably different (Table 4.13). The average value of n-Q exponent (y) for all sites except F2 is -0.28, the values for low and high flow ranges are -0.41 and -0.15 respectively. Similar to other sub-reaches, F2 has a negative y for low flow (-0.35) but positive (0.19) for high flow. This is possibly because of higher resistance from the

hydraulically rough rock walls. The exponents are comparable with many gravel-bed sites from the literature.

The relation of $(8/f)^{1/2}$ $(= V/u^*)$ with relative depth R/D_{84} is plotted and the Manning-Strickler, Keulegan, Bathurst (1985, 2002) and Ferguson (2007a) VPE equations are tested against Trout Beck data. The Manning-Strickler equation appears to be unsuitable for Trout Beck data, but Keulegan-type logarithmic curves and Ferguson's VPE appear to describe the site data reasonably well. The best fit value of k_s/D_{84} in Keulegan equation varies from 2.5 to 9, which is higher than the generally considered 2 to 4 range (Bray, 1979; Hey, 1979; Bathurst, 1985; Ferguson, 2007a; Ferguson, 2013). The 2 to 4 range works well for sub-reaches F4 and F5 but F1 and F3 will be best represented by k_s/D_{84} values 6 and 9 respectively. Ferguson's VPE is particularly useful to predict velocity by a single equation over a wide range of environments (Ferguson, 2007a). This comparison shows that the flow resistance values in Trout Beck alluvial and boulder-riffle sub-reaches (F1 and F3) are higher than predicted by any of the commonly used equations in the literature. However, the equations relating flow resistance to R/D_{84} generally assume that resistance is dominated by grain roughness, but in mountainous streams like Trout Beck the form resistance might be significant (Comiti *et al.*, 2007). Reid and Hickin (2008) found that form roughness is about 90% of the total roughness in the system they studied, therefore is a lot higher than the grain roughness.

The non-dimensional $V^* - q^*$ equation collapses the Trout Beck data from alluvial and semi-alluvial sites except sub-reach F5 which suggests that the D_{84} may not represent the effective roughness of the channel bed in F5. The Trout Beck data also do not collapse onto the trend line proposed by Comiti *et al.* (2007) which is because their equation does not have a slope term. The $V^{**} - q^{**}$ equation suggested by Rickenmann and Recking (2011) does not properly collapse Trout Beck data. Sub-reach F5 plots slightly higher than RR trend line, F4 and F1 are little lower, and F3 is right at the lower edge of their data envelope suggesting that Trout Beck sub-reaches except F5 have more resistance than D_{84} would suggest. The value of effective roughness height (k_s) for each sub-reach which collapses $V^{**} - q^{**}$ data into RR trend are calculated which also shows that the Trout Beck sub-reaches except F5 have more resistance than the measured D_{84} would give.

4.5 Total shear stress

The water flowing in a channel exerts a shear stress (τ) on the channel boundary, the magnitude of which is a function of energy slope and water depth (Eq. 1.20). The shear stress applies tangentially to the sediment surface and is fundamentally important to sediment transport process and a critical control on sediment entrainment. This section discusses how the shear stress varies with the discharge and also how it varies between sub-reaches.

Estimation of total shear stress τ (= ρgRS) for a reach or sub-reach requires mean hydraulic radius R and energy slope S. For each of the five sub-reaches τ is calculated for field measured low Q as well as estimated high Q (Sections 4.2.2 and 4.2.3). The range of τ values for each sub-reach is summarised in three discharge ranges (< 3 m^3 s^{-1}, 3 – 6 m^3 s^{-1} and 6 – 12 m^3 s^{-1}) in Table 4.14. (refer to Tables 4.11 and 4.12 for detailed data).

Table 4.14. Range of shear stress (τ) for the sub-reaches for range of discharges.

Sub-reach	Channel description	τ, N m^{-2}		
		Q range: < 3 m^3 s^{-1}	3 – 6 m^3 s^{-1}	6 – 12 m^3 s^{-1}
F1	Alluvial	15 – 37	37 – 50	50 – 69
F2	Bedrock	24 – 82	82 – 130	130 – 194
F3	Boulder-riffle	28 – 90	90 – 114	114 – 140
F4	Semi-alluvial (70% cover)	13 – 38	38 – 58	58 – 93
F5	Semi-alluvial (20% cover)	17– 57	57 –78	78 –110

Table 4.14 shows that for low to moderate discharges (< 3 m^3 s^{-1}), the highest shear stresses are in F2 and F3, whereas the lowest are in F1 and F4. At moderate flood discharges (3 – 6 m^3 s^{-1}) when sediment transport is expected to occur, the highest shear stresses are again in F2 and F3 and the lowest in F1 and F4. At very high discharges (> 6 m^3 s^{-1}), the maximum shear stresses are in F2 and then in F3, and the lowest are again in F1 and F4. This shows that throughout the discharge range, the bare rock and boulder-riffle sub-reaches have high shear stresses; the sub-reaches with higher sediment cover (F1 and F4) have low shear stresses while the semi-alluvial sub-reach with very low sediment cover (F5) has intermediate shear stresses.

Figure 4.32 plots shear stress against discharge for each sub-reach. As found for hydraulic geometry and flow resistance (Sections 4.3 and 4.4), a single power law is a

poor fit to most sub-reaches so separate low-*Q* and high-*Q* power laws are fitted; the *τ*-*Q* equations are shown in the plot.

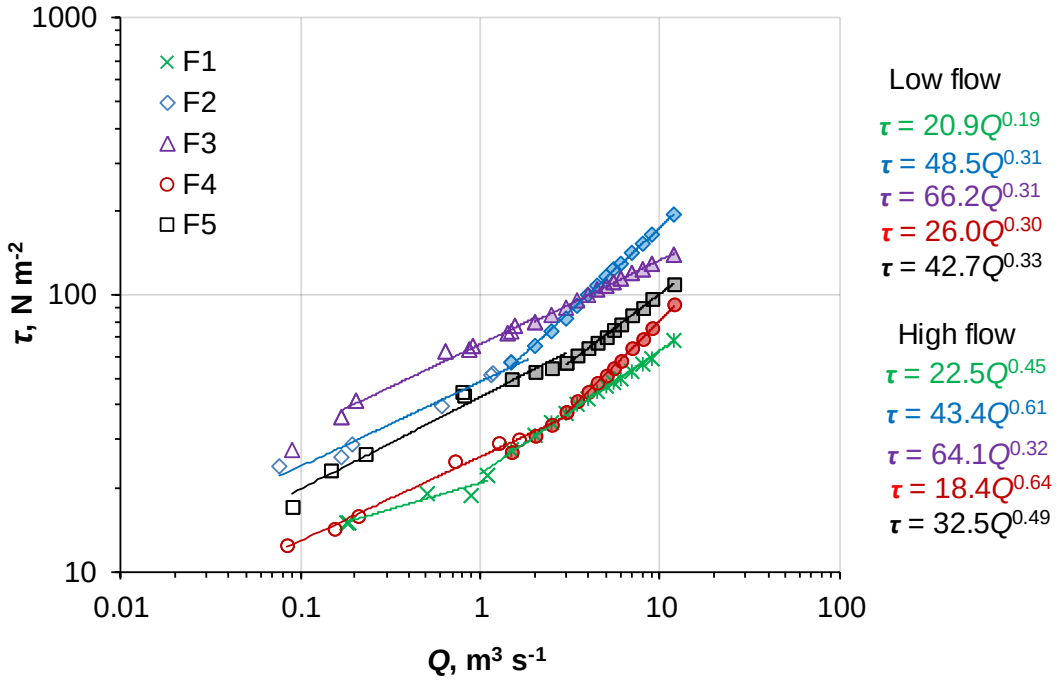

Figure 4.32. Relationship of average shear stress (*τ)* with discharge (*Q)* for each sub-reach: F1 (alluvial) green, F2 (bare rock) blue, F3 (boulder-riffle) purple, F4 (semi-alluvial 70% cover) red, and F5 (semi-alluvial 20% cover) black. Two power law equations (for low *Q* and high *Q*) for each sub-reach are shown. The open markers are the measured data and filled markers are the estimated data. All fitted power-law exponents are significantly different from zero at $p < 0.001$.

The positive exponent in the *τ*-*Q* relation indicates that shear stress increases with discharge, as expected since *S* varies little with *Q* (Figure 4.20) but *R* must increase with *Q*. If *S* is exactly constant, the *τ*-*Q* exponent will be the same as that of *R*-*Q* (~ *d*-*Q)*. For example, in the bare rock sub-reach F2 the *S*-*Q* exponent (Figure 4.20b) is very small (0.09) but the *τ*-*Q* exponent at deep flow is high (0.61) and very similar to the *d*-*Q* exponent (0.60) (Figure 4.23b). Figure 4.32 shows that the boulder-riffle sub-reach F3 experiences the highest shear stress up to 4 $m^3 s^{-1}$ but F2 overtakes it at the highest discharges, while F1 and F4 have the lowest shear stress throughout the discharge range. For bare rock and semi-alluvial sub-reaches the *τ*-*Q* exponents at low flow are very similar ranging from 0.30 to 0.33, but the exponent for the alluvial sub-reach F1 is lower (0.19). However, at higher discharges, F2 and F4 have the highest exponents (0.61 and 0.64), F3 has the lowest (0.32), and F1 and F5 have intermediate values (0.45 and 0.49). Almost the same exponent for low and high *Q* for F3 (0.31 to 0.32) indicates that the shear stress is steadily increasing at almost the same rate over the range of flows, while F2 and F4 have a slow increase at low discharge but a rapid increase at high discharge. The shear stress in the pool (backwater zone of boulder-riffle) is not

calculated in detail but the water surface slope here is only about one third as steep as either F2 or F3, and the depth is only slightly greater than in F2 and smaller than in F3, so the shear stress in the pool is much lower than in F2 and F3.

The mean total shear stress has also been estimated for the slightly longer sub-reaches (between successive pressure transducers located either side of the short sub-reach), for the peak discharges between each successive tracer survey (Table 5.1). These estimates are plotted in Figure 4.33, and summarised in Table 4.15.

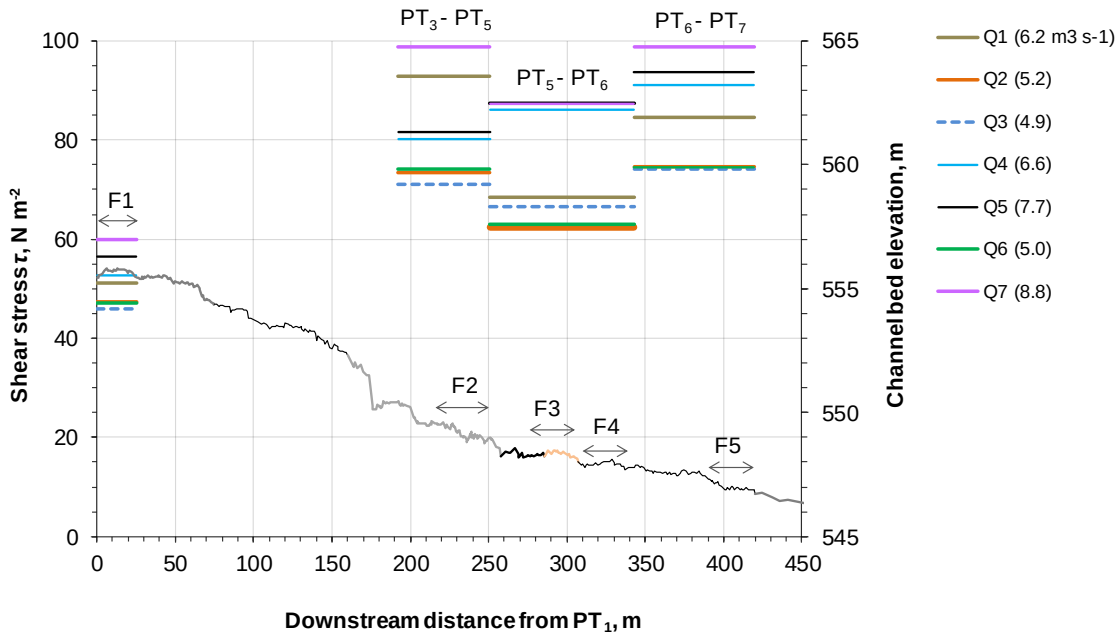

Figure 4.33. The primary y-axis shows the shear stress (τ) values that are plotted for sub-reaches for different peak discharge during the successive survey periods, shown by different colours. For example, Q_4 (6.6) indicates that the peak flow was 6.6 m^3 s^{-1} between the 3rd and 4th survey. The secondary y-axis shows the longitudinal profile starting at PT_1 (0 m) and ending at PT_7 (420 m), F1 to F5 are marked.

Table 4.15. Maximum shear stresses in F1 and longer sub-reaches PT_3 – PT_5 (length 59 m), PT_5 –PT_6 (92 m), and PT_6 – PT_7 (77 m) for the period between successive tracer surveys. Q_1 to Q_7 respectively represent the peak discharges during the first to seventh survey periods.

Sub-reach	Channel description	Maximum τ between two tracer surveys (N m^{-2})						
		Q_1 (6.2 m^3 s^{-1})	Q_2 (5.2)	Q_3 (4.9)	Q_4 (6.6)	Q_5 (7.7)	Q_6 (5.0)	Q_7 (8.8)
F1	Alluvial	51	47	46	53	56	47	60
PT_3 - PT_5	Bedrock	93	73	71	80	82	74	99
PT_5 - PT_6	Semi-alluvial (pool/boulders/gravels~ 55% cover)	69	63	67	86	87	63	87
PT_6 - PT_7	Semi-alluvial (35% cover)	84	75	74	91	94	74	99

The longer sub-reach shear stresses are calculated using the hydraulic radius based on the two cross sections at the respective PTs and the quasi-continuous stage data recorded by PTs. Because of the complex bed topography the hydraulic radius based on two cross-sections for PT_1 to PT_2 section is not accurate; therefore the stress for this longer sub-reach is not calculated. Instead, F1 shear stresses based on the τ-Q power-law relation (Figure 4.32) are shown. Similarly, the shear stress between $PT_2 – PT_3$ is not calculated as there is a knickpoint in between which distorts the energy slope for the upstream and downstream reaches. Figure 4.33 shows how the shear stresses vary between the sub-reaches at the same and different discharges. For the highest flood during the seventh survey-period ($Q_7 = 8.8$ m^3 s^{-1}) both the bare rock sub-reach $PT_3 – PT_5$ and the lower semi-alluvial sub-reach $PT_6 – PT_7$ have the maximum shear stress (99 N m^{-2}), whereas during the same period the upper alluvial sub-reach F1 experiences the minimum shear stress (60 N m^{-2}). Similarly for the lowest peak flood (4.9 m^3 s^{-1}), again $PT_3 – PT_5$ and $PT_6 – PT_7$ have the highest shear stresses (71 and 74 N m^{-2}) and F1 has the lowest shear stress (46 N m^{-2}).

In summary, at low to moderate flows (< 4 m^3 s^{-1}) the highest shear stress is found in the boulder-riffle sub-reach (F3) but at higher discharges the highest shear stress is in the bare rock sub-reach (F2). The lowest shear stresses throughout the flow range are observed in the alluvial sub-reach F1. The shear stresses in short sub-reaches generally tie in with those from the longer sub-reaches. However, though F3 has the highest shear stresses at low to moderate discharge, the longer sub-reach $PT_5 – PT_6$ (mainly alluvial, past F3 and F4) has intermediate shear stresses up to 6.2 m^3 s^{-1}; this is probably because of the effect of the backwater/pool area (~25 m long, upstream of F3) which has lower slope and lower velocity than in the F3 area. However, in high flow conditions the shear stresses for both F3 and $PT_5 – PT_6$ are high. Similarly, the high shear stresses in F2 and F5 agree with high shear stresses in $PT_3 – PT_5$ and $PT_6 – PT_7$ (mainly bedrock, past F5).

4.6 Effective shear stress

The total shear stress values for sub-reaches (Figure 4.32) show that the boulder-riffle sub-reach (F3) has the highest or second-highest shear stress at all discharges. However, it also has the highest flow resistance as measured by f or n (Figure 4.26), presumably because of the form drag exerted by the numerous boulders. This implies that F3 has a lower effective stress (total shear stress τ minus form drag) (Section 1.1.6) available for sediment transport than its total stress would suggest. Moreover, as discussed in section 4.5, while the short boulder sub-reach (F3) has a high total shear stress, the longer sub-

reach $PT_5 - PT_6$ (Pool-F3-F4) (Figure 4.33) has a lower total shear stress because of the inclusion of the low-gradient pool area upstream of the boulder riffle. This also shows that the total shear stress is higher in the boulder area than in other parts of the $PT_3 - PT_5$ section. Since both shear stress and flow resistance are high in the boulder-riffle sub-reach it is not clear what the effective stress is there. The tracer-pebble results discussed later (Chapter 5) suggest that the boulder-riffle area appears to be the area with the lowest effective shear stress in the entire study site. Therefore, an attempt was made to partition the total stress in the boulder sub-reach (F3) into stress borne by mobile grains and stress borne by immobile grains. As explained in section 3.1.6, two approaches- Yager *et al.* (2007) and an alternative method using basic physics are adopted for this study.

4.6.1 Yager *et al.* (2007) stress-partitioning equations

A total of 103 grains with longest visible axis greater than 256 mm (Section 2.4.3) were mapped in the boulder-riffle sub-reach (F3) using dGPS. According to the standard definition of boulders (*b*-axis > 256 mm) there were only 54 boulders in sub-reach F3, but for this analysis all surveyed 103 grains are assumed to be immobile at moderate to high flows and are also termed as 'boulders' for this analysis. The protrusion height for each boulder was also recorded. Figure 4.34 shows the boulders in the study area during this survey and Figure 4.35 shows the surveyed boulders in the DEM.

Figure 4.34. Photograph looking downstream on the day of the boulder survey (17.09.14) showing the boulders in the lower semi-alluvial reach. The boulder-riffle sub-reach (F3) for which the stress-partitioning equations were tested is circled.

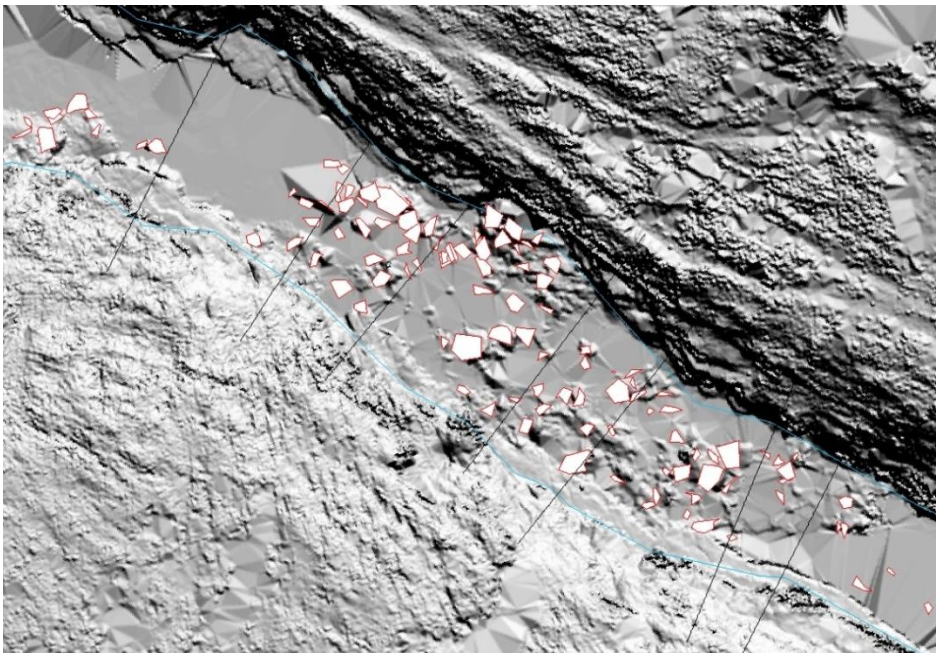

Figure 4.35. A DEM showing the mapped boulders in the boulder-riffle sub-reach F3. The black lines indicate the intermediate cross-sections used in the hydraulic calculations.

A total of eight variables and parameters have to be specified to solve the equations: average channel width (w), energy slope (S), unit discharge (q), diameter of immobile grain (D), protrusion (p) or average top height of mobile sediment above the base of the immobile grains Z_m (= D-p), spacing of the immobile boulders (λ), drag coefficient for mobile sediment (C_m) and drag coefficient for the immobile grains (C_I). The basic equation used in the study is Eq. 3.8 ($\tau_t A_t = \tau_I A_{IP} + \tau_m A_m$, where τ_t, τ_I ,τ_m are respectively the total boundary stress, stress on large immobile grains and stress on mobile bed; and A_t , A_{IP} and A_{m} are the plan areas occupied by total bed, immobile boulders and mobile grains respectively. There are several equations which are used in the calculation (Equation 1 to 13 in Yager *et al*. (2007)) and all of them are not reproduced here. The required parameters were obtained from cross-sections and boulder surveys, flow and water profile measurements and the stage-discharge rating curve. The measured or calculated values of the input parameters are given below, with a brief note of how they were calculated.

1) w = 5.2 m (calculated from DEM).
2) S = 0.018 – 0.020 (calculated from measured water profiles).
3) q = 0.02 – 1.54 $m^2 s^{-1}$ (= Q/w, where Q is the measured and extended discharge ranging from 0.1 – 8 $m^3 s^{-1}$).
4) D = 0.33 m (average b-axis value of 103 immobile grains in sub-reach F3).

5) Z_m = 0.10 m (calculated as boulder diameter minus protrusion = D-p. The protrusion p (= 0.23 m) above the mobile bed was estimated at site and later checked using dGPS data).
6) λ = 1 m (the distance between each successive boulder was calculated and then averaged. This was also calculated by calculating the bed area for one boulder, the square root of which would be an approximate spacing λ= 1.1 m. A sensitivity check is carried out which shows the result with λ = 1 m is close to λ = 1.1 m).
7) C_m = 0.047 (as used by Yager *et al*. (2007)) or 0.44 m as used by Yager et al (2012).
8) C_I = values vary according to flow depth and C_m value (C_I is calibrated by matching the calculated U with observed U; where $U = q.w/(2V_w/\sqrt{3}\lambda)$, q = sqrt[$(8gSV_w^3)/(3\lambda^2 w^2(A_{IF}\,C_I + A_m\,C_m)$], the total water volume $V_w = w\sqrt{3}\lambda h/2 - V_I$; V_I is the total volume of immobile grains, A_{IF} the bed perpendicular area of immobile grains, and h is the flow depth between immobile grains. (Yager *et al.*, 2007).

The flow depth between immobile grains h (or average flow depth h_a) is needed to calibrate C_I and C_m for a particular site. In a personal communication, Yager confirmed that h is more relevant for flume experiments but for natural rivers h can be assumed to be equal to h_a, therefore this study uses $h = h_a$. Drag coefficients C_I and C_m are calibrated comparing the measured and calculated U, which gives slightly better results than calibrating with q. As both these drag coefficients vary with the flow and both are unknowns, C_m is kept constant to calibrate C_I as it is less sensitive to the discharge than C_I. The value of C_m was initially set at 0.047 as used by Yager *et al.* (2007) but in a later study of the Erlenbach step-pool channel (Switzerland), Yager *et al.* (2012) found a much higher value of C_m (0.44 ± 0.09). The calibrated value for C_I (using C_m = 0.047) is shown in Figure 4.36, with best-fit equation $C_I = 23.4(h_a/p)^{-2.41}$. The C_I is also calculated using C_m = 0.44 which gives a best-fit equation $C_I = 18.5(h_a/p)^{-2.44}$ which is significantly different from $C_I = 157(h_a/p_u)^{-1.6}$ found by Yager *et al.* (2012) with C_m = 0.44. Using the chosen C_m and calibrated C_I the shear stress on mobile grains τ_m (= $\rho C_m U^2/2$) is calculated. The total shear stress τ_t (= $\rho g h_a S$) and portion of shear stress that is available for mobile sediments τ_m are plotted in Figure 4.37 which shows that τ_m increases with the increasing depth. Curves of τ_m are plotted for a range of C_m values to investigate the sensitivity of τ_m to C_m.

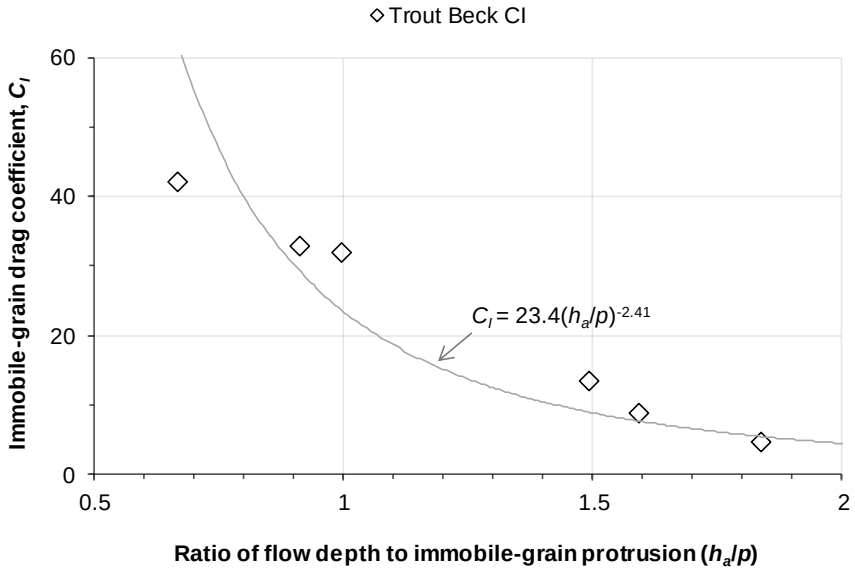

Figure 4.36. The C_I values and the best-fit equation as obtained by fitting measured and calculated velocities (using $C_m = 0.047$).

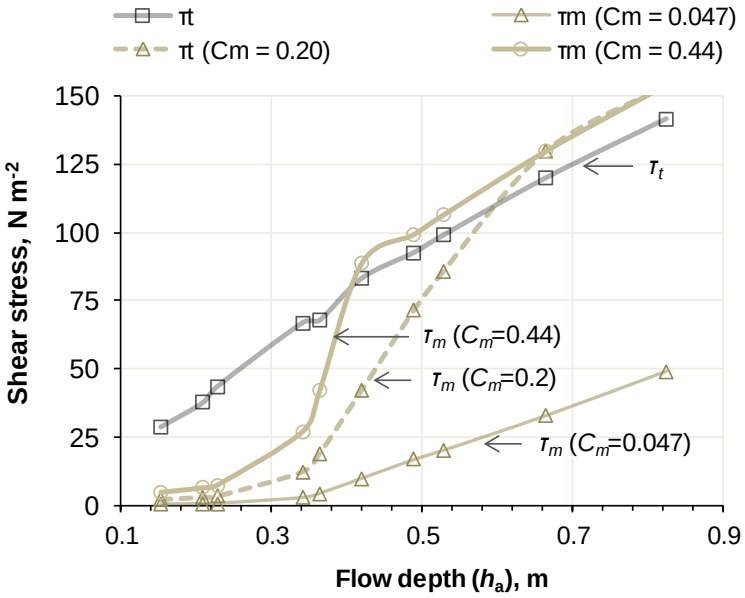

Figure 4.37. The relationships of shear stresses τ_t and τ_m with water depth h_a for boulder-riffle sub-reach F3 for three values of C_m: 0.047 as used by Yager et al (2007) by flume experiment, 0.2 as an intermediate value to compare the result with the other two values, and 0.44 as derived by Yager et al (2012) by field experiment in Erlenbach.

The value of τ_m depends on the velocity U and C_m, therefore an appropriate value of C_m would need to be used to get meaningful value of τ_m. Figure 4.37 shows τ_m is very sensitive to the C_m value but no guidelines have been provided to determine the value of C_m. The results based on $C_m = 0.047$ are presented in Table 4.16. The data show that the ratio τ_m/τ_t increases with the increasing discharge, but these ratios appear to be low, for example even at the high discharge of 8 m^3 s^{-1} (~bankfull discharge) only 35% of the total stress is available for mobile sediment and the rest for the immobile parts of the

channel. However, at this discharge range it is expected that a higher percentage of the total shear stress is available for sediment transport. An increase in τ_m/τ_t implies a decrease in τ_I/τ_t which means the relative magnitude of form drag decreases with the depth. This contradicts Andrews (2000) who found the relative magnitude of form drag increases with the discharge and the form drag at bankfull discharge reduces the stress on the bed surface by ~40%. But as stated above, all these results are very sensitive to the C_m value chosen.

Table 4.16. Summary of stress partitioning results using Yager *et al.*(2007) equations with C_m = 0.047. Discharge Q is in $m^3\ s^{-1}$ and shear stresses are in $N\ m^{-2}$. The low-Q data (0.09 – 1.58 $m^3\ s^{-1}$) were field-measured; high-Q data (2.5 – 8 $m^3\ s^{-1}$) were estimated.

Parameters	Values									
Q	0.09	0.17	0.21	0.65	0.88	1.58	2.5	3.0	5.0	8.0
h_a	0.15	0.21	0.23	0.34	0.36	0.42	0.49	0.53	0.66	0.83
C_I	42.0	32.8	32.0	13.5	8.7	4.6	2.8	2.5	1.7	1.2
$\tau_m = \rho C_m U^2/2$	0.5	0.7	0.8	2.9	4.5	10	17	20	33	49
$\tau_t = \rho g h_a S$	29	38	44	67	68	83	93	99	120	142
τ_m/τ_t	0.02	0.02	0.02	0.04	0.07	0.12	0.18	0.20	0.27	0.35
$\tau_t = (\tau_I A_{IP} + \tau_m A_m)/A_t$	26	35	40	64	65	80	89	96	117	139
$\tau_I = (\tau_t A_t - \tau_m A_m)/A_{IP}$	288	377	437	655	650	757	789	824	920	992
$\tau_I = \rho A_{IF} C_I U^2/2A_{IP}$	262	347	404	622	618	723	757	792	889	963

Table 4.16 shows that the calculated values of shear stress on immobile grains (τ_I) using either of the two available equations [$\tau_I = (\tau_t A_t - \tau_m A_m)/A_{IP}$, or $\rho A_{IF} C_I U^2/2A_{IP}$] are exceptionally high, much higher than the total shear stress (τ_t). However, τ_t based on these high values of τ_I seems about right as the values are close to $\rho g h_a S$. This is perhaps because this analysis uses the force balance principle where $\tau_t A_t = \tau_b A_b + \tau_m A_m$ (Eq. 4.2) but not the stress balance ($\tau_t \neq \tau_b + \tau_m$) unless $A_m = A_b = A_t$, which is not the case here. Therefore it is possible τ_I can be higher than τ_t. However, the power-law equation for drag coefficient (C_I) calibrated for Trout Beck is significantly different from that for the Erlenbach (Yager *et al.*, 2012), so whether this approach can be applicable at Trout Beck is not known. Perhaps this approach is also not appropriate for Trout Beck as the boulders there are not in isolated staggered patterns. As stated above, the C_m values used in Yager *et al.* (2007) and Yager *et al.* (2012) are significantly different, perhaps because of the steps and the resulting hydraulics in steps and pools in Erlenbach whereas the 2007 study was based on flume experiments with a regular staggered array of identical 'boulders'. This analysis shows that a small change in the value of C_m

(Figure 4.37) will affect the value of C_I and hence the τ_m, but it is not known what will be the appropriate value of C_m for Trout Beck. The 2012 equations (Yager *et al.*, 2012) are not attempted here as the site does not have steps and also there are no reliable benchmarks to check the C_I and C_m, as a small change on these values will affect the results significantly. Therefore an alternative approach has been developed to split the shear stress between mobile grains and boulders as discussed below.

4.6.2 Alternative approach for the boulder sub-reach in Trout Beck

Since τ_m is very sensitive to small changes in C_m, whose value is unknown, and also the calibrated value of C_I is very different from the value suggested by Yager *et al.* (2012), an alternative way for randomly-distributed boulders rather than staggered boulders or steps is considered. A simple equation is developed as briefly described below.

The total stress $\tau_t = \rho gRS$ is partitioned between the stress on the immobile grains or boulders (τ_b) and mobile grains (τ_m) assuming the stress on the walls is negligible as discussed earlier. The force balance equation $F_t = F_b + F_m$ (Eq. 3.7) can be written as

$$\tau_t = \frac{\tau_b A_b + \tau_m A_m}{A_t} \qquad \text{Eq. 4.2}$$

where A_b and A_m are the bed areas occupied by boulders and mobile grains in a reach of total bed area A_t. The drag force on immobile boulders is

$$\tau_b A_b = \frac{1}{2}\rho V^2 C_d \Sigma X_b \qquad \text{Eq. 4.3}$$

where V is mean velocity, C_d is the average drag coefficient for a boulder, X_b is the flow-facing cross-section area of each boulder and Σ is the sum over all boulders. Combining equations 4.2 and 4.3 gives

$$\tau_t = \frac{0.5\rho V^2 C_d \sum X_b + \tau_m A_m}{A_t} \qquad \text{Eq. 4.4}$$

Here the one remaining unknown is C_d, and τ_m depends on it plus the various knowns. Eq. 4.4 can be rearranged and written for $\frac{\tau_m}{\tau_t}$ as

$$\tau_m = \frac{\tau_t A_t - 0.5\rho V^2 C_d \sum X_b}{A_m} = \left(\frac{\tau_t A_t}{A_m} - \frac{0.5\rho V^2 C_d \sum X_b}{A_m}\right) = \frac{\tau_t A_t}{A_m}\left(1 - \frac{0.5\rho V^2 C_d \sum X_b}{\tau_t A_t}\right)$$

$$\text{Or, } \frac{\tau_m}{\tau_t} = \left(1 - \frac{0.5\rho V^2 C_d \sum X_b}{\tau_t A_t}\right)\frac{A_t}{A_m} \qquad \text{Eq. 4.5}$$

From the low Q field-measured and extended high Q data the input parameters (hydraulic radius, slope, average velocity, and total shear stress) are calculated. The boulder survey provides the basis for calculating A_m (*i.e.* $A_t - A_b$). The flow-facing cross-sectional area of the boulder (X_b) is approximated by multiplying boulder face-width by water depth (or protrusion above the bed if the water depth is higher than the height of the boulder). The total stress on mobile grains (τ_m) can be calculated by using Eq. (4.5) and the stress on immobile boulders (τ_b) can be calculated by putting the value of τ_m in Equation (4.2) or directly by using

$$\tau_b = \frac{\Sigma F_b}{\Sigma A_b} = \frac{1}{2}\rho V^2 C_d \frac{(X_{b1}+X_{b2}+X_{b3}+\cdots)}{(A_{b1}+A_{b2}+A_{b3}+\cdots)} \qquad \text{Eq. 4.6}$$

By choosing a value for C_d, the value of τ_b is calculated and then τ_m is calculated by using Eq. 4.2. From the boulder survey and DEM A_t, A_b, A_m are found to be 127, 14 and 113 m^2 respectively. The discharge range considered for this analysis is from 0.09 to 8 $m^3\ s^{-1}$ (mean depth = 0.15 to 0.83 m). The total boulder facing area (ΣX_b) increases with stage up to 2.5 $m^3\ s^{-1}$ discharge (mean depth = 0.49) and then remains constant at 10.7 m^2 (Table 4.17). The shear stresses τ_m and τ_b are plotted in Figure 4.38 for different of drag coefficients (C_d) varying from 0.3 to 1. The stress on mobile grains τ_m shown by dotted lines is slightly higher than the mean total stress τ_t at low depth but it starts decreasing as the water depth increases.

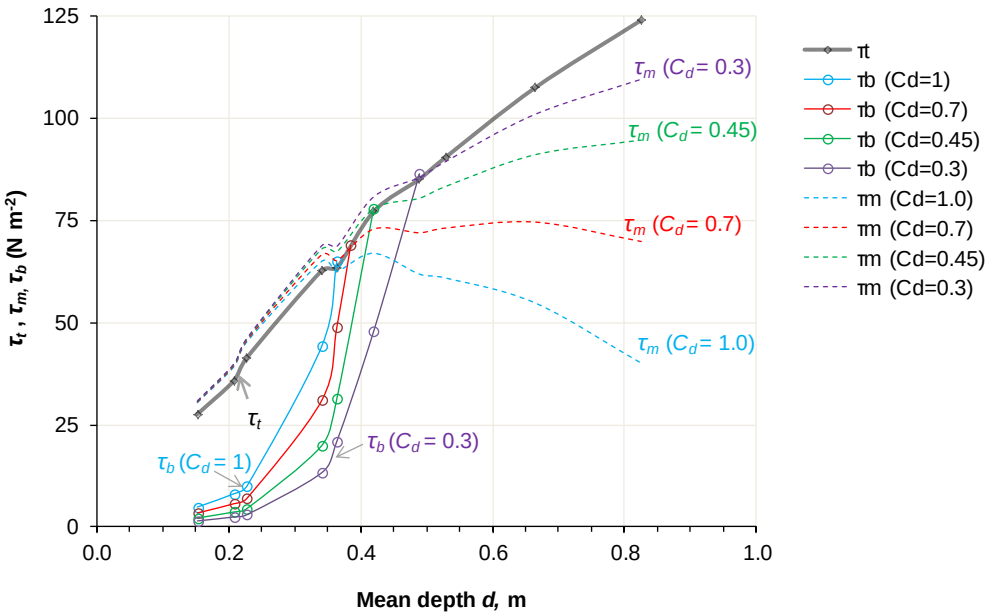

Figure 4.38. The shear stress (τ_t, τ_m, and τ_b) versus mean depth (d). The thick black line is the total stress (τ_t), other solid lines are the stresses on boulders (τ_b) and dashed lines are the stresses available for mobile sediment (τ_m). The blue, red, green and purple lines are the stresses for drag coefficient C_d = 0.3, 0.45, 0.7 and 1.

The plot shows that, if $C_d = 1$ (as for vertical-axis cylinders), then the shear stress on a representative boulder (τ_b) increases rapidly with stage and starts to exceed the mean total shear stress τ_t at a water depth of 0.36 m ($Q \sim 0.88$ m^3 s^{-1}). Also up to this stage ($d = 0.36$ m) τ_m slightly exceeds the total stress τ_t but for $d > 0.36$m τ_m decreases with the increase in d. As in the previous analysis using Yager *et al*. (2007) equations, τ_b here is also even higher than τ_t at high flow. Moreover, it's not possible to assign a single value of C_d over the range of Q as it varies with the Froude number (Fr) and the relative submergence as shown in Figure 4.39 which suggests the C_d varies if $R/D < 4$ and Fr <1.5 (Powell, 2014).

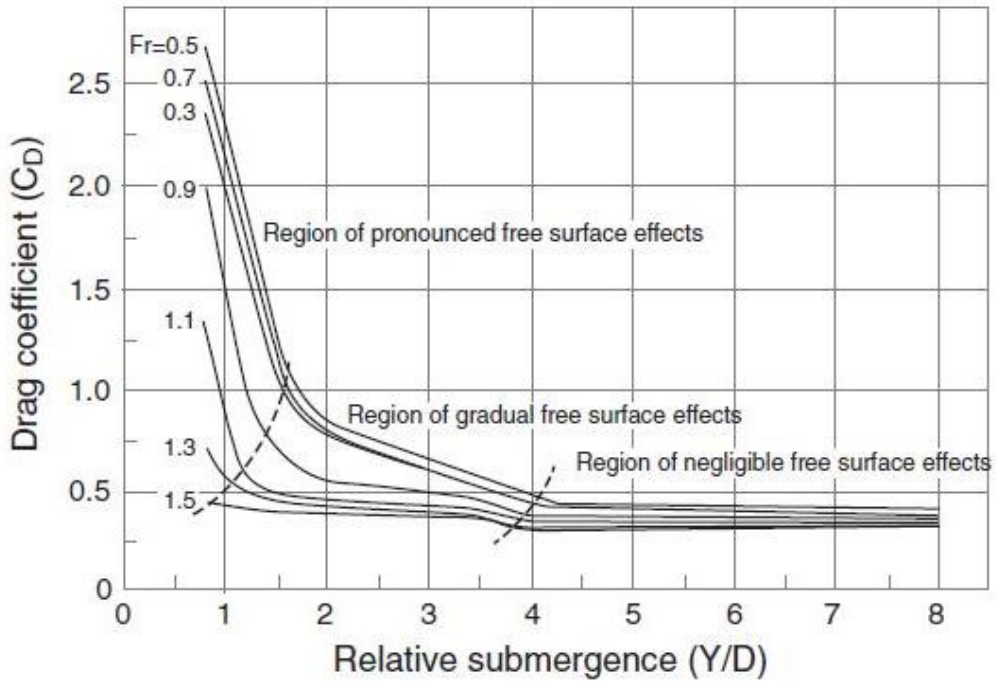

Figure 4.39. Variation of drag coefficient of 6.35 mm diameter hemisphere on smooth surface with Froude number (*Fr*) and relative submergence (*Y*/*D*) showing regions of pronounced, gradual and negligible free surface effects. For *Y*/*D* > 4 and *Fr* >1.5, the drag coefficient is largely independent of *Fr* and *Y*/*D*. For *Y*/*D* <4 and constant F_r, the drag coefficient increases whilst at constant *Y*/*D*, the drag coefficient decreases as *Fr* increases except at low *Fr*. From Powell (2014), but originally from Flammer *et al.* (1970).

The values of F_r and R/D_{84} for the boulder-riffle site vary from 0.12 to 0.51 and 0.80 to 3.8 respectively as Q increases from 0.09 to 8.0 m^3 s^{-1} (Table 4.17). Based on these Froude numbers and submergence ratios the drag coefficient is estimated from Figure 4.39, and then the resulting shear stresses τ_m and τ_b are calculated using Equations 4.2 and 4.6. The results of this calculation are shown in Figure 4.40. The input parameters and the result including the value of C_d are summarised in Table 4.17 which also includes the values of downstream component of total water shear force (F_t), force applied on mobile bed (F_m) and force applied on immobile boulders (F_b). Figure 4.38 is

different from Figure 4.40 in that in the former a constant drag coefficient is used for the entire range of flows whilst the latter uses the varying values of C_d according to Fr and R/D_{84}.

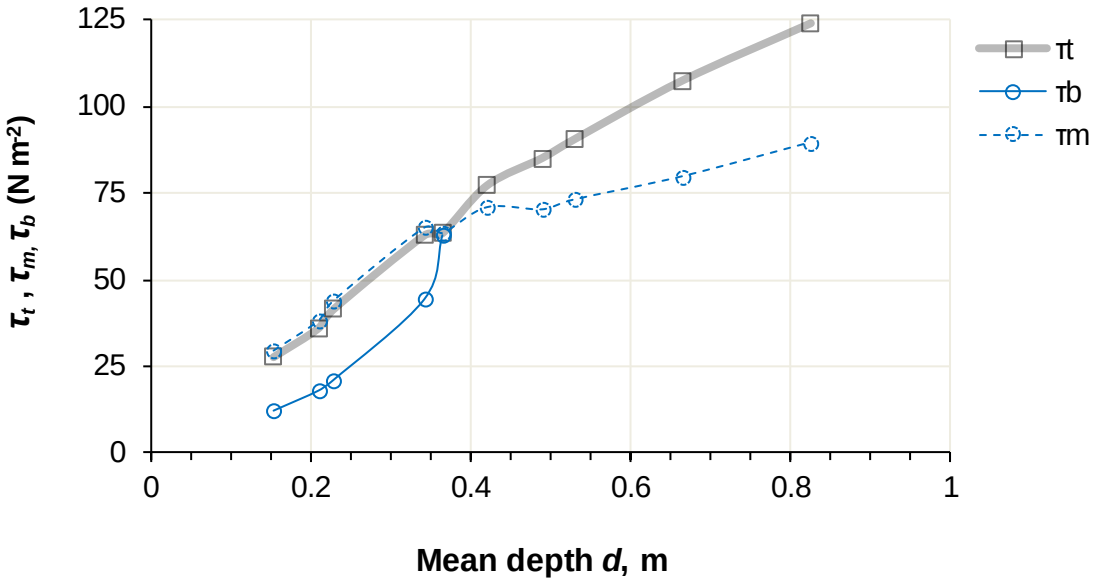

Figure 4.40. Stress partitioning using alternative method: τ_t, τ_b and τ_m versus water depth using the stage-dependent C_d values in Table 4.17.

Table 4.17. The input parameters and results of stress-partitioning using the alternative method – *Q:* discharge, *V:* mean velocity, *d:* mean depth, R/D_{84}: relative submergence, F_r : Froude number, C_d : drag coefficient, $\sum X_b$*:* sum *of* flow facing area of boulders, τ_m : stress available for mobile grains, τ_t: total shear stress, τ_b : stress on boulders, F_t: downstream component of total water force, F_b: downward force applied on boulders, and F_m: downward force applied on mobile grains.

Descriptions	Values									
Q (m^3 s^{-1})	0.09	0.17	0.21	0.65	0.88	1.58	2.5	3	5	8
V (m s^{-1})	0.15	0.17	0.18	0.35	0.44	0.65	0.84	0.93	1.18	1.45
d, m	0.15	0.21	0.23	0.34	0.36	0.42	0.49	0.53	0.66	0.83
R/D_{84}	0.8	1.0	1.1	1.7	1.8	2.1	2.4	2.5	3.1	3.8
Fr	0.12	0.12	0.12	0.19	0.23	0.32	0.39	0.41	0.46	0.51
C_d	2.50	2.20	2.10	1.00	0.90	0.80	0.75	0.70	0.62	0.50
$\sum X_b$, (m^2)	6.2	7.8	8.2	10.0	10.2	10.6	10.7	10.7	10.7	10.7
τ_b (N m^{-2})	12	18	21	44	63	128	205	231	331	402
τ_m (N m^{-2})	30	38	44	65	64	71	70	73	80	90
τ_t (N m^{-2})	28	36	42	63	63	77	85	91	108	124
τ_m/τ_t	1.07	1.06	1.06	1.04	1.00	0.92	0.83	0.81	0.74	0.72
F_b, kN	0.17	0.25	0.29	0.62	0.88	1.78	2.86	3.22	4.62	5.61
F_m, kN	3.33	4.31	4.97	7.35	7.17	8.02	7.95	8.27	9.03	10.14
F_t, kN	3.50	4.56	5.27	7.97	8.05	9.80	10.81	11.48	13.65	15.75
F_m/F_t	0.95	0.95	0.94	0.92	0.89	0.82	0.73	0.72	0.66	0.64
F_b/F_t	0.05	0.05	0.06	0.08	0.11	0.18	0.27	0.28	0.34	0.36

The downward water shear forces F_t, F_b and F_m are also plotted against the mean flow depth in Figure 4.41 and the result also confirm the force balance equation $F_t = F_m + F_b$ (Eq. 3.7). For example at mean depth d = 0.83 m (Q = 8 m^3 s^{-1}), out of 15.75 kN total force 5.61 kN is applied on immobile boulders and the remaining 10.14 kN is available for sediment transport. The ratio F_m/F_t decreases as the depth increases (Table 4.17), but the F_b/F_t ratio increases with the discharge which implies that the relative magnitude of form drag increases with increasing discharge as found by Andrews (2000).

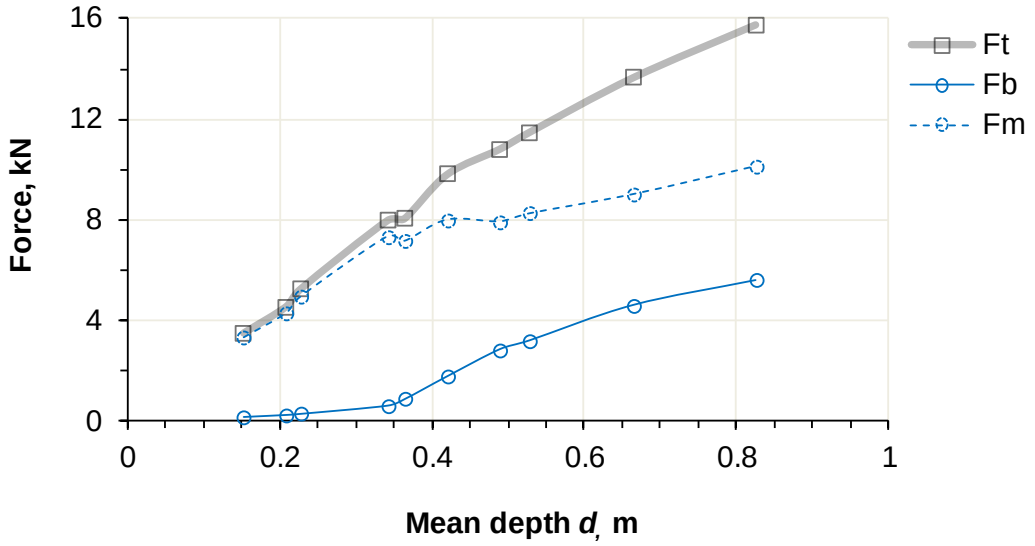

Figure 4.41. Shear forces (F_t, F_b and F_m) versus water depth, where F_t = downstream component of total water force, F_b = downward force applied on boulders, and F_m = downward force applied on mobile grains.

Figure 4.41 and Table 4.17 show that at low submergence up to d = 0.36 m (Q = 0.88 m^3 s^{-1}) almost all the driving force is available for mobile sediment and little is taken by boulders. This is possibly because at low flow the frontal area is small and also the pressure difference upstream and downstream of the boulder to provide form drag is very small. Moreover, the boulder-covered area is only 11 % of the total bed area therefore the force on boulder is negligible compared to the total force at shallow depth, but as the depth increases the form drag also increases. Also all grains smaller than the surveyed grains (*i.e.* *a*-axis <256 mm) are treated as mobile but at low discharge many would actually be immobile and provide additional form drag, as would the rough walls which are not included in F_b. Therefore the total available force for sediment transport could be less than the values obtained for F_b.

The conclusion is that boulder stress partitioning using the method of Yager *et al.* (2007) does not work well in Trout Beck. One possible error in the calculation could be because a proportion p ($0 < p < 1$) of the total facing area should be excluded from the calculation as being in the low-velocity wake zone of other boulders, or equivalently that the effective V^2 approaching a boulder is only p times the reach-average V^2 for the same reason. But it is not obvious how to assign a value to p, and the results of any adjusted calculation depend on this parameter.

4.7 Chapter summary

Bulk hydraulic properties (mean width w, depth d, velocity V, hydraulic radius R, perimeter P, flow resistance n or f and shear stress τ) in each of five sub-reaches of varying bed character (F1 – F5) have been calculated based on the continuity equation, dGPS-measured channel bed and water surface profiles, channel cross-sections, and low to moderate discharge (< 1.6 $m^3 s^{-1}$) measurements by the salt dilution method. For moderate to high discharge conditions (1.5 – 12 $m^3 s^{-1}$) , the rating curves developed for each pressure-transducer, the scaled-down EA discharge data, the field-measured water levels and the dGPS-surveyed channel cross-sections have been used.

At-a-station hydraulic geometry has been examined which can be an effective method to quantify the flow resistance in high-gradient mountain rivers as it describes how the velocity and the depth vary with the discharge in the reach. At each field site, this demonstrates a general trend that the velocity, width and depth increased with the increasing discharge, but with offsets between the reaches. All sub-reaches show a rapid increase in velocity as discharge increases, except at the bare rock site where the rate of increase in velocity becomes slower once the water level rises up the rough walls. The rate of increase in velocity is always higher than that in depth except at higher discharges in the bare rock sub-reach (F2) and one semi-alluvial sub-reach (F5) which has very low sediment cover (20%). A more rapid increase in velocity than in depth implies a rapid decrease in flow resistance with increasing discharge.

For at-a-station hydraulic geometry relations (V-Q, d-Q, w-Q) a single power law over the full range of discharge is not a good fit, therefore two power equations, one for low and another for high discharge, joining at a hinge are fitted for each sub-reach. The hinges are at slightly different Q values for sub-reaches ranging from 1.1 to 3 $m^3 s^{-1}$ (F1 = 1.1 $m^3 s^{-1}$, F2 = 1.5, F3= 2, F4 =3, and F5 = 3 $m^3 s^{-1}$). The grand average value of the V-Q exponent (m = 0.49) d-Q exponent (f = 0.37) and w-Q exponent (b = 0.15) are all

within the range of values previously obtained for steep mountainous streams. However, m = 0.49 is considerably higher than Leopold and Maddock (1953) value of 0.34 for large alluvial rivers, and the b = 0.15 is lower than Comiti *et al*. (2007) value of 0.26 for boulder and step-pool morphology. The high values of m and f in almost-confined channels indicate that the flow resistance declines rapidly with increasing discharge. Going from low to high discharge, the average value of the velocity exponent declines from 0.57 to 0.40, the depth exponent increases from 0.27 to 0.47 and the width exponent decreases slightly from 0.16 to 0.14. This implies that the increased discharge contribute more to increase depth than velocity or width. David *et al.* (2010) found that if $m > f + b$ the grain resistance is likely to be dominant but if $m < f + b$ then the form or spill resistance will dominate. All Trout Beck sites showed $m > f + b$ at low flow and $m < f + b$ at high flow which implies the grain resistance is predominant at shallow depths but form or spill resistance in deep flows. This could mean that at F3 up to 3 $m^3 s^{-1}$ (d = 0.53 m, Table 4.17) (hinge for low and high Q at F3) the form drag is not significant.

Manning's n and Darcy-Weisbach f are calculated for both field-measured low Q and extended high Q data and plotted against discharge. The average values of n and f for Trout Beck are 0.08 and 1.11 respectively, higher than the values recommended by Chow (1959) (0.05) but within the range found elsewhere for shallow and high-gradient mountainous rivers with or without exposed bedrock. However, generally in steep boulder-bed channels, the flow resistance varies rapidly with the depth of the flow, more than in larger and lower gradient alluvial rivers (Reid & Hickin, 2008). The boulder-riffle reach (F3) has the highest n (average 0.124, range 0.068 – 0.273) and f (average 2.37, range 0.39 – 10.1) for all measured discharges, because of lowest velocity, highest depth and coarse grain size distributions including the big boulders. Much higher resistance in this boulder-riffle sub-reach is probably due to higher form drag from the boulders and this could also mean that the flow is primarily affected by channel form and the effect of skin resistance of the bed and banks are comparatively small. The bedrock gorge (F2) has the lowest value of flow resistance (average n = 0.061, f = 0.50) because of faster velocity, despite the rapidly rising depth and higher value of energy slope, and is consistent with the smoothness of its exposed rock bed. The flow resistance coefficients have a rapid decrease from low to moderate discharge and then decrease very slowly in alluvial and semi-alluvial sub-reaches but in the bare rock gorge n and f rapidly decrease to a minimum then increase again at high Q. The rapid drop in n or f as Q increases from low to moderate is similar to what has been

found in steep shallow alluvial channels. The trend of F2 decreasing first and then increasing with discharge is also seen in a big anastomosing bedrock reach of the Sabie River (Heritage *et al.*, 2004). In Trout Beck reaches from low to high range the *n* value varies from 3 to 5 times and *f* from 10 to 36 times.

The coefficients and exponents in *n*-*Q* and *f*-*Q* plots differ between sub-reaches and also from low-moderate to moderate-high discharge, but mostly they are similar to those for alluvial and semi-alluvial sites and are generally similar to those from steep fully alluvial channels. The average *n*-*Q* exponent *y* is -0.28 (low *Q* average -0.41, high *Q* average -0.15). The bare rock site has -0.35 for low *Q* but a positive exponent (0.19) for high flow; this is attributed to the higher resistance from rough walls with protrusions and re-entrants.

The inverse of flow resistance $(8/f)^{1/2}$ (= V/u^*) is plotted against relative submergence (R/D_{84}) to examine how Trout Beck data respond to changing R/D_{84} and compared with commonly used power law and log law based equations. The Manning-Strickler equation is found to be unfit for Trout Beck whilst the Keulegan equation with k_s/D_{84} = 2.5 to 9 and the Ferguson (2007a) VPE seem to describe the site data reasonably well. The best fit value of k_s/D_{84} in the Keulegan equation varies between sub-reaches (F1 = 6, F3 = 9, F4 = 4, F5 = 2.5) and two of these values are well above the generally considered range of 2 to 4. However the equations relating flow resistance to R/D_{84} generally assume that resistance is dominated by grain roughness, but in mountainous stream like Trout Beck the form and spill resistance may be significant. Furthermore, the Keulegan equation is based on the assumption that the velocity varies with depth in the logarithmic way. This may not be the case in steep boulder-bed channels but this equation seems to work well even in bedrock reaches of Trout Beck.

The dimensionless hydraulic geometry approach allows velocity and depth to be estimated from a known or estimated discharge if the channel's slope and grain sizes are known. The dimensionless unit discharge q^* or q^{**} can be a better predictor than d/D_{84} for steep mountainous stream because width is less sensitive to measurement error than depth (Comiti *et al.*, 2007; Ferguson, 2007a). Non-dimensional hydraulic geometry relations, both $V^* - q^*$ and $V^{**} - q^{**}$, are plotted and compared with the curves predicted by equations from Comiti *et al.* (2007) and Rickenmann and Recking (2011). The $V^* - q^*$ equation collapses the data from three of the alluvial and semi-alluvial sub-reaches but one (F5) is slightly offset. The $V^{**} - q^{**}$ equation proposed by Rickenmann and

Recking (2011) (RR) does not perfectly collapse the Trout Beck data but two sub-reaches F5 and F4 are very close to the prediction curves, F1 plots a little lower and F3 plots near the lower edge of the RR data range. All alluvial and semi-alluvial sites but one (F5) plot lower than RR trend lines suggesting that Trout Beck sub-reaches except F5 have more resistance than D_{84} would suggest.

Up to a moderate flood discharge (4 $m^3 s^{-1}$) , the boulder sub-reach (F3) has higher total shear stress τ than the bare rock gorge (F2) but due to higher flow resistance, and probably higher form drag, F3 has a lower effective stress available for sediment transport. The total shear stress averaged over the longer sub-reach $PT_5 - PT_6$ (mainly alluvial, past F3, F4) up to 6.2 $m^3 s^{-1}$ is lower than in F3, probably because of the low gradient of the pool (backwater) area upstream of F3. The high shear stress values for the short sub-reaches F2 and F5 agree well with those estimated for the respective longer sub-reaches $PT_3 - PT_5$ (fully bedrock, past F2) and $PT_6 - PT_7$ (semi-alluvial 35% cover, past F5). The alluvial sub-reach F1 has the lowest shear stresses throughout the discharge range.

Stress partitioning in the boulder-riffle sub-reach F3 has been performed using the method of Yager *et al.* (2007) which splits the total shear stress τ (or τ_t) into stress on mobile beds τ_m (i.e. effective shear stress) and stress on large immobile boulders τ_I. The analysis shows that this approach does not perform well in Trout Beck, mainly because of the uncertainties in the values of drag coefficients for mobile and immobile sediments (C_m and C_I). The general approach in this method is to calibrate C_I for a site assuming a constant value of C_m. The authors of this method had used $C_m = 0.047$ in their original flume experiment (Yager *et al.*, 2007) but later in the field experiment in Erlenbach they found a much higher value 0.44 ± 0.09 (Yager *et al.*, 2012). The two values of C_m give significantly different values of C_I and hence the stress components available for mobile and immobile sediments, therefore without knowing an appropriate value of C_m this approach is less useful and there is no guidance to estimate C_m for a new site.

Using a force balance approach, $F_t = F_m + F_b$, an alternative method has been developed to split the total downstream water force F_t into mobile and immobile components F_m and F_b respectively (Section 4.6.2) which shows that F_m/F_t decreases as the discharge increases which implies the relative magnitude of the form drag increases with the depth. This is consistent with Andrews (2000) but contradicts the previous analysis

based on Yager *et al.* (2007). The analysis shows that at low submergence up to flow depth 0.36 m (Q = 0.9 $m^3 s^{-1}$) almost all the driving force is available for mobile sediment and little is taken by the boulders, whereas at higher submergence (at flow depth 0.83 m, Q = 8 $m^3 s^{-1}$) only 72% of the total stress is available for mobile sediment. This shows that the effective stress is 100% of the total stress at shallow flow (Q ~1 $m^3 s^{-1}$) and 72% at deep flow (8 $m^3 s^{-1}$) (Table 4.17). This is possibly because when the flow is shallow the frontal area is small and also the pressure difference between upstream and downstream side of a boulder which produces form drag is very small. The conclusion on stress-partitioning is that Yager *et al*. (2007) method of stress partitioning does not work in Trout Beck. However the new approach appears to work to split the driving force into grain and form drag components but it is also based on the assumptions on the drag coefficients.

The wider implications of these findings are discussed in chapter 7. The next chapter will present the field results of tracer pebbles experiments that discuss the tracer surveys and recoveries, dispersal and transport distance, grains shape and size, virtual velocities. In particular the chapter investigates the size selectivity and bed load mobility in the contrasting reaches of the study channel.

5 Bedload dynamics

This chapter presents the results of the tracer-pebble experiment to investigate the movement of coarse sediment through a sequence of sub-reaches of contrasting character (alluvial, bare rock and semi-alluvial) in Trout Beck. It answers research questions 2 and 3 as identified in section 1.2 of chapter 1. The data from tracer- pebble resurveys are used to discuss various aspects of bedload transport including dispersal pattern, transport distance, areas of peak concentrations, the role of channel morphology including sediment cover and immobile boulders, grain-size and shape. The tracer data are then analysed with respect to river discharge and shear stress. This analysis compares coarse-sediment mobility and size selectivity over different substrates but under the same flow conditions. This allows comparison of results with other bedrock or gravel bed rivers and establishes a link with the more detailed bulk hydraulics data (Chapter 4) to determine the threshold shear stress which is the main factor driving the sediment transport (Chapter 7). The objectives of this chapter are to:

- assess the variation in sediment mobility according to bed character
- investigate whether the bedload transport in contrasting sub-reaches is size and shape selective
- establish threshold discharge and shear stress for different reach and sub-reaches

In order to achieve these objectives bedload transport was observed for nineteen months using two sets of magnetically-tagged tracer pebbles. The details of the tracer pebbles and search methods have already been described (Chapter 3) but a brief reminder of the experimental design is useful. The upper tracer set "A", placed on a fully alluvial bed, travelled over this bed with some of the tracers continuing into the upper semi-alluvial reach, the bare rock gorge, the lower semi-alluvial reach, and eventually to the lower fully alluvial reach. The lower tracer set "B", placed on bare rock near the head of the gorge, travelled through the gorge into the lower semi-alluvial reach with some continuing into the lower alluvial reach. The tracers were all installed at the same time, and both sets were resurveyed on the same day or only a few days apart, so both sets experienced the same sequence of floods between each successive survey.

This chapter is divided into four sections. Section 5.1 reports the results of tracer surveys and discusses the recovery rates, tracer dispersal and transport distances over the reaches of varying bed character. Section 5.2 describes the factors affecting the

tracer mobility which include bed type, grain characteristics (size and shape selectivity), peak discharge and local shear stress. This section also discusses the threshold discharge and shear stress values. Section 5.3 investigates bedload mobility and size selectivity by using a virtual velocity approach; and finally section 5.4 summarises the chapter.

5.1 Tracer mobility over alluvial, semi-alluvial and bedrock beds

5.1.1 Tracer surveys

Both sets of tracers, n = 270, were put in place on 29 August 2013; set A at 6 m from PT_1 (the first of seven pressure transducers installed along the reach), and set B at 195 m, in the bare rock reach (Figure 3.13). Both sets had the same number of tracers in each half-phi-sized class (Table 3.2) and same median diameter (75 mm) which allows the inter-set comparison of travel distances without any adjustment in the size distribution. Tracer locations were resurveyed at low flow on seven occasions between 29 August 2013 and 10 April 2015. As mentioned in the methods in section 3.2.4, most pebbles were visually located, but magnetic locators (magnetometers) were used to search the buried ones, and mapping was done using differential GPS (dGPS). The first six surveys, over the period of nine months, were carried out at an interval of one to two months, generally after a big flow event. After nine months the pattern of results was clear so the frequency of resurveying was reduced, with just one final survey in April 2015 after a total of 19 months from installation. The tracer relocation error was approximately to be 0.2 m (horizontal distance) which includes the dGPS error and the error in replacing the grain where it was found in resurveys; this value was used to identify which tracers had moved since the last survey. Table 5.1 summarises the information about the surveys including the dates, the type of beds over which the tracers were travelling over the period, peak discharge between the searches (Q_p) and number of competent floods. The river discharge (Q) exceeding the threshold value (Q_c) can be defined as a competent flood for sediment transport. The lowest and highest peak discharges between the survey intervals were 4.9 and 8.8 $m^3 s^{-1}$ respectively. Figures 5.1 and 5.2 show the study period hydrographs, with the survey dates marked.

Table 5.1. Summary information on the 2013 – 2015 tracer-pebble experiment "A" refers to the upper set of tracers placed on a fully alluvial bed, and "B" the lower set placed on bare rock. "Mixed" bed type denotes partial sediment cover. The number of floods exceeding 4 and 5 $m^3 s^{-1}$ (competent discharges for sediment transport, will be discussed in section 5.2.3), the peak discharge (and date) between the survey intervals are shown.

Survey number	Date (dd/mm/yy)		Days (~*months*) after seeding	Bed type traversed by tracers since previous survey		No of floods > 4 $m^3 s^{-1}$	No of floods > 5 $m^3 s^{-1}$	Peak *Q*, $m^3 s^{-1}$(*date)*
	A	B		A	B			
Installed	29.08.13	29.08.13	0 (*0*)	alluvial	bare rock	-	-	-
1	09.10.13	09.10.13	41 (*1.5*)	alluvial	rock then mixed	1	1	6.2 (*15.09.13*)
2	04.11.13	04.11.13	67 (*2*)	alluvial	rock then mixed	2	1	5.2 (*23.10.13*)
3	12.12.13	11.12.13	105 (*3.5*)	alluvial	mainly mixed	1	0	4.9 (*08.12.13*)
4	19.01.14	20.01.14	144 (*5*)	alluvial	mainly mixed	2	1	6.6 (*23.12.13*)
5	30.03.14	31.03.14	214 (*7*)	alluvial	almost all mixed	2	2	7.7 (*23.02.14*)
6	26.05.14	27.05.14	271 (*9*)	alluvial	almost all mixed	2	0	5.0 (*10.05.14*)
7	10.04.15	09.04.15	589 (*19*)	mostly alluvial	almost all mixed	13	9	8.8 (*26.02.15*)
Total						*23*	*14*	

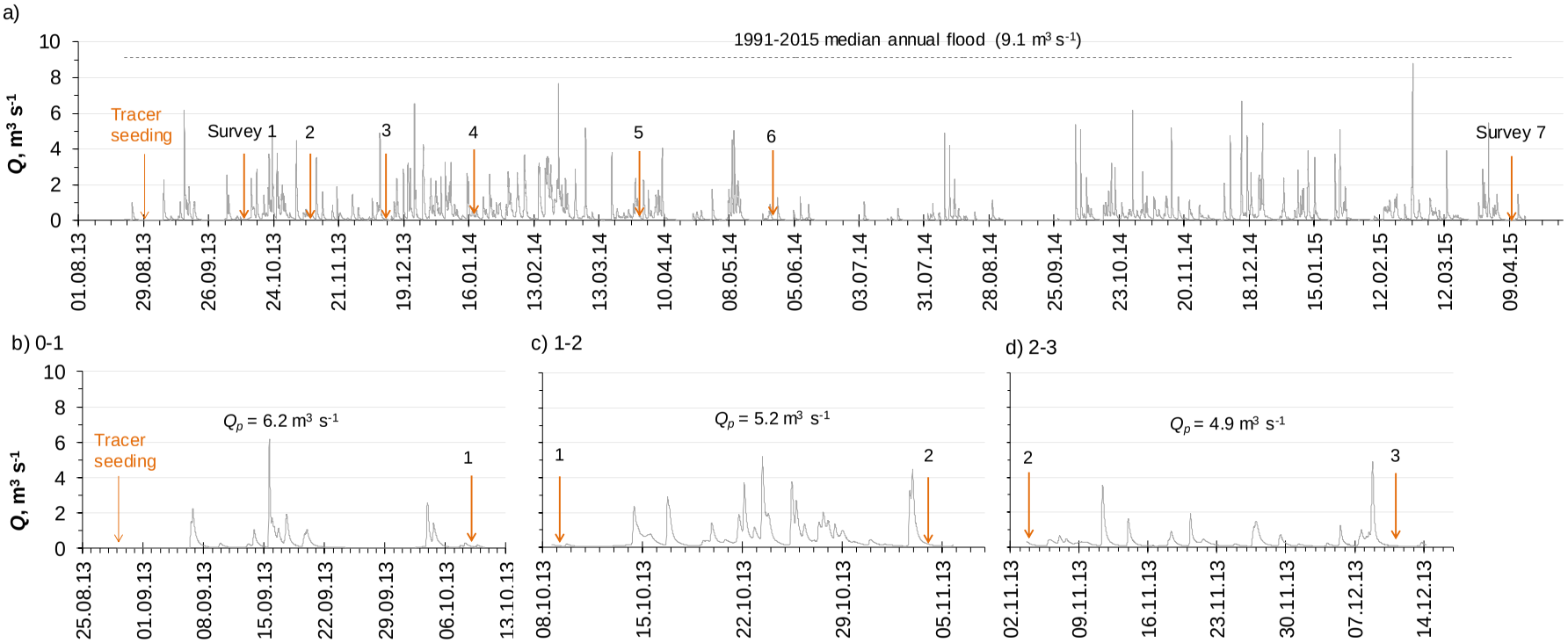

Figure 5.1. (a) 15 min discharge series for entire study period, scaled from EA data. The dates for tracer placement and seven surveys are marked; a dashed-line shows the long-term median annual flood (Table 2.5); (b) to (d) hydrograph for each survey interval: period 0 – 1 (seeding to 1st survey) to period 2 – 3 (between surveys 2 and 3). The peak Q (Q_p) for each period is shown.

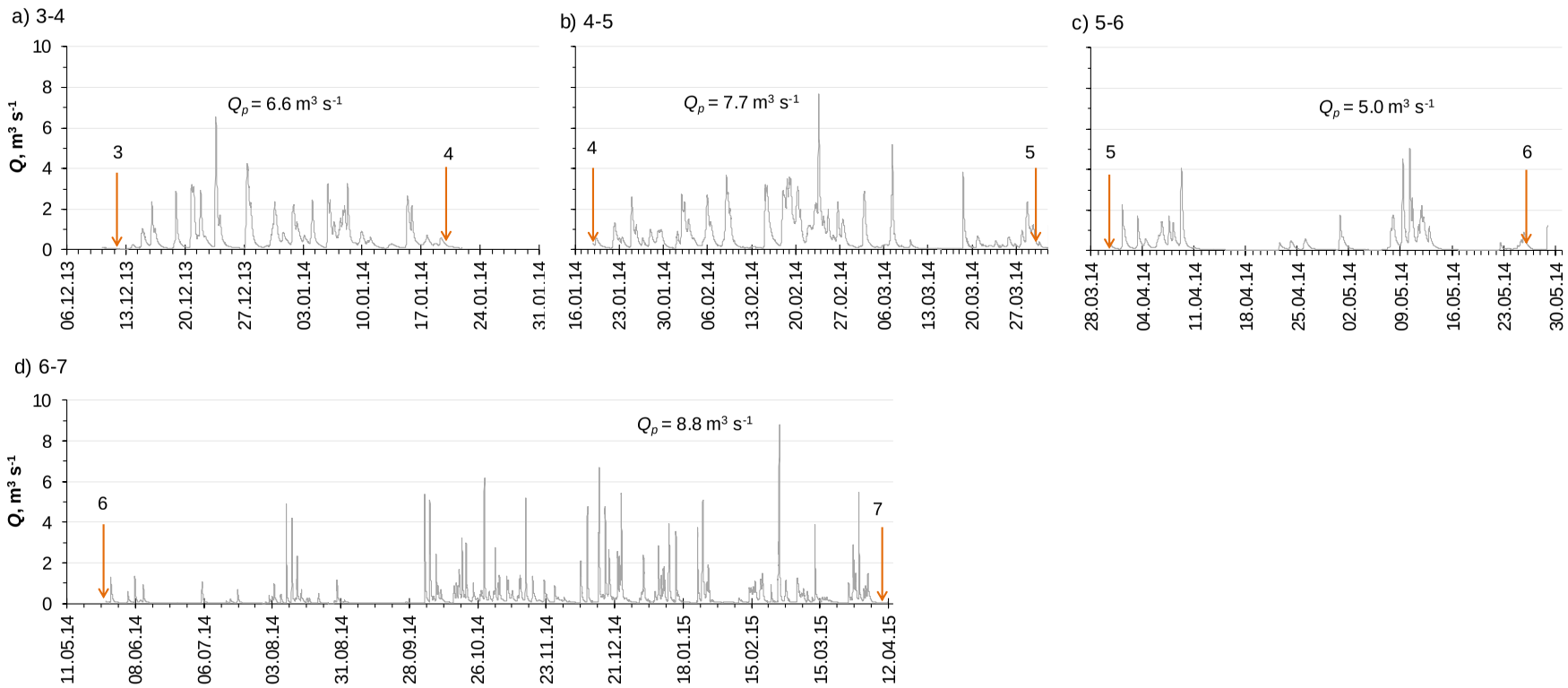

Figure 5.2. Discharge hydrograph for periods 3 – 4 to 6 – 7 (a to d). The peak discharge (Q_p) in $m^3\ s^{-1}$ is shown.

5.1.2 Tracer recovery rates

Recovery rates were generally high for the first six surveys but a rather lower for the final survey by which time the tracers had dispersed over a longer distance and more may have become deeply buried (beyond detection) or travelled beyond the study site. The recovery rates along with the discharge hydrograph are shown in Figure 5.3. In survey 1 almost all of the set A tracers were still in their initial positions and were not logged one by one; only the ten tracers that had moved by 1 m or more were mapped, therefore 100% recovery was assumed overall as well as for each half-phi-sized class of A tracers.

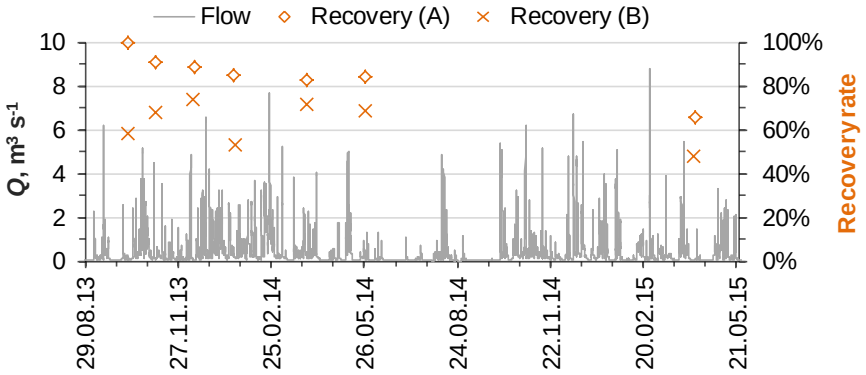

Figure 5.3. Recovery rates along with the *Q* series for set A and B tracers for seven surveys.

Recovery rates were always higher for alluvial-site tracers; the range across the survey periods was 66 – 91% for A tracers (average 85%) and 48 – 74%, (average 63%) for B tracers. Of the total of 270 installed at each site, the final survey found 179 (66%) A tracers and 129 (48%) B tracers. On the second last survey, nine months into the experiment, the recovery rates were 18% higher for A tracers (84%) and 21% higher for B tracers (69%). The slightly lower recovery rates in the final survey were expected because of a prolonged gap and large number of events during the survey interval (Table 5.1). Such recovery rates are consistent with previous studies. Over a period of two years Ferguson and Wathen (1998) found an overall 61% recovery rate of 1,460 tracers seeded in six reaches of a small gravel-bed river in Scotland (Allt Dubhaig), which is slightly lower than the recovery rate of the A tracers in the final survey (66%). Cray (2010) had seeded 800 tracers in the Trout Beck rock gorge in the same place as the present B tracers and recovered 58% over a period of five and a half months. However, Smith (2004) found a high recovery rate of 84% in Trout Beck over a period of five months. Goode and Wohl (2010b) recovered 61, 63 and 70% of painted tracers over a period of three years in three bedrock reaches of Ocoee River in USA.

The recovery rates for each half-phi-sized class are plotted in Figure 5.4. They vary from 24 – 100% for set A and 18 – 100% for set B tracers. The plots illustrate that A tracers had higher recovery rates also in each individual half-phi-sized class; the cobbles (64 – 256 mm) had higher recovery rates than the pebbles (23 – 64 mm). The recovery rates increased with grain size, as previously found by Ferguson and Wathen (1998), except for the B tracers in the final survey. The low recovery rates of small-sized pebbles (23 – 45 mm), particularly in the final search, suggest a greater dispersion of the finer particles (*i.e.* more may have travelled beyond the search limits), associated with the cumulative duration above transport threshold for these sizes. Another factor is probably that smaller pebbles are more likely to filter down into the bed where they are less likely to be recovered. The low recovery rate of the coarsest size B tracers in the final survey is most likely because they were buried and tracing was difficult as they did not have magnets. The recovery rates for both sets of tracers, overall as well as for each half-phi-sized class, are presented in Table 5.2.

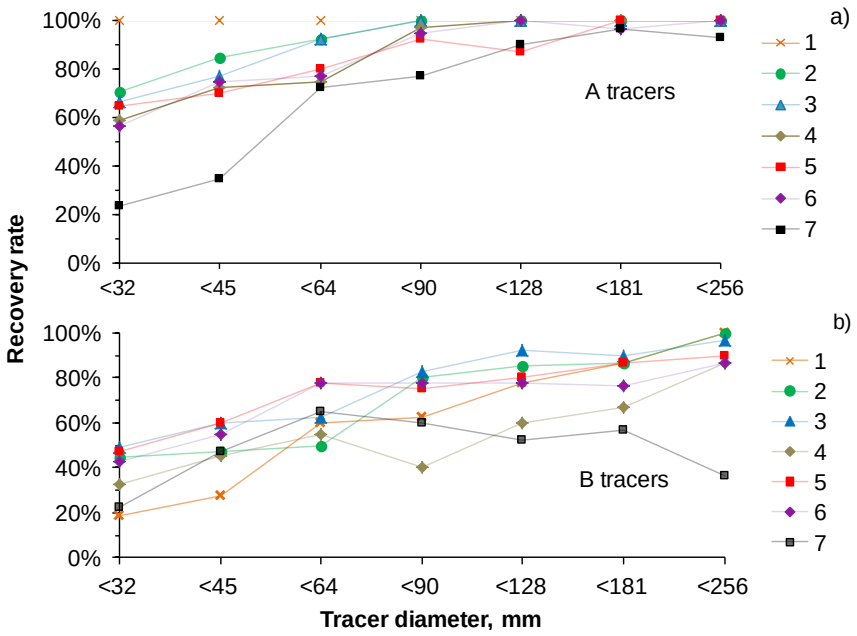

Figure 5.4. A and B tracer recovery rates for each half-phi-sized class ($\varphi = -\log_2 D$, where D is grain diameter in mm). 1 – 7 in the legend refer to successive surveys.

Several tracers, particularly the B tracers, were temporarily missing in a number of searches but were then found in subsequent searches, for example the recovery rate of B tracers increased from 58 to 68 % in survey 2 and 53 to 72% in survey 5 (Table 5.2). In the last few surveys some of the B tracers were discoloured and abraded and their ID numbers were indistinct as they had moved through the steep gorge and boulders and dispersed over a considerable distance. Such tracers were identified by matching their axial dimensions (*a*, *b* and *c*), their previous positions and ID photographs.

Table 5.2. Summary statistics of tracer surveys with peak flows, recovered numbers and recovery rates

Survey number	Peak Q, $m^3 s^{-1}$	No. of recovered tracers		Overall recovery %		% Recovery in each half-phi size class													
						-5 (<32 mm)		-5.5 (<45 mm)		-6 (<64 mm)		-6.5 (<90 mm)		-7 (<128 mm)		-7.5 (<181 mm)		-8 (<256 mm)	
		A	B	A	B	A	B	A	B	A	B	A	B	A	B	A	B	A	B
0																			
1	6.2	270*	156	100	58	100	18	100	28	100	60	100	63	100	78	100	87	100	100
2	5.2	247	183	91	68	71	45	85	48	93	50	100	80	100	85	100	87	100	100
3	4.9	242	199	89	74	67	49	78	60	93	63	100	83	100	93	100	90	100	97
4	6.6	228	142	84	53	59	33	73	45	75	55	98	40	100	60	100	67	100	87
5	7.7	225	193	83	72	65	47	70	60	80	78	93	75	88	80	100	87	100	90
6	5.0	227	185	84	69	57	43	75	55	78	78	95	78	100	78	97	77	100	87
7	8.8	179	129	66	48	24	22	35	48	73	65	78	60	90	53	97	57	93	37
		Overall mean		85	63														

*100% recovery was assumed as almost all tracers were still in the initial position and they were not logged one by one.

Most of the surveys were conducted at low flow when all tracers on bare rock were easily recovered. Sometimes it was difficult to recover tracers in the lower semi-alluvial reach even though the magnetometer detected a signal. This was because either the signal overlapped signals from other tracers or the tracers were underneath boulders or buried deeply in coarse sediment patches. The lower recovery of B tracers in survey 4 (53%) was probably because the flow during the survey was higher than on other occasions, making searching harder, particularly in deeper pools. The dispersal of tracers and its relation to different depositional environments are discussed in next section.

5.1.3 Dispersal and depositional pattern of the tracers

The dispersal and depositional pattern of both sets of tracers varied across the periods of tracer movement, from period 0 – 1 (seeding to survey 1) to period 6 – 7 (between surveys 6 and 7); the period is defined as each interval from one survey to the next. Typically 95% of the recovered A tracers were found on an alluvial surface and only a few (5%) were partly or fully buried at less than 0.1 m depth. The tracers were distributed fairly evenly in the central part of channel. At low flow the talweg is close to the left bank, but during floods the river flows over the full width. Therefore it is likely that some smaller-sized tracers followed the talweg but were then washed away with the floods so they were not seen anywhere downstream within the study reach except in the final survey. Likewise, 85% of the recovered B tracers were found on sediment patches and areas of partial sediment cover; 10% were found buried to a depth of less than 0.15 m; and 5% on bare rock surfaces where they were either isolated or in a small groups. The dispersal and depositional pattern on each survey are discussed below.

Survey 1

The spatial locations of each individual tracer as observed in survey 1 are superimposed on a digital elevation model (DEM) of the field site in Figure 5.5 which together with the channel long-profile demonstrates the dispersion pattern of the tracers along the reaches of varying bed character. The downstream distances shown in the DEM and long profile start from PT_1, the start line of the study reach. The study reach photographs taken during the first survey are shown in Figure 5.6. They show that most of the A tracers were still at the seeding position whereas the majority of the B tracers had left the installation site and were seen in the gorge, pool and even on the boulder-riffle.

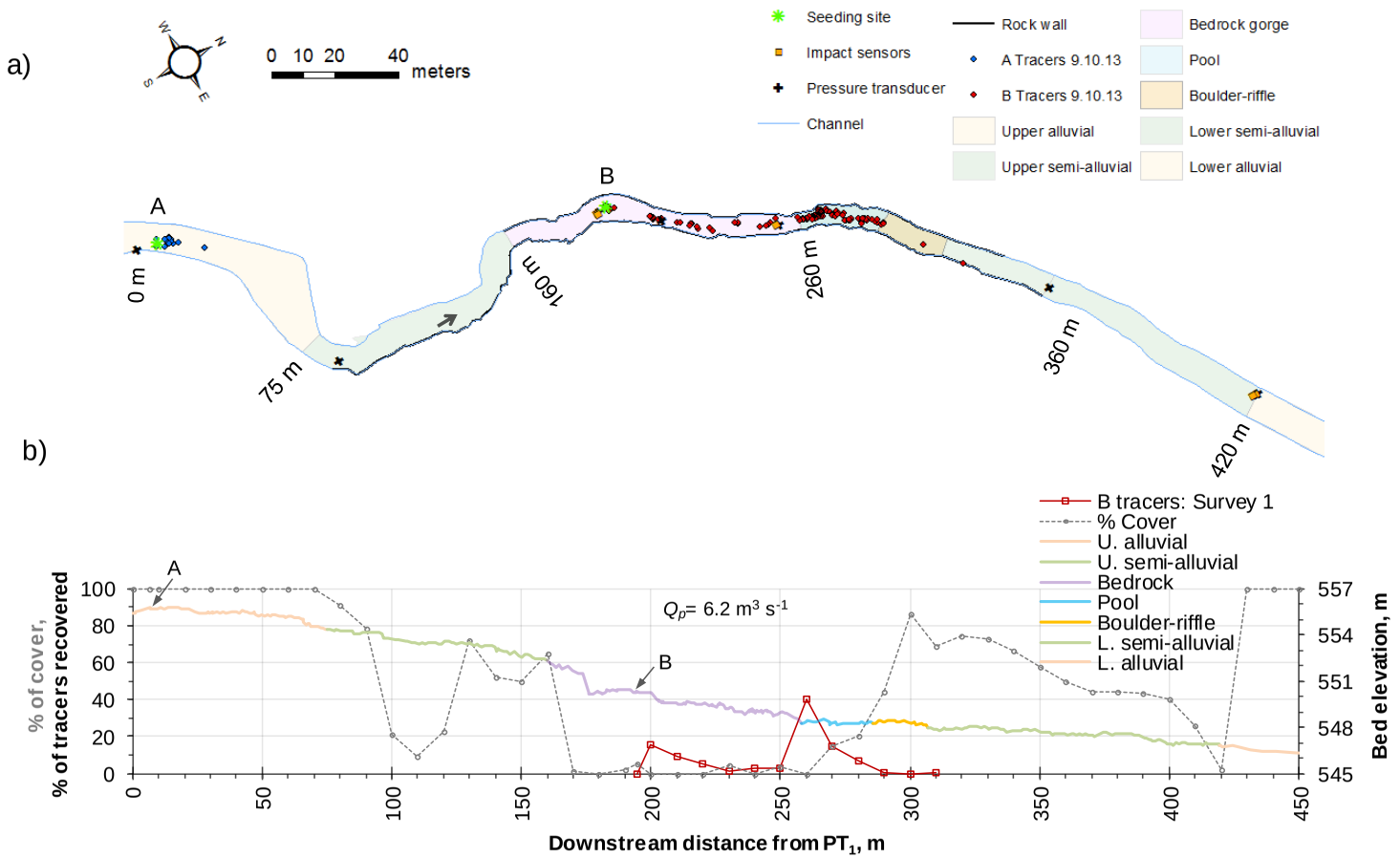

Figure 5.5. Spatial distribution of tracers downstream of respective seeding sites A (at 6 m) and B (at 195 m) as of survey 1; distances shown are from PT_1. (a) Study channel showing seeding sites (green) and coloured reaches/sub-reaches: upper alluvial (0 – 75 m), upper semi-alluvial (75 – 160 m), rock gorge (160 – 260 m), lower semi-alluvial (260 – 420 m) and lower alluvial (> 420 m). The "pool" (260 – 285) and "boulder-riffle" (285 –305) are in the upper part of the lower semi-alluvial reach. The A and B tracers are shown by blue and red dots respectively. The channel map shows the pressure transducers (+), bedload impact sensors (yellow), rock walls and an arrow to indicate flow direction. (b) The primary y-axis shows the percentage alluvial cover (grey line, as of 10.04.14) and % of recovered tracers (B: red, A: not shown) in every 10 m along the channel, whereas secondary y-axis shows the channel bed elevation. The peak Q = 6.2 m^3 s^{-1} during period 0 – 1 is shown. The coloured lines in (b) correspond to coloured reaches in (a).

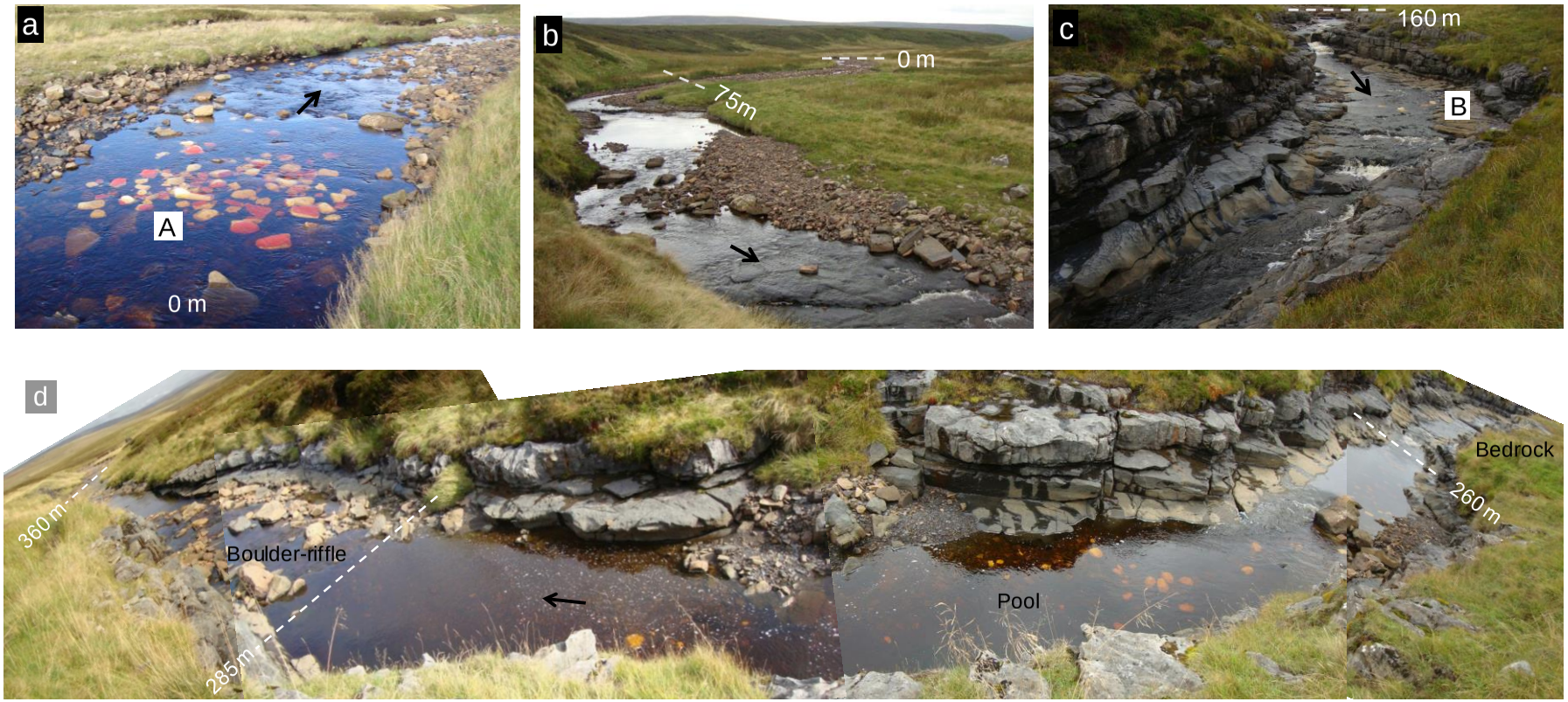

Figure 5.6. Photographs taken during survey 1 illustrating the different reaches of the study site: (a) most of the upper site tracers were still on the surface at the seeding site A; (b) no tracers were found in the upper semi-alluvial reach; (c) head of rock gorge, knickpoint and few lower site tracers were still on the seeding site B; (d) bare rock gorge, pool (B tracers were seen), boulder-rifle (285 – 305 m) and the lower semi-alluvial reach. The distances are from PT_1, arrows indicate the flow direction.

The highest density of boulders (*b*-axis > 256 mm) was in the boulder-riffle at 285 – 305 m along the reach, which is hydraulically rougher than the bedrock gorge and creates a backwater zone in the rock-bed floor at 260 – 285 m at low to medium discharges and is labelled the "pool" in Figures 5.5 and 5.6. As stated earlier only ten tracers of set A were found to have moved in survey 1, the furthest-travelled tracer (*b*-axis = 50 mm) was found at 15 m distance while the other nine were within 7 m from the seeding site. In contrast, the majority of the set B tracers had left their seeding site in the same period of time: 70 out of 156 recovered tracers (45%) were lying on exposed rock in the gorge (0 – 65 m from seeding site), 84 (54%) were in the pool, 1 in the boulder-riffle, and the furthest-travelled tracer (31 mm) was found a bit further down the boulder-riffle. Figure 5.5 shows clearly that tracers tended to accumulate in places where there was a rapid downstream increase of sediment cover. The percentage sediment cover plotted in Figure 5.5b is based on the cover survey dated 10.04.2014 (Section 2.4.1). The size of the furthest-travelled tracer and their distances in each survey are shown in Table 5.3.

Survey 2

Figure 5.7 shows the tracer dispersion at the time of the second survey. A total of 232 out of 247 recovered A tracers (94%) were within 5 m of their initial position; the other 15 including the front-runner (50 mm) were found between 5 to 18 m of their initial position. At the same time, out of 183 recovered B tracers 39 (21%) were found within the rock gorge, 115 (63%) in the pool, 22 (12%) in the boulder-riffle, and 7 (4%) in the lower semi-alluvial reach. The 35-mm diameter front-runner was found at 134 m from the seeding site. These data show that the tracers had moved short distances from the previous survey and about two thirds of the recovered tracers were still in the pool.

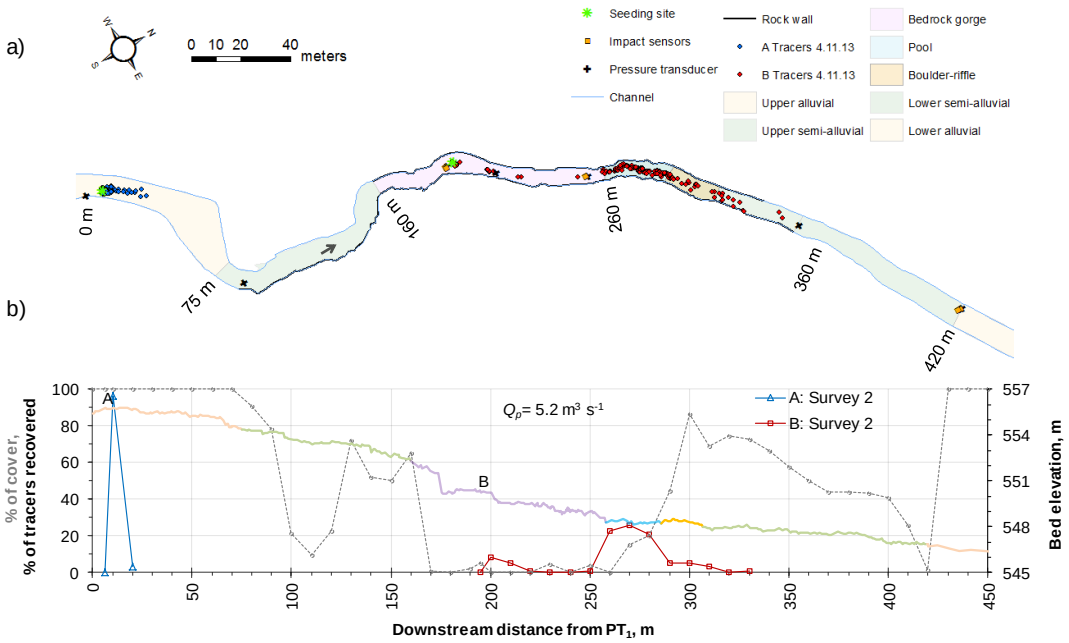

Figure 5.7. (a) Dispersion of A (blue) and B (red) tracers in survey 2. The furthest-travelled tracers from set A and B were found at 18 m and 134 m from the respective seeding sites; (b) % of alluvial cover (grey) and recovered tracers (A: blue, B: red) in every 10 m along the reach.

Survey 3

The tracer distribution as of survey 3 is shown in Figure 5.8. Of 242 recovered A tracers 209 (86%) were found within 5 m, 32 (13%) were between 5 – 18 m, and the front-runner (28 mm) was found at 21 m from the seeding site. Likewise, 36 (18%) out of 199 recovered B tracers were in the gorge, 120 (60%) in the pool, 29 (15%) in the boulder-riffle, and 14 (7%) in the lower semi-alluvial reach. The front-runner (33 mm) was found at 140 m distance from its seeding site, near pressure transducer PT_6. The tracers that were still in the rock gorge were either in small clusters of a few grains, or in small potholes or grooves in the bare rock. The interval between surveys 2 and 3 shows little change in the dispersion pattern and the bulk of the tracers appeared to remain in the pool. As stated earlier, a large majority of the tracers that were recovered in the semi-alluvial reach were found on an alluvial surface; the remaining few were either buried or found on bare rock.

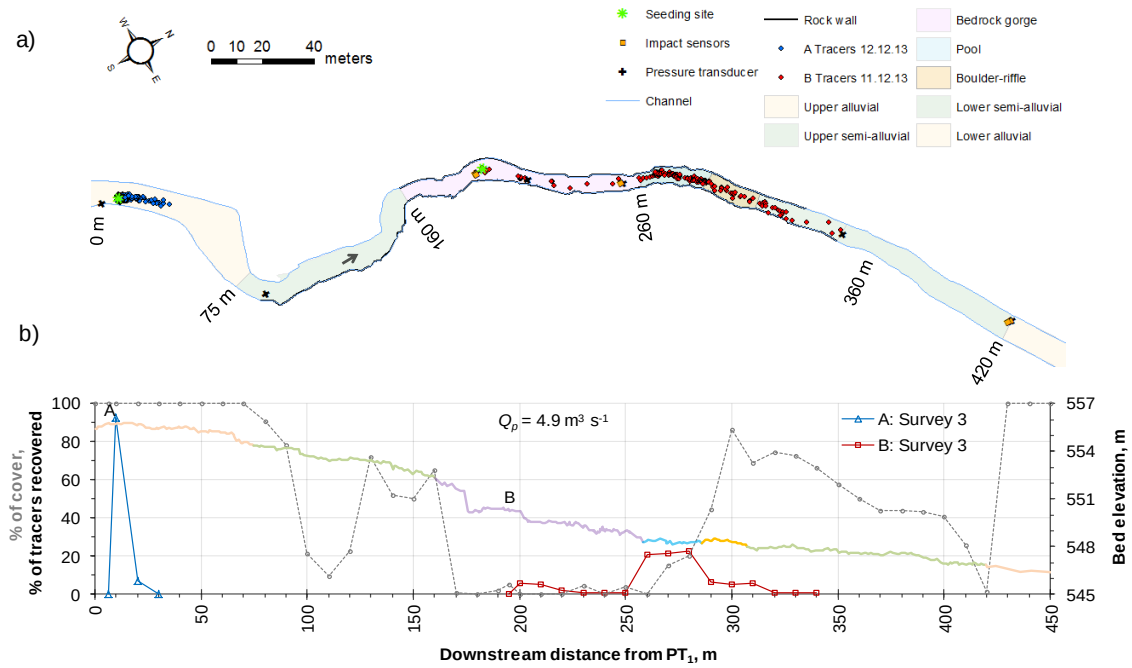

Figure 5.8. (a) Dispersion of A (blue) and B (red) tracers as observed in survey 3. Note the very low mobility since the previous survey, and the peak Q (4.9 $m^3 s^{-1}$) was the lowest of the seven survey intervals.

Survey 4

Figure 5.9 shows the dispersion pattern in the fourth survey. Both sets of tracers were notably more dispersed than previously. The peak discharge of 6.6 $m^3 s^{-1}$ since survey 3 was slightly higher than in the first survey interval. Of a total of 228 recovered A tracers 111 (49%) were found within 5 m and the other 117 (51%) including the front-runner (40 mm) were at 10 – 34 m from the initial position. Likewise, out of 142 recovered B tracers 12 (8%) were found on bare rock, 69 (49%) in the pool, 31 (22%) in the boulder-riffle, 24 (17%) in the semi-alluvial reach and 6 (4%) in the lower alluvial reach. The 38-mm diameter front-runner was found at 234 m from the initial position (429 m from PT_1) in the lower alluvial reach. During this period the first few tracers reached the lower alluvial reach and also there was a significant reduction in the number of tracers in the pool.

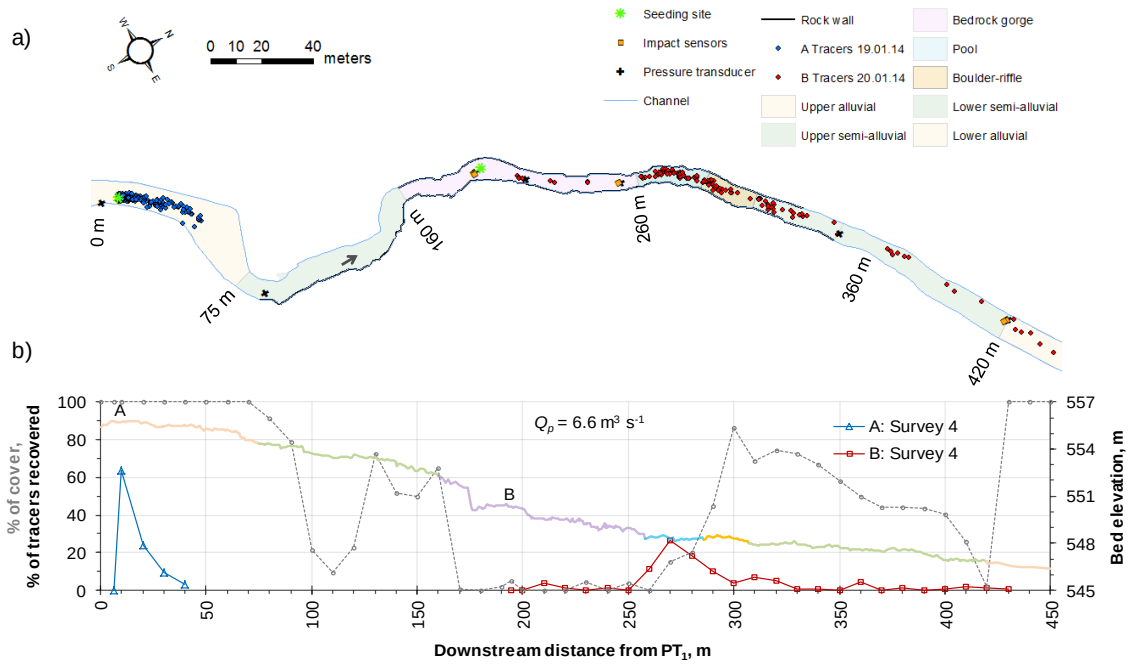

Figure 5.9. Dispersion of tracers in survey 4. Note that the B tracers reached the lower alluvial reach.

Survey 5

The tracer distributions in survey 5 are plotted in Figure 5.10. Out of 225 recovered A tracers 57 (25%) were within 5 m of their initial position, 85 (38%) at 5 – 20 m and 83 (37%) including the front-runner (36 mm) were found at 20 – 66 m distance. The peak *Q* during this period was high (7.7 $m^3 s^{-1}$) and this provides an obvious explanation for why the tracer distributions had shifted further downstream. For example the number of A tracers in the first 5 m decreased from 111 to 57 and also the furthest distance travelled by an A tracer increased from 34 to 66 m since the previous survey. Similarly, out of 193 recovered B tracers, 6 (3%) were within the gorge, 86 (45%) in the pool, 64 (33%) in the boulder-riffle, 33 (17%) in the semi-alluvial reach, and 4 (2%) in the alluvial reach. The front-runner (30 mm) was found in the lower alluvial reach, 233 m downstream of seeding site B. The number of tracers recovered in the pool was more than in survey 4 which had a low recovery rate (Table 5.2). By the time of this survey only a few tracers were left in the rock gorge, mainly in small grooves or as isolated patches of a few grains, and most of them were still in the pool and boulder-riffle areas. Because of the high peak discharge (7.7 $m^3 s^{-1}$) the tracers had gradually started to leave the pool and boulder-riffle area and some had reached an almost flat gravel-bed section in sub-reach F4 (310 – 340 m, Figures 2.36 and 5.10) where they tended to move along the main talweg close to the right bank. Those found downstream of PT_6 (at 343 m) had started to spread across the width of the channel, but were found mainly towards the left

bank as the right side of the channel was dominated by slightly sloping (inclined towards the centre line of the river) exposed rock.

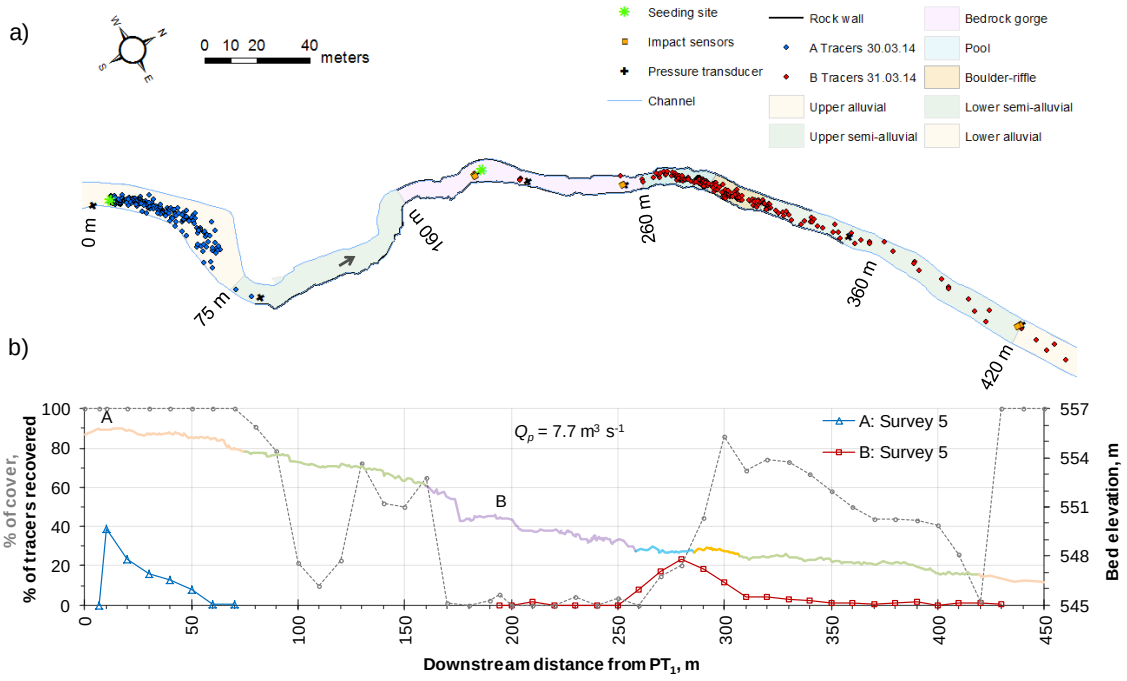

Figure 5.10. Tracers dispersion in survey 5. Note that because of high Q_p, the A tracers moved further down and the peak concentration of B tracers from pool has shifted downward.

Survey 6

The tracer dispersion in survey 6 is shown Figure 5.11. Out of 227 recovered A tracers, 56 (25%) were found 0 – 5 m from the starting point, 91 (40%) at 5 – 20 m, 79 (35%) at 20 – 50 m, and the front-runner (43 mm) at 54 m from the seeding site. Of the 185 recovered B tracers, 6 (3%) were found within the rock gorge, 76 (41%) in the pool, 60 (32%) in the boulder-riffle, 29 (16%) in the semi-alluvial reach, and 14 (8%) in the lower alluvial zone, including the 31-mm front-runner which was found at 302 m from the seeding site. This period (5 – 6) has very low mobility. This can again be attributed to a low peak Q (5.0 m^3s^{-1}) which appeared to be inadequate to entrain the tracers from their resting positions in the pool and the boulder-riffle.

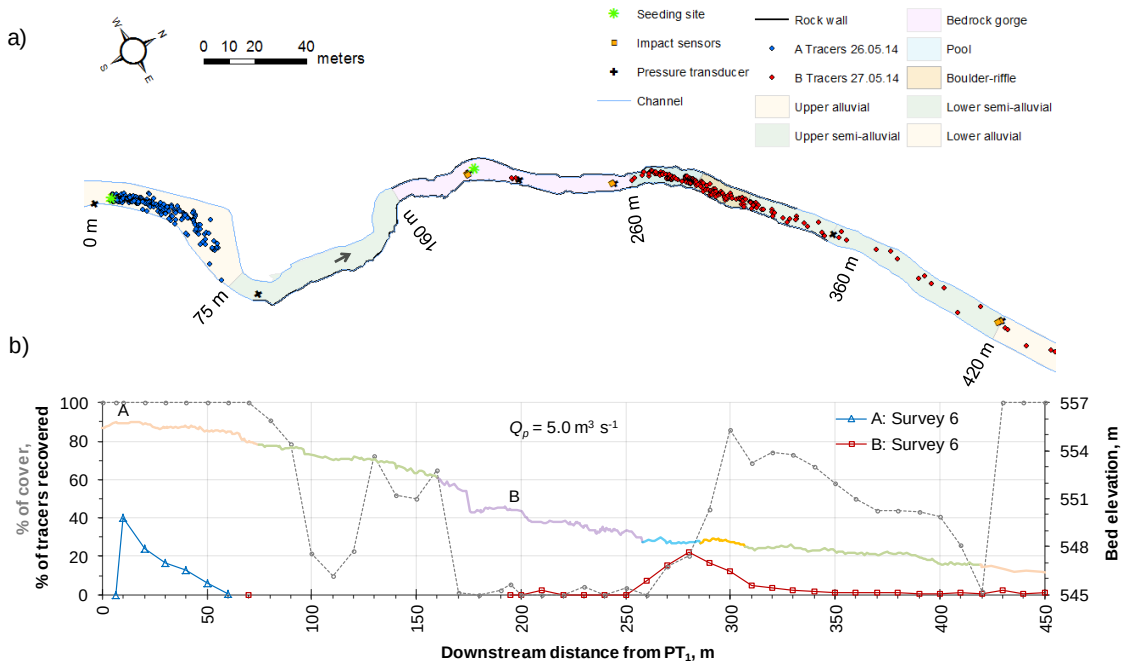

Figure 5.11. Dispersion as of survey 6, both sets of tracers hardly moved during the period. Note the peak *Q* is again very low (5 m^3 s^{-1}).

Survey 7

Finally, Figure 5.12 shows the tracer dispersion in the last survey. The plot demonstrates that some A tracers had moved all the way down to the lower alluvial reach. Out of 179 recovered A tracers, 14 (8%) were still only 0 – 5 m from the starting position, 60 (34%) were at 5 – 20 m, 94 (53%) at 20 – 69 m and still on a fully alluvial bed, 5 (3%) in the upper semi-alluvial, 3 (< 2%) in the pool or boulder-riffle, 2 (1%) in the lower semi-alluvial reach, and the front-runner (35 mm) was 420 m distance from the seeding site and in the lower alluvial reach. Of the 129 recovered B tracers, only 3 (2%) were still on bare rock within the gorge, 10 (8%) were in the pool, 40 (31%) in the boulder-riffle, 46 (36%) in the lower semi-alluvial reach, and 30 (23%) in the lower alluvial reach including the front-runner (30 mm) which was 341 m from the seeding site B.

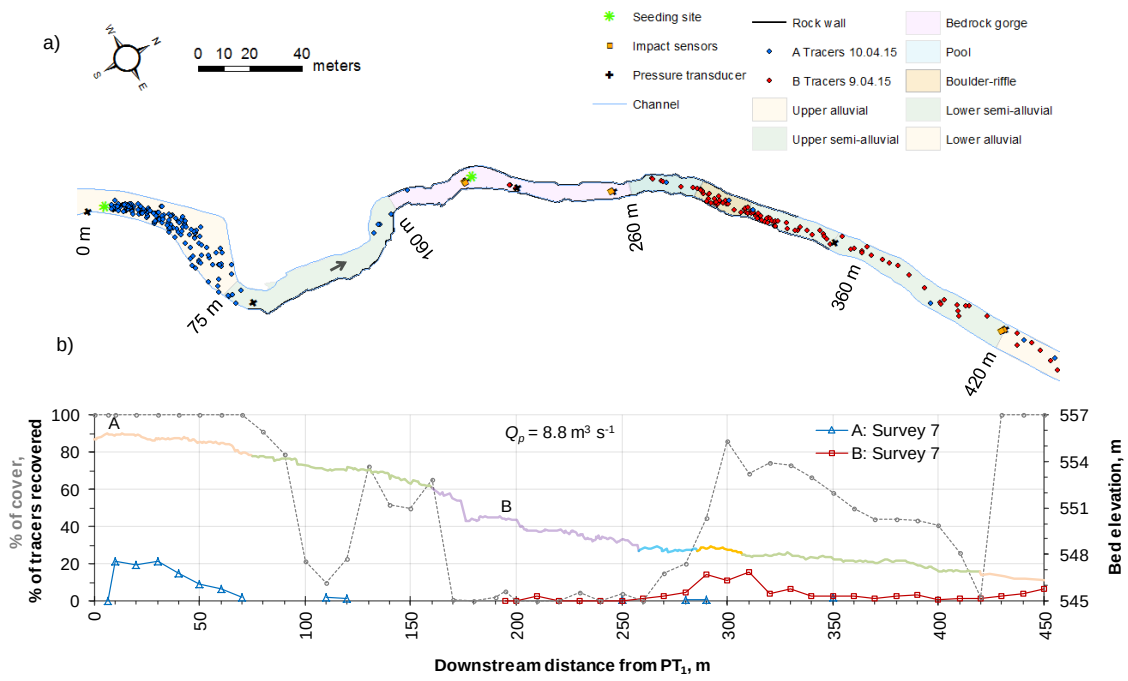

Figure 5.12. Dispersion of A and B tracers in the final survey (survey 7), after a gap of 10 months from the previous survey. The peak Q (8.8 m^3 s^{-1}) during period 6 – 7 is the highest of the study period. The channel plan (a) shows the A tracers (blue) were dispersed thoroughly in upper alluvial reach and the downstream reaches including the lower alluvial reach also contained few of them. The concentration of B tracers is also seen shifting downward from pool and boulder-riffle.

The above data and the plots show that the dispersion of tracers varied throughout the monitoring period. Almost all the tracers were found on an alluvial surface, less than 10% of those recovered were buried, and the main concentration of tracers in semi-alluvial reaches was in the low-velocity pool and hydraulically rough boulder-riffle areas. The periods 1 – 2, 2 – 3 and 5 – 6 did not yield a significant movement of tracers, whereas both sets of tracers were notably mobile in period 6 – 7. The increased dispersal of the tracers on the final survey is attributed to the higher number of flood events, including the highest peak discharge of the entire study period. The majority of the bedrock-site tracers moved through the gorge in the first period whereas the alluvial site tracers had to wait until the final period during which the tracers not only crossed the upper alluvial reach but a few of them reached the lower alluvial reach by travelling 380 m.

5.1.4 Transport distances

This section presents the results of the incremental as well as total travel distances from seeding point at each survey for both sets of tracers, to enable the quantification of the bedload mobility. Table 5.3 summarises the mean, median and maximum travel distances from seeding points, standard deviations and standard errors at each survey.

Table 5.3. Total travel distance (mean, median, maximum) from installation site at each survey, for A and B tracers. Mean and median distances are calculated for all moved tracers, maximum distance is the distance of the furthest-travelled tracer and its grain size is D_{max}, σ is the standard deviation of distances for all tracers, and SE is the standard error of the mean *(*$= \sigma/\sqrt{N}$, where N is the number of recovered tracers*)*.

Survey number	Mean (m)		Median (m)		Maximum (m)		D_{max} (mm)		σ (m)		SE (m)	
	A	B	A	B	A	B	A	B	A	B	A	B
0												
1	6*	51	4.7	65	15	113	50	31	3.5	29	1.0	2.3
2	2.4	70	1.7	75	18	134	50	35	2.6	29	0.2	2.2
3	3.4	73	2.1	75	21	140	28	33	3.6	30	0.2	2.1
4	9.4	94	5.9	84	34	234	40	38	9	42	0.6	3.5
5	18	99	14	90	66	233	36	30	14	35	0.9	2.5
6	17	107	13	93	54	302	43	31	13	51	0.9	3.7
7	37	151	23	118	420	341	35	30	61	71	4.6	6.2

*Mean of only 10 moved tracers therefore distance is higher than in survey 2 and 3

Table 5.3 shows that the total mean travel distance in successive surveys increased, as would be expected. The mean travel distance of recovered A tracers in survey 1 over the period of 1.5 months is shown as 6 m, which is higher than the mean values for the second and third surveys; this is because of very limited number of moved-tracers (< 4%) whereas during the same period the mean distance of B tracers was 51 m as most of the B tracers reached the lower semi-alluvial site. The mean travel distances of A and B tracers in the second survey were 2.4 m and 70 m respectively which increased to 37 m and 151 m in the final survey. Some of the mean distance values are quite different from the median values, as would be expected, because some of the travel distances were high. For example in the final survey a few tracers had travelled quite a long distance, especially the A tracers; therefore the mean values of A and B (37 and 151 m) are higher than their median values (23 and 118 m) (Table 5.3). The travel distance of individual tracers had a quite wide range even within a survey. For example, in the final survey, the individual tracer distance varies from < 1 m up to 420 m for A tracers and up to 341 m for B tracers. The standard deviation (σ) of the tracer distances are moderate and the standard errors of the mean distances are small (Table 5.3). The furthest-travelled A and B tracers in the second last (sixth) survey were found at 54 m and 302 m (grain sizes 43 and 31 mm) from the respective seeding sites, whereas in the final survey they were at 420 m and 341 m respectively. The median values remain unchanged between the second and third surveys (A: 2 m, B: 75 m) and changed very little between the fifth and sixth surveys (A: 14 and 13 m, B: 90 and 93 m) indicating very low mobility in those intervals as discussed in section 5.1.3. The mean values for

the second and third surveys are also close (A: 2 and 3 m, B: 70 and 73 m), as are the standard deviations (A: 2.6 and 3.6, B: 29 and 30). However, in the fifth and sixth surveys the mean values are close for A tracers but are slightly different for B tracers (A: 18 and 17, B: 99 and 107 m), and the same applies to the standard deviations (A: 14 and 13, B: 35 and 51) and standard errors (A: 0.9 and 0.9, B: 2.5 and 3.7). The mean travel distance data reveals that the A tracers were advancing at an average rate of 1.9 m per month, both for first nine-month period and the last ten-month period, despite the lack of movement in the intervals between surveys 2 and 3, and 5 and 6. However, the B tracers advanced at the very high rate of 35 m per month for the first two months (0 – 2), but that decreased to 5.4 m per month for period 2 – 6 and 4.2 m per month for period 6 – 7.

Figure 5.13 shows the period mean transport distance between successive surveys and total (cumulative) mean transport distances at each survey. The plots demonstrate that the total mean distance increases over time but the period mean distance fluctuates according to the river discharges and the spatial location of the tracers. The plots show that the A tracers had their highest mean travel distance in period 6 – 7. The B tracers also travelled farther on average in this period than in any other interval between surveys, but they travelled even farther in period 0 –1 (between seeding and the first search). Table 5.4 summarises the mean, median and maximum travel distance, overall as well as for each half-phi size class, for each of the survey periods.

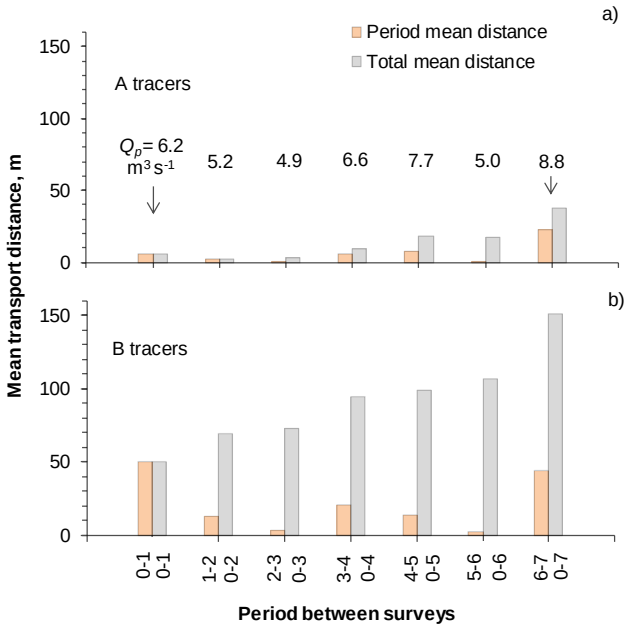

Figure 5.13. Period mean transport distance (orange) and total mean transport distance at each survey (grey) for: a) A tracers; and (b) B tracers. The peak *Q* between surveys (Q_p) is shown.

Table 5.4. The mean (L_{mean}), median (L_{median}) and maximum (L_{max}) travel distance; the *b*-axis of the longest travelled tracer (D_{max}); the standard deviation (σ) of the distances for all tracers, for each period are shown. The mean distances for each half-phi size class are shown. The period 0 – 7 (total distance at the final survey) is shown for comparison. The mean distance for period 2 – 6 during which most of the B tracers were on semi-alluvial bed (will be used in section 5.3), are also shown.

Survey Period	Q_p, $m^3 s^{-1}$	L_{mean} (m)		L_{median} m)		L_{max}, m (D_{max}, mm)		Standard deviation (σ)		Mean distance for each half-phi size class											
										-5.0 <32 mm		-5.5 <45mm		-6 <64 mm		-6.5 <90 mm		-7 <128 mm		-7.5 <181 mm		-8 <256 mm	
		A	B	A	B	A	B	A	B	A	B	A	B	A	B	A	B	A	B	A	B	A	B
0 – 1	6.2	6	51	4.7	65	15 (50)	113 (31)	3	29	6	59	0	53	10	48	0	42	5	59	5	57	4	42
1 – 2	5.2	2.2	13	1.6	6	16 (28)	77 (46)	2	18	4	23	3	24	1.5	18	1.8	14	2.0	12	2	7	1.7	9
2 – 3	4.9	0.9	3	0.2	0.2	11 (35)	52 (75)	2	8	2.2	8	1.4	6	0.8	4	0.9	5	0.3	1.3	0.3	2.4	0.3	0.2
3 – 4	6.6	6	22	3	9	31 (33)	123 (38)	7	29	11	46	11	46	6	27	7	25	4	7	3	8	1.9	12
4 – 5	7.7	7	14	5	6	48 (36)	132 (28)	9	21	20	55	13	28	10	20	7	8	4	7	3	3	1.9	10
5 – 6	5.0	0.5	2.3	0.1	0.1	11 (52)	158 (31)	1	14	0.5	20	2	5	0.5	0.6	0.4	0.4	0.4	0.5	0.2	0.9	0.2	0.2
6 – 7	8.8	23	44	8	24	380 (35)	206 (40)	56	50	66	106	99	78	25	68	21	51	10	20	10	21	6	11
0 – 7	8.8	37	151	23	118	420 (35)	341 (30)	61	71	103	267	113	196	37	175	38	146	21	107	18	96	12	79
2 – 6	7.7	14	34	9	18	53 (43)	184 (31)	12	39	28	114	24	60	18	41	16	28	8	17	7	13	4	22

Table 5.4 shows the highest inter-survey mean travel distance was 23 m for A tracers (period 6 – 7) and 51 m for B tracers (0 – 1). The period 6 – 7 had the highest mean travel distances for each size class except for B tracers in the coarser tail (< 128 to < 256 mm) for which the highest mean distances were in the first period (0 – 1). Similarly, the lowest mean distances were observed in period 5 – 6 (A: 0.5 m, B: 2.3 m), closely followed by 2 – 3 (A: 0.9, B: 3 m). The tracers in the cobble range (64 – 256 mm) moved less than a metre over alluvial or partially alluvial beds in period 5 – 6, during which the peak Q was 5.0 $m^3 s^{-1}$. The A tracers in the alluvial bed moved less than a metre also in period 2 – 3 when the peak Q was 4.9 $m^3 s^{-1}$ but had moved 1.5 – 2.0 m during period 1 – 2 when the peak Q was slightly higher (5.2 $m^3 s^{-1}$). The standard deviations are high for survey periods 0 – 1, 3 – 4 and 6 –7 because these were the periods of high peak Q and some distances were substantially higher than others. The overall and period mean distances were almost always higher in the lower semi-alluvial reach than in the upper alluvial reach (except < 45 mm size class in 6 – 7), though a few A tracers travelled farther than B tracers during the last period. The longest traveller between any two searches was a 35-mm A tracer that travelled 380 m, followed by a 40-mm B tracer that travelled 206 m, both in period 6 – 7 (Table 5.4).

A high proportion of the tracers were found to be stationary in the periods when the peak Q was low. Table 5.5 shows the percentage moved. As noted previously (Section 5.1.1), the tracers that had moved > 0.2 m and were found in both the current survey and immediately previous survey were defined as "moved tracers". The table also shows the percentage moved if the definition of moved tracers considers > 1 m instead of 0.2 m.

Table 5.5. Percentage moved for A and B tracers for each survey period. The percentage is calculated as the number of moved tracers (>0.2 m and >1 m distances) divided by the number of total recovered tracers. The peak discharge (Q_p) is shown.

Survey period	Q_p ($m^3 s^{-1}$)	No of recovered tracers		% moved			
		A	B	A > 0.2 m	A >1 m	B > 0.2 m	B >1 m
0 - 1	6.2	270	156	4	4	99	93
1 - 2	5.2	247	183	98	86	51	45
2 - 3	4.9	242	199	48	22	42	34
3 - 4	6.6	228	142	74	59	83	83
4 - 5	7.7	225	193	73	61	45	42
5 - 6	5.0	227	185	32	13	34	19
6 - 7	8.8	179	129	82	76	74	71

Table 5.5 shows that period 5 – 6 had the lowest percentage of moved to recovered tracers for both sets of tracers: A (32%) and set B (34%). If 1 m is considered to be the threshold of the moved tracers then these percentages will be decreased to 13 (A) and 19 (B) indicating that there was significant number of tracers that had moved less than a metre. The second lowest percentages were in period 2 – 3 (A: 48, B: 42 for > 0.2 m, and A: 22, B: 34 for >1 m). However, despite the higher peak *Q*, period 4 – 5 had a quite low ratio for B tracers (45 for > 0.2 m and 42 for > 1 m) because of two reasons: (i) a significant number of tracers were still in the pool and it seemed some of them did not move at all (Figure 5.10); (ii) the recovery rate of B tracers in survey 4 was quite low (53%) compared to that in survey 5 (72%). Since the definition of "moved tracers" considers only the common tracers that were found in both surveys 4 and 5, the number of moved tracers are low even though the recovery rate in one of the two surveys was high. For example, if a tracer was recovered in survey 5 but not in survey 4 then it is not considered as a moved tracer for period 4 – 5 even if that tracer had moved during that period.

The results discussed above show that the travel distances of the A tracers, placed on a fully alluvial bed and travelling mostly over an alluvial bed, were lower than the travel distances of the B tracers that were placed on bare rock and travelled over bare rock and a semi-alluvial bed. It is evident from the results discussed so far that the variation in travel distances was linked to the type of bed the tracers were traversing, as well as the peak discharge or shear stress during the period. The different size of individual tracers is another factor affecting their travel distances and the next section will therefore discuss the factors affecting the sediment mobility.

5.2 Factors affecting bedload mobility

5.2.1 Bed character – cover type

The bedload movement and travel distances at shorter scales are governed by factors controlling entrainment including relative particle size, shear stress, threshold or critical shear stress (τ_c) or critical discharge Q_c. The effective shear stress (section 4.6) is a key factor for bedload movement and the value of critical stress is entirely dependent on the bed character (morphology, grain size, sediment cover and boulders). The effect of bed character on sediment mobility is investigated in segments of the study channel such as fully alluvial, bare rock, pool, boulder-riffle and rock beds with varying sediment cover.

Figure 5.14a shows the changes along the study site of percentage of sediment cover, as estimated for 10 m increments from the DEM and the dGPS measured boundaries between sediment and exposed rock, on 10th April 2014. The plot also shows the number of boulders (*b*-axis > 256 mm) per 10 m and the mean bankfull channel width (measured from DEM) in each of these 10 m downstream segments. Boulders are present between 260 and 400 m along the reach. The largest boulder of 1.15 m diameter (*b*-axis) was found at 263 m surrounded by a small cluster of other boulders but the highest density of the boulders (4 boulders per 10 m^2 channel area) was in the boulder-riffle (285 – 305 m) zone. The plot shows that the alluvial cover in the pool and boulder-riffle was respectively about 25% and 70%. Figure 5.14b to d shows the number of tracers recovered in every 10 m downstream distance and the channel bed profile; slightly different plots were already seen in section 5.1.3. As mentioned previously (Section 5.1.3), the tracers had the tendency to accumulate in places where there was a sudden downstream increase in sediment cover. The rapid increase in cover from the pool to the boulder-riffle coincides with the highest boulder density, and large numbers of tracers were found in this area in most surveys (Figure 5.14b to d). This shows that even at a flow close to the median annual flood (Figure 5.2d) the boulder-riffle posed a significant barrier to the downstream flux of tracer particles. The upper alluvial reach which had 100 % sediment cover had the lowest mobility (the left-hand set of curves in Figure 5.14b, c, d), the sediment-deprived rock gorge had the highest mobility, and the semi-alluvial bed with partial sediment cover had intermediate mobility (the right-hand set of curves in Figure 5.14 b, c, d). The boulder-riffle where the sediment cover and boulder density were high had very low sediment mobility. All this suggests that there must be a strong relation of bedload mobility with sediment cover and boulder density.

The effective shear stress (Section 4.6) cannot be high unless total shear stress (Section 4.5) is high, and this depends on channel slope. The steep-gradient bare rock gorge (talweg gradient 4.15% for 160 – 260 m, 3.31% for 195 – 260 m) (Figure 5.14b) had higher mobility whereas the almost flat-bed pool (0.04 %) had the lowest mobility; this shows the slope has a strong control on bedload mobility. The upper alluvial reach has a slightly higher slope (1.41%) than the lower semi-alluvial reach (1.00%), but the bedload mobility was slightly higher in the lower semi-alluvial bed. This shows that though slope has a strong link to bedload transport it is not the only variable that determines the transport rate (will be discussed in chapter 7) at a sub-reach scale.

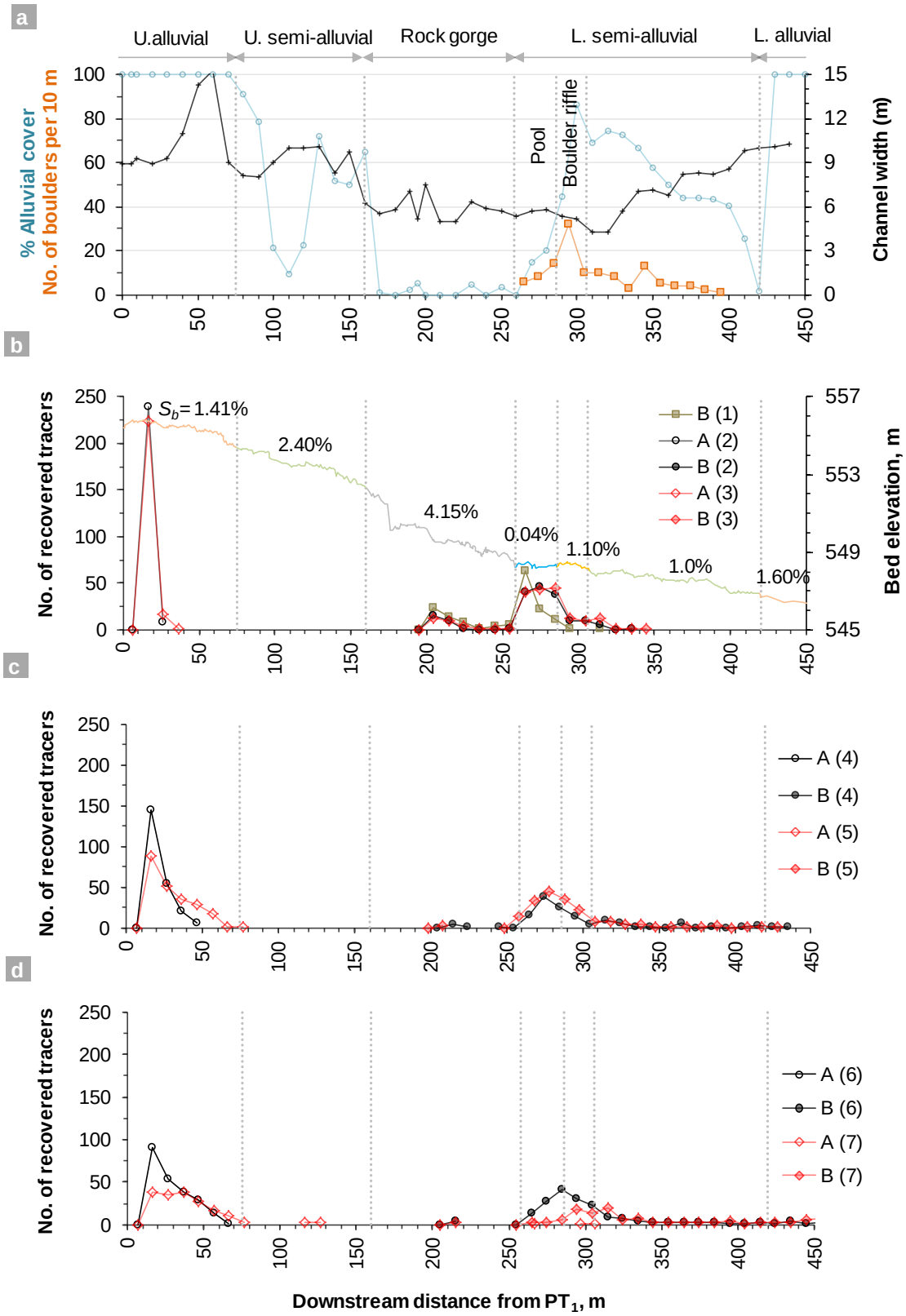

Figure 5.14. (a) Variation in alluvial cover, boulder density and mean bankfull channel width in every 10 m along the reach. (b) Longitudinal profile showing the bed slopes, channel segments of different character (vertical dotted line in all plots). No. of recovered tracers in surveys 1, 2 and 3 along the reach; survey 1 of the A tracers is not shown. (c and d) No. of recovered tracers in surveys 4 and 5, and 6 and 7.

The channel width (Figure 5.14a) affects total shear stress; the narrower the channel the higher will be the flow depth (or hydraulic radius) for a given *Q*. The mean bankfull width along the study reach varies from 9 – 15 m (mean 10.3 m) in the upper alluvial reach to 6 – 10 m (8.7 m) in the upper semi-alluvial reach, 5 – 7.5 m (5.9 m) in bare rock gorge, 4.3 – 7.1 m (5.7 m) in the upper part of the lower semi-alluvial reach, and 6.8 – 10 m (8.5 m) in the lower part of the lower semi-alluvial reach (Figure 5.14a, Table 2.6). The upper alluvial reach has the highest mean width (10.3 m) and the boulder-riffle has the lowest mean width (4.9 m). Both these sections had a very slow movement of the tracer pebbles, which implies that channel width is not the only or main control over bedload mobility.

The notable difference between the mean travel distances of the A and B tracers up to the first two surveys (Table 5.4), when set A had been travelling over an alluvial bed but set B over bare rock, confirms that the tracers were far more mobile on bare rock than in the alluvial reach. Similarly, in the next four surveys (3 to 6) the A tracers were still travelling shorter distances over the upper alluvial bed (mean distance 0.5 – 7 m per period) whereas the B tracers on the lower semi-alluvial bed were transported slightly further (2.3 – 22.0 m per period). This shows that the bedload mobility was slightly higher in the semi-alluvial reach than in the fully alluvial bed, despite the presence of the pool and boulder-riffle. Figure 5.15 plots the cumulative percentage of recovered tracers showing the dispersion of A and B tracers in each survey with respect to the downstream variation in bed character.

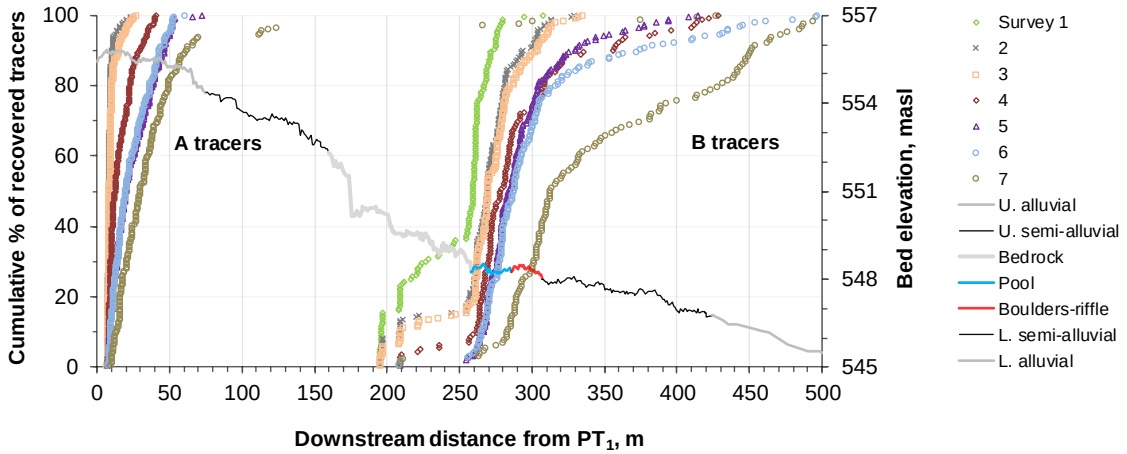

Figure 5.15. Cumulative distribution of tracer travel distances since seeding. The cumulative percentage in primary y-axis is the % of total number of recovered tracers. The secondary y-axis shows the longitudinal profile. The left-hand set of curves are for the A tracers (surveys 2 to 7) while the right-hand set are for the B tracers (surveys 1 to 7). Each survey has different colour curves: 1 (green), 2 (black), 3 (orange), 4 (brown), 5 (purple), 6 (blue) and 7 (khaki).

The A-tracer locations in Figures 5.14 and 5.15 have right-skewed distributions with a single mode, as has been found in previous tracer experiments in alluvial channels (Ferguson *et al.*, 2002), but the B-tracer distributions have two modes (one near the starting point, one near where pool meets boulder riffle) with a relative lack of tracers between those positions.

The first set of curves (A tracers) in Figure 5.15 shows that the tracers were dispersed slowly at a steady pace, whereas the steep parts of the curves in the second set (B tracers) show that the pool and boulder-riffle caused the most evident clustering. The B tracers curve 1 (survey 1) suggests that almost half of the recovered tracers were in the bare rock gorge while the other half were in the pool, whereas the other five curves (2 to 6) show that about two thirds of the recovered tracers were almost stationary in the pool and boulder-riffle. Curve 7 for the A tracers shows that a few tracers from the upper alluvial site travelled all the way to the lower alluvial reach. Similarly, curve 7 for the B tracers shows that a majority of the B tracers got past the pool and boulder-riffle area, a major bottleneck in the system, but about two fifths of the recovered tracers were still there, mainly in the boulder-riffle, despite the many floods experienced by that time. The extended tails of the curves indicate that the tracers that passed through the boulder-riffle had made relatively rapid progress on the less coarse semi-alluvial cover farther downstream. The cumulative percentages based on all seeded tracers, not just those recovered, are plotted in Figure 5.16.

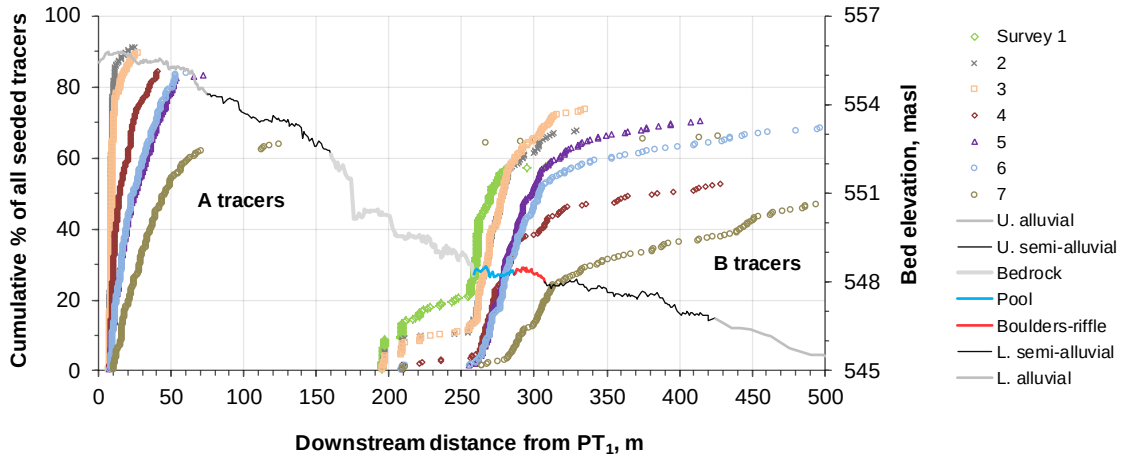

Figure 5.16. Cumulative percentage based on total number of seeded tracers.

The general trends of the curves in Figures 5.15 and 5.16 are broadly similar for the A tracers, except for the last survey which appears slightly different from the others, because of a slightly lower recovery rate. Because of the low recovery rates the B

tracers for surveys 1, 4 and 7 also appear slightly different in these two plots. Table 5.6 shows the percentage storage of B tracers, based on total recovered numbers. For bare rock gorge the percentage based on total seeded numbers are also shown (in brackets) where recovery was presumably ~100 %.

Table 5.6. Percentage storage of B tracers in channel segments of different character based on total recovered number. The percentage storage based on total seeded number is also shown for bare rock gorge (in brackets).

Survey no.	Bare rock gorge	Pool	Boulder-riffle	Lower semi-alluvial	Lower alluvial
1	45 (26)	54	< 1	< 1	0
2	21 (14)	63	12	4	0
3	18 (13)	60	15	7	0
4	8 (4)	49	22	17	4
5	3 (2)	45	33	17	2
6	3 (2)	41	32	16	8
7	2 (1)	8	31	36	23

Table 5.6 shows that total 45% of the B tracers found in the first survey were in the gorge whilst the percentage based on the seeded total was only 26%. The first survey was carried out at low flow and it is unlikely that any tracers that were on bare rock were missed. This implies that by the time of the first survey a high proportion of the B tracers (74%) had already entered the lower semi-alluvial reach. The storage percentage in the pool and boulder-riffle area, based on recovered number of tracers, remained almost the same in surveys 2 to 6 (71 – 78 %), though the centroid of the peak concentration was slightly shifted towards the boulder-riffle. The above discussion further confirm that the tracer mobility was highest on bare rock, intermediate in semi-alluvial and lowest in a fully alluvial bed and also demonstrates that the bed mobility was strongly related to bed slope, alluvial cover and boulder density.

5.2.2 Grain characteristics (size, mass and sphericity)

The analysis so far has viewed the tracer pebbles as a whole, without considering their individual characteristics; therefore the relationship of travel distances with tracer size, mass and shape are discussed in this section. Studies have shown that bedload transport in upland alluvial rivers is both size and shape dependent, with spherical particles tending to move faster than other shapes (e. g. Warburton & Demir, 2000), whereas studies in bedrock channels have shown that the bedload movement was size and shape

independent (e. g. Hodge *et al.*, 2011). Goode and Wohl (2010b) also found a size-independent transport in a reach where bedrock ribs were oblique to flow (~50% cover). Figure 5.17 shows how the transport distances of individual tracers from each set relate to grain size (measured *b*-axis diameter) up to surveys 6 and 7 (over 9 and 19 months), and also for the B tracers up to survey 1 (1.5 months). The A tracers for survey 1 are not shown as only a few had moved. The first survey for the B tracers was included to examine whether their transport over bare rock was size selective, the final survey was an obvious choice to include in the analysis, and the second last survey was included because of its higher recovery rates. Moreover, all the distances travelled by the A tracers in survey 6 were on a fully alluvial bed, however in the final survey 94 % of the recovered tracers were still in the upper alluvial reach, only 6 % had travelled through the bare rock and semi-alluvial beds.

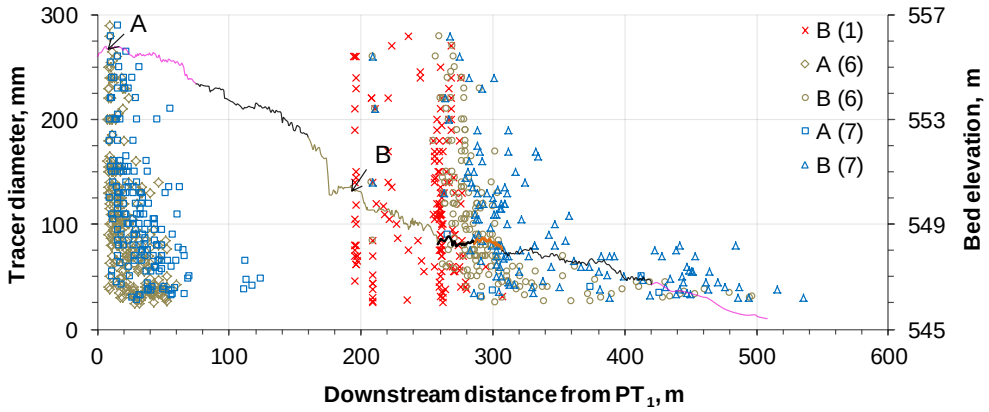

Figure 5.17. Relationship of tracer diameter (*b*-axis) with cumulative transport distance up to surveys 1 (red), 6 (khaki) and 7 (blue) for both sets of tracers. The left-hand data points are for A tracers while the right-hand data are for the B tracers; survey 1 for A tracers is not shown. The tracer installation sites A and B (x= 6 and 195 m) are shown. The channel long-profile shows the morphological reaches in different colour.

The A tracers data for surveys 6 and 7 (Figure 5.17) reveal that the tracers that travelled farther than most were all small ones, whereas the tracers that had hardly moved were of all sizes. This indicates that travel distance was size-dependent. On the other hand in the same period of time, the B tracer distances were not dependent on grain sizes in the first survey but were in the other two surveys. There is considerable scatter in the data but this is perhaps due to other controlling variables such as shape of the tracers, bed structure and positions in the river bed (Schmidt & Ergenzinger, 1992). This plot also shows that the individual distances of B tracers were higher than that of the A tracers.

The mean distances of movement of each half-phi size class between two successive surveys are plotted in Figure 5.18, for all surveys except survey 1 for the A tracers.

These graphs demonstrate the variation in mean distances between each size class across the surveys. The plots also show the 95 % confidence intervals which are appreciable because of the skewness of the distributions of travel distance. A general trend of decreasing mean transport distance with increasing sizes is seen in these plots. The B tracers during interval 0 – 1 (Figure 5.18a) however do not show a decrease in transport distance with increasing grain size, as also shown by Figure 5.17, and curve 1 – 2 shows only a slight decrease in transport distance with increasing size. As discussed in section 5.2.1, by the time of the first survey 74% of the installed tracers had passed through the bare rock gorge and most of the remaining ones did so during intervals 1 – 2 and 3 – 4 (Table 5.6).

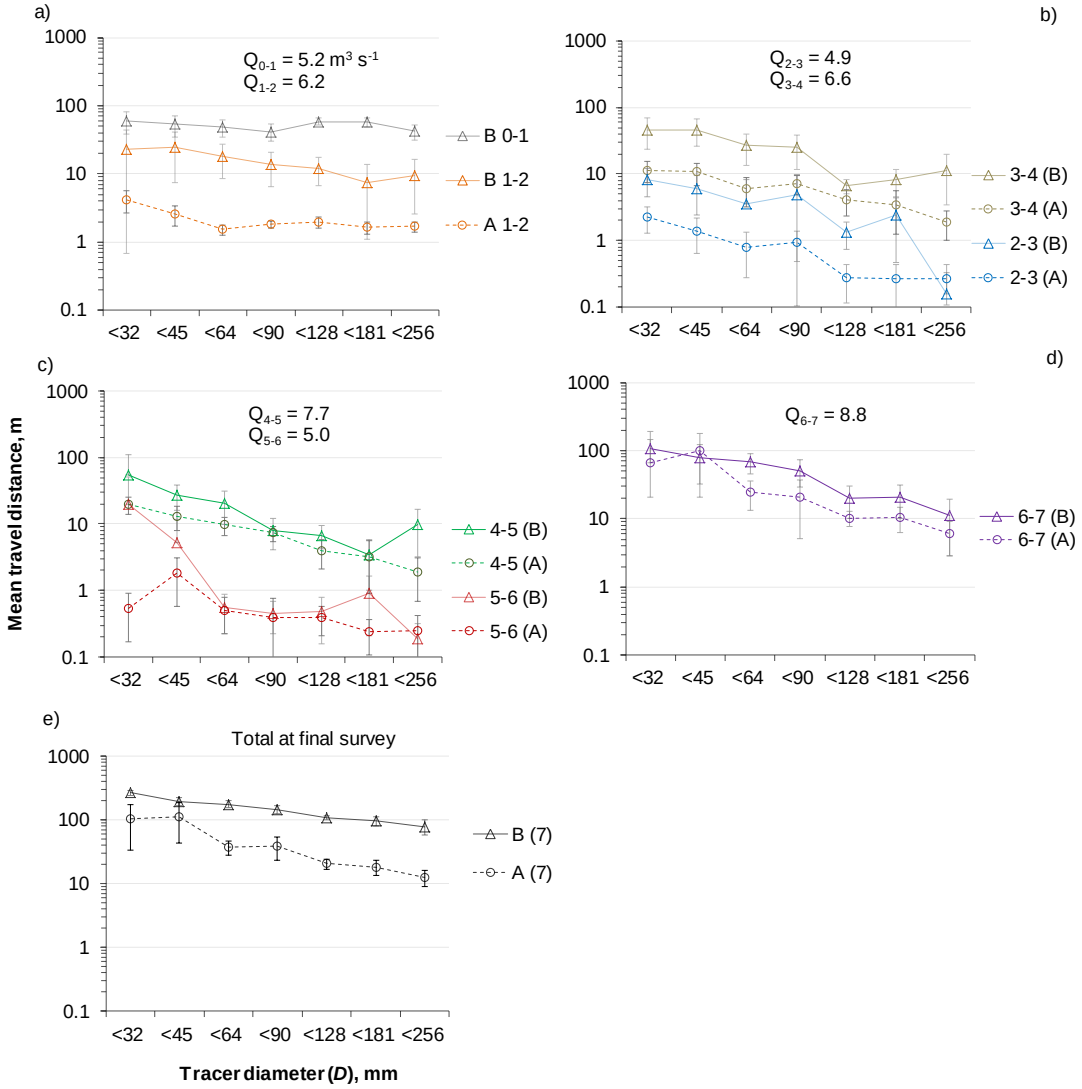

Figure 5.18. Mean transport distance for each half-phi size class for set A (broken lines) and set B (solid lines): (a) survey periods 0 – 1 (grey) and 1 – 2 (orange); (b) periods 2 – 3 (blue) and 3 – 4 (khaki); (c) 4 – 5 (green), 5 – 6 (red); (d) 6 – 7 (purple); (e) total or cumulative in final survey (black). 95% confidence intervals for mean distances are shown.

Period 2 – 3 (Figure 5.18b) generally shows a decrease in distance with increase in size for both set of tracers. However, the coarsest size class for the B tracers had only a small mean travel distance, even smaller than for the A tracer. This was because these tracers were already in the pool and the peak Q (4.9 m^3 s^{-1}) was below the transport threshold for that size in that location. The A tracers in that size range also hardly moved. For period 3 – 4 (Figure 5.18b) in the coarser range (D = 128 – 256), the B tracers show a slight increase in mean transport distance with increasing grain size but the confidence interval for the coarsest class is very wide. The A tracers, however, show a consistent size-selective trend over the full size range in this period.

Periods 4 –5 and 5 – 6 (Figure 5.18c) generally follow the trend of decreasing distance with increasing size, with some exceptions in the fine and coarse size range but the confidence levels are wide. The survey period 6 – 7 (Figure 5.18d) shows a consistent size-selective trend over the full size range for both sets of tracers.

In the final survey (Figure 5.18e), the total mean transport distance from seeding position decreases with increasing grain diameter for both sets of tracers, as found in tracer experiments in alluvial rivers (e.g. Church & Hassan, 1992; Ferguson & Wathen, 1998). However, the slope of the decreasing trend for the semi-alluvial bed (B tracers) is less steep than for the alluvial bed (A tracers) which indicates that the semi-alluvial bed has a slightly lesser degree of size selectivity than the fully alluvial bed. All these plots (Figure 5.18 a – e) reveal that the B tracers always had higher mobility than the A tracers for each period and for each half-phi size class, there are few exceptions but the confidence intervals there are high.

A more detailed statistical analysis was carried out to study the significance of size, mass and shape selectivity using the distances travelled by individual tracers. The analyses were undertaken for the three surveys shown in Figure 5.17 (*i.e*. survey 1 for B tracers, and surveys 6 and 7 for both A and B tracers). The plots are displayed as transport distance versus tracer diameter for each survey in Figure 5.19. Multiple regression analysis of distances travelled by individual tracers (L) is carried out with reference to three potential predictor variables: b-axis diameter D, mass M and Corey sphericity index $C = c/\sqrt{(ab)}$, where a, b, and c are axial dimensions. All variables were log-transformed to allow for nonlinear trends and multiplicative (rather than additive) effects. The appropriate regression model is $y = b_0 x_1^{b1} x_2^{b2} x_3^{b3} \ldots$, where y is the dependent variable L; x_1, x_2 and x_3 are predictor variables D, M and C respectively, b_0 is

the coefficient and b_1, b_2, b_3 are the slopes for respective predictor variables. Seven regressions are carried out for each survey: 3 predictors at a time (*D-M-C*), two at a time (*M-C*, *D-M*, *D-C*) and then individually (*D*, *M*, *C*). To obtain best-fit values of b_0, b_1, b_2, b_3 ... the equation is fitted as

$$\log(L) = A_0 + b_1 \log(D) + b_2 \log(M) + b_3 \log(C) \qquad \text{Eq. 5.1}$$

where A_0 (= log b_0) is the regression intercept.

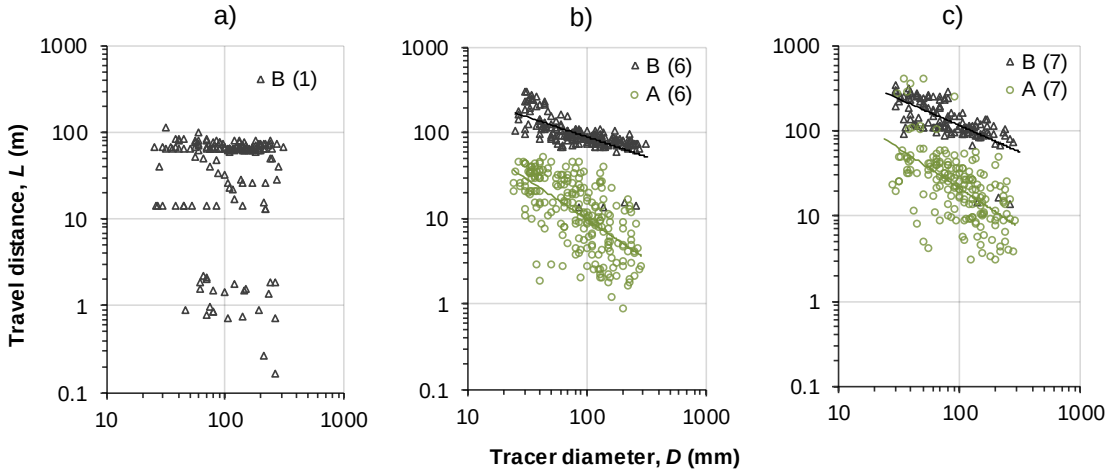

Figure 5.19. Tracer-pebbles travel distances (*L*) in relation to grain size (*D*), with power-law fits where statistically significant, for: (a) survey 1 (1.5 months); (b) survey 6 (9 months); and (c) survey 7 (19 months). The black and green markers represent B and A tracers respectively, and travel distance (*L*) is from the respective seeding site. The A tracers first met bedrock at 69 m whilst B tracers first encountered alluvial cover at 65 m.

The regression analyses of the A tracer travel distances up to survey 6 and 7 are presented in Table 5.7. The *p*-values are significance tests for the effect of each predictor by itself on the dependent variable, with the other predictors held constant; a very small *p*-value (e.g. < 0.05) indicates a statistically significant effect. The value of the coefficient of determination (R^2) was also useful to compare regressions with one, two and three predictors especially to check whether there was any improvement by adding an extra predictor.

The first analysis with three predictors at a time for survey 6 (9 months) data (Table 5.7) shows that the distance (*L*) is dependent on all three variables ($L \propto D^{0.55}M^{-0.50}C^{0.78}$, R^2 = 0.41). The exponent of *M* is negative which means the distance moved varied inversely with mass but the exponent of *D* is positive which cannot be right because for a given diameter (*D*) heavier pebbles tend to travel less far; and also the diameter and mass have a high mutual correlation with R^2 value of 0.94 (Figure 3.11).

Table 5.7. Regression analysis result of A tracers. The coefficients b_1, b_2, and b_3, the p values, adjusted R^2 and the equations are shown. NS = not significant ($p > 0.05$).

Predictors	Coefficients of			p-value			R^2	Equation	Remarks
	log (D)	log (M)	log (C)	log (D)	log (M)	log (C)			
Survey 6									
(i) D, M, C	0.55	-0.50	0.78	0.05	0.00	0.00	0.48	$L \alpha D^{0.55}M^{-0.50}C^{0.78}$	
(ii) M, C		-0.32	0.66		0.00	0.00	0.48	$L \alpha M^{-0.32}C^{0.66}$	
(iii) D, M	-0.03	-0.33		0.90	0.00		0.43	$L \alpha D^{-0.03}M^{-0.33}$	D: NS
(iv) D, C	-0.86		0.51	0.00		0.00	0.42	$L \alpha D^{-0.86}C^{0.51}$	
(v) D	-0.93			0.00			0.40	$L \alpha D^{-0.93}$	
(vi) M		-0.34			0.00		0.43	$L \alpha M^{-0.34}$	
(vii) C			1.00			0.00	0.12	$L \alpha C^{1}$	R^2 very low
Survey 7									
(i) D, M, C	0.38	-0.45	0.67	0.26	0.00	0.00	0.41	$L \alpha D^{0.38}M^{-0.45}C^{0.67}$	D: NS
(ii) M, C		-0.32	0.59		0.00	0.00	0.40	$L \alpha M^{-0.32}C^{0.59}$	
(iii) D, M	-0.09	-0.31		0.79	0.01		0.36	$L \alpha D^{-0.09}M^{-0.31}$	D: NS
(iv) D, C	-0.88		0.44	0.00		0.01	0.36	$L \alpha D^{-0.88}C^{0.44}$	
(v) D	-0.94			0.00			0.34	$L \alpha D^{-0.94}$	
(vi) M		-0.34			0.00		0.37	$L \alpha M^{-0.34}$	
(vii) C			0.83			0.00	0.08	$L \alpha C^{0.83}$	R^2 very low

The second analysis with D omitted from the regression does not reduce the R^2 value; this shows that the three-predictor model was inappropriate because of multicollinearility. The third analysis by omitting C reduces R^2 slightly from 0.48 to 0.43 but D is not significant ($p = 0.90$) again showing multicollinearity, and the fourth analysis by omitting M decreases R^2 slightly (0.42); it seems M predicts L slightly better than D does. The regression predicting L from D alone reduces R^2 slightly (0.40) but the regression from M alone increases R^2 slightly (0.43). The last analysis with C alone has much lower R^2 (0.12) than those predicting L from D or M alone which shows that the shape has less impact compared to M or D.

The survey 7 (19 months) data which relate to tracers moving mostly on alluvial cover give similar results. The regression with one predictor at a time shows that M predicts L slightly better ($R^2 = 0.37$) than D does ($R^2 = 0.34$) and the regression with C alone shows much lower R^2 (0.08) again showing shape has less impact than M or D. These analyses show that the transport distance in alluvial bed was mainly dependent on diameter or mass, but also the shape has some effect (survey 6: $L \alpha D^{-0.86}C^{0.51}$ with $p = 0.00$ for C; survey 7: $L \alpha D^{-0.88}C^{0.44}$ with $p = 0.01$ for C). In a regression of log(L) against log(M) the exponent of M is -0.34 ($p < 0.001$) for both 9 and 19 months' data,

with respective R^2 values of 0.43 and 0.37. Out of nine reaches in their study Ashworth and Ferguson (1989) found three had a significant dependence of L on M with exponent values between -0.29 to -0.33, which are very similar to the above values for the alluvial reach in Trout Beck. Similarly, Ashworth and Ferguson (1989) also found that three of nine regressions of distance against sphericity were significant, with exponents ranging from 0.60 to 1.10 which are very similar to Trout Beck values (0.83 and 1.0, $p < 0.001$). However, the R^2 values are very low (0.08, 0.12) for Trout Beck reaches, whilst these values are not available for the reaches studied by Ashworth and Ferguson (1989). The positive exponents of C show that spherical particles move farther than flat ones, in agreement with previous research (e.g. Komar & Li, 1986; Ashworth & Ferguson, 1989; Warburton & Demir, 2000).

The regression analyses of B tracer travel distances up to survey 1, 6 and 7 are summarised in Table 5.8. The results from the first survey of the B tracers show that the R^2 value for each of the seven analyses was just 0.01 or even less, showing that transport distances could not be predicted at all from any combination of grain characteristics. Likewise all the p-values are > 0.20, showing that none of the predictors had a statistically significant effect on travel distance. Transport in the bare rock gorge was therefore completely unselective with respect to diameter, mass and shape. The other two surveys, after 9 and 19 months, relate to tracer movement predominantly on semi-alluvial beds. The analyses for these surveys show that movement was size (and mass) selective, but not shape selective to a statistically significant degree (survey 6: $L \alpha D^{-0.46}C^{0.05}$ with $p = 0.55$ for C; survey 7: $L \alpha D^{-0.63}C^{0.00}$ with $p = 0.98$ for C). The exponents of the predictors are smaller than for the A tracers. In this respect the degree of selectivity in semi-alluvial beds can be considered as an average of the bare rock (fully non-selective) and alluvial beds (fully selective) or partially selective to size (and mass). This shows the travel distance is statistically significantly related to the grain size in alluvial and semi-alluvial beds, but not on bare rock.

Hodge *et al.* (2011) from a regression of log(L) against log(D) for the bedrock River Calder found $R^2 < 0.001$ and $p = 0.70$ which shows the individual grain size was not significant. This is comparable to $p = 0.41$ and $R^2 < 0.001$ for the Trout Beck bedrock gorge.

Table 5.8. Regression analysis result of B tracers. NS = not significant ($p > 0.05$).

Predictors	Coefficients of			*p*-value			R^2	Equation	Remarks
	Log (*D*)	Log (*M*)	Log (*C*)	Log (*D*)	Log (*M*)	Log (*C*)			
Survey 1									
(i) *D*, *M*, *C*	0.85	-0.37	0.25	0.32	0.22	0.53	0.01		None of the predictors are significant. R^2 very low
(ii) *M*, *C*		-0.08	0.03		0.30	0.92	0.01		
(iii) *D*, *M*	0.56	-0.28		0.43	0.29		0.01		
(iv) *D*,*C*	-0.16		0.01	0.45		0.97	0.00		
(v) *D*	-0.16			0.41			0.00		
(vi) *M*		-0.08			0.28		0.01		
(vii) *C*			0.10			0.75	0.00		
Survey 6									
(i) *D*, *M*, *C*	0.06	-0.18	0.17	0.75	0.00	0.05	0.45	$L \alpha D^{0.06}M^{-0.18}C^{0.17}$	*D:* NS
(ii) *M*, C		-0.16	0.16		0.00	0.03	0.45	$L \alpha M^{-0.16}C^{016}$	
(iii) *D*, *M*	-0.13	-0.12		0.37	0.02		0.44	$L \alpha D^{-0.13}M^{-0.12}$	*D*: NS
(iv) *D*, *C*	-0.46		0.05	0.00		0.55	0.42	$L \alpha D^{-0.46}C^{0.05}$	*C*: NS
(v) *D*	-0.47			0.00			0.43	$L \alpha D^{-0.47}$	
(vi) *M*		-0.17			0.00		0.44	$L \alpha M^{-0.17}$	
(vii) *C*			0.37			0.00	0.09	$L \alpha C^{0.37}$	R^2 very low
Survey 7									
(i) *D*, *M*, *C*	-0.07	-0.20	0.17	0.80	0.03	0.25	0.46	$L \alpha D^{-0.07}M^{-0.20}C^{0.17}$	*D*,*C:* NS
(ii) *M*, *C*		-0.22	0.19		0.00	0.11	0.47	$L \alpha M^{-0.22}C^{0.19}$	*C:* NS
(iii) *D*, *M*	-0.24	-0.15		0.27	0.06		0.46	$L \alpha D^{-0.24}M^{-0.15}$	*D*,*M*: NS
(iv) *D*, *C*	-0.63		0.00	0.00		0.98	0.45	$L \alpha D^{-0.63}C^{0.00}$	*C:* NS
(v) *D*	-0.63			0.00			0.46	$L \alpha D^{-0.63}$	
(vi) *M*		-0.23			0.00		0.47	$L \alpha M^{-0.23}$	
(vii) *C*			0.44			0.01	0.06	$L \alpha C^{0.44}$	R^2 very low

Summary

The regression analysis of distances moved by individual tracers verifies the pattern of size selectivity demonstrated by the mean distances for each half-phi size class (Figure 5.18). The distance has a highly significant ($p < 0.001$) inverse dependence (negative coefficient) on grain diameter (*b*-axis) or grain mass in alluvial and semi-alluvial reaches. But R^2 values are low (0.34 – 0.46) which ties in with the amount of scatter in Figures 5.17 and 5.19; and is also in line with the findings of other researchers (e.g. Hassan *et al.*, 1991; Ferguson & Wathen, 1998). For A tracers, the R^2 value increases only slightly (by 0.02 or less) if the Corey sphericity index of individual tracers is included as a second predictor. The shape effect is statistically significant in the alluvial reach but not in the semi-alluvial reach. In all cases the exponent to *C* was positive as expected (Ferguson & Wathen, 1998; Warburton & Demir, 2000). The above

discussions demonstrate that the transport was size-selective in the alluvial bed with a small but statistically significant shape effect, largely size-independent over the bare rock but started to become size-dependent, once tracers moved onto the semi-alluvial bed.

5.2.3 River discharge

The discussions in section 5.1.4 and Figure 5.18 show that the inter-survey mean transport distances are strongly related to the peak flood discharge in the intervening period. The smaller mean travel distances between surveys 5 and 6 and between surveys 2 and 3 tie in with the lower peak flood values; a peak Q below 5 $m^3 s^{-1}$ did not produce significant movement of the tracer pebbles (Table 5.4). A higher mobility of the A tracers during survey period 6 – 7 was observed (Figure 5.15), which ties in with the highest peak flood during the study period and a longer duration of competent flow associated with a large number of competent events: 9 out of 14 floods with Q values exceeding 5 $m^3 s^{-1}$ occurred during the period 6 – 7 (Table 5.1). River discharge is one of the key attributes that determines the total shear stress (τ) that drives the sediment transport process but a simple relationship between the peak Q and the mean transport distance does not exist because of differences in bed type, grain characteristics, local flow strength and duration of competent flows. This section discusses the temporal differences in peak Q and duration of high Q.

The travel distance of individual tracers between successive searches are plotted in Figure 5.20 against the peak discharge (Q_p) during the periods between searches. The aim of these plots is to try to learn something about threshold discharge.

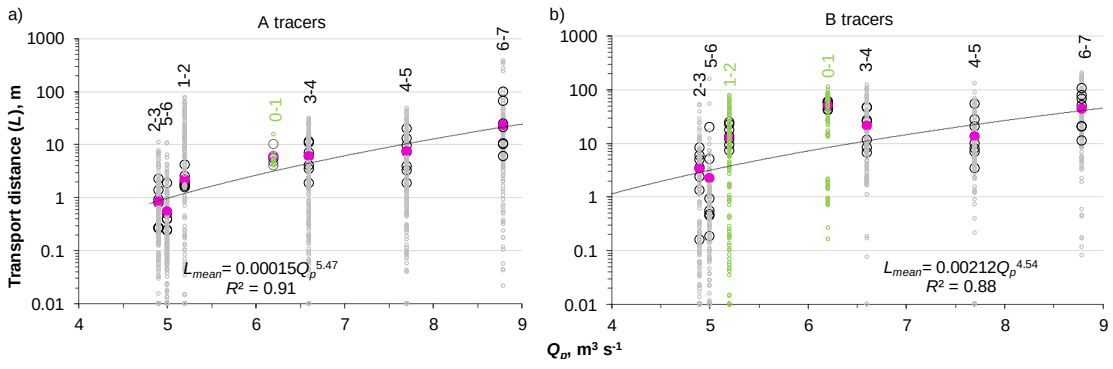

Figure 5.20. Relation between transport distance (L) and peak discharge (Q_p) for A and B tracers for different survey periods. The grey/green circles indicate the travel distance for each individual tracer, the big black circle represent the mean distance for each half-φ size-class and the pink circle shows the overall mean for the period. The power laws shown on the plots are fitted to the mean distances for each period. Periods shown in green (A: 0 –1 and B: 0 – 1, 1 – 2) are not included in the regression. A is significant at $p < 0.01$, and B at $p < 0.05$.

Figure 5.20 demonstrates that the inter-survey mean transport distance (L_{mean}) correlates strongly with the peak Q (R^2 for A and B tracers: 0.91 and 0.88). However, it is to be noted that these correlation are high also because of the averaged data. The A tracer data for the first survey was not included in the regression because only a few tracers had moved. Similarly, the B tracer data for the first two surveys, when the tracers were travelling in the gorge, were not included in the regression as the aim was to establish a relation for the semi-alluvial bed. Omitting the longer intervening period 6 – 7 from the analysis decreases R^2 from 0.91 to 0.84 for the A tracers and from 0.88 to 0.78 for the B tracers. As previously discussed, the 5 $m^3 s^{-1}$ peak discharge in survey period 5 – 6 (Table 5.4) transported the cobbles (64 – 256 mm) up to half a metre on the upper alluvial reach (A tracers) and by less than a metre on the lower semi-alluvial reach (B tracers). This suggests that the threshold discharge should be at least 5 $m^3 s^{-1}$ for the alluvial bed but it could be a little less for the semi-alluvial bed. The regression equation for the A tracers $L_{mean} = 0.00015 Q_p^{5.47}$ ($R^2 = 0.91$) suggests that a peak discharge of 5.0 $m^3 s^{-1}$ will generate a mean distance of 1 m in the alluvial bed (*i.e.* $L_{mean} = 1$ m when $Q_p = 5$ $m^3 s^{-1}$). The threshold discharge can be defined as a discharge which generates an appreciable amount of bedload movement (section 1.1.6), and this analysis shows it is reasonable to assume a threshold of 1 m mean travel distance to define Q_c based on tracer data. Based on this definition for threshold discharge, the equation for B tracers $L_{mean} = 0.00212\ Q_p^{4.54}$ ($R^2 = 0.91$) suggests a Q_c value of 3.9 $m^3 s^{-1}$ for a semi-alluvial bed (*i.e.* $Q_p = 3.9$ $m^3 s^{-1}$ when $L_{mean} = 1$ m). These Q_c values of 5 $m^3 s^{-1}$ for alluvial reach and 3.9 $m^3 s^{-1}$ for semi-alluvial reach will be further investigated in virtual velocity calculations in section 5.3 and also in chapter 7.

Figure 5.21 shows how the mean transport distances of pebbles (23 – 64 mm) and cobbles (64 – 256 mm) vary with peak Q. The plots show that that the mean distances are generally higher for higher peak discharges (except for B tracers for periods 0 – 1 and 1 – 2) and that the pebbles travelled higher mean distances than the cobbles. However, during period 0 – 1 for B tracers the mean distances for pebbles and cobbles are similar (52 and 50 m); this again shows that transport was size-independent in the bare rock gorge, whereas it was size dependent elsewhere.

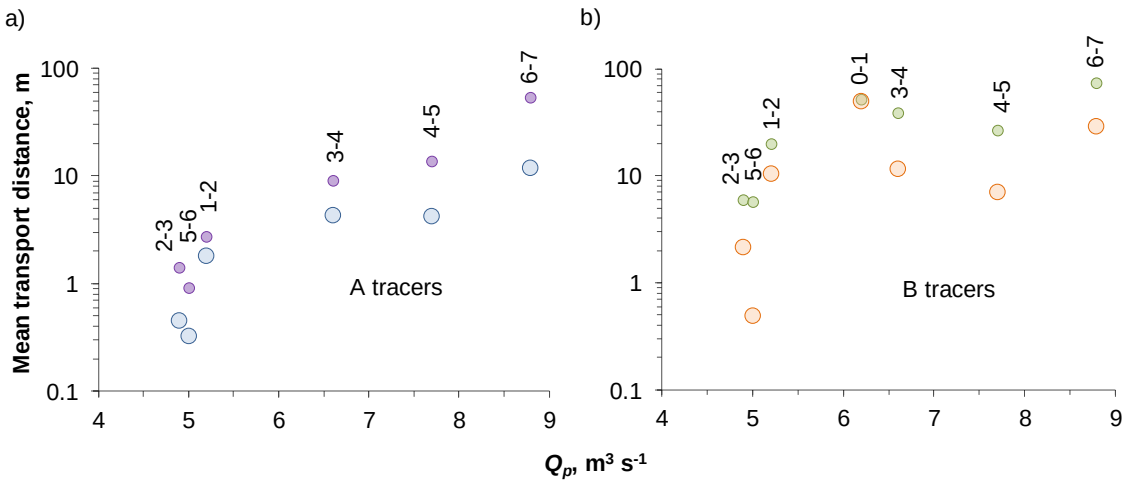

Figure 5.21. The mean distances for pebbles (small circles: purple/green) and cobbles (large circles: blue/orange) in relation to the peak *Q* for different survey periods. Note the B tracers pebbles and cobbles are collapsed for period 0 – 1. A pebbles are significant at $p < 0.001$, A cobbles are significant at $p < 0.01$, B pebbles are significant at $p < 0.05$, but B cobbles are not significant at $p = 0.05$.

Figure 5.20 shows a strong correlation between the peak *Q* and the mean travel distance which is also supported by Figure 5.21. However, to quantify the effect of *Q* on sediment transport it is essential to understand the duration of the competent flow that exceeds the threshold discharge (Q_c), since for similar values of peak *Q* the mobility can be different if the duration of competent flow is different. For example, if the Q_c for bare rock gorge is 3 $m^3 s^{-1}$, then the duration of the competent flow for period 2 – 3 and 5 – 6 will be 7.3 and 13 hours respectively, whereas the peak *Q* for both these periods are about the same (4.9 and 5 $m^3 s^{-1}$). Table 5.9 shows the duration of flow in each survey period that exceeded various alternative values of Q_c, from 2 to 6 $m^3 s^{-1}$. This table shows that a discharge of 5 $m^3 s^{-1}$ was exceeded for only 28 hours during the entire 19-month study period, and out of these 18 hours were during the last survey interval (6 – 7). This explains why some of the A tracers moved substantial travel distances during this interval. Similarly, for period 0 – 1 when the majority of the B tracers had passed through the gorge the number of hours exceeding 3 and 5 $m^3 s^{-1}$ were only 4.5 and 1.8 hours respectively, and the B tracers could have travelled the gorge at relatively lower discharge (impact sensor data in chapter 6 indicates this), however the peak *Q* was fairly high (Table 5.9). The B tracers were still in their original positions at a discharge of 1 $m^3 s^{-1}$ (49 N m^{-2}) 8 days after they were emplaced, so the critical discharge in the gorge was at least that high.

Table 5.9. Number of hours (T) exceeding alternative values of Q_c from 2 – 6 $m^3 s^{-1}$ during each survey interval.

Survey period	Peak Q $m^3 s^{-1}$	Duration (hours) exceeding alternative values of Q_c				
		Q_c = 2 $m^3 s^{-1}$	3	4	5	6
0 – 1	6.2	13	4.5	2.8	1.8	0.5
1 – 2	5.2	37	15	4.3	0.8	0
2 – 3	4.9	13	7.3	2.5	0.0	0
3 – 4	6.6	70	20	6.5	3	1.8
4 – 5	7.7	142	35	7.3	4.5	2.3
5 – 6	5.0	25	13	5.3	0	0
6 – 7	8.8	178	88	46	18	6
Total (0 – 7)	8.8	477	182	74.3	28	10.5

The threshold discharge varies between the reaches and depends on various parameters such as slope, bed roughness, sediment cover, and form drag from in-channel structures. The threshold discharge will be estimated from bed load impact sensor data (Chapter 6) and will be compared with these values in chapter 7. The relationship of travel distance with duration of competent flow for three different values of Q_c = 3, 4 and 5 $m^3 s^{-1}$ is shown in Figure 5.22. These plots show that a power law fits well, with R^2 values ranging from 0.67 – 1.0 for the A tracers and 0.64 – 0.76 for the B tracers for three alternative values of Q_c. As in Figure 5.20, period 0 – 1 for the A tracers and periods 0 – 1 and 1 – 2 for the B tracers are not included in the regression equation.

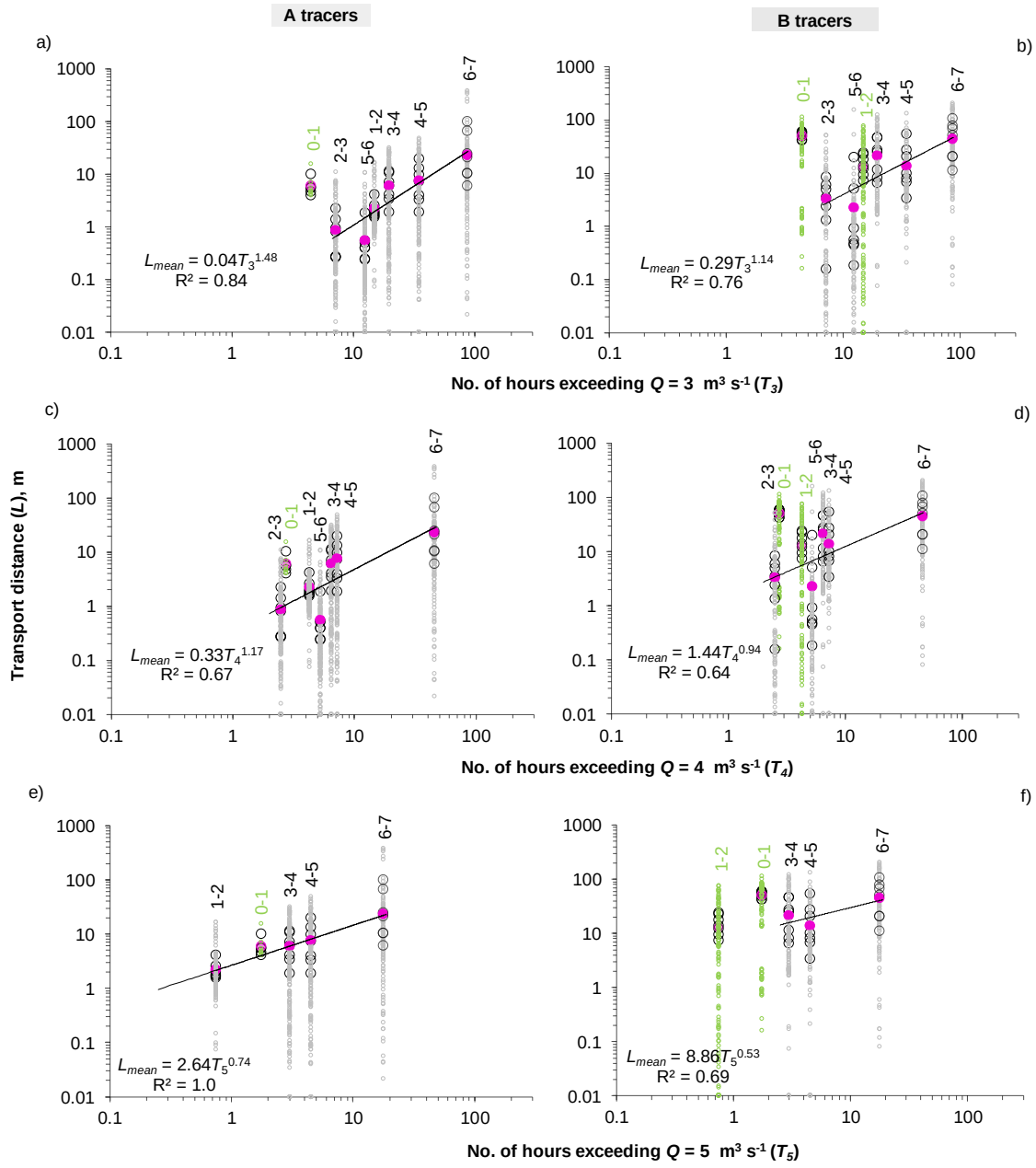

Figure 5.22. Relationship between travel distance and duration of flow exceeding 3 $m^3 s^{-1}$ (a, b), 4 $m^3 s^{-1}$ (c, d) and 5 $m^3 s^{-1}$ (e, f) for A and B tracers. T_3, T_4 and T_5 indicate hours exceeding 3, 4 and 5 $m^3 s^{-1}$ discharges. The left-hand plots (a, c, e) are for A tracers and the right-hand plots (b, d, f) are for B tracers. The power relations are fitted to mean travel distances for each period (pink circles); periods shown in green are not included in the regression. The fitted trends in (b) and (d) are not significantly different from horizontal at the p = 0.05 significance level.

Assuming a critical discharge of 5 $m^3 s^{-1}$, the regression equation for alluvial bed (L_{mean} = 2.64 $T_5^{0.74}$ where T_5 is number of hours the discharge exceeding 5 $m^3 s^{-1}$, Figure 5.22e) suggests that to generate a mean distance of 1 m, the river discharge should be above 5 $m^3 s^{-1}$ for at least 0.27 hours (16 minutes). Likewise, on the semi-alluvial bed (L_{mean} = 8.86 $T_5^{0.53}$, Figure 5.22f) the river discharge should exceed 5 $m^3 s^{-1}$ for 0.02 hours (~1 minute) to produce a mean distance of 1 m.

5.2.4 Shear stress

The other key variable that controls the tracer mobility is the local flow strength, as measured by shear stress or stream power per unit bed area. The shear stress $\tau = \rho gRS$ (Eq. 1.20) takes into account the hydraulic radius R (or depth) and the slope whereas the unit stream power $\omega = \rho gqS$ (where ω is in W m^{-2}, and q the unit discharge in m^2 s^{-1}) uses the unit discharge and slope; this study uses the shear stress approach. Chapter 4 discussed the temporal and spatial differences in shear stress and effective stress (Sections 4.5 and 4.6), therefore this section will only briefly discuss the relation of tracer distances with peak shear stresses in the alluvial and semi-alluvial parts of the study site. As there are only two survey intervals that represent the tracer transport in the rock gorge (B tracers for periods 0 – 1 and 1 – 2), the regression equation for the bare rock part of the study site is not fitted.

The relation between travel distance and maximum shear stress (τ_{max}) for each period is shown in Figure 5.23. The τ_{max} values used for the A tracers is the maximum shear stress value for sub-reach F1 during the survey interval. As discussed in chapter 4 (section 4.5), because of complex bed topography the hydraulic radius for the longer sub-reach PT_1 to PT_2 in the upper alluvial reach is not accurate, so the maximum shear stress associated with the peak discharge during each period is calculated using the equation $\tau_{max} = 22.5Q_p^{0.45}$ (Figure 4.32). The τ_{max} values used for the B tracers are the peak shear stress values in the longer sub-reach (between two PTs) for different survey periods, corresponding to where most of the tracers were: PT_3 – PT_5 for periods 0 – 1 and 1 – 2 when most tracers were on bare rock, PT_5 – PT_6 for periods 2 – 3 to 5 – 6 when most tracers were in the upper part of the lower semi-alluvial reach (160 – 360 m) (Section 2.3.2), and PT_6 – PT_7 for period 6 – 7 when many tracers had moved into the lower part of the lower semi-alluvial reach (360 – 420 m) in which the sediment cover and boulder density decreases downstream before the sudden change to a fully alluvial bed beyond 420 m.

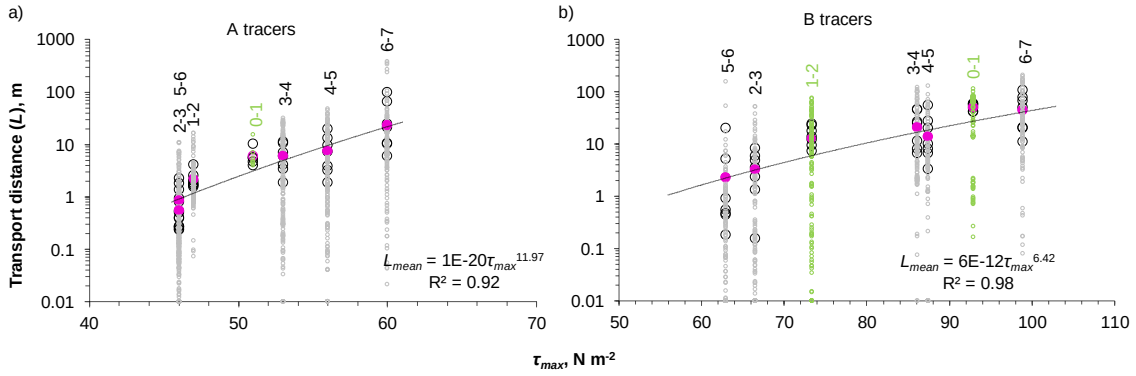

Figure 5.23. Relation between transport distance (L) and maximum shear stress (τ_{max}) for A tracers (a) and B tracers (b) for different survey periods. The grey/green circle represents the travel distance for each individual tracer, the black circle represents the mean distance for each half-phi size class and the pink circle show the overall mean for the period. The power laws are fitted for mean distances for each period and the equations are shown. Periods shown in green are not included in the regression. Both A and B correlations are significant at $p < 0.05$.

Figure 5.23 shows a strong correlation between inter-survey mean transport distance (L_{mean}) and τ_{max} (R^2 = 0.92 for alluvial bed and 0.98 for semi-alluvial bed). The R^2 values suggest the relationship of transport distance with maximum τ appears slightly better defined than with peak Q (Figure 5.20). To yield a mean distance of 1 m the τ values required for the alluvial bed ($L_{mean} = 1 \times 10^{-20} \tau_{max}^{11.97}$) and semi-alluvial bed ($L_{mean} = 6 \times 10^{-12} \tau_{max}^{6.42}$) are 47 and 56 N m^{-2} respectively. If 1 m mean distance is taken to be a transport threshold, as assumed in previous (section 5.2.3), then these values can be considered as critical shear stress (τ_c) values for alluvial and semi-alluvial beds. The lowest peak shear stress between two survey intervals during the entire study period was 46 N m^{-2} for alluvial reach and 63 N m^{-2} for semi-alluvial reach; using the regression equations these lowest τ_{max} values will yield mean distances of 0.80 m in the alluvial and 2.2 m in the semi-alluvial reach. The shear stress in the boulder-riffle area was high (Section 4.5) but the effective stress was also high (and the excess stress τ- τ_c was low) because of high flow resistance from the boulders (Section 4.6); this explains the accumulation of tracer pebbles in the pool and boulder-riffle. The excess shear stresses were high in the bare rock gorge (Chapter 7) which ties in with the high mobility there, but low in the alluvial reach where the bedload mobility was also low.

Summary of threshold discharge (Q_c) and threshold shear stress (τ_c)

The threshold values of discharge and shear stress are estimated from the tracer data by two approaches: based on the dispersion of the tracers, and regression of mean travel distance with the peak discharge or maximum shear stress between successive surveys.

The estimated Q_c and τ_c values are summarised in Table 5.10 and how these values were derived is discussed below.

Table 5.10. Critical discharge Q_c ($m^3 s^{-1}$) and critical shear stress τ_c ($N m^{-2}$) values for alluvial, bare rock and lower semi-alluvial reach from tracer data. Because of limited data, no power law was fitted for the bare rock gorge.

Description	Upper Alluvial		Bare rock gorge		Lower semi-alluvial	
	Q_c	τ_c	Q_c	τ_c	Q_c	τ_c
(i) Tracer dispersion (Section 5.1.3)	5.0	47	<5.2	73	5.0 – 6.6	63 – 91
(ii) Power-law fitting (Sections 5.2.3 and 5.2.4)	5.0	47	-	-	3.9	56

The tracer dispersion discussion in section 5.1.3 shows that there was little movement in the upper alluvial reach at discharge below 5 $m^3 s^{-1}$, therefore it is likely that the critical discharge in the upper alluvial reach should be at least 5 $m^3 s^{-1}$; the respective shear stress (τ_c) value calculated using τ-Q equation is 47 N m^{-2} (Table 4.15). In the bare rock gorge, it is difficult to estimate the critical discharge from tracer data as most of the tracers moved in the first and second survey intervals when the peak discharges were 6.2 and 5.2 $m^3 s^{-1}$ respectively. It is likely that the Q_c in the rock gorge is less than 5.2 $m^3 s^{-1}$ and it could be much lower. The shear stress at 5.2 $m^3 s^{-1}$ discharge in the gorge is 73 N m^{-2} (Table 4.15). In the pool and boulder-riffle area few tracers moved when the flow was around 5 $m^3 s^{-1}$ but appreciable movement occurred when the peak Q was 6.6 $m^3 s^{-1}$. For other parts of the lower semi-alluvial reach the tracer dispersion suggests that Q_c could be a little less than 5 $m^3 s^{-1}$. The equivalent shear stress for 5 and 6.6 $m^3 s^{-1}$ discharges in the lower semi-alluvial reach are 63 and 91 N m^{-2} (Table 4.15).

Assuming a transport threshold of 1 m mean distance, the L_{mean}-Q_p power-law relation gives a Q_c value of 5.0 $m^3 s^{-1}$ for the upper alluvial reach and 3.9 $m^3 s^{-1}$ for the lower semi-alluvial reach. Similarly, the L_{mean}-τ_{max} power-law relation gives τ_c values of 47 and 56 N m^{-2} respectively for the alluvial and lower semi-alluvial reaches.

In this investigation detailed hydraulic calculations were performed for five sub-reaches F1 to F5 (Section 2.5). Here the threshold discharge (Q_c) and threshold shear stress (τ_c) values are also estimated for each sub-reach so that a better link can be established with the detailed bulk hydraulics there. Table 5.11 shows the Q_c and τ_c values for sub-reaches. The Q_c values are same as for three morphological reaches shown in Table

5.10. However, the τ_c values are calculated using the τ-Q power-law equations for respective sub-reaches (Fig 4.32). These values will be further discussed in Chapter 7.

Table 5.11. The critical discharge (Q_c) and critical shear stress (τ_c) for sub-reaches F1 to F5.

Sub-reach	Q_c, $m^3 s^{-1}$	τ_c, $N m^{-2}$
F1	5.0	47
F2	< 5.2	< 119
F3	5.0 – 6.6	107 – 117
F4	3.9 – 5.0	44 – 52
F5	3.9 – 5.0	63 – 72

5.3 Virtual velocities

As mentioned in section 3.2.5 the virtual velocities are calculated to quantify the bedload mobility. Coarse bedload transport is intermittent (Stelczer, 1971); the particles travel in a number of brief steps and remain at rest when the flow in the channel is below the threshold value (Q_c). Virtual velocity (V_v) as initially introduced by Einstein (1937) and used by several researchers (e.g. Hassan *et al.*, 1992; Ferguson & Wathen, 1998; Haschenburger & Church, 1998) allows comparison of sediment movement in rivers with different discharge regimes, and can also be used to estimate sediment transport rate if the width and depth of active transport are known (Haschenburger & Church, 1998). This study will not estimate sediment transport rates but virtual rate of travel will be used to quantify and compare the bedload mobility across different cover types, as done by Hodge *et al.* (2011). The virtual velocities are calculated by dividing the travel distance, mean or individual tracer distance, for each survey intervals by the duration of competent flow. Since the virtual velocity does not include the period when there was no bedload transport, this is a better approach to quantify the bedload mobility.

The calculation of virtual velocity requires the duration of competent flow, which assumes the threshold discharge (Q_c) is known. In this analysis the virtual velocities for different reaches are calculated for various alternative threshold discharges using the mean travel distances for the chosen period. This analysis also estimates the V_v using the individual tracer distances for some assumed values of threshold discharges. The impact sensor data (Chapter 7) show that the Q_c in the rock gorge could be as low as 2.4 $m^3 s^{-1}$ whilst the tracer data shows it could be as high as 5.2 $m^3 s^{-1}$ or even higher (Table 5.10).

Therefore there is no single definite value of Q_c for the bare rock reach but 3 $m^3 s^{-1}$ can be a reasonable approximation for this analysis. Likewise, 5 $m^3 s^{-1}$ for the upper alluvial reach and 4 to 5 $m^3 s^{-1}$ for most part of the lower semi-alluvial reach can be a reasonable approximation of threshold discharges for this analysis (Table 5.10).

Figure 5.24 shows the virtual velocities for the upper alluvial, bare rock and semi-alluvial reaches using various alternative Q_c values. The V_v values in this plot are calculated using the mean travel distances of all recovered tracers (Table 5.4). The duration of competent flows is taken from Table 5.9. Virtual velocity in the bare rock reach is calculated by using the B tracers for survey period 0 – 1 because during that period they were travelling in the gorge. Similarly, the survey interval 2 – 6 is chosen to estimate the virtual velocity in alluvial and semi-alluvial reaches because during that period all A tracers were in the upper alluvial reach and all B tracers were in the lower semi-alluvial reach.

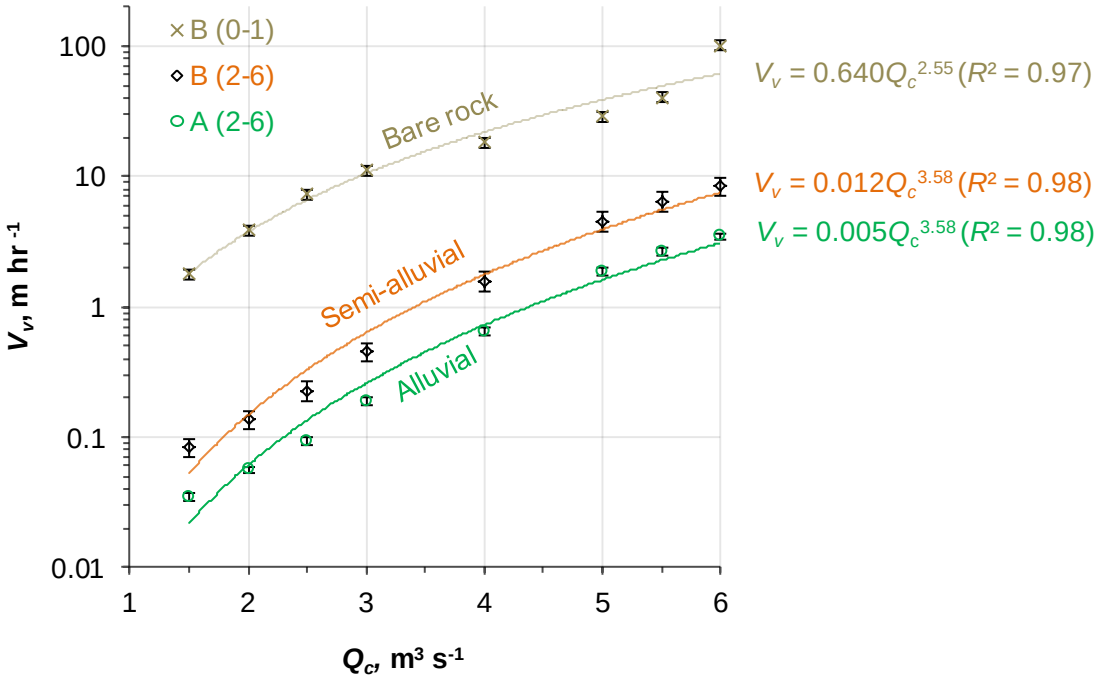

Figure 5.24. Relationship of virtual velocity V_v (based on mean distance and its 95% confidence interval) for various alternative Q_c values for different reaches: bare rock (B: 0 – 1, khaki), semi-alluvial (B: 2 – 6, black) and alluvial (A: 2 – 6, green). The fitted power-law equations and R^2 values are shown.

For any given value of threshold discharge (Q_c), the V_v is highest for the bare rock reach, lowest for the alluvial reach and intermediate for the semi-alluvial reach (Figure 5.24). The threshold values possibly differ between reaches, but this plot can be used to estimate the virtual velocity if the Q_c value for a reach is known. For example, if the

bare rock, semi-alluvial and alluvial reaches have Q_c values of 3, 4 and 5 $m^3 s^{-1}$ respectively, then the virtual velocity values for these reaches will be 10.5, 1.7 and 1.6 m hr^{-1} respectively. These virtual velocity values indicate that the bedload mobility over bare rock reach was 7 times higher than that in the alluvial reach, but the mobility in the semi-alluvial and alluvial reaches is almost the same. However, the travel distances for alluvial and semi-alluvial reaches (Table 5.4 and Figure 5.19 b) suggest that the mobility in the semi-alluvial reach was higher than that in the alluvial reach, so the chosen Q_c of 4 $m^3 s^{-1}$ for the semi-alluvial reach seems to be a little low. This also suggests that the Q_c of 3.9 $m^3 s^{-1}$ as suggested by the power relation of mean travel distance and peak Q (Table 5.10) is low. If the semi-alluvial reach also has a Q_c value of 5 $m^3 s^{-1}$ the virtual velocity will be 3.8 m hr^{-1}, which shows the mobility in semi-alluvial bed is about 2 times as on the alluvial bed and over bare rock was about 3 times as on the semi-alluvial bed.

The virtual velocities are also calculated using the individual tracer distances which are plotted in Figure 5.25. For the bare rock reach the power law-equation for Q_c = 3 $m^3 s^{-1}$ is $V_v = 8.7D^{0.03}$ (Figure 5.25a). The exponent (0.03) and R^2 (0.00) values clearly indicate that the virtual velocities in the bare rock gorge are size independent. This is similar to what Hodge *et al.* (2011) found in the predominantly bedrock River Calder ($V_v = 8.09D^{0.05}$, $R^2 = 0.00$).

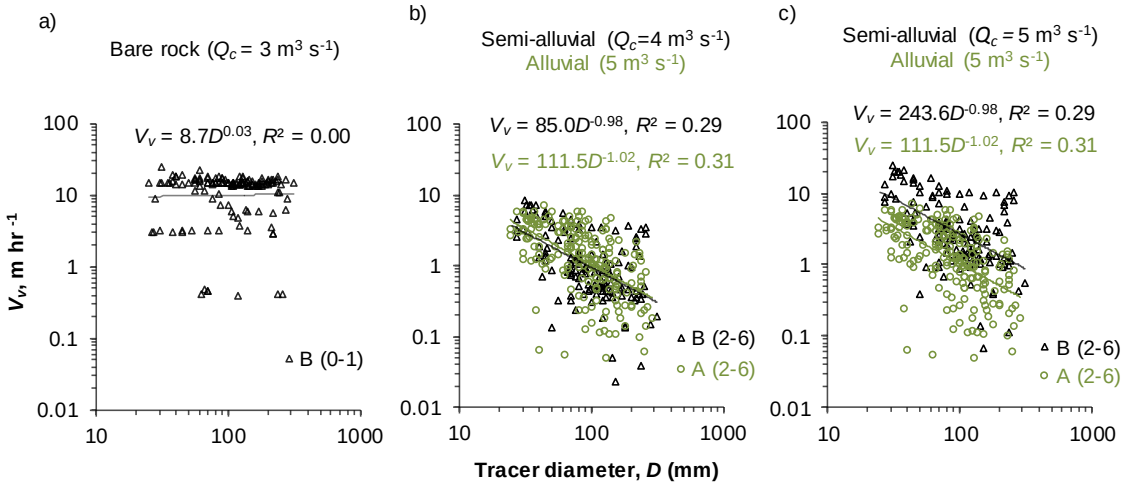

Figure 5.25. Virtual velocity (V_v) against grains diameter (D) for individual tracers: a) B tracers for survey period 0 –1 at Q_c = 3 $m^3 s^{-1}$ (bare rock); b) B tracers with Q_c = 4 $m^3 s^{-1}$ (semi-alluvial: black) and A tracers with Q_c = 5 $m^3 s^{-1}$ (Alluvial: green) for period 2 – 6; c) Q_c = 5 $m^3 s^{-1}$ for both B tracers (semi-alluvial: black) and A tracers (alluvial: green) for period 2 – 6. Best-fit power-law equations are shown. The exponents of the trends in (b) and (c) are significantly different from zero at p <0.05 but those in (a) are not.

The virtual velocity plots for the semi-alluvial reach (with Q_c = 4 m^3 s^{-1}) and alluvial reach (Q_c = 5 m^3 s^{-1}) are shown in Figure 5.25 b. The regression equations for semi-alluvial and alluvial beds are $V_v = 85.0D^{-0.98}$ (R^2 = 0.29) and $V_v = 111.5D^{-1.02}$ (R^2 = 0.31) respectively. These exponent values (<< 0) indicate that the virtual rate of transport was size dependent, though the R^2 values are small. These equations show that the exponents for two reaches are about the same (-0.98 and -1.02) but the coefficients are different (85 for semi-alluvial, and 111.5 for alluvial) which implies that the virtual velocity (or the mobility) in semi-alluvial reach is lower than in the alluvial reach. This arises due to the different threshold values applied to the two bed conditions, and shows similar results to the earlier approach based on mean travel distances (Figure 5.24). Therefore the virtual velocities with Q_c = 5 m^3 s^{-1} for both semi-alluvial and alluvial reaches are plotted in Figure 5.25 c which give the equations $V_v = 243.6\ D^{-0.98}$ (R^2 = 0.29) for semi-alluvial and $V_v = 111.5D^{-1.02}$ (R^2 = 0.31) for the alluvial reaches. The exponents again are about the same but the coefficient for the semi-alluvial equation (243.6) is about 2.2 times higher than that of alluvial reach which indicates that the virtual rate of transport is about 2.2 times higher in semi-alluvial than in an alluvial reach, which is similar to what is suggested by the V_v plot based on mean distances (Figure 5.24). Hodge *et al.* (2011) found $V_v = 172D^{-2.03}$ (R^2 = 0.17) for a semi-alluvial channel with 80 % sediment cover (South Fork Eel) and $V_v = 10.67D^{-0.23}$ (R^2 = 0.02) for a alluvial channel (Allt Dubhaig). This comparison shows that the R^2 values for Trout Beck are higher; however, the exponents vary greatly, possibly because they depend on other variables such as bed character and sediment cover. Hodge *et al.* (2011) showed that the tracer pebbles in River Calder had a higher virtual velocity than in the other two channels with higher sediment cover, and the tracer movement in the bedrock was not size selective whereas it was in the other two rivers; this is similar to what is found in Trout Beck.

In summary, calculation of virtual velocities is useful in order to make a direct comparison of bedload mobility indifferent rivers or in reaches of different bed character, and is also useful to examine size selectivity. The virtual velocities are calculated based on mean travel distances as well as the transport distance of the individual tracers, and both approaches give similar results. With a threshold discharge of 3 m^3 s^{-1} for bare rock and 5 m^3 s^{-1} for semi-alluvial and alluvial reaches, the virtual rate of travel in bare rock was about seven times higher than in an alluvial reach, and 3 times higher than in semi-alluvial reach. Similarly, the virtual transport rate in the semi-alluvial reach was about 2 times higher than in the alluvial reach. The virtual velocity

plots for individual tracers suggest that transport was non-size selective on bare rock but was size-selective in the semi-alluvial and alluvial reaches. These plots demonstrate that virtual velocities are very sensitive to the choice of Q_c, but the analysis of the virtual velocity plots confirms that the threshold discharge of 4 m^3 s^{-1} for semi-alluvial reach is little low but 5 m^3 s^{-1} is plausible.

5.4 Chapter summary

This chapter has reported the results of a tracer pebble experiment in Trout Beck (Research Questions 2 and 3). Tracer movement was monitored for 19 months from August 2013 using two sets (each 270) of magnetic tracer pebbles covering the grain size distribution of the in-situ sediment from 23 to 256 mm. Tracers were placed in the upper alluvial reach (set A) and on bare rock in the gorge (set B), allowing grain dynamics to be tracked over different bed characters but under the same flow conditions. Tracers were resurveyed six times over first nine months during which A tracers moved very slowly, with none found to have reached the distal end of the upper alluvial zone (69 m from seeding site) whilst the B tracers moved at low discharges and dispersed much farther and some of them even entered the lower alluvial reach (225 m from seeding site). By that time the pattern of dispersion was obvious and just one final survey was made, ten months after the previous survey at 19 months. Concurrent measurements of bulk hydraulics (Chapter 4) and bedload impact counts (Chapter 6) at various locations in the channel aided interpretation of the tracer measurements.

The overall average recovery rate from seven surveys was 85% for A tracers and 63% for B tracers. In the final survey, 66% of A tracers were recovered, with a range 24 – 97% for half-phi size classes and 48 % of B tracers were recovered with a range 22 – 65 % for each half-phi size classes. The spatial distribution and depositional pattern of the tracers varied across the survey periods. In the upper alluvial site the tracers were dispersed moderately evenly. Almost all of the A tracers (~95%) in the upper alluvial reach were found on the surface of channel alluvium in isolated form, very few were in small clusters, and only a small number (5%) were partly or fully buried and by no more than 0.10 m. The general pattern of the distribution was that the tracers seeded in the upper alluvial reach moved slowly and remained concentrated within the first 50 m of the reach until the second last survey. By and large most of the tracers in the lower semi-alluvial reach were also found on the alluvial cover, and only about 10% were found buried and by no more than 0.15 m. The few B tracers that were found still in the

rock gorge in the second survey were either in grooves or pot-holes or in small patches. The vast majority of the B tracers were concentrated in the pool and boulder-riffle throughout the study period, and 39% of the recovered tracers (19% of total seeded) were still in the pool or boulder-riffle even in the final survey.

By the time of the first survey after one and a half months a substantial number of the B tracers had quickly dispersed through the bare rock gorge in a fairly high flood of 6.2 $m^3 s^{-1}$, leaving behind only 26% of the seeded tracers (45% of the recovered total) in the gorge, and entered the pool and boulder-riffle area at the start of the lower semi-alluvial reach. During the same period of time only ten tracers had moved in the upper alluvial site and none by more than 15 m. The survey intervals 1 – 2, 2 – 3 and 5 – 6 during which the peak discharges were around 5 $m^3 s^{-1}$ did not yield a significant movement of the tracer pebbles (cobbles moved < 1 m) in the reach as a whole even though some of the smaller tracers moved considerable distances. It was observed that most of the B tracers were concentrated in the pool and boulder-riffle throughout the study period. 75% of the recovered tracers were found in the pool and boulder-riffle area in the second survey and there was little change in this percentage up to the sixth survey, though the peak concentration gradually moved from the pool into the boulder riffle. However during the period between the last two surveys (6 – 7), both sets of tracers were substantially dispersed, because of a much longer duration of competent flow including the highest peak *Q* for the entire study period.

Tracers placed in the bare rock reach were far more mobile than those in the alluvial reach. By the time of the second survey after a period of two months the total mean travel distance of the A tracers, which were travelling in the upper alluvial reach, was only 2.4 m whereas it was 70 m for the B tracers which were travelling in the rock gorge. The transport was largely size independent over the purely bare rock reach because of the lower friction angle and higher effective shear stress, which will be discussed along with the results from bulk hydraulics (Chapter 4) in Chapter 7. Once these tracers reached the lower semi-alluvial reach, transport distances became relatively shorter, though still greater than in the purely alluvial reach (total mean travel distance in month 9 was 17 m for A tracers and 107 m for B tracers), and became size selective. The A tracers displayed size-selective transport throughout the experimental period. The multiple regression analysis of distances travelled by individual tracer pebbles also confirms the pattern of size selectivity shown by the mean distances for

each half-phi size class. The distances in alluvial and semi-alluvial beds have a highly significant inverse dependence on grain size ($p < 0.001$). There is a small but statistically significant shape effect in the alluvial reach, with more spherical tracers tending to travel farther, but not in the semi-alluvial reach.

The tracer data show that the bed character, grain sizes, the peak discharge and local hydraulic conditions are the main controlling factors in the movement of sediment through the reach. The bed type determines the critical discharge for significant transport of the tracer pebbles, therefore is very important for the conveyance of sediment downstream. The analysis shows that the boulder-riffle and its backwater zone at the distal end of the gorge (pool) are the most favourable places for sediment accumulation. Other areas of frequent deposition are gravel bars upstream of large boulders and the exposed bars in the bank, which clearly imply that the bed morphology has a strong control on coarse sediment movement. The cover distribution correlates with the tracers' concentration, the tracers tended to accumulate in places where there was a sudden downstream increase in sediment cover. The sediment mobility also ties in with the percentage cover; very low in the fully alluvial reach, very high in the sediment-free bare rock gorge and intermediate in the semi-alluvial reach. The data clearly demonstrate that the bed mobility was strongly related with bed slope, alluvial cover and boulder density.

The inter-survey mean transport distances are highly correlated with the peak discharges and maximum shear stresses. By considering 1 m mean distance as the definition of a transport threshold the critical discharge (Q_c) values suggested by the power-law fits of mean transport distance versus peak Q are 5 and 3.9 $m^3 s^{-1}$ for alluvial and semi-alluvial reaches respectively, but from the virtual velocity analysis the critical discharge value of 3.9 $m^3 s^{-1}$ seems to be a little low for the semi-alluvial reach. Likewise, the critical shear stress (τ_c) values for alluvial and semi-alluvial reaches are found to be 47 and 56 N m^{-2} respectively. However, the mean transport distances between successive surveys suggest that the threshold values are < 5.2 $m^3 s^{-1}$ (< 73 N m^{-2}) for bare rock gorge, at least 5 $m^3 s^{-1}$ (47 N m^{-2}) for the upper alluvial reach, and 5.0 – 6.6 $m^3 s^{-1}$ (63 – 91 N m^{-2}) for the lower semi-alluvial reach. However, the difference in bedload mobility is dependent on effective shear stress and the excess shear stresses, which were discussed in chapter 4 and will be further discussed in chapter 7. The broader implications of these results are discussed in chapter 7.

6 Bedload transport measurements using bedload impact plates

This chapter reports the results of bedload impact plate measurements which are used to investigate the dynamics of bedload transport along Trout Beck (Research Question 4, Chapter 1, Section 1.4.1). Measuring bedload transport in steep bedrock rivers using bedload samplers, sediment traps and slots is an expensive and difficult task, therefore bedload impact plates are an emerging technology used to indirectly estimate bedload transport (Richardson *et al.*, 2003; Rickenmann & McArdell, 2007; Rickenmann & Fritschi, 2010). Here, data from bedload impact plates are used to discuss variability in bedload dynamics; determine discharge and shear stress thresholds for bedload transport; estimate sediment availability; and illustrate the temporal and spatial relationship of bedload intensity with discharge and shear stress. This analysis allows the start and end of the coarse sediment movement to be identified which quantifies the threshold conditions for bedload motion (Richardson *et al.*, 2003; Beylich & Laute, 2014; Downs *et al.*, 2016). Threshold values are used to estimate the bedload transport rate which is generally considered to be a power function of excess shear stress or discharge above the threshold value (e.g. Meyer-Peter & Müller, 1948; Fernandez Luque & Van Beek, 1976; Rickenmann, 2001). The two main objectives of this chapter are to:

- examine the impact plate data to determine differences in flow and shear stress at initiation and cessation of bedload motion along the reaches of fully alluvial, fully bedrock and partially exposed rock beds. The threshold values obtained from this analysis will be compared with the tracer-pebble data and other empirical relations in Chapter 7.
- observe the variability in bedload transport during high-flow events.

In order to achieve these objectives five impact plates (also called impact sensors or loggers) were installed in three different locations (Fig 3.15). The details of the impact plates experiment have already been described (Chapter 3) but a brief description is provided here for context. This project uses the slightly modified version of the impact sensor described by Carling *et al.* (2002a) and Richardson *et al.* (2003). This consists of an accelerometer connected to a metal plate (15 cm x 13 cm x 0.6 cm) which is mounted flush with the river bed. The sensors have a maximum sensitivity of 1 impact in 0.2 seconds and the sensors reach saturation at 255 impacts (impulses) within a time

interval of 5 minutes which gives a mean transport rate of 0.85 grains per second. Data were downloaded in every 1 to 2 months (memory capacity of 55 days) at low flow conditions then analysed alongside measured discharge and shear stress (Chapter 4).

This chapter is divided into five sections. Section 6.1 presents an overview and discusses the general trends of the data recorded at different sensor locations; section 6.2 calculates the threshold values of discharge and shear stress from bedload impacts; section 6.3 analyses the intra-event variability of the impact counts over a range of storm events; section 6.4 briefly discusses the advantages and limitations of the bedload impact sensor and factors affecting the impact counts; and finally section 6.5 summarises the main findings of the chapter.

6.1 Overview and general pattern of bedload impacts

Five impact plates were installed in the reach: three in August 2013, one in September and the final one in December 2013 and all were monitored until April 2015, 20 months from first installation (Section 3.3.2). Figure 6.1 shows the plan and longitudinal profile of the channel bed showing the locations of the impact sensors and other monitoring equipment.

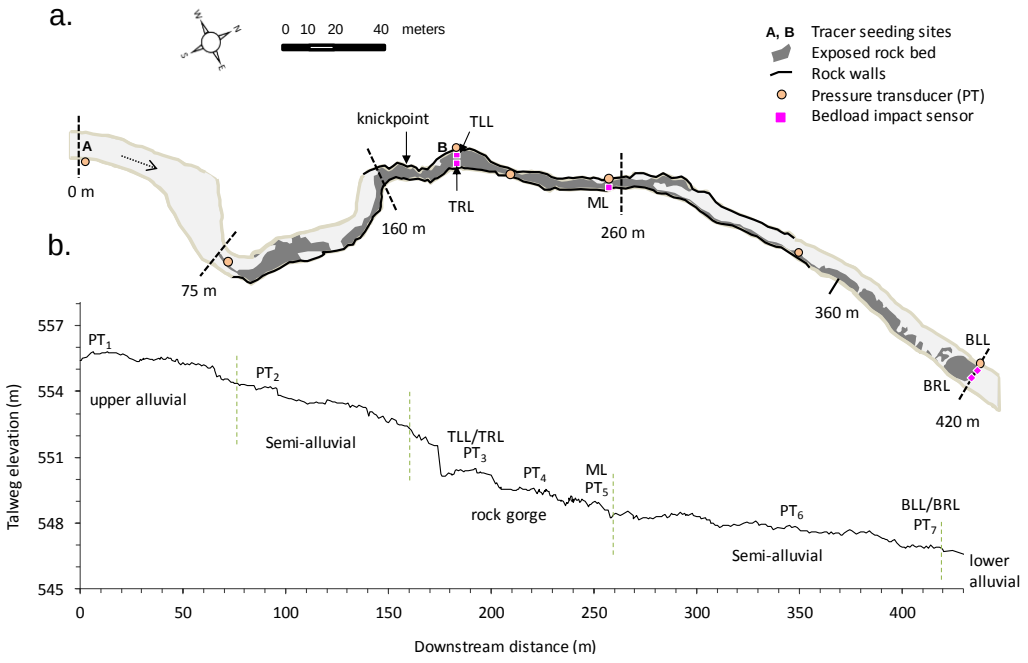

Figure 6.1. (a) Plan view of study reach showing the exposed rock bed and different reaches marked by dashed-lines. Five bedload impact sensors TLL, TRL, ML, BLL and BRL (pink), seven pressure transducers (orange) and tracer seeding sites (A and B) are shown. The dashed-arrow shows the flow direction, and the distances shown are from PT_1; (b) the longitudinal profile of talweg showing the pressure transducers PT_1 to PT_7 and five impact sensors.

The top two sensors TLL (Top Left Logger) and TRL (Top Right Logger) were installed adjacent to each other next to PT_3 in the rock gorge, the middle plate ML (Middle Logger) next to PT_5 near the bottom of the gorge, and the lower two BLL (Bottom Left Logger) and BRL (Bottom Right Logger) adjacent to each other next to PT_7 at the end of the lower semi-alluvial reach. Over the study period some data are missing because of equipment breakdown or because the water level in the channel was too high to retrieve the logger. Consequently, the focus of this chapter is a comparison between the rock gorge (upper three impact sensors TLL, TRL and ML) and the semi-alluvial reach (lower two sensors BLL and BRL). The general pattern of impact counts is that the top right and bottom left sensors (TRL and BLL) recorded many bedload impacts but the other three sensors registered very low impact counts under all conditions.

Figure 6.2 shows the time series of impact counts per 5 min interval (I) for each of the five sensors which illustrate the temporal variability in coarse sediment transport, its relation with the discharge (Q) and the reach-averaged shear stress (τ). The Q series used in this study, unless mentioned otherwise, is based on PT_6 stage data and rating curve which is selected because of its higher logging frequency, shorter averaging time and lower errors (mean error = 0.00 $m^3 s^{-1}$, root-mean-square = 0.29 $m^3 s^{-1}$) (Section 4.1.4). It is to be noted that the study site discharges based on the local stages are slightly different from EA scaled discharges mainly because of the different averaging time. The shear stresses for TRL and BLL shown in these plots (Figure 6.2c, e) and elsewhere in this chapter, unless expressed otherwise, are reach-averaged shear stresses between PT_3 to PT_5 and PT_6 to PT_7 respectively. Figure 6.2 shows that generally the impact peaks agree well with the discharge and shear stress peaks. The rock gorge has very little sediment on its bed so any impacts registered by the sensors in the gorge (TLL, TRL and ML) are because of sediment supplied from the upstream semi-alluvial and alluvial reaches (Figure 6.1). However, the lower sensors in the lower semi-alluvial reach receive sediment entrained locally within the reach as well as from upstream reaches. As discussed in the tracer-pebble results in chapter 5 there were several competent floods (Table 5.1) when bedload transport was active and this has also been confirmed by these time series plots of bedload impact counts. The number of counts in each 5 min period at TRL is much higher than at TLL even though they were only few metres apart in the same cross-section, and this is also the case with the lower section where BLL records notably higher number of counts than BRL does. Figure 6.2 (a, b, f)

shows that the TLL and BRL sensors only record significant impacts at very high flows ≥ 5 to 6 $m^3 s^{-1}$.

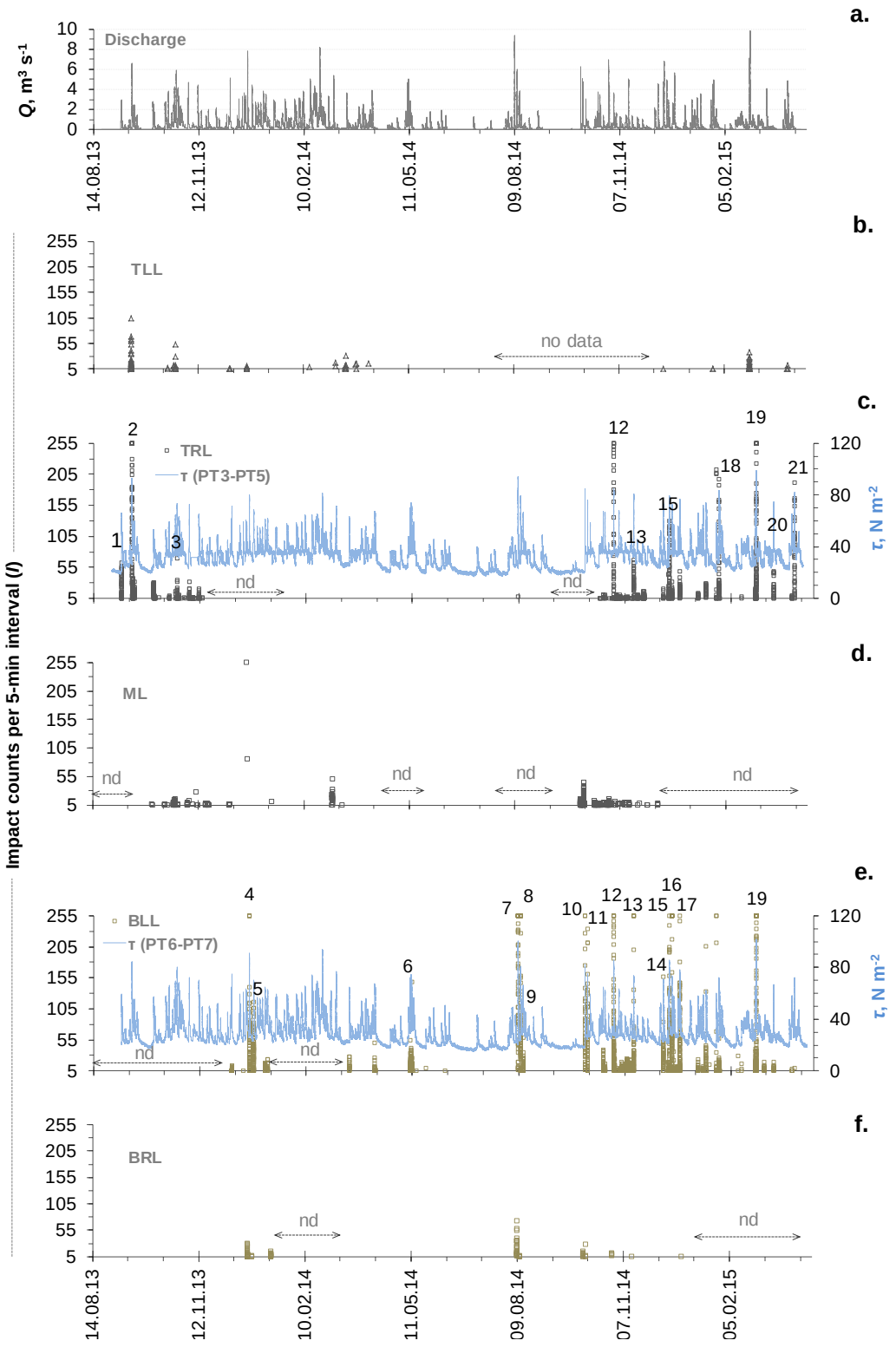

Figure 6.2. (a) 5 min discharge series during the study period; (b) to (f) the impact counts at each of the five impact sensors (TLL, TRL, ML, BLL, BRL) from August 2013 until April 2015. The events which will be discussed in subsequent sections are marked by event numbers 1 to 21 (Table 6.2). The 'nd' indicates 'no data' for that sensor. The shear stresses (blue) in the gorge and lower semi-alluvial reach are superimposed against TRL and BLL counts (c, e).

Table 6.1 summarises the bedload impact data (number of non-zero periods) and shows that TLL is the least active sensor with the lowest number of non-zero periods (787: 0.6% of the total no. of periods) whilst the TRL and ML are very active with higher number of non-zero periods respectively 7 414 (5% of total) and 7 006 (7% of total). The BLL has a moderate number of non-zero periods (5 627: ~5% of total no. of periods) but the intensity of impacts is high. BLL has 1 527 periods (27% of total non-zero periods) that exceed 10 counts and 444 periods (8%) exceeding 50 counts, whilst these figures for TRL are 11% and 3% respectively.

Table 6.1. Summary information of the impact counts, each period refers 5 min interval.

Description	Bedload impact sensors				
	TLL	TRL	ML	BLL	BRL
Total number of periods	130 612	141 114	102 325	125 756	124 815
Number of non-zero periods (% of total no. of periods)	787 (0.6%)	7 414 (5%)	7 006 (7%)	5 627 (~5%)	1 161 (1%)
No. of periods exceeding 10 counts (% of total non-zero periods)	54 (7%)	791 (11%)	117 (2%)	1,527 (27%)	47 (4%)
No. of periods exceeding 50 counts (% of total non-zero periods)	6 (1%)	236 (3%)	3 (0.04%)	444 (8%)	3 (0.3%)

The TLL and TRL were only few metres apart in the same cross-section but over 90% of the total non-zero periods recorded at this section were for TRL and less than 10% for TLL. The very low number of impacts at TLL is probably because the bedload momentum was concentrated in the centre of the channel (Figures 3.16b and 6.1). Richardson *et al.* (2003) also found that a sensor located on the outer bend recorded a very low number of impacts compared to the other two in the same cross-section. Similarly, in the lower section BLL recorded 83% of non-zero periods whilst the adjacent BRL only registered 17%. This is most likely because the main flux was passing along the talweg on the left hand side of the channel where the BLL was sited. Downs *et al.* (2016) also reported similar lateral and longitudinal variability in the bedload movement using impact loggers sited in the same cross-section. Table 6.1 and Figure 6.2 indicate that there is a large variation in the bedload transport in downstream and cross-section directions.

Figure 6.2(b to f) shows some data gaps which were either because of sensor malfunction or the downloading was not possible because of high water levels. Since the TLL, ML and BRL have a very low number of impact counts the subsequent

analysis has been undertaken on TRL and BLL data only. Although the ML sensor is just 60 m downstream of the upper sensors in the gorge and records a large number of non-zero periods (7 006), the intensity of impacts is very low as 98% of the non-zero periods record less than 10 counts which appear to be the background noise with little structure to the data (Table 6.1). Figure 6.3 shows the relationship of impact counts with discharge Q and shear stress τ at TRL and BLL.

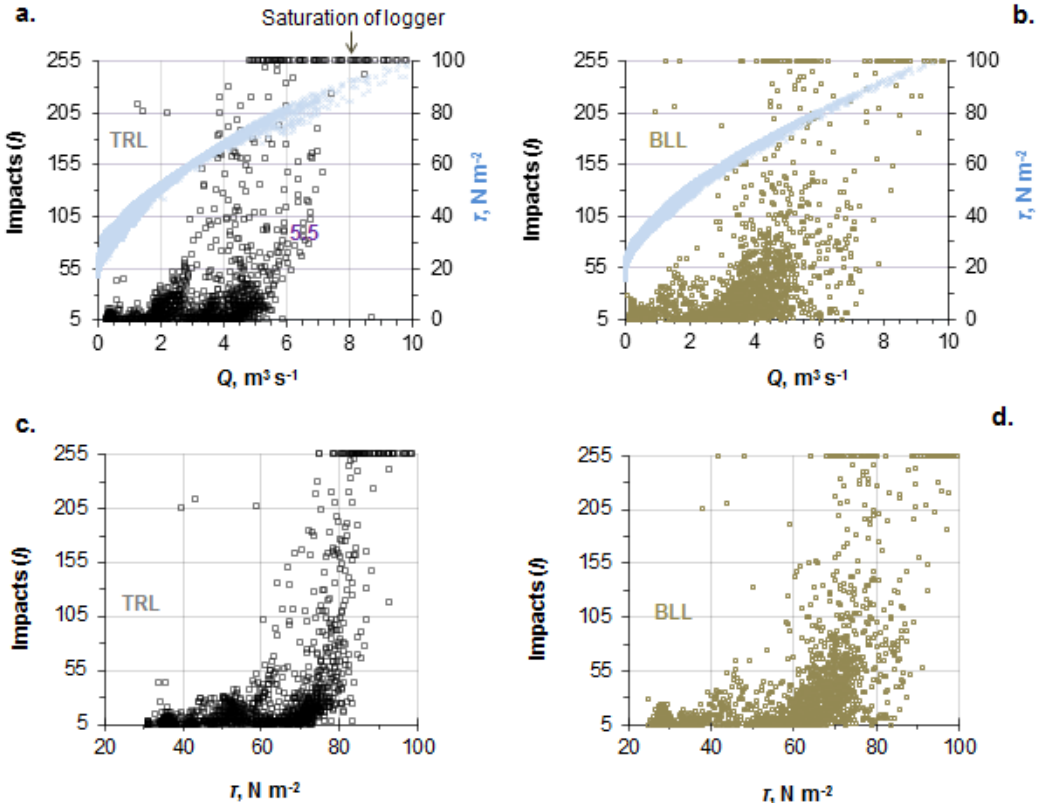

Figure 6.3. Relationship of impact counts per 5 min interval (I) with discharge Q and shear stress τ for all data (includes both rising and falling limbs) during the study period; a) I-Q for TRL and the τ (blue) in the gorge; b) I-Q for BLL and the τ in the lower semi-alluvial reach; (c) I: τ for TRL; and d) I: τ for BLL. Logger's saturation at 255 counts.

The plots of bedload impacts against discharge and shear stress in Figure 6.3 show a non-linear upwards trend with considerable scatter; the majority of data for both the loggers lie within Q = 3 to 6 m^3 s^{-1} and τ = 60 to 85 N m^{-2}. The lack of a clear single impact threshold is expected given the plots consist of all data during the study period and include different states of rise depending on the type of Q event, supply conditions and variable bed character. For example, for TRL the sediment is supplied from the upper semi-alluvial and alluvial reaches and the threshold values at these two reaches are expected to be different. Similarly, the lower semi-alluvial reach comprises the pool-boulder area and the partially alluvial areas (Figure 6.1) with varying bed exposure which probably also have different threshold discharges. The variability in impact

counts at high flow relates to bed material sediment supply limitations and variability; changes in the type of bedload motion as sliding, rolling and saltation; local intermittent control on transport (e.g. a large clast becoming temporally lodged upstream of the plate); and instrument response to differing impacts (e.g. a particle hitting the plate edge rather than the centre). Factors affecting the counts will be further discussed in section 6.4.

During the study period there were 23 flood events (Table 5.1) which exceeded 4 $m^3 s^{-1}$ and 14 events which exceeded 5 $m^3 s^{-1}$ discharges. There were 21 flood events with significant bedload movement (> 50 counts in 5 min period) which are listed in Table 6.2; the Event numbers are also labelled in Figure 6.2.

Table 6.2. Event numbers, dates and the sensor data for further analysis. Event numbers with impact data to both TRL and BLL are highlighted. The peak *Q* during the event, tracer survey number (Table 5.1) and the ranking based on peak *Q* are shown. A brief note why there is a lack of common data to both sensors is included for 12 largest events ($Q > 5\ m^3 s^{-1}$).

Event number	Date	TRL	BLL	Peak *Q*, $m^3\ s^{-1}$	Survey number	Rank as per peak *Q*	Remarks
1	06.09.13	√		2.3		20	
2	15.09.13	√		6.2	1	4	BLL no data
3	23.10.13	√		5.2	2	9	BLL no data
4	23.12.13		√	6.6	4	3	TRL no data
5	27.12.13		√	4.2		17	
6	09.05.14		√	4.5	6	16	
7	08.08.14		√	8.7		13	
8	10.08.14		√	4.2		18	
9	13.08.14		√	2.3		21	
10	04.10.14		√	5.4		7	TRL no data
11	06.10.14		√	5.1		11	TRL no data
12	28.10.14	√	√	6.2		5	5th largest event
13	14.11.14	√	√	5.2		10	10^{th} largest event
14	09.12.14		√	4.8		14	
15	14.12.14	√	√	6.7		2	2nd largest event
16	17.12.14		√	4.8		15	
17	23.12.14		√	5.4		8	TRL counts <50
18	25.01.15	√		5.1		12	BLL counts <50
19	26.02.15	√	√	8.8	7	1	Largest event
20	12.03.15	√		3.9		19	
21	30.03.15	√		5.5		6	BLL counts <10

These 21 events include ten TRL events, 15 BLL events and four are common to both. Out of these 21 events, only four events have common data ranked as 1 (Event no 19, the largest event during the study period), 2, 5 and 10 and all these common events have peak $Q > 5$ m^3s^{-1}. The reason why all other events exceeding 5 $m^3 s^{-1}$ (rank 1 to 12) lack common data is one of the sensors has no data (sensor break down or memory full) or it has less than 50 counts in 5 minute period (Table 6.2). The Event 7 is the thunderstorm-caused event. The next section will estimate the threshold of motion based on the impacts data from these events.

6.2 Threshold of motion

The threshold of motion refers to the condition when the sediment starts to move; the discharge and shear stress associated with this initial motion are called threshold or critical discharge (Q_c) and critical shear stress (τ_c) (Sections 1.1.6). Estimates of threshold values based on the tracer-pebble experiment are discussed in sections 5.2.3 and 5.2.4 of chapter 5. This section firstly describes the limitation of impact plates in detecting a threshold value of grain size (or energy) to cause an impact count on the plates and then "threshold impact count" which refers to the number of counts in 5 minutes period that represents an appreciable movement of the bedload particles is discussed. Subsequently the threshold discharges and shear stresses are calculated using three approaches: analysis of frequency of 5 min periods exceeding the threshold impact count, power-law fitting to event $I - Q$ plots, and event start-stop analysis.

6.2.1 Threshold grain size to cause an impact count

Calibration of the bedload impact plates to determine the minimum grain size/energy needed to get the impact sensor to record a threshold is difficult as it is not only a function of grain size, but also of grain momentum (which is the product of grain mass and velocity) (Richardson *et al.*, 2003). Downs *et al.* (2016) reported that this type of impact plate is capable of detecting the impact of a grain size with a minimum size of 9 – 12 mm. The critical grain size to cause an impulse with a piezoelectric bedload impact sensor (PBIS) as found by Rickenmann and McArdell (2007) was 10 to 30 mm for a spherical quartz grain, but those plates were bigger (0.36 m x 0.50 m x 0.015 m) than the plates used in this research (0.15 m x 0.13 m x 0.006 m). An attempt to establish the threshold impact count was made by dropping various sizes of pebbles (n = 23, b-axis diameter = 5 to 40 mm, mass = 0.30 to 66 g) on the surface of the sensor plate from different heights, with the plate both in horizontal and tilted positions. It was found that

all the grains including the 5-mm sized particle caused an impact count in the sensor even for a sub-centimetre drop. The grains also produced multiple rebounds which complicated identification of a definite value for the threshold. This experiment was undertaken in air and it appeared that grain sizes as small as 5 mm could produce at least one count and possibly a few rebounds depending on how and where the grain strikes the plate. However, it is expected that a larger size particle will be needed to cause an impact in water and also rebound multiple readings are less likely in the flow as the particle is swept away from the plate.

6.2.2 Threshold impact counts

A low number of impact counts does not necessarily represent the bedload movement. Determining a single value of impact counts that represents the threshold condition is not straightforward. For example whether 10 counts in 5 min period (*i.e*. 1 count in 30 seconds) or 50 counts in 5 min period (*i.e*. 1 count in six seconds) represents the threshold of bedload movement is difficult to estimate. Two simple calculations are performed to estimate a reasonable value for threshold impact count. The preferred definition of threshold is the discharge that moves the sediment at a predefined threshold or reference rate. Some previous researchers have used a low reference rate of $\varphi = 0.0001$, where

$$\varphi = \frac{q_s}{(gRD_{50}^3)^{1/2}} \qquad \text{Eq. 6.1}$$

is Einstein's non-dimensional transport rate, q_s the volumetric transport rate per unit width ($m^3\ m^{-1}\ s^{-1}$), D_{50} the median diameter, and R is the submerged specific gravity (Ferguson, 2012). Others follow Parker *et al.* (1982) in using a different approach with $W_* = 0.002$, where

$$W_* = \frac{\varphi}{(\tau^*)^{3/2}} \qquad \text{Eq. 6.2}$$

and τ^* is the non-dimensional shear stress or Shields number.

The assumptions used here are that the sensor width is 0.15 m, pebbles shapes are spherical and submerged specific gravity is 1.65. In the Einstein's φ approach, the number of grains over a sensor plate in a 5 min period (*i.e*. threshold count assuming one grain produces one impact) is calculated for each single grain size (e.g. 5, 8, 10, 20 mm) by multiplying the grain transport rate (grains $m^{-1}\ s^{-1}$) by the width of the plate and the duration (300 s). The grain transport rate (t_r) is calculated by dividing the

volumetric transport rate q_s (Eq. 6.1) by the grain volume ($\pi D^3/6$). The threshold count in the Parker's W_* method is also calculated in the same way where q_s in Eq. 6.1 is calculated by using $\varphi = W \times \tau^{*3/2}$ (Eq. 6.2). The estimated threshold impact counts based on these approaches are summarised in Table 6.3. The first block of Table 6.3 shows the Einstein's φ approach gives threshold counts of 98 for 5 mm, 48 for 8 mm, 35 for 10 mm and 12 for 20 mm grain sizes over the impact plate in a 5 min sampling interval, which corresponds to 2.17 to 0.27 pebbles per metre width per second.

Table 6.3. Threshold impact count per 5 min interval based on critical value of Einstein's φ =0.0001 (first block) and Parker's W_* = 0.002 (second block).

Bedload grain size D (mm)	Based on φ = 0.0001	
	Grain transport rate, t_r (grains m^{-1} s^{-1})	No. of grains over sensor plate (threshold impact count)
5	2.17	98
8	1.07	48
10	0.77	35
20	0.27	12
30	0.15	7
40	0.10	4
50	0.07	3

Bedload grain size D (mm)	Based on W_* = 0.002		
	Threshold impact count for τ_c^* =		
	0.045	0.06	0.10
5	19	29	62
8	9	14	31
10	7	10	22
20	2	4	8
30	1	2	4
40	1	1	3
50	1	1	2

The second block in Table 6.3 shows the threshold impact counts based on Parker's W_* approach for a range of dimensionless critical shear stress (τ_c^*). The τ_c^* for gravel bed river ranges from 0.03 – 0.086 (Buffington & Montgomery, 1997) (Section 1.1.6), and may be a little higher for Trout Beck gorge (slope ~3%). For τ_c^* = 0.10 the threshold counts are 62, 31, 22, and 8 for typical grain size of 5, 8, 10 and 20 mm respectively which shows that the threshold counts based on W_* = 0.002 are lower than those from φ = 0.0001; the φ = 0.0001 itself is a very low rate indeed (Shvidchenko & Pender, 2000; Ferguson, 2012). Moreover, these values are for a single grain size whereas the bedload comprises a mix of different sizes. Therefore the threshold impact counts equivalent to "one grain moving per metre channel width per second" based on Einstein's φ = 0.0001 is considered to be a reasonable "threshold" in the sensor data to identify an appreciable amount of bedload movement; this gives around 50 counts per 5 minutes interval (Table 6.3). All subsequent analysis will therefore assume the threshold of bedload entrainment occurs when the impact sensor first records 50 counts in a 5 minutes period on the rising limb, and the threshold of cessation occurs when the sensors records the last 50 counts on the falling limb of the hydrograph. Qualitative

support for this threshold is indicated in Figure 6.3 as impact counts increase markedly above a threshold value of 50.

6.2.3 Threshold calculation based on frequency of 5 min periods exceeding 50 counts

The threshold values of entrainment for discharge and shear stress have been estimated by analysing the frequency of 5 min interval logger counts that exceed the threshold impact count (I = 50). Figure 6.4 shows the percentage of periods with >50 counts plotted against discharge and shear stress classes (bin sizes Q = 0.5 m^3 s^{-1}; τ = 5 N m^{-2}).

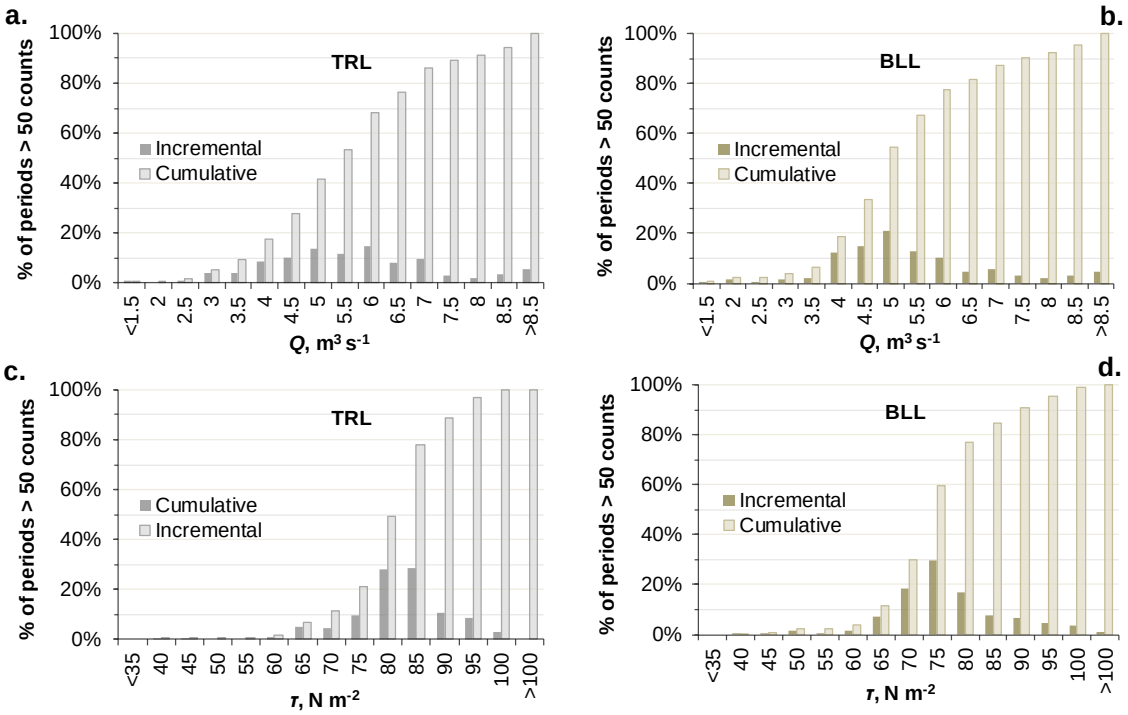

Figure 6.4. Percentage of total periods with I >50 against discharge and shear stress classes; the cumulative values are also shown; a) TRL periods against Q; b) BLL periods against Q; c) TRL periods against τ in the gorge; and d) BLL periods against τ in the lower semi-alluvial reach.

The TRL plots in Figure 6.4 (a, c) show that the threshold for appreciable recording of impacts (the plots indicate ~5% of the periods exceeding 50 counts) can be considered as Q_c = 3 m^3 s^{-1} and τ_c = 65 N m^{-2}. The cumulative bar of TRL plots indicate that 50% of the total periods occur at Q less than 5.5 m^3 s^{-1} and τ less than 80 N m^{-2}. Similarly, the BLL plots (Figure 6.4 b, d) show that the threshold for appreciable recording of contacts (plots suggest ~10% of the periods >50 counts) can be considered as Q_c = 4 m^3 s^{-1} and τ_c = 65 N m^{-2}; the cumulative bars indicate that half of the periods occur at Q less than 5 m^3 s^{-1} and τ less than 75 N m^{-2}.

6.2.4 Threshold calculation from *I*-*Q* power law

Figures 6.5 and 6.6 show power-law relationships fitted to plots of bedload impacts per 5 min interval (I) and discharge (Q), with the form

$$I = a\,(Q - Q_0)^{\,b} \qquad \text{Eq. 6.3}$$

where Q is discharge, Q_0 is discharge when $I = 0$, and a and b are constants. From Eq. 6.3 Q_c is calculated, where Q_c is Q when $I = 50$. The Q_c is calculated for seven TRL and ten BLL events and also for all data at these sensors.

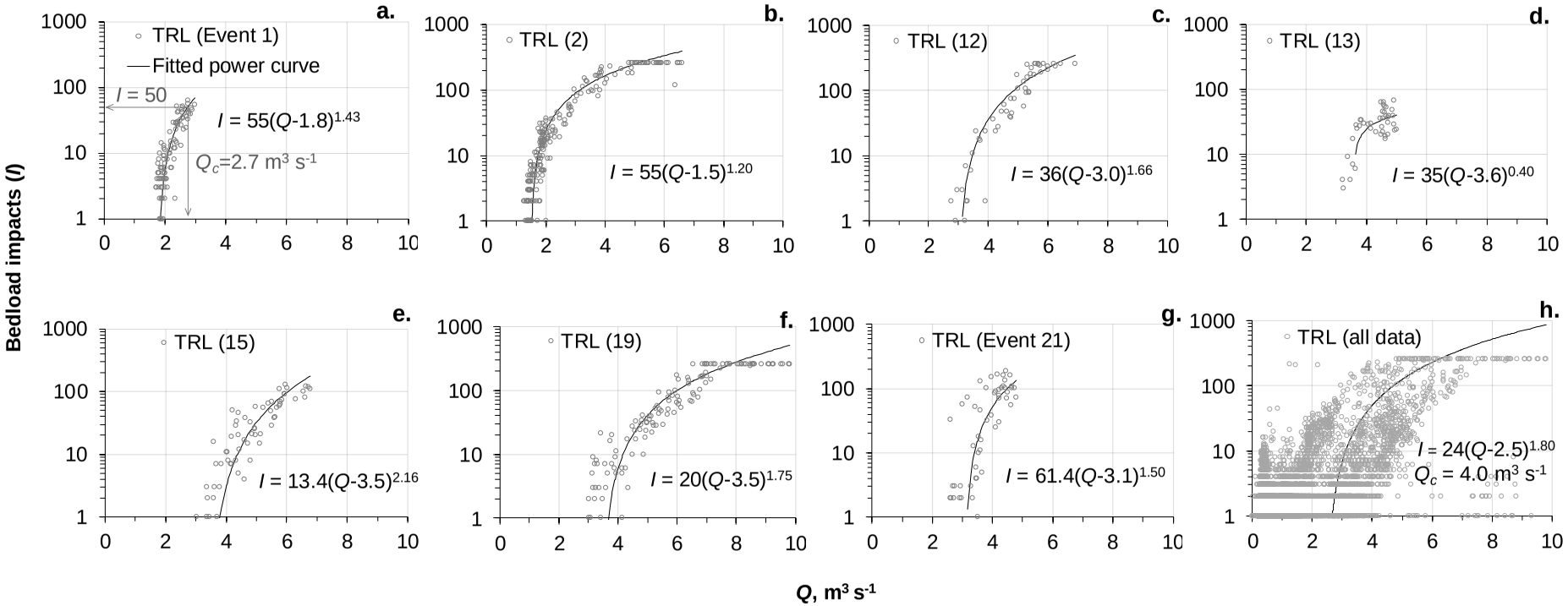

Figure 6.5. Semi-log plots of TRL impact counts per 5 min interval (I) against Q for seven different events (a to g) and the entire data during the study period (h). Fitted power-law equations in the form $I = a\ (Q - Q_0)^b$ are shown. The threshold discharge Q_c (*i.e.* Q when $I = 50$) is illustrated in first a).

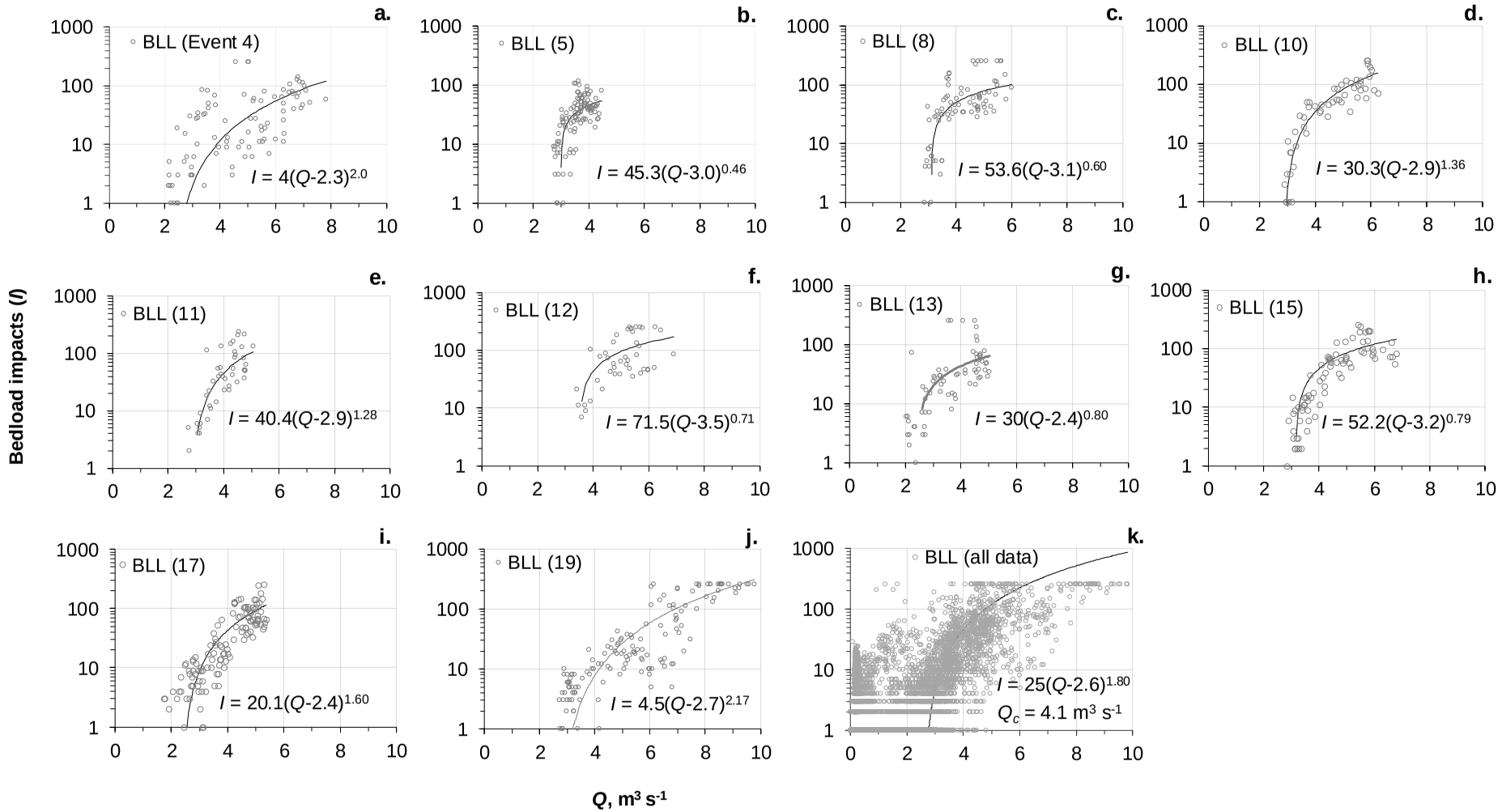

Figure 6.6. Semi-log plots of BLL impact counts per 5 min interval (I) against discharge (Q) for ten different flood events (a to j) and the entire data (k). Fitted power-law equations in the form $I = a\ (Q - Q_0)^b$ are shown.

Figures 6.5 and 6.6 show some scatter but overall the power-law fits well for a single event, however the threshold values are different across the events. The derived Q_c values are plotted in Figure 6.7 and summarised in Table 6.4. Based on the plots of individual events, the critical discharge range from 2.4 to 6.0 $m^3 s^{-1}$ (average 4.3 $m^3 s^{-1}$) for TRL and 4 to 5.8 $m^3 s^{-1}$ (average 4.5 $m^3 s^{-1}$) for BLL. However, the plots based on all data (Figures 6.5h and 6.6k) give very similar values of threshold discharge for TRL and BLL, 4.0 and 4.1 $m^3 s^{-1}$ respectively.

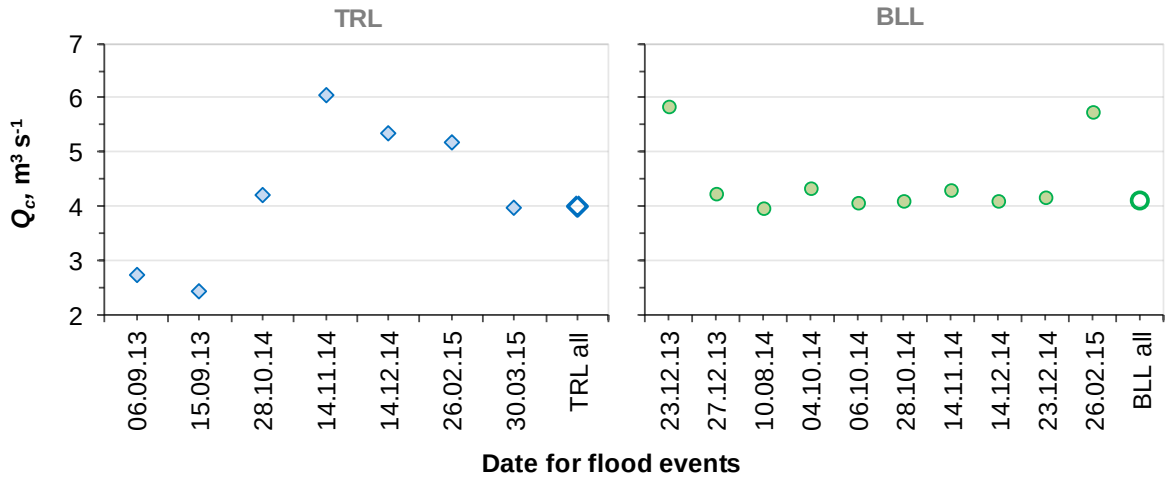

Figure 6.7. The Q_c values for TRL (closed blue diamond) and BLL (closed green circle) for different events derived with I = 50 in the I-Q equations shown in Figures 6.5 and 6.6. The Q_c estimates from all data (TRL: open blue diamond, BLL: open green circle) are also shown for comparison.

Table 6.4. The critical discharge (Q_c) in $m^3 s^{-1}$ for TRL and BLL for different events.

Event number	Q_c $m^3 s^{-1}$	
	TRL	BLL
1	2.7	
2	2.4	
4		5.8
5		4.2
8		4.0
10		4.3
11		4.1
12	4.2	4.1
13	6.0	4.3
15	5.3	4.1
17		4.2
19	5.2	5.8
21	4.0	
Range	*2.4 – 6.0*	*4.0 – 5.8*
Average	*4.3*	*4.5*
All data	*4.0*	*4.1*

The scatter in the values of Q_c between events and between TRL and BLL is mainly because the location of the grains in the channel has a strong control on grain entrainment (as shown by tracer results, Chapter 5) and bed material supply is limited (which will be further discussed in Section 6.3.2). Moreover, the gorge does not have sediment on its bed therefore the TRL data must represent grains entrained in the upper semi-alluvial and upper alluvial reach. The threshold values vary between events, which was also found in another bedrock channel (Richardson *et al.*, 2003) and gravel bed rivers (e.g. Reid *et al.*, 1985; Garcia *et al.*, 2000). The studies in alluvial rivers show that these variations in threshold values between channels with similar size and shape of sediment depend on form resistance, channel morphology (Buffington & Montgomery, 1999; Millar, 1999) and packing effects (Brayshaw, 1985; Powell & Ashworth, 1995).

6.2.5 Threshold for the start and end of bedload transport

The threshold discharge and shear stress at the start and end of transport have been analysed for all 21 events (Table 6.2) following the method of Turowski *et al.* (2011). The histograms of frequency of discharge and shear stress at the start and end of transport (*Q*-start; *Q*-stop; *τ*-start; *τ*-stop) are shown in Figure 6.8 for TRL and Figure 6.9 for BLL. The *Q*-start and *Q*-stop are the threshold discharges that cause respectively the first and last 50-count in an event, so are the *τ*-start and τ-stop.

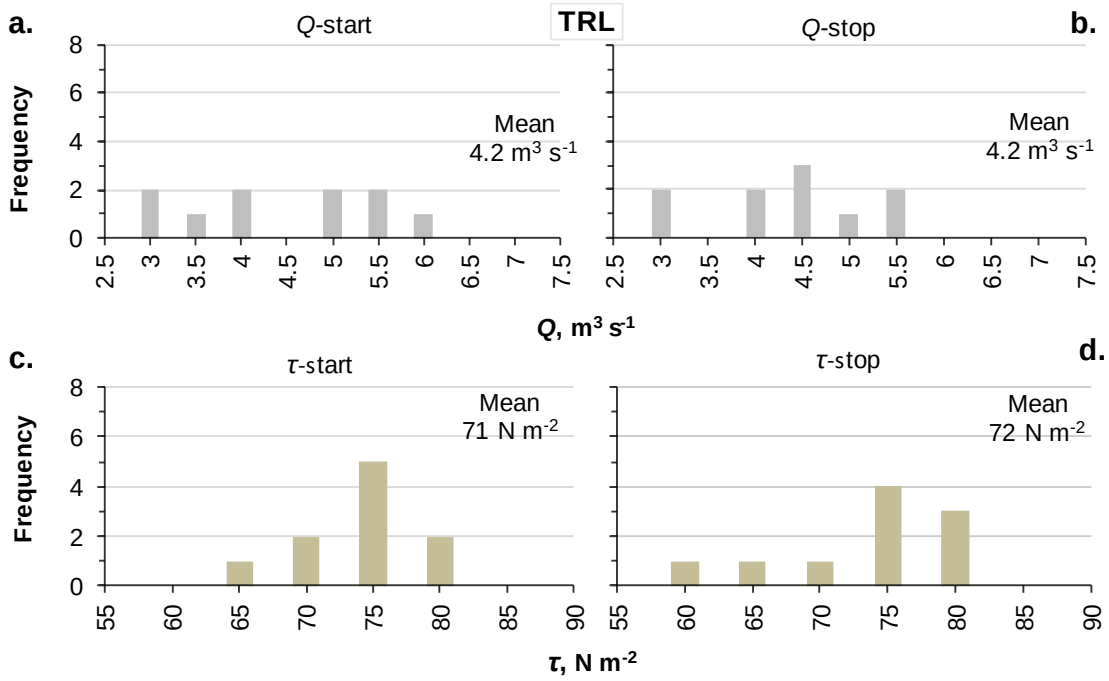

Figure 6.8. TRL histograms (bin size Q = 0.5 m^3 s^{-1}; τ =5 N m^{-2}): a,b) the discharge at the start and end of bedload transport; c,d) The shear stress at the start and end of bedload transport.

The TRL plots in Figure 6.8 show that the *Q*-start and *Q*-stop vary across the events but the overall range for start and stop of bedload transport are very similar; 2.75 to 5.75 $m^3 s^{-1}$ for entrainment and 2.75 to 5.25 $m^3 s^{-1}$ for cessation. The mean threshold discharge for both start and stop of transport is 4.2 $m^3 s^{-1}$. Similarly, the shear stress for entrainment is 63 – 78 N m^{-2} and for cessation 58 – 78 N m^{-2}. The plots reveal that the highest number of entrainment and cessation both occurred at τ = 73 N m^{-2}.

The BLL plots in Figure 6.9 show that the overall range of threshold values for entrainment and cessation in the lower semi-alluvial reach are also similar. The discharge range to start and end the bedload transport are respectively 3.25 – 6.75 $m^3 s^{-1}$ (mean 4.1 $m^3 s^{-1}$) and 3.25 – 5.75 $m^3 s^{-1}$ (mean 4.1 $m^3 s^{-1}$). Similarly, the shear stress to start and stop the transport are 63 – 83 N m^{-2} (mean 68 N m^{-2}) and 63 – 78 N m^{-2} (mean 67 N m^{-2}) respectively. The highest number of events entrained and ceased at shear stress of 63 N m^{-2}.

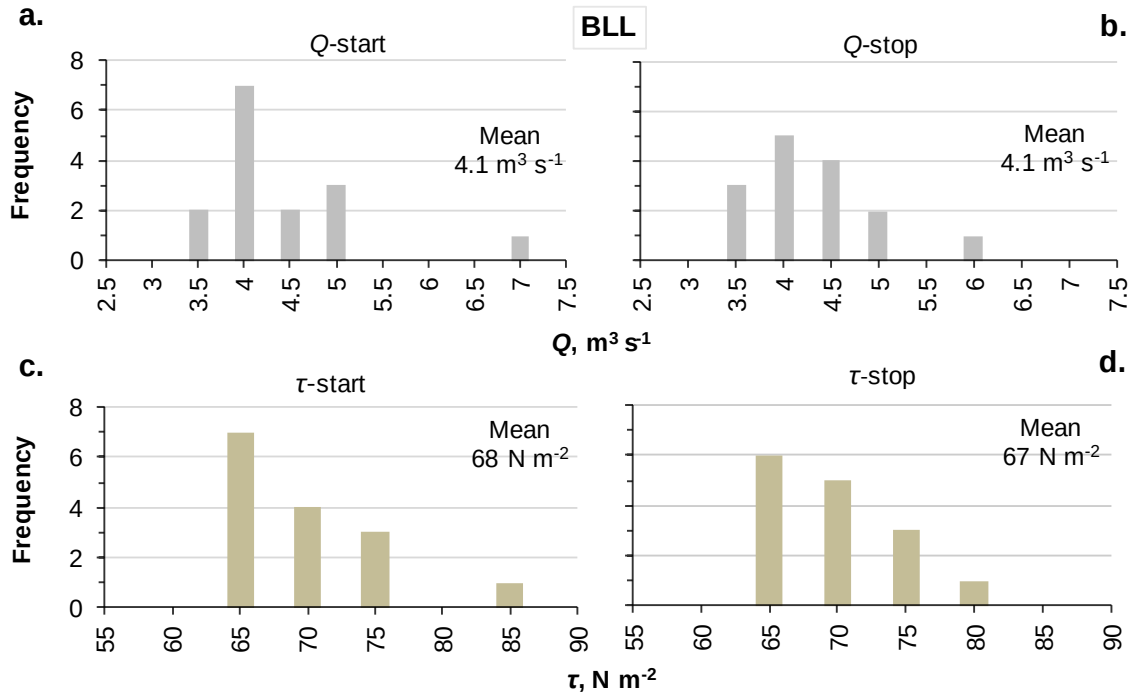

Figure 6.9. a, b) Histogram of the discharge at the start and end of bedload transport at BLL; c,d) histogram of the shear stress at start and end of transport.

The start-stop plots for both sets of data show that the distribution of discharge and shear stress at the start and end of bedload motion are generally similar. The events with low threshold values in the upper sensor may indicate the bedload entrainment from the patches in upper semi-alluvial reach; and the events with high threshold values may reflect the entrainment from fully alluvial reach. Similarly, low threshold values at BLL

are perhaps due to the start of motion of the readily available material from the patches in the lower semi-alluvial reach; and high threshold values are likely to represent the bedload entrainment in the pool, boulder-riffle areas, and alluvial surface (both in upper alluvial and lower semi-alluvial reach) where the sediment is not readily available for entrainment. The data used in above plots are presented in Table 6.5. The calculated shear stress values in Table 6.5 are slightly different, even for the same discharges, due to small variations in hydraulic radius and energy slope ($\tau = \rho g R S$). As mentioned earlier in section 6.1, the shear stresses used in these analyses are calculated using the stage data recorded at 5 minute sampling intervals between PT_3 to PT_5 for TRL and PT_6 to PT_7 for BLL.

Table 6.5. Discharge and shear stress at the start and end of the bedload transport at TRL and BLL.

Event number	Event date	TRL				BLL			
		Q_{start}	Q_{stop}	τ_{start}	τ_{stop}	Q_{start}	Q_{stop}	τ_{start}	τ_{stop}
1	06.09.2013	2.8	2.6	66	59				
2	15.09.2013	2.8	2.8	61	62				
3	23.10.2013	5.2	5.2	72	72				
4	23.12.2013					6.7	3.6	85	62
5	27.12.2013					3.6	3.7	64	64
6	09.05.2014					3.9	4.2	67	69
7	08.08.2014					4.6	3.4	72	62
8	10.08.2014					3.7	3.6	65	65
9	13.08.2014					3.5	3.5	63	63
10	04.10.2014					4.8	3.7	73	65
11	06.10.2014					3.8	3.4	66	62
12	28.10.2014	4.8	4.4	72	75	3.3	4.8	61	72
13	14.11.2014	4.6	4.6	75	77	3.6	4.7	64	72
14	09.12.2014					3.6	4.1	64	68
15	14.12.2014	5.8	4.2	72	69	4.1	4.3	68	67
16	17.12.2014					4.2	3.9	68	67
17	23.12.2014					3.6	4.5	65	71
18	25.01.2015	3.6	4.4	71	79				
19	26.02.2015	5.3	5.5	77	78	4.8	5.7	71	77
20	12.03.2015	3.8	3.9	72	75				
21	30.03.2015	3.2	4.0	67	75				
Average value		4.2	4.2	71	72	4.1	4.1	68	67
Range		2.8-5.8	2.6-5.5	61-77	59-79	3.3-6.7	3.4-5.7	61-85	62-77

The relationship between discharge at the start of transport against the discharge at the end of previous event shown in Figure 6.10 (a,b), following the method of Turowski *et al.* (2011). Similar plots for shear stress are also shown in Figure 6.10 (c, d).

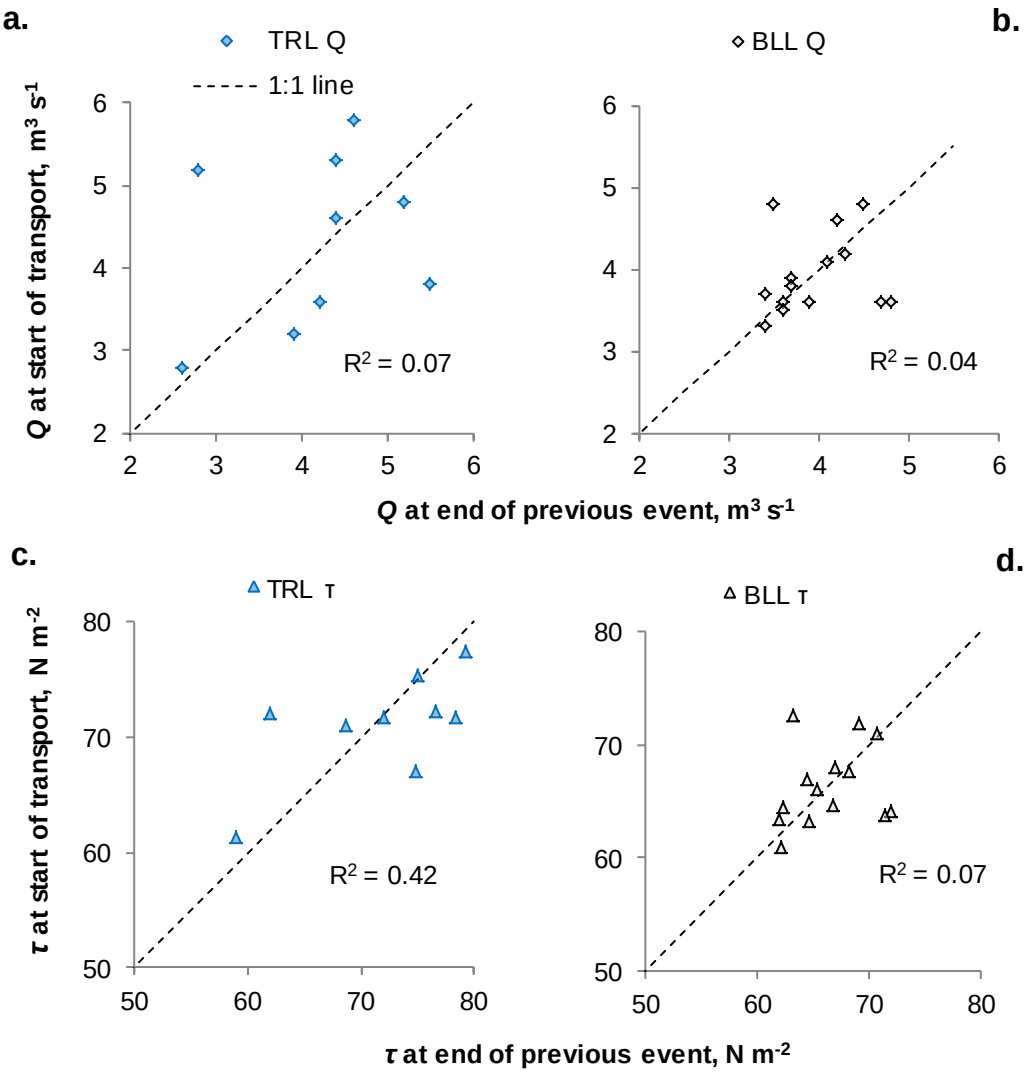

Figure 6.10. a and b. Discharge at the start of bedload transport against the discharge at the end of transport in the previous event at TRL and BLL; c and d. Shear stress at the start of transport against the shear stress at the end of transport in the previous event at TRL and BLL. The 1:1 line (dashed), the linear regression line (black line) with the equation and R^2 value are shown for comparison. The R^2 values of the correlations are shown, none of the correlations is statistically significant at the 0.05 level.

The TRL data in Figure 6.10 (a, c) show large scatter , however the BLL data show reduced scatter around the one-to-one line . This differs from the near-perfect collapse along the one-to-one line as found by Turowski *et al.* (2011) in their study streams. The patterns of discharge and shear stress are similar though the shear stress plots appear to be slightly less scatter. It is to be noted that there are a lot fewer data points than in Turowski *et al.* (2011). In summary, the threshold discharge or threshold shear stress varies between the events and also between the channel locations. Start-stop analysis

shows that there is no single threshold discharge or shear stress value that represents the Trout beck reaches. This is consistent with results from the previous two approaches (Sections 6.2.3 and 6.2.4). Bedload comprises a mix of grains of different sizes, and the grain size distribution also varies temporally and spatially according to the channel discharge and the sediment supply, therefore a single threshold value of entrainment was not expected. Such variability in threshold values is also reported in many gravel-bed rivers (e.g. Einstein, 1950; Kirchner *et al.*, 1990; Buffington *et al.*, 1992; Turowski *et al.*, 2011).

Summary of threshold discharge (Q_c) *and threshold shear stress* (τ_c)

The range of threshold discharge and shear stress estimated from three different approaches are summarised in Table 6.6. The average threshold discharges suggested by two sensors are not significantly different (4 to 4.5 $m^3 s^{-1}$) but the values for individual events vary up to 2.5 to 3 times (Table 6.6).

Table 6.6. The range of critical discharge Q_c and critical shear stress τ_c for TRL (rock gorge) and BLL (lower semi-alluvial). The average values are shown in brackets. The sources from which these values are obtained are given within parenthesis in first column. The shear stresses for power-law fitting are calculated using τ-Q relation for sub-reaches F2 and F5 (TRL: $\tau = 43.4Q^{0.61}$, and BLL: $\tau = 32.5Q^{0.49}$ from Figure 4.32).

Description	Q_c ($m^3 s^{-1}$)		τ_c ($N m^{-2}$)	
	TRL	BLL	TRL	BLL
(i) Based on frequency of periods with >50 counts (Figure 6.4)	3.0	4.0	65	65
(ii) Power-law fitting (Table 6.4)	2.4 – 6.0 (average 4.3)	4.0 – 5.8 (4.5)	74 – 129 (106)	64 – 77 (68)
(iii) Start-stop analysis (Table 6.5)	2.6 – 5.8 (average 4.2)	3.3 – 6.7 (4.1)	59 – 79 (72)	61 – 85 (68)

The variability in threshold values may occur mainly due to three reasons. Firstly, supply variation results in the variation in threshold values. Supply at TRL is more variable as the sediment depends on what is the gorge/upstream which may vary between events, whereas at BLL the sediment is locally sourced , and so supply is more consistent between events as shown by Figures 6.7 and 6.1. Secondly, small fluctuations in discharge and turbulent sweeps can affect the hydraulic forces on grains (Grass, 1970) but the average flow characteristics do not fully describe the forces on the grains. Therefore the threshold values vary randomly and no definite trend can be expected.

Thirdly, the GSD of the bed material, in the study area as well as upstream, may have changed between the events (Turowski *et al.*, 2011). If the GSD of the bed material remains unchanged from event to event then the spatial location of the grains, friction angles and grain protrusions may have changed between the events (Wiberg & Smith, 1987; Kirchner *et al.*, 1990; Buffington *et al.*, 1992). The GSD measurement carried out at different dates suggests that there were some changes in GSD. In the lower semi-alluvial reach, the discharge and shear stress at the start of the bedload transport generally matches the discharge and shear stress at the end of the previous transport (Figure 6.10) which implies that the random fluctuation due to turbulent sweep may not be a dominant factor there, as also argued by Turowski *et al.* (2011) for their streams for which the *Q*-start of the bedload transport collapsed with the *Q*-end of the previous events. Therefore the main reason of threshold variation in the lower semi-alluvial is perhaps the variation in GSD or the grain arrangement, whereas for upper alluvial reach supply variation and changing local hydraulic conditions can be the reasons of variations as the data their do not lie along one-to-one line (Figure 6.10) and also the scatter in the threshold discharges is large compared to the BLL values (Figure 6.7).

This thesis performs the detailed hydraulic calculations in five sub-reaches F1 to F5 of the study site (Section 2.5) in chapter 4, therefore it is interesting to estimate the Q_c and τ_c values for these five sub-reaches and compare the results from tracer pebbles and empirical equations. The comparison of the sub-reach threshold values are made in chapter 7 (Section 7.1.4) but this section estimates the Q_c and τ_c values for five sub-reaches based on the Q_c and τ_c values for TRL and BLL (Table 6.7). The Q_c values for TRL which range from 2.4 – 6 $m^3 s^{-1}$ (Table 6.6) are also assumed to be the Q_c values for sub-reaches F1 (upper alluvial) and F2 (rock gorge). Similarly, Q_c for BLL (3.3 – 6.7 $m^3 s^{-1}$, Table 6.6) is assumed to be the Q_c for three sub-reaches F3, F4 and F5 in lower semi-alluvial reach. The respective threshold shear stresses for each sub-reach are then calculated using the τ-Q relation for each sub-reach as shown in Figure 4.32.

Table 6.7. The range of critical discharge Q_c and critical shear stress τ_c for sub-reaches F1 to F5.

Sub-reach	Q_c, $m^3 s^{-1}$	τ_c, $N m^{-2}$
F1	2.4 – 6.0	33 – 50
F2	2.4 – 6.0	74 – 129
F3	3.3 – 6.7	94 – 118
F4	3.3 – 6.7	40 – 62
F5	3.3 – 6.7	58 – 83

Bedload transport rates are normally calculated using a single threshold value for a reach but the above analysis suggests that the actual threshold values in a reach vary, which implies that the bedload transport rate based on a single threshold value cannot accurately predict the actual bedload flux. The average threshold discharges suggested by two sensors are not significantly different (4 to 4.5 $m^3 s^{-1}$) but the values for individual events vary up to 2.5 to 3 times (Table 6.6). Therefore consideration should be given to how the variable threshold values can be incorporated in the bedload formulas. More research is also needed to develop a robust method to estimate the threshold values for different varieties of bedrock channels.

6.3 Intra-event bedload counts and bedload dynamics

This section analyses the impact counts during individual bedload transport events (Table 6.2). This helps to visualise the relationship between sediment transport activity with discharge and shear stress and also to learn about the sediment availability and transport rate during the rising and falling stage of a flood. Studies in gravel-bed rivers indicate that sediment transport rate may not be in phase with discharge (Reid *et al.*, 1985; Hassan & Church, 2001; Ryan *et al.*, 2005; Rickenmann & McArdell, 2007) therefore hysteresis curves are also plotted to assess differences in bedload transport within flow events. The hysteresis loops are useful in identifying difference in sediment supply during the rising and falling stages of the hydrograph. In a clockwise hysteresis the impact counts I during the rising stage are higher than in the falling stage for a given discharge Q, hence the I/Q ratio is higher on the rising limb than in the falling limb. With anticlockwise hysteresis the ratio will be higher in the falling limb. The hysteresis curves are quantified for fourteen events which have higher number of impact counts (Figure 6.2) using the hysteresis index proposed by Lawler *et al.* (2006).

6.3.1 Hysteresis index

This section quantifies the magnitude and the direction of the hysteresis curves using a Hysteresis index (HI_{mid}) as described by Lawler *et al.* (2006). The index is based on the fatness of the loop at the mid-point discharge of the event (Q_{mid}) which is calculated as

$$Q_{mid} = k\,(Q_{max} - Q_{min}) + Q_{min} \qquad \text{Eq. 6.4}$$

where Q_{max} and Q_{min} are respectively the maximum and onset discharge for the event and k determines the position where the loop breadth is measured. The k value is generally assumed to be 0.5 but more complex hysteresis such as multiple figure-of-eight loops (Williams, 1989) may have different values of k to bring Q_{mid} around the centre of the hysteresis. The I_{RL} and I_{FL} are the impacts associated with Q_{mid} on the rising and falling limbs respectively. The Hysteresis index (HI_{mid}) for clockwise loop is

$$HI_{mid} = (I_{RL}/I_{FL}) - 1 \qquad \text{Eq. 6.5}$$

and for anticlockwise hysteresis

$$HI_{mid} = (-1/(I_{RL}/I_{FL})) + 1 \qquad \text{Eq. 6.6}$$

The parameters used in the calculation of HI_{mid} are shown in a typical example in Figure 6.11.

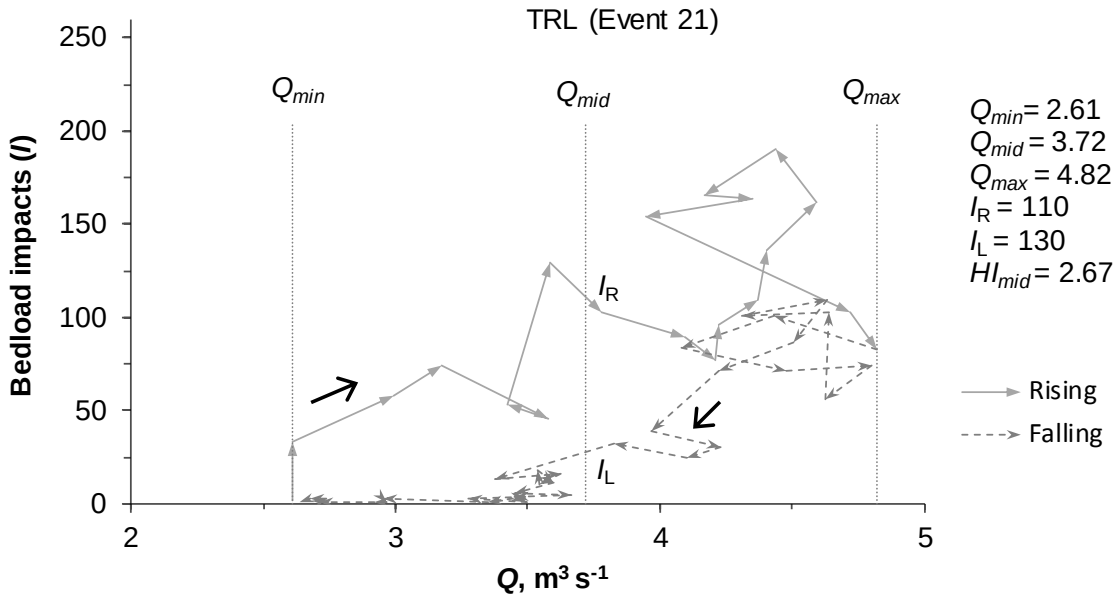

Figure 6.11. An example of clockwise *I*-*Q* hysteresis (Event 21) with k = 0·5. The Q_{min}, Q_{mid} and Q_{max} which are the Q at the start of the event, the mid-event Q and the maximum Q that are required to calculate the hysteresis index (Lawler *et al.*, 2006) are shown.

This hysteresis index is simple; the greater the hysteresis the higher the index and the positive index indicates clockwise hysteresis and negative the counter-clockwise. A zero value of the index indicates that no hysteresis is present. The hysteresis indexes for selected 14 events are presented in Table 6.8 which shows that the TRL has highest index for Event 21 (2.7) and lowest for Events 2 and 10 (0.4), whilst the BLL has highest for Event 19 (-6.7) and lowest for Event 15 (-0.2). The last column in Table 6.8 shows six representative events which are analysed in greater detail in section 6.3.2. These include Events 2 and 4 which show the impact patterns at TRL and BLL respectively; Event 7 is included to show the impacts pattern during a thunderstorm; and Events 12, 15 and 19 to compare the TRL and BLL impacts during the same event.

The positive index indicates a clockwise hysteresis whilst the negative index indicates an anticlockwise loop. Out of seven TRL events presented in Table 6.8, four are positive and three negative whereas out of 11 BLL events six are positive and five negative which indicates that number of clockwise and anticlockwise events are approximately equal. The clockwise and anticlockwise relationships show that the delivery of bedload is not concurrent with the discharge peak. However, it also depends on the size of the index, for example 0.2 suggests that the bedload and *Q* are fairly concurrent. The clockwise hysteresis indicates higher number of counts on the rising limb for a certain discharge and is generally known as "intra-event" or "first-flush effects" in which much of the available bed material is entrained by the first storm, leaving little for later transport even at higher stages (Lawler *et al.*, 2006). The clockwise hysteresis can arise when erosion or remobilisation of sediment accumulated in previous events occurs (Lewkowicz & Wolfe, 1994; Bogen, 2004), multi-peaked events minimise sediment availability in the catchment (Moliere *et al.*, 2004) or bed material in the upstream reach is stripped down (Lenzi & Marchi, 2000). The anticlockwise hysteresis may occur from a rapid increase in bed material availability after peak discharge due to increased availability of sediment sources. The anticlockwise hysteresis indicates that sediment supply is not limited, either within individual flood event or through sequence of events. Both positive and negative indexes in Trout Beck indicate the occurrence of both first-flush as well as the sediment entrainment after the discharge peak.

Table 6.8. Lawler Hysteresis index for TRL and BLL for different storm events. Index direction is shown positive '+' for clockwise hysteresis and negative '-'for anticlockwise hysteresis and the index associated with saturated counts (I > 255) is also marked by (S). The last column shows some typical events which will be discussed in section 6.3.2.

Event number	Sensors		Discharge ($m^3 s^{-1}$)								HI_{mid}		Hysteresis direction		Events selected for further analysis (Peak Q)
	TRL	BLL	TRL				BLL				TRL	BLL	TRL	BLL	
			k	Q_{min}	Q_{max}	Q_{mid}	k	Q_{min}	Q_{max}	Q_{mid}					
1	√		0.55	1.9	3.0	2.5					-1.2		-		
2	√		0.25	3.4	6.6	4.2					0.4		+(S)		Event 2
4		√					0.5	2.5	7.8	5.2		-4.5		-	Event 4
5		√					0.5	2.9	4.5	3.7		-3.2		-	
7		√					0.6	0.1	9.3	5.6		-1.7		-(S)	Event 7
8		√					0.5	2.6	6.0	4.3		1.5		+	
10		√					0.7	3.0	6.3	5.1		2.3		+	
11		√					0.7	2.8	5.1	4.3		0.9		+	
12	√	√	0.6	2.8	6.9	5.2	0.5	2.5	6.9	4.7	-1.0	2.4	-	+(S)	Event 12
13	√	√	0.6	3.2	5.0	4.3	0.5	0.8	5.0	2.9	0.4	0.9	+	+	
15	√	√	0.5	3.5	6.8	5.1	0.5	3.1	6.8	4.9	-1.8	-0.2	-	-	Event 15
17		√					0.7	1.7	5.7	4.3		4.8		+	
19	√	√	0.5	3.1	9.8	6.5	0.5	2.7	9.8	6.3	1.4	-6.7	+(S)	-(S)	Event 19
21	√		0.5	2.6	4.8	3.7					2.7		+		

Applying this hysteresis index for bedload rather than suspended load transport, for which the index was originally derived (Lawler *et al.*, 2006), should be borne in mind when interpreting the data because patterns of bedload transport in upland channels are intrinsically more complex than suspended load variations. Furthermore, if the bedload impact time series are truncated because of saturation in the logger at higher transport rates (*i.e.* $I > 255$), it is very difficult to fully interpret the form of the hysteresis relationship and calculating the hysteresis index is likely to be flawed because the overall form of the relation is not known; such events are marked as 'S' in Table 6.8. The next section will illustrate hysteresis loops from six representative events (Table 6.8) and discuss the pattern of bedload material impacts in relation to discharge variations. The Events 2, 4, 7, 12, 15 and 19 have the peak discharges 6.2, 6.6, 8.7, 6.2, 6.7 and 8.8 $m^3 s^{-1}$ respectively (Table 6.2).

6.3.2 Events analysis

Event 2

The time series of TRL impact counts, discharge and shear stress during the event of 15 September 2013 and the associated hysteresis are shown in Figure 6.12. This is a fairly big flood (peak Q = 6.2 $m^3 s^{-1}$, Table 6.2) and the impact count generally tracks the discharge and shear stress. The bedload activity starts by registering 1 impact count at 12:05 at Q = 1.7 $m^3 s^{-1}$ and τ = 51 N m^{-2}, rapidly increases to reach saturation in one and a half hours at 13:35, remains at saturation for just over two hours until 15:45 and then decreases for about four and a half hours until the impact count reduces to near-zero at 20:05 at Q = 1.8 $m^3 s^{-1}$ (51 N m^{-2}), and again continues with a small secondary spike at 22:00.

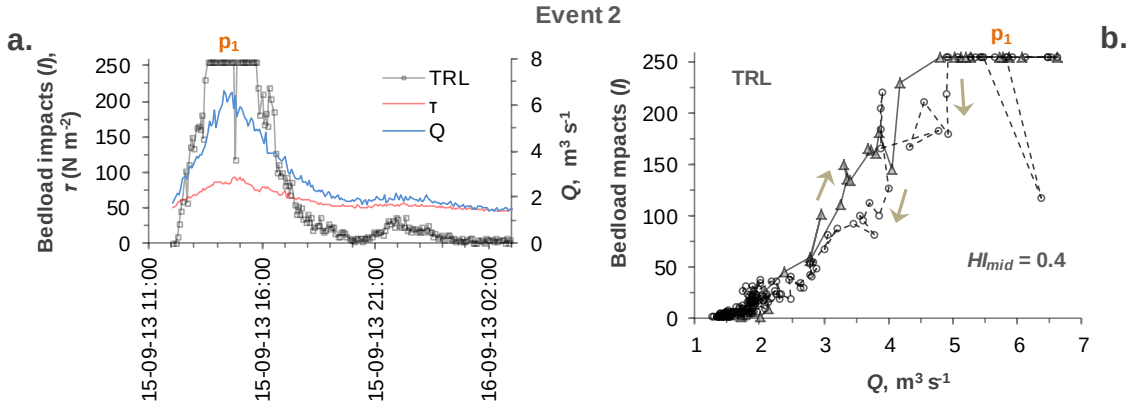

Figure 6.12. Bedload impact during Event 2, 15 September 2013: (a) time series of TRL impact counts, τ and Q; (b) a clockwise hysteresis with index HI_{mid} = 0.4. The impact peak is labelled as p1.

The threshold discharge Q_c *i.e.* the discharge associated with 50 impact counts is 2.8 $m^3 s^{-1}$ both for entrainment and cessation (Table 6.5). The clockwise hysteresis (HI_{mid} = 0.4) generally indicates the bedload movement occurs as per the availability of the sediment and there is slight deficit of supply in the falling limb. One reason for lower count in recession could be that the most-easily moved grains (e.g. small but in exposed positions) will move on the rising limb, so same shear stress on falling limb cannot move so many grains. This is very likely in this case as there is no evidence of a lag between discharge and impact counts as it would take some time for upstream supply to impact on this locally.

Event 4

Figure 6.13 shows the BLL impact counts and associated hysteresis during the event of 23 December 2013. It is a fairly big flood (peak Q = 6.6 $m^3 s^{-1}$) but with low impact counts. The sediment activity starts at 13:20 at 2.5 $m^3 s^{-1}$ (55 N m^{-2}), but the counts remains near-zero until 14:50 (6 $m^3 s^{-1}$) , then increase with the increasing Q (or τ), reaching a peak p_1 at 15:50 which is 40 minutes after the peak Q at 15:10, then decreases and suddenly rises again at 17:30 to saturation point (p_2) where it remains for 20 minutes, then drops again and fluctuates before it finally ceases at 21:00 at 2.1 $m^3 s^{-1}$ (52 N m^{-2}).

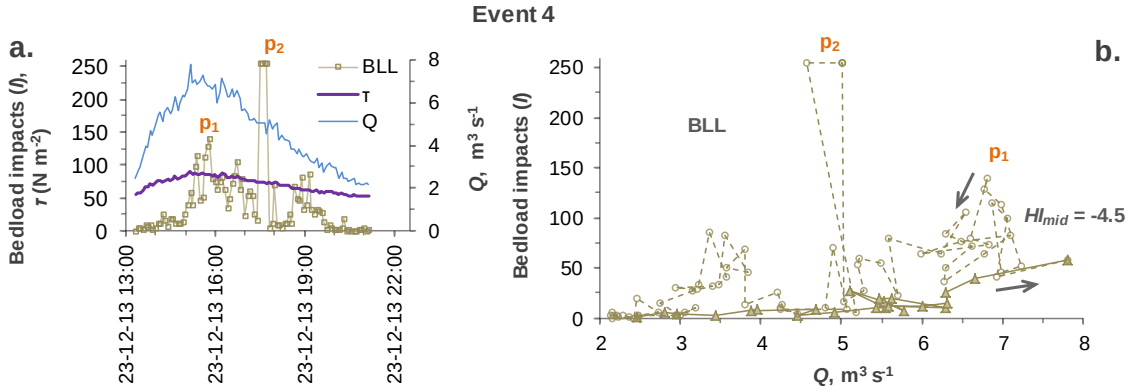

Figure 6.13. Bedload impact during the fourth event, 23 December 2013: (a) time series of BLL impact counts, the shear stress τ, and Q; (b) hysteresis.

The threshold discharge Q_c associated with 50 counts is 6.7 $m^3 s^{-1}$ on entrainment and 3.6 $m^3 s^{-1}$ on cessation (Table 6.5). The negative but complex hysteresis (HI_{mid} = - 4.5) suggests that the supply is generally limited on the rising limb and the multiple pulses on the falling limb indicate the intensity of impacts is uneven. The impact peak p_2 on the falling limb at Q = 5 $m^3 s^{-1}$ appears to be a local phenomenon possibly related to a

local bank collapses or migration of a small sediment patch or temporary switch of main transport path.

Event 7

The BLL impact counts and associated hysteresis during the event of 8 August 2014 are shown in Figure 6.14. This is a thunderstorm-caused big flood (peak Q = 8.7 m^3 s^{-1}) with very low starting Q and may not be comparable to other events hydrologically. The impact count tracks the discharge and shear stress and the impact peak coincides with the discharge peak. The bedload movement starts at 16:50 at < 0.5 m^3 s^{-1}, rises rapidly on the ascending limb and reaches saturation (p_1) in less than half an hour at 17:10, remains at saturation for an hour and a quarter until 18:25, decreases another half an hour until 19:00 and then increases again to give a spike (p_2) at 19:20 which remains at saturation for only five minutes, fluctuates again and finally the transport ceases at 22:50 at 2.3 m^3 s^{-1} (53 N m^{-2}).

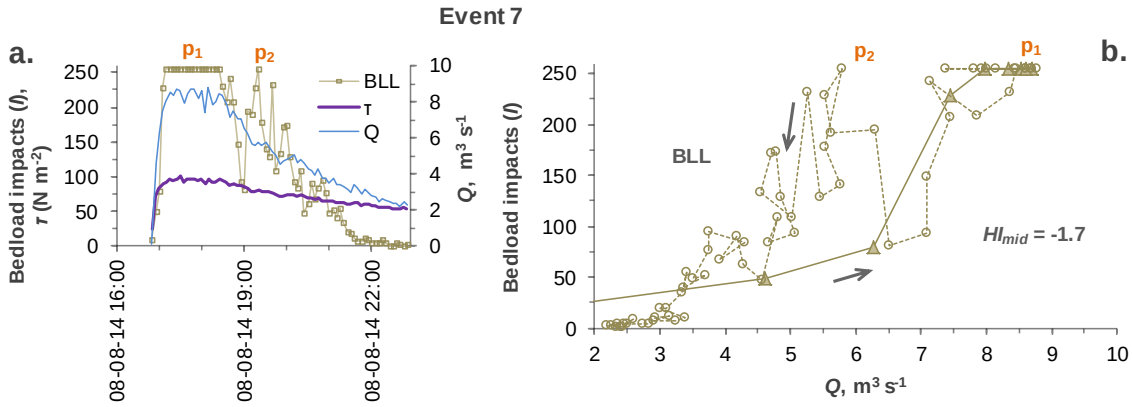

Figure 6.14. Bedload impact during thunderstorm-caused Event 7, 8 August 2014: (a) time series of BLL impact counts, τ and Q; (b) hysteresis.

The threshold discharge Q_c associated with 50 impact counts is 4.6 m^3 s^{-1} on entrainment and 3.4 m^3 s^{-1} on cessation (Table 6.5). The negative hysteresis (HI_{mid} = -1.7) indicates that the supply is generally limited on the rising limb and the multiple pulses on the falling limb suggest the intensity of impacts is uneven.

Event 12

Figure 6.15 shows the event of 28 October 2014 which is a fairly big flood (peak Q = 6.2 m^3 s^{-1}) and has the impact data from both TRL and BLL, thus allowing a direct comparison of the two. The impact count tracks Q at TRL and this event is very similar to Event 2, whilst the BLL does not track Q. The bedload transport at TRL starts at 15:40 at 2.8 m^3 s^{-1} (61 N m^{-2}), rises for an hour and a quarter to reach saturation (p_2),

remains at saturation for just over half an hour until 17:20 and then declines for two and a half hours until the bedload transport ends at 19:55 at 2 $m^3 s^{-1}$ (55 N m^{-2}). The bedload motion at BLL starts at 15:35 at 2.5 $m^3 s^{-1}$ (55 N m^{-2}), reaches to saturation (p_1) at 16:30 and remains there for 20 minutes until 16:50, declines to a low level (I = 35) at 17:25, fluctuates and again rises to another peak (p_3) at 19:45 and reaches to near-zero counts at 21.20 at 2.0 $m^3 s^{-1}$ (51 N m^{-2}) and continues, with a small spike at 22:55. The threshold discharge Q_c for entrainment and cessation are 4.8 and 4.4 $m^3 s^{-1}$ for TRL and 3.3 $m^3 s^{-1}$ and 4.8 $m^3 s^{-1}$ for BLL respectively (Table 6.5). The TRL has a very narrow hysteresis loop with a negative index (HI_{mid} = - 1.0). The BLL hysteresis is generally clockwise (HI_{mid} = 2.4) indicating the supply is limited on the recession limb. The impact count time series shows that the first bedload pulse occurs in the lower semi-alluvial reach before it occurs in the gorge which may suggest that the threshold discharge in the upstream alluvial reach is higher than in the lower semi-alluvial reach, and also that the first pulse (p_1) is generated by the sediment entrained within the lower semi-alluvial reach. But it is possible that this is a random occurrence where the threshold is higher at TRL than at BLL.

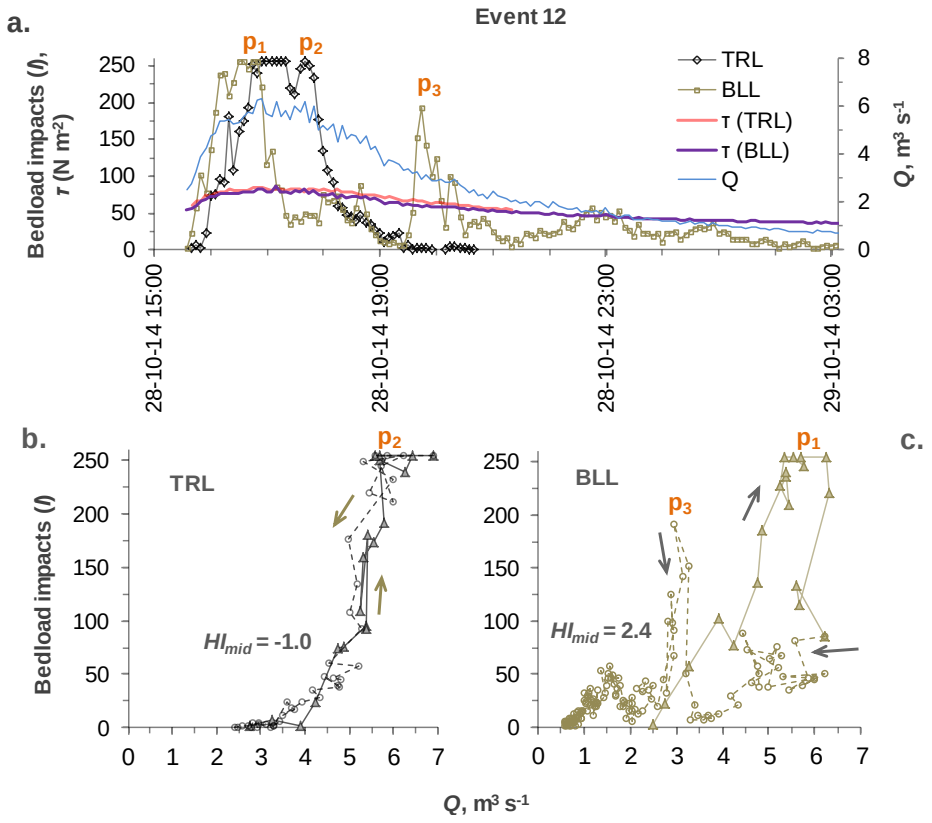

Figure 6.15. Bedload impact during the 12th event, 28 October 2014: (a) time series of TRL and BLL impact counts, Q and τ; (b) TRL hysteresis; and (c) BLL hysteresis.

The plots also suggest that the peak in the gorge (p_2) is generated by the sediment entrained from the upstream reaches which is followed two and a half hours later by a second peak in the lower semi-alluvial reach (p_3). Bedload movement still continues at lower discharges because it is in motion and the armoured bed is broken /disturbed. The impact peak matches the discharge peak for TRL but not for BLL and the impacts have strong relationship with discharge for TRL with coefficient of determination $R^2 = 0.78$ but weak for BLL with $R^2 = 0.45$.

Event 15

Figure 6.16 shows an event on 14 December 2014 which is a fairly big flood (peak Q = 6.7 $m^3 s^{-1}$) with bedload impact data from both loggers. As in other previous events the impact count tracks Q for TRL but does not for BLL. As in previous events the TRL has only one peak (p_2) but BLL has multiple peaks and its major peak (p_3) does not coincide with the discharge peak.

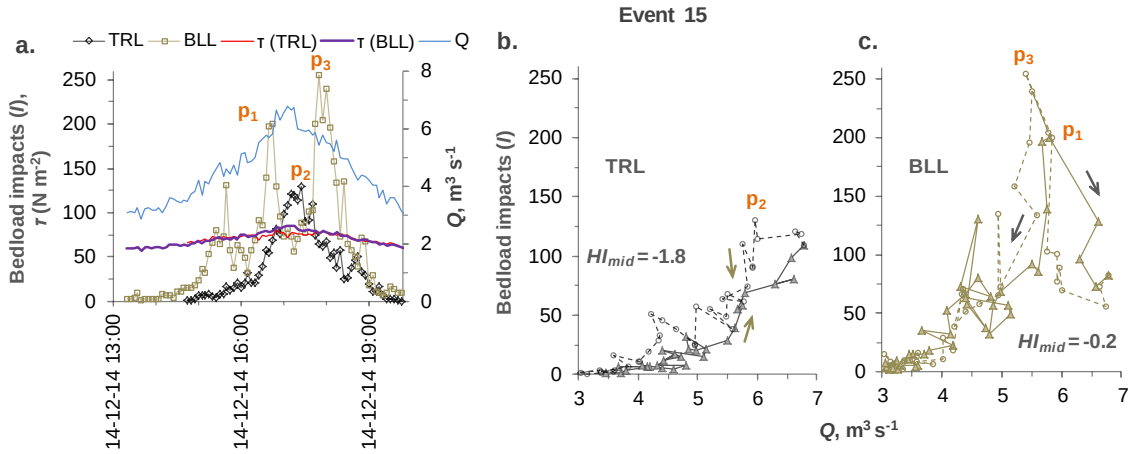

Figure 6.16. Bedload impact during 15th event, 14 December 2014: (a) time series of TRL and BLL impact counts, τ and Q; (b) TRL hysteresis; and (c) BLL hysteresis.

The bedload motion at TRL starts at 14:45 at 3.5 $m^3 s^{-1}$ (65 N m^{-2}), reaches peak p_2 at 17:25 and ceases at 20:35 at 2.8 $m^3 s^{-1}$ (56 N m^{-2}). The bedload motion at BLL starts at 13:20 (about one and a half hour earlier than at TRL) at 3 $m^3 s^{-1}$ (59 N m^{-2}), reach peak p1 at 16:45, drops and again reaches the major peak p3 at 17:50, declines and ends at 20:00 at 2.9 $m^3 s^{-1}$ (58 N m^{-2}). The threshold discharges Q_c for entrainment and cessation are 5.8 and 4.2 $m^3 s^{-1}$ for TRL and 4.1 and 4.3 $m^3 s^{-1}$ for BLL respectively. The TRL has a narrow and anticlockwise hysteresis pattern (HI_{mid} = - 1.8) with low transport rates on the rising limb, whereas BLL has a complex hysteresis pattern (HI_{mid} = - 0.2).

Event 19

Both sets of data, TRL and BRL, during the largest event (peak Q = 8.8 m^3 s^{-1}) in the study period on 26th February 2015 are plotted in Figure 6.17. The nearly-linear relationship of TRL counts with Q and narrow hysteresis pattern of bedload transport (HI_{mid} = 1.4) follows the discharge hydrograph quite closely. However, unlike in previous Events 12 and 15, the first impact peak (p_1) occurs at TRL. The bedload activity at TRL starts at 02:30 at 3.1 m^3 s^{-1} (62 N m^{-2}), reaches saturation after four and a half hours at 07:00, remains at saturation for three hours until 10:00, declines for three hours and ceases at 13:00 at 3.4 m^3 s^{-1} (64 N m^{-2}). The plot shows that BLL lags Q and TRL at first, but peaks about peak discharge.

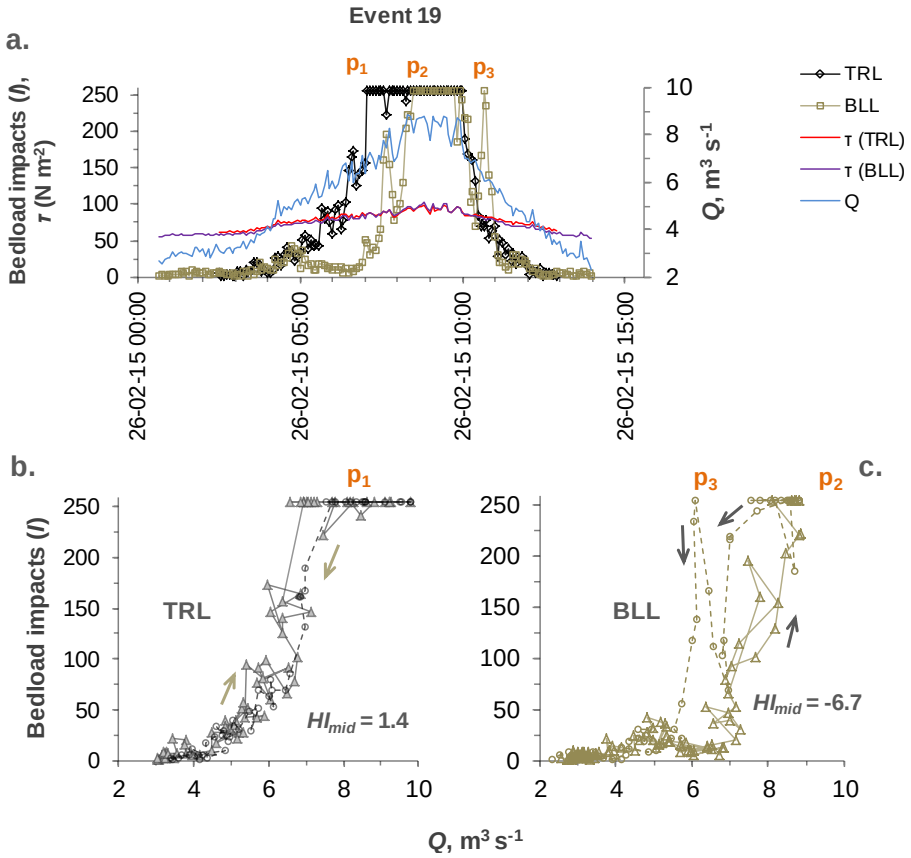

Figure 6.17. Bedload impact during 19th event, 26 February 2015: (a) time series of TRL and BLL impact counts, τ and Q; (b) TRL hysteresis; and (c) BLL hysteresis.

The bedload movement at BLL starts at 00:40, about two hours earlier than TRL, at 2.7 m^3 s^{-1} (56 N m^{-2}) and reached saturation (p_2) after eight hours at 08:30, remains at saturation for an hour and a quarter until 09:45, declines until 10:25 and increases to reach saturation (p_3) at 10:40, remains at saturation for 5 minutes and then drops to a near-zero counts at 12:30 at 4.1 m^3 s^{-1} (65 N m^{-2}). The threshold discharge Q_c for entrainment and cessation are 5.3 and 5.5 m^3 s^{-1} for TRL and 4.8 m^3 s^{-1} and 5.7 m^3 s^{-1}

for BLL respectively. The anticlockwise hysteresis at BLL (HI_{mid} = -6.7) suggests limited transport on the rising limb of the hydrograph.

Summary

The impact count curves for individual events are variable but some trends can be identified. The impact data in the upper sensor in the gorge (TRL) generally have a single peak showing a stronger linear relationship with discharge, whilst the sensor in the lower semi-alluvial reach (BLL) shows multiple pulses showing a weaker linear relationship with discharge. However, the start-stop analysis shows that the threshold values at the start of transport are related with the threshold values at the end of previous transport with a slightly stronger relation for BLL than TRL (Figure 6.10). The power-law fitting also shows that there is less variability in BLL threshold values (Figure 6.7). The start-stop analysis shows no significant variability between entrainment and deposition in either TRL or BLL (Figures 6.8 and 6.9). The TRL records the sediment entrained from upstream alluvial areas whilst the BLL receives sediment entrained locally as well as from upper reaches. The impact counts versus discharge curves are generally hysteretic; the numbers of events with clockwise and anticlockwise are almost equal. Most hysteresis curves are complex comprising both clockwise and anticlockwise loops but the TRL loops are relatively narrow and simple than the BLL. The multiple pulses in the lower logger data are possibly attributed to sudden release of sediment from the semi-alluvial patches or local erosion within the reach. The variable and pulsing nature of the bedload transport in lower sensor data has also been reported in both bedrock channels (Richardson *et al.*, 2003) and gravel bed rivers (Brayshaw, 1985; Reid *et al.*, 1985; Garcia *et al.*, 2000).

6.4 Advantages, disadvantages and factors affecting the impact counts

The main advantage of sediment impact sensors is that they provide quasi-continuous information of bedload transport intensities (Rickenmann & Fritschi, 2010) and provide information on the start and end of bedload transport including the duration of movement (Turowski *et al.*, 2011). These data are useful in establishing threshold discharge and shear stress values, and can be used to infer sediment supply and transport rate.

Furthermore, they are affordable, easy to maintain and are largely non-invasive. The disadvantages are they need calibration to estimate the actual bedload flux and do not provide direct information on the grain size distribution of the bed load. On-going

research linking the sensors data to bedload particle size (e.g. Wyss *et al.*, 2014; Barrière *et al.*, 2015) is promising therefore estimation of bedload transport rate (Rickenmann *et al.*, 2014) from impact sensor data may be possible in the future. The analysis in this chapter is solely based on the number of impact counts recorded by the sensors, which are dependent on a number of factors:

Size and shape of the particles

The particle size and mass from fines to pebbles and cobbles in the bed load mix affect the signal response of the impact sensor. In a flume experiment with pebbles and gravels using PBIS, Etter (1996) found that the number of impulses per unit mass reduces almost linearly with grain size, however this should also depend on the number of grains per unit mass. Other research (Böckli, 2011; Rickenmann *et al.*, 2014) has shown that up to 40 mm particle size, the impulse increases with grain size and then starts decreasing again. Particle shape can also affect the impact counts as it affects the mode of transport; for example, a spherical particle tends to roll and is likely to generate more impulses than similar-sized particles of other shapes which travel by saltation or sliding (Turowski & Rickenmann, 2009). The study on Swiss geophones conducted by Wyss *et al.* (2014) has shown that the sensor signal can be related to the maximum size of the transported material. In a flume and field study on a piezoelectric hydrophone mounted under a steel plate Barrière *et al.* (2015) studied the amplitude and frequency of a single impact and developed a technique to relate the D_{50} of the transported material with the sensor signal properties. Though these are some different types of systems that record different types of data and the impact plates used in this study do not record signal size but all these show that grain size and shape affect the sensors data, factors which have not been explicitly accounted for in this study.

Impact location on the plate

Studies have shown that the amplitude of the voltage response reduces from the sensor therefore the sensor response to a single strike is a function of grain size as well as the location of the strike. Marr *et al.* (2011) investigated this by dropping a 100 mm diameter particle on the surface of geophone plate at various distance from the centre (0, 5, and 20 cm) and found that the highest voltage response was at the centre and the lowest at 20 cm from the centre. This shows the same size particle can have different responses depending on where it hits the plate.

Mode of bedload motion

The middle logger ML which was in a narrow section only 60 m downstream of the top loggers (Figure 6.1) did not record all the impacts that were recorded by the TRL, and the most likely reason is that pebbles that were passing through the ML plate were saltating, not sliding or rolling. A small step in the bed immediately upstream of the plate location would also enhance this effect. Turowski and Rickenmann (2009) from a flume experiment on Swiss geophone plate and Krein *et al.* (2008) from a hydrophone experiment found that the mode of bedload transport has an influence on the impulse response. The study conducted by Tsakiris *et al.* (2014) on geophone plates showed that rolling particles generated a stronger response at lower frequency (100 – 200 kHz) and weaker response in higher frequency (380 – 480 kHz) whereas the saltating particles behaved the other way round. Since the sensor response determines the quantity and size of signal spikes, the type of bedload motion appears to influence the recorded bedload impacts.

Flow velocity

Flow velocity has a strong control on bedload transport rate, if sediment supply is unlimited. This analysis has shown that Trout Beck is generally supply limited. Though the impact count generally tracks for the upper sensor (TRL) for most of the events it does not track for the lower sensor (BLL) because of the complex bed character comprising pool, boulders and varied sediment cover. In a geophone experiment, Rickenmann *et al.* (2014) found that the number of impulses per unit mass tended to decrease with increasing mean velocity as the idea is that at higher flow the saltation length increases and therefore the grains jump over the impact plate. The impact count is not only a result of grain mass (or size) but also a function of grain momentum *i.e.* the product of mass and velocity (Richardson *et al.*, 2003). Flume studies have shown that saltation height and the step length of the grains depend on excess shear stress (Lajeunesse *et al.*, 2010).

Thread of maximum bedload transport

At the upper and lower cross-sections, the impact plate located in the main thread of the flow recorded a higher number of impulses; hence the location of the plate within the cross-section dictates the number of counts. The upper sensor TRL recorded many more impacts than the TLL which was next to it, and this also happened in the lower section

where BLL recorded far more impacts than BRL. Part of the reason could be differences in sensitivity of the loggers but since it happened in almost all events it is likely that the reason is related to the thread of maximum bedload transport. Richardson *et al.* (2003) also observed that their sensor located on an abraded track (area of maximum bedload transport) recorded a much greater number of impacts than the sensor just 1.1 m apart in the same cross-section but outside the abraded track.

Range of supply factors

The multiple peaks and the hysteric loops of the impact counts (Section 6.3.2) suggest the sediment supply in Trout Beck was at times supply-limited; hence supply factors are also important in determining the bedload counts. For the upper sensors the supply was from upstream reaches whereas for the lower sensors the local supply was also available. In addition, there were a few places (Fig 2.21) which could potentially produce small bank collapses and supply sediment to the channel and therefore some of the small pulses in the lower sensor could be attributed to such lateral failures.

6.5 Chapter summary

This chapter has presented the analysis of bedload impact sensors data from Trout Beck (Research Question 4, Section 1.4.1). Bedload impulses were monitored for 20 months from August 2013 using five sets of impact sensors installed in three different locations (2-1-2) in the study site. The general pattern of the data is that the right side sensor in the rock gorge recorded over 90% of the total non-zero periods in that cross-section whilst the left sensor recorded less than 10 %. Similarly in the lower semi-alluvial reach, the left sensor recorded 83% of the non-zero periods leaving only 17% for the right sensor. The middle sensor at the bottom of the bedrock gorge recorded an appreciable number of transport events but the number of counts in each 5 minutes period was very low. This shows a large variation in the bedload activity in longitudinal as well as transverse directions. A detailed analysis has been undertaken using the data from upper sensor TRL and lower sensor BLL. Though the TRL was located in the gorge, its data represent grain entrainment in the upper alluvial reach where the supply was sourced from, whereas BLL received locally entrained sediment as well as sediment from upstream reaches.

A low reference transport rate of 50 counts per 5 minutes interval has been estimated to be a reasonable “threshold impact count” based on which the threshold discharge (Q_c)

and shear stress (τ_c) have been calculated by three approaches: frequency of periods exceeding 50 counts; power-law equations from impact counts versus discharge plots; and the start-stop analysis of the bedload transport following the method of Turowski *et al.* (2011). The period analysis approach gives the threshold values Q_c = 3 $m^3 s^{-1}$ and τ_c = 65 N m^{-2} for the upper sensor and 4.0 $m^3 s^{-1}$ and 65 N m^{-2} for the lower sensor (Table 5.10). The power-law equations give the Q_c values from 2.4 – 6.0 $m^3 s^{-1}$ (average 4.3 $m^3 s^{-1}$) for the upper sensor and 4 – 5.8 $m^3 s^{-1}$ (average 4.5 $m^3 s^{-1}$) for the lower sensor. The start-stop analysis shows that the threshold for entrainment is approximately similar to the threshold of cessation for both the sensors and the threshold values Q_c and τ_c are 2.6 – 5.8 $m^3 s^{-1}$ and τ_c = 59 – 79 N m^{-2} (average: 4.2 $m^3 s^{-1}$, 71 N m^{-2}) for the upper sensor; and 3.3 – 6.7 $m^3 s^{-1}$ and 61 – 85 N m^{-2} (average: 4.1 $m^3 s^{-1}$, 68 N m^{-2}) for the lower sensor. All these results show that Trout Beck does not have a single threshold value, which is as expected, and an overall range of threshold discharge is 2.4 – 6 $m^3 s^{-1}$ for upper sensor and 3.3 – 6.7 $m^3 s^{-1}$ for lower sensor. The relationship between discharge at the start of transport against the discharge at the end of previous event are also analysed using the method of Turowski *et al.* (2011). The results show a large scatter of the data for upper sensor and they do not plot along a one-to-one line; however they are less scatter and close to one-to-one line for the lower sensor.

A conceptual summary diagram showing the threshold values for five sub-reaches (F1 to F5) in three morphological reaches (upper alluvial, bare rock and lower semi-alluvial) has been presented in Figure 6.18. The three blocks in this diagram show the channel bed, sediment supply and transport, grain entrainment and location of impact plates in upper alluvial reach, bedrock gorge and lower semi-alluvial reach. The threshold values that represent sub-reach F1 to F5 are shown, which will be further discussed in chapter 7. The broader implications of these findings are discussed in chapter 7.

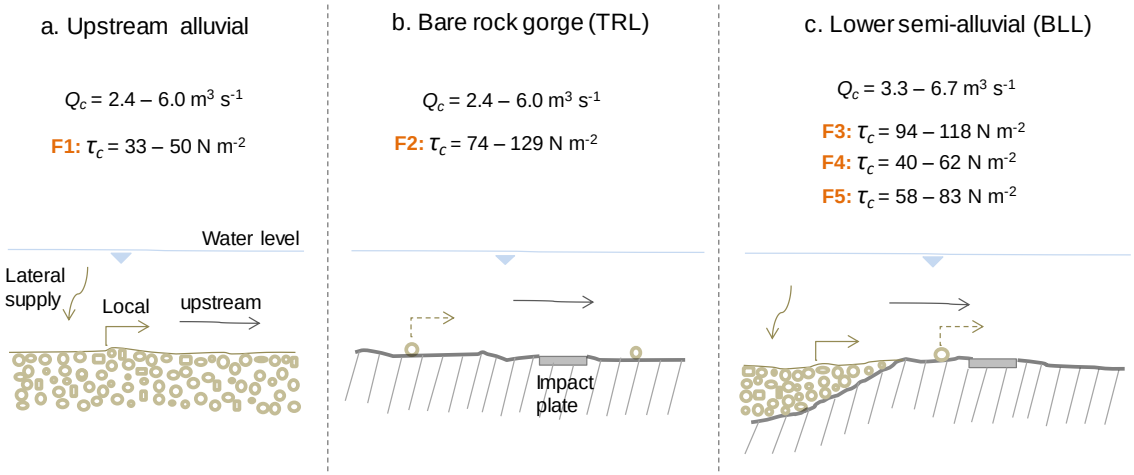

Figure 6.18. Summary diagram showing sediment dynamics in the upstream alluvial, bare rock gorge and lower semi-alluvial channel reaches. Critical discharge Q_c and shear stress τ_c values at five sub-reaches F1 to F5 are shown: a) typical upper alluvial bed showing the supply from upstream and sides, entrainment from bed, and water depth in the channel; b) bare rock gorge showing the impact plate, supply from upstream and occasional entrainment (dotted arrow); and c) lower semi-alluvial reach showing the impact plate, the mix of alluvial and exposed surfaces, the lateral and upstream supply, entrainment from alluvial patches and exposed surfaces.

The intra-event variability of bedload activity has been analysed. A hysteresis index has been used to quantify the hysteresis curves and the result shows both positive (clockwise) and negative (anticlockwise) indexes. This indicates that first-flush entrainment, as well as the entrainment following the peak *Q* occur at both sites. Analysis of the event count time series has shown that the upper sensor has a simple response and consistent behaviour, with one major peak generally coinciding with the discharge peak, narrow hysteresis and at times limited sediment supply. However the lower sensor has multiple peaks, is generally sediment supply-limited and has a complex response due to intervening channel architecture and sedimentology. The discharge and shear stress to initiate and cease the bedload motion varies temporally and spatially which clearly shows that the bedload formulas which use a single threshold value do not accurately predict the actual sediment transport through a reach.

7 Discussion and conclusions

This discussion is based on the results of field measurements of channel morphology, bulk hydraulics, tracer pebbles and sediment impact counts as described in detail in chapters 2, 4, 5 and 6 respectively. This chapter is divided into six sections. Section 7.1 restates the aims of this research, offers answers to the research questions identified in section 1.4.1, and discusses the major findings and their relationship to previous work. The following three sections put the Trout Beck results into a wider context and discuss their implications for other academic work and practical applications. Section 7.2 considers alluvial-to-bedrock transitions along rivers more generally, and the various ways in which the necessary downstream changes in stream power and sediment conveyance could be triggered. Section 7.3 takes a longer-term perspective, discussing what might happen in extreme floods and how gradual incision of bedrock channels could feed back to the local flow and bedload transport processes. Section 7.4 identifies some findings from Trout Beck that cast doubt on assumptions commonly made in incision models and sediment studies and suggests how models and practice could be modified if the Trout Beck findings are more generally applicable. Section 7.5 reviews the research overall and identifies future avenues of research. Finally section 7.6 provides the conclusions of the thesis.

7.1 Scope and main findings of the study

The aim of this study was to further understand the sediment transport processes in bedrock reaches by acquiring field data from contrasting sub-reaches. This research has investigated the sediment dynamics by establishing links between channel geometry, sediment transport and local reach hydraulics. The details about the findings relating to each of the four research questions (RQs) have been discussed and summarised within the respective chapters: RQ 1 in chapter 4, RQs 2 and 3 in chapter 5, and RQ 4 in chapter 6. Each research question is reproduced and answered in the following sections. For the convenience of the reader, Figure 7.1 presents a reach map illustrating five morphological reaches (upper alluvial, upper semi-alluvial, bare rock, lower semi-alluvial, and lower alluvial), five hydraulic sub-reaches (F1: upper alluvial, F2: bare rock, F3: boulder-riffle, F4: lower semi-alluvial with 70 % sediment cover, and F5: lower semi-alluvial with 20 % cover) alongside a summary of the key findings of this research which will be discussed in the following sections.

a.

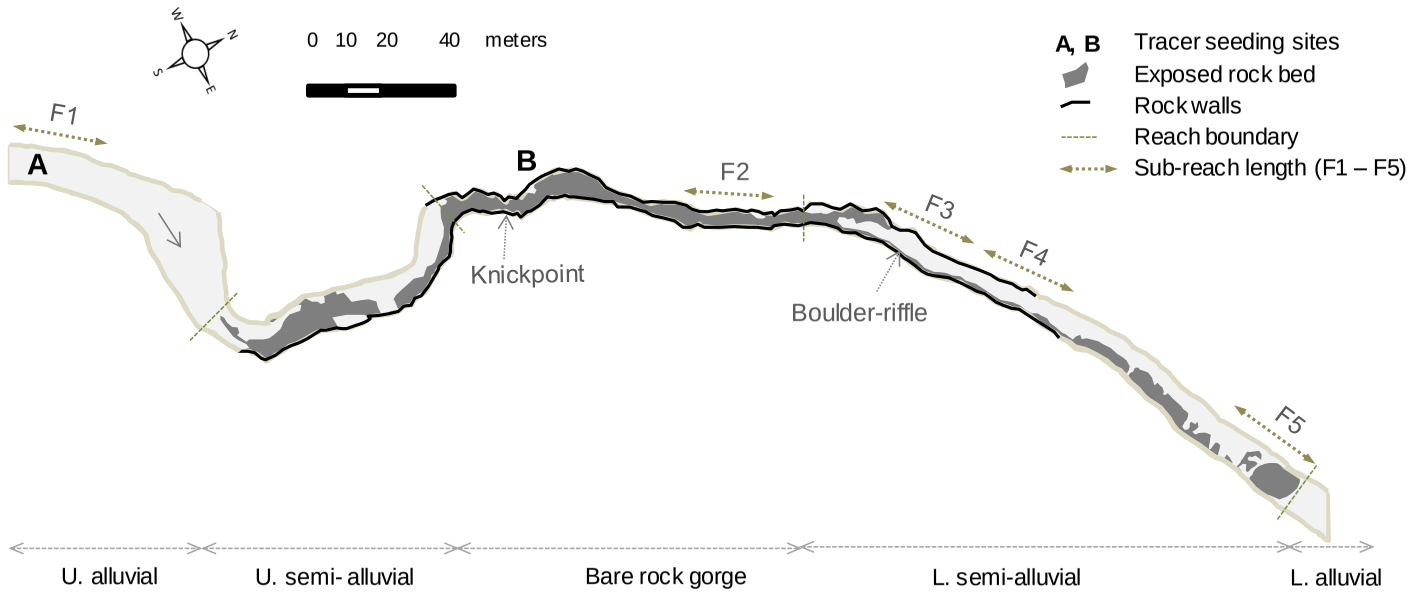

b.

Sub-reach (type)	% cover	Bed slope	Energy Slope, *S*	D_{50} (mm)	D_{84} (mm)	Manning's *n* (s m$^{-1/3}$)	Darcy-Weisbach *f*	τ (N m^{-2})	τ_c (N m^{-2})	τ^*_c	Bedload mobility	Size selectivity
F1 (alluvial)	100	0.015	0.009 – 0.011	36	116	0.046 – 0.156	0.19 – 3.6	15 – 69	47	0.081	very low	yes
F2 (bare rock)	1	0.019	0.016 – 0.025	-	-	0.046 – 0.128	0.25 – 2.5	24 – 194	< 119	-	very high	no
F3 (boulder-riffle)	70	0.013	0.017 – 0.020	84	190	0.068 – 0.273	0.39 – 10.1	28 – 129	107– 117	0.079 – 0.086	very low	yes
F4 (70% cover)	70	0.003	0.007 – 0.012	68	190	0.049 – 0.230	0.21 – 7.5	13 – 93	44 – 52	0.040 – 0.047	moderate	yes
F5 (20% cover)	20	0.014	0.017 – 0.023	64	140	0.041 – 0.151	0.16 – 3.8	17 – 110	63 – 72	0.061 – 0.070	high	no data

Figure 7.1. (a) Reach map showing 5 reaches and 5 sub-reaches. Sub-reach length (F1 – F5) varies from 24 to 28 m. (b) Key results for Trout Beck. The τ, τ_c and τ^*_c are respectively the total shear stress, critical shear stress and non-dimensional critical shear stress. The range of values shown for *S*, *n*, *f* and τ correspond to the discharge range 1 –12 m^3 s^{-1}. The τ_c and τ^*_c are based on tracer data (Table 7.2) The study site mean flow and mean annual flood are 0.39 and 10.6 m^3 s^{-1} respectively.

7.1.1 RQ 1: How do bulk flow properties vary according to bed character and with discharge?

The variation in at-a-station hydraulic geometry, flow resistance (n and f) and shear stress (τ) with river discharge (Q) have been examined in five short sub-reaches F1 to F5 (Section 2.5) using the measured discharge, stage and water surface profiles. Hydraulic geometry relations (Section 4.3) are a valuable tool in studying flow resistance (Ferguson, 1986; David *et al.*, 2010) which varies with depth and velocity (Section 1.1.3). A single power law (V-Q, d-Q, w-Q) is not appropriate for Trout Beck sub-reaches, therefore separate power laws for low and high Q have been fitted (Figure 4.23), as also done by Navratil and Albert (2010) in their 15 alluvial river reaches. Navratil and Albert (2010) suggested that the discontinuities at their sites were due to the lateral gravel bars, the hydraulic conditions of riffle cross-sections and change in flow resistance with depth (vegetation, sediment influence). However, in Trout Beck the discontinuities appear to be due to the change in flow resistance with depth as the data show that the kinks in both at-a-station hydraulic geometry (Figure 4.23) and flow resistance (Figure 4.26) plots are at same discharge values. The hydraulic geometry plots show that the velocity (V) increases more rapidly with discharge than depth (d) or width (w) at low to moderate flow, but at an only slightly higher rate than depth at high flows. However, in the bare rock gorge (F2) depth increases more rapidly than velocity at higher flows. This is most likely because the rock walls have numerous re-entrants and spurs (Figure 2.34) which provide higher flow resistance. The nearly-vertical walls in the gorge also restrict the width increment and therefore depth increases more strongly. The sub-reach F5 (20% cover) has a similar trend but depth increases less rapidly than in F2, possibly also because of smoother bed than the walls. The average values of the hydraulic geometry exponents for velocity (m), depth (f) and width (b) are broadly in line with other researchers' findings in steep mountain streams (Figure 4.25) (Judd & Peterson, 1969; Knighton, 1975; Beven *et al.*, 1979; Knighton, 1979; Bathurst, 1993; Lee & Ferguson, 2002; Comiti *et al.*, 2007), but different from those for large alluvial rivers studied by Leopold and Maddock (1953). The width exponent (b) value in Rio Cordon (Comiti *et al.*, 2007) was also higher than in Trout Beck. The observed greater increase of velocity than depth at low to moderate Q suggests a rapid decrease of flow resistance with discharge which also implies that roughness components are exposed to a smaller portion of the flow. All Trout Beck sites show $m > f + b$ at low

flows and $m < f + b$ at high flows (Table 4.8). According to David *et al.* (2010) this suggests grain resistance dominates the shallow flows and form or spill resistance dominates the deep flows.

The overall average values of Manning's *n* and Darcy-Weisbach *f* calculated over a wide range of discharges for five sub-reaches are 0.08 and 1.11 respectively (Table 4.9), which are within the range found elsewhere for shallow and high-gradient mountain rivers with or without exposed bedrock (Table 4.10) (e.g. Lee & Ferguson, 2002; Heritage *et al.*, 2004; Reid & Hickin, 2008). However, both *n* and *f* vary greatly both with discharge at a site and between sub-reaches at the same discharge. The fully and partly alluvial sub-reaches show a general trend of *n* and *f* decreasing with increasing *Q*, which is consistent with the findings from other shallow alluvial channels (Figure 4.27) (Kellerhals *et al.*, 1972; Hicks & Mason, 1991; Lee & Ferguson, 2002). However, in the bare rock gorge (F2) *n* and *f* decrease rapidly at low flow, but increase again at high flow, most likely because of rough rock walls. This is consistent with the findings of Heritage *et al.* (2004) in a bedrock reach of the Sabie River.

At any flow, the boulder-riffle sub-reach (F3) has the highest flow resistance, most probably due to higher form drag from its coarser grains including numerous boulders (e.g. Yager *et al.*, 2007) which results in lowest velocity and highest depth. Similarly, sub-reach F2 has the lowest value of flow resistance at low to moderate flow because of its smoother bed, which results in faster velocity. The other three sub-reaches F1, F4 and F5 have intermediate values of *n* and *f*.

The standard resistance laws do not accurately predict flow in the Trout Beck sub-reaches; however some resistance laws fit better than others. Manning-Strickler substantially underestimates flow resistance and none of the sites follow simple power laws (section 4.4.4). The Keulegan log law fits Trout Beck data better but for a boulder sub-reach a very high value of k_s/D_{84} (9) is required to fit the trend line. Ferguson (2007a) VPE performs well for sub-reach F4, slightly under predicts F1 and F3, and over predicts F5. Rickenmann and Recking (2011) non-dimensional hydraulic geometry ($v^{**} - q^{**}$) trend line fits better than the other relations, but still under predicts F3 and F1 (Fig 4.31a). Comparison of Trout Beck plots with prediction curves from various resistance laws (Figures 4.29, 4.31) shows that D_{84} is not necessarily a very good

estimate of the true effective roughness height (k_s). The value of k_s which collapses Trout Beck data into Rickenmann and Recking (2011) prediction curve is calculated (Figure 4.31 b), which shows that D_{84} under predicts the flow resistance in alluvial and semi-alluvial sub-reaches, except F5 (20% cover). A possible explanation is that the alluvial and semi-alluvial sites (F1, F3, F4) have very poorly sorted grains, include the boulders even up to 1 m or above sizes as well as the rough walls. The estimation of *f* or *n* using grain sizes D_{84} or D_{50} has some limitations as the flow resistance is the result of both the grains and the form drag on elements such as immobile boulders, morphology of walls, rock characteristics and bedforms. In semi-alluvial sub-reaches *ks* for rock bed is probably less than sediment D_{84}, though k_s for rock walls will be higher than D_{84}. And D_{84} may not be very precise when based on only 100 counts; and on very coarse cover, flow resistance depends on shape and arrangement of obstacles (via drag coefficient and hiding effects) as well as average size.

For all these reasons some scatter in the flow resistance plots would be expected, and the analysis has shown that huge changes in k_s (away from D_{84}, that is) would not be needed to bring each sub-reach into line (Figure 4.29). The direction of the required change in k_s is what would be expected: higher than D_{84} in F3, lower than D_{84} in F5 (Figure 4.31).

Total shear stress (τ) increases with increasing discharge because the hydraulic radius also increases with the discharge, while energy slope remains almost constant within a sub-reach. The slope does, however, differ considerably between sub-reaches (Figure 4.20), and this along with differences in width and roughness leads to considerable spatial differences in total shear stress at any given discharge. Shear stress in F2 is far higher than in F1 because of higher slope at the bare rock gorge; the hydraulic radii (or depths) are similar at both sites. The shear stress at F3 is even higher than in F2 up to moderate flow because of the higher depth, but shear stress at high flows in F3 is slightly lower than in the gorge. The shear stress in the pool immediately upstream of boulder-riffle is lower than in F2 and F3 because of very low bed slope and energy slope. Sub-reaches F4 and F5 have intermediate shear stresses, higher than F1 but lower than F2 or F3. The boulder sub-reach F3 has the highest or second highest shear stress but the tracer data suggest that the bedload mobility through that segment is very low

which clearly implies that the shear stress is not the only controlling variable. Other parameters which also affect bedload mobility are discussed below in relation to RQ 2.

7.1.2 RQ 2: How does sediment mobility vary according to bed character?

To investigate the relative sediment mobility in different parts of the study reach, two sets of 270 tracer pebbles one installed in the upper alluvial reach (set A) and the other in the bare rock gorge (set B), were monitored for nineteen months. The data from the first survey, after one and a half months, showed high mobility on the bare rock but very low mobility in the alluvial channel. In subsequent survey intervals, even at higher peak discharges, bedload mobility in the semi-alluvial and alluvial zones always remained lower than that it had been in the bare rock gorge during the first survey interval. This clearly shows that bare rock sub-reach conveyed the sediment more rapidly than alluvial or semi-alluvial sub-reaches. The particle dynamics also plays a role here as the threshold stress depends on friction angle and grain protrusion (Kirchner *et al.*, 1990). The smoother rock in the gorge produces high near-bed velocity and low friction angles resulting in lower threshold values for particle entrainment. Once the particles are entrained it is very likely that they won't stop until they meet an alluvial patch, therefore travel distances in the bare rock gorge are longer than elsewhere. This is also a reason why particle transport in the gorge was non-selective for size and shape but selective in alluvial and semi- alluvial segments, which will be discussed in the next section (Section 7.1.3).

The tracer mobility also differs quite significantly between the alluvial sub-reach (F1) and the sub-reaches within the semi-alluvial part of the river (F3, F4, and F5). If bedload mobility is a function of excess shear stress ($\tau - \tau_c$) or stress ratio (τ/τ_c), then since both the total stress (τ) and the threshold stress (τ_c) vary according to the channel geometry and bed character the potential bedload transport rate should also vary along the channel for contrasting sub-reaches. The boulder-riffle sub-reach (F3) and the immediate upstream backwater zone or "pool" (Figures 2.32, 5.6 d) significantly impede the natural downstream movement of the tracers. This suggests that the shear stress in the pool-boulder area only exceeds the threshold shear stress in major floods. In the boulder-riffle sub-reach, even though the total stress is high, the excess shear stress must be low compared to the gorge. The rapid movement of the tracers through the rock gorge, which experiences shear stresses similar to those in the boulder-riffle,

indicates that the excess shear stress in the gorge is high because of a low threshold stress (τ_c). In contrast, the boulder-riffle zone which accumulates the tracers must have very low excess stress because of the highest threshold stress, which is also shown by the highest values of *n* and *f* (Figure 4.26). Much of this higher resistance is likely to be the form drag component which is not available for sediment transport for the mobile sediment which means the effective stress (total shear stress τ minus form drag component) at sub-reach F3 is very low. The shear stress in sub-reach F4 (70% cover) is slightly higher than in the fully alluvial sub-reach F1 (Figure 4.32), but the threshold stress is similar, therefore the bedload conveyance in F1 is slightly higher than in F4. Both the shear stress and threshold stress in sub-reach F5 (20% cover) are higher than in F1 and F4, but lower than in F2 and F3; the excess stress and the bedload conveyance are second highest in F5, after the rock gorge.

The virtual velocity calculation assuming threshold values of 3, 5 and 5 $m^3 s^{-1}$ for bare rock, semi-alluvial and alluvial reaches suggest that virtual rates of transport in bare rock and semi-alluvial reaches are respectively 7 and 2 times higher than in the alluvial reach (Section 5.3).

Stress partitioning was attempted in the boulder-riffle sub-reach (F3) using the method of Yager *et al.* (2007) which splits the total shear stress into stress on mobile beds (i.e. effective shear stress) and stress on large immobile boulders. This method could not be made to work, and an alternative approach gave inconclusive results, which were heavily dependent on assumptions about drag coefficients.

7.1.3 RQ 3: How selective is bedload transport?

The alluvial site tracers (A) recovered in the 9-month survey were all still in the upper alluvial channel. Mean travel distances of different size classes showed size selectivity, with smaller tracers travelling farther on average. The majority of the A tracers recovered in the 19-month survey were also still in the upper alluvial reach and the mean travel distances for size classes again showed dispersion was size-dependent. The size-selective transport in the alluvial reach is consistent with the findings from several previous studies (e.g. Church & Hassan, 1992; Ferguson & Wathen, 1998).

In contrast, the bare rock site tracers (B), by the time of the first survey, dispersed rapidly through the gorge. The mobile tracers in the rock gorge included all sizes and

did not show any indication of size selectivity; similarly the tracers that remained in the gorge included all sizes except the smallest ones. The lack of size-selective transport in the bare rock gorge is consistent with the findings of Goode and Wohl (2010b) and Hodge *et al.* (2011).

The 9- and 19-month surveys, when most of the B tracers were travelling along the lower semi-alluvial reach, show that larger grains were less mobile than finer ones. This demonstrates that the transport distances are size-independent on bare rock but size-dependent in partially covered zones. However, the degree of selectivity in the partial-cover zone can be interpreted as slightly less than on a fully alluvial bed (Figure 5.19 b).

The multiple regression analysis of transport distances of individual tracer pebbles in relation to their diameter, mass and shape confirmed these interpretations. The B tracers result of first survey (Table 5.8) shows that R^2 value for regression on all three predictors (size, mass and Corey sphericity) is 0.01 and no predictor is statistically significant, which confirms the dispersion in bare rock was non-selective with respect to either size or shape. The analysis of 9- and 19-month data for both sets of tracers (Tables 5.7 and 5.8) shows that the movement was size-selective and for A tracers the particle shape has a small but significant secondary effect which is consistent with the findings of Warburton and Demir (2000) who showed the transport in gravel-bed rivers was selective to both shape and size of the particles. Overall, this study shows that bedload transport is selective in the alluvial reach, still selective in the semi-alluvial reach though possibly less so, but non-selective in the bare rock reach.

7.1.4 RQ 4: How do the flow and shear stress at initiation and cessation of bedload transport compare and vary according to bed character?

The threshold of initial motion refers to the flow stage at which grains start to move in a channel, and the threshold of cessation refers to the flow stage at which grains stop moving. This simple concept is quite complex in practice because of complications such as the wide range of grain shapes and sizes present in coarse-bedded streams, differences in packing arrangement and bed structure, the consequent variance in friction angle and the effects of bed forms. Despite its complexity, the threshold of motion is a very important attribute which is used in predictions of bed load flux. The quantification of the threshold values of discharge and shear stress and their variation according to the bed character have been discussed in sections 5.2.3, 5.2.4 and 6.2. This

section briefly discusses these values obtained from the tracer and impact count data, and compare these with values from empirical relations proposed by Schoklitsch (1962), Parker *et al.* (2011), Mueller *et al.* (2005), and Lamb *et al.* (2008b) (Section 1.1.6).

The visual observation of tracer dispersion indicates that the threshold discharge in the alluvial reach is higher than in the bare rock gorge and lower part of the semi-alluvial reach. However, the tracer data indicate that the pool and the boulder-riffle in the upper part of the lower semi-alluvial reach have very high threshold discharges similar to, or even higher than that of the alluvial sub-reach (F1). The lower mobility of the A tracers suggests lower values of excess stress, but that is most likely due to the low total stress in the upper alluvial channel. The start-stop analysis, as done by Turowski *et al.* (2011), showed no significant variability between initiation and cessation of bedload transport in Trout Beck reaches (Section 6.2.5).

The Schoklitsch equation (Eq. 1.24) is based on combining Shields' criterion (τ_c^* = constant, thus relating critical depth to slope and grain size) with Manning-Strickler flow resistance (to obtain critical discharge from critical depth and grain size). It is often used in steep mountain rivers to estimate q_c or Q_c (Schoklitsch, 1962; Warburton, 1990; Ferguson, 1994). Table 7.1 summarises the critical discharge (Q_c) values estimated from tracer and impact count data (Tables 5.11 and 6.7) along with the estimates from Schoklitsch (1962) and an approximation assuming the critical value of non-dimensional stream power (ω^*_c) = 0.1 (Eq. 1.27) as suggested by Parker *et al.* (2011) and Ferguson (2012).

Table 7.1. Critical discharges Q_c ($m^3 s^{-1}$) from field data (Tables 5.11 and 6.7) and empirical relations. The grain sizes (D_{40} and D_{50}) are undefined for F2 as there is no sediment on the main part of the bed, therefore the Q_c from empirical formulas are missing for F2.

Sub-reach (type)	Field studies		Equations from Literature	
	Tracer	Bedload impacts	Schoklitsch (1962)	Approximation assuming ω_{*c}=0.1 (Parker *et al*., 2011)
F1 (alluvial)	5.0	2.4 – 6.0	5.9	4.0
F2 (bare rock)	< 5.2	2.4 - 6.0	-	-
F3 (boulder-riffle)	5.0 - 6.6	3.3 - 6.7	6.6	5.6
F4 (semi-alluvial 70 % cover)	3.9 - 5	3.3 - 6.7	11.3	7.9
F5 (semi-alluvial, 20 % cover)	3.9 - 5	3.3 - 6.7	5.5	4.3

The tracer pebble data suggests that the tracers did not experience appreciable movement in the alluvial and boulder-riffle segments at discharges below 5 $m^3 s^{-1}$. This is consistent with the Q_c values shown in Table 7.1, and also with the analysis of impact count data in chapter 6. The Q_c estimates from Schoklitsch's equation appear to be broadly in line with the field estimates for three out of four sites, but not for F4 (70% cover). Lopes *et al.* (2001) found that Schoklitsch's equation worked well in eight out of 22 alluvial streams in USA which includes 2 out of 4 supply-limited channels. Bathurst *et al.* (1987b) also showed that Schoklitsch's equation worked well for supply-limited conditions. However, it is rather surprising that the Schoklitsch equation gives reasonable-looking estimates of Q_c in Trout Beck when one of its components, the Manning-Strickler resistance equation, drastically underestimates the measured flow resistance in Trout Beck (Figure 4.29). It is possible that both the flow resistance and the value of τ^*_c are too low in Schoklitsch's derivation and the two errors more or less cancel out to give reasonable results for Q_c. The rule of thumb ω_{*c} = 0.1 yields reasonable values, though they are a little high for F4 and a little low for F1. Parker *et al.* (2011) suggested it based on an analysis of flume data (Fig. 7 in Parker *et al.*, 2011) and Ferguson (2012) provided some theoretical backing for it using the VPE resistance law.

Table 7.2 shows the non-dimensional critical shear stress (τ^*_c) values for sub-reaches which are calculated from the field-estimated τ_c values (Tables 5.11 and 6.7) and the local bed D_{50} grain size. The table also shows the τ^*_c predicted by the slope-dependent

empirical formulas proposed by Mueller *et al.* (2005) and Lamb *et al.* (2008b), and the respective τ_c values.

Table 7.2. Critical shear stress (τ_c, N m^{-2}) and non-dimensional critical shear stress (τ^*_c) from the tracer and impact count data and empirical relations. The D_{50} is undefined for the sediment-free rock gorge; hence some values for F2 are missing.

Sub-reach	Tracer		Impact count		Mueller *et al.* (2005)		Lamb *et al.* (2008b)	
	τ_c	τ^*_c	τ_c	τ^*_c	τ^*_c	τ_c	τ^*_c	τ_c
F1	47	0.081	33 - 50	0.057 - 0.086	0.044	25	0.048	28
F2	< 119	-	74 - 129	-	0.072	-	0.059	-
F3	107 - 117	0.079 - 0.086	94 - 118	0.069 - 0.087	0.061	83	0.055	75
F4	44 - 52	0.040 - 0.047	40 - 62	0.036 - 0.056	0.041	45	0.046	51
F5	63 - 72	0.061 - 0.070	58 - 83	0.056 - 0.080	0.071	74	0.058	61

In semi-alluvial sub-reaches (F3, F4 and F5), there is a mix of exposed rock and sediment cover, and τ_c on rock could well be different from τ_c on the partial cover but it is assumed that to generate bedload transport the flow has to entrain sediment from the patches so that it is their D_{50} that matters. As with the Q_c estimates (Table 7.1), the τ_c estimates from tracer pebbles and impact counts generally agree (Table 7.2). They suggest that the lowest and the second lowest values of τ_c are in F1 (alluvial) and F4 (70% cover) and the highest in F2 (bare rock) and F3 (boulder-riffle) (Table 7.2). However, the τ_c estimates for F2 from field data (tracers: < 119 N m^{-2}, impact counts: 74 – 129 N m^{-2}) appear to be too high and have a wide range. Based on tracer pebbles, the lowest inter-survey peak Q when the tracers had travelled in the gorge was 5.2 m^3 s^{-1} (τ-Q relation gives τ = 119 N m^{-2}) but the tracers might have moved in a lower discharge than this, therefore there is an uncertainty in the Q_c and τ_c values for the gorge (F2). There is even bigger uncertainty in the F2 estimates from bedload impact counts. The impact sensor in the gorge (TRL) (Figure 6.1) gave a Q_c range 2.4 – 6 m^3 s^{-1} (τ_c = 74 – 129 N m^{-2}) but these values probably represent the threshold value in the upstream alluvial reach from where the sediment was supplied to the gorge, which does not have any coarse sediment on its bed. From visual observation, it appears that the τ_c in the gorge is in the lower end of the range (2.4 – 6 m^3 s^{-1}), say 2.4 – 3 m^3 s^{-1} (τ_c = 74 – 85 N m^{-2}) but there are no data to support this interpretation; therefore the wide range of 2.4 – 6 m^3 s^{-1} is shown for both F1 and F2 (Table 7.1). The B tracers did not move when they were installed in August 2013, at Q = 0.020 m^3 s^{-1}, but tests on subsequent

visits showed that small pebbles (up to 45 mm size) could be entrained from smooth rock surfaces in discharges as low as 0.5 $m^3 s^{-1}$. However, most of the tracers were still in their original positions at a discharge of 1 $m^3 s^{-1}$ (τ_c = 49 N m^{-2}) 8 days after they were installed, so Q_c in the rock gorge is at least that high. This shows that it is impossible to identify τ_c in F2 because transport there is limited by supply from upstream.

The τ^*_c estimate from field data (Table 7.2) shows that F3 and F1 have the highest values and F4 the lowest, The τ^*_c values calculated from sub-reach slope using the empirical relation of Mueller *et al.* (2005) vary from 0.041 to 0.072, or 0.046 to 0.059 using Lamb *et al.* (2008b) relation. In both cases the highest τ^*_c is for F2 and the lowest for F4; F3 has a value intermediate between F1 and F2. When these slope-based estimates of τ^*_c are converted to estimates of τ_c by using the local bed D_{50} grain size (Table 7.2), the values for F1 and F3 are much lower than those inferred from tracer mobility and impact counts, but the values for F4 and F5 are comparable.

Table 7.2 suggests that threshold shear stress (τ_c) and threshold Shields stress (τ^*_c) both vary according to the bed character, but numerical values vary considerably according to the chosen method of estimation. Moreover, the impact counts events analysis (section 6.3.2) suggests that threshold values can also vary temporally because of packing effects (e.g. Brayshaw, 1985; Powell & Ashworth, 1995) and intervening channel architecture and sedimentology (e.g. Buffington & Montgomery, 1999; Millar, 1999). The temporal variation in threshold stress is consistent with previous works (e.g. Garcia *et al.*, 2000; Richardson *et al.*, 2003). The variable thresholds of initial motion and the stochastic nature of the sediment supply add further uncertainty to the bedload rating curves and flux estimates (Batalla, 1997; Habersack *et al.*, 2001), but these aspects are not studied in this thesis.

7.2 Sediment conveyance through mixed bedrock-alluvial systems

To study flow processes and sediment mobility in detail in the field required a great deal of fieldwork and data reduction and necessarily restricted the study to a single field site. The details of the findings regarding streamwise changes in shear stress, threshold stress and bedload mobility are inevitably specific to this particular field site, but an alternation between alluvial and bedrock segments occurs along many other rivers. In all cases the change from fully alluvial bed to partly or completely exposed bedrock

implies that the flow in the bedrock segment is capable of transporting more bedload than is supplied from the upstream alluvial segment. In this section various possible causes of such a change are discussed, to help put the Trout Beck study into a wider context.

The variability in bed character in many bedrock reaches arises mainly because of variation in alluvial cover, GSD and roughness of the exposed boundary, which are the result of changes in channel width, slope and planform. The changes in location of the patches, patch GSD and roughness of both the patches and exposed surfaces determine the flow field (depth, velocity, flow resistance, shear stress) which affects the sediment transport process. Bedrock reaches where alluvial cover may vary from 0 up to 100 % are important features to investigate in order to determine fluvial landscape evolution and better understand the sediment delivery downstream.

To estimate downstream sediment flux through an alluvial-bedrock-alluvial sequence, the potential bedload conveyance of each differing segment reach needs to be assessed. This is generally done by considering the shear stress and threshold shear stress in each reach. If the potential transport rate per unit width (q_t) is related to excess shear stress ($\tau - \tau_c$) or stress ratio (τ/τ_c) by a power-law relation, the bedload conveyance (Q_t) in each channel segment depends on channel width (w) and the excess shear stress (or stress ratio). As the reach-averaged shear stress (τ) is a function of flow depth and slope, the conveyance Q_t is a function of slope, width, depth and critical shear stress (τ_c). The depth is dictated by slope, width and bed roughness and τ_c also depends mainly on bed character (sediment D_{50} or rock roughness). The Trout Beck data at competent flow (high Q) show that sub-reaches F2, F3 and F4 have similar depths (slightly lower for the bare rock sub-reach F2) but the order of the shear stresses are F2 > F3 > F4 (Figure 7.1 b) which ties in with width F2 < F3 ~ F4 (Table 4.6) and energy slope F2 > F3 > F4 (Table 4.12, Figure 4.20). A simple calculation to show how the potential transport rates in the bare rock and semi-alluvial sub-reaches compare with the supply rate from the alluvial sub-reach are shown in Table 7.3. These values are calculated using an excess stress law of the type proposed by Meyer-Peter and Müller (1948) (Eq. 1.30), then expressed as ratios of the calculated bedload transport rate in the upstream alluvial reach.

Table 7.3. Potential bedload transport conveyance of each sub-reach, expressed as a ratio of the supply rate from the alluvial sub-reach F1 for a range of competent discharges. The average τ_c values are estimated from tracer data (Table 7.2) and the width (w) and shear stress (τ) are taken from Table 4.6 and 4.12 respectively. The ratio shown in bracket for F2 is for τ_c = 74 N m^{-2} (Q_c = 2.4 m^3 s^{-1}) which is the lowest threshold value suggested by the impact count data (Table 7.1).

Sub-reach (type)	Average τ_c (N m^{-2})	Relative bedload conveyance of a sub-reach in relation to alluvial sub-reach at Q =		
		6 m^3 s^{-1}	7 m^3 s^{-1}	8 m^3 s^{-1}
F1 (alluvial)	47	1	1	1
F2 (bare rock)	119 (74)	4 (46)	5 (24)	4 (15)
F3 (boulder-riffle)	112	0.4	1.1	1.0
F4 (semi-alluvial, 70% cover)	48	4	3	3
F5 (semi-alluvial, 20% cover)	68	6	5	4

Table 7.3 shows that sub-reaches F2, F4 and F5 are each potentially capable of conveying all bedload supplied to them from F1, but that F3 is barely able to do so at discharges of 7-8 m^3 s^{-1} and would accumulate sediment at a discharge of 6 m^3 s^{-1}. However, the calculations are sensitive to the assumed value of τ_c. As mentioned earlier in section 7.1.4, it is very likely that the τ_c for the gorge is less than the value used in this calculation (119 N m^{-2}), and if a lower value of τ_c is used then the bedload conveyance in the gorge will be even higher than elsewhere. For example if τ_c = 74 N m^{-2} (equivalent to Q_c = 2.4 m^3 s^{-1}) is used, which is the lowest value in the range suggested by impact counts, the bedload conveyance in the gorge at 6, 7 and 8 m^3 s^{-1} river discharges will be respectively 46, 24 and 15 times higher than in the alluvial sub-reach compared to 4, 5 and 4 for τ_c = 119 N m^{-2}. This shows that depending on the true value of τ_c, bare-rock sub-reach F2 might have by far the highest bedload conveyance but might be equalled or even slightly exceeded by F5.

The bedload conveyance in the boulder-sub reach (F3) is only 40 % that of the alluvial sub-reach (F1) at Q = 6 m^3 s^{-1} (Table 7.3), but at higher discharges both F1 and F3 have similar conveyances. This implies that, at Q up to somewhere between 6 and 7 m^3 s^{-1}, the bedload conveyance of F3 is less than the sediment supply from F1 so some of the sediment flushed through F2 will accumulate in F3. It is to be noted that these are the ratios of bedload conveyance and not bedload flux which will be lower in supply-limited reaches such as Trout Beck. Table 7.3 shows the ranking of bedload conveyance

as F2~ F5 > F4 > F3 ~ F1, whereas the ranking of total shear stress (τ) is F2 > F3 > F5 > F4 > F1 (Figure 7.1) and of critical shear stress (τ_c) is F2~F3 > F5 > F1 ~ F4 (Figure 7.1). This shows that the ranking of τ and τ_c does not always tie in with the ranking of bedload conveyance.

An increase in bedload conveyance in the alternating sequence from alluvial to semi-alluvial to bare rock segments therefore is a result of one or more of three possible downstream changes – narrowing of the channel by rock walls, an increase in channel slope (which increases τ), or a reduction in threshold stress (τ_c) due to a smoother bed. The data shows τ_c is higher in the bare rock gorge than in the upper alluvial reach but the channel is narrower and the shear stress (τ) is very high, giving a high bedload conveyance. In other rivers with mixed bedrock-alluvial systems also it is expected that one or more of these downstream changes will occur when the stream passes on from alluvial to bedrock. In situations where the bedrock segment is of limited length and the river becomes alluvial again farther downstream, it can be inferred that bedload flushed through the bedrock segment during floods starts to accumulate. This implies a downstream reduction in the ability of the flow to transport coarse sediment. As with the alluvial to bedrock transition, this could occur through a change in any or all of the controlling factors of width, slope and bed roughness, but this time in the opposite direction.

7.3 Long-term perspective and major floods

This thesis is necessarily a short-term study of flow and bedload transport in an unchanged channel geometry. Moreover, the fieldwork period happened not to contain any major floods: the highest flood peak was less than the long-term mean annual flood. This section puts the study findings into a multi-decade context based on what is known about the flood history of Trout Beck, and discusses how in the much longer term the channel geometry might evolve through gradual incision and sedimentation, possibly at different rates in different sub-reaches.

Long-term channel processes may cause changes in the three main variables that control the bedload conveyance of the river *i.e.* the width, slope and roughness. In the alluvial segments lateral erosion may occur because of the tool effect (Turowski *et al.*, 2008b) and as a result it may widen the section, decrease the local shear stress and increase

sediment deposition. In the long run the boundaries between the segments may also shift. The upstream movement of the knickpoint or the incision at the head of rock gorge may make the proximal end of the upper alluvial zone steeper which may increase the sediment supply to the gorge. This will reduce the slope of the gorge and the sediment cover will be increased at the toe of the gorge. The increased cover would then reduce the exposed area and reduce the incision rate in the gorge.

The partial cover and the evolution of channel profile in the long run also depends on whether the channel is flood cleaning or flood depositing (Turowski *et al.*, 2013). The historical data shows that Trout Beck is a flood-cleaning system; a 200-year event in July 2002 cleared all sediment except the dispersed boulders from the lower semi-alluvial reach (Figure 2.25). The 2002 – 2003 cover maps show most of the patches re-formed within six months and a comparison of current maps with a 2009 map shows there has been no significant change in the sediment pattern since then. The bed will be exposed to erosion after such big floods but how long it takes to re-form the patches depends on the supply from upstream.

7.4 Implications for landscape modelling, engineering design and studying mixed bedrock-alluvial systems

Although the Trout Beck results are from a single site, they relate to five contrasting sub-reaches with big differences in bed character, bank type, and bulk flow variables. How representative the results are of bedrock channels generally is impossible to say, but some of the findings are common to each sub-reach. In particular, there is a clear common tendency for flow resistance as quantified by n and f to decrease with increasing discharge. This has also been found by the few previous researchers to make field measurements of n or f in bedrock channels ((e.g. Heritage *et al.*, 2004; Richardson & Carling, 2006)), so it may be a general tendency. This section begins by considering the implications this has for models of bedrock incision processes and for practical engineering calculations in bedrock channels. It then discusses the wider implications of some of the other findings from trout Beck.

Most models of bedrock incision processes and rates, and some models of landscape evolution, use shear stress to predict bedload transport rates and calculate shear stress from discharge. To do this requires the assumption of a flow resistance law and the value of its roughness coefficient, but field data to guide this choice are lacking. As

discussed in more detail below, most models use standard resistance laws developed for low-gradient large alluvial channels but recent studies indicate that these relations do not perform well for steep/shallow/coarse alluvial streams (Lee & Ferguson, 2002; Comiti *et al.*, 2007; Ferguson, 2007a; Recking *et al.*, 2008; Nitsche *et al.*, 2011; Rickenmann & Recking, 2011; Powell, 2014). In addition to this, the bare rock and partial-cover segments in bedrock reaches further complicate the flow resistance calculation. This study has a number of implications for landscape evolution models, engineering designs and monitoring of mixed alluvial-bedrock systems. Some of the key implications are discussed below.

1) Total shear stress (τ) and critical shears tress (τ_c)

To study the sediment transport process it is essential to understand how the reach-averaged shear stress (τ) and the threshold shear stress (τ_c) vary along the channel and with discharge. Incision models generally calculate shear stress from unit discharge (q) and slope (S) which involves the use of a flow resistance law and a specific value for its roughness coefficient (e.g. Howard, 1994; Whipple & Tucker, 1999; Turowski *et al.*, 2007; Chatanantavet & Parker, 2008; Turowski *et al.*, 2008a; Zhang *et al.*, 2015). For example, mean depth (d) could be calculated as $(qn)^{0.6} S^{0.3}$ using a fixed value of Manning's n . However, as there are no specific equations developed for bedrock channels, modellers use standard alluvial-river equations such as Manning's assuming a constant value of n (e.g. Lague, 2010), or Manning-Strickler with n scaled on grain size or rock-bed roughness relative to flow depth (e.g. Johnson, 2014) or a constant value of Darcy-Weisbach friction factor f (e.g. Zhang *et al.*, 2015). A clear message from this study is that n or f varies with discharge, therefore incision models (or other flow and sediment transport models for bedrock channels) should not use constant n or f to estimate shear stress, if the model has options for variable Q (unsteady and non-uniform flows). The resistance laws (e.g. logarithmic, variable-power or variable power based $V^{**} - q^{**}$) which are acceptable for shallow gravel-bed channels are likely to be acceptable for semi-alluvial channels. However, there is a need for more field data and better ways to quantify k_s in boulder-rich channels such as the boulder-riffle segment in Trout Beck which works as a barrier for sediment conveyance downstream. In Trout Beck, all sub-reaches except F1 (alluvial) have two roughness scales: rock and sediment in the semi-alluvial sub-reaches (F3, F4 and F5); and rock bed and rock walls in the

bare rock sub-reach (F2). The measured D_{84} gives an approximation of k_s for an alluvial bed, but the overall k_s will be some kind of average of $k_{sediment}$ and k_{rock} as done by Johnson (2014) (Section 1.3.1). Furthermore, the standard flow resistance laws based on representative diameter (D_{50} or D_{84}) cannot predict the flow resistance in bare rock reaches because they lack sediment on the channel bed. In addition, the pattern of variation in flow resistance with discharge is different in the rock gorge with rough walls than in other reaches. So there is a need for new ways to quantify effective k_s in bed rock reaches, including the possibility of different k_s in different parts of the wetted perimeter (smooth rock, rough rock, sediment patch).

Another parameter required to understand the grain entrainment is threshold stress (τ_c) which varies along the channel length according to bed character. This study has shown that the estimation of threshold stress in bedrock reaches is a difficult task even in the field. The general approach, in the absence of field data, is to assume a value of the dimensionless critical shear stress τ^*_c and calculate τ_c from it and the (assumed) median diameter of the bed material D_{50} (e.g. Lague, 2010) but flume results and field data from coarse gravel and boulder-rich channels show that τ^*_c appears to be higher (e.g. Mueller *et al.*, 2005; Mao *et al.*, 2008) in steep and/or shallow channels with large/immobile roughness elements as some of the total shear stress is consumed by these roughness components and not available for sediment transport (Yager *et al.*, 2007; Lamb *et al.*, 2008b; Ferguson, 2012; Johnson, 2014). However on a smooth and relatively steep rock surface the τ^*_c is low.

2) Sediment supply and channel morphology in the fluvial system

The source of sediment supply and the spatial arrangement of different reaches and their morphology in the channel system need to be considered in river models, and in carrying out field studies or engineering design. For example to study the sediment transport process through the gorge in Trout Beck a full understanding of how the sediment is supplied from upstream reaches must be achieved. In addition, the pool-boulder area is acting as a barrier for sediment conveyance downstream. The tracer data shows that even at the 9-month survey (survey 6) half of the total B tracers or about three quarter of the recovered number of tracers (Figure 5.16, Table 5.6) were still in

this area; once they crossed this obstacle the rate of downstream dispersion increased again.

A simple power law relation between bedload transport rate (Q_b) and river discharge (Q) has been generally accepted for many gravel-bed rivers (Barry *et al.*, 2004) but Trout Beck data do not follow this trend. The bedload flux in bedrock reaches is limited by the supply from upstream, so may not be closely related to flow conditions within the reach. The field data suggest that significant transport occurs in the upper alluvial reach only in floods peaking above 5 $m^3 s^{-1}$ (Table 7.1) which is ~50% of the mean annual flood and is exceeded less than 1% of time. In a mixed alluvial-bedrock channel the transport rate in the upstream alluvial segment controls the sediment supply to downstream bedrock reaches. The shear stresses in alluvial segments are often below or not far above the critical threshold for entrainment; therefore a simple power function of discharge cannot accurately predict the sediment supply to downstream reaches. This implies that flux calculations based on a simple power law function of Q with no threshold, such as in the model of Lague (2010), will overestimate the transport rate in moderate floods. The sensitivity of results in such models needs to be checked. The flood cleaning or flood depositing behaviour using a simple $Q_t - Q$ relation (Turowski *et al.*, 2013) might also have different outcomes if threshold discharge is considered; or maybe if different threshold discharges for different bed characters are considered.

3) Relation between sediment flux and sediment cover

Many incision models assume that the proportion of sediment cover in a bedrock reach depends on the ratio of sediment supply to bedload coveyance. The Trout Beck results suggest that the bedload conveyance and sediment supply for different segments vary and also that the bedload conveyance calculated for the overall reach may be higher than the bedload conveyance of some of its sub-reaches. In Trout Beck the bedload conveyance of the boulder-riffle segment is likely to be lower than that for the entire reach, which implies overestimation of flux through the reach. In addition to the sediment flux, the cover also depends on channel morphology, for example the Trout Beck gorge is almost sediment free and whatever amount of sediment is supplied, normally the sediment does not stay there in the form of cover. In contrast, the boulder-riffle section and its backwater zone affect the bulk hydraulics and enhance the

sediment storage there; therefore the presence or absence of boulders may also be another control in deciding the sediment cover. This indicates that the presence of numerous boulders in a channel segment, whether derived from rock wall collapse or bed plucking or lateral inputs, may cause the growth of sediment patches in immediate downstream areas which may inhibit further bedrock erosion. This finding is consistent with the flume experiment results of Chatanantavet and Parker (2008).

7.5 Review of the research plan and future avenues of research

The study has been completed according to the research plan and is considered to have addressed all the research questions. This research has extended knowledge about sediment dynamics in bedrock reaches, in particular addressing the interrelationships among channel form, flow and sediment. In addition to this, the study has provided detailed datasets on reach-scale sediment dynamics which are very useful for those studying the bedrock reaches in light of the shortage of field data in this area. It is worth mentioning the following points which may be useful in informing future studies.

- The sediment patch surveys were carried out three times over the period of nine months; all showed very similar patterns of sediment cover and no significant changes occurred as there were no big floods during the entire study period. In the absence of big floods some potential research questions, e.g. how cover varies in major floods, could not be studied. However, by comparing the study-period cover maps with the historic 200-year flood of 2002 and another map of 2009, it has been demonstrated that Trout Beck is a flood-cleaning stream which evacuates sediment during extreme floods and deposits during small and intermediate events.
- All floods during the 20-month study period had peak discharges lower than the mean annual flood, and the highest peak discharge during the study period ($8.8\ m^3\ s^{-1}$) lasted only a few hours and was during the night. Therefore because of the flashiness of the channel the direct measurement of discharge above $2\ m^3\ s^{-1}$ proved to be difficult. However, the data for high-Q have been indirectly derived using the continuous record of stage data, Environment Agency discharge data, the low-Q measured discharges and the channel cross-sections without compromising the outcomes of the analysis. The methods developed to do this may be useful in other studies of flashy streams.

As also mentioned earlier in section 7.4, there is a need to have more field data on sediment dynamics in various types of bedrock reaches which will help modellers to decide appropriate resistance laws and threshold shear stresses. The possible areas of further research include:

- Additional studies of the type conducted here will help document results from varieties of bedrock reaches from different settings and provide more confidence and choices to the modellers. More sophisticated methods such as radio-frequency identification (RFID) technology instead of magnet-tagged tracers could be considered as this provides higher recoveries of the tracers, with no disturbance, and possibly some additional information such as tracking of paths of individual tracers.
- The study shows that the critical shear stress τ_c varies spatially and temporally and the estimated values also vary according to the methods used. This highlights the difficulty of estimating a representative τ_c for different channel segments. In bare rock reaches and exposed parts of the semi-alluvial reaches there will be no bed material, therefore for such beds an effective roughness height (k_s) would need to be worked out. The D_{84} also does not accurately represent the effective roughness in reaches with high boulders density. It is strongly advised that research is done on methods to estimate the critical shear stress τ_c and a composite roughness height (k_s-composite) for bedrock reaches.
- Direct entrainment tests of some kind at a range of discharges might be a useful way to investigate bare rock threshold stress (τ_c).
- It would be interesting to modify a one-dimensional flow and sediment transport model to allow for bedrock, calibrate it to the field site, and test with additional field data so that it can be used elsewhere.
- Further research on stress-partitioning in boulder-rich areas is needed. The model of Yager *et al.* (2007), which gave plausible results for their field site, did not perform well in Trout Beck. Future studies could usefully test their approach, and the alternative developed in this research, in other channels, or indeed develop and test new models.
- In this study the two impact sensors were placed next to each other in a cross-section but it is also advisable to install two sensors next to each other but in line

with the flow direction in order to check the reliability of the data measured by the other sensor, as was done by Reid *et al.* (2007). Several sensors across a rock bed, to see to what extent transport varies laterally, would also be more useful. It is also advisable to produce a better calibration of the sensors (e.g. Rickenmann *et al.*, 2014).

7.6 Conclusions

This thesis reports the results of a field-based study undertaken to examine coarse sediment transport processes in a mixed alluvial-bedrock channel. It is hypothesised that in this type of fluvial system, where there is an alternation of alluvial and bedrock reaches, the presence of exposed rock implies potential sediment transport rate exceeds sediment supply, and transport rate will be higher than in alluvial reaches. Greater knowledge of the hydraulics and bedload dynamics in mixed alluvial bedrock channels is important for better understanding of flow resistance, river bed incision, sediment patch dynamics and the downstream continuity in sediment transport. However, detailed field data to describe these processes are lacking. This study has investigated this hypothesis in the field by measuring bulk hydraulics in short sub-reaches and tracking tracer pebbles through a sequence of contrasting channel sections. The bulk hydraulics provide insights into at-a-station hydraulic geometry, flow resistance, and total shear stress whereas the sediment transport observations describe dispersion patterns, bedload mobility, thresholds of motion, and size selectivity. The research has sought to establish links between flow, channel form and sediment-type to explain sediment transport processes. This has involved making inferences from the results about threshold discharge and threshold stress, and thus excess stress and bedload conveyance. Results are compared between the contrasting channel segments for a range of flow conditions and also with published literature. The major findings of this study are as follows.

1. Flow resistance in alluvial and semi-alluvial reaches decreases rapidly with discharge at low to moderate flow then decreases at a slower rate at higher flows. However, in the bare rock reach resistance rapidly decreases at low to moderate flow but increases at high flow, due to increased resistance of the rough rock walls.

2. Manning's n and Darcy-Weisbach f differ between reaches at same discharge, with lower resistance the more bare rock there is and higher resistance the coarser the sediment cover is.
3. Flow resistance in semi-alluvial segments resembles that in steep shallow gravel-bed rivers. The general pattern of variation of flow resistance with relative submergence (R/D_{84}) is captured by logarithmic and variable-power laws, but quantitative agreement would require replacing sediment D_{84} with an effective reach-average roughness height (k_s) that is lower than D_{84} in some reaches (those with entirely/mainly rock bed) but higher in others.
4. Tracers seeded on the exposed rock dispersed more rapidly along the steep and narrow bare rock gorge than in the fully alluvial reach. In the first two months of the experiment tracers in the bare rock reach moved 29 times further than in the fully alluvial reach.
5. Tracers seeded in the proximal alluvial segment moved more gradually until they reached the semi-alluvial zone upstream of the gorge. The alluvial segment is wider and less steep compared to the gorge and regulates the sediment supply to the gorge.
6. The mobility of the tracers that started in the gorge decreased when they entered the semi-alluvial reach, though they remained more mobile than in the fully alluvial reach. From month 2 to month 9, the tracers in the semi-alluvial reach moved 2.4 times further than in the fully alluvial reach. The tracers were concentrated in a partial-sediment cover zone with numerous boulders with a backwater zone immediately upstream. The mobility of tracers in this pool-boulder area was very low but once they crossed this obstacle their mobility increased.
7. Bedload transport was size selective in the fully and partially alluvial zones, with smaller tracers tending to travel farther, but non-selective on bare rock. Dispersion over the fully alluvial bed was also shape selective, with more spherical tracers tending to travel farther.
8. The tracer movement has been explained by streamwise changes in excess shear stress (total stress minus threshold stress). The bedload conveyance is highest in reaches with entirely or mainly rock bed due to higher shear stress (steep gradient) and relatively low threshold stress (smooth bed). The bedload

conveyance is lowest on the upstream alluvial segment, which has the lowest shear stress at any given discharge, and in the boulder-riffle which has high total shear stress but also high threshold stress. The high threshold stress in the boulder area is associated with very high flow resistance, presumably due to form drag. The bedload conveyance in the semi-alluvial zone downstream of the boulder-riffle is moderate where the total stress and threshold stress are intermediate between fully alluvial and fully bare rock zones.

9. The calculated bedload conveyance of the bare rock reach is very sensitive to the assumed threshold stress and this is much less well constrained than in the other reaches.
10. The tracer experiment showed that the coarse bedload transport in alluvial and semi-alluvial reaches was significant only when the peak discharge was above 5 $m^3 s^{-1}$ but the impact sensors showed that, some sediment, presumably finer, passes at lower discharge. Flow over bare rock was probably competent to move sediment at quite low discharge (Q), but there is no direct evidence of this since transport there is supply-limited from upstream i.e. no sediment is supplied until Q is sufficient to entrain sediment from alluvial channel.

Reference List

Aberle, J., & Smart, G. (2003). The influence of roughness structure on flow resistance on steep slopes. *Journal of Hydraulic Research, 41* (3), 259-269.

Anders, N. S., Seijmonsbergen, A. C., & Bouten, W. (2009). Modelling channel incision and alpine hillslope development using laser altimetry data. *Geomorphology, 113* (1), 35-46.

Andrews, E. (2000). Bed material transport in the Virgin River, Utah. *Water Resources Research, 36* (2), 585-596.

Andrews, E. D. (1983). Entrainment of gravel from naturally sorted riverbed material. *Geological Society of America Bulletin, 94* (10), 1225-1231.

Archer, D., & Stewart, D. (1995). The installation and use of a snow pillow to monitor snow water equivalent. *Water and Environment Journal, 9* (3), 221-230.

Ashley, G. M., Renwick, W. H., & Haag, G. H. (1988). Channel form and processes in bedrock and alluvial reaches of the Raritan River, New Jersey. *Geology, 16* (5), 436-439, http://dx.doi.org/10.1130/0091-7613(1988)016<0436:CFAPIB>2.3.CO;2.

Ashworth, P. J., & Ferguson, R. I. (1986). Interrelationships of Channel Processes, Changes and Sediments in a Proglacial Braided River. *Geografiska Annaler. Series A, Physical Geography, 68* (4), 361-371, doi:10.2307/521527.

Ashworth, P. J., & Ferguson, R. I. (1989). Size-selective entrainment of bed load in gravel bed streams. *Water Resources Research, 25* (4), 627-634, doi:10.1029/WR025i004p00627.

Bagnold, R. (1980). An empirical correlation of bedload transport rates in flumes and natural rivers. In *Proceedings of the Royal Society of London A: Mathematical, Physical and Engineering Sciences* (Vol. 372, pp. 453-473).

Bänziger, R., & Burch, H. (1991). Geschiebetransport in Wildbächen–Messung mittels eines neuartigen Sensors. *Schweizer Ingenieur und Architekt, 24*, 576-579.

Barrière, J., Krein, A., Oth, A., & Schenkluhn, R. (2015). An advanced signal processing technique for deriving grain size information of bedload transport from impact plate vibration measurements. *Earth Surface Processes and Landforms, 40* (7), 913-924.

Barry, J. J., Buffington, J. M., & King, J. G. (2004). A general power equation for predicting bed load transport rates in gravel bed rivers. *Water Resources Research, 40* (10).

Batalla, R. J. (1997). Evaluating Bed-material Transport Equations using Field Measurements in a Sandy Gravel-bed Stream, Arbúcies River, NE Spain. *Earth Surface Processes and Landforms, 22* (2), 121-130, doi:10.1002/(SICI)1096-9837(199702)22:2<121::AID-ESP671>3.0.CO;2-7.

Bathurst, J. (1978). Flow resistance of large-scale roughness. *Journal of the Hydraulics Division, 104* (12), 1587-1603.

Bathurst, J. (1985). Flow resistance estimation in mountain rivers. *Journal of hydraulic engineering, 111* (4), 625-643.

Bathurst, J., Graf, W., & Cao, H. (1987a). Bed load discharge equations for steep mountain rivers. *Sediment Transport in Gravel-Bed Rivers. John Wiley and Sons New York. 1987. p 453-491, 8 fig, 5 tab, 55 ref.*

Bathurst, J., Leeks, G., & Newson, M. (1987b). Discussion of bed-load transport measurements by the vortex-tube trap on Virgilio Creek, Italy. *Sediment transport in gravel-bed rivers*, 611-614.

Bathurst, J. (1993). Flow resistance through the channel network. *Channel network hydrology*, 69-98.

Bathurst, J. (2002). At-a-site variation and minimum flow resistance for mountain rivers. *Journal of hydrology, 269* (1), 11-26.

Bauer, B. O., Sherman, D. J., & Wolcott, J. F. (1992). Sources of Uncertainty in Shear Stress and Roughness Length Estimates Derived from Velocity Profiles. *The Professional Geographer, 44* (4), 453-464.

Beven, K., Gilman, K., & Newson, M. (1979). Flow and flow routing in upland channel networks/L'écoulement et le calcul du cheminement de l'écoulement dans les réseaux des canaux montagneux. *Hydrological Sciences Journal, 24* (3), 303-325.

Beylich, A. A., & Laute, K. (2014). Combining impact sensor field and laboratory flume measurements with other techniques for studying fluvial bedload transport in steep mountain streams. *Geomorphology, 218*, 72-87, http://dx.doi.org/10.1016/j.geomorph.2013.09.004.

Böckli, M. (2011). Laborversuche zum Verhalten von Geophon-Sensoren. *Master's thesis, ETH Zürich and WSL*.

Bogen, J., & Møen, K. (2001). Bed load measurements with a new passive ultrasonic sensor. *Erosion and Sediment Transport Measurement: Technological and Methodological Advances, International Association of Hydrological Sciences, Oslo*, 19-21.

Bogen, J. (2004). Erosion and sediment yield in the Atna river basin. *Hydrobiologia, 521* (1-3), 35-47.

Bray, D. I. (1979). Estimating average velocity in gravel-bed rivers. *Journal of the Hydraulics Division, 105* (9), 1103-1122.

Brayshaw, A. C. (1985). Bed microtopography and entrainment thresholds in gravel-bed rivers. *Geological Society of America Bulletin, 96* (2), 218-223.

Buffington, J. M., Dietrich, W. E., & Kirchner, J. W. (1992). Friction angle measurements on a naturally formed gravel streambed: Implications for critical boundary shear stress. *Water Resources Research, 28* (2), 411-425, doi:10.1029/91WR02529.

Buffington, J. M., & Montgomery, D. R. (1997). A systematic analysis of eight decades of incipient motion studies, with special reference to gravel-bedded rivers. *Water Resour. Res., 33* (8), 1993-2029, doi:10.1029/96wr03190.

Buffington, J. M., & Montgomery, D. R. (1999). Effects of hydraulic roughness on surface textures of gravel-bed rivers. *Water Resources Research, 35* (11), 3507-3521.

Bunte, K., & Ergenzinger, P. (1989). New tracer techniques for particles in gravel bed rivers. *Bulletin de la Société Géographique de Liege, 25*, 85-90.

Bunte, K., Abt, S., Bogen, J., Fergus, T., & Walling, D. (2003). Sampler size and sampling time affect bed load transport rates and particle sizes measured with bed load traps in gravel-bed streams. In *Erosion and sediment transport measurement in rivers: technological and methodological advances: Workshop, Oslo, Norway, 19-21 June, 2002.* (pp. 126-133). IAHS Press.

Bunte, K., Abt, S. R., Potyondy, J. P., & Ryan, S. E. (2004). Measurement of coarse gravel and cobble transport using portable bedload traps. *Journal of hydraulic engineering, 130* (9), 879-893.

Bunte, K., Swingle, K. W., & Abt, S. R. (2007). Guidelines for using bedload traps in coarse-bedded mountain streams: construction, installation, operation, and

sample processing. In *Stream Notes*. Stream Systems Technology Center, Rocky Mountain Research Station.

Bunte, K. (2010). Measurements of Gravel Transport Using the Magnetic Tracer Technique: Temporal Variability Over a Highflow Season and Field-Calibration. *Gray, JR, Laronne, JB, and Marr, JDG, Bedload-surrogate monitoring technologies: US Geological Survey Scientific Investigations Report, 5091*, 85-106.

Burbank, D. W., Anderson, R. S., & Brozovic, N. (1996). Bedrock incision, rock uplift and threshold hillslopes in the northwestern Himalayas. *Nature, 379* (6565), 505-510.

Burt, T., Labadz, J., & Butcher, D. (1997). The hydrology and geomorphology of blanket peat: implications for integrated catchment management., Blanket mire degradation: causes, consequences and challenges. In *Proceedings of a conference of the Mires Research Group of the British Ecological Society* (pp. 121-127). Macauley Land Use Research Institute on behalf of Mires Research Group, Manchester University.

Butterworth, J. A., Hewitt, E. J., & McCartney, M. P. (2000). Discharge Measurement Using Portable Dilution Gauging Flowmeters. *Water and Environment Journal, 14* (6), 436-441, doi:10.1111/j.1747-6593.2000.tb00291.x.

Byrd, T. C., Furbish, D. J., & Warburton, J. (2000). Estimating depth-averaged velocities in rough channels. *Earth Surface Processes and Landforms, 25* (2), 167-173.

Campbell Scientific, I. (2003). CR10X Measurement and Control Module Operator's Manual, Revision 2/03. *Retrieved from, https://s.campbellsci.com/documents/us/manuals/cr10x.pdf*.

Campbell Scientific, I. (2016). Instruction Manual, CS547A Conductivity and Temperature Probe and A547 Interface, Revision 4/16. *Retrieved from, https://s.campbellsci.com/documents/us/manuals/cs547a.pdf*.

Carbonneau, P. E., Bergeron, N., & Lane, S. N. (2005). Automated grain size measurements from airborne remote sensing for long profile measurements of fluvial grain sizes. *Water Resources Research, 41* (11).

Carling, P. A. (1983). Threshold of coarse sediment transport in broad and narrow natural streams. *Earth Surface Processes and Landforms, 8* (1), 1-18, doi:10.1002/esp.3290080102.

Carling, P. A. (1995). Flow-separation berms downstream of a hydraulic jump in a bedrock channel. *Geomorphology, 11* (3), 245-253.

Carling, P. A., & Tinkler, K. (1998). Conditions for the entrainment of cuboid boulders in bedrock streams: An historical review of literature with respect to recent investigations. In *Rivers Over Rock: Fluvial Processes in Bedrock Channels* (Vol. 107, pp. 19-34). AGU, Washington, DC.

Carling, P. A., Benson, I., & Richardson, K. (2002a). A new instrument to record sediment movement in bedrock channels. ICCE/IAHS: Erosion and Sediment Transport Measurement: Technological and Methodological Advances. In *Oslo Workshop*.

Carling, P. A., Hoffmann, M., Silke-Blatter, A., & Dittrich, A. (2002b). Drag of emergent and submerged rectangular obstacles in turbulent flow above bedrock surface. In A. J. Schleiss & E. Bollaert (Eds.), *[Papers in proceedings of] International Workshop on "Rock Scour"* (pp. 83-94). Balkema.

Carling, P. A. (2006). The hydrology and geomorphology of bedrock rivers. *Geomorphology, 82* (1–2), 1-3, http://dx.doi.org/10.1016/j.geomorph.2005.08.017.

Castellarin, A., Kohnová, S., Gaal, L., Fleig, A., Salinas, J., Toumazis, A., Kjeldsen, T., & Macdonald, N. (2012). Review of applied-statistical methods for flood-frequency analysis in Europe: WG2 of COST Action ES0901. In. (NERC) Centre for Ecology & Hydrology.

Chanson, H. (1999). Comment on "Critical flow constrains flow hydraulics in mobile-bed streams: A new hypothesis" by GE Grant. *Water Resources Research, 35* (3), 903-905.

Chatanantavet, P., & Parker, G. (2008). Experimental study of bedrock channel alluviation under varied sediment supply and hydraulic conditions. *Water Resour. Res., 44* (12), W12446, doi:10.1029/2007wr006581.

Chatanantavet, P., & Parker, G. (2009). Physically based modeling of bedrock incision by abrasion, plucking, and macroabrasion. *Journal of Geophysical Research: Earth Surface, 114* (F4).

Chatanantavet, P., Whipple, K. X., Adams, M. A., & Lamb, M. P. (2013). Experimental study on coarse grain saltation dynamics in bedrock channels. *Journal of Geophysical Research: Earth Surface, 118* (2), 1161-1176, doi:10.1002/jgrf.20053.

Chow, V. T. (1959) *Open-channel hydraulics*. McGraw-Hill.

Church, M. A., & Kellerhals, R. (1970). Stream gauging techniques for remote areas using portable equipment. *Department of Energy, Mines and Resources, Inland Waters Branch, Ottawa, Ont. Technical Bulletin No. 25*.

Church, M. A., & Hassan, M. A. (1992). Size and distance of travel of unconstrained clasts on a streambed. *Water Resources Research, 28* (1), 299-303.

Comiti, F., Mao, L., Wilcox, A., Wohl, E. E., & Lenzi, M. A. (2007). Field-derived relationships for flow velocity and resistance in high-gradient streams. *Journal of hydrology, 340* (1), 48-62.

Conway, V., & Millar, A. (1960). The hydrology of some small peat-covered catchments in the northern Pennines. *J. Instn Wat. Engrs, 14*, 415-424.

Cowie, P. A., Whittaker, A. C., Attal, M., Roberts, G., Tucker, G. E., & Ganas, A. (2008). New constraints on sediment-flux–dependent river incision: Implications for extracting tectonic signals from river profiles. *Geology, 36* (7), 535-538, doi:10.1130/g24681a.1.

Cray, A. (2010). *The Dynamics of Coarse Sediment Transfer in an Upland Bedrock River*. MSc Thesis, Durham University, available at Durham E-Theses Online: http://etheses.dur.ac.uk/209/.

Crisp, D. (1966). Input and output of minerals for an area of Pennine moorland: the importance of precipitation, drainage, peat erosion and animals. *Journal of Applied Ecology*, 327-348.

Crowe, S., & Warburton, J. (2007). Significance of large peat blocks for river channel habitat and stream organic budgets. *Mires and Peat, 2*, 1-15.

D'Agostino, V., & Lenzi, M. A. (1999). Bedload transport in the instrumented catchment of the Rio Cordon: Part II: Analysis of the bedload rate. *Catena, 36* (3), 191-204.

David, G. C., Wohl, E., Yochum, S. E., & Bledsoe, B. P. (2010). Controls on at-a-station hydraulic geometry in steep headwater streams, Colorado, USA. *Earth Surface Processes and Landforms, 35* (15), 1820-1837.

Davis, J., Sklar, L., Demeter, G., Johnson, J., & Whipple, K. (2005). The influence of bed roughness on partial alluviation in an experimental bedrock channel. In *AGU Fall Meeting Abstracts* (Vol. 1, pp. 0508).

Day, T. J. (1975). Longitudinal dispersion in natural channels. *Water Resources Research, 11* (6), 909-918.

Day, T. J. (1976). On the precision of salt dilution gauging. *Journal of hydrology, 31* (3), 293-306.

Day, T. J. (1977a). Field procedures and evaluation of a slug dilution gauging method in mountain streams. *Journal of Hydrology(New Zealand), 16* (2).

Day, T. J. (1977b). Observed mixing lengths in mountain streams. *Journal of hydrology, 35* (1), 125-136, http://dx.doi.org/10.1016/0022-1694(77)90081-6.

Demir, T. (2000). *The influence of particle shape on bedload transport in coarse-bed river channels.*, PhD Thesis, Durham University, available at Durham E-Theses Online: http://etheses.dur.ac.uk/4375/.

Dietrich, W. E., & Whiting, P. (1989). Boundary shear stress and sediment transport in river meanders of sand and gravel. *Water Resources Monograph, 12*, 1-50.

Downs, P. W., Soar, P. J., & Taylor, A. (2016). The anatomy of effective discharge: the dynamics of coarse sediment transport revealed using continuous bedload monitoring in a gravel-bed river during a very wet year. *Earth Surface Processes and Landforms, 41* (2), 147-161, doi:10.1002/esp.3785.

Eddy, A., Welch, D., & Rawes, M. (1968). The vegetation of the Moor House national nature reserve in the northern Pennines, England. *Vegetatio, 16* (5-6), 239-284.

Einstein, H. (1937). Bedload transport as a probability problem. *Sedimentation (reprinted in 1972). Water Resources Publications, Colorado*, 105-108.

Einstein, H. A. (1950). *The bed-load function for sediment transportation in open channel flows*. US Department of Agriculture.

Elder, K., Kattelmann, R., & Ferguson, R. (1990). Refinements in dilution gauging for mountain streams. In *Hydrology in Mountainous Regions. I–Hydrological Measurements; the Water Cycle. International Association for Hydrological Science Proceedings of two Lausanne symposia, August 1990. IAHS Publication No* (Vol. 193, pp. 247-254).

Ergenzinger, P., & Conrady, J. (1982). A new tracer technique for measuring bedload in natural channels. *Catena, 9* (1–2), 77-80, http://dx.doi.org/10.1016/S0341-8162(82)80006-4.

Ergenzinger, P., & Schmidt, K. (1990). Stochastic elements of bed load transport in a steppool mountain river. *Hydrology in mountainous regions. II—Artificial reservoirs, water and slopes: International Association of Hydrological Sciences Publication, 194*, 39-46.

Etter, M. (1996). *Zur Erfassung des Geschiebetransportes mit Hydrophonen ('Recording bedload transport with hydrophones').* PhD thesis, Univ. of Berne, Berne, Switzerland, Swiss Federal Research Institute WSL, Birmensdorf, Switzerland.

Evans, M., Burt, T., Holden, J., & Adamson, J. (1999). Runoff generation and water table fluctuations in blanket peat: evidence from UK data spanning the dry summer of 1995. *Journal of hydrology, 221* (3), 141-160.

Ferguson, R. I. (1986). Hydraulics and hydraulic geometry. *Progress in Physical Geography, 10* (1), 1-31.

Ferguson, R. I. (1994). Critical discharge for entrainment of poorly sorted gravel. *Earth Surface Processes and Landforms, 19* (2), 179-186, doi:10.1002/esp.3290190208.

Ferguson, R. I., Hoey, T., Wathen, S., & Werritty, A. (1996). Field evidence for rapid downstream fining of river gravels through selective transport. *Geology, 24* (2), 179-182.

Ferguson, R. I., & Paola, C. (1997). Bias and precision of percentiles of bulk grain size distributions. *Earth Surface Processes and Landforms, 22* (11), 1061-1077.

Ferguson, R. I., & Wathen, S. J. (1998). Tracer-pebble movement along a concave river profile: Virtual velocity in relation to grain size and shear stress. *Water Resources Research, 34* (8), 2031-2038, doi:10.1029/98WR01283.

Ferguson, R. I., Bloomer, D. J., Hoey, T. B., & Werritty, A. (2002). Mobility of river tracer pebbles over different timescales. *Water Resour. Res., 38* (5), 1045, 10.1029/2001wr000254.

Ferguson, R. I., & Hoey, T. B. (2002). Long-term slowdown of river tracer pebbles: Generic models and implications for interpreting short-term tracer studies. *Water Resour. Res., 38* (8), 1142, doi:10.1029/2001wr000637.

Ferguson, R. I. (2005). Estimating critical stream power for bedload transport calculations in gravel-bed rivers. *Geomorphology, 70* (1–2), 33-41, http://dx.doi.org/10.1016/j.geomorph.2005.03.009.

Ferguson, R. I. (2007a). Flow resistance equations for gravel-and boulder-bed streams. *Water resources research., 43*, W05427.

Ferguson, R. I. (2007b). 2 Gravel-bed rivers at the reach scale. *Developments in Earth Surface Processes, 11*, 33-53.

Ferguson, R. I. (2010). Time to abandon the Manning equation? *Earth Surface Processes and Landforms, 35* (15), 1873-1876, doi: 10.1002/esp.2091.

Ferguson, R. I. (2012). River channel slope, flow resistance, and gravel entrainment thresholds. *Water Resources Research, 48* (5), http://dx.doi.org/10.1029/2011WR010850.

Ferguson, R. I. (2013). Reach-scale flow resistance. *Treatise on Geomorphology, Fluvial Geomorphology, edited by J. Schroder and E. Wohl, Elsevier, New York, 9*.

Fernandez Luque, R., & Van Beek, R. (1976). Erosion and transport of bed-load sediment. *Journal of Hydraulic Research, 14* (2), 127-144.

Finnegan, N. J., Sklar, L. S., & Fuller, T. K. (2007). Interplay of sediment supply, river incision, and channel morphology revealed by the transient evolution of an experimental bedrock channel. *J. Geophys. Res., 112* (F3), F03S11, doi:10.1029/2006jf000569.

Flammer, G. H., Tullis, J. P., & Mason, E. S. (1970). Free surface, velocity gradient flow past hemisphere. *Journal of the Hydraulics Division, 96* (7), 1485-1502.

Folk, R. L., & Ward, W. C. (1957). Brazos River bar: a study in the significance of grain size parameters. *Journal of Sedimentary Petrology, 27* (1), 3-26.

Furbish, D. (1987). Conditions for geometric similarity of coarse stream-bed roughness. *Mathematical Geology, 19* (4), 291-307, doi:10.1007/BF00897840.

Garcia, C., Laronne, J. B., & Sala, M. (2000). Continuous monitoring of bedload flux in a mountain gravel-bed river. *Geomorphology, 34* (1), 23-31.

Garnett, M., Ineson, P., & Adamson, J. (1997). A long-term upland temperature record: No evidence for recent warming. *Weather, 52* (11), 342-351.

Gees, A. (1990). Flow measurement under difficult measuring conditions: Field experience with the salt dilution method. *Hydrology in Mountainous Regions I. Hydrological Measurements; The Water Cycle, edited by: Lang, H. and Musy, A., IAHS Publ, 193*, 255-262.

Gemini. (2014). Tinytag Explorer Software, Quick Start Guide. *Retrieved from, http://gemini2.assets.d3r.com/pdfs/original/1733-9800-0028.pdf*.

Gilbert, G. (1877). Report on the geology of the Henry Mountains: US Geographical and Geological Survey. *Rocky Mountain Region, Report*.

Gleason, C. J., & Smith, L. C. (2014). Toward global mapping of river discharge using satellite images and at-many-stations hydraulic geometry. *Proceedings of the National Academy of Sciences, 111* (13), 4788-4791.

Gleason, C. J. (2015). Hydraulic geometry of natural rivers A review and future directions. *Progress in Physical Geography*, doi:10.1177/0309133314567584

Goode, J. R., & Wohl, E. (2010a). Substrate controls on the longitudinal profile of bedrock channels: Implications for reach-scale roughness. *J. Geophys. Res., 115* (F3), F03018, doi:10.1029/2008jf001188.

Goode, J. R., & Wohl, E. (2010b). Coarse sediment transport in a bedrock channel with complex bed topography. *Water Resour. Res., 46* (11), W11532, doi:10.1029/2009wr008135.

Grant, G. E. (1997). Critical flow constrains flow hydraulics in mobile-bed streams: A new hypothesis. *Water Resources Research, 33* (2), 349-358.

Grass, A. J. (1970). Initial instability of fine bed sand. *J. Hydraul. Div. Am. Soc. Civ. Eng., 96*, 619-632.

Gregory, K. J., & Goudie, A. (2011). Introduction to the discipline of geomorphology. *The SAGE Handbook of Geomorphology. London: SAGE*, 1-20.

Griffiths, G. A. (1981). Flow resistance in coarse gravel bed rivers. *Journal of the Hydraulics Division, 107* (7), 899-918.

Griffiths, G. A. (1989). Form resistance in gravel channels with mobile beds. *Journal of hydraulic engineering, 115* (3), 340-355.

Habersack, H., Nachtneb El, H., & Laronne, J. (2001). The continuous measurement of bedload discharge in a large alpine gravel bed river. *Journal of Hydraulic Research, 39* (2), 125-133.

Hancock, G. S., Anderson, R. S., & Whipple, K. X. (1998). Beyond power: Bedrock river incision process and form. *Rivers Over Rock: Fluvial Processes in Bedrock Channels*, 35-60.

Haschenburger, J. K., & Church, M. (1998). Bed material transport estimated from the virtual velocity of sediment. *Earth Surface Processes and Landforms, 23* (9), 791-808, doi:10.1002/(SICI)1096-9837(199809)23:9<791::AID-ESP888>3.0.CO;2-X.

Hassan, M. A., Schick, A. P., & Laronne, J. B. (1984). The recovery of flood dispersed coarse sediment particles, a three dimensional magnetic tracing method. *Channel Processes; Water, Sediment and Catchment Controls: Catena Supplement, 5*, 153-162.

Hassan, M. A., Church, M., & Schick, A. P. (1991). Distance of movement of coarse particles in gravel bed streams. *Water Resources Research, 27* (4), 503-511.

Hassan, M. A., Church, M. A., & Ashworth, P. J. (1992). Virtual rate and mean distance of travel of individual clasts in gravel-bed channels. *Earth Surface Processes and Landforms, 17* (6), 617-627.

Hassan, M. A., & Church, M. A. (2001). Sensitivity of bed load transport in Harris Creek: Seasonal and spatial variation over a cobble-gravel bar. *Water Resources Research, 37* (3), 813-825.
Hassan, M. A., & Ergenzinger, P. (2003). Use of tracers in fluvial geomorphology. *Tools in fluvial geomorphology*, 397-423.
Helley, E. J., & Smith, W. (1971). Development and calibration of a pressure-difference bedload sampler. Open-File Report 73-108. In. United States Department of the Interior Geological Survey, Water Resources Division.
Heritage, G. L., Moon, B., Broadhurst, L., & James, C. (2004). The frictional resistance characteristics of a bedrock-influenced river channel. *Earth Surface Processes and Landforms, 29* (5), 611-627.
Heritage, G. L., & Milan, D. J. (2009). Terrestrial laser scanning of grain roughness in a gravel-bed river. *Geomorphology, 113* (1), 4-11.
Herschy, R. W. (1993). The velocity-area method. *Flow measurement and instrumentation, 4* (1), 7-10.
Herschy, R. W. (1998). *Hydrometry: principles and practice*. John Wiley & Sons Ltd.
Hey, R. D. (1979). Flow resistance in gravel-bed rivers. *Journal of the Hydraulics Division, 105* (4), 365-379.
Hey, R. D. (1988). Bar form resistance in gravel-bed rivers. *Journal of hydraulic engineering, 114* (12), 1498-1508.
Hicks, D. M., & Mason, P. D. (1991). *Roughness characteristics of New Zealand Rivers: A handbook for assigning hydraulic roughness coefficients to river reaches by the" visual comparison" approach*. Water Resources Survey.
Hirsch, R. M. (1979). An evaluation of some record reconstruction techniques. *Water Resources Research, 15* (6), 1781-1790.
Hodge, R. A., Brasington, J., & Richards, K. (2009a). In situ characterization of grain-scale fluvial morphology using Terrestrial Laser Scanning. *Earth Surface Processes and Landforms, 34* (7), 954-968.
Hodge, R. A., Brasington, J., & Richards, K. (2009b). Analysing laser-scanned digital terrain models of gravel bed surfaces: linking morphology to sediment transport processes and hydraulics. *Sedimentology, 56* (7), 2024-2043.
Hodge, R. A., Hoey, T. B., & Sklar, L. S. (2011). Bed load transport in bedrock rivers: The role of sediment cover in grain entrainment, translation, and deposition. *J. Geophys. Res., 116* (F4), F04028, doi:10.1029/2011jf002032.
Holden, J. (2000). *Runoff production in blanket peat covered catchments.* PhD Thesis, Durham University, available at Durham E-Theses Online: http://etheses.dur.ac.uk/4264/.
Holden, J., & Adamson, J. (2002). The Moor House long-term upland temperature record: New evidence of recent warming. *Weather, 57* (4), 119-127.
Holden, J., & Burt, T. P. (2003). Runoff production in blanket peat covered catchments. *Water Resources Research, 39* (7 (art. no. 1191)), 6-1.
Hongve, D. (1987). A revised procedure for discharge measurement by means of the salt dilution method. *Hydrological processes, 1* (3), 267-270, doi:10.1002/hyp.3360010305.
Howard, A. D. (1980). Thresholds in river regimes. *Thresholds in geomorphology*, 227-258.
Howard, A. D., & Kerby, G. (1983). Channel changes in badlands. *Geological Society of America Bulletin, 94* (6), 739-752.

Howard, A. D. (1994). A detachment-limited model of drainage basin evolution. *Water Resour. Res., 30* (7), 2261-2285, doi:10.1029/94wr00757.

Howard, A. D., Dietrich, W. E., & Seidl, M. A. (1994). Modeling fluvial erosion on regional to continental scales. *Journal of Geophysical Research: Solid Earth, 99* (B7), 13971-13986.

Howard, A. D. (1998). Long profile development of bedrock channels: Interaction of weathering, mass wasting, bed erosion, and sediment transport. In *Rivers Over Rock: Fluvial Processes in Bedrock Channels* (Vol. 107, pp. 297-319). AGU, Washington, DC.

Hudson, R., & Fraser, J. (2002). *Alternative methods of flow rating in small coastal streams*. British Columbia Forest Service, Vancouver Forest Region.

Hudson, R., & Fraser, J. (2005). The mass balance (or dry injection) method. *Streamline Watershed Management Bulletin, 9*, 6-12.

Inoue, T., Izumi, N., Shimizu, Y., & Parker, G. (2014). Interaction among alluvial cover, bed roughness, and incision rate in purely bedrock and alluvial-bedrock channel. *Journal of Geophysical Research: Earth Surface, 119* (10), 2123-2146, doi:10.1002/2014JF003133.

Jarrett, R. D. (1984). Hydraulics of high-gradient streams. *Journal of hydraulic engineering, 110* (11), 1519-1539.

Johnson, G. A. L. (1963). *The geology of Moor House: a national nature reserve in north-east Westmorland*. HM Stationery Office.

Johnson, J. P. L., & Whipple, K. X. (2007). Feedbacks between erosion and sediment transport in experimental bedrock channels. *Earth Surface Processes and Landforms, 32* (7), 1048-1062, doi:10.1002/esp.1471.

Johnson, J. P. L., Whipple, K. X., Sklar, L. S., & Hanks, T. C. (2009). Transport slopes, sediment cover, and bedrock channel incision in the Henry Mountains, Utah. *J. Geophys. Res., 114* (F2), F02014, doi:10.1029/2007jf000862.

Johnson, J. P. L., & Whipple, K. X. (2010). Evaluating the controls of shear stress, sediment supply, alluvial cover, and channel morphology on experimental bedrock incision rate. *J. Geophys. Res., 115* (F2), F02018, doi:10.1029/2009jf001335.

Johnson, J. P. L. (2014). A surface roughness model for predicting alluvial cover and bedload transport rate in bedrock channels. *Journal of Geophysical Research: Earth Surface*, 2013JF003000, doi:10.1002/2013JF003000.

Judd, H. E., & Peterson, D. F. (1969). Hydraulics of large bed element channels. In *Reports. Paper 285.* http://digitalcommons.usu.edu/water_rep/285. Utah State University.

Katul, G., Wiberg, P., Albertson, J., & Hornberger, G. (2002). A mixing layer theory for flow resistance in shallow streams. *Water Resources Research, 38* (11).

Keller, E. A., & Melhorn, W. N. (1978). Rhythmic spacing and origin of pools and riffles. *Geological Society of America Bulletin, 89* (5), 723-730, doi:10.1130/0016-7606(1978)89<723:rsaoop>2.0.co;2.

Kellerhals, R., Neill, C. R., & Bray, D. I. (1972). *Hydraulic and geomorphic characteristics of rivers in Alberta*. Alberta Cooperative Research Program in Highway and River Engineering.

Keulegan, G. H. (1938). *Laws of turbulent flow in open channels* (Vol. 21). National Bureau of Standards US.

Kidson, R., Richards, K., & Carling, P. (2006). Hydraulic model calibration for extreme floods in bedrock-confined channels: case study from northern Thailand. *Hydrological processes, 20* (2), 329-344.

Kirchner, J. W., Dietrich, W. E., Iseya, F., & Ikeda, H. (1990). The variability of critical shear stress, friction angle, and grain protrusion in water-worked sediments. *Sedimentology, 37* (4), 647-672, doi:10.1111/j.1365-3091.1990.tb00627.x.

Kite, G. (1994). Measuring glacier outflows using a computerized conductivity system. *Journal of Glaciology, 40* (134), 93-96.

Knighton, A. D. (1975). Variations in at-a-station hydraulic geometry. *American Journal of Science, 275* (2), 186-218.

Knighton, A. D. (1979). Comments on log-quadratic relations in hydraulic geometry. *Earth Surface Processes, 4* (3), 205-209.

Knighton, D. (1998). *Fluvial forms and processes: a new perspective (Ed. 2)*. Arnold, Hodder Headline, PLC

Komar, P. D., & Li, Z. (1986). Pivoting analyses of the selective entrainment of sediments by shape and size with application to gravel threshold. *Sedimentology, 33* (3), 425-436.

Korup, O., McSaveney, M. J., & Davies, T. R. H. (2004). Sediment generation and delivery from large historic landslides in the Southern Alps, New Zealand. *Geomorphology, 61* (1–2), 189-207, doi:10.1016/j.geomorph.2004.01.001.

Krein, A., Klinck, H., Eiden, M., Symader, W., Bierl, R., Hoffmann, L., & Pfister, L. (2008). Investigating the transport dynamics and the properties of bedload material with a hydro-acoustic measuring system. *Earth Surface Processes and Landforms, 33* (1), 152.

Lague, D., Hovius, N., & Davy, P. (2005). Discharge, discharge variability, and the bedrock channel profile. *Journal of Geophysical Research: Earth Surface, 110* (F4).

Lague, D. (2010). Reduction of long-term bedrock incision efficiency by short-term alluvial cover intermittency. *J. Geophys. Res., 115*, F02011, doi:10.1029/2008jf001210.

Lajeunesse, E., Malverti, L., & Charru, F. (2010). Bed load transport in turbulent flow at the grain scale: Experiments and modeling. *Journal of Geophysical Research: Earth Surface, 115* (F4).

Lamarre, H., MacVicar, B., & Roy, A. G. (2005). Using Passive Integrated Transponder (PIT) Tags to Investigate Sediment Transport in Gravel-Bed Rivers. *Journal of Sedimentary Research, 75* (4), 736-741, doi:10.2110/jsr.2005.059.

Lamarre, H., & Roy, A. G. (2008a). The role of morphology on the displacement of particles in a step–pool river system. *Geomorphology, 99* (1), 270-279.

Lamarre, H., & Roy, A. G. (2008b). A field experiment on the development of sedimentary structures in a gravel-bed river. *Earth Surface Processes and Landforms, 33* (7), 1064-1081.

Lamb, M. P., Dietrich, W. E., & Sklar, L. S. (2008a). A model for fluvial bedrock incision by impacting suspended and bed load sediment. *Journal of Geophysical Research: Earth Surface, 113* (F3).

Lamb, M. P., Dietrich, W. E., & Venditti, J. G. (2008b). Is the critical Shields stress for incipient sediment motion dependent on channel-bed slope? *Journal of Geophysical Research: Earth Surface, 113* (F2), F02008, doi:10.1029/2007JF000831.

Lane, S. (1995). The dynamics of dynamic river channels. *Geography, 80* (2), 147-162.

Lane, S. N., Tayefi, V., Reid, S. C., Yu, D., & Hardy, R. J. (2007). Interactions between sediment delivery, channel change, climate change and flood risk in a temperate upland environment. *Earth Surface Processes and Landforms, 32* (3), 429-446, doi:10.1002/esp.1404.

Laronne, J., & Carson, M. (1976). Interrelationships between bed morphology and bed-material transport for a small, gravel-bed channel. *Sedimentology, 23* (1), 67-85.

Lawler, D. M., Petts, G. E., Foster, I. D., & Harper, S. (2006). Turbidity dynamics during spring storm events in an urban headwater river system: The Upper Tame, West Midlands, UK. *Science of the Total Environment, 360* (1), 109-126.

Lawless, M., & Robert, A. (2001). Scales of boundary resistance in coarse-grained channels: turbulent velocity profiles and implications. *Geomorphology, 39* (3–4), 221-238, http://dx.doi.org/10.1016/S0169-555X(01)00029-0.

Lee, A. J., & Ferguson, R. I. (2002). Velocity and flow resistance in step-pool streams. *Geomorphology, 46* (1), 59-71.

Leica. (2008). Leica RX1200 User Manual, Version 7, English. *Retrieved from, http://www.surveyequipment.com/PDFs/RX1200_User_en.pdf*.

Lenzi, M. A., Marchi, L., & Scussel, G. R. (1990). Measurement of coarse sediment transport in a small alpine stream. In *International Conference on Water Resources in Mountainous Regions, Lausanne, Switzerland* (Vol. 27, pp. 283-290).

Lenzi, M. A., & Marchi, L. (2000). Suspended sediment load during floods in a small stream of the Dolomites (northeastern Italy). *Catena, 39* (4), 267-282.

Leopold, L. B., & Maddock, T. (1953). The hydraulic geometry of stream channels and some physiographic implications. In. U.S. Geological Survey Professional Paper 252 (pp. 56).

Leopold, L. B. (1970). An improved method for size distribution of stream bed gravel. *Water Resources Research, 6* (5), 1357-1366.

Lewkowicz, A. G., & Wolfe, P. M. (1994). Sediment transport in Hot Weather Creek, Ellesmere Island, NWT, Canada, 1990-1991. *Arctic and Alpine Research*, 213-226.

Lopes, V., Osterkamp, W., & Espinosa, M. (2001). Evaluation of selected bedload equations under transport-and supply-limited conditions. In *Proceedings of the Seventh Federal Interagency Sedimentation Conference* (pp. 25-29).

Manley, G. (1936). The climate of the northern Pennines: the coldest part of England. *Quarterly Journal of the Royal Meteorological Society, 62* (263), 103-115.

Mao, L., Uyttendaele, G. P., Iroumé, A., & Lenzi, M. A. (2008). Field based analysis of sediment entrainment in two high gradient streams located in Alpine and Andine environments. *Geomorphology, 93* (3), 368-383.

Marcus, W. A., Roberts, K., Harvey, L., & Tackman, G. (1992). An evaluation of methods for estimating Manning's n in small mountain streams. *Mountain Research and Development*, 227-239.

Marr, J., Hilldale, R. C., & Randle, T. (2011). *Laboratory Research and Development of Bedload Impact-plate Sensors*. US Department of the Interior, Bureau of Reclamation.

Meshkova, L. V., Carling, P. A., & Buffin-Bélanger, T. (2012). Nomenclature, Complexity, Semi-Alluvial Channels and Sediment-Flux-Driven Bedrock Erosion. In *Gravel-Bed Rivers* (pp. 424-431). John Wiley & Sons, Ltd.

Meyer-Peter, E., & Müller, R. (1948). Formulas for bed-load transport. In *Proceedings, Second Congress, International Association for Hydraulic Structures Research, Stockholm* (pp. 39-64).

Millar, R. G. (1999). Grain and form resistance in gravel-bed rivers Résistances de grain et de forme dans les rivières à graviers. *Journal of Hydraulic Research, 37* (3), 303-312.

Miller, J. R. (1991a). The influence of bedrock geology on knickpoint development and channel-bed degradation along downcutting streams in south-central Indiana. *The Journal of Geology*, 591-605.

Miller, J. R. (1991b). Controls on channel form along bedrock-influenced alluvial streams in south-central Indiana. *Physical Geography, 12* (2), 167-186.

Mizuyama, T., Laronne, J., Nonaka, M., Sawada, T., Satofuka, Y., Matsuoka, M., Yamashita, S., Sako, Y., Tamaki, S., & Watari, M. (2010). Calibration of a passive acoustic bedload monitoring system in Japanese mountain rivers. *US Geological Survey Scientific Investigations Report, 5091*, 296-318.

Moliere, D., Evans, K., Saynor, M., & Erskine, W. (2004). Estimation of suspended sediment loads in a seasonal stream in the wet-dry tropics, Northern Territory, Australia. *Hydrological processes, 18* (3), 531-544.

Montgomery, D. R., Abbe, T. B., Buffington, J. M., Peterson, N. P., Schmidt, K. M., & Stock, J. D. (1996). Distribution of bedrock and alluvial channels in forested mountain drainage basins. *Nature, 381* (6583), 587-589.

Montgomery, D. R., & Buffington, J. M. (1998). Channel processes, classification, and response. *River ecology and management, 112*, 1250-1263.

Montgomery, D. R., & Gran, K. B. (2001). Downstream variations in the width of bedrock channels. *Water Resources Research, 37* (6), 1841-1846.

Mosley, M., & Tindale, D. (1985). Sediment variability and bed material sampling in gravel-bed rivers. *Earth Surface Processes and Landforms, 10* (5), 465-482.

Mueller, E. R., Pitlick, J., & Nelson, J. M. (2005). Variation in the reference Shields stress for bed load transport in gravel-bed streams and rivers. *Water Resources Research, 41* (4).

Mulhofer, L. (1933). Untersuchungen uber die Schwebestoff und Geschiebefurungdes Inns bei Kirchbichl. *Die Wasserwirtschaft H, 2*.

Navratil, O., & Albert, M.-B. (2010). Non-linearity of reach hydraulic geometry relations. *Journal of hydrology, 388* (3), 280-290.

Neill, C. (1968). Note on initial movement of coarse uniform bed-material. *Journal of Hydraulic Research, 6* (2), 173-176.

Nelson, P. A., & Seminara, G. (2011). Modeling the evolution of bedrock channel shape with erosion from saltating bed load. *Geophysical Research Letters, 38* (17).

Nelson, P. A., & Seminara, G. (2012). A theoretical framework for the morphodynamics of bedrock channels. *Geophysical Research Letters, 39* (6).

Nikuradse, J. (1933). Stromungsgesetz in rauhren rohren, vDI Forschungshefte361 (English translation: Laws of flow in rough pipes). Tech. Rep. NACA Technical Memorandum 1292. National Advisory Commission for Aeronautics, Washington, DC, USA (1950).

Nitsche, M., Rickenmann, D., Turowski, J. M., Badoux, A., & Kirchner, J. W. (2011). Evaluation of bedload transport predictions using flow resistance equations to account for macro-roughness in steep mountain streams. *Water Resources Research, 47* (8).

Papanicolaou, A., Diplas, P., Dancey, C., & Balakrishnan, M. (2001). Surface roughness effects in near-bed turbulence: Implications to sediment entrainment. *Journal of Engineering Mechanics, 127* (3), 211-218.

Parker, C., Clifford, N. J., & Thorne, C. R. (2011). Understanding the influence of slope on the threshold of coarse grain motion: Revisiting critical stream power. *Geomorphology, 126* (1), 51-65.

Parker, G., Klingeman, P. C., & McLean, D. G. (1982). Bedload and size distribution in paved gravel-bed streams. *Journal of the Hydraulics Division, 108* (4), 544-571.

Parker, G. (1990). Surface-based bedload transport relation for gravel rivers. *Journal of Hydraulic Research, 28* (4), 417-436, doi:10.1080/00221689009499058.

Parker, G., Wilcock, P. R., Paola, C., Dietrich, W. E., & Pitlick, J. (2007). Physical basis for quasi-universal relations describing bankfull hydraulic geometry of single-thread gravel bed rivers. *Journal of Geophysical Research: Earth Surface, 112* (F4).

Petit, F., Gob, F., Houbrechts, G., & Assani, A. (2005). Critical specific stream power in gravel-bed rivers. *Geomorphology, 69* (1), 92-101.

Powell, D. M., & Ashworth, P. J. (1995). Spatial pattern of flow competence and bed load transport in a divided gravel bed river. *Water Resources Research, 31* (3), 741-752.

Powell, D. M. (2014). Flow resistance in gravel-bed rivers: Progress in research. *Earth-Science Reviews, 136*, 301-338, http://dx.doi.org/10.1016/j.earscirev.2014.06.001.

Rantz, S. E. (1982). Measurement and computation of streamflow: volume 2, computation of discharge. In U. N. Series (Ed.), *Water Supply Paper* (pp. 285-631).

Raven, E. K., Lane, S. N., Ferguson, R. I., & Bracken, L. J. (2009). The spatial and temporal patterns of aggradation in a temperate, upland, gravel-bed river. *Earth Surface Processes and Landforms, 34* (9), 1181-1197, doi:10.1002/esp.1783.

Raven, E. K., Lane, S. N., & Ferguson, R. (2010). Using sediment impact sensors to improve the morphological sediment budget approach for estimating bedload transport rates. *Geomorphology, 119* (1–2), 125-134, http://dx.doi.org/10.1016/j.geomorph.2010.03.012.

Rawes, M. (1981). Moor House 22nd annual progress report. *The Nature Conservancy, Moor House Field Station*.

Recking, A., Frey, P., Paquier, A., Belleudy, P., & Champagne, J. Y. (2008). Feedback between bed load transport and flow resistance in gravel and cobble bed rivers. *Water Resources Research, 44* (5), W05412, doi:10.1029/2007WR006219.

Reid, D. E., & Hickin, E. J. (2008). Flow resistance in steep mountain streams. *Earth Surface Processes and Landforms, 33* (14), 2211-2240.

Reid, I., Layman, J., & Frostick, L. (1980). The continuous measurement of bedload discharge. *Journal of Hydraulic Research, 18* (3), 243-249.

Reid, I., Frostick, L. E., & Layman, J. T. (1985). The incidence and nature of bedload transport during flood flows in coarse-grained alluvial channels. *Earth Surface Processes and Landforms, 10* (1), 33-44.

Reid, S. C., Lane, S. N., Berney, J. M., & Holden, J. (2007). The timing and magnitude of coarse sediment transport events within an upland, temperate gravel-bed river. *Geomorphology, 83* (1–2), 152-182, doi:10.1016/j.geomorph.2006.06.030.

Rhodes, D. D. (1977). The bfm diagram; graphical representation and interpretation of at-a-station hydraulic geometry. *American Journal of Science, 277* (1), 73-96.

Richards, K. (1973). Hydraulic geometry and channel roughness; a non-linear system. *American Journal of Science, 273* (10), 877-896.
Richards, K., & Milne, L. (1979). Problems in the calibration of an acoustic device for the observation of bedload transport. *Earth Surface Processes, 4* (4), 335-346.
Richards, K. (1982). *Rivers from and process in alluvial channels*. Methuen, London.
Richards, K., & Clifford, N. J. (2011). The nature of explanation in geomorphology. *The SAGE Handbook of Geomorphology. London: SAGE*, 36-58.
Richardson, K., Benson, I., Carling, P., Bogen, J., Fergus, T., & Walling, D. (2003). An instrument to record sediment movement in bedrock channels. In *Erosion and sediment transport measurement in rivers: technological and methodological advances: Workshop, Oslo, Norway, 19-21 June, 2002.* (pp. 228-235). IAHS Press.
Richardson, K., & Carling, P. A. (2006). The hydraulics of a straight bedrock channel: Insights from solute dispersion studies. *Geomorphology, 82* (1–2), 98-125, http://dx.doi.org/10.1016/j.geomorph.2005.09.022.
Rickenmann, D. (1991). Hyperconcentrated flow and sediment transport at steep slopes. *Journal of hydraulic engineering, 117* (11), 1419-1439.
Rickenmann, D. (1994). Bedload transport and discharge in the Erlenbach stream. In *Dynamics and Geomorphology of Mountain rivers* (pp. 53-66). Springer.
Rickenmann, D. (1997). Sediment transport in Swiss torrents. *Earth Surface Processes and Landforms, 22* (10), 937-951.
Rickenmann, D., Hofer, B., & Fritschi, B. (1997). Geschiebemessungen mittels Hydrophon (Hydrophone measurement of Bed Load Transport). *Østerrechische Wasser und Abfallwirtschaft, 49* (11-12), 219-228 (213 ref.).
Rickenmann, D. (2001). Comparison of bed load transport in torrents and gravel bed streams. *Water Resources Research, 37* (12), 3295-3305.
Rickenmann, D., & McArdell, B. W. (2007). Continuous measurement of sediment transport in the Erlenbach stream using piezoelectric bedload impact sensors. *Earth Surface Processes and Landforms, 32* (9), 1362-1378.
Rickenmann, D., & McArdell, B. (2008). Calibration of piezoelectric bedload impact sensors in the Pitzbach mountain stream. *Geodinamica Acta, 21* (1-2), 35-52.
Rickenmann, D., & Fritschi, B. (2010). Bedload transport measurements using piezoelectric impact sensors and geophones. In *Bedload-surrogate Monitoring Technologies*, , Gray JR, Laronne JB, Marr JDG (eds), US Geological Survey Scientific Investigations Report 2010–5091. US Geological Survey: Reston, VA; 407–423.
Rickenmann, D., & Recking, A. (2011). Evaluation of flow resistance in gravel-bed rivers through a large field data set. *Water Resources Research, 47* (7).
Rickenmann, D., Turowski, J. M., Fritschi, B., Klaiber, A., & Ludwig, A. (2012). Bedload transport measurements at the Erlenbach stream with geophones and automated basket samplers. *Earth Surface Processes and Landforms, 37* (9), 1000-1011.
Rickenmann, D., Turowski, J. M., Fritschi, B., Wyss, C., Laronne, J., Barzilai, R., Reid, I., Kreisler, A., Aigner, J., & Seitz, H. (2014). Bedload transport measurements with impact plate geophones: comparison of sensor calibration in different gravel-bed streams. *Earth Surface Processes and Landforms, 39* (7), 928-942.
Riegl. (2015). Data Sheet, RIEGL VZ-1000, 2015-03-24. *Retrieved from, http://www.riegl.com/uploads/tx_pxpriegldownloads/DataSheet_VZ-1000_2015-03-24.pdf*.

Robert, A. (1990). Boundary roughness in coarse-grained channels. *Progress in Physical Geography, 14* (1), 42-70, doi:10.1177/030913339001400103.
Robert, A. (1997). Characteristics of velocity profiles along riffle-pool sequences and estimates of bed shear stress. *Geomorphology, 19* (1–2), 89-98, http://dx.doi.org/10.1016/S0169-555X(96)00049-9.
Ryan, S. E., & Troendle, C. (1999). Measuring bedload with handheld samplers in coarse-grained mountain channels. *Stream Notes*, 1-4.
Ryan, S. E., Porth, L. S., & Troendle, C. (2005). Coarse sediment transport in mountain streams in Colorado and Wyoming, USA. *Earth Surface Processes and Landforms, 30* (3), 269-288.
Sargent, R. (1979). Variation of Manning's n roughness coefficient with flow in open river channels. *Journal of the Institution of Water Engineers and Scientists, 33* (3).
Schlumberger. (2014). Diver Manual, November 2014. *Retrieved from, http://www.novametrixgm.com/pdfs/equipment/Diver_manuals/Diver_Product_Manual_en.pdf*.
Schmidt, K., & Ergenzinger, P. (1992). Bedload entrainment, travel lengths, step lengths, rest periods—Studied with passive (iron, magnetic) and active (radio) tracer techniques. *Earth Surface Processes and Landforms, 17* (2), 147-165.
Schmidt, K., & Gintz, D. (1995). Results of bedload tracer experiments in a mountain river. *River geomorphology*, 37-54.
Schneider, J., Hegglin, R., Meier, S., Turowski, J., Nitsche, M., & Rickenmann, D. (2010). Studying sediment transport in mountain rivers by mobile and stationary RFID antennas. In *River flow* (Vol. 2010, pp. 1723-1730). Bundesanstalt für Wasserbau: Karlsruhe, Germany.
Schoklitsch, A. (1962). Handbuch des Wasserbaues. *Springer, Vienna* (3rd ed.).
Shaw, E. (1994). Hydrology in practice. *Hydrology in practice.* (Ed. 3).
Shields, A. (1936). Application of similarity principles and turbulence research to bedload movement.
Shvidchenko, A., & Pender, G. (2000). Initial motion of streambeds composed of coarse uniform sediments. In *Proceedings of the Institution of Civil Engineers-Water and Maritime Engineering* (Vol. 142, pp. 217-227). Thomas Telford Ltd.
Siddiqui, A., & Robert, A. (2010). Thresholds of erosion and sediment movement in bedrock channels. *Geomorphology, 118* (3–4), 301-313, doi:10.1016/j.geomorph.2010.01.011.
Sklar, L. S., & Dietrich, W. E. (1998). River longitudinal profiles and bedrock incision models: Stream power and the influence of sediment supply. *Rivers Over Rock: Fluvial Processes in Bedrock Channels*, 237-260.
Sklar, L. S., & Dietrich, W. E. (2004). A mechanistic model for river incision into bedrock by saltating bed load. *Water Resour. Res., 40* (6), W06301, doi:10.1029/2003wr002496.
Smith, H. M. (2004). *Significance of Bedrock Channel Morphology and Sediment Dynamics in a UK Upland River.* MSc Thesis, Durham University, available at Durham E-Theses Online: http://etheses.dur.ac.uk/2976/.
Sneed, E. D., & Folk, R. L. (1958). Pebbles in the lower Colorado River, Texas a study in particle morphogenesis. *The Journal of Geology*, 114-150.
Snell, J., & Sivapalan, M. (1995). Application of the meta-channel concept: Construction of the meta-channel hydraulic geometry for a natural catchment. *Hydrological processes, 9* (5-6), 485-505.

Stelczer, K. (1971). Etude stochastique du mouvement de charriage. *International Association of Scientific Hydrology. Bulletin, 16* (3), 9-18.

Strickler, A. (1923). *Contributions to the question of a velocity formula and roughness data for streams, channels and closed pipelines (Beiträge zur Frage der Geschwindigkeitsformel und der Rauhigkeitszahlen für Ströme, Kanäle und geschlossene Leitungen)*, In: Roesgan, T., Brownie, W.R. (Eds.), W. M. Keck Lab of Hydraulics and Water Resources, Calif. Inst. Tech., Pasadena, Calif. January 1981, 16. Mitteilungen des Eidgenossischen Amtes fur Wasserwirtschaft, Bern, Switzerland (Translation T-10).

Sykes, J., & Lane, A. (1996). *The United Kingdom Environmental Change Network: protocols for standard measurements at terrestrial sites*. London: The Stationery Office, Centre for Ecology & Hydrology.

Tancock, M. (2014). *The dynamics of upland river confluences.* PhD Thesis. Durham University, available at Durham E-Theses Online: http://etheses.dur.ac.uk/10527/.

Tinkler, K., & Wohl, E. (1998a). Field studies of bedrock channels. *Rivers Over Rock: Fluvial Processes in Bedrock Channels*, 261-277.

Tinkler, K., & Wohl, E. (1998b). A primer on bedrock channels. In *Rivers Over Rock: Fluvial Processes in Bedrock Channels* (Vol. 107, pp. 1-18). AGU, Washington, DC.

Tsakiris, A. G., Papanicolaou, A. N., & Lauth, T. J. (2014). Signature of bedload particle transport mode in the acoustic signal of a geophone. *Journal of Hydraulic Research, 52* (2), 185-204.

Turowski, J. M., Lague, D., & Hovius, N. (2007). Cover effect in bedrock abrasion: A new derivation and its implications for the modeling of bedrock channel morphology. *J. Geophys. Res., 112* (F4), F04006, doi:10.1029/2006jf000697.

Turowski, J. M., Hovius, N., Meng-Long, H., Lague, D., & Men-Chiang, C. (2008a). Distribution of erosion across bedrock channels. *Earth Surface Processes and Landforms, 33* (3), 353-363, doi:10.1002/esp.1559.

Turowski, J. M., Hovius, N., Wilson, A., & Horng, M.-J. (2008b). Hydraulic geometry, river sediment and the definition of bedrock channels. *Geomorphology, 99* (1–4), 26-38, doi:10.1016/j.geomorph.2007.10.001.

Turowski, J. M., & Rickenmann, D. (2009). Tools and cover effects in bedload transport observations in the Pitzbach, Austria. *Earth Surface Processes and Landforms, 34* (1), 26-37, doi:10.1002/esp.1686.

Turowski, J. M., Badoux, A., & Rickenmann, D. (2011). Start and end of bedload transport in gravel-bed streams. *Geophysical Research Letters, 38* (4).

Turowski, J. M., & Rickenmann, D. (2011). Measuring the Statistics of Bed-Load Transport Using Indirect Sensors. *Journal of hydraulic engineering, 137* (1), 116-121.

Turowski, J. M. (2012). Semi-Alluvial Channels and Sediment-Flux-Driven Bedrock Erosion. In *Gravel-Bed Rivers* (pp. 399-418). John Wiley & Sons, Ltd.

Turowski, J. M., Badoux, A., Leuzinger, J., & Hegglin, R. (2013). Large floods, alluvial overprint, and bedrock erosion. *Earth Surface Processes and Landforms, 38* (9), 947-958.

Valeport. (2011). Datasheet Reference: Model 801 version 2A, Feb 2011. *Retrieved from, http://www.valeport.co.uk/Portals/0/Docs/Datasheets/Valeport_Model801_v2a.pdf.*

Valla, P. G., Van Der Beek, P. A., & Lague, D. (2010). Fluvial incision into bedrock: Insights from morphometric analysis and numerical modeling of gorges incising glacial hanging valleys (Western Alps, France). *Journal of Geophysical Research: Earth Surface, 115* (F2).

Van Der Beek, P., & Bishop, P. (2003). Cenozoic river profile development in the Upper Lachlan catchment (SE Australia) as a test of quantitative fluvial incision models. *Journal of Geophysical Research: Solid Earth, 108* (B6).

Waldon, M. G. (2004). Estimation of average stream velocity. *Journal of hydraulic engineering, 130* (11), 1119-1122.

Warburton, J. (1990). Comparison of bed load yield estimates for a glacial meltwater stream. In *Proceedings International Conference on Water Resources in Mountainous Regions, IAHS Publication* (Vol. 193, pp. 315-322).

Warburton, J. (1992). Observations of Bed Load Transport and Channel Bed Changes in a Proglacial Mountain Stream. *Arctic and Alpine Research, 24* (3), 195-203, doi:10.2307/1551657.

Warburton, J., & Demir, T. (2000). Influence of bed material shape on sediment transport in gravel-bed rivers—a field experiment. *Tracers in Geomorphology: Chichester, UK, John Wiley & Sons*, 401-410.

Warburton, J., Holden, J., & Mills, A. J. (2004). Hydrological controls of surficial mass movements in peat. *Earth-Science Reviews, 67* (1), 139-156.

Warburton, J., & Evans, M. (2011). Geomorphic, sedimentary, and potential palaeoenvironmental significance of peat blocks in alluvial river systems. *Geomorphology, 130* (3), 101-114.

Whipple, K. X., & Tucker, G. E. (1999). Dynamics of the stream-power river incision model: Implications for height limits of mountain ranges, landscape response timescales, and research needs. *Journal of Geophysical Research: Solid Earth, 104* (B8), 17661-17674.

Whipple, K. X., & Tucker, G. E. (2002). Implications of sediment-flux-dependent river incision models for landscape evolution. *J. Geophys. Res., 107* (B2), 2039, doi:10.1029/2000jb000044.

Whipple, K. X. (2004). Bedrock rivers and geomorphology of active orogens. *Annual Review of Earth and Planetary Sciences, 32* (1), 151-185, doi:10.1146/annurev.earth.32.101802.120356.

Whittaker, J. G., & Jaeggi, M. N. (1982). Origin of step-pool systems in mountain streams. *Journal of the Hydraulics Division, 108* (6), 758-773.

Wiberg, P. L., & Smith, J. D. (1987). Calculations of the critical shear stress for motion of uniform and heterogeneous sediments. *Water Resources Research, 23* (8), 1471-1480, doi:10.1029/WR023i008p01471.

Wiberg, P. L., & Smith, J. D. (1991). Velocity distribution and bed roughness in high-gradient streams. *Water Resources Research, 27* (5), 825-838.

Wilcock, D. N. (1971). Investigation into the relations between bedload transport and channel shape. *Geological Society of America Bulletin, 82* (8), 2159-2176.

Wilcock, P. R. (1996). Estimating Local Bed Shear Stress from Velocity Observations. *Water Resour. Res., 32* (11), 3361-3366, doi:10.1029/96wr02277.

Williams, G. P. (1989). Sediment concentration versus water discharge during single hydrologic events in rivers. *Journal of hydrology, 111* (1), 89-106.

Wohl, E. (1999). Incised bedrock channels. *Incised river channels*, 187-217.

Wohl, E. (2000). *Mountain rivers* (Vol. 14). American Geophysical Union.

Wohl, E., & Merritt, D. M. (2001). Bedrock channel morphology. *Geological Society of America Bulletin, 113* (9), 1205-1212, doi:10.1130/0016-7606(2001)113<1205:bcm>2.0.co;2.

Wohl, E., & David, G. C. (2008). Consistency of scaling relations among bedrock and alluvial channels. *Journal of Geophysical Research: Earth Surface, 113* (F4).

Wohl, E. (2013). *Mountain rivers revisited* (Vol. 19). John Wiley & Sons.

Wolman, M. G. (1954). *A method of sampling coarse river-bed material* (Vol. 35, No. 6). Transactions, American Geophysical Union.

Wyss, C., Rickenmann, D., Fritschi, B., Turowski, J., Weitbrecht, V., & Boes, R. (2014). Bedload grain size estimation from the indirect monitoring of bedload transport with Swiss plate geophones at the Erlenbach stream. In *River Flow* (pp. 1907-1912).

Yager, E., Kirchner, J., & Dietrich, W. (2007). Calculating bed load transport in steep boulder bed channels. *Water Resources Research, 43* (7).

Yager, E., Dietrich, W., Kirchner, J., & McArdell, B. (2012). Prediction of sediment transport in step-pool channels. *Water Resources Research, 48* (1).

Yanites, B. J., Tucker, G. E., Hsu, H.-L., Chen, C.-c., Chen, Y.-G., & Mueller, K. J. (2011). The influence of sediment cover variability on long-term river incision rates: An example from the Peikang River, central Taiwan. *J. Geophys. Res., 116* (F3), F03016, doi:10.1029/2010jf001933.

Zhang, L., Parker, G., Stark, C., Inoue, T., Viparelli, E., Fu, X., & Izumi, N. (2015). Macro-roughness model of bedrock-alluvial river morphodynamics. *Earth Surface Dynamics, 3* (1), 113-138, doi:10.5194/esurf-3-113-2015.

Zingg, T. (1935). *Beitrag zur schotteranalyse.* Diss. Naturwiss. ETH Zürich, Nr. 849, 1935 Ref.: Niggli, P.; Korref.: Burri, C. http://dx.doi.org/10.3929/ethz-a-000103455.